Transactions of the ASME, Journal of Heat Transfer (ISSN 0022-1481) is published monthly by The American Society of Mechanical Engineers, Three Park Avenue, New York, NY 10016. Periodicals postage paid at New York, NY and additional mailing offices. POSTMASTER: Send address changes to Transactions of the ASME, Journal of Heat Transfer, c/o THE AMERICAN SOCIETY OF MECHANICAL ENGINEERS, 22 Law Drive, Box 2300, Fairfield, NJ 07007-2300. **CHANGES OF ADDRESS** must be received at Society headquarters seven weeks before they are to be effective. Please send old label and new address.

Journal of Heat Transfer

Published Monthly by ASME

VOLUME 131 • NUMBER 6 • JUNE 2009

RESEARCH PAPERS

(**Contents continued on inside back cover**)

This journal is printed on acid-free paper, which exceeds the ANSI Z39.48-1992 specification for permanence of paper and library materials. ♾™
♻ 85% recycled content, including 10% post-consumer fibers.

Journal of Heat Transfer **Volume 131, Number 6** **JUNE 2009**

The ASME Journal of Heat Transfer is abstracted and indexed in the following:

Applied Science and Technology Index, Chemical Abstracts, Chemical Engineering and Biotechnology Abstracts (Electronic equivalent of Process and Chemical Engineering), Civil Engineering Abstracts, Compendex (The electronic equivalent of Engineering Index), Corrosion Abstracts, Current Contents, E & P Health, Safety, and Environment, Ei EncompassLit, Engineered Materials Abstracts, Engineering Index, Enviroline (The electronic equivalent of Environment Abstracts), Environment Abstracts, Environmental Engineering Abstracts, Environmental Science and Pollution Management, Fluidex, Fuel and Energy Abstracts, Index to Scientific Reviews, INSPEC, International Building Services Abstracts, Mechanical & Transportation Engineering Abstracts, Mechanical Engineering Abstracts, METADEX (The electronic equivalent of Metals Abstracts and Alloys Index), Petroleum Abstracts, Process and Chemical Engineering, Referativnyi Zhurnal, Science Citation Index, SciSearch (The electronic equivalent of Science Citation Index), Theoretical Chemical Engineering

Solid-State Thermal Rectification With Existing Bulk Materials

C. Dames
Department of Mechanical Engineering and Materials Science and Engineering Program, University of California, Riverside, A311 Bourns Hall, Riverside, CA 92521

A two-terminal thermal device exhibits thermal rectification if it transports heat more easily in one direction than in the reverse direction. Within the framework of classical heat conduction by Fourier's law, thermal rectification occurs in a two-segment bar if the thermal conductivities of the segments have different dependencies on temperature. The general solution to this problem is a pair of coupled integral equations, which in previous work had to be solved numerically. In this work the temperature dependencies of the thermal conductivities are approximated using power laws, and perturbation analysis at low thermal bias leads to a simple algebraic expression, which shows that the rectification is proportional to the difference in the power-law exponents of the two materials, multiplied by a geometric correction function. The resulting predictions have no free parameters and are in good agreement with the experimental results from the literature. For maximum rectification, the thermal resistances of the two segments should be matched to each other at low thermal bias. For end point temperatures of 300 K and 100 K, using common bulk materials it is practical to design a rectifier with rectification of well over one hundred percent. A new quantity, the normalized thermal rectification, is proposed to better facilitate comparisons of various rectification mechanisms across different temperature ranges. [DOI: 10.1115/1.3089552]

Keywords: thermal diode, thermal rectification, perturbation theory

1 Introduction

A thermal rectifier is the heat-transfer analog to the familiar electrical diode. Consider a two-terminal thermal device whose left-hand end is connected to a hot reservoir at temperature T_H and whose right-hand end is connected to a cold reservoir at T_C, and define the magnitude of this heat flow as Q_{LR}. After exchanging the temperatures of the two reservoirs, the heat flow reverses direction and assumes a new magnitude Q_{RL}. If $Q_{LR} \neq Q_{RL}$, the device exhibits thermal rectification.

Thermal rectification is of broad interest because of its potential to open up new ground for the control of heat transport, inspiring analogies to the tremendous boom in the microelectronics industry following the invention of such nonlinear elements as the transistor and the diode. Possible applications of thermal rectification include thermal barrier coatings that resist heat uptake while releasing heat easily, nanostructured thermoelectrics [1], or powering a heat engine by using a thermal-bridge rectifier to exploit the daily temperature oscillations near the earth's surface.

Thermal rectification requires an asymmetry and a nonlinearity. In fluidic systems thermal rectification is well-known in the form of natural convection, where the gravitational field couples with buoyancy to cause asymmetric heat transport, for example, between the upper and lower surfaces of an enclosure. Focusing on solid-state systems, at least five different rectification mechanisms have been suggested. One mechanism is the effect of thermal expansion on the pressure between two rough materials in contact, which changes the thermal boundary resistance, leading to thermal rectification if the two materials have different thermal expansion coefficients [2–4]. A second mechanism is based on detailed atomistic calculations of the thermal transport in one-dimensional atomic chains with idealized anharmonic interatomic potentials [5–11]. A third mechanism is based on models of the scattering of ballistic phonons or other energy carriers by asymmetric nanostructures [1,12,13]. Fourth, thermal rectification was recently measured in individual nanotubes with asymmetric mass loading [14], an effect which was attributed to solitons. The final mechanism, and focus of this paper, uses the framework of classical heat conduction by Fourier's law in a two-segment bar with segments that have thermal conductivities with different temperature dependencies.

The classical Fourier law rectification mechanism was first observed experimentally in the 1970s [15–17]. Although these papers correctly identified the basic rectification mechanism to be the different temperature-dependent thermal conductivities of the two segments, quantitative theory was not presented [18]. The authors of Ref. [17] subsequently described a simplified theory, which assumed that thermal conductivity could be represented as the sum of spatially-dependent and temperature-dependent terms [19]; Hudson [20] gave an argument based on nonplanar isotherms; and Kokshenev et al. [21] attempted to relate the rectification to the acoustic mismatch at the interface, but none of these approaches are appropriate for the experiments considered [15–17] or the system studied in the present work. The proper classical theory was given by Hoff [22], who expanded the heat flow as a power series in the temperature difference. However, the resulting nonlinear equations had to be solved numerically, and the comparison to experiments was only qualitative [23]. More recently Hu et al. [10] and Peyrard [9] also modeled rectification due to the temperature-dependent thermal conductivity of two-segment bars. However, these calculations were not compared with experiments, because they focused on mathematically-idealized material properties (thermal conductivity functions and/or interatomic Hamiltonians), which are difficult to relate to real engineering materials.

This paper advances the previous situation by deriving a simple linearized theory, which yields a single algebraic equation for the rectification. This equation is immediately applicable to a broad range of practical materials and includes a criterion for geometric optimization. Furthermore, the theory has no free parameters and agrees well with the available experimental data for both metal-metal [15] and dielectric-dielectric systems [16], comparisons that were not made in the previous detailed theoretical papers.

Contributed by the Heat Transfer Division of ASME for publication in the JOURNAL OF HEAT TRANSFER. Manuscript received March 30, 2008; final manuscript received September 30, 2008; published online March 31, 2009. Review conducted by Pamela M. Norris.

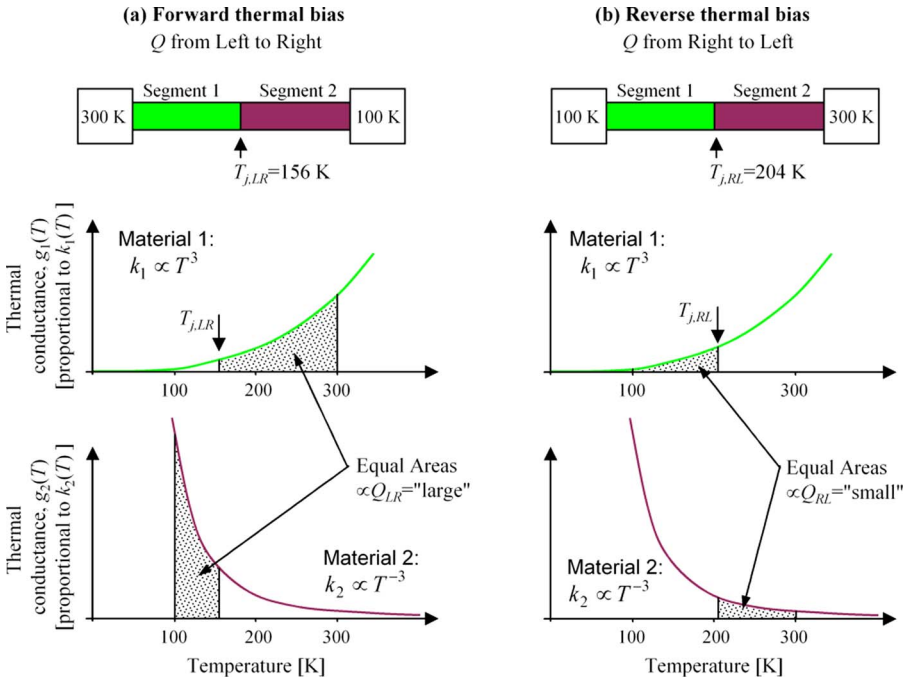

Fig. 1 Basic concept of thermal rectification due to temperature-dependent thermal conductivity $k(T)$. A two-segment bar is made of materials with different trends in their $k(T)$, for example, $k_1 \propto T^3$ and $k_2 \propto T^{-3}$. (*a*) For heat flow from left to right, segment 1 is relatively hot while segment 2 is relatively cold, causing both segments to have relatively high k. (*b*) These trends are reversed for heat flow from right to left, causing both segments to have relatively low k. Thus this structure exhibits thermal rectification. The graphical interpretation is that T_j must be chosen so that the appropriate areas under each $g(T)$ curve are equal.

2 Derivation of Governing Equations

2.1 Qualitative Picture. The basic idea of classical thermal rectification due to temperature-dependent thermal conductivity $k(T)$ is shown in Fig. 1. A two-segment bar is made of materials with opposite trends in their $k(T)$. For heat flow from left to right, segment 1 is relatively hot and segment 2 is relatively cold. Because k increases with T for segment 1 but decreases with T for segment 2, both segments are in a regime of relatively high thermal conductivity. Thus the thermal resistance in this "forward thermal bias" condition is relatively low. When the heat flow direction is reversed, segment 1 becomes relatively cold while segment 2 is relatively warm. In this case both segments have relatively low thermal conductivity, and now the thermal resistance in "reverse thermal bias" is relatively high. Thus, this structure exhibits thermal rectification. From the sketches in Fig. 1, it is clear that the rectification arises from the opposite trends in $k(T)$ of the two materials. As shown in Fig. 2, it is apparent that for any given temperature real materials can be identified with vastly different $k(T)$ behaviors, so this effect is accessible over a broad range of temperatures.

2.2 General Analysis. The thermal rectification γ can be defined as [17]

$$\gamma(T_H, T_C) = (Q_{LR} - Q_{RL})/Q_{RL} \tag{1}$$

where this expression assumes that $Q_{LR} > Q_{RL}$ (if not, swap Q_{LR} and Q_{RL} in Eq. (1)). Thus our task is to evaluate Q_{LR} and Q_{RL} for a given T_H and T_C. We focus on a two-segment bar ($i=1,2$), assuming perfect thermal contacts at the junction between segments and to the thermal reservoirs at both ends. Convection and radiation are neglected. The left and right ends of the bar are at temperatures T_L and T_R, respectively, and the junction between the segments is at T_j. This junction temperature may be different for heat flow from left to right ($T_{j,LR}$) and from right to left ($T_{j,RL}$). Each bar has cross-sectional area A_i and length L_i in the x direction. From Fourier's law, the heat flow Q is given by

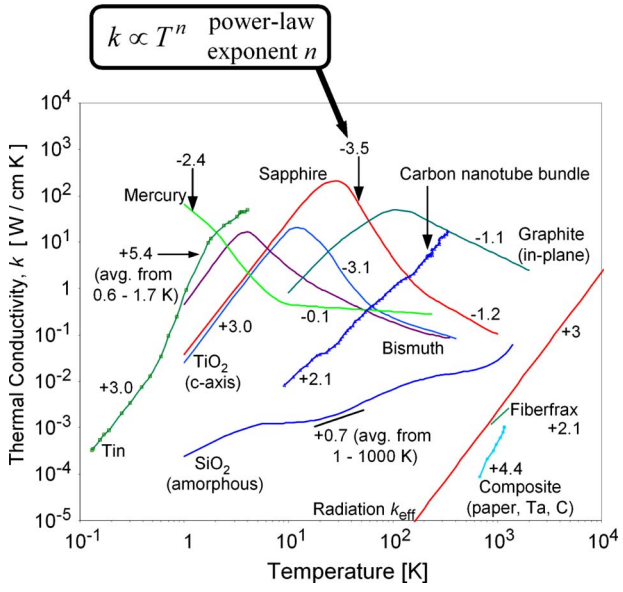

Fig. 2 Temperature-dependent thermal conductivity of selected materials, showing that the power-law exponents n commonly range from −3 to +3, with extreme values from −3.5 to +5.4 noted here. The data are from Refs. [28–31].

$$Q_i = -k_i(T)A_i\frac{dT}{dx} \tag{2}$$

For convenience, define

$$g_i(T) = A_i k_i(T)/L_i \tag{3}$$

which is the thermal conductance in the limit of constant temperature. Combining Eqs. (2) and (3), separating variables, and integrating for each of the two segments, we have

$$Q = \int_{T_j}^{T_L} g_1(T)dT \tag{4}$$

$$Q = \int_{T_R}^{T_j} g_2(T)dT \tag{5}$$

or simply

$$\int_{T_j}^{T_L} g_1(T)dT = \int_{T_R}^{T_j} g_2(T)dT \tag{6}$$

For a particular choice of T_L and T_R, and known materials and geometry, this integral equation defines the unknown junction temperature T_j. After finding T_j, the heat flow is then found using Eq. (4) or Eq. (5). The graphical interpretation is indicated in Fig. 1. The value of T_j is chosen such that the area between T_j and T_L for the curve $g_1(T)$ exactly balances the area between T_R and T_j for the curve $g_2(T)$. If the left-side and right-side temperatures are swapped, the value of T_j may or may not change, but due to the opposing $k(T)$ trends the areas to be balanced do change, and thus so does the magnitude of Q, leading to rectification.

2.3 Simplifications for Materials With Power-Law Thermal Conductivity. To proceed further analytically we now focus on materials whose temperature-dependent thermal conductivity can be approximated by a power law over a limited range of temperatures:

$$k_i(T) = k_{0,i}(T/T_{\text{ref}})^{n_i} \tag{7}$$

where T_{ref} is a reference temperature and n_i is the power-law exponent. This approximation was not considered in the previous related modeling work [9,10,21–23]. Without loss of generality, for convenience we set T_{ref} equal to the average temperature T_0. That is, $T_{\text{ref}}=T_0=(T_H+T_C)/2$. The power-law approximation of Eq. (7) is relevant to most practical engineering materials. As shown in Fig. 2, common values of n_i range from about +3 to −3, depending on the temperature range and the dominant mechanisms of heat conduction.

Defining the dimensionless temperature as

$$\theta = T/T_0 \tag{8}$$

the functions g take the form

$$g_i(T) = A_i k_{0,i}\theta^{n_i}/L_i \tag{9}$$

For convenience define

$$m_i = n_i + 1 \tag{10}$$

and

$$R_{0,i} = L_i/k_{0,i}A_i = 1/g_i(T_0) \tag{11}$$

where $R_{0,i}$ is the thermal resistance of leg i at uniform temperature T_0. Define the resistance ratio

$$\rho = R_{0,2}/R_{0,1} \tag{12}$$

and dimensionless heat flux

$$q = Q(R_{0,1} + R_{0,2})/T_0 \tag{13}$$

Finally, substituting these simplifications back into Eqs. (4) and (5) gives

$$q = (\theta_L^{m_1} - \theta_j^{m_1})(1+\rho)/m_1 \tag{14}$$

$$q = (\theta_j^{m_2} - \theta_R^{m_2})(1+\rho^{-1})/m_2 \tag{15}$$

These two equations in the two unknowns q, θ_j are analogous to Eqs. (4) and (5) and determine the thermal rectification in a device where the temperature dependence of the thermal conductivity each leg follows a power law.

2.4 Low-Bias Limit: Perturbative Solution. Although we are unaware of a general solution to Eqs. (14) and (15), a convenient closed-form solution is possible in the common limit of small rectification. We first note that the zeroth order solution (k independent of T) is readily found from the elementary application of Fourier's law and can be expressed in our dimensionless notation as

$$q_0 = \Delta \tag{16}$$

$$\theta_{j0} = 1 + \frac{\Delta}{2}\left(\frac{\rho-1}{\rho+1}\right) \tag{17}$$

where we have defined the dimensionless temperature difference $\Delta=(T_L-T_R)/T_0$, which further implies

$$\theta_L = 1 + \Delta/2 \tag{18}$$

$$\theta_R = 1 - \Delta/2 \tag{19}$$

In the perturbative limit, θ_j deviates only slightly from θ_{j0}, which we quantify by defining $d=\theta_j-\theta_{j0}$. Thus

$$\theta_j = 1 + d + \frac{\Delta}{2}\left(\frac{\rho-1}{\rho+1}\right) \tag{20}$$

The key simplification in the low-bias limit is that θ_L, θ_R, and θ_j are all close to unity, so we replace them by their second-order expansions, for example, $\theta_L^m \approx 1+\frac{1}{2}m\Delta+\frac{1}{8}m(m-1)\Delta^2$. The resulting algebraic equations contain numerous terms but are conveniently solved with the help of a symbolic math software [24], finally yielding the following compact result:

$$q = \Delta + \frac{(n_1-n_2)}{2(\rho^{1/2}+\rho^{-1/2})^2}\Delta^2 \tag{21}$$

From the definition of rectification in Eq. (1),

$$\gamma = \frac{q(\Delta)+q(-\Delta)}{-q(-\Delta)} \tag{22}$$

which assumes that the segments are labeled such that $n_1>n_2$. Substituting Eq. (21) into Eq. (22) gives

$$\gamma = \left[\frac{(n_1-n_2)\Delta}{(\rho^{1/2}+\rho^{-1/2})^2}\right]\Big/\left[1-\frac{(n_1-n_2)\Delta}{2(\rho^{1/2}+\rho^{-1/2})^2}\right] \tag{23}$$

Finally, retaining only the leading power in Δ gives

$$\gamma = \frac{(n_1-n_2)}{(\rho^{1/2}+\rho^{-1/2})^2}\Delta \tag{24}$$

This is the most useful analytical result of the paper. It shows that the rectification in this low-bias limit is linearly proportional to (a) the dimensionless thermal bias $(T_H-T_C)/T_0$, (b) the difference in power-law exponents n_1-n_2, and (c) a simple function of the thermal resistance ratio ρ. We emphasize that point (a) was previously identified by Hoff [22,23], while points (b) and (c) are new results. Compared with the exact solutions of Eqs. (14) and (15) presented below, Eq. (24) is conservative in that it always underpredicts the true rectification and is a good approximation (that is, $|\gamma_{\text{approx}}-\gamma_{\text{exact}}|/\gamma_{\text{exact}}<0.1$) for rectification of up to 20%.

The most important feature of Eq. (24) is that maximum rectification is achieved by maximizing the difference in power-law exponents between the two materials, consistent with the qualitative sketch of Fig. 1. Although previous discussions of this effect

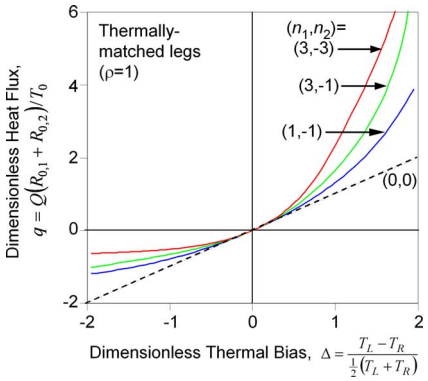

Fig. 3 Heat flux as a function of thermal bias for materials with several different combinations of power-law exponents (n_1,n_2). This plot is closely analogous to the "*I-V* curve" of a conventional electrical diode.

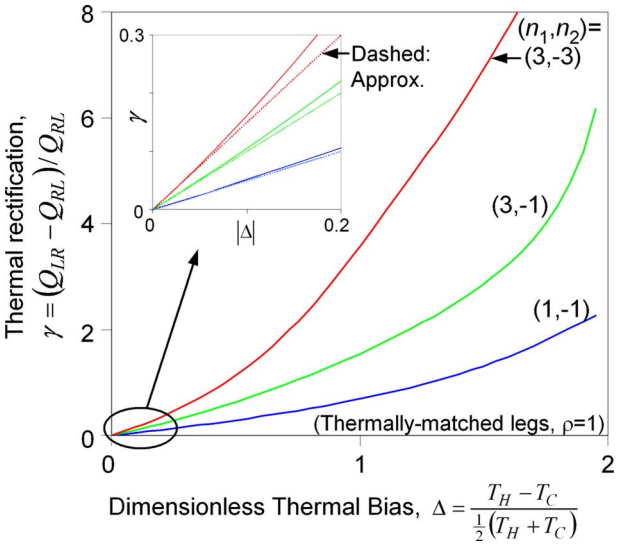

Fig. 4 Thermal rectification γ as a function of thermal bias for materials with several different combinations of power-law exponents (n_1,n_2). Inset: detail at low bias, including the linearized approximation from Eq. (24) (dashed lines).

have focused on suggestions that the two materials should have opposite temperature derivatives [21–23], by considering materials with power-law thermal conductivities here we see that in this low-bias limit it is only the *difference* in exponents that matters. For example, a thermally balanced ($\rho=1$) system with $(n_1,n_2)=(3,1)$ will exhibit exactly the same rectification as a balanced system with $(n_1,n_2)=(1,-1)$.

Equation (24) also suggests that theoretical and experimental reports about thermal diodes should be specified not only by their rectification γ but also by their dimensionless temperature difference $\Delta=(T_H\text{-}T_C)/T_0$, because it is easy to get large rectification simply by increasing the dimensionless thermal bias. In fact, we expect that γ should be linear in Δ to leading order for almost any type of rectification mechanism, because this follows directly from the expansion of q into the first and second powers of Δ, as in Eqs. (21) and (22). Indeed, we have also observed $\gamma \propto \Delta$ at low bias in a study of thermal rectification by ballistic-elastic phonons in asymmetric nanostructures, an entirely unrelated mechanism [13]. Considering the universality of $\gamma \propto \Delta$, we therefore suggest that it may be more meaningful to speak in terms of a "normalized thermal rectification" $\hat{\gamma}$ as follows:

$$\hat{\gamma} \equiv \gamma/\Delta = \frac{\gamma(T_H+T_C)}{2(T_H-T_C)} \tag{25}$$

because, to leading order, this quantity is independent of T_H and T_C. In particular, in the low-bias limit for these classical thermal diodes.

$$\hat{\gamma} = \frac{(n_1-n_2)}{(\rho^{1/2}+\rho^{-1/2})^2} \tag{26}$$

This form is appealing because $\hat{\gamma}$ is now independent of both the average temperature and the thermal bias (assuming that n_1 and n_2 can be treated as constants). With some attention to thermal matching ($\rho \approx 1$), we note that it is practical to achieve $\hat{\gamma}$ larger than 1 with common bulk materials. (Refer to Fig. 2, which shows that material pairs with $(n_1\text{-}n_2)$ greater than 4 are available over a wide temperature range.)

3 Results and Discussion

3.1 Rectification Curves. We have solved Eqs. (14) and (15) numerically for several values of n_1, n_2, and ρ. We focus on $(n_1,n_2)=(1,-1)$, (3, −1), and (3, −3). For thermally-matched legs ($\rho=1$), Fig. 3 shows the calculated heat current as a function of thermal bias (analogous to the familiar plot of electrical current versus voltage for an electrical diode). In this figure recall that a value of $\Delta=1$ corresponds to end point temperatures (T_L,T_R) of $\left(\frac{3}{2}T_0,\frac{1}{2}T_0\right)$, while $\Delta=-1$ corresponds to $\left(\frac{1}{2}T_0,\frac{3}{2}T_0\right)$. Thus this bias of $\Delta=\pm 1$ can be applied to the common laboratory situation of thermal transport between 300 K (room temperature) and 100 K (slightly above liquid nitrogen temperature), in which case $T_0=200$ K. Thermal rectification is clearly present in Fig. 3. Of the three scenarios considered, rectification is strongest for $(n_1,n_2)=(3,-3)$, followed by (3, −1), and then (1, −1). The thermal rectification is quantified in Fig. 4. At the dimensionless bias of $\Delta=1$, the thermal rectification for the three scenarios is 357%, 154%, and 69%, respectively. As a specific example, for a system operating between 100 K and 300 K with $(n_1,n_2)=(3,-3)$, the dimensionless heat transfer in the forward direction is $q_{LR}=2.348$. If the temperatures are reversed to 300 K and 100 K, the new heat transfer is only $q_{RL}=0.514$. Thus the rectification in this example is 357%.

3.2 Effect of Thermal Matching. Figure 5 shows the effect of ρ on rectification for the three different choices of (n_1,n_2), for both the linearized and full calculations. The main plot applies to high bias ($\Delta=1$), and shows that the optimum choice of ρ depends on both the bias and the choice of n_1,n_2, and may be somewhat different from unity. The inset applies to low bias ($\Delta=0.1$), and shows that at low bias, the rectification is always maximized for $\rho=1$, that is, the two segments should be thermally matched, consistent with Eq. (24). From the inset we also note that the linearized and full calculations are in good agreement at low bias, with the largest error at $\Delta=0.1$ being 7.4% for $(n_1,n_2)=(3,-3)$. However, the main plot shows that at high bias the linearized calculation is a poor approximation, underpredicting the exact calculation by a factor of 2 or more, especially for large values of n_1 and n_2.

Figures 2 and 5, along with Eq. (24), also help explain why the rectification effect is usually not observed in everyday heat-transfer applications. In most thermal systems with two legs, the legs are designed with identical materials $(n_1\text{-}n_2=0)$ and/or have very different geometries ($\rho \ll 1$ or $\rho \gg 1$), in either case leading to negligible rectification. The thermal matching of the legs need only be approximate: For example, as long as $0.520<\rho<1.93$, the rectification at low bias will be at least 90% of the value for thermally-matched legs; likewise, for $0.172<\rho<5.83$ the rectification will be at least 50% of the thermally-matched value. Still, most applications are unlikely to have even this level of thermal matching unless it was specifically designed for. Material selec-

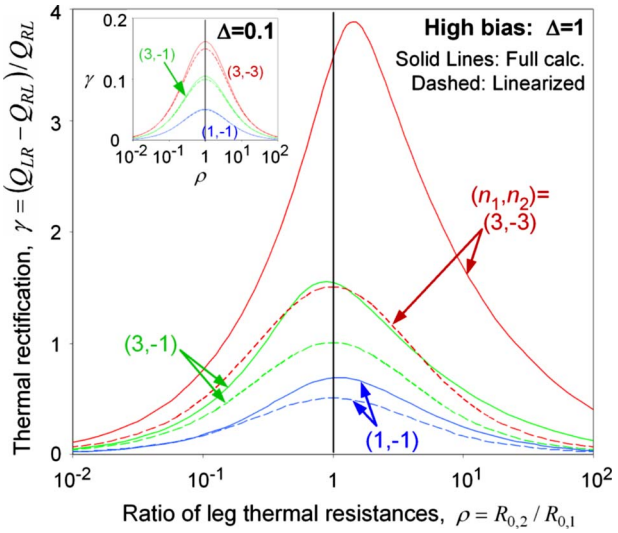

Fig. 5 Effect of the thermal matching parameter ρ on the rectification for materials with several different combinations of power-law exponents (n_1,n_2). Main plot: high thermal bias ($\Delta=1$). Inset: low thermal bias ($\Delta=0.1$). The full calculation refers to Eqs. (14) and (15), while the linearized calculation is Eq. (24).

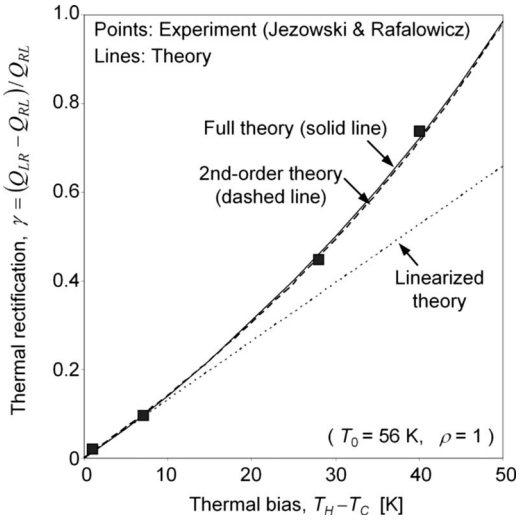

Fig. 6 Comparison with the experimental measurements of Jezowski and Rafalowicz [16] for a bar made of graphite and quartz. "Full theory" denotes the numerical solution of Eqs. (1)–(6) based on the reported $k(T)$ for bulk graphite and bulk quartz from Ref. [16]. Linearized theory and "second-order theory" denote Eqs. (24) and (23) respectively, which approximate the reported bulk $k(T)$ by power laws with our fits for n_1 and n_2.

tion is another important consideration; particularly at ambient temperature, Fig. 2 suggests that materials chosen at random are likely to have $|n_1-n_2|<2$, even though values >4 are readily accessible. Finally, the temperature difference should be some reasonable fraction of the absolute average; for example, at 300 K, if the temperature drop is only 10 K the corresponding Δ is so small that the rectification will almost certainly be less than 5% regardless of the materials and geometry. These examples point out the need for careful design of Δ, n_1-n_2, and ρ to achieve large rectification; nevertheless, recall from the calculations above (Fig. 4) that with care it is practical to design a system for rectification of well over 100%.

3.3 Comparison With Experiments. Our theoretical analysis can be compared with previous experimental results on two-segment bars in metal-metal [15] and dielectric-dielectric systems [16]. We first focus on the results of Jezowski and Rafalowicz [16] for graphite and quartz. As shown in Fig. 6, the full theory of Eqs. (1)–(6) and the second-order theory of Eq. (23) are both in very good agreement with the experimental results for all four of the reported thermal biases. Furthermore, the linearized theory of Eq. (24) is in good agreement with the data at low bias. We emphasize that these calculations have no free parameters; the measured $k(T)$ for graphite (k_1) and quartz (k_2) [16] were used to calculate $\gamma(T_H$-$T_C)$ directly, from the complete $k_1(T)$ and $k_2(T)$ curves in the case of the full theory, and from our fit n_1 and n_2 (1.27 and −1.68, respectively) in the case of the linearized and second-order theories. For the full theory calculations, because of the limited temperature range of data provided for pure graphite, it was necessary to extrapolate k_1 above 65 K, using the power-law fit of n_1. Similarly, k_2 (quartz) was extrapolated below 49 K using n_2. We note that these rectification measurements were not previously explained quantitatively. Although Ref. [16] qualitatively identified the rectification to be caused by the different $k(T)$ trends of graphite and quartz, they did not attempt to model their data quantitatively. Later these data were revisited by Kokshenev et al. [21], who essentially argued that the data should follow $\gamma \propto \Delta$ by assuming the effect is due to acoustic mismatch, but the proportionality constant was not derived.

We now turn to the results of Balcerek and Tyc [15] for two-segment bars of brass and tin (Fig. 7). As in Fig. 6, the theoretical curves of Fig. 7 include both the full calculation (based on the $k(T)$ for bulk brass and bulk tin extracted from Ref. [15]) as well as the linearized theory of Eq. (24) based on our fits for the temperature-dependent n_1 and n_2 (see Table 1). As shown in Fig. 7, the calculated curves are in reasonably good agreement with the experimental rectification measurements extracted from Ref. [15]. This plot includes cases where ρ deviates significantly from the ideal matched value of unity and shows that our analysis also

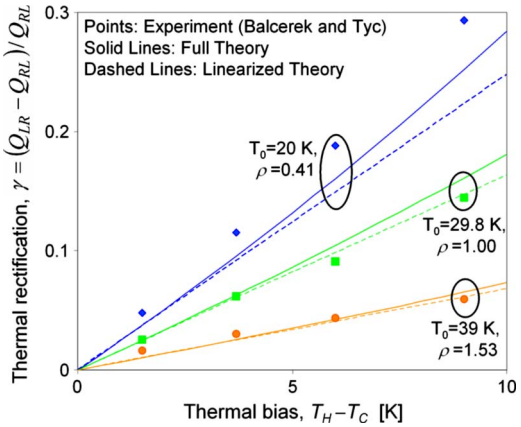

Fig. 7 Comparison with the experimental measurements of Balcerek and Tyc [15] for a bar made of brass and tin. Full theory denotes the numerical solution of Eqs. (1)–(6) based on the reported $k(T)$ for bulk brass and bulk tin from Ref. [15]. Linearized theory denotes Eq. (24), which approximates the reported bulk $k(T)$ by power laws with our fits for n_1 and n_2.

Table 1 Parameters used to analyze the experimental data of Balcerek and Tyc [15] in Fig. 7

Average temperature, T_0 (K)	20	29.8	39
Exponent n_1 (α-brass)	0.97	0.78	0.50
Exponent n_2 (tin)	−1.43	−1.17	−0.61
Resistance ratio, ρ	0.41	1.00	1.53

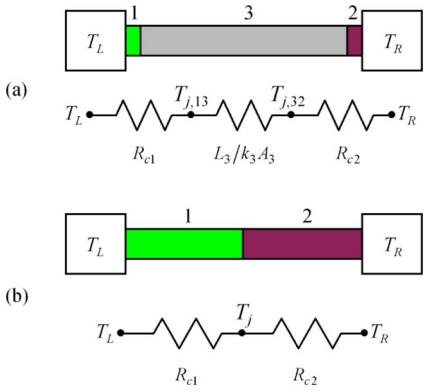

Fig. 8 Modeling temperature-dependent contact resistances in the present framework of a two-segment bar. (*a*) Contact resistances (1) and (2) in series with a bar of thermal conductivity k_3. (*b*) When the thermal resistance of the central bar (3) is negligible, the system becomes formally equivalent to a two-segment bar (as in Fig. 1).

agrees with the experiments over this range. Balcerek and Tyc [15] also reported that the classical Fourier theory can successfully model these measurements. Although the details of their approach were not given, their fits have significantly less error than our curves in Fig. 7, which we attribute to their access to more accurate $k(T)$ data for their bulk tin and bulk brass materials. Because we determined the bulk $k(T)$ by graphically processing figures from Ref. [15], which had a logarithmic scale, our uncertainty in the bulk $k(T)$ is estimated at around 5%. The uncertainty in n_1 and n_2 is particularly important and is estimated at around 10%. The relative uncertainty in our calculation of linearized γ is estimated at around 20% (e.g., $\gamma=0.4\pm0.08$), and the absolute uncertainty in extracted experimental γ is estimated as 0.01 (e.g., $\gamma=0.4\pm0.01$). Thus, the agreement between theory and experiment in Fig. 7 is within this level of uncertainty.

We comment briefly on the recent experiments of Chang et al. [14], which reported rectification of up to $\gamma=7\%$ in boron nitride nanotubes. Assuming a background temperature of 300 K, the implied temperature extremes in their data are $T_H=324$ K and $T_C=303$ K. Thus $\Delta=0.067$, and the normalized rectification is $\hat{\gamma}=1.04$. Although this effect was attributed to solitons in the nanotubes, it should be noted that the classical phenomena described in this paper could also be used to achieve this degree of rectification with existing bulk materials, by selecting materials with power laws that differ by n_1-$n_2=4.16$ (Fig. 2).

3.4 Relationship to Contact Resistances. It has been pointed out that the temperature dependence of contact resistances is another source of classical thermal rectification [25]. The present analysis can be used to calculate upper bounds for the contact-resistance rectification effect as follows. As shown in Fig. 8(*a*), we consider a third segment between 1 and 2, with materials 1 and 2 shrunk to thin layers localized at the contacts. This could represent a nanotube or nanowire spanning between two reservoirs with different contact resistances at each end. The contact-resistance rectification effect is strongest if the temperature drops are localized across the contacts, with negligible temperature drop across the central segment 3. In this case the central segment no longer influences the heat transfer and the system simplifies to the two-leg schematic of Fig. 8(*b*).

The system of Fig. 8(*b*) can be analyzed in two different ways depending on the detailed treatment of the contact resistance. First, if the contacts are treated as thin heat conductors that are still several times thicker than the mean free path of the energy carriers, then a classical Fourier treatment is appropriate. The analysis given above in Sec. 2 is directly applicable, where L_i, A_i, and k_i now all refer to the properties of contact i. The rectification can thus be calculated from the numerical solution of Eqs. (1)–(6), or Eq. (24) in the linearized limit of power-law $k(T)$ for the contact materials.

Second, the thickness of the contact material layer may be assumed to be much thinner than the mean free path of the energy carriers, in which case the contact resistance is typically characterized through a contact conductance per unit area G with units of $\mathrm{W/m^2\,K}$, which depends on the materials on either side of the interface. In this case materials 1 and 2 vanish from Fig. 8(*a*), and the resistances R_{c1} and R_{c2} in Fig. 8(*b*) correspond to the contact resistances between the central bar and the left and right reservoirs, respectively. In general the quantitative prediction of $G(T)$ for an arbitrary pair of interface materials is a complicated and unsolved problem. Standard theories include the diffuse mismatch model and the acoustic mismatch model, but these often disagree with measurements by up to an order of magnitude [26,27]. However, to study the rectification effect here we focus only on the temperature trends, which typically range from $G\propto T^3$ at low temperatures (due to the Debye specific heat law) to $G=$const. at high temperatures (due to the law of Dulong and Petit). It is important to note that the standard convention when measuring or modeling $G(T)$ is to focus on temperature drops across the contact that are much smaller than the average temperature. Thus, our discussion is limited to the low-bias limit of $\Delta\ll1$. For a planar contact of uniform thickness, $G(T)$ is related to $g(T)$ simply through

$$g_i = A_i G_i \tag{27}$$

In this way temperature-dependent contact resistances (or conductances) can be mapped into Eqs. (4)–(6). The resistance ratio ρ is calculated as before from Eqs. (11) and (12), and Eq. (24) can be applied in the case of power-law $G(T)$ for small Δ. However, for the standard theories of contact resistance the maximum value of $(n_1$-$n_2)$ will be no more than 3, which is significantly less than the values of $(n_1$-$n_2)$ accessible in bulk materials (Fig. 2).

4 Conclusions

Thermal rectification requires an asymmetry and a nonlinearity. Within the framework of the classical Fourier law of heat conduction, these conditions are met by a two-segment bar if the thermal conductivities of the two segments have different dependencies on temperature. The general solution to this problem involves two coupled integral equations, which are usually solved numerically. In the common case of low thermal bias and thermal conductivities with power-law temperature dependencies, the maximum thermal rectification is given by a simple algebraic expression, $\gamma_{\max}\approx\frac{1}{4}(n_1-n_2)(T_H-T_C)/T_0$. As long as the thermal resistances of the two segments of the bar are closely-matched (within a factor of approximately two of each other), the rectification will be within 10% of this maximum value. Finally, we suggest that the normalized thermal rectification $\hat{\gamma}=\gamma/\Delta$ is a more meaningful figure of merit than γ when evaluating the intrinsic capabilities of a material or device to provide thermal rectification.

Acknowledgment

The author would like to thank Li Shi and Joseph V. Mantese for helpful discussions.

References

[1] Saha, S., Shi, L., and Prasher, R., 2006, "Monte Carlo Simulation of Phonon Backscattering in a Nanowire," ASME International Mechanical Engineering Congress and Exposition, Chicago, p. 15668.
[2] Barzelay, M. H., Tong, K. N., and Holloway, G. F., 1955, "Effects of Pressure on Thermal Conductance of Contact Joints, NACA Technical Note 3295," Technical Report No. 3295.
[3] O'Callaghan, P. W., Probert, S. D., and Jones, A., 1970, "A Thermal Rectifier," J. Phys. D, **3**(9), pp. 1352–1358.
[4] Walker, D. G., 2006, "Thermal Rectification Mechanisms Including Noncon-

tinuum Effects," Joint ASME-ISHMT Heat Transfer Conference, Guwahati, India.
[5] Terraneo, M., Peyrard, M., and Casati, G., 2002, "Controlling the Energy Flow in Nonlinear Lattices: A Model for a Thermal Rectifier," Phys. Rev. Lett., **88**(9), p. 094302.
[6] Li, B., Wang, L., and Casati, G., 2004, "Thermal Diode: Rectification of Heat Flux," Phys. Rev. Lett., **93**(18), p. 184301.
[7] Segal, D., and Nitzan, A., 2005, "Spin-Boson Thermal Rectifier," Phys. Rev. Lett., **94**(3), p. 034301.
[8] Eckmann, J.-P., and Mejia-Monasterio, C., 2006, "Thermal Rectification in Billiardlike Systems," Phys. Rev. Lett., **97**(9), p. 094301.
[9] Peyrard, M., 2006, "The Design of a Thermal Rectifier," Europhys. Lett., **76**(1), pp. 49–55.
[10] Hu, B., He, D., Yang, L., and Zhang, Y., 2006, "Thermal Rectifying Effect in Macroscopic Size," Phys. Rev. E, **74**(6), p. 060201.
[11] Ming, Y., Wang, Z. X., Li, Q., and Ding, Z. J., 2007, "Nonlinear Thermal Properties of Three-Terminal Mesoscopic Dielectric Systems," Appl. Phys. Lett., **91**(14), p. 143508.
[12] Roberts, N. A., and Walker, D. G., 2008, "Monte Carlo Study of Thermal Transport of Frequency and Direction Dependent Reflecting Boundaries in High Kn Systems," ITHERM: 11th Intersociety Conference on Thermal and Thermomechanical Phenomena in Electronic Systems, Orlando, FL, pp. 993–998.
[13] Dames, C., and Miller, J. P., "Ballistic-Elastic Thermal Rectification," in preparation.
[14] Chang, C. W., Okawa, D., Majumdar, A., and Zettl, A., 2006, "Solid-State Thermal Rectifier," Science, **314**(5802), pp. 1121–1124.
[15] Balcerek, K., and Tyc, T., 1978, "Heat Flux Rectification in Tin-Alpha-Brass System," Phys. Status Solidi A, **47**(2), pp. K125–K128.
[16] Jezowski, A., and Rafalowicz, J., 1978, "Heat-Flow Asymmetry on a Junction of Quartz With Graphite," Phys. Status Solidi A, **47**(1), pp. 229–232.
[17] Marucha, C., Mucha, J., and Rafałowicz, J., 1975, "Heat Flow Rectification in Inhomogeneous GaAs," Phys. Status Solidi A, **31**(1), pp. 269–273.
[18] Although Balcerek and Tyc stated that they made theoretical calculations based on Fourier's law, which appear to be in very good agreement with their experiments, no modeling details were given.
[19] Marucha, C., Mucha, J., and Rafalowicz, J., 1976, "Phenomenological Interpretation of Heat Flux Volume Rectification in Non-Homogeneous Media," Phys. Status Solidi A, **37**(1), pp. K5–K7.
[20] Hudson, P. R. W., 1976, "Heat Flow Rectification," Phys. Status Solidi A, **37**(1), pp. 93–96.
[21] Kokshenev, V. B., Balcerek, K., Tyc, T., and Jezowski, A., 1984, "Discussion of the Heat-Flux Rectification in the Solid-Solid System in the Acoustic-Mismatch Theory Framework," Phys. Status Solidi A, **81**(1), pp. 171–176.
[22] Hoff, H., 1985, "Asymmetrical Heat Conduction in Inhomogeneous Materials," Physica A, **131**(2), pp. 449–464.
[23] Hoff, H., and Jung, P., 1993, "Experimental Observation of Asymmetrical Heat Conduction," Physica A, **199**(3–4), pp. 502–516.
[24] MAPLE, accessed through MATLAB.
[25] Shi, L., and Mingo, N., 2007, private communication.
[26] Swartz, E. T., and Pohl, R. O., 1989, "Thermal-Boundary Resistance," Rev. Mod. Phys., **61**(3), pp. 605–668.
[27] Cahill, D. G., Ford, W. K., Goodson, K. E., Mahan, G. D., Majumdar, A., Maris, H. J., Merlin, R., and Phillpot, S. R., 2003, "Nanoscale Thermal Transport," J. Appl. Phys., **93**(2), pp. 793–818.
[28] Touloukian, Y. S., ed., 1970, *Thermophysical Properties of Matter*, IFI/Plenum, New York.
[29] Kim, P., Shi, L., Majumdar, A., and Mceuen, P. L., 2001, "Thermal Transport Measurements of Individual Multiwalled Nanotubes," Phys. Rev. Lett., **87**(21), pp. 215502.
[30] Unifraxcorp., Fiberfrax Low-Con Felt Datasheet, http://www.fiberfrax.com/.
[31] Note: The effective thermal conductivity for thermal radiation is estimated using the radiation convection coefficient $h_{rad}=4\sigma T^3$ where σ is the Stefan–Boltzmann constant, and k is calculated from $k=h_{rad}^{*}\times \mathrm{MFP}$, where MFP is a photon mean free path taken as ~ 1 mm.

Microscale Temperature Measurements Near the Triple Line of an Evaporating Thin Liquid Film

Hemanth K. Dhavaleswarapu

Suresh V. Garimella[1]
e-mail: sureshg@purdue.edu

Jayathi Y. Murthy

Cooling Technologies Research Center,
School of Mechanical Engineering,
and Birck Nanotechnology Center,
Purdue University,
585 Purdue Mall,
West Lafayette, IN 47907-2088

Thin-film evaporation from a meniscus in a confined space, which is the basis for many two-phase cooling devices, is experimentally investigated. The meniscus formed by heptane, a highly wetting liquid, on a heated fused quartz wafer is studied. Microscale infrared temperature measurements performed near the thin-film region of the evaporating meniscus reveal the temperature suppression caused by the intensive evaporation in this region. The high spatial resolution (~6.3 μm) and high temperature sensitivity (~20 mK) of the infrared camera allow for improved accuracy in the measurements. The effects of evaporation rate, applied heat flux, and channel width on the thin-film heat transfer distribution are also explored. [DOI: 10.1115/1.3090525]

Keywords: meniscus, thin liquid film, evaporation, diffusion, triple line

1 Introduction

Evaporation from a meniscus serves as the basic mechanism in many two-phase cooling devices such as heat pipes, thermosyphons, vapor chambers, two-phase cold plates, and capillary pumped loops. Thin-film evaporation, which takes place near a solid-liquid-vapor junction, has long been believed to be the dominant mode of heat transfer in such systems [1]. The efficacy of heat transfer in thin films is attributed to a high disjoining pressure gradient [2], which results in liquid being pulled into the thin-film region, as well as the very low thermal resistance resulting from the small film thickness. The intensive evaporation near the triple line creates a temperature gradient along the meniscus. This results in a surface tension gradient that gives rise to thermocapillary convection. Both the evaporation from the thin film as well as the thermocapillary convection induced have been reported in the literature [3,4] to play a major role in the total heat transferred. However, the exact role and nature of these processes is still not completely understood.

Wayner [5] carried out extensive theoretical and experimental studies in this field and delineated several important factors influencing thin-film evaporation. Ma and Peterson [6] developed experimentally verified models for evaporation from V-grooves to predict their maximum heat transport limit. Holm and Goplen [7] were the first to develop an approximate method for predicting heat transfer from capillary grooves. They found that nearly 80% of the total heat transfer takes place from the thin-film transition region. Stephan and Busse [8] developed a model to describe the heat and mass transport in the microregion of the meniscus in a V-groove. Their numerical model agreed well with the measured heat transfer data and showed that up to 50% of the entire evaporation can take place in the microregion despite its small geometrical dimensions. Other researchers [9,10] have attributed as much as 90% of heat transfer to the thin-film region. However, Park and Lee [11] suggested that the thin-film contributed less than 5% of total heat transfer due to its small geometrical extent. A recent model developed by Wang et al. [12] showed that 20% of the heat transfer takes place from the thin-film region, but as much as 60% of the overall heat transfer takes place from a 1 μm thick microregion.

In terms of experimental investigations, interferometry and ellipsometry have been widely employed in the study of thin liquid films. Mirzamoghadam and Catton [13] considered a two-dimensional (2D) meniscus generated on an inclined, partially submerged, heated flat plate in a pool of liquid. They studied the temperature in the liquid using laser holographic interferometry. The general characteristics of the meniscus region, where the combined influence of natural convection, conduction, and surface tension gradients are important, were deduced. Xu and Carey [9] assumed that heat transfer occurs only through the thin-film region and developed a model whose results were in reasonable agreement with their experiment. Dasgupta et al. [14] studied a 2D extended meniscus of heptane using ellipsometry and found high mass fluxes in the thin-film region using a semi-empirical model. However, their model neglected vapor diffusion effects. Panchamgam et al. [15] conducted interferometry experiments with pentane on a quartz substrate under saturation conditions and demonstrated for the first time that the disjoining pressure controls fluid flow within an evaporating, completely wetting, thin film.

Höhmann and Stephan [16] and Buffone and Sefiane [17] used liquid crystals to measure local temperatures underneath an evaporating meniscus. Thermochromic liquid crystals (TLCs) are organic compounds that reflect light when their temperature falls within a certain range, usually termed as their event temperature range. The color displayed by the TLCs can be related to the temperature of the surface. However, this technique suffers from large uncertainties and from the limited lifetime of the TLCs (ranging from a few minutes to 1–2 h).

With advances in technology, infrared thermography is fast becoming an attractive option due to its nonintrusive nature, high resolution, and high temperature sensitivity. Jiang et al. [18] and Buffone and Sefiane [19] demonstrated temperature measurements on a meniscus surface with an infrared (IR) camera. Jiang et al. [18] carried out experiments on a thin film on a cylinder and concluded that nearly 20–40% of the heat transfer occurs through the thin-film region. It is to be noted that the actual emissivities of the surfaces were not considered in Refs. [18,19], and all surfaces were assumed to have an emissivity of unity. The design of these experiments did not allow for the temperature distribution all

[1]Corresponding author.

Contributed by the Heat Transfer Division of ASME for publication in the JOURNAL OF HEAT TRANSFER. Manuscript received May 11, 2008; final manuscript received January 26, 2009; published online April 2, 2009. Review conducted by Louis C. Chow.

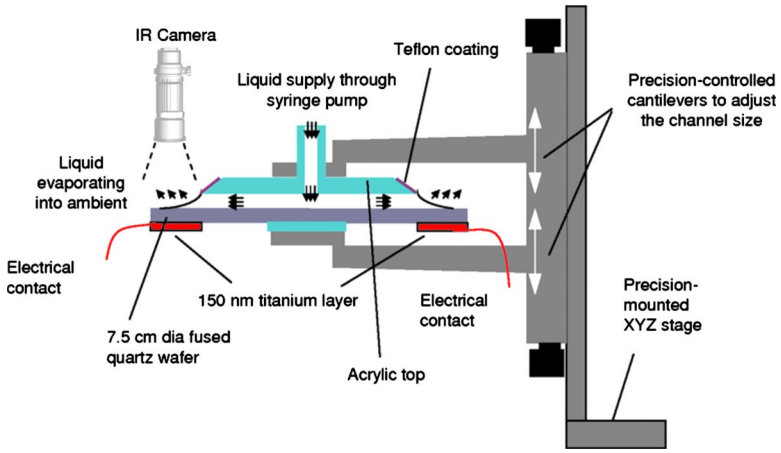

Fig. 1 Schematic diagram of the test setup in side view

along the meniscus to be obtained. The temperature drop in the all-important thin-film region was also not clearly observed.

In the present work, a steady two-dimensional meniscus in a channel subjected to a constant heat flux is studied. The fluid lost to evaporation is replenished using a syringe pump to achieve a constant evaporation rate. The effects of applied heat flux and evaporation rate on thin-film evaporation are investigated. A high-end, science-grade IR camera is used for temperature measurements. This camera provides a spatial resolution of ~ 6.3 μm and a temperature sensitivity of 20 mK. The test setup allows for temperature measurements to be made right at the triple line; resolution to this scale has hitherto not been achieved. The measurements allow for critical parameters to be evaluated in situ and then used to obtain additional details concerning the evaporation process. A subregion of the meniscus of length 50 μm is examined. A heat balance analysis is carried out to delineate the contribution of the subregion heat transfer to the total.

2 Experimental Setup and Procedures

2.1 Test Setup. Figure 1 shows details of the test setup. The vertical space between a 76.2 mm diameter, 500 μm thick fused quartz wafer and a 58.42 mm outer diameter, 5.08 mm thick acrylic top piece acts as the channel of interest. This "channel" is mounted on a linear stage that enables precise control of the channel width (accuracy of ~ 10 μm). A constant heat flux is provided to the thin film using a 100 nm titanium layer deposited on the underside of the quartz wafer with standard microfabrication procedures. The titanium heat source is annular in geometry with the annulus inner and outer diameters being 58.42 mm and 76.2 mm, respectively. Liquid continuously fed from a syringe pump (PHD 2000, Harvard Apparatus) enters the test piece through an axial inlet, emerges from the slit, and forms a meniscus right above the heat source, causing it to evaporate into the atmosphere. The meniscus so formed has two solid-liquid-vapor junctions, one on the quartz wafer and the other at the edge of the acrylic top piece. The circular geometry naturally eliminates any edge effects that would be present in a rectangular domain.

Prevention of the formation of a thin film at the edge of the acrylic top piece proved to be challenging. Even a small amount of liquid spread on the acrylic formed liquid fingers because of microscopic surface irregularities, rendering difficult an accounting of the net liquid-vapor interfacial area. A hydrophobic Teflon coating on the angled edge of the acrylic was found to be effective in containing the liquid film precisely, without creeping on to the acrylic. An IR camera (Merlin, FLIR Inc.) with a 4× objective is used to capture the temperature contours and a goniometer (CAM 100, KSV Instruments Ltd.) with 2× magnification, and a backlit light emitting diode (LED) light is used to image the meniscus. The IR camera was carefully calibrated with a high-sensitivity, high-stability blackbody (2000 series, SBIR Inc.). Performing an in situ calibration effectively removed the effect of background radiation.

High purity heptane (Sigma-Aldrich, 99.99%), a highly wetting liquid with a boiling point of 98°C, is used as the test fluid. The quartz wafer is solvent cleaned, blow dried with extra-dry grade nitrogen, and later rinsed with heptane before each run. To ensure that the system had reached a steady state, the evaporation process was allowed to occur for over 2 h in each test before recording data. Since the field of view of the IR camera, 2×1.5 mm^2, does not capture the entire annular region, images are taken at four different locations along the ring on the top and the bottom of the wafer to verify the uniformity of temperature along the perimeter of the meniscus. The absolute temperature distribution is found to be uniform within a confidence interval of ± 1°C. All other subsequent experiments are conducted at a fixed location. Data sets in which any foreign particles were observed on the surface were discarded. Liquid menisci formed at three different evaporation rates and five different input power levels in two different channel widths are investigated for this work.

In order to determine the net applied heat flux, it is essential to estimate the heat losses in the system. The conduction losses through the wafer and the convection and radiation losses to the surroundings are estimated by performing a dry run. Wafer with no liquid in the system is tested. A series of tests at different power levels is conducted for this configuration, and the average steady-state heater temperature (T_{bottom}) is recorded with the IR camera at each power level. A relationship between the input power and the heater temperature is then obtained as a curve fit to the results. The heat losses for each test with the liquid are then calculated by substituting the measured average heater temperature into the curve-fit relationship, and the heat input on the bottom of the channel (q_s) is obtained by subtracting the losses from the input power. Thus estimated heat flux q_s'' is a function of the input power and the evaporation rate. However, no discernible difference is noted for q_s'' with variation in evaporation rate, and hence q_s'' is only a function of the input power. On average, the heat losses are found to be nearly 30–40% of the input power. The uncertainty in determining the input heat flux by this method is $\pm 10\%$.

This analysis, however, does not take into account the heat lost to the liquid, in other words, the sensible heat gained by the liquid while flowing through the channel. As clarified later, this has a negligible impact on the heat transfer from the 50 μm region. The uncertainty in the flow rate principally results from the step resolution of the syringe pump and is $\pm 0.35\%$.

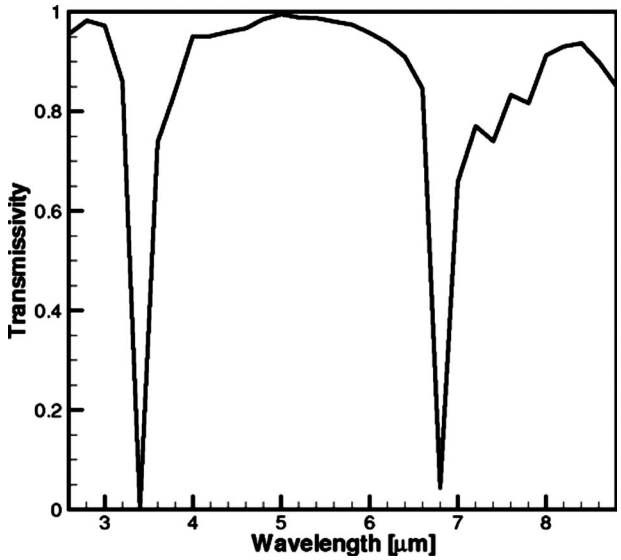

Fig. 2 Transmissivity of an 80 μm thick heptane layer

2.2 Transmissivity of Heptane. Assuming the fluid to behave as a semitransparent solid [20], its transmissivity based on the complex index of refraction [21] in the infrared regime is calculated for obtaining an accurate estimation of liquid temperatures. Figure 2 shows the transmissivity of an 80 μm thick heptane layer. It is noticed that the liquid remains nearly transparent in the bulk of the infrared regime (3–8 μm).

Figure 3(*a*) shows the image of a heptane meniscus on a 500 μm thick polished fused quartz wafer that is heated from below. Taking advantage of the IR transparency of heptane near the contact line, infrared measurements are used to capture the

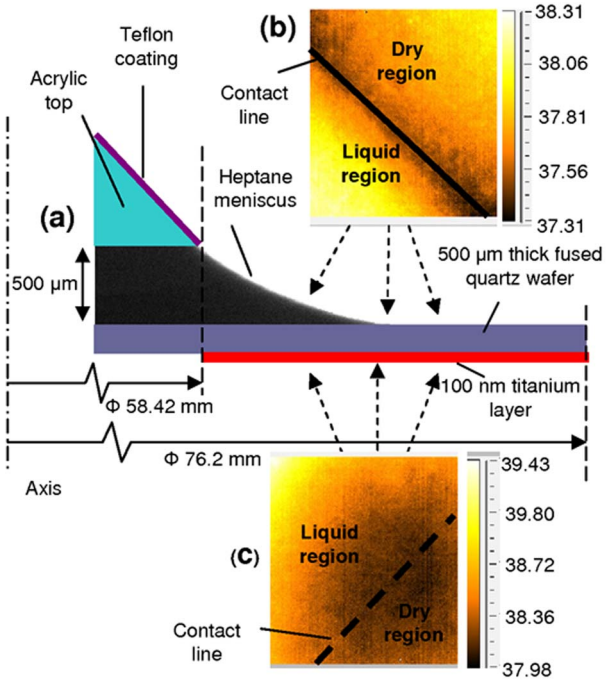

Fig. 3 (*a*) Image of heptane meniscus on fused quartz wafer (q_s''=950 W/m^2, Ψ=8.35×10^{-7} kg/s). (*b*) Infrared image of wafer top (T_{top}) near the contact line. (*c*) Infrared image of the titanium layer on the underside of the wafer near the contact line (T_{bottom}).

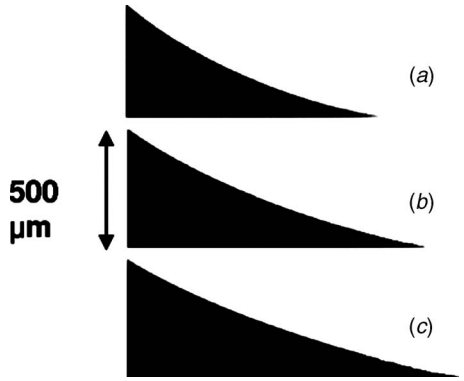

Fig. 4 Two-dimensional meniscus images at a heat flux of 990 W/m^2 and different evaporation rates: (*a*) 8.35×10^{-7} kg/s, (*b*) 8.8×10^{-7} kg/s, and (*c*) 9.35×10^{-7} kg/s

temperature of the wafer top surface (T_{top}) and the temperature of the titanium layer on the underside of the meniscus (T_{bottom}). Both these measurements are carried out with a single IR camera at different time periods after the system has attained steady state. As published values for emissivity for quartz and titanium span a range of values, an in situ calibration of the emissivities of both the surfaces is performed. This is achieved by coating half the surface with black paint (Krylon 1602) of known emissivity of 0.95 [22]. The wafer is then heated, and thermal images are recorded. Using the software RTOOLS (FLIR Inc.) and assuming that a 500 μm long region at the interface between the black and the unpainted surface (i.e., the surface whose emissivity is desired) is at a uniform temperature, the emissivity of the nonblack surface is adjusted until it reads the temperature of the black surface. The emissivities were thus found to be 0.80 and 0.47 for the quartz and titanium layers, respectively.

A typical shape of the liquid-vapor interface is presented in Fig. 3(*a*), in which the liquid region is opaque and the air is transparent. Figures 3(*b*) and 3(*c*) are raw thermal images of the wafer top and titanium layer. The "liquid region" in the IR images corresponds to the wetted portion of the image while "dry region" indicates the superheated surface adjacent to the liquid meniscus. In both images, it is seen that the thin-film region near the contact line is the point of lowest temperature indicating its high efficiency. The temperature drop is less evident on the wafer underside than on the wafer top because of the smearing caused by the lateral conduction in the wafer. Similar temperature drops under the thin film were observed in Refs. [16,17].

3 Results and Discussion

The dependence of meniscus shape, channel width, and temperature distribution near the meniscus on the heat flux and evaporation rate is first considered. The extent of heat transfer taking place from a 50 μm long region near the contact line is then discussed.

3.1 Dependence of Meniscus Shape on Evaporation. The meniscus shape is an important parameter in determining the heat flux through the thin-film region [12]. The meniscus shape, and thus the effective area of evaporation, is varied in the experiments by controlling three independent parameters—evaporation rate (Ψ), applied heat flux (q_s''), and channel width (w).

The effect of mass flow rate on the film profile at a constant applied heat flux of 990 W/m^2 is shown in Fig. 4. It is seen that the meniscus shape varies significantly with mass flow rate. At a constant heat flux, increasing the evaporation rate requires a larger interfacial area for evaporation, thereby changing the film profile. This is observed in Figs. 4(*a*)–4(*c*) where the contact line extends

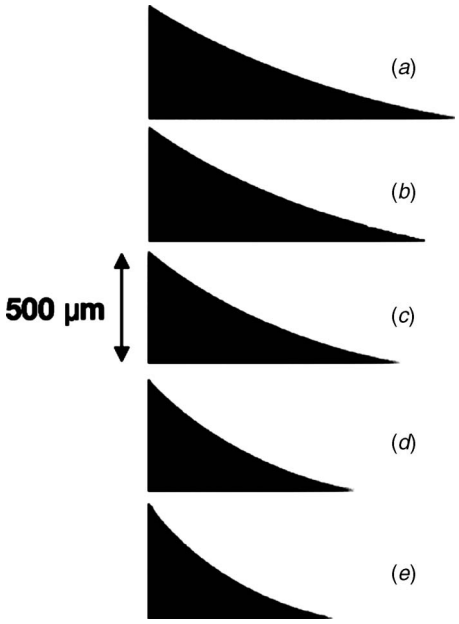

Fig. 5 Two-dimensional meniscus images at an evaporation rate of 8.35×10^{-7} kg/s and different heat fluxes: (*a*) 810 W/m^2, (*b*) 950 W/m^2, (*c*) 990 W/m^2, (*d*) 1030 W/m^2, and (*e*) 1190 W/m^2

forward with increasing evaporation rate. To evaluate the apparent contact angle, the profile of the meniscus is extracted from the digital images using an edge-detection algorithm in MATLAB [23]. A tangent to the curve-fitted profile at the contact line gives the contact angle. Thus evaluated apparent contact angles for all the cases are found to be in the range of 7–12 deg. The accuracy of the measurement technique is ±1 deg.

The effect of heat flux on the film profile at a constant mass flow rate of 8.35×10^{-7} kg/s is illustrated in Fig. 5. At a constant evaporation rate, increasing the heat flux requires a smaller interfacial area for evaporation. This is observed in Figs. 5(*a*)–5(*e*) where the contact line recedes and the apparent contact angle increases with an increase in applied heat flux, which is in agreement with the trends found in Ref. [12]. A higher heat flux necessitates a higher capillary pressure gradient for intensive evaporation near the contact line and hence causes an increase in apparent contact angle.

The width of the channel was found to have only a minor effect on the film profile over the small range of widths tested, as demonstrated in Fig. 6; the effect of increasing the channel width from 500 μm and 600 μm is shown at identical values of heat flux and mass flow rate. The remaining results in this work consider only the channel width of 500 μm.

Fig. 6 Two-dimensional meniscus images at an evaporation rate of 9.35×10^{-7} kg/s and a heat flux of 820 W/m^2 in different channel widths: (*a*) 500 μm and (*b*) 600 μm

3.2 Microscale Temperature Measurements. Figure 7 depicts the measured temperatures in a 400 μm region surrounding the contact line at an applied heat flux of 1190 W/m^2 and at different evaporation rates. Each plot shows the time- and area-averaged temperature distribution along the wafer top (T_{top}), the wafer underside (T_{bottom}), and the mean (T_{mean}), where T_{mean} is the mean of T_{top} and T_{bottom}. The *x*-axis represents the radial position, with the wetted and nonwetted regions identified (see Fig. 7(*c*)). Only a subset of data points obtained is included to improve clarity. Each solid line represents the curve-fitted temperature, while the dotted-line envelopes represent the uncertainty in the measurements due to thermal noise and time- and area-averaging; several images are averaged to improve the confidence of the averaged temperatures.

As the heat flux is supplied from the titanium layer on the bottom, T_{bottom} is greater than T_{top} as expected. The lowest temperature point is at the contact line, signifying the sink effect and high efficiency of heat removal in the thin-film region. Lateral conduction in the quartz wafer leads to a smearing of the temperature valley on the underside; with a silicon wafer (of higher conductivity), the temperature valley is not observed. Höhmann and Stephan [16] observed a $\sim$0.2 K temperature drop near the contact line over a region of 35 μm length on the underside of the wafer, but this was within the error limits of the measurement technique. Also, Jiang et al. [18] observed a $\sim$0.4 K temperature drop near the contact line over a region of $\sim$300 μm length; however, because of experimental constraints only three data points were obtained over the region. The length over which the temperature drop is seen is a strong function of the experimental setup. The improved test setup used in the present work allows for a relatively large temperature drop of $\sim$1 K to be resolved on the wafer top over a length of 400 μm, as seen in Fig. 7.

It is noticed that the difference in temperature at the contact line between T_{top} and T_{bottom} decreases with an increase in evaporation rate, suggesting a decrease in effective thermal resistance with an increase in evaporation rate. Figure 8 illustrates the heat flux effect on the temperature contours near the contact line at a constant evaporation rate of 8.35×10^{-7} kg/s. The plots reveal that the difference in temperature at the contact line between T_{top} and T_{bottom} increases with an increase in applied heat flux. This is in agreement with the results of Ref. [18].

3.3 Subregion Heat Transfer. While this is a multimode and three-dimensional heat transfer problem with conjugate conduction effects, an approximate heat balance analysis is carried out here based on the temperature measurements in Figs. 7 and 8 to obtain an estimate of the heat transfer through a small region near the contact line. A subregion of length 50 μm (corresponding to a $\sim$10 μm thick liquid layer) is defined as the region of interest. A heptane layer up to 80 μm thick is essentially transparent to IR. Since this thickness is achieved at a distance of approximately $\sim$250 μm along the wafer from the contact line, T_{top} in the liquid region from 0 μm (contact line) to -250 μm can be treated as the temperature of the wafer top surface.

Treating the wafer as a fin and assuming 1D conduction along its radius, an approximate heat transfer analysis is conducted. The 1D conduction assumption in the annular subregion is justified as the length of the subregion ($\sim$50 μm) is negligible compared with its radial position $\sim$59 mm (see Fig. 3). Neglecting heat losses, the heat balance for the control volume, shown in Fig. 9, is given by

$$q_r - q_{r+\delta r} + q_s = q_d \tag{1}$$

where q_r is the heat conducted per unit depth in the *r*-direction, q_s is the heat input on the bottom of the control volume per unit depth due to the electric heating, and q_d is the heat dissipated per unit depth by evaporation from the meniscus. Using Fourier's law

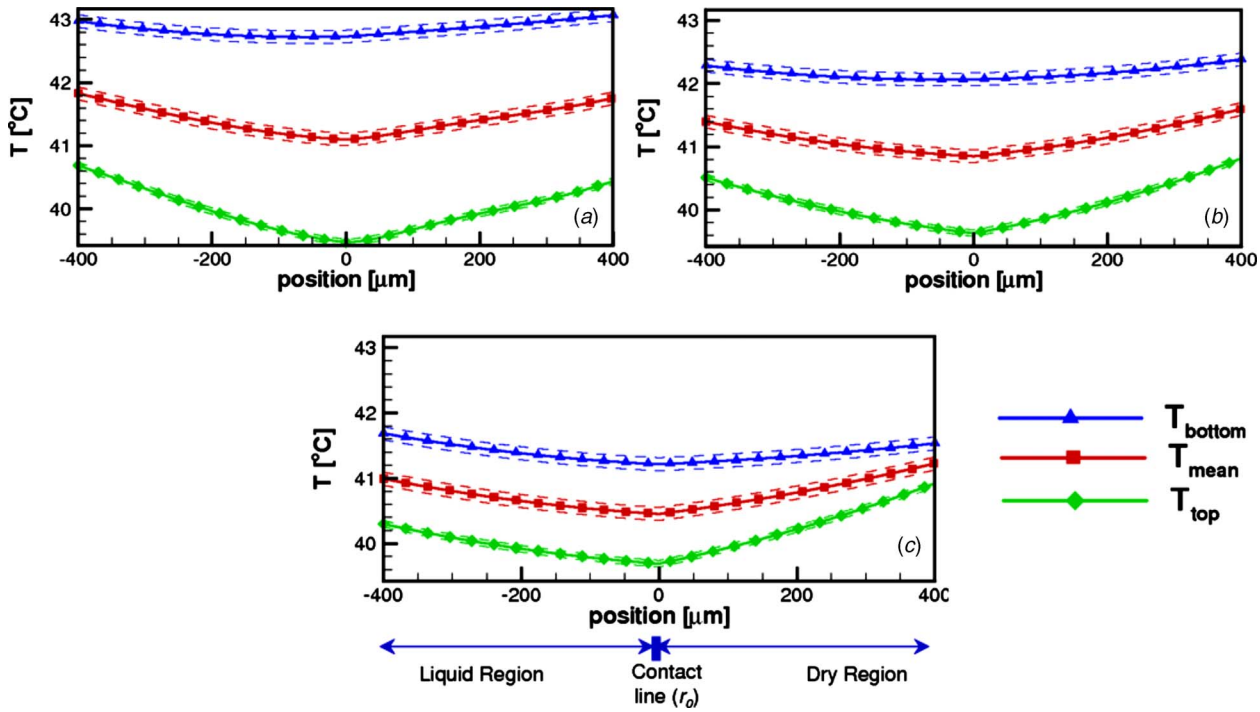

Fig. 7 Infrared temperature maps of T_{top} and T_{bottom} at a heat flux of 1190 W/m^2 and different evaporation rates: (*a*) 8.35 $\times 10^{-7}$ kg/s, (*b*) 8.8$\times 10^{-7}$ kg/s, and (*c*) 9.35$\times 10^{-7}$ kg/s

and assuming profiles of T_{mean} such as those shown in Figs. 7 and 8 to represent the 1D temperature profiles in the wall, we have

$$k\frac{d^2T_{mean}}{dr^2}t\delta r + q_s = q_d \tag{2}$$

Since the heat source q_s is of a constant value, when the dissipation heat flux q_d reaches a maximum, d^2T_{mean}/dr^2 also reaches a maximum. The temperature maps in Figs. 7 and 8 show that the location of maximum d^2T_{mean}/dr^2 is at the contact line.

Integrating Eq. (2) along the length of the subregion (Δr) and multiplying by the perimeter of the contact line gives the subregion heat transfer ($q_{subregion}$) as

$$q_{subregion} = q_I + q_{II}$$

where

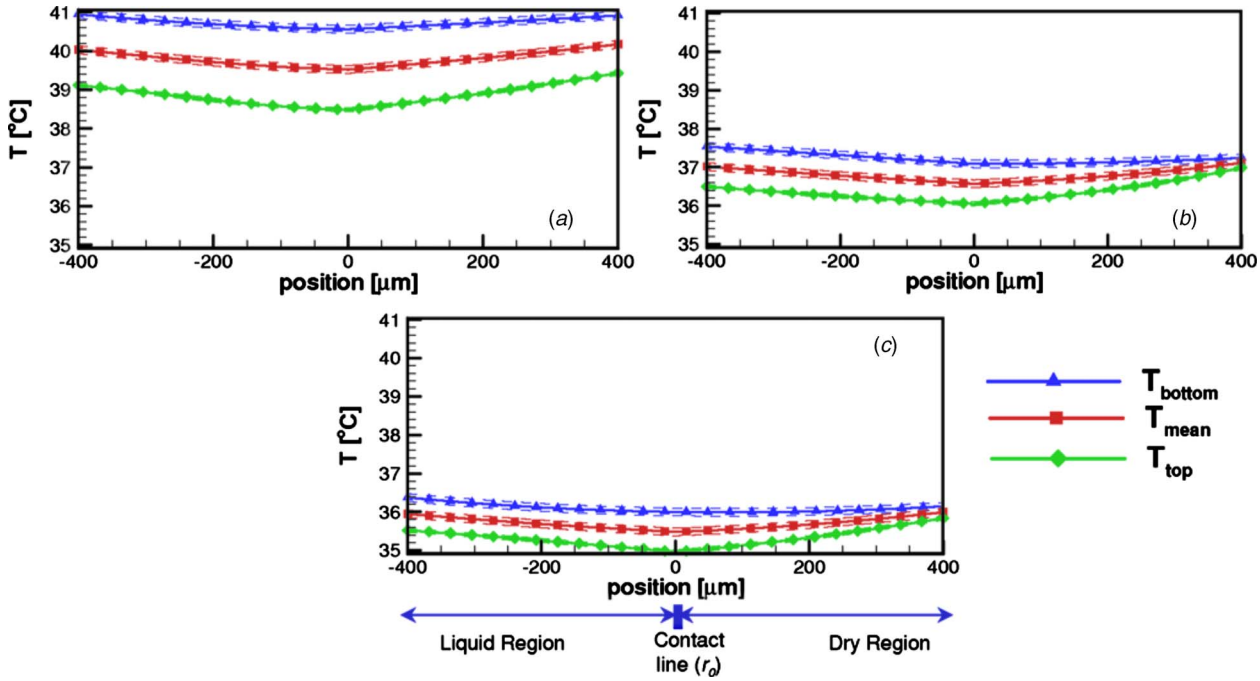

Fig. 8 Infrared temperature maps of T_{top} and T_{bottom} at an evaporation rate of 8.35$\times 10^{-7}$ kg/s and different heat fluxes: (*a*) 1030 W/m^2, (*b*) 950 W/m^2, and (*c*) 810 W/m^2

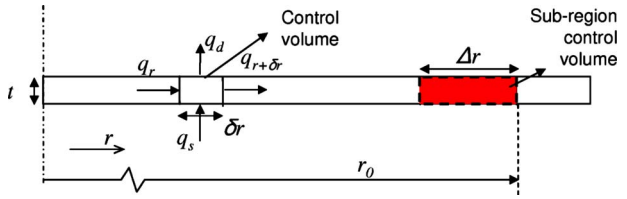

Fig. 9 The heat balance over a control volume of extent δr in the wafer

$$q_{\mathrm{I}} = \left(k \left. \frac{dT_{\mathrm{mean}}}{dr} \right|_{r_0-\Delta r}^{r_0} 2\pi r_0 t \right) \quad \text{and} \quad q_{\mathrm{II}} = (q_s'' \Delta r 2\pi r_0) \tag{3}$$

where $dT_{\mathrm{mean}}/dr|_{r_0-\Delta r}^{r_0}$ represents the difference in temperature gradient evaluated at the ends of control volume and k is the thermal conductivity of the wafer. The first term in Eq. (3), q_{I}, represents the heat conducted in from both sides of the control volume, while the second term q_{II} indicates the heat added from the heater. The fraction of heat being transferred through the meniscus subregion is given by

$$\eta = \frac{q_{\mathrm{subregion}}}{\Psi h_{fg}} \tag{4}$$

Taking $k \sim 1.34$ W/m K, $t \sim 500$ μm, $\Delta r \sim 50$ μm, and $h_{fg} \sim 350.6$ kJ/kg (320 K, 1 atm), the values of η are estimated. The uncertainty in the value of η is estimated to be $\pm 10\%$. For the case $q_s'' = 810$ W/m^2 and $\Psi = 9.35 \times 10^{-7}$ kg/s, using the temperature data (Fig. 8(*c*)) and Eq. (3) gives $q_{\mathrm{subregion}} = 0.22$ W, $q_{\mathrm{I}} = 0.21$ W, and $q_{\mathrm{II}} = 0.01$ W. This shows that the applied heat flux (q_{II}) contributes very little ($<5\%$) to the subregion heat transfer; similar behavior is observed in all the experimental results. Therefore, a small change in q_s'' does not change the value of $q_{\mathrm{subregion}}$ and consequently of η. Table 1 summarizes the percentage contribution of subregion heat transfer to total heat transfer for all the experimental results obtained in this work. Nearly 70% of the heat is seen to be dissipated through the subregion. This value is in reasonable agreement with reports in the literature [7,8,12]. While a more rigorous analysis including vapor-diffusion-coupled evaporation [24] would yield a more accurate value of η, two important trends may be noted from the results in Table 1: η increases with an increase in evaporation rate and an increase in heat flux. For a constant heat flux and with increasing evaporation rate, the average meniscus thickness in the subregion falls (see Fig. 4), thus bringing down the associated thermal resistance (as observed in Sec. 3.2) and enhancing η. As explained in Sec. 3.1, for a constant evaporation rate, the contact angle increases with an increase in heat flux. This increases the capillary pressure and consequently the liquid supply into the subregion, which results in an increase in η.

Table 1 Variation in the percentage contribution of the subregion heat transfer to the total (η,%) with heat flux (q_s'') and evaporation rate (Ψ)

	Ψ		
q_s''	8.35×10^{-7} kg/s	8.8×10^{-7} kg/s	9.35×10^{-7} kg/s
810 W/m^2	66	67	69
950 W/m^2	70	73	78
990 W/m^2	68	73	78
1030 W/m^2	76	79	84
1190 W/m^2	77	80	87

4 Conclusions

A novel experiment has been designed to investigate the heat transfer characteristics of the thin-film region in a two-dimensional meniscus. The effects of applied heat flux, evaporation rate, and channel width on thin-film evaporation are investigated. The liquid-vapor interfacial area increases with decrease in heat flux and increase in evaporation rate, and remains unaffected by small changes in channel width. Microscale infrared thermography revealed a distinct temperature drop at the triple line, indicating the effectiveness of thin-film heat transfer. This temperature drop was found to increase with increasing heat flux. An approximate heat balance analysis shows that nearly 70% of the heat transfer takes place from a subregion defined as a 50 μm long extent of the meniscus adjacent to the contact line. The subregion heat transfer is found to increase with an increase in heat flux and increase in evaporation rate.

In an ongoing work, a micro-particle image velocimetry (μPIV) study is being conducted to visualize flow into the thin-film region so that the mass flow feeding evaporation may be more accurately determined. A comprehensive model and a numerical simulation of the experiment are also being developed.

Acknowledgment

The authors acknowledge financial support for this work from members of the Cooling Technologies Research Center, a National Science Foundation Industry/University Cooperative Research Center at Purdue University.

Nomenclature

h_{fg} = latent heat of vaporization (kJ/kg)
k = thermal conductivity (W/m K)
q_s'' = applied heat flux (W/m^2)
$q_{\mathrm{subregion}}$ = heat flow through the subregion (W)
T = temperature (°C)
t = thickness of the wafer (μm)
w = channel width (μm)
r_0 = distance of contact line from axis (m)

Greek Symbols

η = fraction of heat flow through the subregion (%)
Ψ = evaporation rate (kg/s)
δr = differential length along the wafer
Δr = length of the subregion (μm)

Subscripts

bottom = titanium layer on the wafer underside
mean = mean of top and bottom temperatures
subregion = subregion near the contact line
top = wafer top surface

References

[1] Potash, M., Jr., and Wayner, P. C., Jr., 1972, "Evaporation From a Two-Dimensional Extended Meniscus," Int. J. Heat Mass Transfer, **15**, pp. 1851–1863.
[2] Derjaguin, B. V., 1955, "Definition and the Concept of and Magnitude of the Disjoining Pressure and Its Role in the Statics and Kinetics of Thin Layers of Liquids," Colloid J. USSR, **17**, pp. 191–197.
[3] Ward, C. A., and Duan, F., 2004, "Turbulent Transition of Thermocapillary Flow Induced by Water Evaporation," Phys. Rev. E, **69**, p. 056308.
[4] Dhavaleswarapu, H. K., Chamarthy, P., Garimella, S. V., and Murthy, J. Y., 2007, "Experimental Investigation of Steady Buoyant-Thermocapillary Convection Near an Evaporating Meniscus," Phys. Fluids, **19**, p. 082103.
[5] Wayner, P. C., 1999, "Intermolecular Forces in Phase-Change Heat Transfer: 1998 Kern Award Review," AIChE J., **45**, pp. 2055–2068.
[6] Ma, H. B., and Peterson, G. P., 1996, "Experimental Investigation of the Maximum Heat Transport in Triangular Grooves," ASME J. Heat Transfer, **118**, pp. 740–746.
[7] Holm, F. W., and Goplen, S. P., 1979, "Heat Transfer in Meniscus Thin Film Transition Region," ASME J. Heat Transfer, **101**, pp. 543–547.
[8] Stephan, P. C., and Busse, C. A., 1992, "Analysis of the Heat Transfer Coefficient of Grooved Heat Pipe Evaporator Walls," Int. J. Heat Mass Transfer, **35**, pp. 383–391.

[9] Xu, X., and Carey, V. P., 1990, "Film Evaporation From a Microgrooved Surface—An Approximate Heat Transfer Model and Its Comparison With Experimental Data," J. Thermophys. Heat Transfer, **4**, pp. 512–520.
[10] Demsky, S. M., and Ma, H. B., 2004, "Thin Film Evaporation on a Curved Surface," Microscale Thermophys. Eng., **8**, pp. 285–299.
[11] Park, K., and Lee, K., 2003, "Prediction of the Transport Phenomena in the Micro Capillary Tube of a CPL System," ASME International Mechanical Engineering Congress, Washington, D.C.
[12] Wang, H., Garimella, S. V., and Murthy, J. Y., 2007, "Characteristics of an Evaporating Thin Film in a Microchannel," Int. J. Heat Mass Transfer, **50**, pp. 3933–3942.
[13] Mirzamoghadam, A. V., and Catton, I., 1988, "Holographic Interferometry Investigation of Enhanced Tube Meniscus Behavior," ASME J. Heat Transfer, **110**, pp. 208–213.
[14] Dasgupta, S., Schonberg, J. A., and Wayner, P. C., Jr., 1993, "Investigation of Evaporating Extended Meniscus With Augmented Young–Laplace Equation," ASME J. Heat Transfer, **115**, pp. 201–208.
[15] Panchamgam, S. S., Gokhale, S. J., Plawsky, J. L., Dasgupta, S., and Wayner, P. C., Jr., 2005, "Experimental Determination of Disjoining Pressure of Shear in the Contact Line Region of a Moving Evaporating Thin Film," ASME J. Heat Transfer, **127**, pp. 231–243.
[16] Höhmann, C., and Stephan, P., 2002, "Microscale Temperature Measurement at an Evaporating Liquid Meniscus," Exp. Therm. Fluid Sci., **26**, pp. 157–162.
[17] Buffone, C., and Sefiane, K., 2005, "Temperature Measurement Near the Triple Line During Phase Change Using Thermochromic Liquid Crystal Thermography," Exp. Fluids, **39**, pp. 99–110.
[18] Jiang, J., Tao, Y.-X., and Byrd, L., 2000, "Evaporative Heat Transfer From Thin Liquid Film on a Heated Cylinder," Int. J. Heat Mass Transfer, **43**, pp. 85–99.
[19] Buffone, C., and Sefiane, K., 2004, "IR Measurements of Interfacial Temperature During Phase Change in a Confined Environment," Exp. Therm. Fluid Sci., **29**, pp. 65–74.
[20] Viskanta, R., and Anderson, E. E., 1975, "Heat Transfer in Semitransparent Solids," Adv. Heat Transfer, **2**, pp. 318–434.
[21] Tuntomo, A., Tien, C. L., and Park, S. H., 1992, "Optical Constants of Liquid Hydrocarbon Fuels," Combust. Sci. Technol., **84**, pp. 133–140.
[22] NASA Jet Propulsion Laboratory Web Site, URL: http://masterweb.jpl.nasa.gov/reference/paints.htm
[23] 2005, MATLAB, The Language of Technical Computing, Version 7.1, The Mathworks Inc., Natick, MA.
[24] Wang, H., Garimella, S. V., and Murthy, J. Y., 2008, "Transport From a Volatile Meniscus in a Microtube," Int. J. Heat Mass Transfer, **51**, pp. 3007–3017.

Influence of Film-Hole Shape and Angle on Showerhead Film Cooling Using PSP Technique

Zhihong Gao[1]

Je-Chin Han

Department of Mechanical Engineering,
Turbine Heat Transfer Laboratory,
Texas A&M University,
College Station, TX 77843-3123

The effect of film-hole geometry and angle on turbine blade leading edge film cooling has been experimentally studied using the pressure sensitive paint technique. The leading edge is modeled by a blunt body with a semicylinder and an after-body. Two film cooling designs are considered: a heavily film cooled leading edge featured with seven rows of film cooling holes and a moderately film cooled leading edge with three rows. For the seven-row design, the film holes are located at 0 deg (stagnation line), ±15 deg, ±30 deg, and ±45 deg on the model surface. For the three-row design, the film holes are located at 0 deg and ±30 deg. Four different film cooling hole configurations are applied to each design: radial angle cylindrical holes, compound angle cylindrical holes, radial angle shaped holes, and compound angle shaped holes. Testing was done in a low speed wind tunnel. The Reynolds number, based on mainstream velocity and diameter of the cylinder, is 100,900. The mainstream turbulence intensity is about 7% near of leading edge model and the turbulence integral length scale is about 1.5 cm. Five averaged blowing ratios are tested ranging from $M=0.5$ to $M=2.0$. The results show that the shaped holes provide higher film cooling effectiveness than the cylindrical holes, particularly at higher average blowing ratios. The radial angle holes give better effectiveness than the compound angle holes at $M=1.0-2.0$. The seven-row film cooling design results in much higher effectiveness on the leading edge region than the three-row design at the same average blowing ratio or same amount coolant flow. [DOI: 10.1115/1.3082413]

Keywords: leading edge film cooling, pressure sensitive paint (PSP), shaped hole, compound angle

1 Introduction

Thermal efficiency and power output of gas turbine engines increase with increasing rotor inlet temperatures. The operating temperatures are far above the permissible metal temperatures. Advanced cooling technologies must be applied to ensure that the metal can withstand these extreme conditions. Han et al. [1] described many cooling techniques that are commonly used in various combinations to increase the lifetime of turbine blades. Film cooling has been widely accepted as an active cooling method in high pressure and high temperature blades. In a film cooled component, relatively cooler air is ejected through discrete holes or slots to provide a protective film between the hot mainstream gas and the turbine component to maintain the surface at acceptable temperature thus protecting the turbine component surface.

The leading edge of the turbine blades is subject to the greatest heat load due to flow stagnation. Many researchers used a cylinder or semicylinder to model the blade leading edge. The leading edge film cooling has been investigated under different freestream flow conditions. Luckey et al. [2] simulated the airfoil leading edge using a cylinder with several film cooling rows. They correlated their results for the optimum blowing ratio and injection angle. Karni and Goldstein [3] studied the effect of blowing ratio and injection location on the mass transfer coefficient. Mick and Mayle [4] studied the effects of coolant blowing ratio and film cooling hole location on the stagnation region. Mehendale and Han [5,6] investigated the effects of Reynolds number and turbulence on heat transfer and film cooling effectiveness. Ou et al. [7] presented the effects of film-hole location and inclined film slots on leading edge film cooling heat transfer. Ekkad et al. [8] presented the effects of coolant density and freestream turbulence. Using the same test facility, Gao et al. [9] assessed the pressure sensitive paint (PSP) and transient infrared thermography techniques. Funazaki et al. [10] studied the effects of unsteady wake on the leading edge film cooling effectiveness. Ou and Rivir [11] examined the effects of turbulence intensity, blowing ratio, and Reynolds number.

Some studies have been conducted in cascade environment. Nirmalan and Hylton [12] studied the effects of various parameters on film cooling in a turbine vane cascade under conditions similar to the ranges of actual engines. Abuaf et al. [13] presented heat transfer coefficients and film effectiveness on a film cooled vane. Cruse et al. [14] studied the effect of leading edge shape. Ekkad et al. [15] studied the combined effects of unsteady wake and freestream turbulence on the film cooling effectiveness and the heat transfer coefficients with air and CO_2 film injection. Cutbirth and Bogard [16] studied the effects of coolant density ratio on film cooling effectiveness on a simulated turbine vane. Mhetras and Han [17] studied the effects of upstream wake on the leading edge film cooling effectiveness in a five-blade linear cascade. Some researchers studied leading edge film cooling under rotating environment. Dring et al. [18] investigated film cooling performance in a low speed rotating facility. Takeishi et al. [19] also reported the film cooling effectiveness distributions on a low speed stator-rotor stage using a rotating rig with a one-stage turbine model. Abhari and Epstein [20] investigated time-resolved measurements of heat transfer on a cooled transonic turbine stage. Using a short-duration blowdown turbine test facility, they simulated full engine parameters. Ahn et al. [21,22] studied film cooling effectiveness on the leading edge with two-row and three-row hole injections under rotating conditions in a three-stage turbine using the PSP technique.

[1]Present address: Siemens Energy, 11842 Corporate Blvd., Orlando, FL 32817.

Contributed by the Heat Transfer Division of ASME for publication in the JOURNAL OF HEAT TRANSFER. Manuscript received June 4, 2007; final manuscript received December 4, 2008; published online March 30, 2009. Review conducted by Sai C. Lau.

The film cooling holes used in the above studies were cylindrical, angled in the radial direction; more recently, shaped holes have come into consideration for the leading edge film cooling. Mouzon et al. [23] compared the film performance between laidback and cylindrical holes on a three-row leading edge model. The holes were located at 0 deg and ±20 deg, inclined at 45 deg to the surface and angled in the radial (spanwise) direction. They found that the laidback holes resulted in much higher net heat flux reduction than the cylindrical holes. Falcoz et al. [24] investigated cylindrical holes, conical holes, and laidback (forward diffused) holes on a leading model. Four rows of film holes were located at ±22.5 deg and ±7.5 deg. The holes were angled in the radial direction and inclined 45 deg to the surface. The hole-to-hole spacing was $p=4d$. Their results indicated that the laidback holes showed a better lateral coverage. The best spanwise averaged film cooling effectiveness was achieved by conical holes. Kim and Kim [25] studied cylindrical holes and laidback holes and tear-drop shaped (both laterally and forward expanded) holes. Three rows of radial angle holes were located at 0 deg and ±23 deg with a hole-to-hole spacing of $p/d=7.5$. The holes were inclined 30 deg to the surface. They showed that the holes with a laidback type widened exits gave higher film cooling effectiveness than tear-drop shaped holes. Both laidback holes and tear-drop shaped holes were found to perform better than cylindrical holes. Reiss and Bölcs [26] studied the effects of shaped holes with compound angle orientation. They compared cylindrical holes, laidback (forward diffused) holes, and fan-shaped (laterally diffused) holes. Five rows of leading edge film holes were located at 0 deg, ±20 deg, and ±40 deg. The holes at stagnation row were angled in the radial direction while the other rows were angled 60 deg to the mainstream direction. The holes were inclined 45 deg to the surface. They found that laidback holes gave the best overall film cooling performance. The fan-shaped holes performed better than cylindrical holes, but not as well as laidback holes. Lu et al. [27] also studied the effects of hole orientation and hole shape on leading edge film cooling. They examined compound angle cylindrical holes and compound angle laidback fan-shaped holes. Three rows of film cooling holes were located at 0 deg and ±15 deg with a hole-to-hole spacing of $p/d=4$. These holes were inclined 30 deg to the surface. The compound angle holes were angled at 30 deg or 45 deg with respect to the local mainstream direction. They found that the shaped holes gave much higher effectiveness than cylindrical holes. For the compound angle holes, the effectiveness was improved at lower blowing ratios, but reduced at higher blowing ratios due to jet liftoff.

There are a lot of constraints pertaining to leading edge film cooling. The limited space, small wall thickness, and high curvature are obstacles to leading edge film cooling study. The research on shaped holes and varying hole angles is limited, especially for heavily film cooled designs. It is a challenge to acquire accurate effectiveness data in a heat transfer experiment. An error due to thermal conduction always exists in effectiveness measurements using conventional heat transfer methods, such as IR, transient liquid crystal, etc. Correction for conduction error becomes more difficult for film holes with close spacing and large incline angles. In this study, the PSP technique is used to measure the adiabatic film cooling effectiveness. Since the PSP method is based on the heat and mass transfer analogy, the conduction error associated with heat transfer measurement is eliminated. In addition, the PSP measurement is not limited by surface curvature. Two leading edge film cooling designs are investigated: a heavily film cooled design with seven rows of film holes and a moderately film cooled design with three rows. Four different film-hole configurations will be applied to the two designs: radial angle cylindrical holes, compound angle cylindrical holes, radial angle shaped holes, and compound angle shaped holes.

2 Experimental Facility

Figure 1 schematically shows the experimental setup. The mainstream flow travels through a nozzle and into the test tunnel. The test section is placed in the wind tunnel. The center of the cylinder is located at 73.7 cm downstream of the nozzle exit. The mainstream flow was adjusted to maintain a Reynolds number of 100,900 (based on the cylinder diameter). To increase the

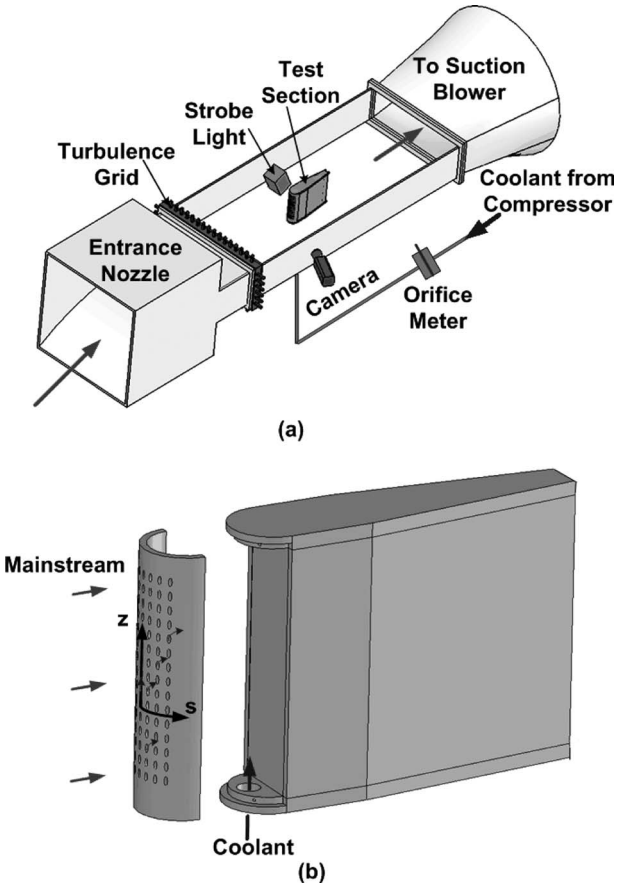

Fig. 1 (*a*) Test facilities and (*b*) test section

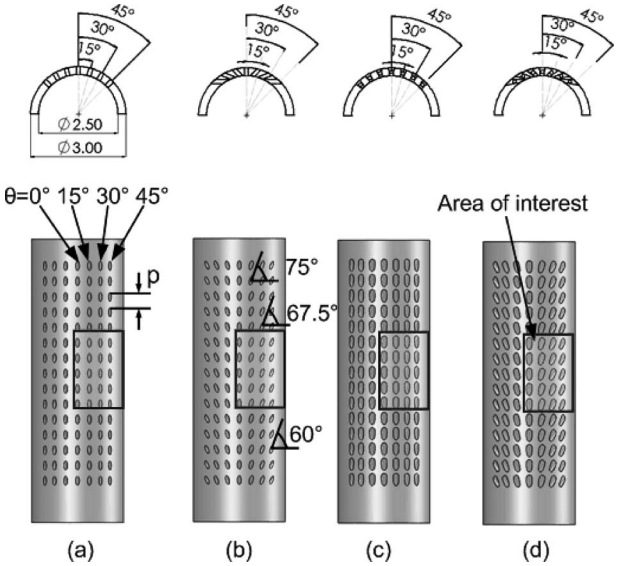

Fig. 2 Seven-row film cooled leading edge models: (*a*) radial angle cylindrical holes, (*b*) compound angle cylindrical holes, (*c*) radial angle shaped holes, and (*d*) compound angle shaped holes

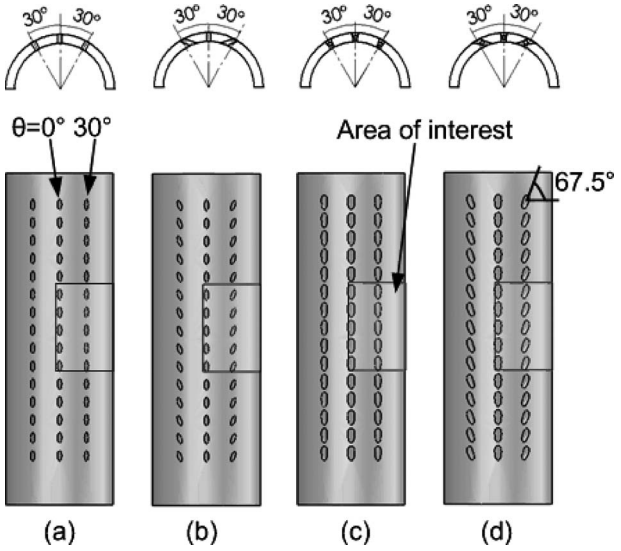

Fig. 3 Three-row film cooled leading edge models: (*a*) radial angle cylindrical holes, (*b*) compound angle cylindrical holes, (*c*) radial angle shaped holes, and (*d*) compound angle shaped holes

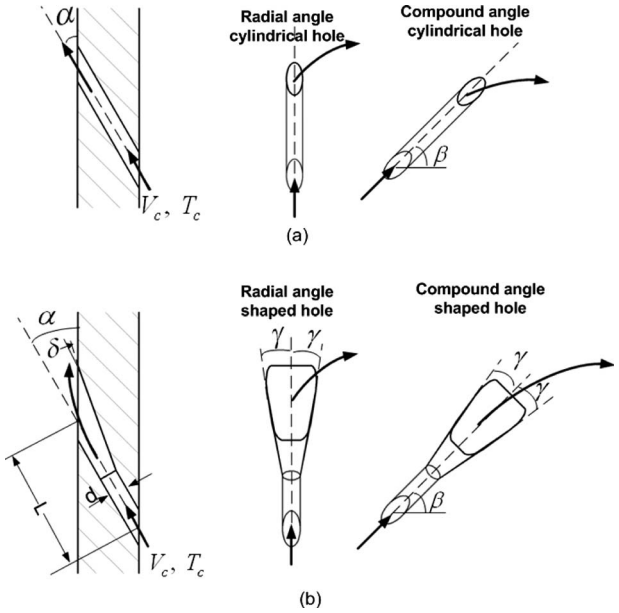

Fig. 4 Definition of hole shape and orientations: (*a*) cylindrical hole and (*b*) shaped hole

freestream turbulence of the mainstream flow, a turbulence grid is added at the exit of the nozzle. With the grid, a turbulence intensity of 7% with a turbulence integral length scale of about 1.5 cm was measured near the cylinder. The test tunnel was made of Plexiglas for optical access. The excitation light and camera for PSP measurement are placed outside of the wind tunnel, as indicated in Fig. 1. A close view of the test section is shown in Fig. 1(*b*). The airfoil leading edge is modeled as a blunt body with a semicylinder and an after-body. The semicylinder, made using stereolithography (SLA), can be detached from the after-body when changing the film-hole configuration. The semicylinder has a diameter of 7.62 cm, height of 25.4 cm, and wall thickness of 0.64 cm. The hollow semicylinder serves as a coolant plenum. Coolant flow travels through an orifice flow meter and enters the test model from the bottom. The coolant ejects to mainstream through the film cooling holes. Definition of the coordinate system that is used to present the effectiveness data in the later section of this paper can also be found in Fig. 1(*b*).

Figure 2 shows the seven-row film-hole configurations. The seven rows are located at 0 deg (stagnation line), ±15 deg, ±30 deg, and ±45 deg on either side of the leading edge model. For the radial angle holes (either cylindrical holes or shaped holes), the holes are oriented in the radial (spanwise) direction and orthogonal to the local mainstream direction. For the compound angle holes, each row is oriented at different angles with respect to the local mainstream due to the constraint of the space. As shown in Figs. 2(*b*) and 2(*d*), the holes are oriented (β) at 90 deg, 75 deg, 67.5 deg, and 60 deg to the local mainstream flow for the row 0 deg, ±15 deg, ±30 deg, and ±45 deg, respectively. Figure 3 shows the three-row film-hole configurations. Three rows of holes are located at 0 deg (stagnation line) and ±30 deg. Holes at ±30 deg are oriented at 67.5 deg to the local mainstream direction in the compound angle design. The stagnation row is always angled to the radial direction. For both seven-row and three-row designs, each row has 15 holes with a hole-to-hole spacing $p=4d$ in the spanwise direction. The film-hole orientations and the shaped-hole angles are shown in Fig. 4. All these holes are angled (α) at 25 deg to the model surface and arranged inline pattern. The shaped holes are laidback fan-shaped holes with lateral expansion (γ) of 5 deg from the film-hole axis, and additional 5 deg (δ) forward expansion to the surface. The metering part of the shaped holes has the same diameter ($d=0.32$ cm) as the cylindrical holes. Expansion of shaped holes starts in the middle of each hole. This

Table 1 Film cooling hole configurations

	Design 1 (seven-row)				Design 2 (three-row)			
	Cylindrical holes		Shaped holes		Cylindrical holes		Shaped holes	
Hole configurations	Radial angle	Compound angle	Radial angle	Compound angle	Radial angle	Compound angle	Radial angle	Compound angle
Hole diameter (d) (cm)	0.3715	0.3715	0.3715	0.3715	0.3715	0.3715	0.3715	0.3715
Diameter ratio (D/d)	24	24	24	24	24	24	24	24
Hole-to-hole spacing (p/d)	4d	4d	4d	4d	4d	4d	4d	4d
Ratio of hole length to diameter (L/d)	4.73	4.73–5.46	4.73	4.73–5.46	4.73	4.73–5.46	4.73	4.73–5.46
Lateral expansion angle (γ) (deg)	0	0	5	5	0	0	5	5
Forward expansion angle (δ) (deg)	0	0	5	5	0	0	5	5
Angle to surface (α) (deg)	25	25	25	25	25	25	25	25
Streamwise angles (β) (deg)	90	90/75/67.5/60	90	90/75/67.5/60	90	90/67.5	90	90/67.5
Ratio of hole breakout area to metering cross-section area	1.0	1.0	1.9	1.9/1.94/1.98/2.1	1.0	1.0	1.9	1.9/1.98

results in an area ratio about 2 between the expanded cross section at the film-hole exit and the metering part. Details of holes' dimension can be found in Table 1.

3 Film Cooling Effectiveness Measurement Theory and Data Analysis

Data for film cooling effectiveness were obtained using the PSP technique. PSP is a photoluminescent material that emits light when excited, with the emitted light intensity inversely proportional to the partial pressure of oxygen. This light intensity is recorded using a charge coupled device (CCD) camera. The image intensity obtained from PSP by the camera during data acquisition is normalized with a reference image intensity (I_{ref}) taken under no-flow condition. Background noise in the optical setup is removed by subtracting the image intensities with the image intensity obtained under no-flow conditions and without light excitation (I_{blk}). The resulting intensity ratio can be converted to pressure ratio using a predetermined calibration curve and can be expressed as

$$\frac{I_{\text{ref}} - I_{\text{blk}}}{I - I_{\text{blk}}} = f\left(\frac{(P_{O_2})_{\text{air}}}{(P_{O_2})_{\text{ref}}}\right) = f(P_{\text{ratio}}) \tag{1}$$

where I denotes the intensity obtained for each pixel and $f(P_{\text{ratio}})$ is the relationship between intensity ratio and pressure ratio obtained after calibration.

Correlation between the PSP emitting intensity and the oxygen partial pressure is necessary for determining the film cooling effectiveness. Calibration of the PSP emitting intensity versus oxygen partial pressure was performed in a vacuum chamber by varying the pressure from 0 atm to 1.0 atm. A PSP coated test specimen was placed in the vacuum chamber. The top wall of the vacuum chamber was made of Plexiglas for optical access. The distance and orientation of the exciting light and the CCD camera for the calibration tests were the same as used in showerhead film cooling experiments. The calibration curve is shown in Fig. 5. PSP is also sensitive to temperature with higher temperatures resulting in lower light emission. During the tests, all the test facilities and flow were maintained at 22°C.

To obtain film cooling effectiveness, air and nitrogen are used alternately as coolant. Nitrogen, which has nearly the same molecular weight as that of air, mixes with the oxygen molecules on the surface causing a change in the emitted light intensity from PSP. By noting the difference in partial pressure between the air and nitrogen injection cases, the film cooling effectiveness can be determined using the following equation:

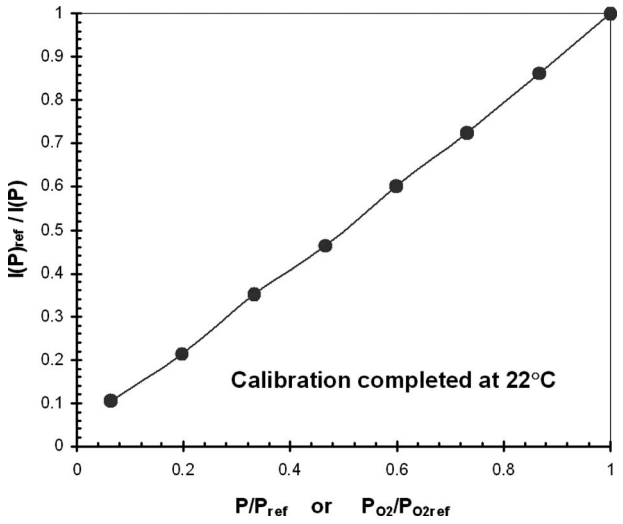

Fig. 5 PSP calibration curve

$$\eta = \frac{C_{\text{mix}} - C_{\text{air}}}{C_{N_2} - C_{\text{air}}} = \frac{C_{\text{air}} - C_{\text{mix}}}{C_{\text{air}}} = \frac{(P_{O_2})_{\text{air}} - (P_{O_2})_{\text{mix}}}{(P_{O_2})_{\text{air}}} \tag{2}$$

where C_{air}, C_{mix}, and C_{N_2} are the oxygen concentrations of mainstream air, air/nitrogen mixture, and nitrogen on the test surface, respectively. The definition of film effectiveness in Eq. (2) based on heat and mass transfer analogy assumes similar form as that of adiabatic film cooling effectiveness given in Eq. (3)

$$\eta = \frac{T_{\text{mix}} - T_m}{T_c - T_m} \tag{3}$$

The semicylinder test section under investigation was coated with PSP using an air brush. It was excited by a strobe light fitted with a narrow band-pass interference filter (optical wavelength = 520 nm). Upon excitation, the PSP coated surface emitted light with a wavelength longer than 600 nm. A 12-bit scientific grade CCD camera (Cooke Sensicam QE with CCD temperature maintained at −15°C using two-stage Peltier cooler), fitted with a 35 mm lens and a 600 nm long-pass filter, was used for recording images. The filter mounted on the camera is chosen so that it does not allow any reflected light from the illumination source to pass through. The camera and the strobe light were triggered simultaneously using a transistor-transistor logic (TTL) signal from a function generator. A total of 200 tagged image file (TIF) images were captured and ensemble averaged to get the individual intensities. The spatial resolution of each image was 0.8 mm/pixel. A computer program was used to convert these pixel intensities into pressure using the calibration curve and then into film cooling effectiveness. The coolant flow rate into the test section was set using an orifice meter based on prior calculation for the desired average blowing ratio.

Uncertainty calculations were performed based on a confidence level of 95% based on the uncertainty analysis method of Coleman and Steele [28]. Lower effectiveness magnitudes have higher uncertainties. For an effectiveness magnitude of 0.3, uncertainty was around ±1% while for an effectiveness magnitude of 0.05, uncertainty was as high as ±8%. This cumulative uncertainty is the result of uncertainties in calibration (4%), image capture (1%), and blowing ratio (4%).

4 Results and Discussion

4.1 Local Blowing Ratio Distribution. Film cooling effectiveness was measured at five average blowing ratios ranging from $M = 0.5$ to $M = 2.0$. The average blowing ratio is defined as $M = \rho_c V_c / \rho_m V_m$, i.e., the coolant mass flux to the freestream mass flux ratio. The coolant to mainstream density ratio in the current study is unity; therefore, the mass flux ratio is reduced to velocity ratio. Based on the above definition, the coolant mass flow rate ($\dot{m}_c$) for a given averaged blowing ratio was determined by Eq. (4) and supplied to the coolant plenum

$$\dot{m}_c = nM\rho_m V_m(\pi d^2/4) \tag{4}$$

The driving force for the coolant ejection through the holes is pressure differential between the total pressure inside the coolant plenum and external static pressure on the cylinder surface. The higher the pressure differential, the more the coolant ejects through the holes. The actual coolant velocity from the film holes $V_{c,\text{local}}$ is subject to the spanwise variation in internal total pressure and circumferential variation in outer static pressure. To obtain the actual coolant mass flow rate from each hole, the discharge coefficient C_D is calculated by

$$\dot{m}_c = \sum_{i=1}^{n} C_D \cdot \rho_c \cdot \frac{\pi}{4} d^2 \cdot \sqrt{2(P_{t,\text{plenum}} - P)/\rho_c} \tag{5}$$

The pressure inside the coolant plenum was measured by pressure taps. Three pressure taps were placed along the middle five-hole span region. Uniform internal pressure was found in the middle

five-hole span region. Therefore, the effect of spanwise variation in internal pressure on coolant ejection flow can be eliminated in the area of interest. Therefore, the coolant ejection flow can be determined by the outer pressure variation in the circumferential direction. The outer pressure P on the cylinder surface was measured by PSP. In Eq. (5), a constant discharge coefficient C_D is assumed for all the holes at a given averaged blowing ratio M. It should be noted that the constant assumption of C_D may not be true as C_D depends on not only the film-hole geometry but also the external and internal flow conditions. It is assumed that the deviation in the discharge coefficients from hole to hole is not significant and hence an average value can be used without introducing significant error. By solving Eqs. (4) and (5), the C_D can be obtained for a given M. Once the C_D for a given M is determined, the coolant velocity from the holes in a row is calculated by

$$V_{c,\text{local}} = C_D \cdot \sqrt{2(P_{t,\text{plenum}} - P)/\rho_c} \tag{6}$$

It is found that the coolant mass flow rate increases from the stagnation to downstream. The higher outer pressure prohibits the coolant exiting from the stagnation row. More coolant goes to the downstream rows where the outer static pressure is relatively lower. To better understand the effect of blowing ratio, the local blowing ratio, defined as $M_{\text{local}} = \rho_c V_{c,\text{local}} / \rho_m V_{m,\text{local}}$, is examined for film holes at row 15 deg, 30 deg, and 45 deg. $V_{m,\text{local}}$ is the local mainstream velocity, determined from the local static pressure on the model surface and freestream total pressure. The local static pressure P was measured by PSP. Since the local mainstream velocity in the stagnation line is 0, the freestream velocity is used to normalize the coolant velocity for the stagnation row to indicate how much coolant is released from the stagnation row. Although a different denominator is used for the stagnation row, the same notation (M_{local}) is used to present the local blowing ratios. Figure 6 shows the local blowing ratio distribution with compound angle holes. It can be seen that the difference in local blowing ratio for cylindrical and shaped holes is very small. For the seven-row design, the higher $V_{m,\text{local}}$ results in a lower local blowing ratio in the downstream rows, although more coolant ejects from the downstream holes. Local blowing ratios for the stagnation row (if normalized with $V_{m,\text{local}}$) and 15 deg row are significantly higher than the other two rows. M_{local} values for rows at 30 deg and 45 deg are comparable. Local blowing ratio distributions for the three-row design with compound angle holes are presented in Fig. 6(*b*). Local blowing ratios for the radial angle holes are similar in value to corresponding compound angle holes and are omitted from this presentation.

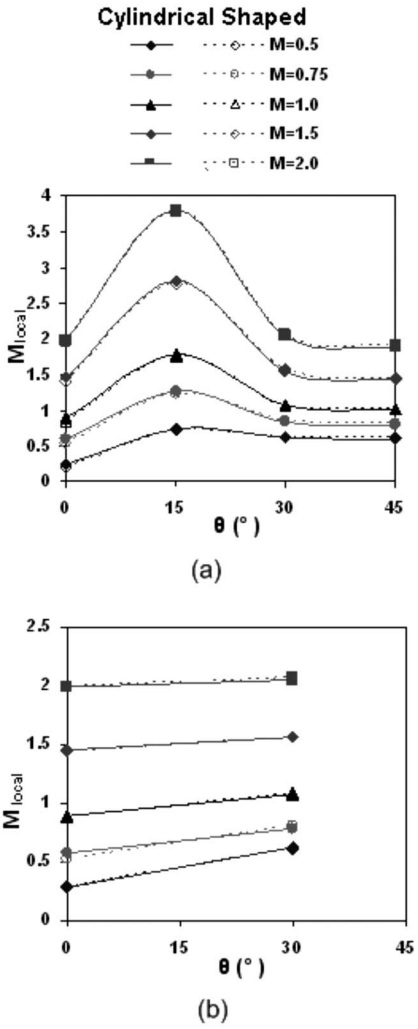

Fig. 6 Schematic of local coolant mass flow rate distribution and local blowing ratio: (*a*) seven-row design and (*b*) three-row design

5 Film Cooling Effectiveness on the Leading Edge Models

Due to the flow symmetry, film cooling effectiveness on one side of the cylinder in the middle five-hole region was measured with the PSP technique. The film cooling effectiveness distribution for the seven-row design is shown in Fig. 7. The first row of the film holes represents the stagnation row. Radial angle cylindrical holes (which are commonly used in gas turbine airfoils) are chosen as the baseline. The film cooling effectiveness data for the baseline case are shown in Fig. 7(*a*). In the stagnation region, the mainstream momentum is small; the coolant from the stagnation row is ejected along the radial direction without being deflected. In the downstream region, the mainstream momentum increases. Subject to the mainstream, the coolant jets are deflected. The interaction between coolant and mainstream is determined by the momentum ratio. When the local blowing ratio increases, the coolant to mainstream momentum ratio also increases. With increased momentum ratio, the coolant jet tends to follow the ejection direction and is less deflected. For a given averaged blowing ratio M, the local blowing ratios from the upstream rows are larger than the local blowing ratios from the downstream rows. Consequently, the coolant traces from the upstream holes follow the ejection directions and are less deflected. Similarly, for a given row of cooling holes, the jets are less deflected at higher average blowing ratios (because M_{local} increases with M). At low and medium average blowing ratios ($M = 0.5–1.0$), the coolant jets are deflected to the streamwise direction, so the coolant accumulation effect is evident downstream of film cooling rows. This is observed by the elevated film cooling effectiveness in the downstream region. The coolant accumulation in the radial direction is not significant at these lower average blowing ratios. However, at higher average blowing ratios ($M = 1.5$ and 2.0), the upper portion of the leading edge model (with larger z/d) shows higher effectiveness due to coolant trace accumulation in the radial direction. In the stagnation region ($0 < s/d < 3$), the film effectiveness seems to increase with increasing average blowing ratio. More coolant accumulates around the stagnation region with more coolant injection. In the downstream region ($s/d > 10$), with increasing average blowing ratio, the accumulated film effectiveness region increases in the radial direction but decreases in the streamwise direction. This is because more coolant accumulates in the radial direction with higher average blowing ratios. Inside the film cooling holes, the film cooling effectiveness is slightly less than 1 because some mixing with mainstream occurs inside the hole.

The effect of hole angle can be detected by comparing Figs. 7(*a*) and 7(*b*). For the compound angle holes, the angle of film

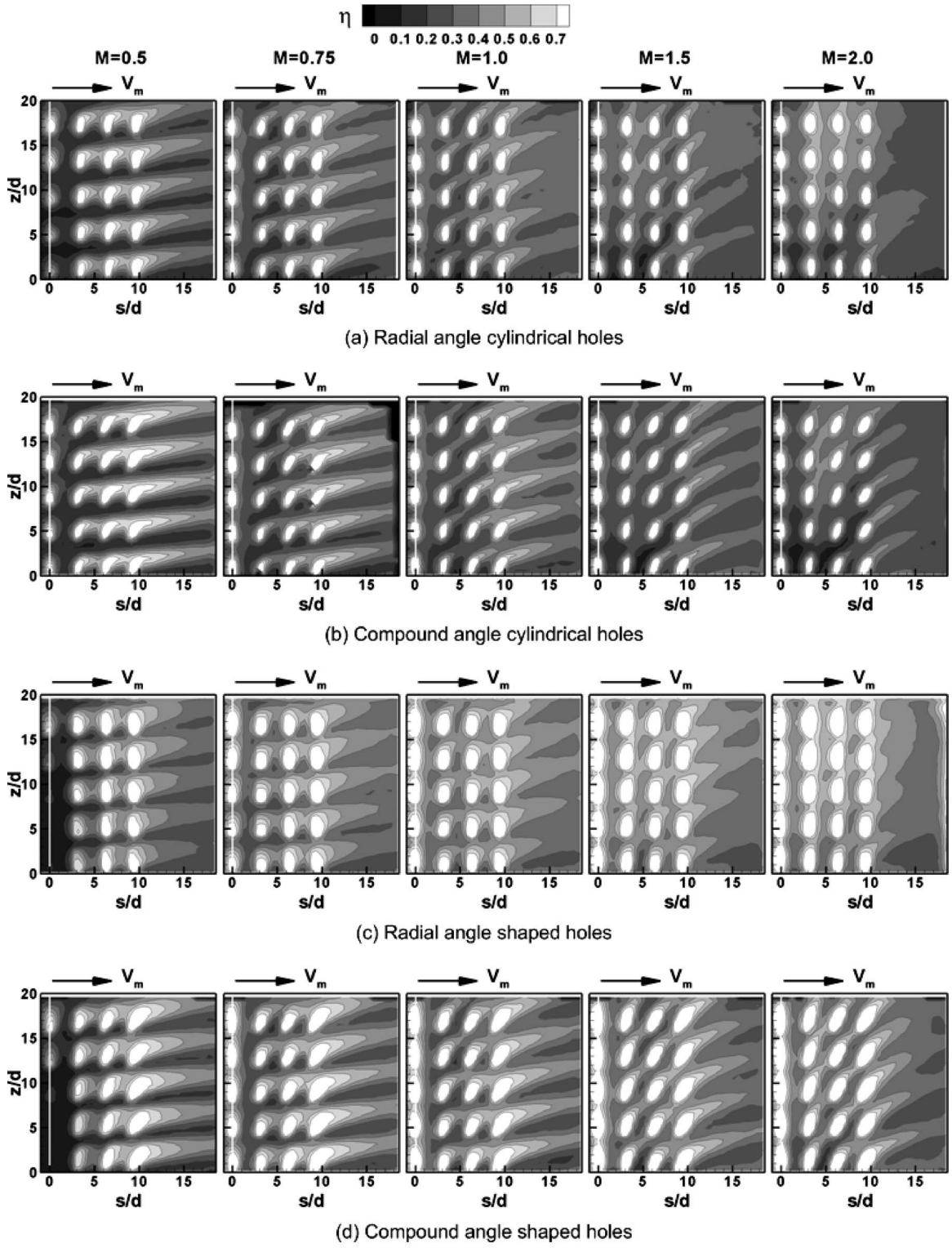

Fig. 7 Film cooling effectiveness distribution for seven-row design

holes to mainstream reduces (except for the stagnation row). The coolant jets are less deflected by the mainstream. Consequently, the coolant traces with elevated effectiveness become narrower and longer instead of spreading out more. The coolant accumulation in the radial direction, compared with radial angle holes, is less significant even at the highest average blowing ratio $M=2.0$. At lower averaged blowing ratios ($M=0.5$ and $M=0.75$), it seems that the compound angle holes result in higher effectiveness than the radial angle holes. However, at higher average blowing ratios ($M=1.5$ and $M=2.0$), the effectiveness from compound angle cylindrical holes becomes lower than from radial angle cylindrical holes. This is largely due to the jet spreading out less due to the compound angle holes.

The film cooling effectiveness distribution for radial angle shaped holes is shown in Fig. 7(*c*). Compared with the cylindrical holes (both radial angle and compound angle), the effectiveness

for the shaped holes significantly increases except for the stagnation row at $M=0.5$. The coolant jet momentum reduces due to the shaped-hole expansion. With lower jet momentum, the coolant jet tends to stay closer to the surface. The interaction between the coolant jet and mainstream flow also reduces. Therefore, coolant jet is less mixed with the mainstream flow resulting in better film protection. The advantage of the shaped holes becomes more evident at higher average blowing ratios. Similar to the radial angle cylindrical holes, the streamwise coolant accumulation is more noticeable at lower average blowing ratios; the spanwise (radial direction) coolant accumulation is more evident at higher average blowing ratios. The film effectiveness between the hole rows ($0<s/d<10$) increases with the increase in average blowing ratio. This is consistent with the observation on the radial angle cylindrical holes. Further downstream, ($s/d>10$), the effectiveness for the radial angle shaped hole increases from $M=0.5$ to $M=1.5$. At $M=2.0$, more coolant goes to the radial direction, resulting in a slightly lower effectiveness in the downstream region.

Figure 7(*d*) shows the effectiveness distribution for the compound angle shaped holes. Compared with the corresponding radial angle holes, the coolant trace with elevated effectiveness for the compound angle shaped holes becomes narrower and longer. This is similar to the observation for the cylindrical holes with

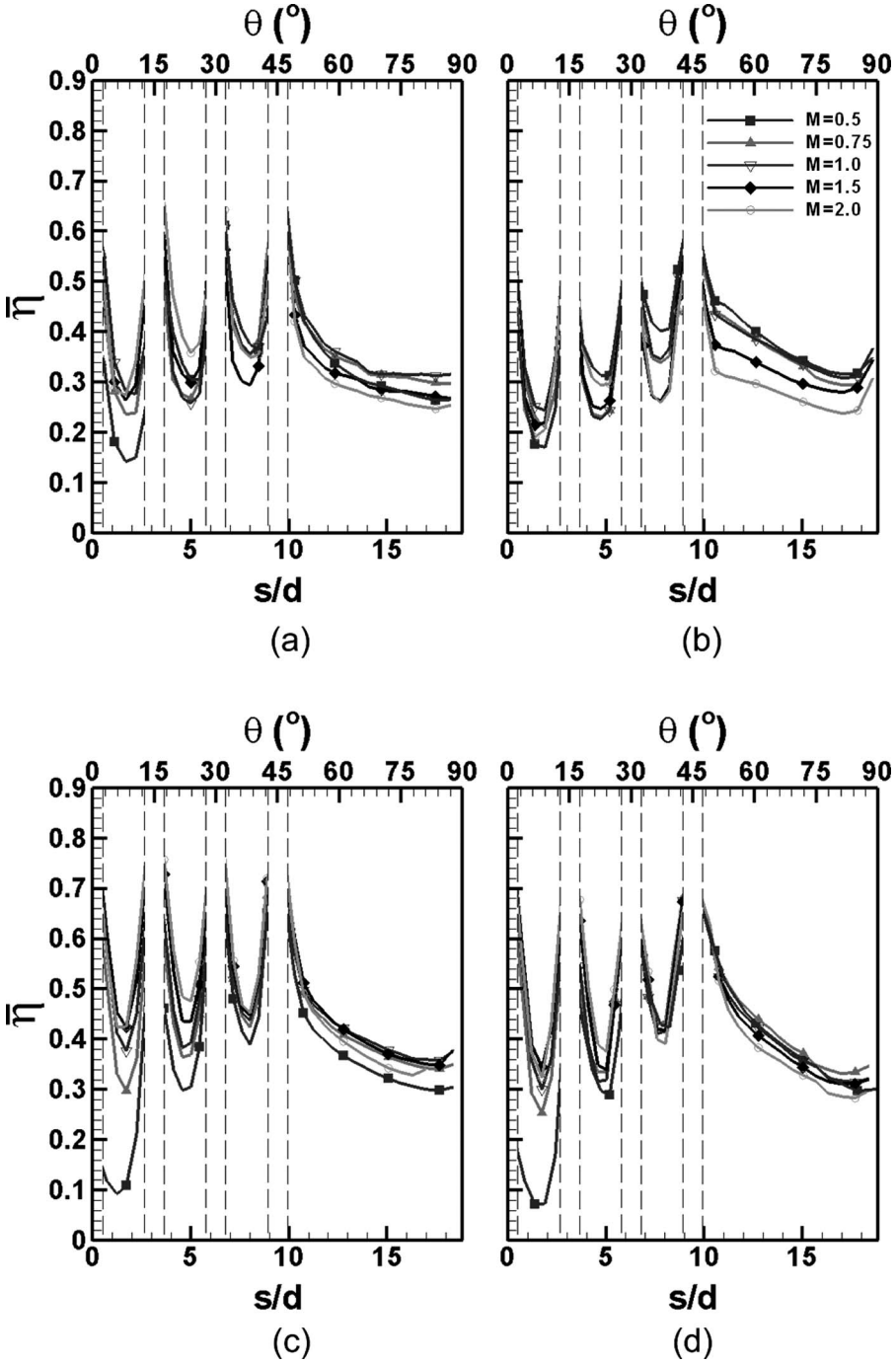

Fig. 8 Effect of blowing ratio on spanwise averaged film effectiveness (seven-row design): (*a*) radial angle cylindrical holes, (*b*) compound angle cylindrical holes, (*c*) radial angle shaped holes, and (*d*) compound angle shaped holes

different hole angles. At higher average blowing ratios $M=1.5$ and $M=2.0$, the effectiveness reduces because the coolant jets spread out less. The area between the holes (in the spanwise direction) is less protected. At lower average blowing ratios $M=0.5-1.0$, the compound angle shaped holes seem to offer better effectiveness than radial angle shaped holes for the region downstream of film holes ($s/d>10$).

Figures 8 and 9 are the spanwise averaged effectiveness for the seven-row models. The data are presented in terms of s/d and θ (angle to the stagnation line), which are depicted in the bottom and top x-axes, respectively. The effectiveness along the hole-row locations is masked; only the effectiveness on the cylinder surface is presented. Figure 8 shows the influence of average blowing ratio on the film cooling effectiveness. The film cooling effectiveness near the stagnation region ($s/d<6$ or $\theta<30$ deg) increases with the increase in average blowing ratio. Further downstream ($s/d>10$ or $\theta>45$ deg), the trend is reversed. With multiple rows of film cooling design, the coolant accumulation effect can be detected from the elevated effectiveness in the downstream region. The variation in effectiveness with averaged blowing ratio is relatively small for the shaped holes, particularly, for the compound angle shaped holes.

Figure 9 shows the effect of film-hole configuration on film cooling effectiveness. For the stagnation rows, the holes are all angled to the radial direction; therefore, the lines for the same hole shape fall together. In general the shaped holes give better effectiveness than the cylindrical holes except for the very low average blowing ratio $M=0.5$. Between the hole rows ($0<s/d<10$), the radial angle holes (both cylindrical and shaped) offer higher effectiveness than the corresponding compound angle holes. Downstream of the film holes ($s/d>10$), the compound angle holes offer higher effectiveness at low average blowing ratios ($M=0.5$ and $M=0.75$). At high average blowing ratios ($M=1.5$ and $M=2.0$), the effectiveness from the radial angle shaped holes is slightly higher than that from compound angle shaped holes. However, the film cooling effectiveness from compound angle cylindrical holes is higher than the corresponding radial angle cylindrical holes.

Figure 10 shows the film cooling effectiveness distribution for the three-row film cooling design. It can be seen that effectiveness level decreases significantly when compared with the seven-row design shown in Fig. 7. However, some film cooling characteristics observed in the seven-row design are also evident in the three-row design. When the average blowing ratio increases, the effectiveness in the stagnation region (between the film holes) increases. The coolant comes out of the film holes and disperses near the stagnation region. More coolant is accumulated in this region when the blowing ratio increases. Further downstream ($s/d>7$), the coolant spreads out from the second row of film holes and provides fairly good film cooling coverage at low blowing ratios. As the blowing ratios increase, the interaction between the coolant jet and mainstream flow is enhanced. When jet momentum increases, jets (less deflected by the mainstream) tend to penetrate the mainstream. Therefore, the effectiveness on the surface reduces. For the same hole geometry (either cylindrical hole or shaped hole), it can be seen that the coolant traces from compound angle holes are narrower than from corresponding radial angle holes. Coolant traces spread out less and film coverage reduces. When compared with the cylindrical holes, the superiority of shaped holes in film coverage is obvious, particularly at higher average blowing ratios.

Figure 11 shows the effect of average blowing ratio on spanwise averaged effectiveness for the three-row design. When the average blowing ratio increases, the effectiveness in the area between the stagnation row and downstream row ($s/d<5$) increases for all the hole configurations. However, the trend reverses in the region further downstream ($s/d>7$). The effectiveness for the shaped holes is relatively insensitive to average blowing ratios in this region ($s/d>7$), particularly for the radial angle shaped holes.

The effect of film-hole configurations on the spanwise averaged film cooling effectiveness for the three-row design is shown in Fig. 12. The radial angle shaped holes give the best film cooling coverage especially at higher averaged blowing ratios. In general, shaped holes yield higher effectiveness than cylindrical holes; radial angle holes yield higher effectiveness than compound angle holes.

To evaluate the film cooling performance, the comparison of the spanwise averaged film cooling effectiveness at the downstream region $s/d=12.5$ is presented in Fig. 13 for different film cooling hole configurations. The abscissa is coolant mass flow rate normalized with the seven-row flow at $M=1$. Consuming a similar amount of coolant, the seven-row design produces much better effectiveness than the three-row. At this downstream location ($s/d=12.5$), the spanwise averaged effectiveness from the shaped holes is significantly higher than the cylindrical holes for both seven-row and three-row designs. In general, the radial angle holes offer higher effectiveness than compound angle holes. The radial angle shaped holes yield the best film effectiveness at medium and high blowing ratios.

6 Conclusions

Two showerhead film cooling designs were investigated: a heavily film cooled model with seven rows of film holes and a

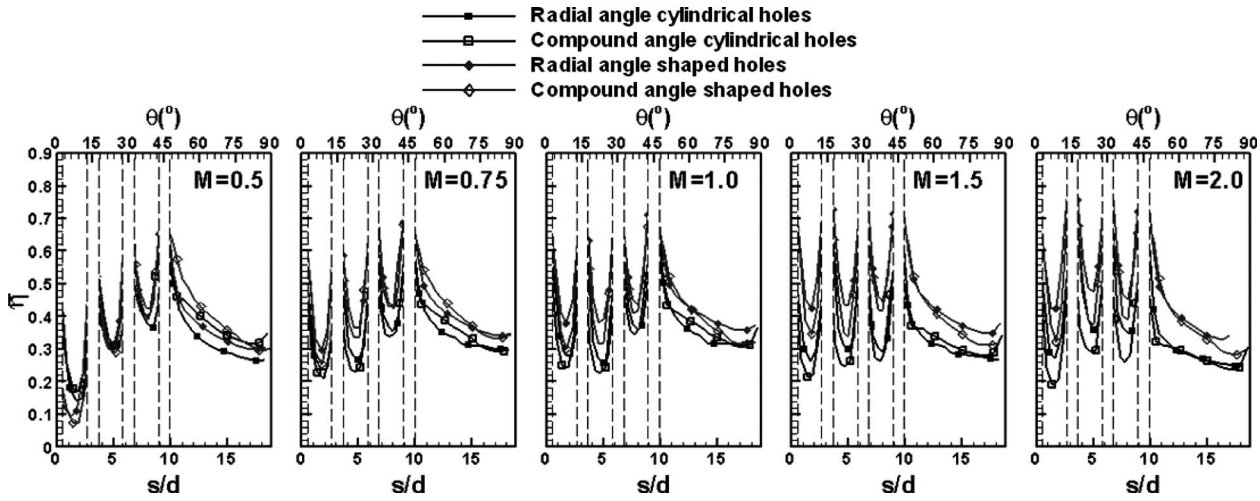

Fig. 9 Effect of hole configuration on spanwise averaged film effectiveness (seven-row design)

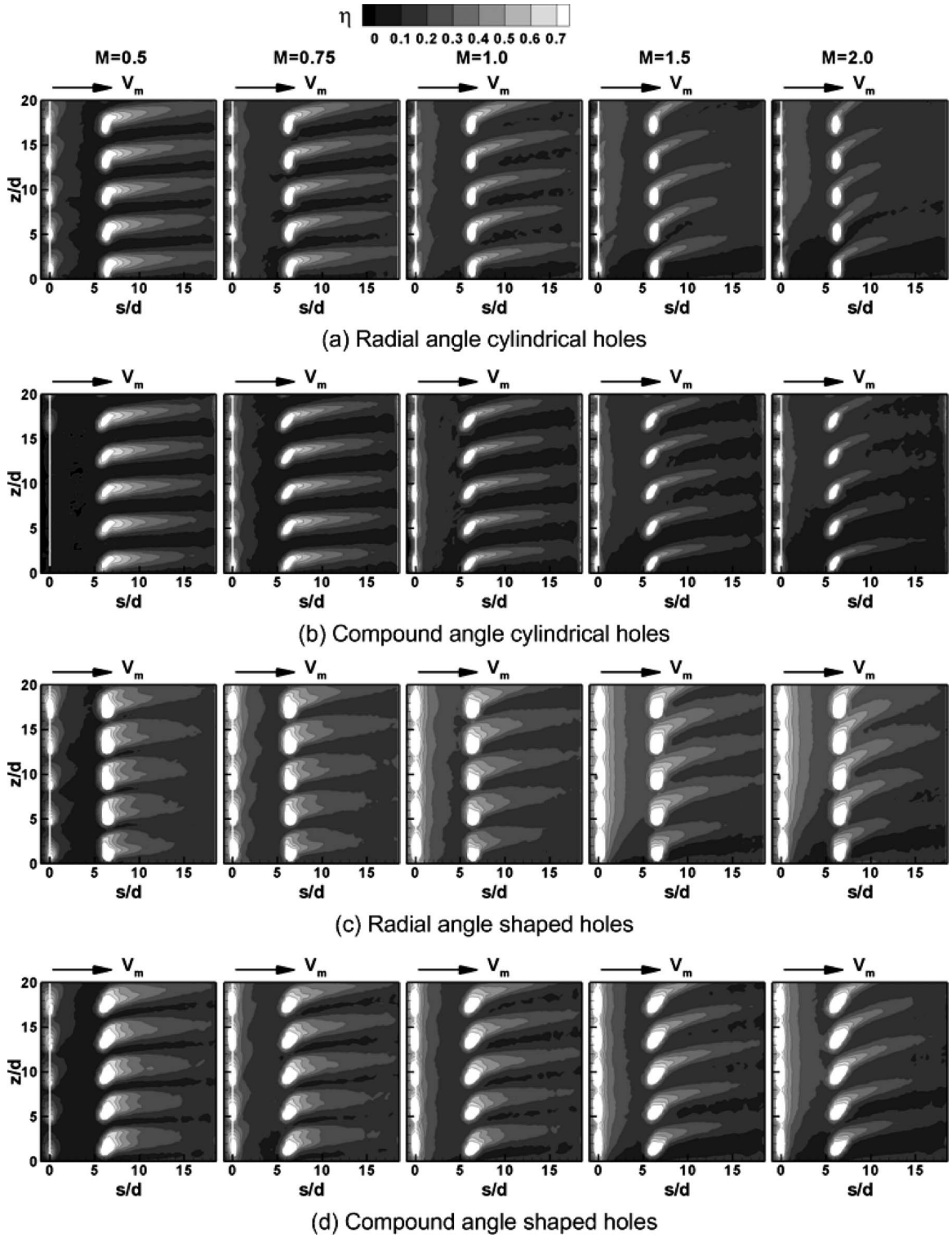

Fig. 10 Film cooling effectiveness distribution for three-row design

moderately film cooled model with three rows of film holes. For each design, four different film-hole configurations were studied. PSP experiments were performed to measure the film cooling effectiveness on the leading edge models. The PSP method is a convenient method to determine the film cooling effectiveness, especially for the surfaces with heavily distributed film holes. Because the PSP technique relies on the mass transfer analogy, heat conduction problems nearby the film-hole region are eliminated. Main findings from this study are as follows.

1. The film cooling effectiveness for the seven-row design is much higher than the three-row design at the same average blowing ratio or at the same amount of coolant flow. This is because the seven-row design has more film accumulation from row to row than the three-row design.
2. In general, shaped holes offer higher effectiveness than cylindrical holes at intermediate and high average blowing ratios ($M=0.75-2.0$) for both three-row and seven-row designs. The advantage of shaped holes is more evident at

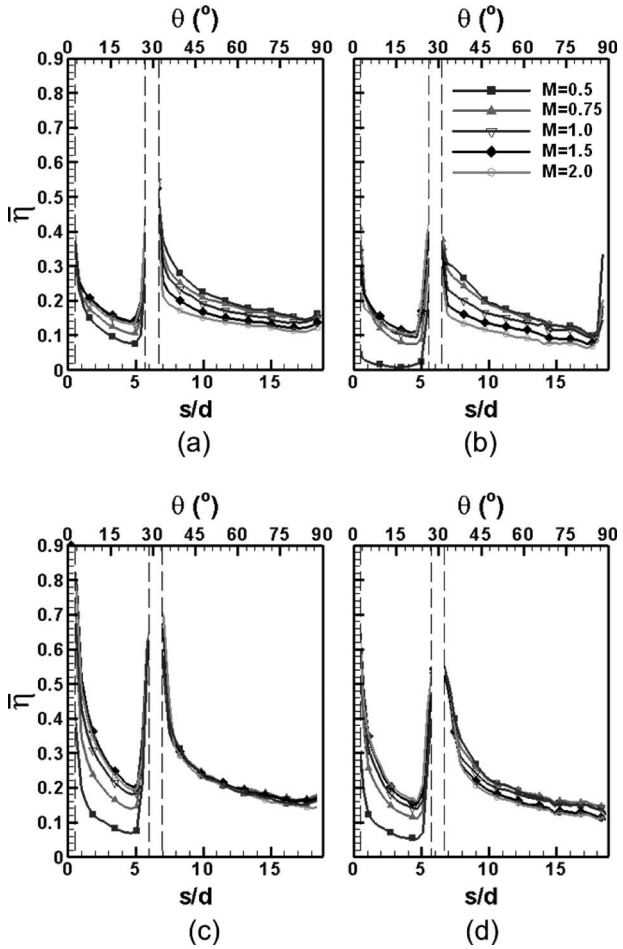

Fig. 11 Effect of blowing ratio on spanwise averaged film effectiveness (three-row design): (*a*) radial angle cylindrical holes, (*b*) compound angle cylindrical holes, (*c*) radial angle shaped holes, and (*d*) compound angle shaped holes

higher average blowing ratios ($M=1.5$ and 2.0). Due to the increased breakout area, the jet momentum from shaped holes is reduced. Therefore, coolant jets stay closer to the surface and result in higher effectiveness.

3. Compared with compound angle holes, the coolant jets from radial angle holes are more deflected by the mainstream and cover a wider surface area. For the three-row model, the radial angle holes provide higher effectiveness than the corresponding compound angle holes. Similar behavior is observed on the seven-row model at higher average blowing ratios ($M=1.0-2.0$).
4. For both three-row and seven-row designs, the film cooling effectiveness increases with increasing average blowing ratio near the stagnation region. In the downstream region, however, the effectiveness decreases at higher blowing ratios due to the enhanced interaction (mixing) between the coolant jets and mainstream flow.

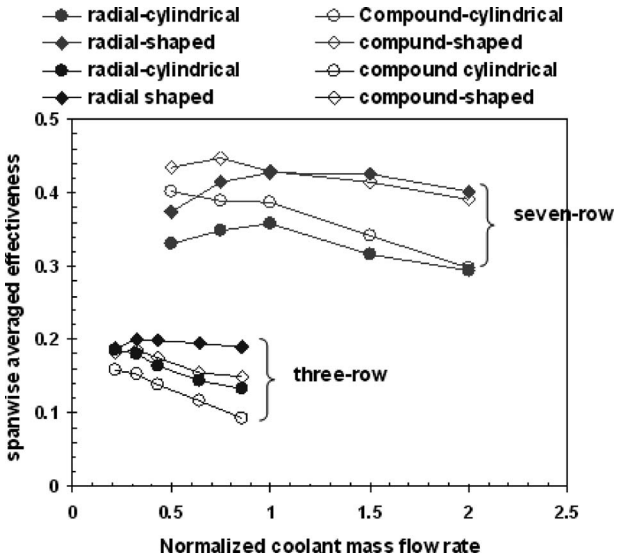

Fig. 13 spanwise averaged effectiveness at $\theta=60$ deg ($s/d=12.5$)

Acknowledgment

This work has been supported through the Marcus Easterling Endowment Fund.

Nomenclature

C = oxygen concentration
C_D = discharge coefficient
d = film cooling hole diameter

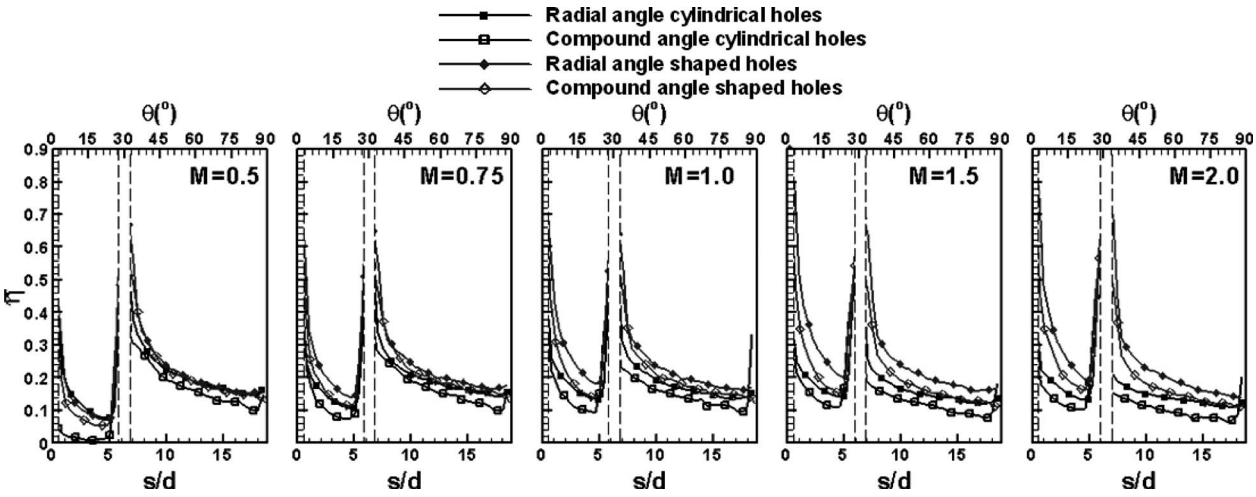

Fig. 12 Effect of hole configuration on spanwise averaged film effectiveness (three-row design)

D = diameter of the leading edge model (semicylinder)
I = PSP emission intensity
L = length of the film hole
s = distance from the stagnation line
M = average blowing ratio
n = number of film cooling holes
p = hole-to-hole spacing in the spanwise direction
P = static pressure
P_t = total pressure
P_{O_2} = partial pressure of oxygen
T_c = coolant temperature
T_f = film temperature
T_m = mainstream temperature
V_c = average velocity of coolant from the film cooling hole row
V_m = mainstream velocity
V_∞ = freestream velocity
z = distance along the blade span measured from the bottom of the measured area

Greek Symbols

α = film cooling hole incline angle to the surface
β = film cooling hole incline angle to the streamwise direction
δ = film cooling hole lateral expansion angle
γ = film cooling hole forward expansion angle
η = local film cooling effectiveness
$\bar{\eta}$ = spanwise averaged film cooling effectiveness
θ = angle to stagnation line
ρ_c = density of coolant
ρ_m = density of mainstream air

Subscripts

air = mainstream air with air as coolant
mix = mainstream air with nitrogen as coolant
ref = reference image with no mainstream and coolant flow
blk = image without illumination (black)

References

[1] Han, J. C., Dutta, S., and Ekkad, S. V., 2000, *Gas Turbine Heat Transfer and Cooling Technology*, Taylor & Francis, New York.
[2] Luckey, D. W., Winstanley, D. K., Hames, G. J., and L'Ecuyer, M. R., 1977, "Stagnation Region Gas Film Cooling for Turbine Blade Leading Edge Applications," AIAA J. Aircr., **14**, pp. 494–501.
[3] Karni, J., and Goldstein, R. J., 1990, "Surface Injection Effect on Mass Transfer From a Cylinder in Crossflow: A Simulation of Film Cooling in the Leading Edge Region of a Turbine Blade," ASME J. Turbomach., **112**, pp. 418–427.
[4] Mick, W. J., and Mayle, R. E., 1988, "Stagnation Film Cooling and Heat Transfer Including Its Effect Within the Hole Pattern," ASME J. Turbomach., **116**, pp. 730–737.
[5] Mehendale, A. B., and Han, J. C., 1992, "Influence of High Mainstream Turbulence on Leading Edge Film Cooling Heat Transfer," ASME J. Turbomach., **114**, pp. 707–715.
[6] Mehendale, A. B., and Han, J. C., 1993, "Reynolds Number Effect on Leading Edge Film Effectiveness and Heat Transfer Coefficient," Int. J. Heat Mass Transfer, **36**, pp. 3723–3730.
[7] Ou, S., Mehendale, A. B., and Han, J. C., 1992, "Influence of High Mainstream Turbulence on Leading Edge Film Cooling Heat Transfer: Effect of Film Hole Row Location," ASME J. Turbomach., **114**, pp. 716–723.
[8] Ekkad, S. V., Han, J. C., and Du, H., 1998, "Detailed Film Cooling Measurements on a Cylindrical Leading Edge Model: Effect of Free-Stream Turbulence and Coolant Density," ASME J. Turbomach., **119**, pp. 594–600.
[9] Gao, Z., Wright, L. M., and Han, J. C., 2005, "Assessment of Steady State PSP and Transient IR Measurement Techniques for Leading Edge Film Cooling," ASME Paper No. IMECE2005-80146.
[10] Funazaki, K., Yokota, M., and Yamawaki, K., 1997, "The Effect of Periodic Wake Passing on Film Effectiveness of Discrete Holes Around the Leading Edge of a Blunt Body," ASME J. Turbomach., **119**, pp. 292–301.
[11] Ou, S., and Rivir, R. B., 2001, "Leading Edge Film Cooling Heat Transfer With High Free Stream Turbulence Using a Transient Liquid Crystal Image Method," Int. J. Heat Fluid Flow, **22**, pp. 614–623.
[12] Nirmalan, N. V., and Hylton, L. D., 1990, "An Experimental Study of Turbine Vane Heat Transfer With Leading Edge and Downstream Film Cooling," ASME J. Turbomach., **112**, pp. 477–487.
[13] Abuaf, N., Bunker, R., and Lee, C. P., 1997, "Heat Transfer and Film Cooling Effectiveness in a Linear Airfoil Cascade," ASME J. Turbomach., **119**, pp. 302–309.
[14] Cruse, M. W., Yuki, U. M., and Bogard, D. G., 1997, "Investigation of Various Parametric Influences on Leading Edge Film Cooling," ASME Paper No. 97-GT-296.
[15] Ekkad, S. V., Mehendale, A. B., Han, J. C., and Lee, C. P., 1997, "Combined Effect of Grid Turbulence and Unsteady Wake on Film Effectiveness and Heat Transfer Coefficient of a Gas Turbine Blade With Air and CO_2 Film Injection," ASME J. Turbomach., **119**, pp. 594–600.
[16] Cutbirth, J. M., and Bogard, D. G., 2003, "Effects of Coolant Density Ratio on Film Cooling Performance on a Vane," ASME Paper No. 2003-GT-38582.
[17] Mhetras, S. P., and Han, J. C., 2006, "Effect of Unsteady Wake on Showerhead Film Cooling Protection for a Gas Turbine Blade," International Heat Transfer Conference, Sydney, Australia.
[18] Dring, R. P., Blair, M. F., and Hoslyn, H. D., 1980, "An Experimental Investigation of Film Cooling on a Turbine Rotor Blade," ASME J. Eng. Power, **102**, pp. 81–87.
[19] Takeishi, K., Matsuura, M., Aoki, S., and Sato, T., 1990, "An Experimental Study of Heat Transfer and Film Cooling on Low Aspect Ratio Turbine Nozzles," ASME J. Turbomach., **112**, pp. 488–496.
[20] Abhari, R. S., and Epstein, A. H., 1994, "An Experimental Study of Film Cooling in a Rotating Transonic Turbine," ASME J. Turbomach., **116**, pp. 63–70.
[21] Ahn, J., Schobeiri, M. T., Han, J. C., and Moon, H., 2006, "Film Cooling Effectiveness on the Leading Edge Region of a Rotating Turbine Blade With Two Rows of Film Cooling Holes Using Pressure Sensitive Paint," ASME J. Heat Transfer, **128**(9), pp. 879–888.
[22] Ahn, J., Schobeir, M. T., Han, J. C., and Moon, H. K., 2007, "Effect of Rotation on Leading Edge Region Film Cooling of a Gas Turbine Blade With Three Rows of Film Cooling Holes," Int. J. Heat Mass Transfer, **50**, pp. 15–25.
[23] Mouzon, B. D., Terrell, E. J., Ablert, J. E., and Bogard, D. G., 2005, "Net Heat Flux Reduction and Overall Effectiveness for a Turbine Blade Leading Edge," ASME Paper No. GT2005-69002.
[24] Falcoz, C., Weigand, B., and Ott, P., 2006, "Experimental Investigation on Showerhead Cooling on a Blunt Body," Int. J. Heat Mass Transfer, **49**, pp. 1287–1298.
[25] Kim, Y. J., and Kim, S. M., 2004, "Influence of Shaped Injection Holes on Turbine Blade Leading Edge Film Cooling," Int. J. Heat Mass Transfer, **47**, pp. 245–256.
[26] Reiss, H., and Bölcs, A., 2000, "Experimental Study of Showerhead Cooling on a Cylinder Comparing Several Configurations Using Cylindrical and Shaped Holes," ASME J. Turbomach., **122**, pp. 161–169.
[27] Lu, Y., Allison, D., and Ekkad, S. V., 2006, "Influence of Hole Angle and Shaping on Leading Edge Showerhead Film Cooling," ASME Paper No. GT2006-90370.
[28] Coleman, H. W., and Steele, W. G., 1989, *Experimentation and Uncertainty Analysis for Engineers*, Wiley, New York, Chaps. 3 and 4.

Heat Transfer to Supercritical Water in a Horizontal Pipe: Modeling, New Empirical Correlation, and Comparison Against Experimental Data

Majid Bazargan
Assistant Professor
Department of Mechanical Engineering,
K. N. Toosi University of Technology,
Tehran 1999 143 344, Iran
e-mail: bazargan@kntu.ac.ir

Daniel Fraser
Assistant Professor
Department of Mechanical and Industrial Engineering,
University of Manitoba,
Winnipeg, MB, R3T 5V6, Canada
e-mail: fraser@cc.umanitoba.ca

Enhancement of heat transfer to supercritical fluids has drawn the attentions of many researchers within the past few decades. Modeling and predicting heat transfer to turbulent flow of supercritical fluids, however, are very complicated due to severe variations of fluid properties near the critical point. Large discrepancies between available heat transfer data are greatly due to confusion of forced convection and mixed convection data. The data unaffected by buoyancy have been selected cautiously from a large database generated in this study. Such data have been used to develop a 1D numerical model as well as a semi-empirical correlation to predict forced convection heat transfer to turbulent flow of supercritical water. In the numerical model, radial variations of heat flux and shear stress are taken into account. Modifications to turbulent Prandtl number and wall shear stress formulations have been applied to a law of the wall type of model to fit supercritical conditions. The model shows good agreement with experiments. In the experimental part, the extensive database obtained on a full-scale test facility in the present study, plus a new conceptual approach, has been employed together to develop a semi-empirical heat transfer correlation. It accurately predicts the experiments.
[DOI: 10.1115/1.3082403]

Keywords: supercritical water, forced convection heat transfer, variable property flow, semi-empirical heat transfer correlation

1 Introduction

At supercritical pressures, thermodynamic and transport properties of fluids change dramatically near the critical temperature. The critical points for pure water are 22.1 MPa and 374°C. Figure 1 shows the variations of some water properties at $P=24$ MPa. Those properties not shown in the figure also demonstrate severe changes. For example, variations of thermal conductivity with temperature follow the same pattern as of viscosity.

For a given supercritical pressure, the temperature at which the fluid thermal expansion is maximum is called the pseudocritical temperature. This temperature tends to increase slightly with increasing pressure. A fluid at supercritical pressure, with temperatures before and after the pseudocritical temperature, is referred to as liquidlike and vaporlike, respectively. Because of large property variations, heat transfer rates are dramatically enhanced near the critical region. For a flow in a channel, heat transfer enhancement occurs when wall temperatures (T_w) exceed the pseudocritical point (T_{pc}) while bulk fluid temperatures (T_b) are below it, i.e., $T_b < T_{pc} < T_w$. This has made supercritical fluids an excellent heat transfer medium for some applications (e.g., rocket propulsion systems, supercritical water oxidation (SCWO), nuclear reactors, and now, potentially, geothermal systems).

SCWO, as a waste remedial technique, sparked considerable interest [1]. SCWO is a powerful process for the thorough destruction of organic and inorganic wastes. For example, destruction efficiencies for toxic substances such as polychlorinated biphenyls (PCBs) can reach 99.99%. Other recent applications of supercritical fluids are direct-cycle supercritical water-cooled fast breeder reactors considered as early as 1992 [2] and Generation IV nuclear reactors [3]. Interest in such supercritical water reactors (SCWRs) has grown considerably to include General Atomics in the USA (GAT), Atomic Energy of Canada Limited (AECL), and many others worldwide [4]. Supercritical geothermal systems are also gaining considerable interest. The potential for such systems is worldwide and gaining momentum quickly [5,6]. In some modern military aircraft, fuel is pressurized above its critical point and used as a coolant to remove heat from the aircraft engine and/or wings. There are other potential uses for supercritical fluids being currently investigated worldwide, in particular, in Iceland [7] and Japan [8]. In addition, there is a fast growing interest in extracting valuable minerals such as gold, and rare earth elements from supercritical saline geothermal systems [9]. There is also growing interest in supercritical geothermal resources in the volcanic Aleutian Islands, Alaska [10]. A thorough understanding of forced convection heat transfer is crucial toward the optimal design of such systems, in particular, heat exchanger design.

The purpose of this study was to expand knowledge and data on forced convection heat transfer to supercritical water. This purpose was served in two ways, analytically and experimentally. In the analytical part of this study, a numerical model was established to account for dramatic variations in flow properties. The model reveals details on the heat transfer mechanism to supercritical fluids. The turbulence model was based on the well known law of the wall. Modifications on turbulent Prandtl number were also incorporated into the model.

Contributed by the Heat Transfer Division of ASME for publication in the JOURNAL OF HEAT TRANSFER. Manuscript received August 23, 2007; final manuscript received August 23, 2008; published online March 31, 2009. Review conducted by Louis C. Chow.

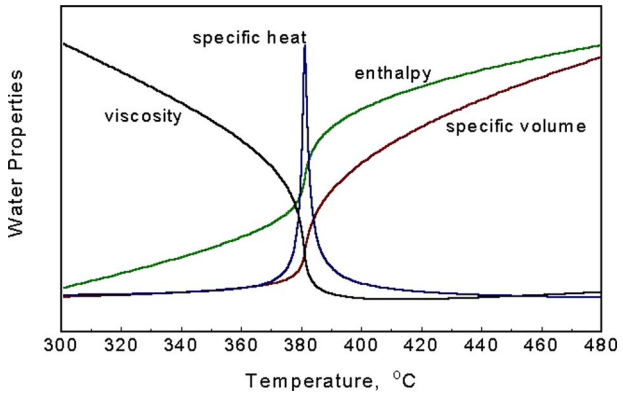

Fig. 1 Variations of properties of water with temperature at $P = 24$ MPa

A systematic experimental study was also performed producing a large database. Based on the data obtained and findings from the analytical model, a new approach was employed to develop a semi-empirical correlation.

It is important to make sure that the flow under study is unaffected by buoyancy. Such data are the basis of the new semi-empirical correlation developed and is essential as for evaluation of numerical model established in this study. It was extensively explained by Bazargan et al. [11] that buoyancy effects are much more readily experienced in supercritical fluid flows compared with constant property flows. Much of the data reported in literature to represent the problem of forced convection heat transfer to supercritical fluids, in fact, were reflecting mixed convection situations. The results of Ref. [11] were used to select relevant (i.e., buoyancy unaffected) data for the present study. It should be also noted that according to Ref. [11], for flow conditions of this study, once buoyancy effect is negligible, the insignificance of acceleration effect is guaranteed.

2 Experimental Apparatus

A SCWO pilot plant, details of which were explained in Ref. [11], was constructed at the University of British Columbia in collaboration with NORAM, a Vancouver based company. This experimental facility was used in the present work to study the convection heat transfer to pure water at supercritical pressures. A schematic of the apparatus is shown in Fig. 2.

The test section was 3 m long. The inner diameter of the test section was 6.42 mm. The uncertainty in pressure was 0.5% or (0.12 MPa at 24 MPa). The uncertainty in bulk temperature measurement was 0.4%, i.e., 1.5°C at 380°C. Thirty intrinsic thermocouples were welded to the tube surface and used to measure the wall temperature at different locations along the test section. To account for peripheral variations of surface temperature due to buoyancy effects [11], they were evenly distributed between the top and bottom surfaces of the test section.

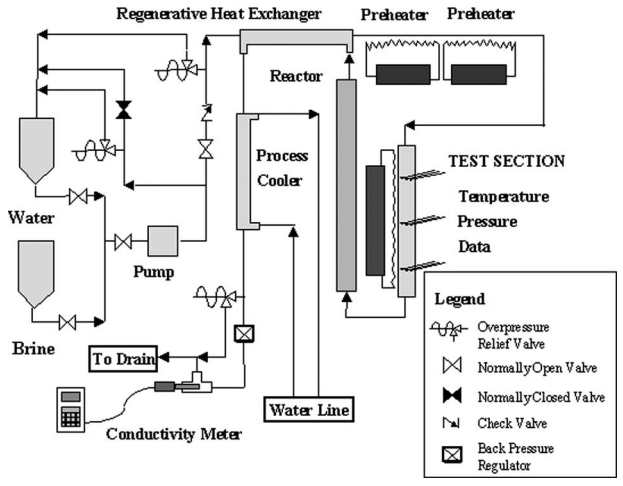

Fig. 2 Schematic of the SCWO facility

Maximum achievable heat flux was 310 kW/m^2. Mass flow rates varied between 330 kg/m^2 s and 1200 kg/m^2 s. Uncertainty in volumetric flow measurements was less than 1%. Controlled variables were pressure, mass flow, inlet temperature to the test section, and heat flux. Surface thermocouples were mounted far enough from the flow inlet to exclude entry region effects for entry temperatures.

3 Numerical Model

Most numerical studies have concentrated on flows under influences of buoyancy in a vertical pipe. Under certain conditions, buoyancy and/or acceleration effects may lead to heat transfer deterioration. Due to flow symmetry, a 2D model is theoretically adequate to address such effects. For this reason, vast majority of past studies have focused on vertical flows. However, little can be learned from a 2D code for horizontal flows since it is restricted to account for acceleration effects without buoyancy. This only occurs in very small diameter pipes. In pipe diameters such as those used in the current study or larger, such phenomena are closely coupled. A full 3D computational fluid dynamics (CFD) code, with special care given to extreme variations of fluid properties near critical point, is required to model these effects. Such model has not been developed yet.

A 1D model, however, is adequate for flows with negligible effects of buoyancy and/or acceleration. Such conditions occur with higher flow rates and/or lower heat fluxes in a horizontal pipe. Within this study, using finite difference method, a 1D model to account for radial variations of the flow was developed. An extension of earlier models to include recent advances in law of the wall modeling (e.g., newer definitions of the turbulent Prandtl number) was incorporated.

3.1 Governing Equations. Simplifying assumptions made into momentum and energy equations are as follows. Convection terms of momentum are negligible compared with momentum transferred by shear stresses. The gravitational term (buoyancy effect) is ignored; hence the flow is axisymmetric. Terms for radial convection, axial conduction, and dissipation in the energy equation are negligible compared with the axial convection term. Thus, the balance equations for shear stress and heat fluxes are obtained as

$$\frac{\tau}{\rho} = (\nu + \varepsilon_m)\frac{du}{dy} \tag{1}$$

$$\frac{q}{\rho C_P} = -(\alpha + \varepsilon_h)\frac{dT}{dy} \tag{2}$$

where ε_m and ε_h are momentum and heat eddy diffusivity and reflect the effects of turbulent velocity and temperature fluctuations, respectively. The turbulent Prandtl number is defined as $\mathrm{Pr}_t = \varepsilon_m/\varepsilon_h$. Available data for flow of water at normal conditions show that Pr_t is very close to unity. For supercritical fluid flow, ε_m and ε_h are assumed to be equal as a first approximation, i.e., $\varepsilon_m = \varepsilon_h = \varepsilon$. The influence of variations in Pr_t will be discussed later.

The model provides a solution to the boundary layer equations based on the law of the wall. The wall coordinates y^+ and u^+ are used to make the equations nondimensional. Note that the inner layer of the boundary layer, where the radial variations of velocity and temperature are sharp, is under main considerations here and the outer layer corrections where the profiles are flat do not significantly affect the results. Given the flow rate, pressure, wall temperature, and heat flux, the nondimensionalized equations of

Table 1 Some of available expressions for the universal velocity profiles

The equation of universal velocity profile	Range of validity	Investigator
$u^+=y^+$	$0\le y^+\le 11.5$	
$u^+=2.5\ln y^+ +5.5$	$11.5<y^+$	Prandtl–Taylor
$u^+=y^+$	$0\le y^+\le 5$	
$u^+=5\ln y^+ -3.05$	$5\le y^+\le 30$	von Kármán
$\frac{du^+}{dy^+}=\frac{2}{1+\{1+4\kappa^2 y^{+2}[1-e^{(-y^+/A^+)}]\}^{1/2}}$	All $y+$	
	$\kappa=0.4$, $A=26$	Van Driest
$u^+=14.53\tanh(y^+/14.53)$	$0\le y^+\le 27.5$	
$u^+=2.5\ln y^+ +5.5$	$27.5<y^+$	Rannie
$u^+=2.5\ln(1+0.4y^+)+7.8[1-e^{(-y+/11)}-(y^+/11)e^{(-0.33y+)}]$	All $y+$	Reichardt
$\frac{du^+}{dy^+}=\frac{1}{1+n^2u^+y^+[1-e^{(-n^2u^+y^+)}]}$	$n=0.124$	
	$0\le y^+\le 26$	
$u^+=2.78\ln y^+ +3.8$	$26<y^+$	Deissler
$\frac{\varepsilon_m}{\nu}=0.001(y^+)^3$	$y^+\le 5$	
$\frac{\varepsilon_m}{\nu}=0.5[1+4k^2y^{+2}(1-e^{(-y^+/A^+)})]^{1/2}$	$5<y^+$	
	$\kappa=0.4$, $A=26$	This study

shear stress and heat flux were integrated simultaneously from the wall to the center. Values of temperature and shear stress at the wall were first estimated by educated guesses and were corrected later as a result of the iteration. Supercritical water properties were obtained from The International Association for the Properties of Water and Steam (IAPWS) [12]. The outputs of the numerical model are velocity and temperature profiles. Bulk temperatures were calculated from the temperature profile. The relation $h=q/(T_w-T_b)$ was used to calculate local heat transfer coefficients.

3.2 The Effect of the Choice for the Universal Velocity Profile. The expression describing the relationship between y^+ and u^+ is called the universal velocity profile. Well known expressions for the universal velocity profile are listed in Table 1. It is useful to see how the results of our numerical model vary with each expression. Variations of local heat transfer coefficients along the test section were calculated by the model and are shown in Fig. 3. Experimental data obtained in the present study are also shown.

The solution based on the expression of Prandtl–Taylor largely underpredicts the data. Predictions based on von Kármán, Van Driest, and Rannie law of the wall expressions led to similar results though they better approximated the data. Using the expression of Reichardt largely overpredicted the data and is only partially shown in Fig. 3. This behavior was observed in many other cases not shown here. The expression of Deissler also resulted in an overestimation of the data in this example, that is, while all expressions mentioned above lead to same predictions once applied to a constant property flow.

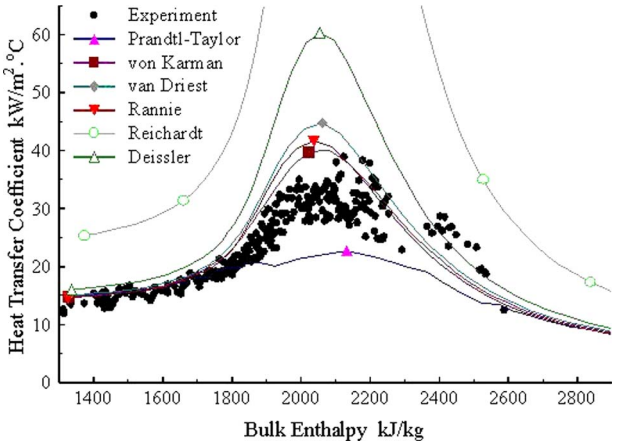

Fig. 3 Comparison of predictions of the present model utilizing various expressions for eddy diffusivity with experiments; $P=25.2$ MPa, $q''=307$ kW/m^2, and $G=964$ kg/m^2 s

In order to improve the present model, the first step was to consider which expression for eddy diffusivity provided the best agreement with the data. A comprehensive comparison was thus performed. The expressions of von Kármán, Van Driest, and Rannie constitute a family of solutions resulting in better agreement with our experiments.

Jackson and Hall [13] speculated that since the expression of eddy diffusivity suggested by Van Driest contained a damping factor (e^{-y+}), it could better cope with variable property conditions. However, our results showed that the expression of von Kármán provided similar results without containing such a factor.

According to the suggestion of Kays [14], at small y^+, ε_m/ν varies corresponding to $(y^+)^3$. Accordingly, the following relationships are used for eddy diffusivity in the current study:

$$\frac{\varepsilon_m}{\nu}=0.001(y^+)^3 \quad \text{for} \quad y^+\le 5 \tag{3}$$

$$\frac{\varepsilon_m}{\nu}=0.5[1+4k^2y^{+2}(1-e^{(-y^+/A^+)})]^{1/2} \quad \text{for} \quad 5<y^+ \tag{4}$$

where $k=0.4$ and $A^+=26$.

3.3 Modifications of the Models for Variable-Property Flows. The empirical formulations in most models consider constant property flow data. Hence, different techniques have been applied to adjust models to fit variable property conditions. Some of those were incorporated in the present model. One example is the integrated form of y^+ and u^+ (introduced originally by Goldmann [15]). Another example is the use of correction factors in the expression of eddy diffusivity (initiated by Hsu and Smith [16] and modified further by others). It can be shown, however, that neither of these modifications appreciably affected the predictions.

The main parameters accounted for in the current study that were found to influence the model predictions were equations used for the wall shear stress and turbulent Prandtl number. These will be addressed individually in Secs. 3.4 and 3.5.

3.4 Effect of Wall Shear Stress. The wall coordinates, y^+ and u^+, are estimated based on values of the wall shear stress, τ_w. Furthermore, radial variations in the shear stress are usually expressed as a function of shear stress at the wall. It is therefore

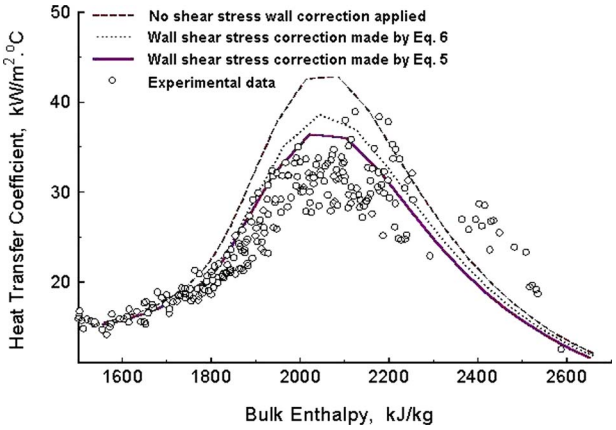

Fig. 4 Effect of the expression used for shear stress at the wall on heat transfer; P=25.2 MPa, G=965 kg/m^2 s, and q'' =307 kW/m^2

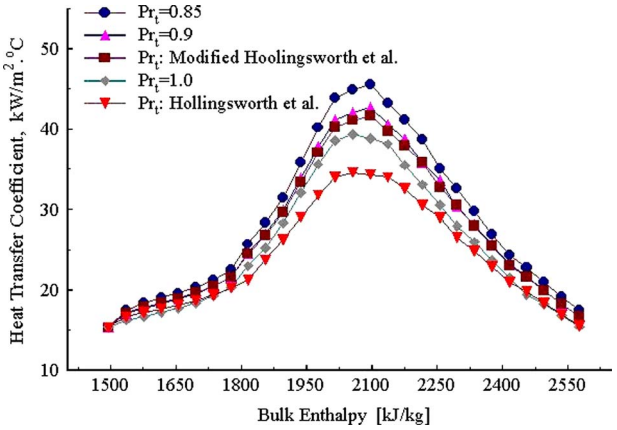

Fig. 5 The effect of Pr$_t$ on local heat transfer coefficients; P =25.2 MPa, G=965 kg/m^2 s, and q''=307 kW/m^2

important to investigate how a supercritical environment can affect the shear stress at the wall. Petukhov et al. [17] suggested the following correction factor of Popov to account for property variations near the critical region:

$$\frac{\tau_w}{(\tau_w)_0} = \left(\frac{\rho_w}{\rho_b}\right)^{0.4} \tag{5}$$

$(\tau_w)_0$ is the wall shear stress at constant property conditions. A more recent correction factor, introduced by Razumovskiy et al. [18], is

$$\frac{\tau_w}{(\tau_w)_0} = \left(\frac{\rho_w}{\rho_b} \cdot \frac{\mu_w}{\mu_b}\right)^{0.18} \tag{6}$$

Variations in the local heat transfer coefficient along the test section, with and without applying correction factors for shear stress at the wall, are shown in Fig. 4. As shown, the better agreement with experiment is obtained once Eq. (5) is used.

3.5 The Effect of Turbulent Prandtl Number, Pr$_t$. For fluids with a molecular Prandtl number close to 1, like water at normal pressure and temperature, the turbulent Prandtl number is assumed to be unity. As such, the Reynolds analogy holds. There are no data available for supercritical fluid flows. Measuring turbulent shear stress and velocity profiles to determine ε_m is extremely difficult. In addition, simultaneous measurements of turbulent heat flux and temperature profiles to determine ε_h make Pr$_t$ nearly impossible to be evaluated.

In most analytical studies on supercritical water, Pr$_t$ was assumed to be unity. Furthermore, changing Pr$_t$ from 1.0 to 0.9 or 0.85 appeared to not affect the results significantly in previous studies. However, the present model, as will be shown, is sensitive to the values of Pr$_t$.

Kays [14] showed varying results of direct numerical solutions and experiments for Pr$_t$. For high Reynolds numbers, Pr$_t$ approaches 0.85 in the core region of the flow. Near the wall Pr$_t$ may be greater than 1. Hollingsworth et al. [19] fitted their data to a curve, which correlated Pr$_t$ with y^+ as follows:

$$\mathrm{Pr}_t = 1 + 0.855 - \tanh[0.2(y^+ - 7.5)] \tag{7}$$

At very small y^+, the equation of Hollingsworth et al. [19] suggests values much greater than 1 for Pr$_t$, which is not acceptable. For this reason, Kays [14] suggested that Eq. (7) may be applied at $y^+ > 5$ and for smaller values of y^+, Pr$_t$ can be assumed to be constant and equal to unity. The limit of $y^+ > 5$ was further modified in this study to $y^+ > 13.8$ in order to avoid discontinuities in values of Pr$_t$. This formulation for Pr$_t$ is referred to as "modified Hollingsworth et al." in upcoming results. The effect of variations of Pr$_t$ on heat transfer coefficients calculated by the present model is shown in Fig. 5. For the sake of a better comparison, flow parameters were chosen to be the same as those shown earlier in Fig. 4.

The results, with constant values of 0.85, 0.9, and 1.0 for Pr$_t$, show that the greater the value for Pr$_t$, the smaller the heat transfer coefficients. The modified expression of Hollingsworth et al. [19], i.e., Eq. (7) with Pr$_t$=1.0 at the wall region, in fact, is a sort of combination of Pr$_t$=0.85 and Pr$_t$=1.0. That is because the original Eq. (7) approaches to 0.85 asymptotically as y^+ grows. Thus, it is not surprising to see that the corresponding heat transfer coefficients shown in Fig. 5 lie between the results obtained for Pr$_t$ =0.85 and Pr$_t$=1.0 and very close to the curve attributed to Pr$_t$ =0.9. Applying the relationship of Hollingsworth et al. [19] without any modifications, on the other hand, yields interesting results for the heat transfer coefficients. The close agreement with experiments is striking and shown separately in Fig. 6.

4 A New Empirical Correlation

Empirical Nusselt number correlations are capable to predict heat transfer coefficients satisfactorily for constant property pipe flows over a wide range of flow conditions. Furthermore, they may offer acceptable results for variable property flows provided that fluid properties vary monotonically with temperature. The dramatic property changes a supercritical fluid undergoes near the critical region, however, complicate the problem. More than 20 different correlations were developed over the past few decades. Some of the most common expressions are listed in Table 2. For a

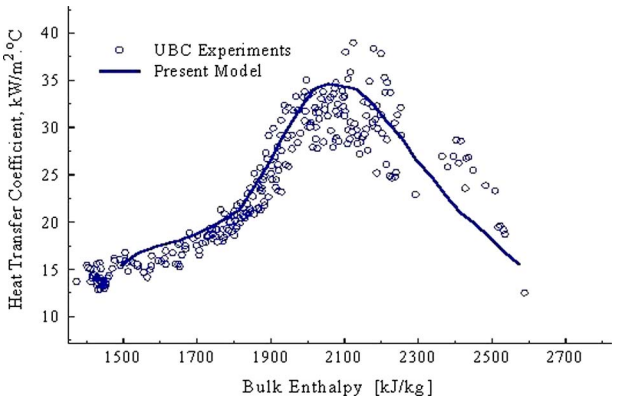

Fig. 6 Comparison of model predictions (equation of Hollingsworth et al. [19] used for Pr$_t$) with experiments. Test conditions are the same as Fig. 5.

Table 2 Empirical correlations for forced convection heat transfer to supercritical fluids

	$\mathrm{Nu}_b = 0.023\ \mathrm{Re}_b^{0.8}\ \mathrm{Pr}_{\min}^{0.8}$
Miropolski-Shitsman [25]	$\mathrm{Pr}_{\min}$ is the smaller of Pr_b and Pr_w
	$\mathrm{Nu}_b = \dfrac{\frac{C_f}{2}\mathrm{Re}_b\ \mathrm{Pr}_b}{12.7\sqrt{\frac{C_f}{2}}(\mathrm{Pr}_b^{2/3}-1)+1.07}\left(\dfrac{\mu_w}{\mu_b}\right)^{-0.11}\left(\dfrac{\kappa_w}{\kappa_b}\right)^{0.33}\left(\dfrac{\overline{\mathrm{Cp}}}{\mathrm{Cp}_b}\right)^{0.35}$
	where
	$\overline{\mathrm{Cp}} = \dfrac{i_w - i_b}{T_w - T_b}$
Petukhov et al. [26]	
	$\mathrm{Nu}_w = 0.00459\ \mathrm{Re}_w^{0.923}\ \overline{\mathrm{Pr}}_w^{0.613}\left(\dfrac{\rho_w}{\rho_b}\right)^{0.231}$
Swenson et al. [24]	$\overline{\mathrm{Pr}}_w = \mu_w\overline{\mathrm{Cp}}/\kappa_w$
	$\mathrm{Nu}_b = 0.0135\ \mathrm{Re}_b^{0.85}\ \mathrm{Pr}_b^{0.8}F_c$
	where
	$E = \dfrac{T_{\mathrm{pc}} - T_b}{T_w - T_b}$
	$F_c = 1.0$ for $1 < E$
	$F_c = 0.67\ \mathrm{Pr}_{\mathrm{pc}}^{-0.5}\left(\dfrac{\overline{\mathrm{Cp}}}{\mathrm{Cp}_b}\right)^{n1}$
	for $0 \le E \le 1$
	$F_c = \left(\dfrac{\overline{\mathrm{Cp}}}{\mathrm{Cp}_b}\right)^{n2}$
	for $E < 0$
	$n_1 = -0.77(1 + 1/\mathrm{Pr}_{\mathrm{pc}}) + 1.49$
	$n_2 = 1.44(1 + 1/\mathrm{Pr}_{\mathrm{pc}}) - 0.53$
Yamagata et al. [23]	$\mathrm{Pr}_{\mathrm{pc}}$ is the Pr number at the pseudocritical temperature.
	$\mathrm{Nu}_b = \dfrac{\frac{C_f}{2}\mathrm{Re}_b\ \mathrm{Pr}_b}{12.7\sqrt{\frac{C_f}{2}}(\mathrm{Pr}_b^{2/3}-1)+1.07}\left(\dfrac{\rho_w}{\rho_b}\right)^{0.3}\left(\dfrac{\overline{\mathrm{Cp}}}{\mathrm{Cp}_b}\right)^{n}$
	where $n = 0.4$ for $T_b < T_w < T_{\mathrm{pc}}$ or $1.2T_{\mathrm{pc}} < T_b < T_w$
	$n = 0.4 + 0.2[(T_w/T_{\mathrm{pc}}) - 1]$ for $T_b < T_{\mathrm{pc}} < T_w$
Krasnoshchekov and Protopopov [27]	$n = 0.4 + 0.2[(T_w/T_{\mathrm{pc}}) - 1]\{1 - 5[(T_b/T_{\mathrm{pc}}) - 1]\}$ for $T_{\mathrm{pc}} < T_b < 1.2T_{\mathrm{pc}}$

relatively complete listing of these correlations, see Ref. [20]. The discrepancies between predictions of various correlations are apparent and have been addressed by a number of researchers [21]. The need for a reliable empirical correlation applicable for a wide range of flow conditions is vital. This cannot be reached unless sources of discrepancies among available correlations would be thoroughly understood and explained.

It has been shown [22] that in contrast with what is widely stated in literature, the use of different properties appears not to be the major cause of discrepancies between various correlations.

Neglecting buoyancy is claimed by Bazargan et al. [11] to be the most important source of discrepancy between the predictions of various empirical correlations. Many early investigations did not distinguish between vertical and horizontal flows. In some earlier studies the orientation of the test section was not even reported. For horizontal test sections, some did not specify if measurements were done at the top or bottom surface of the tube. In a number of studies with vertical test sections, the differences between upward and downward flows were not accounted for. In most such studies the effect of buoyancy was already assumed to be negligible before it was investigated. Thus, many experimental results intended to represent forced convection heat transfer, in fact, likely reflect mixed convection situations. Empirical correlations are highly affected by such ambiguity. To emphasize the misleading effects of neglecting buoyancy the reader is referred to Fig. 7. The predictions of a few correlations for the test conditions for which Yamagata et al. [23] showed the effect of natural convection was zero are presented.

What makes heat transfer to a supercritical fluid flow to be different from other examples of variable property flows is the peculiar way of variation of fluid properties. Within thermodynamic critical region the variations of some properties with temperature are not monotonic. For instance, once $T_b < T_{\mathrm{pc}} < T_w$, specific heat capacity increases near the wall as we move away from the wall toward the flow centerline. Maximum value of specific heat occurs at some distance from the wall where the pseudocritical temperature is reached. Further away from the wall, it decreases again toward a certain value at the flow centerline. It means that the sign of the derivative of specific heat with respect to radius (i.e., temperature) changes as it crosses the critical region. That explains why implementation of a simple correction

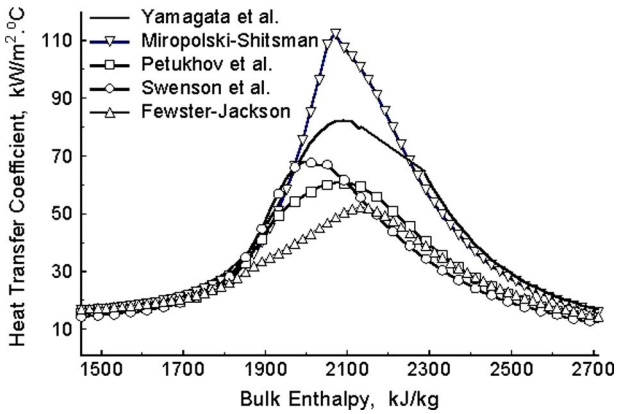

Fig. 7 Comparison of correlations under no buoyancy conditions tried by Yamagata et al. [23]; $P = 24.5$ MPa, $q'' = 233$ kW/m^2, $G = 1260$ kg/m^2 s, and $D = 7.5$ mm

factor in form of the wall-to-bulk ratio of one of the properties into empirical correlations, as applied to other flows with variable properties, is inadequate in the case of supercritical fluid flows. Substituting wall or bulk Cp by averaged Cp defined as $(i_w - i_b)/(T_w - T_b)$ was an effective step ahead. Nevertheless, correction factors so defined do not fully reflect the effect of Cp profile as well as other property profiles across the flow.

The Nusselt type correlation is developed through a semi-empirical approach. It stems from the "fully developed flow" assumption. Under supercritical conditions this assumption in its restrictive sense may not be helpful anymore, i.e., the velocity and temperature profiles are expected to change when the pseudocritical region spans the flow radially from the wall to bulk. If $T_w < T_{pc}$ or if $T_{pc} < T_b$, the variations in velocity and temperature profiles along the flow are not large. Thus, the available empirical correlations may predict the data satisfactorily. For $T_b < T_{pc} < T_w$, Reynolds and Prandtl numbers only partially characterize the flow. The question of at what temperature they should be evaluated is more difficult than any other situation to answer. Further information about the radial location of the pseudocritical region (zone of severe variations of fluid properties) seems to be necessary. In other examples of variable property flow there may exist a large difference of properties between wall and bulk, but there is no region, which is of particular importance. On the contrary, in supercritical fluid flow, as we learned from the results of our analytical modeling, it is vital to know whether the pseudocritical temperature is experienced in the buffer layer of the boundary layer or not. Available empirical correlations do not fully reflect the physics explained and thus they are case dependent and may produce unreliable results if flow conditions were different from those under which they were developed. It leads us to the idea of allowing the reference temperature to vary with flow conditions along the test section.

4.1 A Different Approach. Calculating non-dimensional numbers at temperatures such as that of the bulk or wall, as widely practiced, cannot reflect the different regions of flow along the tube. At one point, the pseudocritical region may be reached in the laminar sublayer, thus not promoting heat transfer substantially. Downstream at some other point where the pseudocritical temperature is shifted to the buffer layer, turbulence activities increase and heat transfer is enhanced. To comply with the variant nature of flow along the test section, it is suggested here to evaluate Reynolds and Prandtl numbers at a variable reference temperature, T_{ref}. This way the assumption of fully developed flow in a specific sense has been applied. That is, heat transfer may be determined from local fluid properties and is independent of the flow history. The question is what temperature can best represent the flow at each axial location, i.e., how to define T_{ref}.

In order to explain the new approach employed in this study, we need to use a traditional, constant property based, Nusselt number correlation as our framework. Since all such correlations are inadequate to predict heat transfer to supercritical fluid flows, it really does not matter which one of them is selected for the starting point of our method here. Let us pick the well known Dittus–Boelter correlation for its amazing simple form. We know from previous studies [22] that Dittus–Boelter correlation overpredicts the peak of heat transfer coefficients for supercritical flows. Note that the Reynolds and Prandtl numbers are evaluated at bulk temperature in Dittus–Boelter correlation, i.e., $T_{ref} = T_b$. Now, let us find out at what temperature should Reynolds and Prandtl numbers be estimated in order that the Dittus–Boelter correlation provides the best agreement with the experiments. The temperature resulting in the best agreement with experiment was called the equivalent temperature and denoted by T_{eq}. Thus, there will be one temperature, T_{eq}, associated with each flow cross section for which the predicted heat transfer coefficient almost equals the experimental value, i.e., $h_{correlation} \approx h_{expt}$. Hence, the Dittus–Boelter correlation can accurately predict the heat transfer coefficient provided that T_{ref} is chosen to be T_{eq} at any point. Further inspection showed that there indeed exists a T_{eq} at each flow cross section. The variation of T_{eq} along the test section is shown in Fig. 8.

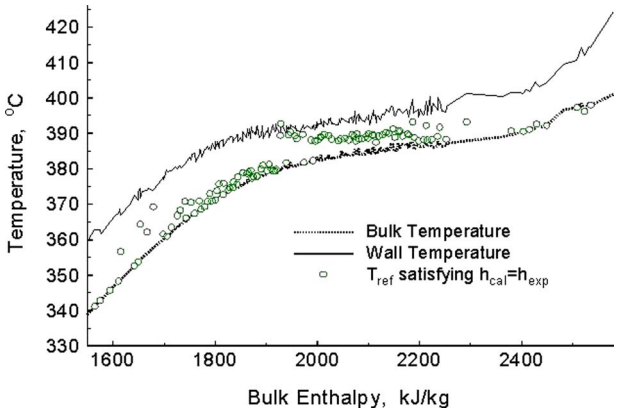

Fig. 8 Variations of T_{ref} with respect to T_b and T_w along the test section; P=25.2 MPa, q''=307 kW/m^2, G=965 kg/m^2 s, and D=6.3 mm

As shown, in both subcritical $(T_b < T_w < T_{pc})$ and postcritical $(T_w > T_b > T_{pc})$ regions, it appears that $T_{eq} \approx T_b$. In the vicinity of the pseudocritical temperature, T_{eq} jumps from T_b to some values close to T_w. It then remains almost constant until the bulk is raised to that temperature. More trials in the subcritical region confirmed that the small scatter of data can be safely ignored and the major trend observed in variation of T_{eq} may be relied on.

Note that the use of enthalpy for horizontal axis is preferable over temperature. That is because the heat flux is constant and thus fluid energy (bulk enthalpy) changes linearly along the test section. Enthalpy at T_{ref} is denoted as i_{ref} and estimated by

$$i_{ref} = i_b + i_{fac}(i_w - i_b) \tag{8}$$

where i_w and i_b are the wall and bulk enthalpies. The enthalpy factor, i_{fac}, is to be specified for different zones of flow. In order to study the variation of i_{fac} along the flow, we define the dimensionless number "enthalpy zone," i_{zone}, as

$$i_{zone} = \frac{i_{pc} - i_b}{i_{pc} - i_w} \tag{9}$$

where i_{pc} is the fluid enthalpy at the pseudocritical temperature. Wall temperature is estimated first by Dittus–Boelter correlation using $T_{ref} = T_b$ and corrected later by iteration. Variation of i_{zone} with flow enthalpy along the test section is shown in Fig. 9.

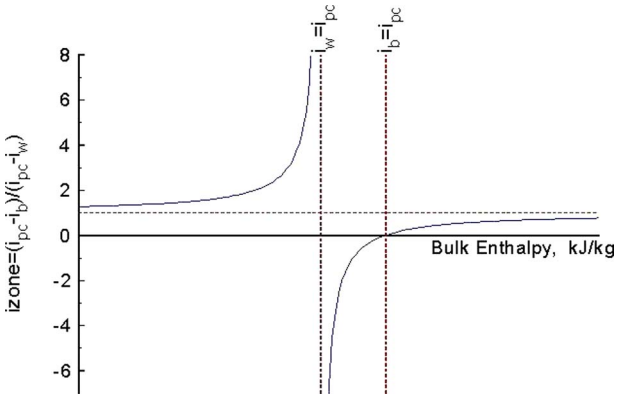

Fig. 9 Typical variation of $i_{zone} = (i_{pc} - i_b)/(i_{pc} - i_w)$ along the test section

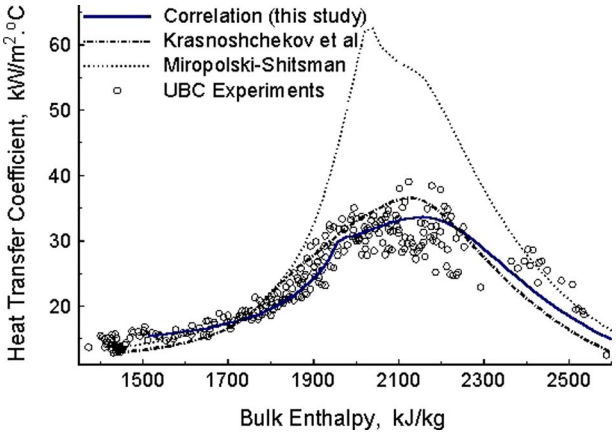

Fig. 10 Results of the correlation of this study compared with others and experiment; P=25.2 MPa, q''=307 kW/m^2, G =965 kg/m^2 s, and D=6.3 mm

Before the pseudocritical temperature is reached at the wall (i.e., $i_b < i_w < i_{pc}$), i_{zone} is greater than 1. It goes to positive infinity asymptotically as T_w approaches T_{pc}. For this range of values of i_{zone}, Fig. 8 suggests that $T_{ref}=T_b$ (i.e., $i_{ref}=i_b$) is adequate. Where $i_b < i_{pc} < i_w$, i_{zone} has a negative number, $T_{ref}=T_b$ still leads to satisfactory results for T_w values close to T_{pc}. It was confirmed by the experimental results that this region expands to values of i_{zone} from negative infinity up to about -0.9. Starting from this critical i_{zone} number (≈ -0.9) to the point where the bulk is at pseudocritical temperature ($i_{zone}=0$) and even at postcritical region (i.e., $i_b > i_{pc}$), i_{ref} varies with temperature.

From Fig. 8 it is clear that there is a jump in T_{ref} from T_b to a value close to T_w in the near critical region. This can be modeled using value of $i_{zone}=-0.9$ and the parameter "enthalpy factor," i_{fac}, defined as

$$i_{fac} = \frac{1 - i_{zone}}{1 - (-0.9)} \cdot \frac{i_{pc}}{i_w} = \frac{(1 - i_{zone})i_{pc}}{1.9 i_w} \quad \text{for} \quad -0.9 < i_{zone} < 1$$

$$i_{fac} = 0 \quad \text{for} \quad i_{zone} \le -0.9 \quad \text{or} \quad 1 \le i_{zone} \tag{10}$$

According to the above definitions, variations of i_{zone}, i_{fac}, and T_{ref} may be summarized as follows. At subcritical temperatures up to where the wall is just into critical region, i_{fac} is 0 and $T_{ref}=T_b$. As i_{zone} crosses the critical value of -0.9, i_{fac} jumps from 0 to (i_{pc}/i_w), which is slightly smaller than unity. Accordingly, T_{ref} will jump to a value close to T_w. Further downstream of the flow i_{fac} vanishes to 0 again as i_{zone} approaches 1 at the postcritical region.

Heat transfer coefficients obtained from the correlation with T_{ref} defined as above were compared against experimental results, and very good agreement was obtained. An example is shown in Fig. 10. The predictions of a few other correlations are also shown. It is clear that best agreement with experiment is provided by the correlation of this study.

To demonstrate the capability of the present correlation in predicting the results of other investigations for horizontal flows, we need to find those measurements that are not affected by buoyancy. Not many of such data are available in literature. In the following example measurements of Yamagata et al. [23] are compared with predictions of the others and present correlation. To avoid congestion of too much data on a single graph the results of Yamagata et al. [23] and the present study are shown separately. Figure 11 shows the data of Yamagata et al. [23] for four different test conditions. The graph with the largest peak heat transfer coefficients corresponds to the test conditions where the buoyancy effects are negligible. This can be learned from the fact that the heat transfer coefficients measured at the bottom and the top surfaces, as shown in Fig. 11, are identical. This is among rare data for horizontal flows in which the effects of natural convection were shown to be negligible.

Eight different correlations (Refs. [13,17,19,23–27]) were tried and the predictions of the best two of them (compared with the data of Yamagata et al. [23], Fig. 11), together with those of the present correlation, were shown in Fig. 12. Most of the other correlations largely overpredicted the data. The closer agreement of peak heat transfer coefficients ($\sim$75 kW/m^2 °C) predicted by this study with the data of Yamagata et al. [23] is striking.

It should be re-emphasized that the correlation developed in this chapter is valid for axisymmetric flows where natural convec-

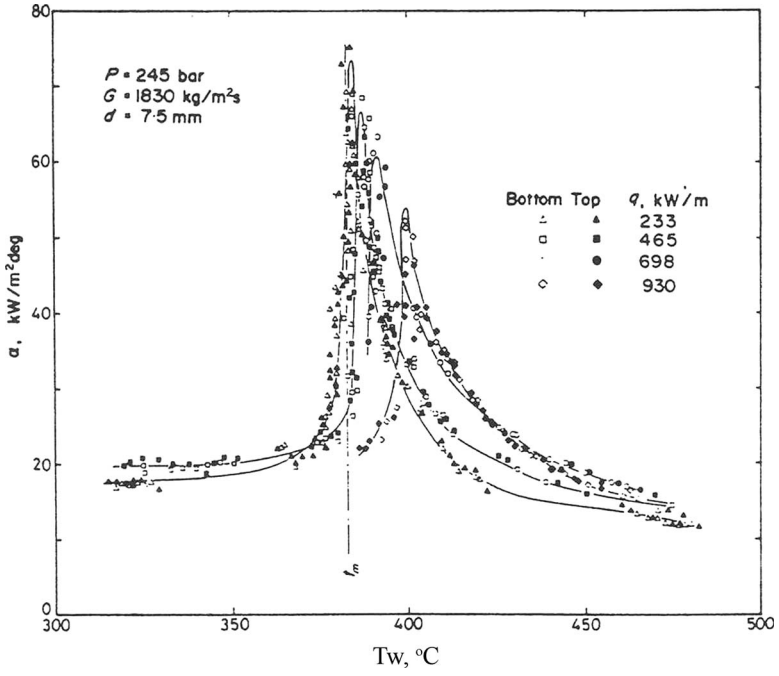

Fig. 11 Heat transfer coefficients measured by Yamagata et al. [23]

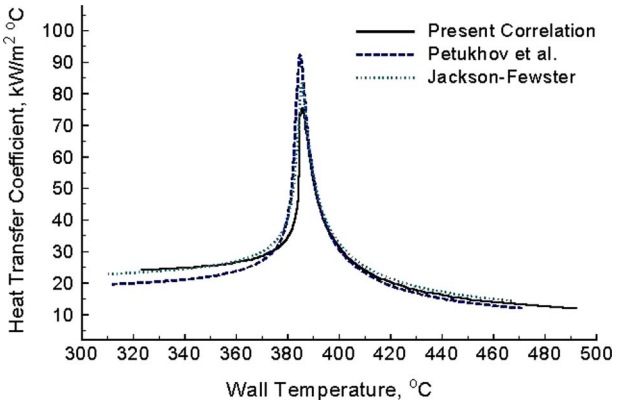

Fig. 12 Heat transfer coefficients predicted by the empirical correlations of this and other studies. Test conditions are the same as Fig. 11.

tion, as well as the effect of acceleration, is negligible. Depending on test conditions, it happens that in some cases one of the available correlations may predict heat transfer coefficients satisfactorily and be compatible with the present correlation. Nevertheless, none of those earlier correlations are as widely applicable to various test conditions as the present one.

5 Summary and Conclusions

A model was developed that provides a solution to the boundary layer equations based on the law of the wall. Model predictions were compared against experimental data for flows unaffected by buoyancy. Good agreements were reached. In addition to this, a new empirical correlation has been developed, which provides accurate prediction compared with the data of this study as well as others.

The following main conclusions were drawn from this work.

- Most of the popular expressions for universal velocity profiles were tried. Variations in the predictions were shown. It was found that using the expressions offered by Van Driest, von Kármán, and Rannie provided the best prediction to the data obtained in the current study. Others were shown to dramatically overpredict, or in the case of Prandtl–Taylor, underpredict the data of the current study.
- Incorporating different expressions for the wall shear stress also affects the prediction of the model. The correction of Popov, reported by Petukhov et al. [17], to account for variable properties was found to predict the current data well.
- The effect on the choice of turbulent Prandtl number was also studied. Here it was found that a slight modification made to original expression of Hollingsworth et al. [19] provides the best prediction.
- The model developed was shown to predict the data obtained in the current study better than others' predictions.
- The semi-empirical correlation developed during this study was shown to predict the data obtained in this study as well as the data of others for cases with negligible buoyancy and/or acceleration effects.

6 Recommendations

A 1D model was shown to be adequate to predict flows where buoyancy and/or acceleration effects are unimportant. It can be shown that under most conditions, both buoyancy and acceleration are closely coupled in horizontal flows. The exception would be for small diameter tubes that may have acceleration effects (due to decreasing density as the fluid passes through the pseudocritical temperature) without buoyancy effects (due to the small diameter). To properly account for both buoyancy and acceleration in a horizontal flow, a 3D model is imperative. It is essential to investigate how turbulence structure may be affected by dramatic variations of flow properties at supercritical conditions. That is, while vast majority of numerical models available have assumed that the structure of turbulence is not changed in a variable property flow and in order to account for property variations, simply the local value of each property has been taken in calculations.

With respect to experimental work, lack of data for horizontal supercritical fluid flows with clarifications about buoyancy effects is evident. Such data are very much needed, especially for supercritical water and for a wide range of flow parameters, to better evaluate models and empirical correlations.

Nomenclature

$\underline{\mathrm{Cp}}$ = specific heat capacity, kJ/kg °C
$\overline{\mathrm{Cp}}$ = averaged specific heat capacity, kJ/kg °C
D = tube diameter, mm
f = friction factor
G = mass flux, kg/m^2 s
h = heat transfer coefficient, kW/m^2 °C
i = specific enthalpy, kJ/kg
i_{fac} = enthalpy factor defined in Eq. (8)
i_{zone} = enthalpy zone parameter defined in Eq. (9)
N = total number of grids
Nu = Nusselt number
P = pressure, MPa
$\underline{\mathrm{Pr}}$ = Prandtl number
$\overline{\mathrm{Pr}}$ = averaged Prandtl number, $\overline{\mathrm{Cp}}\cdot\mu/\kappa$
Pr_t = turbulent Prandtl number
q'' = heat flux, kW/m^2
Re = Reynolds number
r = radial distance from center of the tube, mm
r_0 = tube radius, mm
T, t = temperature, °C
u = fluid velocity in axial direction, m/s
v = fluid velocity in radial direction, m/s DF
α = thermal diffusivity, m^2/s
β = volumetric expansion coefficient, 1/K
ε = momentum and thermal eddy diffusivity once Pr_t=1.0, m^2/s
ε_h = thermal eddy diffusivity, m^2/s
ε_m = momentum eddy diffusivity, m^2/s
κ = thermal conductivity, W/m °C
μ = dynamic viscosity, kg/m s
ν = kinematic viscosity, m^2/s
ρ = density, kg/m^3
τ = shear stress, N/m^2
τ_t = turbulent shear stress, N/m^2

Subscript

b = bulk
pc = pseudocritical
ref = reference
w = wall

References

[1] Modell, M., Gaudet, G., Simson, M., Hong, G., and Biemann, K., 1982, "Supercritical Water, Testing Reveals New Process Holds Promise," Solid Wastes Management Magazine, August, pp. 26–30.
[2] Oka, Y., Koshizuka, S., and Yamasaki, T., 1992, "Direct Cycle Light Water Reactor Operating at Supercritical Pressure," J. Nucl. Sci. Technol., **26**(6), pp. 585–588.
[3] 2006, "Generation IV Nuclear Reactors," UIC Briefing Paper No. 77, Jul., available on the web at http://www.uic.com.au/nip77.htm.
[4] Condie, K. G., 2005, "Design Description for INL Supercritical Water Heat Transfer Test Section for Inclusion Into the Benson Loop," Idaho National Laboratories, Report. http://nuclear.inl.gov/deliverables/docs/test_section_design_summary.pdf
[5] Fridleifsson, G. O., Elders, W. A., and Saito, S., 2001, "The Icelandic Deep Drilling Project (IDDP): Obtaining Supercritical Geothermal Fluid From Hot Spot Ridge Interaction," American Geophysical Union, Fall Meeting.
[6] Fraser, D. W. H., 2004, "Supercritical Geothermal Worldwide Resources as a

Challenge to the Oil and Mining Industries," Second Conference on Future Energy (COFE), Washington, DC.
[7] Fraser, D. W. H., 2002, "A Method for Bringing the Geothermal Saline Fluids to the Surface for Mineral Extraction," Second International Workshop and Conference on IDDP, Reykjavik, Iceland, Oct., available on CD.
[8] Hashida, T., Hayashi, K., Niitsuma, H., Matsuki, N., Tsuchiya, N., and Nakatsuka, K., 2000, "Investigation of Heat Extraction From Supercritical Geothermal Reservoirs," *Proceedings of the World Geothermal Congress*, Japan, pp. 3725–3730.
[9] Fraser, D. W. H., 2006, "Mineral Extraction From High Temperature Supercritical Aqueous Chloride Solutions From Near Surface Magmatic Systems," Conference on Mineral Extraction From Geothermal Brines, Tucson, AZ, Sept.
[10] Fraser, D. W. H., 2004, "Transportable Geothermal Energy and the Possible Use of Methanol as a Hydrogen Carrier, The Aleutian Islands Potential," presented at the 2004 Geothermal Summit at Chena Hot Springs, Chena Hot Springs, Alaska, Aug. 10–12, available on CD.
[11] Bazargan, M., Fraser, D. W. H., and Chatoorgan, V., 2005, "Buoyancy Effects During the Horizontal Flow of Supercritical Water," ASME J. Heat Transfer, **127**(8), pp. 897–902.
[12] Pruß, A., and Wagner, W., 1995, *Physical Chemistry of Aqueous Systems: Meeting the Needs of Industry, Proceedings of the 12th International Conference on the Properties of Water and Steam*, H. J. White, Jr., J. V. Sengers, D. B. Neumann, and J. C. Bellows, eds., Begell House, New York, p. 66.
[13] Jackson, J. D., and Hall, W. B., 1979, "Forced Convection Heat Transfer to Fluids at Supercritical Pressure," *Turbulent Forced Convection in Channels and Bundles*, Vol. 2, S. Kakac and D. B. Spalding, eds., Hemisphere, New York, p. 563.
[14] Kays, W. M., 1994, "Turbulent Prandtl Number—Where Are We?," ASME J. Heat Transfer, **116**, pp. 284–295.
[15] Goldmann, K., 1954, "Heat Transfer to Supercritical Water and Other Fluids With Temperature Dependent Properties," Chem. Eng. Prog., Symp. Ser., **50**(11), pp. 105–113.
[16] Hsu, Y. Y., and Smith, J. M., 1961, "The Effect of Density Variation on Heat Transfer in the Critical Region," ASME J. Heat Transfer, **83**, pp. 176–182.
[17] Petukhov, B. S., Kurganov, V. A., and Ankudinov, V. B., 1983, "Heat Transfer and Flow Resistance in the Turbulent Pipe Flow of a Fluid With Near-Critical State Parameters," Teplofiz. Vys. Temp., **21**(1), pp. 92–100 1983 [High Temp., **21**(1), pp. 81–89].
[18] Razumovskiy, V. G., Ornatskiy, A. P., and Mayevskiy, Y. M., 1990, "Local Heat Transfer and Hydraulic Behavior in Turbulent Channel Flow of Water at Supercritical Pressure," Heat Transfer-Sov. Res., **22**(1), pp. 91–102.
[19] Hollingsworth, D. K., Kays, W. M., and Moffat, R. J., 1989, "Measurement and Prediction of the Turbulent Thermal Boundary Layer in Water on Flat and Concave Surfaces," Thermosciences Division, Department of Mechanical Engineering, Stanford University, Report No. HMT-41.
[20] Kakac, S., 1987, "The Effect of Temperature-Dependent Fluid Properties on Convective Heat Transfer," *Handbook of Single Phase Convective Heat Transfer*, S. Kakac, R. K. Shah, and W. Aung, eds., Wiley, New York, Chap. 18.
[21] Fraser, D. W. H., and Bazargan, M., 2001, "Effect of Natural Convection on Heat Transfer in a Horizontal Tube With Supercritical Water," Fifth World Conference on Experimental Heat Transfer, Fluid Mechanics and Thermodynamics, Thessaloniki, Greece, Sept.
[22] Bazargan, M., 2001, "Heat Transfer to Turbulent Flow of Supercritical Water in a Horizontal Flow," Ph.D. thesis, University of British Columbia, Vancouver, B.C. Canada
[23] Yamagata, K., Nishikawa, K., Hasegawa, S., Fujii, T., and Yoshida, S., 1972, "Forced Convective Heat Transfer to Supercritical Water Flowing in Tubes," Int. J. Heat Mass Transfer, **15**, pp. 2575–2593.
[24] Swenson, H. S., Carver, J. R., and Kakarla, C. R., 1965, "Heat Transfer to Supercritical Water in Smooth-Bore Tubes," ASME J. Heat Transfer, **87**, pp. 477–484.
[25] Miropolski, Z. L., and Shitsman, M. E., 1957, "Heat Transfer to Water and Steam at Variable Specific Heat (In Near-Critical Region)," Zh. Tekh. Fiz., **27**(10), pp. 2359–2372 1957 [Sov. Phys. Tech. Phys., **27**(10), pp. 2196–2208].
[26] Petukhov, B. S., Krasnoshchekov, E. A., and Protopopov, V. S., 1961, "An Investigation of Heat Transfer to Fluids Flowing in Pipes Under Supercritical Conditions," *Proceedings of the 1961–1962 Heat Transfer Conference on International Development in Heat Transfer*, Aug. 28, 1961–Jan. 12, 1962, University of Colorado, Boulder, CO.
[27] Krasnoshchekov, E. A., and Protopopov, V. S., 1966, "Experimental Study of Heat Exchange in Carbon Dioxide in the Supercritical Range at High Temperature Drops," Teplofiz. Vys. Temp., **4**(3), pp. 389–398 1966 [High Temp., **4**(3), pp. 375–382].

Flow and Heat Transfer Over a Stretched Microsurface

Suhil Kiwan[1]
e-mail: kiwan@just.edu.jo

M. A. Al-Nimr

Department of Mechanical Engineering,
Jordan University of Science and Technology,
P.O. Box 3030,
Irbid, 22110, Jordan

The convection heat transfer induced by a stretching flat plate has been studied. Similarity conditions are obtained for the boundary layer equations for a flat plate subjected to a power law temperature and velocity variations. It is found that a similarity solution exists only for a linearly stretching plate and only when the plate is isothermal. The analysis shows that three parameters control the flow and heat transfer characteristics of the problem. These parameters are the velocity slip parameter K_1, the temperature slip parameter K_2, and the Prandtl number. The effect of these parameters on the flow and heat transfer of the problem has been studied and presented. It is found that the slip velocity parameter affect both the flow and heat transfer characteristics of the problem. It is found that the skin friction coefficient decreases with increasing K_1 and most of the changes in the skin friction takes place in the range $0<K_1<1$. A correlation between the skin friction coefficient and K_1 and Re_x has been found and presented. It is found that $c_f=\frac{2}{3}Re_x^{-0.5}(K_1+0.64)^{-0.884}$ for $0<K_1<10$ with an error of $\pm 0.8\%$. Other correlations between Nu and K_1 and K_2 has been found and presented in Eq. (28).
[DOI: 10.1115/1.3090811]

Keywords: similarity solution, stretched microsurface, rarefied gas, velocity slip parameter, temperature jump parameter

1 Introduction

In the past few years the hydrodynamic and thermal behaviors of different systems at a microscale level have attracted the attention of many researchers. This is due to the rapid growth of novel techniques applied in micro-electro-mechanical systems (MEMS) that found applications in many industrial and biomedical fields. An excellent review for the fundamentals, theory, and applications of these microscale systems may be found in Refs. [1–3]. As a result of this revolution that raised interest in these microscale systems, researchers revisited many macroscale mechanical components and focused on investigating and predicting the change in their thermal and hydrodynamic behaviors if they are fabricated at microscale sizes. Recently, electrostatic, magnetic, electromagnetic, pneumatic, and thermal actuators, motors, valves, gears, cantilevers, diaphragms, and tweezers less than 100 μm in size have been fabricated. These have been used as sensors for pressure, temperature, mass flow, velocity, sound and chemical composition; as actuators for linear and angular motions; and as simple components for complex systems such as robots, microheat-engines, and microheat-pumps [1–3].

The flow characteristics in these small devices differ from those in macroscopic systems and cannot always be predicted from the classical flow and energy models such as the Navier–Stokes and energy equations with no-slip and no-jump boundary conditions at a fluid-solid interface. Slip flow, temperature jump, thermal creep, rarefaction, compressibility, viscous dissipation, intermolecular forces, and other unconventional effects may have to be taken into account. For gases, microfluid hydrodynamic and thermal behaviors have been studied by incorporating slip and jump boundary conditions, thermal creep, viscous dissipation, and compressibility effects into the continuum equations of motion and energy. Molecular-based models have also been used for certain ranges of the operating parameters. Moreover, the presence of slip and temperature jump is not strictly associated with microscale applications. On a macroscale level, if the pressure of the gas is reduced sufficiently, the slip and temperature jump conditions exist.

On the macroscale level, many investigators studied the heat transfer and fluid flow adjacent to a continuously moving macrosurface through a quiescent fluid. This was motivated by the many engineering applications that can be modeled by a stretching surface, and the fact that the study of heat transfer and flow field is necessary in many applications to determine the quality of the final products. These applications include manufacturing processes of a continuous casting, glass fiber production, metal extrusion, geothermal reservoirs, many processes involving polymer composites, hot rolling, manufacturing of plastics, textiles, paper productions etc. The heat and mass characteristics of continuously moving surfaces in a fluid with no-slip conditions has been investigated over the years by many researches [4–8].

The problem under consideration, to the best of the author's knowledge, has not been reported in the literature.

2 Problem Formulation

Consider the steady two-dimensional laminar flow induced by a continuously stretching horizontal plate in a quiescent fluid as shown in Fig. 1. The plate will induce the fluid to move. The plate motion could be produced by two equal and opposite forces so that the plate is stretched keeping the origin fixed. Only the right hand side of the plate will be considered for the analysis (see Fig. 1).

On the basis of the boundary layer approximations with constant thermophysical properties, the conservation of momentum and mass equations are given by

$$\frac{\partial u}{\partial x}+\frac{\partial v}{\partial y}=0 \tag{1}$$

$$u\frac{\partial u}{\partial x}+v\frac{\partial u}{\partial y}=\nu\frac{\partial^2 u}{\partial y^2} \tag{2}$$

[1]Corresponding author.

Contributed by the Heat Transfer Division of ASME for publication in the JOURNAL OF HEAT TRANSFER. Manuscript received May 24, 2008; final manuscript received October 15, 2008; published online April 9, 2009. Review conducted by Sung Jin Kim.

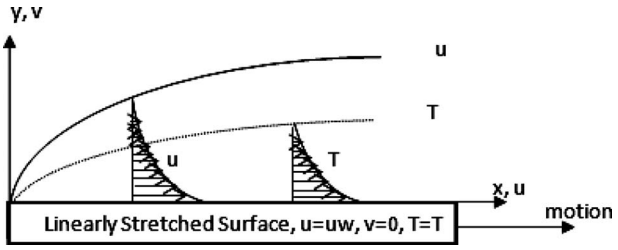

Fig. 1 Schematic for the problem under consideration

$$\rho c_p\left(u\frac{\partial T}{\partial x}+v\frac{\partial T}{\partial y}\right)=k\left(\frac{\partial^2 T}{\partial y^2}\right) \tag{3}$$

For flow at rarefied length scales, the flow and temperature fields are subjected to the following boundary conditions [2].

The velocity slip at the wall for the nonisothermal wall is

$$u_s=u-u_w=\frac{(2-\sigma_v)}{\sigma_v}\lambda\left.\frac{\partial u}{\partial y}\right|_w+\frac{3}{4}\frac{\mu}{\rho T_{wg}}\left.\frac{\partial T}{\partial x}\right|_w \tag{4a}$$

where T_{wg} is the temperature of the gas at the surface. The temperature jump at the wall is as follows:

$$T_s=T-T_w=2\frac{(2-\sigma_T)}{\sigma_T}\lambda\left.\frac{\partial T}{\partial y}\right|_w \tag{4b}$$

The impermeable wall is given by

$$v=0 \quad \text{at} \quad y=0 \tag{4c}$$

Away from the wall, as $y\to\infty$

$$u\to 0, \quad T\to T_\infty \tag{4d}$$

In order to find the condition for similarity solution to exist, assume that the wall is moving by a horizontal velocity given in the form $u_w=U_o x^m$ and the wall temperature is given by $T_w-T_\infty=Cx^n$. The following similarity transformations are defined [3]:

$$u=U_o x^m f'(\eta), \quad T-T_\infty=Cx^n\theta(\eta) \tag{5}$$

$$\eta=y\sqrt{\frac{m+1}{2}}\sqrt{\frac{U_o x^m}{\nu x}}=\frac{y}{x}\sqrt{\frac{m+1}{2}}\sqrt{\mathrm{Re}_x} \tag{6}$$

$$v=-x^{m-1/2}\sqrt{\frac{2\nu U_o}{m+1}}\left(\frac{m+1}{2}f+\frac{m-1}{2}f'\eta\right) \tag{7}$$

Substituting the above parameters into the governing equations yields

$$f'''+ff''-\frac{2m}{m+1}f'^2=0 \tag{8}$$

$$\theta''+\mathrm{Pr}\left(f\theta'-\frac{2n}{m+1}f'\theta\right)=0 \tag{9}$$

The transformed boundary conditions are

$$f(0)=0, \quad f'(\infty)=0, \quad \theta(\infty)=0 \tag{10}$$

To simplify the analysis (without loss of generality), it is assumed that $T_\infty=0$. Thus, the slip velocity condition becomes

$$f'(0)=1+K_1 f''(0)x^{m-1/2}\sqrt{\frac{m+1}{2}}+\frac{3}{4}\frac{\mu}{\rho}\frac{n}{U_o x^{m+1}\theta(0)} \tag{11}$$

And the temperature jump becomes

$$\theta(0)=1+K_2\theta'(0)x^{m-1/2}\sqrt{\frac{m+1}{2}} \tag{12}$$

Equations (8)–(12) indicate that the similarity solution exists only when $m=1$ and $n=0$. That is, for linearly stretching isothermal plate.

In general, for the case where $m=1$ and $n=0$, Eqs. (5)–(7) are reduced to

$$u=U_o x f'(\eta), \quad \frac{(T-T_\infty)}{(T_w-T_\infty)}=\theta(\eta) \tag{13}$$

$$\eta=y\sqrt{\frac{U_o}{\nu}}=\frac{y}{L}\sqrt{\mathrm{Re}_L} \tag{14}$$

$$v=-f\sqrt{\nu U_o} \tag{15}$$

Also, the governing equations become

$$f'''+ff''-f'^2=0 \tag{16}$$

$$\theta''+\mathrm{Pr}\,f\theta'=0 \tag{17}$$

and the velocity slip and temperature jump boundary conditions are reduced to

$$f'(0)=1+K_1 f''(0) \tag{18}$$

$$\theta(0)=1+K_2\theta'(0) \tag{19}$$

where,

$$K_1=\frac{(2-\sigma_v)}{\sigma_v}\lambda\sqrt{\frac{U_o}{\nu}}=\frac{(2-\sigma_v)}{\sigma_v}K_n\,\mathrm{Re}_L^{1/2} \tag{20}$$

$$K_n=\lambda/L \tag{21}$$

and

$$K_2=2\frac{(2-\sigma_T)}{\sigma_T}\lambda\sqrt{\frac{U_o}{\nu}}=2\frac{(2-\sigma_T)}{\sigma_T}K_n\,\mathrm{Re}_L^{1/2} \tag{22}$$

The expression for the shear stress can be developed from the similarity solution for $m=1$ in the following form:

$$c_f=\frac{2\tau}{\rho u^2(x)}=\frac{2f''(\eta)}{\sqrt{\mathrm{Re}_x}} \tag{23}$$

At the moving surface, $f''(0)=0.5C_f\sqrt{\mathrm{Re}_x}$. It should be noted that Reynolds number is based on the wall velocity not the flow velocity. This will simplify the comparison for different values of Kn. The local heat transfer coefficient h can be expressed as

$$h=\frac{-k\left.\frac{\partial T}{\partial y}\right|_{y=0}}{(T_w-T_\infty)} \tag{24}$$

and in dimensionless form the Nusselt number is

$$\mathrm{Nu}=\frac{h\sqrt{\nu/U_o}}{k}=-\theta'(0) \tag{25}$$

Finally, the displacement and the thermal boundary layer thicknesses are defined, respectively, as

$$\delta=\int_0^\infty f''d\eta=-f'(0) \tag{26}$$

$$\eta_{T0.99}=\eta(\theta(\eta)=0.01) \tag{27}$$

3 Numerical Solution Procedure

The system of differential equations given by Eqs. (16) and (17) along with the boundary conditions at two points given by Eq. (10), (18), and (19) are solved using a variable order, variable step size finite difference method with deferred corrections. The solution method is based on the subprogram of Pereyra [9]. The first

Table 1 Comparison between the present code results and that obtained by Ali [4] for $m=0$, $n=0$, $K_1=0$ and $K_2=0$

	Nu				
	Pr=0.72	Pr=1.0	Pr=3.0	Pr=10.0	c_f
Present Code	0.4631	0.582	1.1632	2.3035	1.0000
Ali [4]	0.4617	0.5801	1.1599	2.2960	1.0000
% Error	0.30	0.33	0.28	0.33	0.00

step in the solution is to reduce the governing equations to a system of first order differential equations. The basic discretization of the first order differential equations is the trapezoidal rule over a nonuniform mesh. This mesh is chosen adaptively, to make the local error approximately the same size everywhere. Higher-order discretizations are obtained by deferred corrections. Global error estimates are produced to control the computation. The resulting nonlinear algebraic system is solved by Newton's method with step control. The linearized system of equations is solved by Gauss elimination.

The solution of $f'(\eta)$ and $\theta(\eta)$ is obtained iteratively on η. The solution is first obtained by assuming a certain value of η, then η increased until the values of $f'(\eta)$ and $\theta(\eta)$ at infinity decay exponentially to zero (at least of order 10^{-4}). The maximum possible value of η is taken. Table 1 shows a comparison between the present code results and that obtained by Ali [4] for classical stretching problem when $n=0$ and $m=1$. The comparison shows an excellent agreement. Furthermore, other validation cases are presented by the first author of the current paper in Ref. [5].

4 Results and Discussion

The governing equations and the boundary conditions of the problem indicate that there are three parameters that control the flow and heat transfer characteristics of the problem. The slip parameter K_1, the temperature jump parameter K_2, and the Prandtl number Pr. The effect of each parameter is studied and will be presented next.

Figure 2 represents the variation of the dimensionless transverse velocity component $f(\eta)$ with the similarity independent variable η. As predicted, v increases as η increases since large values of η apply for locations far from the plate (large y). For this case the amount of flow that escapes the boundary layer and leaves in the form of transverse velocity component increases. Near the leading edge the boundary layer thickness is growing with x and more flow escaped the layer in the transverse direction and far away of the plate the flow that escapes the boundary layer accumulates as y increases, yielding larger values for v. The same figure shows that $f(\eta)$ decreases as K_1 increases. As K_1 increases, the slip at the plate surfaces increases, and the penetration of the wall stretching through the fluid decreases. This leads to a reduction in the displacement thickness as will be seen later. This reduction in the displacement thickness leads to a reduction in the flow that escapes the layer and hence a reduction in v.

Figure 3 shows the variation in the dimensionless axial velocity component $f'(\eta)$ with the similarity independent variable η. The velocity component u decreases as η increases to reach zero far away from the plate when the penetration effect of the driving stretching surface diminishes. Note that the fluid dimensionless velocity at the wall is 1 when $K_1=0$, which presents the no-slip case. As the hydrodynamics slipping parameter K_1 increases, the differences between the wall and the fluid velocities adjacent to the wall increase. Again, it is clear that as the slipping parameter increases, the penetration of the stretching effect through the fluid domain decreases, leading to a reduction in the hydrodynamic boundary layer measured by the displacement thickness. Increasing the slipping factor may be looked at as a miscommunication between the source of motion (the plate) and the fluid domain. Note that hydrodynamic behavior of the problem under consideration is more sensitive to the variations in small values of K_1 as compared with the variations in large values of K_1. Table 2 shows that, for example, increasing K_1 from 0 to 1 leads to an increase in the slip velocity at the wall from 0 to 0.43 while increasing K_1

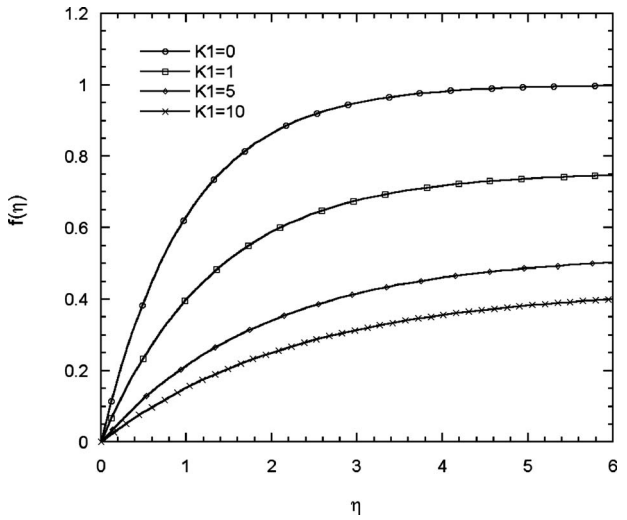

Fig. 2 Variation in the dimensionless transverse velocity distribution with the similarity parameter η at different slip parameter K_1

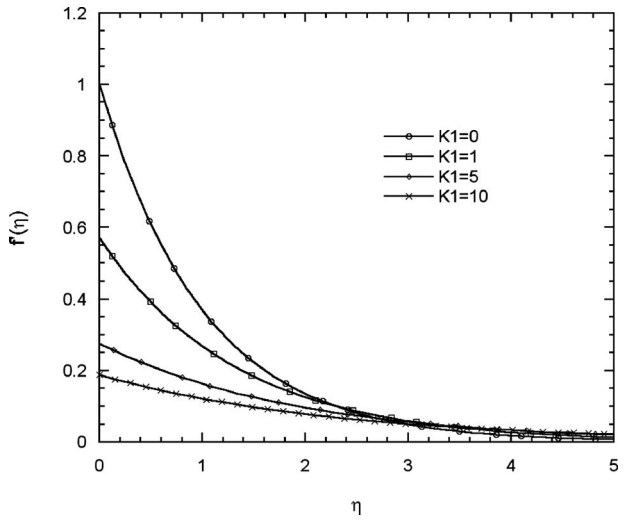

Fig. 3 Variation in the dimensionless axial velocity distribution with the similarity parameter η at different slip parameter K_1

Table 2 Numerical results of the momentum and thermal problem

Pr	K_1	K_2	$f'(0)$	$-f''(0)$	$\theta(0)$	$-\theta'(0)$
0.7	0	0	1.000	1.000	1.000	0.454
	0.5		0.704	0.591	0.724	0.276
	1.0		0.570	0.430	0.745	0.255
	5.0		0.276	0.145	0.808	0.192
	10.0	1	0.188	0.081	0.836	0.164
1	0	0	1.000	1.000	1.000	0.582
	0.5		0.704	0.591	0.672	0.328
	1.0		0.570	0.430	0.695	0.305
	5.0		0.276	0.145	0.766	0.234
	10.0	1	0.188	0.081	0.799	0.201
	1	0.5	0.570	0.430	0.820	0.360
		1.0	0.570	0.430	0.695	0.305
		5.0	0.570	0.430	0.313	0.137
		10.0	0.570	0.430	0.185	0.081
		20.0	0.570	0.430	0.102	0.045

from 1 to 5 leads to an increase in the wall slip velocity from 0.43 to 0.75. The sensitivity of u and v to the variations in K_1 within its lower range is obvious in Figs. 2 and 3.

Figure 4 shows the variation in the shear parameter f'' with the independent similarity parameter η. Note that f'' is equal to -1 at the wall when $K_1=0$, and this is the exact value known for a flow over a stretching surface with no-slip boundary conditions [5,10]. As predicted the shear parameter f'' decreases as η increases since the penetration of the stretching driving force decreases as one marches into the fluid domain. Also, f'' decreases as K_1 increases due to the increase in the slip conditions at the stretching plate since as slip conditions increase, the flow will be less aware of the stretching effects.

Figure 5 shows the variation of the dimensionless temperature θ with η at different values of the hydrodynamics slip parameter K_1 and for the temperature jump parameter $K_2=0.5$. As the velocity slip parameter K_1 increases, less flow will be induced close to the plate layer as a result of its stretching effect. As a result, the hot plate heats less amount of fluid and this causes higher increases in the fluid temperature. It will be shown later that the problem thermal behavior is much more sensitive to the variations in K_2 as compared with the variations in K_1. The parameter K_2 has direct effects on the fluid thermal behavior because K_2 is a measure for the temperature jump at the wall. On the other hand, K_1 affects the fluid hydrodynamics behavior directly, and this hydrodynamics behavior affects the problem thermal behavior indirectly through the enthalpy flow in the energy equation. Also, note that the temperature profile becomes almost linear for small η as K_1 increases. Less motion will be induced within the fluid as K_1 increases, and a pure heat conduction mode will prevail in this case yielding the linear looking profile for the temperature. The limiting case $K_1 \rightarrow \infty$ implies that the fluid layer above the stretching plate is stagnant because it is completely unaware of the stretching effect. This implies that the available mode for heating the fluid by the plate is a pure heat conduction mode that is described by a sort of error function which looks linear very close to the plate.

Figure 6 shows the variation in θ' with η and for different values of K_1 at $K_2=0.5$. The parameter θ' is a measure for the heat transfer within the domain and this parameter decreases as η increases because the penetration of the hot plate heating effect decreases as η increases. Also, note that negative values for θ' imply positive heat transfer rates in the positive η direction, because the heat transfer is proportional to $-\theta'(0)$. Also, increasing K_1 leads to a reduction in the amount of heat transfer near the plate surface. This has been explained before since the heat transfer mode shifts from the convection to conduction mode as K_1 increases. The conduction mode is less efficient as compared with the convection mode. It is important to draw the reader's attention to the fact that although higher fluid temperatures are attained as

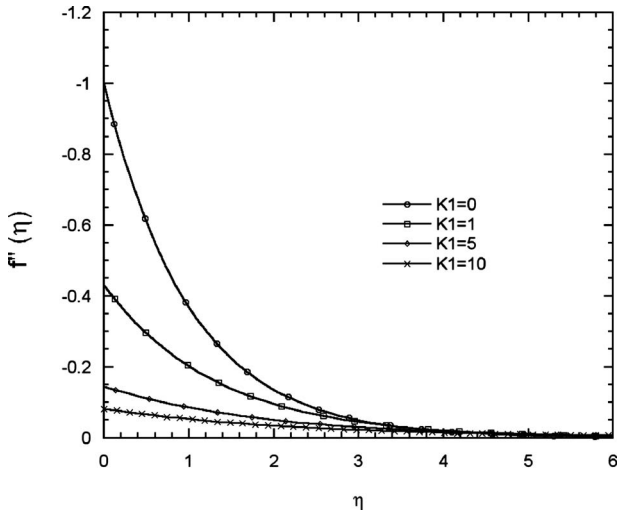

Fig. 4 Variation in the dimensionless shear parameter distribution with the similarity parameter η at different slip parameter K_1

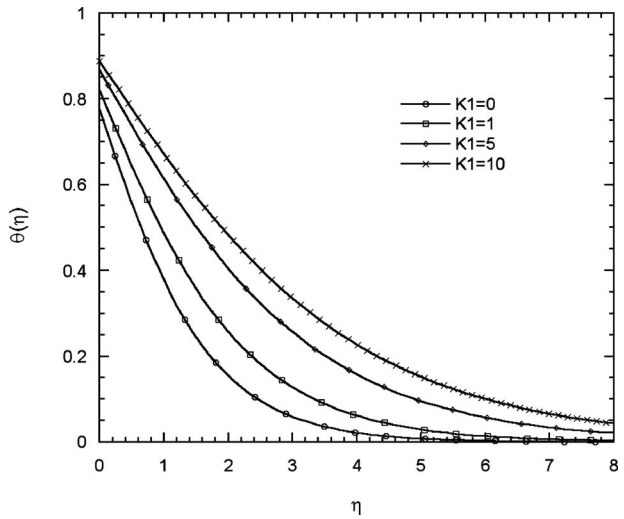

Fig. 5 Variation in the dimensionless temperature distribution with the similarity parameter η at different slip parameter K_1

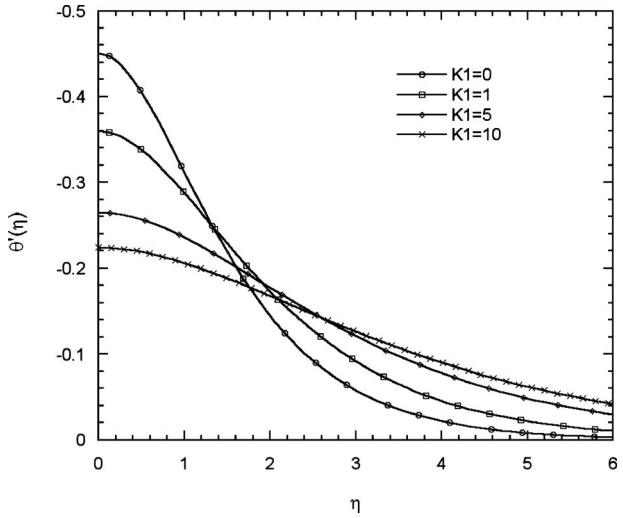

Fig. 6 Variation in the dimensionless temperature gradient distribution with the similarity parameter η at different slip parameter K_1

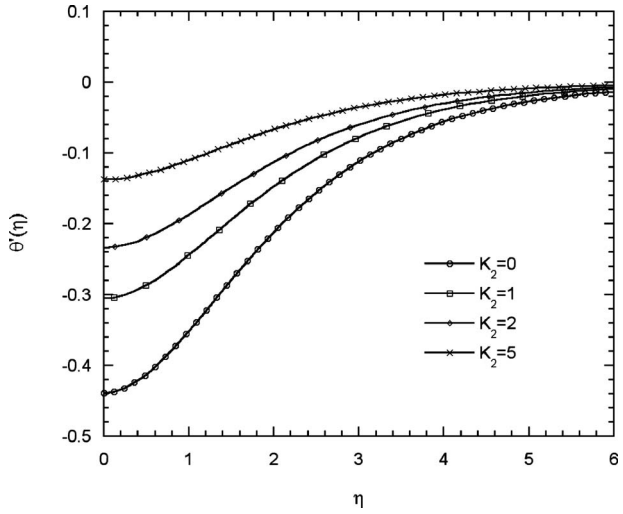

Fig. 8 Variation in the dimensionless temperature gradient distribution with the similarity parameter η at different jump parameters K_2, K_1=1, Pr=1

K_1 increases, but less heat transfer has been observed. Increasing K_1 leads to a less amount of induced flow and then to less amount of heat transfer. But this little amount of heat is supposed to heat less amount of fluid, and as a result, yields higher temperatures.

Figure 7 shows the variation in the dimensionless temperature θ with the similarity parameter η and at different values of K_2. As predicted, increasing the temperature jump parameter K_2 leads to a reduction in the fluid temperature. As the temperature jump parameter K_2 increases, the fluid will not sense the heating effects of the plate and less amount of heat will be extracted from the hot plate to the fluid. Also, the problem thermal behavior is more sensitive to the variations in lower range of K_2 as compared with the variations in the higher ranges of K_2. As an example, increasing K_2 from 0 to 1 yields to an increase in the wall temperature jump from 0 to 0.3 while increasing K_2 from 2 to 5 raises the temperature jump at the wall from 0.475 to 0.68.

Figure 8 shows the effect of the temperature jump parameter K_2 on the distribution of θ'. As predicted, less amount of heat transfer generates within the fluid domain as K_2 increases. This is due to the thermal miscommunication between the hot wall and the fluid as the temperature jump parameter increases. The fluid will not be aware of the wall thermal conditions due to the increase in the temperature jump parameter. Note that temperature gradients, and hence heat transfer, diminishes outside the thermal boundary layer.

Figure 9 shows the effect of Pr on the temperature distribution for $K_1=1$ and $K_2=0.5$. As predicted lower Pr leads to higher temperatures. Lower Pr implies fluids having higher thermal diffusivity α and lower viscosities μ. The heating effect of the hot wall is able to penetrate deeper and deeper through the fluid as α increases, and this yields higher fluid temperatures. Also, the stretching plate will induce less flow as μ decreases, and the hot plate is supposed to heat less amount of fluid. This, in turn, yields higher temperatures for the plate.

Figure 10 shows the effect of Pr on θ' distribution. The parameter—θ' is proportional to the heat transfer through the fluid domain and this convicted heat is proportional to Pr as explained previously. It is known that all heat transfer correlations predict that q is proportional to Pr.

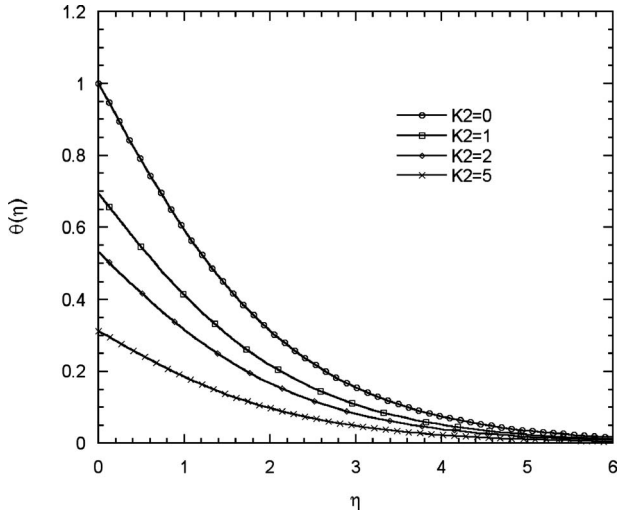

Fig. 7 Variation in the dimensionless temperature distribution with the similarity parameter η at different jump parameters K_2, K_1=1, Pr=1

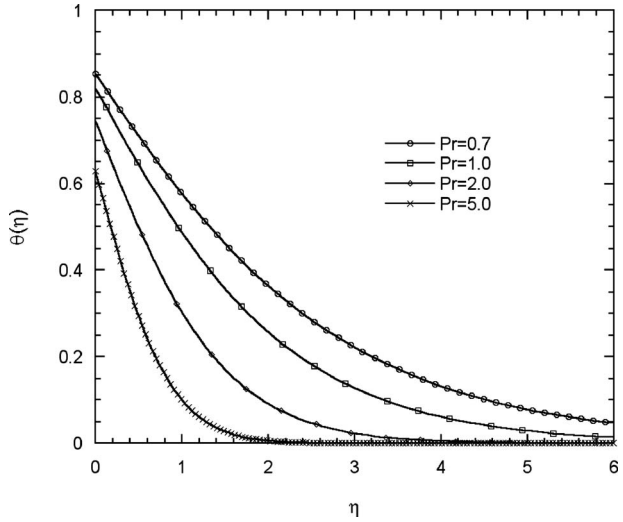

Fig. 9 Variation in the dimensionless temperature distribution with the similarity parameter η at different Prandtl numbers for K_1=1, K_2=0.5

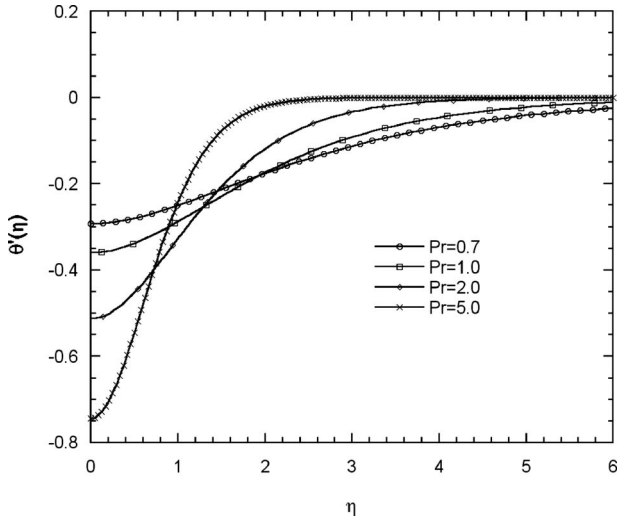

Fig. 10 Variation in the dimensionless temperature gradient with the similarity parameter η at different Prandtl numbers for $K_1=1$, and $K_2=0.5$

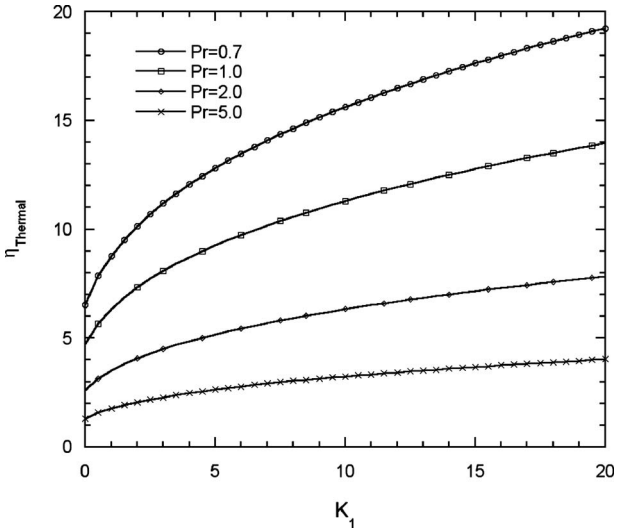

Fig. 12 Variation in the thermal boundary layer thickness with the variation of slip parameter K_1 for different Prandtl numbers and $K_2=1$

Figure 11 shows the variation in the displacement thickness with the velocity slip parameter K_1. The displacement thickness decreases as K_1 increases because the fluid is not able to sense the stretching effect generating at the wall as the slip parameter increases. As a result, the stretching effect does not penetrate deeply through the fluid due to this hydrodynamics miscommunication. Note that there is an asymptotic lower limit for the effect of K_1 on the hydrodynamics boundary layer thickness. Figure 11 also indicates that changing Pr has no effect on the displacement thickness at all values of K_1. This can simply be explained by inspecting Eq. (10) and Eqs. (16)–(18). They showed that (for isothermal surface) the momentum equation is uncoupled from the energy equation, and the Pr effect appears only in the energy equation (i.e., Eq. (10)). Hence, it is expected that changing Pr has no effect on the momentum equation and, therefore, on the displacement thickness.

Figure 12 shows the effect of K_1 on the thermal boundary layer thickness and at different values of Pr. As predicted decreasing Pr increases the thermal boundary layer thickness because Pr decreases as the fluid thermal diffusivity increases and this enable the heating effects of the hot wall to penetrate deeper into the fluid. This, in turn, causes the thickening of the thermal boundary layer. Also, increasing K_1 leads to an increase in the thermal boundary layer. This has been explained previously because as K_1 increases, less fluid motion will be induced due to the stretching effect. As a result, the hot wall heating effect will penetrate deeper into the fluid because it will heat less amount of fluid.

Figure 13 shows the effect of temperature jump parameter K_2 on the thermal boundary layer thickness and for different values of Pr. The increase in the thermal boundary layer thickness with decreasing Pr has been justified and discussed before. The reduction in the thermal boundary layer thickness with K_2 is obvious because K_2 represents the temperature jump at the wall. The fluid will not sense the heating effect of the hot wall as K_2 increases, and this causes less thermal penetration through the fluid domain.

Figure 14 shows the effect of K_1 on the skin friction dimensionless parameter $0.5c_f\,\mathrm{Re}_x^{0.5}$. As predicted, the increase in the velocity slip parameter yields a reduction in the skin friction parameter because velocity gradients near the wall decreases. In the limiting

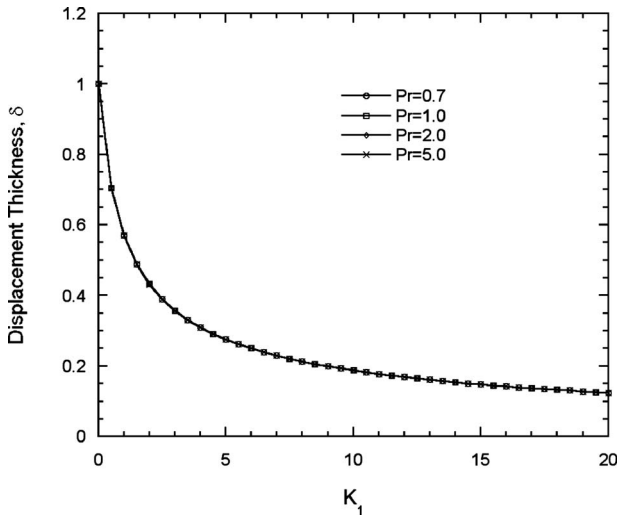

Fig. 11 Variation in the displacement thickness with the variation in the slip parameter K_1 for all values of K_2 and Pr

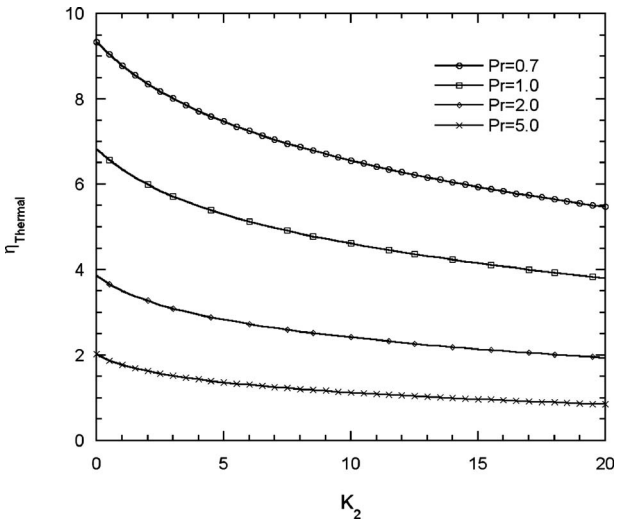

Fig. 13 Variation in the thermal boundary layer thickness with the variation of jump parameter K_2 for different Prandtl numbers and $K_1=1$

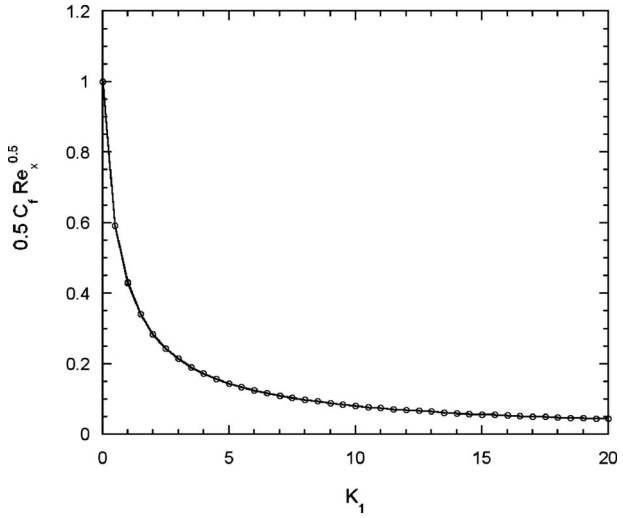

Fig. 14 Variation in skin friction parameter with the variation of slip parameter K_1 for all values of Pr and K_2

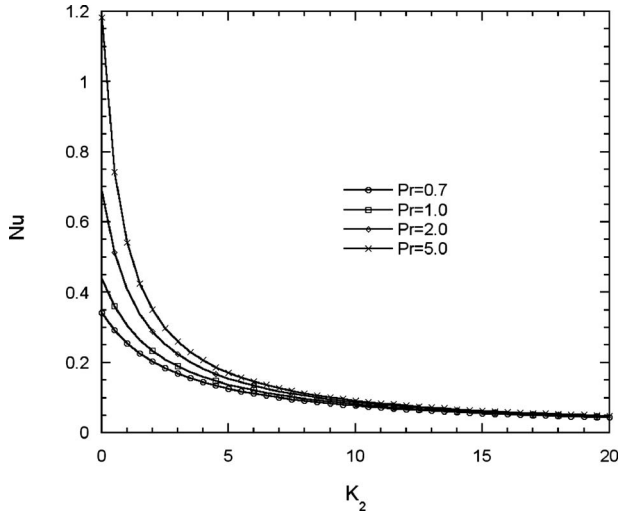

Fig. 16 Variation in Nusselt number with the variation of jump parameter K_2 for different values of Pr and $K_1=1$

case as $K_1 \to \infty$, the fluid is not aware of the stretching effect of the wall and the fluid will not resist this effect, which implies that shear stress at the wall is almost zero. The variation of the skin friction coefficient has been correlated with the variation in K_1. It is found that $c_f = \frac{2}{3}\mathrm{Re}_x^{-0.5}(K_1+0.64)^{-0.884}$ for $0 < K_1 < 10$ with an error of $\pm 0.8\%$. While $c_f = 0.68\,\mathrm{Re}_x^{-0.5}(K_1+0.66)^{-0.9}$ for $0 < K_1 < 20$ with an error of $\pm 1.7\%$. Figure 15 shows the effect of K_1 on Nu for different values of Pr. It has been mentioned previously that heat transfer increase as Pr increases and, as predicted, Nu increases by increasing Pr. However, Nu decreases as K_1 decreases because increasing K_1 induces less amount of fluid due to the stretching effect. This reduction in the fluid induced motion shifts the heat transfer mode from a convection strong mode to a conduction weak mode as explained previously.

Figure 16 shows the effect of K_2 on Nu and at different values of Pr. The increase in Nu with increasing Pr has been explained before. On the other hand, increasing K_2 causes the thermal miscommunication between the hot wall and the fluid, and this justifies the reduction in Nu with increasing K_2. The variation of Nu with the variation of K_1 and K_2 at Pr=1 has been correlated. It is found that

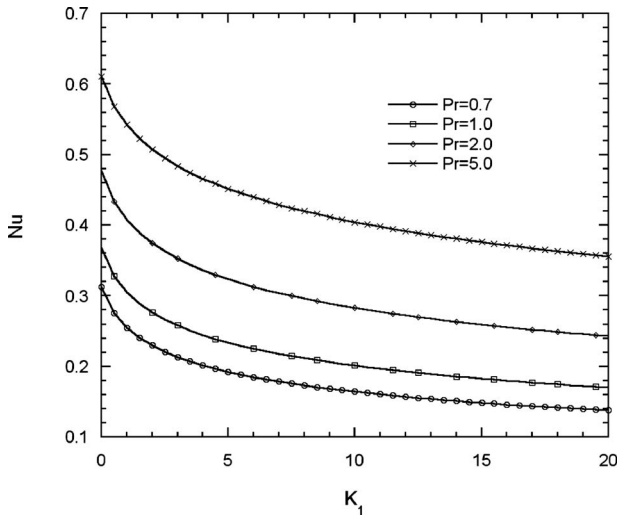

Fig. 15 Variation in Nusselt number with the variation of slip parameter K_1 for different values of Pr and $K_2=1$

$$\mathrm{Nu} = 0.55 \times 10^{-0.2(K_1+2K_2)} \quad 0.025 < K_1, K_2 \leq 1 \text{ with max error} \pm 4.6\%$$

$$\mathrm{Nu} = 0.55 \times 10^{-0.04(K_1+4.25K_2)} \quad 1 < K_1, K_2 \leq 5 \text{ with max error} \pm 8\% \tag{28}$$

5 Conclusions

Heat transfer and flow field characteristics of a stretching horizontal surface are studied. The similarity solution was found to exist for one case only: a linearly stretching surface with constant wall temperature. It is found that three parameters control the flow and heat transfer characteristics of the problem: K_1, K_2, and Pr. The effect of these parameters have been studied and presented. The variation of skin friction and Nusselt number are presented for different values of K_1, K_2, and Pr. Correlations for skin friction parameter and Nusselt numbers are found and presented.

Nomenclature

c_f = skin friction coefficient (J kg^{-1} K^{-1})
f = transformed variable
h_x = local heat transfer coefficient (W m^{-2} K^{-1})
K_1 = slip velocity parameter, Eq. (20)
K_2 = temperature jump parameter, Eq. (22)
K_n = Knudsen number, Eq. (21)
k = thermal conductivity (W m^{-1} K^{-1})
Nu = Nusselt number for $m=1$, $n=0$, $(h\sqrt{\nu/U_o}/k)$
Pr = Prandtl number, (ν/α)
Re_x = local Reynolds number $(u_w x/\nu)$
T = temperature (K)
u = velocity component along the moving plate (m s^{-1})
v = velocity component normal to the plate (m s^{-1})
x, y = coordinate along and normal to the plate (m)
α = thermal diffusivity (m^2/s)
η = transformed variable
θ = dimensionless temperature
λ = molecular mean free path length (m)
ν = kinematic viscosity (m^2/s)
σ_v = thermal accommodation coefficient
σ_T = momentum accommodation coefficient

Subscripts

w = conditions at wall
∞ = ambient conditions
$( )'$ = derivative with respect to η

References

[1] Duncan, G. P., and Peterson, G. P., 1994, "Review of Microscale Heat Transfer," Appl. Mech. Rev., **47**(9), pp. 397–428.
[2] Gad-el-Hak, M., 1999, "The Fluid Mechanics of Microdevices—The Freeman Scholar Lecture," ASME J. Fluids Eng., **121**, pp. 5–33.
[3] Gad-el-Hak, M., 2002, "Flow Physics in Microdevices," *The Handbook of MEMS*, CRC, Boca Raton, FL.
[4] Ali, M. E., 1994, "Heat Transfer Characteristics of a Continuous Stretching Surface," Waerme- Stoffuebertrag., **29**, pp. 227–234.
[5] Kiwan, S., 2006, "Laminar Mixed Convection Heat Transfer Induced by a Stretching Flat Plate in a Porous Medium," Heat Technol., **24**(2), pp. 29–35.
[6] Ali, M. E., and Al-Yousef, F., 2002, "Laminar Mixed Convection Boundary Layer Induced by a Linearly Stretching Permeable Surface," Int. J. Heat Mass Transfer, **45**, pp. 4241–4250.
[7] Elbashbeshy, E. M. A., 1998, "Heat Transfer Over a Stretching Surface With Variable Heat Flux," J. Phys. D, **31**, pp. 1951–1955.
[8] Elbashbeshy, E. M. A., and Bazid, M. A. A., 2004, "Heat Transfer in a Porous Medium Over a Stretching Surface With Internal Heat Generation and Suction and Blowing," Appl. Math. Comput., **158**, pp. 799–807.
[9] Pereyra, V., 1978, "PASVA3: An Adaptive Finite-Difference FORTRAN Program for First Order Nonlinear Boundary Value Problems," *Lecture Notes in Computer Science*, Springer-Verlag, Berlin, p. 76.
[10] Andersson, H. I., 1995, "An Exact Solution of the Navier–Stokes Equation for Magnetohydrodynamic Flow," Acta Mech., **113**, pp. 241–244.

Large-Eddy Simulation of Turbulence-Radiation Interactions in a Turbulent Planar Channel Flow

Ankur Gupta

Michael F. Modest[1]
Fellow ASME
e-mail: mfmodest@psu.edu

Daniel C. Haworth

Department of Mechanical and Nuclear Engineering,
The Pennsylvania State University,
University Park, PA 16802

Large-eddy simulation (LES) has been performed for planar turbulent channel flow between two infinite, parallel, stationary plates. The capabilities and limitations of the LES code in predicting correct turbulent velocity and passive temperature field statistics have been established through comparison to direct numerical simulation data from the literature for nonreacting cases. Mixing and chemical reaction (infinitely fast) between a fuel stream and an oxidizer stream have been simulated to generate large composition and temperature fluctuations in the flow; here the composition and temperature do not affect the hydrodynamics (one-way coupling). The radiative transfer equation is solved using a spherical harmonics (P1) method, and radiation properties correspond to a fictitious gray gas with a composition- and temperature-dependent Planck-mean absorption coefficient that mimics that of typical hydrocarbon-air combustion products. Simulations have been performed for different optical thicknesses. In the absence of chemical reactions, radiation significantly modifies the mean temperature profiles, but temperature fluctuations and turbulence-radiation interactions (TRI) are small, consistent with earlier findings. Chemical reaction enhances the composition and temperature fluctuations and, hence, the importance of TRI. Contributions to emission and absorption TRI have been isolated and quantified as a function of optical thickness. [DOI: 10.1115/1.3085875]

Keywords: large-eddy simulation, thermal radiation, turbulence-radiation interactions, chemical reaction, channel flow

1 Introduction

Most practical combustion systems involve turbulent flow and operate at high temperatures where thermal radiation acts as an important mode of heat transfer. In such systems there are highly nonlinear interactions between chemistry, turbulence, and thermal radiation. Accurate treatments of chemistry, radiation, and turbulence in turbulent reacting flow, even without interactions, are quite challenging and complex on their own; therefore, the interactions between turbulence and radiation (turbulence-radiation interaction (TRI)) have traditionally been ignored in the modeling of turbulent reacting flows.

TRI arises due to highly nonlinear coupling between the fluctuations in temperature, radiative intensity, and species concentrations. TRI takes place over a wide range of length scales. A complete treatment requires consideration of the full range of scales, which is computationally intractable for flows with high Reynolds number, as is the case with chemically reacting turbulent flows of practical interest. Numerical simulation of such systems requires either computing the mean flow while modeling the effects of fluctuations at all scales (Reynolds-averaged approach) or explicitly resolving the large scales while modeling the effects of subfilter-scale (SFS) fluctuations (large-eddy simulation (LES) approach). LES is expected to be more accurate and general since the large energy-containing, flow-dependent scales are captured explicitly and only the (presumably) more universal small-scale dynamics require modeling. LES is also expected to capture phenomena that are difficult to accommodate in Reynolds-averaged approaches, such as large-scale unsteadiness. There is a wide and rapidly growing body of evidence that demonstrates quantitative advantages of LES in modeling studies of laboratory flames [1,2] and in applications to gas-turbine combustors [3–5], internal combustion (IC) engines [6–8], and other combustion systems. LES, therefore, promises to be an accurate and computationally feasible tool for investigations of TRI in chemically reacting turbulent flows.

The importance of TRI has long been recognized [9–16]. Studies have shown that the effects of TRI can be as significant as those of turbulence-chemistry interaction (TCI). TRI is known to result in higher heat loss due to increased radiative emission, reduced temperatures, and, consequently, significant changes in key pollutant species (particularly NO_x and soot) in chemically reacting turbulent flows. Faeth and co-workers [12–16] showed that, with the inclusion of TRI, radiative emission from a flame may be 50–300% higher (depending on the type of fuel) than that expected with radiation but no TRI. With consideration of TRI, Coelho [17] reported a nearly 50% increase in radiative heat loss for a nonpremixed methane-air turbulent jet flame; Tessé et al. [18] reported a 30% increase in the radiative heat loss for a sooty nonpremixed ethylene-air turbulent jet flame. Modest and coworkers [19,20] observed about 30% increase in the radiative heat flux with TRI in their studies of nonpremixed turbulent jet flames. Wu et al. [21] conducted direct numerical simulation (DNS) of an idealized one-dimensional premixed turbulent flame to study TRI along with a high-order photon Monte Carlo (PMC) scheme (of order commensurate with the underlying DNS code) to calculate the radiative heat source. They isolated and quantified the various contributions to TRI for different optical thicknesses. Deshmukh et al. [22] applied the same approach to DNS of an idealized,

[1]Corresponding author.

Contributed by the Heat Transfer Division of ASME for publication in the JOURNAL OF HEAT TRANSFER. Manuscript received March 10, 2008; final manuscript received November 7, 2008; published online April 13, 2009. Review conducted by Ofodike A. Ezekoye. Paper presented at the 2007 ASME-JSME Thermal Engineering Conference Summer Heat Transfer Conference (HT2007), July 8–12, 2007, Vancouver, BC, Canada.

statistically homogeneous, nonpremixed system with full consideration of TRI. Chandy et al. [23] performed large-eddy simulation of an idealized nonpremixed jet flame using the optically thin eddy approximation [24] and treating emission TRI through a filtered mass density function (FMDF) approach. Coelho [25] surveyed various computational approaches to account for TRI and reviewed TRI studies based on those approaches.

In this work large-eddy simulation with a P1 radiation model is used to isolate and quantify TRI effects for a range of optical thicknesses for nonreacting and reacting channel flow configurations. The objectives are to provide fundamental physical insight into TRI in chemically reacting flows, to provide guidance for model development, and to establish the suitability of LES for investigating TRI in chemically reacting flows. The remainder of this paper is organized as follows: Section 2 presents the underlying theory behind turbulent-radiation interactions; the problem formulation is outlined in Sec. 3; results and discussion for the two configurations are presented in Sec. 4, followed by conclusions in Sec. 5.

2 Thermal Radiation and Turbulence-Radiation Interactions

The radiative source term in the instantaneous energy equation is expressed as the divergence of the radiative heat flux. For a gray medium,

$$\nabla \cdot \boldsymbol{q}_{\text{rad}} = 4\kappa_P \sigma T^4 - \kappa_P G \tag{1}$$

where κ_P is the Planck-mean absorption coefficient, σ is the Stefan–Boltzmann constant, and $G \equiv \int_{4\pi} I d\Omega$ is the direction-integrated intensity, or incident radiation, which is obtained by solving the radiative transfer equation (RTE) [26]. The radiative source term consists of an emission part and an absorption part: these are the first and second terms on the right-hand side of Eq. (1), respectively.

TRI can be brought into evidence by taking the mean of Eq. (1),

$$\langle \nabla \cdot \boldsymbol{q}_{\text{rad}} \rangle = 4\sigma \langle \kappa_P T^4 \rangle - \langle \kappa_P G \rangle \tag{2}$$

In the emission term, TRI appears as a correlation between the Planck-mean absorption coefficient and the fourth power of temperature: $\langle \kappa_P T^4 \rangle = \langle \kappa_P \rangle \langle T^4 \rangle + \langle \kappa_P' (T^4)' \rangle$, where a prime denotes a fluctuation about the local mean. The presence of TRI in the emission term is further manifested in the temperature self-correlation ($\langle T^4 \rangle \neq \langle T \rangle^4$). In the absorption term, TRI appears as a correlation between the Planck-mean absorption coefficient and the incident radiation: $\langle \kappa_P G \rangle = \langle \kappa_P \rangle \langle G \rangle + \langle \kappa_P' G' \rangle$.

In the present study, we explore the effects of resolved-scale fluctuations on mean and rms temperature profiles and their contribution to TRI using LES. With "$\tilde{}$" denoting a filtered (resolved-scale) value, the principal quantities examined are the mean ($\langle \tilde{T} \rangle$) and rms ($\langle \tilde{T}'^2 \rangle$) temperature profiles, the normalized temperature self-correlation ($\langle \tilde{T}^4 \rangle / \langle \tilde{T} \rangle^4$), the Planck-mean absorption coefficient and simplified Planck function (i.e., T^4) correlation ($\langle \widetilde{\kappa_P \tilde{T}^4} \rangle / \langle \widetilde{\kappa_P} \rangle \langle \tilde{T}^4 \rangle$), and the Planck-mean absorption coefficient and incident radiation correlation ($\langle \widetilde{\kappa_P \tilde{G}} \rangle / \langle \widetilde{\kappa_P} \rangle \langle \tilde{G} \rangle$). In the absence of TRI, each of the latter two quantities would be equal to unity. The expression for temperature self-correlation indicates that in the presence of thermal radiation there would always be TRI for the level of turbulent fluctuations seen in reacting flows. The departures of each of the correlations, stated above, from unity allow different contributions to TRI to be isolated and quantified. In the remainder of the paper, the "$\tilde{}$" notation is dropped for clarity, and all quantities correspond to resolved-scale values, unless noted otherwise.

A nondimensional optical thickness $\kappa_P L$ is introduced, where L is an appropriate length scale. Previous studies [24,27,28] have suggested that the fluctuations in κ_P (determined by local properties) and in incident radiation G (a nonlocal quantity) are uncorrelated (i.e., $\langle \kappa_P G \rangle \approx \langle \kappa_P \rangle \langle G \rangle$) if the mean free path for radiation is much larger than the turbulence eddy scale. This is the optically thin fluctuation approximation (OTFA) ($\kappa_P L \ll 1$). At the other extreme ($\kappa_P L \gg 1$), the optical thickness may be large compared with all hydrodynamic scales and chemical scales. In that case, the fluctuations in intensity are generated locally and are expected to be correlated strongly with those of the absorption coefficient. A diffusion approximation [26] can be used to model such cases. Between the two extremes are the cases where the smallest scales (Kolmogorov scales and/or flame thickness) are optically thin while the largest (integral scales) are optically thick. Modeling of such transitional cases is an outstanding challenge in TRI and is a primary motivation for this study.

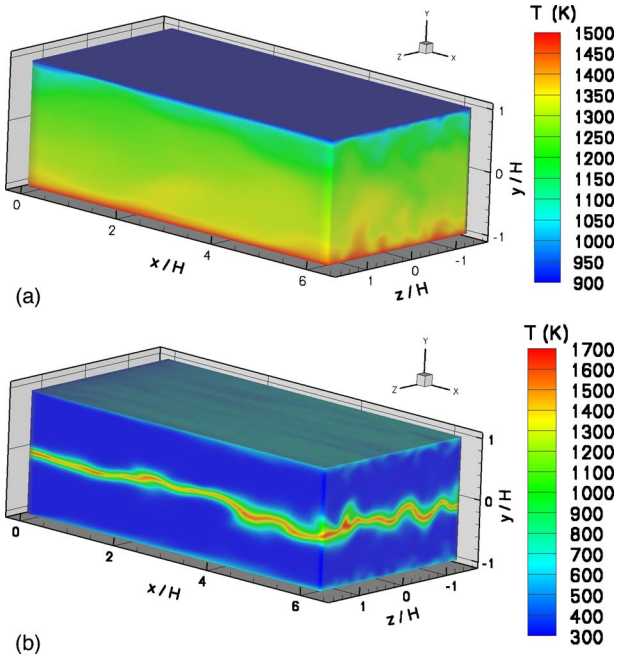

Fig. 1 Instantaneous temperature contours for (*a*) nonreacting flow and (*b*) reacting flow

3 Problem Formulation

3.1 Geometric Configuration. A statistically stationary and one-dimensional turbulent planar channel flow is considered. Turbulent channel flow is a classic configuration in the study of fluid dynamics and has been the subject of numerous DNS and LES investigations [29–32]. This configuration has also been used to study passive scalar statistics [33]. Moreover, a channel domain is a logical extension of classical one-dimensional "slab" problems often used in the study of radiation heat transfer.

The computational domain is a rectangular box with dimensions $(2\pi, 2, \pi)$ in some unit H in the x-, y-, and z-directions (Fig. 1), with solid boundaries at the bottom ($y=-H$) and top ($y=+H$). Mean-flow statistics vary only in the wall-normal direction (y). Periodic boundaries are used in the streamwise (x) and the spanwise (z) directions for flow. The flow is driven by an artificial streamwise body force that balances the friction at the walls, thus allowing the pressure to be periodic with zero mean pressure gradient in the computational domain. Two cases are considered: a nonreacting case and a reacting case.

3.2 Physical and Numerical Models

3.2.1 CFD Code. OPENFOAM [34,35], an open-source CFD code, has been used to perform the large-eddy simulation for this configuration. The code has been validated by comparing com-

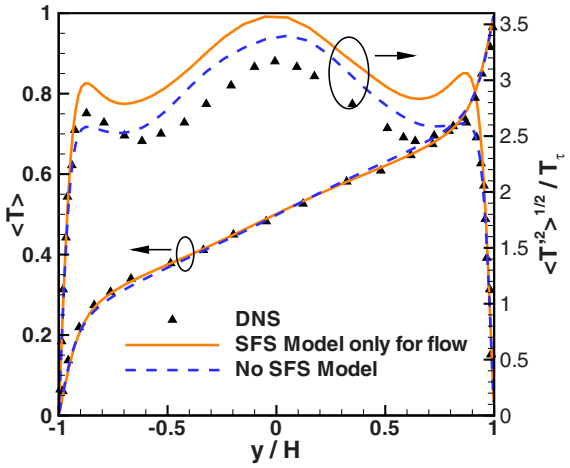

Fig. 2 Computed mean and rms passive scalar profiles and their comparison with DNS of Debusschere and Rutland [33]

puted mean and rms velocity profiles with published DNS data from the literature for the same Reynolds number (Re_τ=180, where Re_τ is a Reynolds number based on the wall-friction velocity) [29]. This included a mesh size and time step sensitivity study and a comparison of results obtained in the presence or absence of an explicit SFS turbulence model [36]. A second study confirmed that computed mean and rms passive scalar statistics are in good agreement with DNS data [33]. While the code might not suffice for high-fidelity LES of near-wall turbulence dynamics, it is quite satisfactory for generating a reasonable level of temperature and composition fluctuations for the present purpose of studying thermal radiation and TRI. Quantitative comparisons between LES and DNS mean and rms temperature (passive scalar) profiles are shown in Fig. 2. There is excellent agreement between the LES mean temperature profiles and the DNS data. The mean temperature profile has a steep gradient near the walls due to the formation of turbulent boundary layers and is relatively flat in the core of the channel as a result of turbulent mixing. The rms profiles of temperature fluctuations are normalized by the wall-friction temperature (T_τ), which is defined as [33]

$$T_\tau = \frac{q_w}{\rho c_P u_\tau} = \left.\frac{k}{\rho c_P u_\tau}\frac{d\langle T\rangle}{dy}\right|_{\text{wall}} \tag{3}$$

Here q_w is the wall heat flux, c_P is the specific heat, k is the thermal conductivity, and u_τ is the wall-friction velocity. The LES rms temperature profile in the absence of a SFS model is within 10% of the DNS data. The maximum temperature fluctuations are at the centerline of the channel, in contrast to the near-wall maximum that is seen for the velocity fluctuations [29]. This is due to the nonzero mean temperature gradient at the centerline of the channel, which results in the production of temperature fluctuations at that location.

Based on the above validation studies, all simulations reported here were performed with no explicit subfilter-scale model using second-order spatial (central differencing) and temporal (Crank–Nicholson) discretizations. This corresponds to the monotone integrated LES (MILES) approach for SFS modeling [37], where the SFS model is implicit in the numerical method. The finite-volume grid used has 30, 60, and 50 cells in the x-, y-, and z-directions, respectively, for the nonreacting case and 60, 96, and 60 cells in the x-, y-, and z-directions, respectively, for the reacting case. The computational time step corresponds to a maximum material Courant number of 0.3.

3.2.2 Physical Models. An incompressible formulation is used. There is no feedback of thermochemistry to the hydrodynamics. The body force and fluid properties are set to achieve the desired Reynolds number (Re_τ=186) [33], where Re_τ is defined as

$$\mathrm{Re}_\tau = \frac{u_\tau H}{\nu} \tag{4}$$

u_τ is given by $\sqrt{\tau_w/\rho}$, and τ_w is the shear stress at the wall. The kinematic viscosity, ν, is calculated using Eq. (4) with u_τ equal to unity. The wall-friction velocity, u_τ, is also used to determine the total wall friction and thus the magnitude of the streamwise body force that is required to sustain the flow.

For the nonreacting case, the top and bottom walls are isothermal at temperatures of 900 K and 1500 K, respectively (Fig. 1(*a*)). The laminar Prandtl number is set to 0.7. The channel boundaries in the spanwise and streamwise directions are periodic. The top and bottom walls are treated as black and diffuse for thermal radiation computations. The participating medium has a Planck-mean absorption coefficient of the form

$$\kappa_p = C_\kappa\left[c_0 + c_1\left(\frac{A}{T}\right) + c_2\left(\frac{A}{T}\right)^2 + c_3\left(\frac{A}{T}\right)^3 + c_4\left(\frac{A}{T}\right)^4 + c_5\left(\frac{A}{T}\right)^5\right] \tag{5}$$

where the coefficients c_0–c_5 and A have been taken from a radiation model suggested for water vapor [38]. Here C_κ is a coefficient that allows the optical thickness to be varied systematically and independently of the other parameters. The values of C_κ used in this study are 0.0005, 0.005, 0.05, 2.5, and 50. The Planck-mean absorption coefficient has an inverse temperature dependence, and it varies up to a factor of 3 over the temperature range of interest.

For the reacting case, the species fields are superposed on the flow field; i.e., the hydrodynamics is solved as in the nonreacting case, and the flow field is used to transport species through the channel. The species and the energy variables are periodic only for the channel boundaries in the spanwise direction; fixed-value inlet and zero-gradient outlet boundaries are used in the streamwise directions for species and energy variables.

A nonpremixed system with one-step, irreversible, infinitely fast chemistry is considered:

$$F + O \rightarrow P \tag{6}$$

A conserved scalar mixture-fraction formulation is used where ξ =0.0 for pure oxidizer, ξ=1.0 for pure fuel, and $\xi=\xi_{st}$=0.5 for pure products. The Lewis number is set to unity.

A mixture-fraction profile is specified at the channel inlet, with ξ=1 (pure fuel) near the upper ($y=+H$) wall, ξ=0 (pure oxidizer) near the lower ($y=-H$) wall, and a narrow transition zone around y=0,

$$\xi = \frac{1}{2}\left(1 + \tanh 15\frac{y}{H}\right) \tag{7}$$

A zero-normal-gradient boundary condition is used for the mixture fraction at the channel outlet and at the top and bottom walls. Species mass fractions Y_F, Y_O, and Y_P are simple piecewise linear functions of ξ, as shown in Fig. 3. In the absence of thermal radiation, the temperature is also a piecewise linear function of mixture fraction and has a functional dependence exactly similar to that for pure products. This piecewise linear function along with the inlet mixture-fraction profile (Eq. (7)) is used to calculate the temperature distribution at the inlet. In the presence of thermal radiation, however, a separate energy (enthalpy) equation is solved. The specific absolute mixture enthalpy h is

$$h = \sum_\alpha (h_\alpha^\circ Y_\alpha + C_{p\alpha} Y_\alpha [T - 300]) \tag{8}$$

where h_α° is the formation enthalpy of species α, Y_α is its mass fraction, $C_{p\alpha}$ is its specific heat, and T is the temperature. At the channel inlet, a profile for enthalpy is calculated from the above

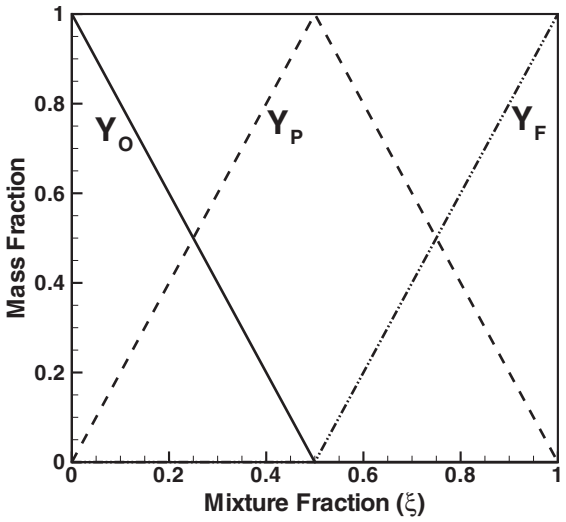

Fig. 3 Species mass fractions as a function of mixture fraction, ξ

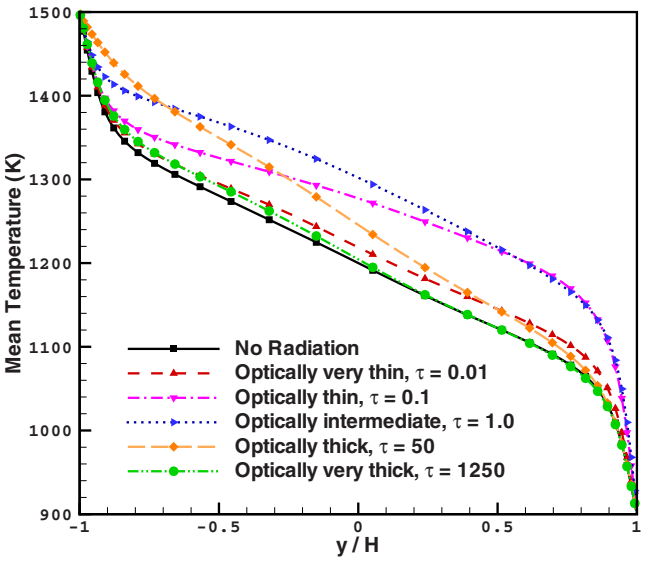

Fig. 4 Computed mean temperature profiles with variations in optical thickness for the nonreacting case

expression and is assigned as the inlet boundary condition. The specific absolute enthalpy is assumed to have a zero gradient at the outlet. The channel walls are thermally insulated; there is zero net heat flux to the wall,

$$q_{\text{rad}} + q_{\text{diff}} = q_{\text{rad}} - k\,\nabla T \cdot \hat{n} = 0 \tag{9}$$

where q_{rad} is the net radiative heat flux to the wall, q_{diff} is the diffusive heat flux to the wall, and $\hat{n}$ is the outward unit-normal vector at the wall.

The RTE is solved for incident radiation G using a P1 spherical harmonics method, requiring the solution of an elliptic partial differential equation (PDE) [26],

$$\nabla \cdot (\Gamma \nabla G) = -\kappa_P(4\pi I_b - G) \tag{10}$$

Here I_b is the Planck function, and Γ is the optical diffusivity of the medium, which, for a nonscattering medium, is given by

$$\Gamma = \frac{1}{3\kappa_P} \tag{11}$$

For the reacting case the channel walls again are black and diffuse. The inlet is assumed to act as a black wall at the local temperature. The channel outlet is assumed to be radiatively insulated, with zero gradient for the incident radiation at the outlet boundary.

The participating medium has a Planck-mean absorption coefficient that is similar to Eq. (5) but includes an explicit dependence on product mass fraction (Y_P),

$$\kappa_p = \max\left\{ C_\kappa Y_P \left[c_0 + c_1\left(\frac{A}{T}\right) + c_2\left(\frac{A}{T}\right)^2 + c_3\left(\frac{A}{T}\right)^3 + c_4\left(\frac{A}{T}\right)^4 + c_5\left(\frac{A}{T}\right)^5 \right], \kappa_{P\min} \right\} \tag{12}$$

where $\kappa_{P\min}$ is a very small absorption coefficient ($\sim$0.01). The values of C_κ used in this study are 0.0008, 0.008, 0.08, 0.16, 0.8, 4, and 16.

4 Results and Discussion

For each configuration, results are presented for different optical thicknesses τ. Here τ is defined as

$$\tau = \begin{cases} \langle \kappa_P \rangle_{y=0} H & \text{for the nonreacting case} \\ \displaystyle\int_{-H}^{+H} \langle \kappa_P \rangle dy|_{x=2\pi H} & \text{for the reacting case} \end{cases} \tag{13}$$

where H is the half-channel height and $y=0$ is the channel centerline location.

In each case, the initial flow field consisted of uniform streamwise velocity with high velocities in the wall-normal and spanwise directions in a small region at the core of the channel to promote the production of turbulence. A statistically stationary turbulent flow field was established by allowing the initial flow field to develop for approximately 100 flow-through times. The temperature (or mixture-fraction in the reacting configuration) field was introduced only after establishing the statistically stationary turbulent flow field. The initial temperature field used in nonreacting configuration was simply a linear profile between the two walls. The initial mixture-fraction field used in reacting configuration was the inlet mixture-fraction profile of Eq. (7) propagated through the entire channel. The temperature field (or mixture fraction) was then allowed to evolve for approximately 40–50 flow-through times before switching on thermal radiation, and the system was allowed to evolve for another 70–80 flow-through times to establish statistically stationary fields. Averaging was performed over approximately 100 flowthrough times to get proper time-averaged statistics.

4.1 Configuration I: Nonreacting Turbulent Planar Channel Flow. For this statistically stationary and statistically one-dimensional configuration, mean quantities correspond to averages over time and over planes parallel to the walls. Computed mean temperature profiles in the absence of radiation and for different optical thicknesses are shown in Fig. 4. As thermal radiation is introduced, initially (optically very thin medium, $\tau=0.01$) most of the thermal radiative energy emitted by the hot wall penetrates through the medium, and only a small amount is absorbed. The mean temperature increases slightly from the no-radiation case, with the departure increasing steadily from the hot wall to the cold wall. This can be explained from the inverse temperature dependence of the Planck-mean absorption coefficient: the low-temperature zones have a higher absorption coefficient. With an increase in optical thickness ($\tau=0.1$), most of the thermal energy radiated by the hot wall still penetrates through the medium near the hot wall but is absorbed near the cold wall. In this case, the

mean temperature profile deviates significantly from the no-radiation case. As the optical thickness is increased further ($\tau = 1.0$), the medium near the hot wall also has a large absorption coefficient and absorbs some of the radiative energy emitted by the hot wall. For this case, significant radiative energy still reaches the region near the cold wall, resulting in large temperature departures from the no-radiation case. A further increase in optical thickness ($\tau = 50$) results in most of the emitted thermal energy getting absorbed in the region near the hot wall, and the departure from the no-radiation mean temperature distribution has a decreasing trend as one moves from hot wall to cold wall. With further increase in the optical thickness ($\tau = 1250$), the medium becomes essentially opaque, and any radiation emitted is absorbed locally close to the point of emission, and the mean temperature distribution approaches the no-radiation temperature distribution. In the limit of large optical thickness, thermal radiation acts as a diffusive process with a diffusivity proportional to $4\sigma T^3/3\kappa_R$, where κ_R is a Rosseland-mean absorption coefficient [26]. For large κ_R the diffusivity due to thermal radiation is negligible, and the mean and rms temperature profiles in the optically thick limit are the same as those in the no-radiation case.

Both emission TRI and absorption TRI are negligible for this case (not shown). This is consistent with findings from earlier studies for nonreacting turbulent flows [11,39,40] and can be attributed to the relatively low level of temperature fluctuations (approximately 3% of the mean temperatures) that are found in nonreacting flows.

Here the effect of varying optical thickness on a nonreacting high-temperature system has been studied for optical thicknesses ranging from very thin ($\tau = 0.01$) to very thick ($\tau = 1250$). For comparison, we note that a 7 mm thick high-temperature region ($T \sim 1500$ K) of typical combustion products (CO_2 and H_2O, at partial pressures of about 0.1 bar) would have an optical thickness of approximately 0.01. On the other hand, a high-temperature region ($T \sim 1500$ K) about 50 m thick with 10 ppm soot would correspond to an optical thickness of approximately 1000. Thus an optical thickness of 1250 is extremely large and serves here only to confirm that the model system exhibits the correct behavior in the optically thick limit. In a practical system, an optical thickness of approximately 15 or greater would correspond to an optically thick medium.

4.2 Configuration II: Chemically Reacting Nonpremixed Turbulent Channel Flow. For this configuration, mean quantities vary with both x and y, and, thus, mean quantities are estimated by averaging over time and over z. A further averaging is performed about the $y = 0$ plane to take advantage of the statistical symmetry of the problem and to reduce the statistical errors in estimating mean quantities.

The mean temperature profiles at the exit of the computational domain ($x = 2\pi H$) are shown in Fig. 5. The mean temperature peaks at the center of the channel and drops to 300 K away from the flame. When thermal radiation is considered, the flame loses heat due to radiative energy emission that heats up the adiabatic walls. Because of the heat loss from the flame, the flame core temperature is decreased while the temperature of the gas adjacent to the heated walls increases due to the formation of a thermal boundary layer. As the optical thickness increases, the flame loses more heat, resulting in higher wall temperatures and further reduction in the flame core mean temperature. However, for very large optical thicknesses, emitted radiation is absorbed locally, and the mean temperature profile returns to that of the no-radiation case.

The rms temperature profiles at $x = 2\pi H$ are shown in Fig. 6 for different optical thicknesses. Turbulent flapping of the flame about the center-plane of the channel causes large variations in temperature near the edges of the flame and gives rise to a double-peak profile. Thermal radiation significantly alters the temperature fluctuations in the core of the flame.

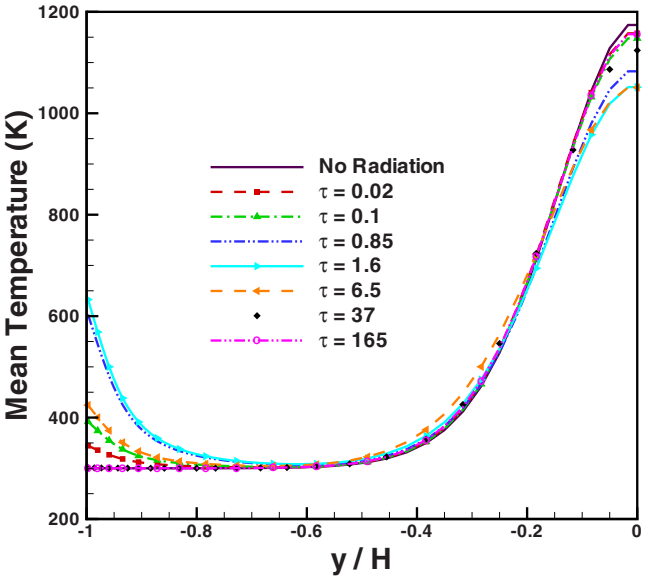

Fig. 5 Computed mean temperature profiles with variations in optical thickness for the reacting case

The temperature self-correlation at the exit is shown in Fig. 7. The shape of the profile can be attributed to the two-peak structure of the rms temperature. The location of the peak depends on the level of temperature fluctuations relative to the mean temperature. Like the rms temperatures, initially the temperature self-correlation decreases with increasing optical thickness, and once the optical thickness attains a sufficiently high value, the temperature self-correlation increases again with increasing optical thickness. The temperature self-correlation is found to be significant for all optical thicknesses considered due to the high level of temperature fluctuations in the presence of chemical reactions.

Figure 8(*a*) presents the contribution to emission TRI of the correlation between Planck-mean absorption coefficient and fourth power of temperature at the $x = 2\pi H$ location. This contribution to emission TRI is found to be significant for all optical thicknesses studied except for the optically very thin case ($\tau = 0.02$). The behavior and shape of the correlation can be ex-

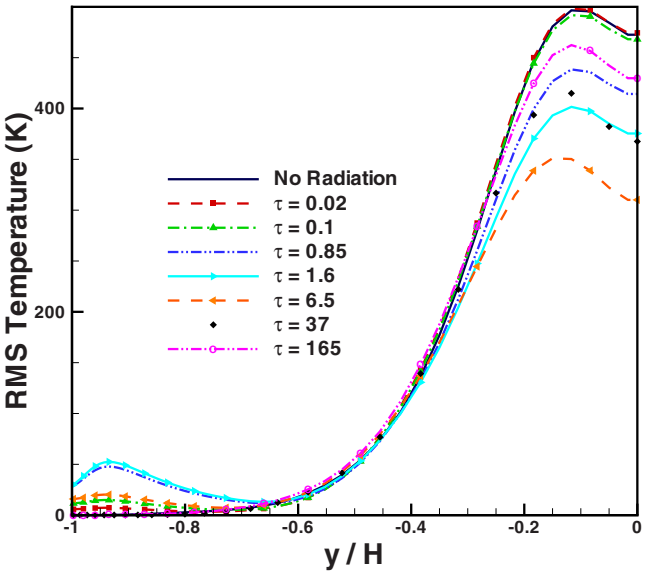

Fig. 6 Computed rms temperature profiles with variations in optical thickness for the reacting case

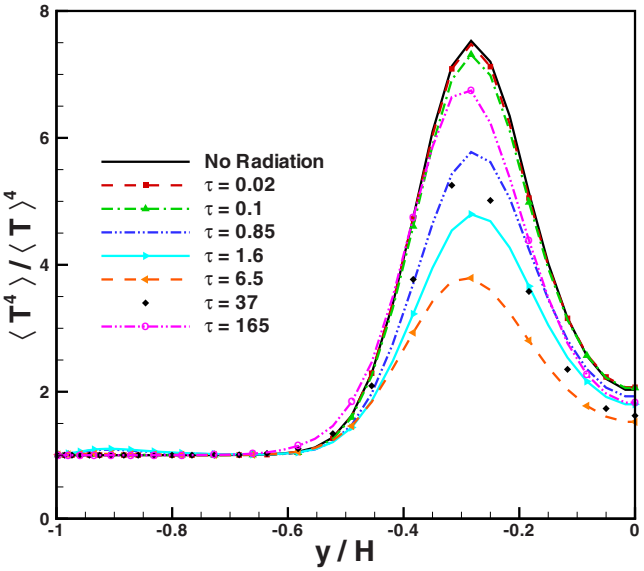

Fig. 7 Temperature self-correlation for several optical thicknesses for the reacting case

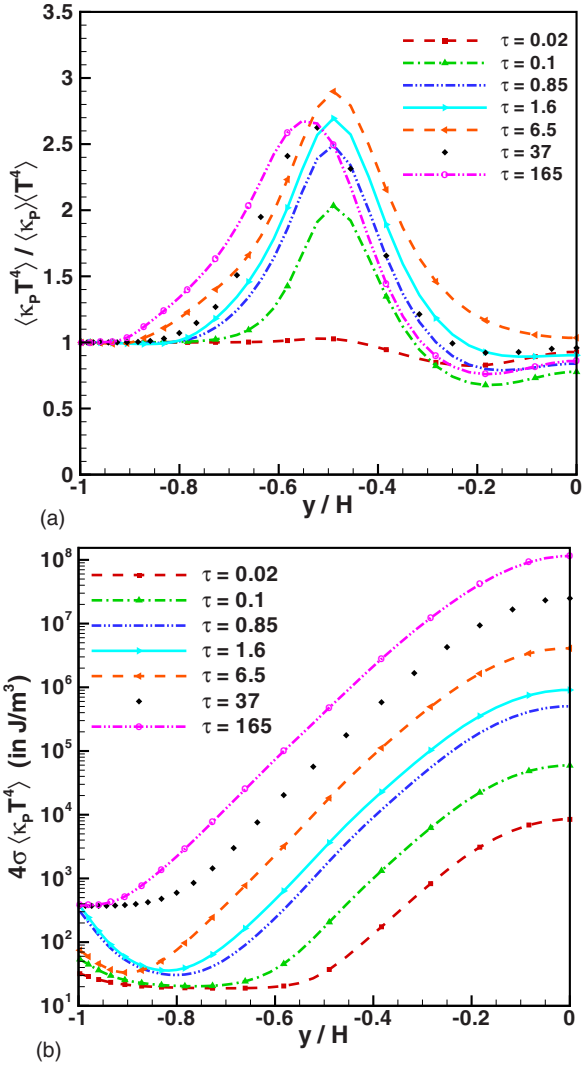

Fig. 8 Correlation between κ_P and T^4 for several optical thicknesses for the reacting case

plained from the assumed functional dependence of the Planck-mean absorption coefficient on temperature and Y_P: κ_P is inversely proportional to temperature but directly proportional to Y_P. Therefore, the fluctuations in temperature and κ_P are negatively correlated at constant Y_P, and fluctuations in product mass fraction and κ_P are positively correlated at constant temperature. These two opposing phenomena compete with one another to determine the overall correlation. In the region near the flame edge, the temperature fluctuations have a dominant impact on κ_P fluctuations, thereby resulting in a correlation less than unity. Similarly, in regions slightly away from the flame edge, Y_P fluctuations are dominant, resulting in correlations much greater than unity. However, it is important to realize that the region where the $\kappa_P - T^4$ correlation is most significant has about two orders of magnitude lower mean emission than the maximum mean emission, which occurs at $y=0$, as seen in Fig. 8(b). The $\kappa_P - T^4$ correlation is close to unity at $y=0$, whereas at the same location the temperature self-correlation is close to 2, as seen in Fig. 7. These numbers and the plots for temperature self-correlation, $\kappa_P - T^4$ correlation, and mean heat emission indicate that here the temperature self-correlation is the dominant contributor to emission TRI.

Absorption TRI at $x=2\pi H$ is shown in Fig. 9(a) for different optical thicknesses and is seen to be negligible for optically thin flames, consistent with the OTFA. Absorption TRI becomes significant at higher optical thicknesses; there thermal radiation travels relatively short distances, and the local incident radiation has some correlation with local emission and, therefore, with the local Planck-mean absorption coefficient. Regions where the $\kappa_P - G$ correlation is most significant have one-to-two orders of magnitude lower mean absorption rates than the maximum mean absorption rate, as seen in Fig. 9(b).

The plots for the temperature self-correlation, the $\kappa_P - T^4$ correlation, and the $\kappa_P - G$ correlation (Figs. 7, 8(a), and 9(a), respectively) reveal that in the optically thin limit where $\tau=0.02$, the temperature self-correlation is primarily the sole contributor to TRI, and it remains an important contributor to TRI for the entire range of optical thickness considered. This is because the temperature self-correlation is significant in the region with large mean emission rates (i.e., $|y| \leq 0.3$) as opposed to the $\kappa_P - T^4$ correlation and the $\kappa_P - G$ correlation, which are dominant in the regions with mean rates one or two orders of magnitude lower than the maximum mean emission and mean absorption rates, respectively (see Figs. 8(b) and 9(b)). The $\kappa_P - T^4$ correlation is important at all optical thicknesses except in the optically thin limit, whereas absorption TRI ($\kappa_P - G$ correlation) is important only in the optically intermediate to thick regions. Note that for very large optical thicknesses both emission TRI and absorption TRI are strong, but their net effect is small due to cancellation (Figs. 8 and 9): in the optically thick limit local values of G approach $4\pi I_b$, and, therefore, the fluctuations in G are directly proportional to the fluctuations in T^4. Absorption TRI (Fig. 9(a)) has a similar shape and behavior as emission TRI (Fig. 8(a)) for very large optical thicknesses. Similarly, it can be seen from the mean emission and mean absorption plots (Figs. 8(b) and 9(b)) that the mean emission rate is identical to the mean absorption rate for very large optical thicknesses, resulting in mean temperatures approaching those of the no-radiation case, as seen in Fig. 5.

5 Conclusions

Large-eddy simulation of incompressible turbulent planar channel flow has been conducted, including thermal radiation. Cases without and with chemical reaction were considered with systematic variation in optical thickness. In the absence of chemical reactions, radiation significantly modifies the mean temperature fields, but emission TRI and absorption TRI were found to be negligible. The no-radiation results are recovered in both the op-

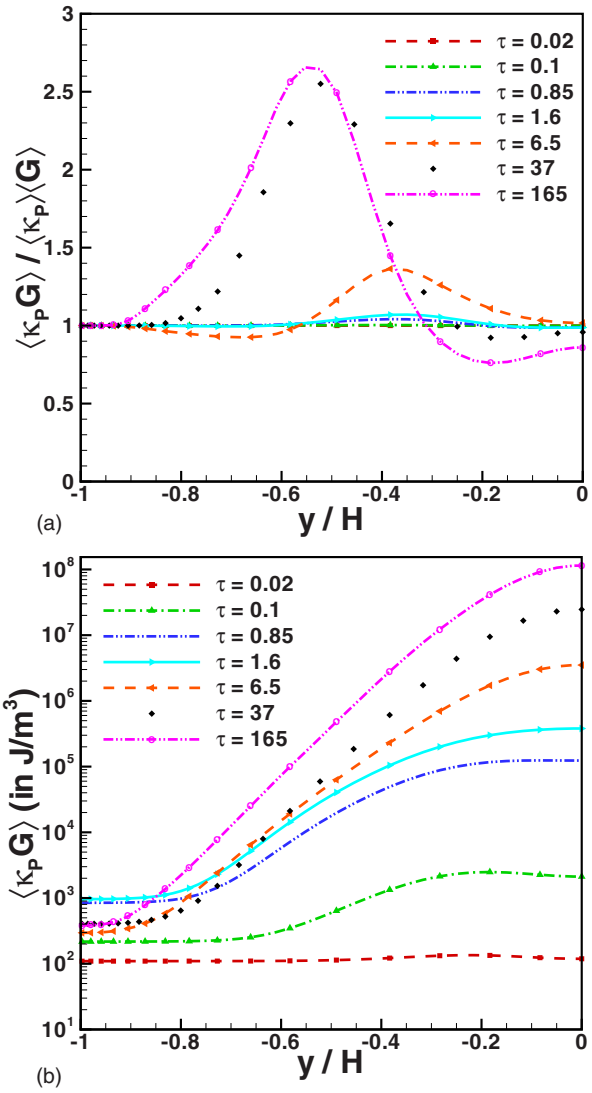

Fig. 9 Absorption TRI for several optical thicknesses for the reacting case

tically thin and optically thick limits. With chemical reactions, emission TRI is important at all optical thicknesses, while absorption TRI increases with increasing optical thickness. For the present configuration, the temperature self-correlation makes the most important contribution to emission TRI. The other noted contribution to emission TRI is Planck-mean absorption coefficient–Planck function correlation. Absorption TRI is as significant as emission TRI at large optical thicknesses, and the two tend to cancel each other out.

Because of the number of simplifications made in this analysis, results from this idealized case should be considered as qualitative. The proposed next steps are as follows: (1) finite-rate chemistry with a filtered density function (FDF) method to accommodate TCI, (2) nongray thermal radiation properties, and (3) a more accurate RTE solver such as the PMC method or a higher-order $P-N$ method.

Acknowledgment

This work has been supported by the National Science Foundation (Grant No. CTS-0121573) and NASA (Award No. NNX07AB40A).

References

[1] Pitsch, H., 2002, "Improved Pollutant Predictions in Large-Eddy Simulations of Turbulent Non-Premixed Combustion by Considering Scalar Dissipation Rate Fluctuations," Proc. Combust. Inst., **29**, pp. 1971–1978.
[2] Sheikhi, M. R. H., Drozda, T. G., Givi, P., Jaberi, F. A., and Pope, S. B., 2005, "Large Eddy Simulation of a Turbulent Nonpremixed Piloted Methane Jet Flame (Sandia Flame D)," Proc. Combust. Inst., **30**, pp. 549–556.
[3] Moin, P., and Apte, S. V., 2004, "Large-Eddy Simulation of Realistic Gas Turbine Combustors," AIAA Paper No. AIAA-2004-330.
[4] James, S., Zhu, J., and Anand, M. S., 2005, "Large-Eddy Simulations of Gas Turbine Combustors," AIAA Paper No. 2005-0552.
[5] Flohr, P., 2005, "CFD Modeling for Gas Turbine Combustors," *Turbulent Combustion* (Lecture Series 2005-02), L. Vervisch, D. Veynante, and J. P. A. J. Van Beeck, eds., von Karman Institute for Fluid Dynamics, Rhode-Saint-Genèse, Belgium
[6] Celik, I., Yavuz, I., and Smirnov, A., 2001, "Large-Eddy Simulations of In-Cylinder Turbulence for IC Engines: A Review," Int. J. Engine Res., **2**, pp. 119–148.
[7] Haworth, D. C., 2005, "A Review of Turbulent Combustion Modeling for Multidimensional In-Cylinder CFD," SAE Trans., **114**(3), pp. 899–928.
[8] Richard, S., Colin, O., Vermorel, O., Benkenida, A., Angelberger, A., and Veynante, D., 2007, "Towards Large-Eddy Simulation of Combustion in Spark-Ignition Engines," Proc. Combust. Inst., **31**, pp. 3059–3066.
[9] Townsend, A. A., 1958, "The Effects of Radiative Transfer on Turbulent Flow of a Stratified Fluid," J. Fluid Mech., **4**, pp. 361–375.
[10] Song, T. H., and Viskanta, R., 1987, "Interaction of Radiation With Turbulence: Application to a Combustion System," J. Thermophys. Heat Transfer, **1**, pp. 56–62.
[11] Soufiani, A., Mignon, P., and Taine, J., 1990, "Radiation-Turbulence Interaction in Channel Flows of Infrared Active Gases, *Proceedings of the International Heat Transfer Conference*, Vol. 6, ASME, New York, pp. 403–408.
[12] Gore, J. P., and Faeth, G. M., 1986, "Structure and Spectral Radiation Properties of Turbulent Ethylene/Air Diffusion Flames," 21st Symposium (International) on Combustion, The Combustion Institute, pp. 1521–1531.
[13] Gore, J. P., and Faeth, G. M., 1988, "Structure and Spectral Radiation Properties of Luminous Acetylene/Air Diffusion Flames," ASME J. Heat Transfer, **110**, pp. 173–181.
[14] Kounalakis, M. E., Gore, J. P., and Faeth, G. M., 1988, "Turbulence/Radiation Interactions in Non-Premixed Hydrogen/Air Flames," 22nd Symposium (International) on Combustion, The Combustion Institute, pp. 1281–1290.
[15] Kounalakis, M. E., Sivathanu, Y. R., and Faeth, G. M., 1991, "Infrared Radiation Statistics of Nonluminous Turbulent Diffusion Flames," ASME J. Heat Transfer, **113**(2), pp. 437–445.
[16] Faeth, G. M., Gore, J. P., Shuech, S. G., and Jeng, S. M., 1989, "Radiation From Turbulent Diffusion Flames," Annu. Rev. Numer. Fluid Mech. Heat Transfer, **2**, pp. 1–38.
[17] Coelho, P. J., 2004, "Detailed Numerical Simulation of Radiative Transfer in a Nonluminous Turbulent Jet Diffusion Flame," Combust. Flame, **136**, pp. 481–492.
[18] Tessé, L., Dupoirieux, F., and Taine, J., 2004, "Monte Carlo Modeling of Radiative Transfer in a Turbulent Sooty Flame," Int. J. Heat Mass Transfer, **47**, pp. 555–572.
[19] Mazumder, S., and Modest, M. F., 1999, "A PDF Approach to Modeling Turbulence-Radiation Interactions in Nonluminous Flames," Int. J. Heat Mass Transfer, **42**, pp. 971–991.
[20] Li, G., and Modest, M. F., 2002, "Application of Composition PDF Methods in the Investigation of Turbulence-Radiation Interactions," J. Quant. Spectrosc. Radiat. Transf., **73**(2–5), pp. 461–472.
[21] Wu, Y., Haworth, D. C., Modest, M. F., and Cuenot, B., 2005, "Direct Numerical Simulation of Turbulence/Radiation Interaction in Premixed Combustion Systems," Proc. Combust. Inst., **30**, pp. 639–646.
[22] Deshmukh, K. V., Haworth, D. C., and Modest, M. F., 2007, "Direct Numerical Simulation of Turbulence/Radiation Interactions in Nonpremixed Combustion Systems," Proc. Combust. Inst., **31**, pp. 1641–1648.
[23] Chandy, A. J., Glaze, D. J., and Frankel, S. H., 2007, "Mixing Models and Turbulence-Radiation Interactions in Non-Premixed Jet Flames via the LES/FMDF Approach, Fifth US Combustion Meeting, San Diego, CA, Mar. 25–28.
[24] Kabashnikov, V. P., and Kmit, G. I., 1979, "Influence of Turbulent Fluctuations on Thermal Radiation," J. Appl. Spectrosc., **31**(2), pp. 963–967.
[25] Coelho, P., 2007, "Numerical Simulation of the Interaction Between Turbulence and Radiation in Reactive Flows," Prog. Energy Combust. Sci., **33**, pp. 311–383.
[26] Modest, M. F., 2003, *Radiative Heat Transfer*, 2nd ed., Academic Press, New York.
[27] Kabashnikov, V. P., 1985, "Thermal Radiation of Turbulent Flows in the Case of Large Fluctuations of the Absorption Coefficient and the Planck Function," J. Eng. Phys., **49**(1), pp. 778–784.
[28] Kabashinikov, V. P., and Myasnikova, G. I., 1985, "Thermal Radiation in Turbulent Flows—Temperature and Concentration Fluctuations," Heat Transfer-Sov. Res., **17**(6), pp. 116–125.
[29] Moser, R. D., Kim, J., and Mansour, N. N., 1999, "Direct Numerical Simulation of Turbulent Channel Flow Up to Re_τ=590," Phys. Fluids, **11**(4), pp. 943–945.
[30] Horiuti, K., 1989, "The Role of the Bardina Model in Large Eddy Simulation of Turbulent Channel Flow," Phys. Fluids A, **1**(2), pp. 426–428.
[31] Piomelli, U., Moin, P., and Ferziger, J. H., 1988, "Model Consistency in Large

Eddy Simulation of Turbulent Channel Flows," Phys. Fluids, **31**, pp. 1884–1891.
[32] Moin, P., and Kim, J., 1982, "Numerical Investigation of Turbulent Channel Flow," J. Fluid Mech., **118**, pp. 341–377.
[33] Debusschere, B., and Rutland, C. J., 2004, "Turbulent Scalar Transport Mechanisms in Plane Channel and Couette Flows," Int. J. Heat Mass Transfer, **47**, pp. 1771–1781.
[34] Weller, H. G., Tabor, G., Jasak, H., and Fureby, C., 1998, "A Tensorial Approach to Continuum Mechanics Using Object Oriented Techniques," Comput. Phys., **12**(6), pp. 620–631.
[35] See www.openfoam.org, January 2006.
[36] Gupta, A., 2007, "Large-Eddy Simulation of Turbulence/Chemistry/Radiation Interactions in Planar Channel Flow," MS thesis, The Pennsylvania State University, University Park, PA.
[37] Boris, J. P., Grinstein, F. F., Oran, E. S., and Kolbe, R. J., 1992, "New Insights Into Large Eddy Simulation," Fluid Dyn. Res., **10**, pp. 199–228.
[38] Sandia National Laboratories Combustion Research Facility, 2002, International Workshop on Measurement and Computation of Turbulent Nonpremixed Flames.
[39] Mazumder, S., and Modest, M. F., 1999, "Turbulence-Radiation Interactions in Nonreactive Flow of Combustion Gases," ASME J. Heat Transfer, **121**, pp. 726–729.
[40] Singh, V., 2005, "Study of Turbulence Radiation Interactions Using LES of Planar Channel Flow," MS thesis, The Pennsylvania State University, University Park, PA.

The Air-Side Thermal-Hydraulic Performance of Flat-Tube Heat Exchangers With Louvered, Wavy, and Plain Fins Under Dry and Wet Conditions

Young-Gil Park
e-mail: ypark5@uiuc.edu

Anthony M. Jacobi[1]
e-mail: a-jacobi@uiuc.edu

Department of Mechanical Science and Engineering,
University of Illinois,
1206 West Green Street,
Urbana, IL 61801

The air-side thermal-hydraulic performance of flat-tube aluminum heat exchangers is studied experimentally for conditions typical to air-conditioning applications, for heat exchangers constructed with serpentine louvered, wavy, and plain fins. Using a closed-loop calorimetric wind tunnel, heat transfer and pressure drop are measured at air face velocities from 0.5 m/s to 2.8 m/s for dry- and wet-surface conditions. Parametric effects related to geometry and operating conditions on heat transfer and friction performance of the heat exchangers are explored. Significant differences in the effect of geometrical parameters are found for dry and wet conditions. For the louver-fin geometry, using a combined database from the present and the previous studies, empirical curve-fits for the Colburn j- and f-factors are developed in terms of a wet-surface multiplier. The wet-surface multiplier correlations fit the present database with rms relative residuals of 21.1% and 24.4% for j and f multipliers, respectively. Alternatively, stand-alone Colburn j and f correlations give rms relative residuals of 22.7% and 29.1%, respectively.
[DOI: 10.1115/1.3089548]

Keywords: louver, flat tube, heat exchanger, heat transfer, friction, correlation, wet-surface multiplier

1 Introduction

Flat-tube aluminum heat exchangers are commonly used in air-conditioning applications where compactness is desired, such as for automotive systems. Among the advantages of the flat-tube design over the round-tube design are higher compactness and reduced material costs, reduced refrigerant charge, lower fan power, and improved suitability for high tube-side operating pressures. On the other hand, flat-tube designs may require higher manufacturing costs and can be subject to more severe performance degradation by air-side surface fouling, condensate retention, and frost accumulation. Engineers must consider such trade-offs based on a sound understanding of the thermal-hydraulic performance characteristics under various operating conditions.

For flat-tube louver-fin heat exchangers, extensive studies of the air-side parametric effects have been reported for dry-surface conditions [1–7]. Davenport [1] found louver spacing to be more relevant than hydraulic diameter for the basis of Reynolds number. Systematic experimental studies of the geometrical parameters (e.g., fin spacing, louver spacing, louver angle, louver length, and fin length) showed that Colburn j and Fanning friction factors tend to increase with larger louver angle [1,6], and the j-factor increases with a larger louver length [1] and a shorter air-flow depth [6]. Most commonly, flat-tube heat exchangers are configured with serpentine folded fins; however, Achaichia and Cowell [3] tested 15 samples of louvered plate-fin heat exchangers with one or two tube rows. Perhaps because of the unique plate-fin-and-tube geometry and the very small unlouvered-fin length, these samples showed somewhat higher Colburn j-factors in comparison to the conventional serpentine fin geometry. Flat-tube louver-fin heat exchangers often exhibit a significantly flattened j-factor (or Stanton number) at low Reynolds numbers, especially for a small louver spacing, a large fin spacing, and a low louver angle [1,3]. Such a behavior is generally attributed to a change in flow pattern, from a louver-directed flow to a duct-directed flow with decreasing Reynolds number [3]. The extent to which a louver-directed flow is achieved is often described as *flow efficiency* [8,9].

Some experimental data show inconsistencies and complexities that are often difficult to explain. Webb and Jung [4] tested six heat exchangers, some with standard serpentine louver fins and some with a splitter-fin geometry. While a similar pressure drop was measured for both geometries, it was found that the low-Re heat transfer flattening occurred only for the splitter-fin geometry, not for the standard fins. Another example is the report by Rugh et al. [5] who tested a very compact flat-tube louver-fin heat exchanger used for automotive systems. They reported that offset-strip fins had higher j and f than louver fins, which is contrary to the usual findings in literature (e.g., Ref. [2]).

Some common misinterpretations of trends in data may be due to an assumption of a monotonic parametric effect. An example is the effect of unlouvered fin length; numerical work by Cui and Tafti [10] explains the increased heat transfer for a small unlouvered fin length (as reported by Achaichia and Cowell [3]); however, a total elimination of unlouvered fin length can actually reduce heat transfer [10]. Similarly, Kim and Bullard [6] noticed that a nonmonotonic variation of heat transfer occurred for a range of louver angle from 15 deg to 29 deg—this trend can be an indication of the existence of multiple suboptimal louver configurations due to the thermal wake effect, as proposed by Suga and Aoki [11]. Kim and Bullard [6] also observed a stronger effect of

[1]Corresponding author.

Contributed by the Heat Transfer Division of ASME for publication in the JOURNAL OF HEAT TRANSFER. Manuscript received March 20, 2008; final manuscript received December 1, 2008; published online March 30, 2009. Review conducted by Sai C. Lau.

louver angle on heat transfer at a higher Re—an example of combined parametric effects. Kim et al. [7] conducted heat transfer, friction experiments on 12 louvered-fin heat exchangers using 2:1 model geometries, representing large louver angles and small-fin spacing (i.e., F_p/L_p). They argued that an optimal performance exists at a louver angle between 20 deg and 25 deg, a range lower than the more typical optimal values [6]. Also, their friction factors were considerably lower than those reported by others for a similar geometry, and an unexpected flattening at low Re appeared in the friction factor data.

There are far fewer studies of wet-surface performance of these heat exchangers, when compared with dry-surface work. Furthermore, differences and inconsistencies in data reduction, and failure to recognize and report some important parameters (such as wettability) make it difficult to compare the results reported in these studies. Recognizing the importance of surface wettability for condensing conditions, Goodremote and Hartfield [12] studied the effect of a hydrophilic coating on the performance of a serpentine-tube louver-fin automotive evaporator. They reported that a hydrophilic coating reduced pressure drop but did not affect heat transfer. Unfortunately, they did not report fin geometry, and it is difficult to compare their work with other studies. A similar limitation exists in generalizing the work by Chiou et al. [13] who tested automotive evaporators under dry and wet conditions, because they calculated wet-surface fin efficiency by McQuistion's method [14], which Wu and Bong [15] later showed to be overly simplistic. As a result, the fin efficiency (and heat transfer coefficient) reported by Chiou et al. [13] depended highly on relative humidity, even for fully wet conditions. Chiou et al. [13] did not report louver angle and surface wettability.

McLaughlin and Webb [16] studied sensible heat transfer and friction characteristics of five automotive evaporators under wet conditions. The differences in heat transfer and pressure drop with varying louver spacing, flow depth, and surface coating were insignificant under dry conditions. However, under wet conditions, they found a 30–40% higher heat transfer coefficient and 10–15% higher pressure drop for a louver spacing of 1.3 mm in comparison to 1.1 mm. They attributed these differences to increased interlouver bridging for a smaller louver spacing. In contrast to the finding by Goodremote and Hartfield [12], McLaughlin and Webb [16] reported that a hydrophilic coating increased heat transfer by 25% but showed an insignificant impact on pressure drop. They conjectured that bridging was reduced by the coating and that their measurements reflected those effects.

Kaiser and Jacobi [17] studied condensate retention effects on the air-side thermal-hydraulic performance of automotive evaporators. Their data showed a decreased sensible heat transfer coefficient under condensing conditions in comparison to the dry data, with a larger effect for smaller louver spacing. The data also showed that a small louver spacing with a large louver angle increases heat transfer and pressure drop. Tang and Jacobi [18] also reported a significant decrease in air-side heat transfer and an increase in pressure drop under wet conditions. In these studies [17,18], heat exchangers retaining less condensate tended to have better wet-surface heat transfer and pressure drop performance. They reported contact angles typical to untreated aluminum, but geometrical differences obfuscated the effect of wettability. The pressure drop results reported by Jacobi and co-workers [17,18] is counter to that of McLaughlin and Webb [16] (and to the findings of this study), perhaps due to differing parametric ranges.

Kim and Bullard [19] conducted heat transfer and pressure drop measurements for flat-tube louver-fin heat exchangers under wet conditions. The effects of Re_{Lp}, a, F_p, and F_d on wet-surface performance were studied using 30 samples. They reported that both sensible heat transfer and pressure drop increased for a large louver angle, indicating fewer condensate bridges. The ratio of pressure drop under wet conditions to that under dry conditions was always greater than 1 (over 2 for certain cases). On the other hand, the ratio for heat transfer coefficient spanned from 0.7 to 1.6—a large increased sensible heat transfer occurred for a large louver angle (27 deg) with small-fin spacing (1.0, 1.2 mm). They proposed Colburn j- and f-factor correlations for wet-surface conditions using simple power-law-based functions. They did not report contact angles, nor consider the effects of surface wettability. Currently in the open literature, their wet-surface j and f correlations are the only correlations for flat-tube heat exchangers under wet conditions. A detailed discussion of the existing performance correlations of flat-tube louver-fin heat exchangers under dry conditions is presented in a related paper [20].

For uninterrupted fin geometries such as wavy or plain fins, extensive experimental and numerical studies with model geometries can be found in literature (e.g., Refs. [21–23]). However, there are few experimental investigations of flat-tube heat exchangers with uninterrupted fins, and none for wet conditions. Recently, Dong et al. [24] used 11 samples of flat-tube wavy-fin heat exchangers to explore the effect of geometrical parameters including fin spacing, wave amplitude, wavelength, and fin length. For dry conditions, they developed correlations for Colburn j and Fanning friction factors using a simple power-law fit. For uninterrupted fins, a serpentine folded configuration—common for louvered designs—can be potentially disadvantageous due to limited availability of condensate water drainage passages. Such a question has not been addressed in literature to our knowledge.

Numerous studies of the performance of flat-tube louver-fin heat exchangers under dry conditions are available in literature. However, the descriptions of parametric effects in individual reports are often case-dependent, due to limited ranges of parameters. The complexity of the combined effects of geometrical and operational parameters makes it difficult to explain inconsistent observations, and power-law-based curve-fits cannot capture nonmonotonic behavior. For these reasons, many existing performance correlations inadequately represent known parametric trends [20]. For wet conditions, where the parametric effects are even more complex, much less research has been reported, data reduction methods are inconsistent, and some important parameters are overlooked. While there are numerous reports in literature for round-tube heat exchangers many fewer studies of flat-tube heat exchangers appear, and the performance of flat-tube heat exchangers with uninterrupted fins under wet-surface conditions has not been reported in the open literature.

In this study we experimentally examine dry- and wet-surface thermal-hydraulic performances of flat-tube heat exchangers, including wavy and plain fins in addition to typical serpentine louver fins. We consider parameters important to condensate retention and drainage, such as contact angle and heat exchanger inclination. Louver-fin data under dry conditions are compared with previously reported data, and trends in the data are explored—particularly the novel data for uninterrupted fins under dry and wet conditions. For the louver-fin geometry, using a combined database from the present and previous studies, empirical correlations of Colburn j- and f-factors are developed in terms of their wet-surface multipliers, as well as stand-alone j and f correlations.

2 Experimental Approach and Data Analysis

The apparatus and procedures used in this work are described in detail elsewhere [25] and are summarized here only in enough detail to support the veracity of the data. A closed-loop wind tunnel was used for dry- and wet-surface experiments. The temperature, humidity, and velocity of the air flow approaching the heat exchanger were controlled with electrical heaters, steam injection, an axial blower, and a digital control system. The air temperature was measured using T-type thermopile grids (6 channels upstream and 12 channels downstream), and chilled-mirror hygrometers were used to measure the upstream and downstream dew points. The cross-sectional flow area in the test section was 30 cm wide and 20 cm high. Following the ASME standard, the air-flow rate was measured with a flow nozzle and a differential

Table 1 Summary of measurement uncertainties in wind-tunnel experiments

Parameters	Uncertainty
Air temperature	±0.1°C
Coolant temperature	±0.03°C
Nozzle discharge coefficient	±2%
Core pressure drop	±0.17 Pa
Nozzle pressure drop	±0.087 Pa
Coolant mass flow rate	±0.1% of reading
Dew point	±0.2°C
Data acquisition system	±0.1% F.S.

pressure transducer; the velocity ranged from 0.5 m/s to 5 m/s in the test section. A pressure transducer was used to measure air-side pressure drop across the test section. A single-phase aqueous solution of ethylene glycol (55% by weight) was used as the tube-side fluid. A chiller system, two large coolant reservoirs, a proportional-integral-derivative (PID)-controlled electric heater, and a gear pump delivered a conditioned tube-side flow (steady to within 0.1°C) at a capacity up to 20 kW. Coolant inlet and outlet temperatures were measured using resistance temperature detectors (RTDs) with an uncertainty less than 0.05°C. A Coriolis-effect flow meter located in the downstream coolant pipe was used to measure coolant mass flow rate. The experimental uncertainties associated with the wind-tunnel experiments are given in Table 1.

Some specimens had face dimensions different from those of the test section, and it was necessary to either cover a part of the heat exchanger face or install an additional flow contraction upstream and a diffuser downstream of the test specimen. The heat exchangers were mounted in the test section, and the entire wind tunnel, test specimen, steam pipes, and coolant pipes were well insulated. Steady-state conditions were considered to prevail when all measurement fluctuations were within instrument uncertainties. For wet tests, however, an initial condensation period of at least 40 min was mandated to ensure fully developed condensate retention. The data stream was sampled for a period long enough to ensure that the average readings were independent of temporal fluctuations.

The test conditions are given in Table 2. For each combination of specimen and surface condition, steady-state data were obtained at air velocities of 0.5 m/s, 0.7 m/s, 1.0 m/s, 1.4 m/s, 2.0 m/s, and 2.8 m/s, and at each velocity, four data sets were recorded at different coolant flow rates, mitigating uncertainties in coolant-side heat transfer. Most experimental data were collected under dry-surface or fully wet-surface conditions, and it was necessary to adjust the operating conditions, depending on local weather conditions and specimen performance, to ensure partially wet-surface conditions were avoided. With nearly 200 heat exchanger experiments (each at multiple coolant flow rates), 88% of the experiments reflected an energy balance within 5%, and all experiments had an energy balance within 10%.

All the specimens used in these experiments were made of aluminum fins brazed to flat, extruded aluminum tubes. Contact angle data for the specimens are provided in Table 3, and geometric data are provided in Table 4 corresponding to the schematic provided in Fig. 1.

Table 2 Test conditions for dry/wet wind-tunnel testing

Condition	$T_{air,1}$ (°C)	$T_{cool,1}$ (°C)	$T_{dew,1}$ (°C)
Dry	30	15	–
Wet1	27	7	15
Wet2	11	0	5

Table 3 Contact angles measured on fins from test specimens

Specimen No.	θ_A (deg)	θ_R (deg)
1, 2, 3	96	30
4, 5, 6, 7, 8	72	Less than 10
9, 10	106	Less than 10

For dry-surface conditions, the air-side, coolant-side, and the average heat transfer rates were calculated using Eqs. (1)–(3). The overall heat transfer coefficient was calculated from an effectiveness-*NTU* relation [26]. The example shown in Eq. (4) is for a single-pass, cross-flow configuration with both fluids unmixed; note that the air-side heat rate capacity was always lower than that of the coolant flow.

$$Q_{air} = C_{air}(T_{air,1} - T_{air,2}) \tag{1}$$

$$Q_{cool} = C_{cool}(T_{cool,2} - T_{cool,1}) \tag{2}$$

$$Q_m = (Q_{air} + Q_{cool})/2 \tag{3}$$

$$\varepsilon = 1 - \exp\{C_r^{-1} NTU^{0.22}[\exp(-C_r NTU^{0.78}) - 1]\}$$
$$\text{with} \quad C_r = C_{min}/C_{max} \tag{4}$$

$$\varepsilon = Q_m/(C_{air}(T_{air,1} - T_{cool,1})) \tag{5}$$

$$NTU = UA/C_{air} \tag{6}$$

The total thermal resistance from the air to the coolant is formulated as shown in Eq. (7), with the fin efficiency calculated assuming symmetry (see Ref. [26]).

$$\frac{1}{UA} = \frac{1}{h_{cool}A_{cool}} + \frac{\delta_t}{(kA)_{tube}} + \frac{1}{\eta_o h_{air} A_{air}} \tag{7}$$

$$\eta_o = 1 - A_f(1 - \eta)/A_{air} \tag{8}$$

$$\eta = \tanh(mL)/(mL) \tag{9}$$

$$m^2 = (h_{air}P_f)/(k_f A_{f,c}) \tag{10}$$

The coolant flow was always laminar ($Re < 100$), with Pr from 10 to 100; thus, the coolant flow was considered hydrodynamically developed and thermally developing. Because the air-side heat transfer resistance was dominant in most cases, a constant wall heat flux boundary condition can be assumed for coolant flow. This allowed the use of well-known tabular data (Ref. [27], p. 218) to obtain the coolant heat transfer coefficient. Thus, Eqs. (1)–(10) yielded the air-side convection coefficient, which was cast as a Colburn *j*-factor. The friction factor was determined including entrance and exit effects. Finally, we have

$$j = \frac{h_{air}}{c_{p,air}G_c}\mathrm{Pr}_{air}^{2/3} \tag{11a}$$

$$f = \frac{A_c}{A_{air}}\frac{\rho_m}{\rho_1}\left[\frac{2\rho_1\Delta P}{G_c^2} - (1+\sigma^2)\left(\frac{\rho_1}{\rho_2} - 1\right)\right] \tag{11b}$$

For wet wind-tunnel tests, the data reduction differs slightly from the dry-surface case. The enthalpy difference was used as the driving potential instead of the temperature difference, following Threlkeld [28]. The air-side heat transfer rate was calculated using Eq. (12). Equivalent enthalpies for coolant and wall surfaces were that of saturated air at that temperature. The wet fin efficiency was calculated as shown below, based on the analogy between heat and mass transfer and on the assumption that $Le \approx 1$ for air-water vapor mixture. In Eq. (15), *b* is the slope of saturated enthalpy line between fin base temperature and fin tip temperature.

Table 4 Detailed geometrical data of heat exchanger specimens

No.	External dimensions ($H\times W\times D$) (all in mm)	Fin type	L_p (mm)	F_p (mm)	F_l (mm)	L_l (mm)	α (deg)	δ_f (mm)	F_d (mm)	T_p (mm)
1	406×381×16	Louver	1.40	1.06	7.93	6.93	27	0.102	15.9	9.86
2	406×381×28	Louver	1.40	2.12	7.93	6.93	27	0.102	27.9	9.86
3	406×381×28	Louver	1.40	1.06	7.93	6.93	27	0.102	27.9	9.86
4	210×314×26	Louver	1.14	5.1	12.43	11.15	29±3	0.114	25.4	14.26
5	210×314×26	Louver	1.14	2.1	12.43	11.15	29±3	0.114	25.4	14.26
6	210×314×26	Louver	1.14	1.4	12.43	11.15	29±3	0.114	25.4	14.26
7	210×314×26	Wavy	12.7[a]	2.1	12.43	NA	1.9[b]	0.114	25.4	14.26
8	210×314×26	Wavy	12.7[a]	3.6	12.43	NA	1.9[b]	0.114	25.4	14.26
9	237×265×100	Wavy	9.5[a]	4.43	20.0	NA	1.3[b]	0.20	100	24.0
10	237×265×100	Plain	NA	4.43	20.0	NA	NA	0.20	100	24.0

[a]For wavy fins, wavelength (mm).
[b]For wavy fins, wave height (mm), i.e., offset from valley to hill.
Note that all wavy-fin heat exchangers have in-phase sinusoidal patterns.

$$Q_{w,\text{air}} = \dot{m}_{\text{air}}(i_{\text{air},1} - i_{\text{air},2}) \tag{12}$$

$$\eta_w = \tanh(m_w L)/(m_w L) \tag{13}$$

$$m_w^2 = m^2 b_f / c_{p,\text{air}} \tag{14}$$

$$b_f = (i_{s,b} - i_{s,t})/(T_b - T_t) \tag{15}$$

The same ε-NTU relation as for dry condition was used for wet condition but C_r and $C_{\min}$ are determined using

$$C_{\text{air},w} = Q_m/(i_{\text{air},1} - i_{\text{air},2}) \tag{16}$$

and

$$C_{\text{cool},w} = Q_m/(b_i'(T_{\text{cool},2} - T_{\text{cool},1})) \tag{17}$$

where b_i' was defined in the same way as b_f in Eq. (15) but evaluated at the average tube internal surface temperature. The overall heat transfer coefficient for wet condition follows from

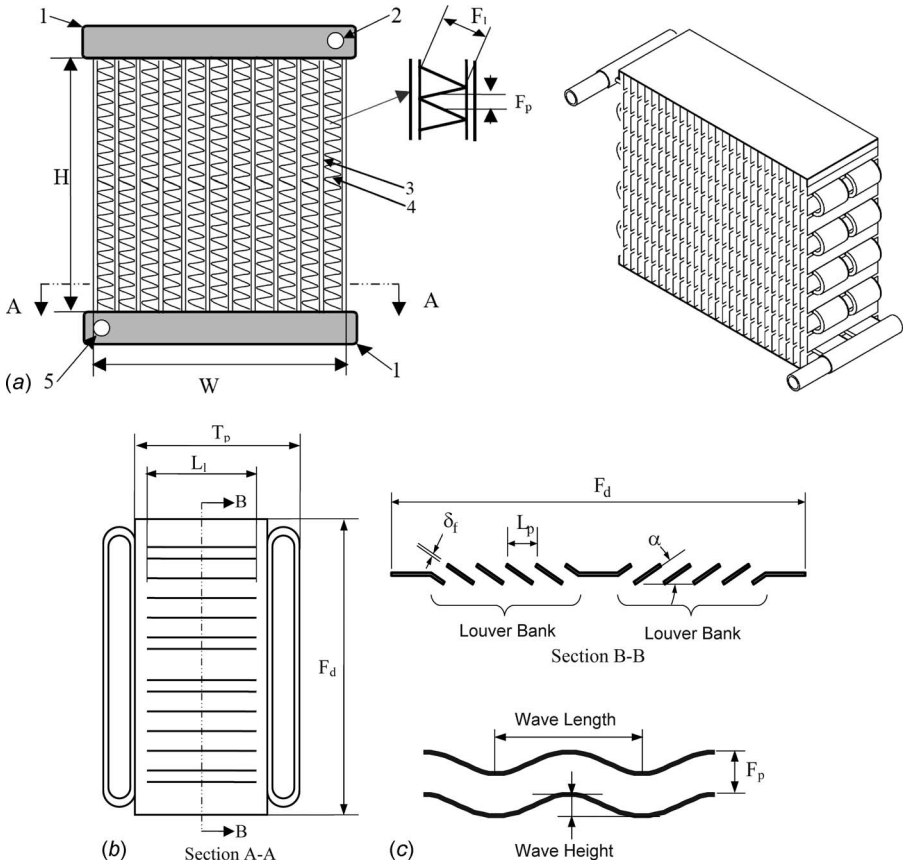

Fig. 1 Schematic of test specimen: (*a*) frontal view, with (1) manifold, (2) coolant outlet, (3) flat tubes, (4) louvered fins, (5) coolant inlet, the air flow is into the page, and the coolant flow is from bottom to top; the geometry on the right is for specimens 9 and 10, with all others configured as shown on the left; (*b*) tube-fin cross-sectional view, with coolant flow out of the page, and air flow from bottom to top; (*c*) louver-fin cross-sectional view, showing the louver configuration (upper); wavy-fin cross-sectional view (lower)

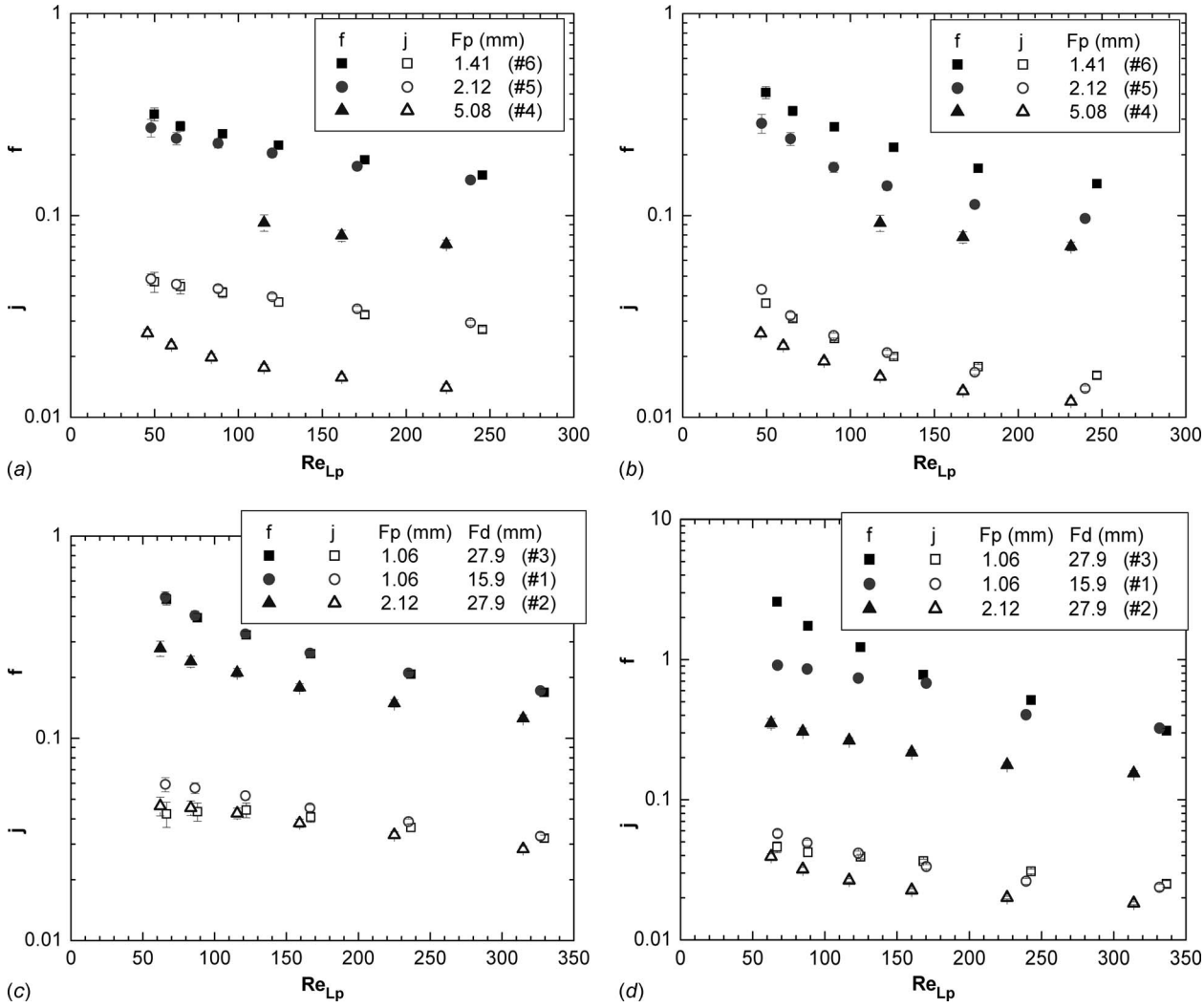

Fig. 2 Geometrical effects on dry- and wet-surface performance of louvered-fin heat exchangers. The effect of fin spacing (specimen Nos. 6, 5, and 4): (*a*) dry condition and (*b*) wet condition. The effect of fin spacing and flow depth (specimen Nos. 2, 3, and 1): (*c*) dry condition and (*d*) wet condition. The error bars show 95%-confidence intervals for the data.

$$\frac{1}{C_{\min,w}NTU_w} = \frac{1}{UA_{\text{air},w}} = \frac{b_i'}{h_{\text{cool}}A_{\text{cool}}} + \frac{b_i'\delta_t}{(kA)_{\text{tube}}} + \frac{c_{p,\text{air}}}{\eta_{o,w}h_{\text{air}}A_{\text{air}}} \tag{18}$$

An error propagation analysis was undertaken using standard methods [29] to calculate the uncertainties of Table 1 and the measured data. The results will be presented with 95%-confidence intervals for each point.

3 Experimental Results

The effect of fin spacing on louver-fin heat exchanger performance is shown in Fig. 2, for identical specimens, except for the fin spacing. Under dry conditions, the F_p=1.41 mm and F_p =2.12 mm heat exchangers have very similar *j*- and *f*-factors, whereas the F_p=5.08 mm heat exchanger has far lower *f*- and *j*-factors. For wet conditions, louver-fin heat exchangers can have a decreased *f*-factor as condensate bridges the louver gaps and a transition from louver- to duct-directed flow occurs. As seen by comparing Figs. 2(*a*) and 2(*b*), at high Re, the *f*-factor is decreased under wet conditions for the F_p=1.41 mm and F_p =2.12 mm heat exchangers. However, a blockage by interfin bridging occurs at low Re, and the F_p=1.41 mm heat exchanger shows an increased *f* when the air-flow forces are not large enough to stop such bridging. Consistent with these explanations, McLaughlin and Webb [16] reported a reduced pressure drop for samples with a small louver spacing; however, there are contrasting studies [17–19] (perhaps due to different geometrical features). Also shown in Figs. 2(*c*) and 2(*d*) are the effects caused by fin spacing and flow depth for louver-fin heat exchangers. Under dry and wet conditions, both *f*- and *j*-factors depend on fin spacing but are essentially independent of flow depth in the high-Re range. The F_p=1.06 mm heat exchanger shows higher *f* and *j* than the F_p=2.12 mm heat exchanger. The heat exchanger with high fin density (F_p=1.06 mm) shows a noticeable reduction in *j*-factor at low Reynolds numbers, especially for longer air-flow depth (F_d=27.9 mm). This finding is consistent with earlier work and suggests the small-fin spacing manifests a transition to duct-directed flow at low Re.

Continuing an examination of geometrical effects, the two heat exchangers for which the data of Figs. 3(*a*) and 3(*b*) were obtained have the same fin spacing (2.12 mm) and similar flow depth (25.4, 27.9 mm). Their major differences are louver spacing and fin length (tube spacing). Under dry conditions, the thermal-hydraulic performances are similar. This behavior indicates that within the range of these changes the impact of louver spacing and tube spacing is small under dry conditions. However, under wet conditions, there is a significant difference in *f*-factors and a difference in *j*-factors. The small changes in *j* buttress the data

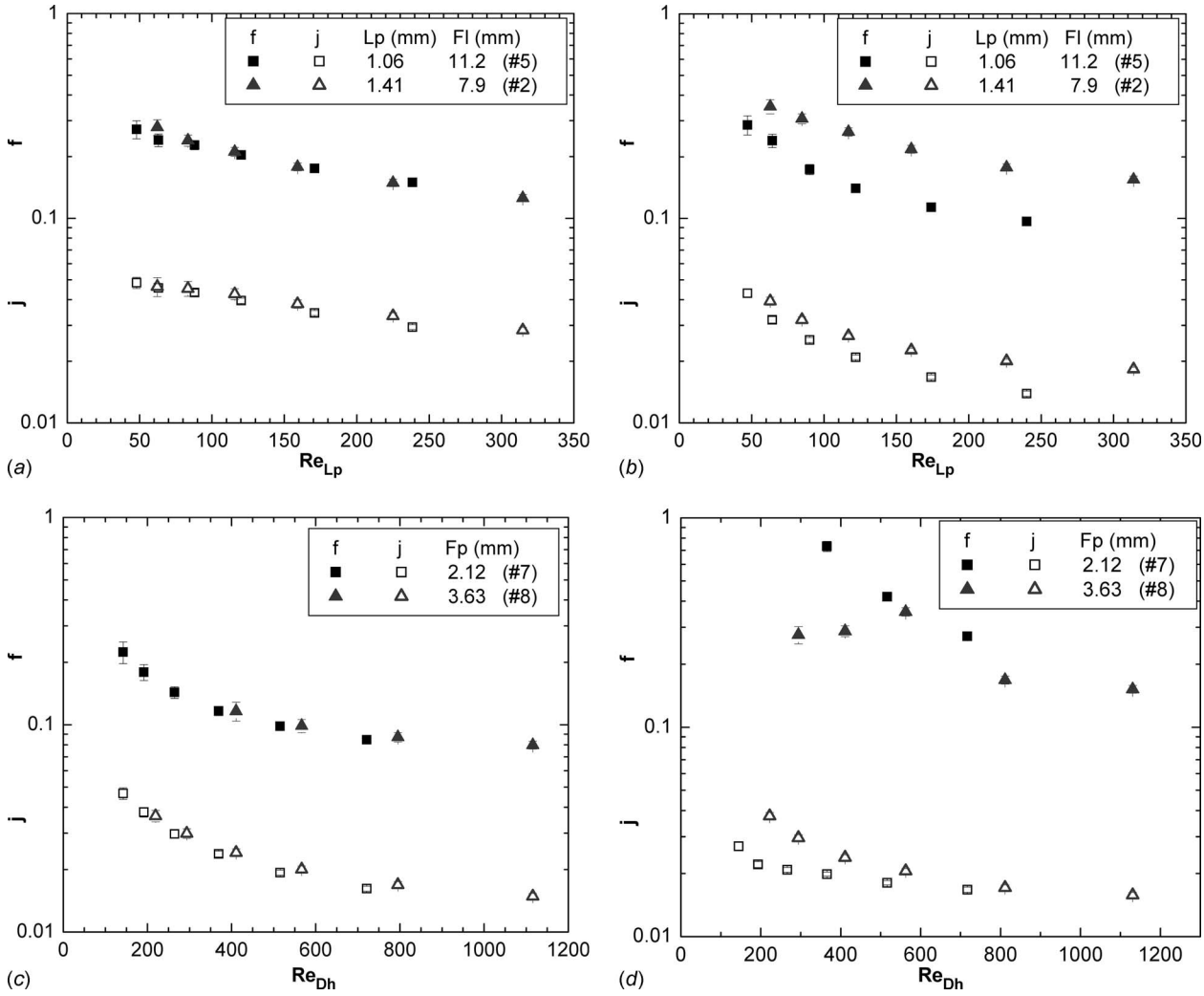

Fig. 3 Geometrical effects fin spacing on dry- and wet-surface performance of heat exchangers. The effect of louver spacing and tube spacing louvered-fin heat exchangers (specimen Nos. 5 and 2; F_p=2.12 mm both): (*a*) dry condition and (*b*) wet condition; the effect of fin spacing on wavy-fin heat exchangers (specimen Nos. 7 and 8): (*c*) dry condition and (*d*) wet condition.

reduction scheme for wet fins. If an inappropriate data reduction scheme is used, artificial changes in j might occur. It is unlikely that real changes in j could have occurred in a way to be canceled out by artifacts in data interpretation: The j-factor did not change much because there were no significant changes, and the data reduction scheme did not introduce an artificial change. The gap between neighboring louvers is smaller for a smaller louver spacing (at the same louver angle) and thus interlouver bridges more readily formed at a smaller louver spacing. The differences in f may have been caused by interlouver bridging inducing duct-directed flow. In contrast to the behavior under dry conditions, j-factors under wet conditions follow a power-law relationship more closely in Fig. 3(*b*).

It is easy to contrast the louver-fin performance with the wavy-fin performance by comparing to Figs. 3(*c*) and 3(*d*). The wavy-fin heat exchangers used to obtain the data shown in Figs. 3(*c*) and 3(*d*) have the same geometry, except for fin spacing. For dry conditions, fin spacing causes a negligible effect for the wavy-fin heat exchangers in the present parameter space. For wet conditions, the f-factor is increased significantly with a reduced fin spacing, but the j-factor decreased with a reduced fin spacing. For these heat exchangers, very poor condensate drainage was observed, owing to the uninterrupted horizontal fins and collection of condensate in the fin valleys (see Ref. [25] for details). The unusual peak in the f data is a result of the significant fluctuations in the amount of condensate retention.

The two heat exchangers for which the data in Figs. 4(*a*) and 4(*b*) were obtained have vertical fins and horizontal flat tubes—they have identical geometry, except that one has plain fins and the other has wavy fins. The wavy-fin heat exchanger has a higher f-factor than the plain-fin heat exchanger under dry conditions. For both dry and wet conditions, the plain fin has a slightly higher j-factor at low Re and a slightly lower j at high Re. The more noticeable change in the slope of j and f with Re for the wavy-fin geometry may be due to the effect of flow unsteadiness that propagates upstream with an increasing Reynolds number, as Rush et al. [22] observed for laminar flows in an in-phase wavy channel.

In Figs. 4(*c*) and 4(*d*), data from two wavy-fin heat exchangers (Nos. 8 and 9) with similar fin spacing but very different wave geometry and flow depth are compared. In comparison to specimen No. 9, specimen No. 8 has an overall larger wave pattern (height and length), shorter fin length (tube spacing), and shorter air-flow depth. Under both dry and wet conditions, specimen No. 8 shows significantly larger f and j than does specimen No. 9. If flow depth has an insignificant effect on f for wavy-fin heat exchangers (as Fig. 2 indicates for louver-fin heat exchangers), then

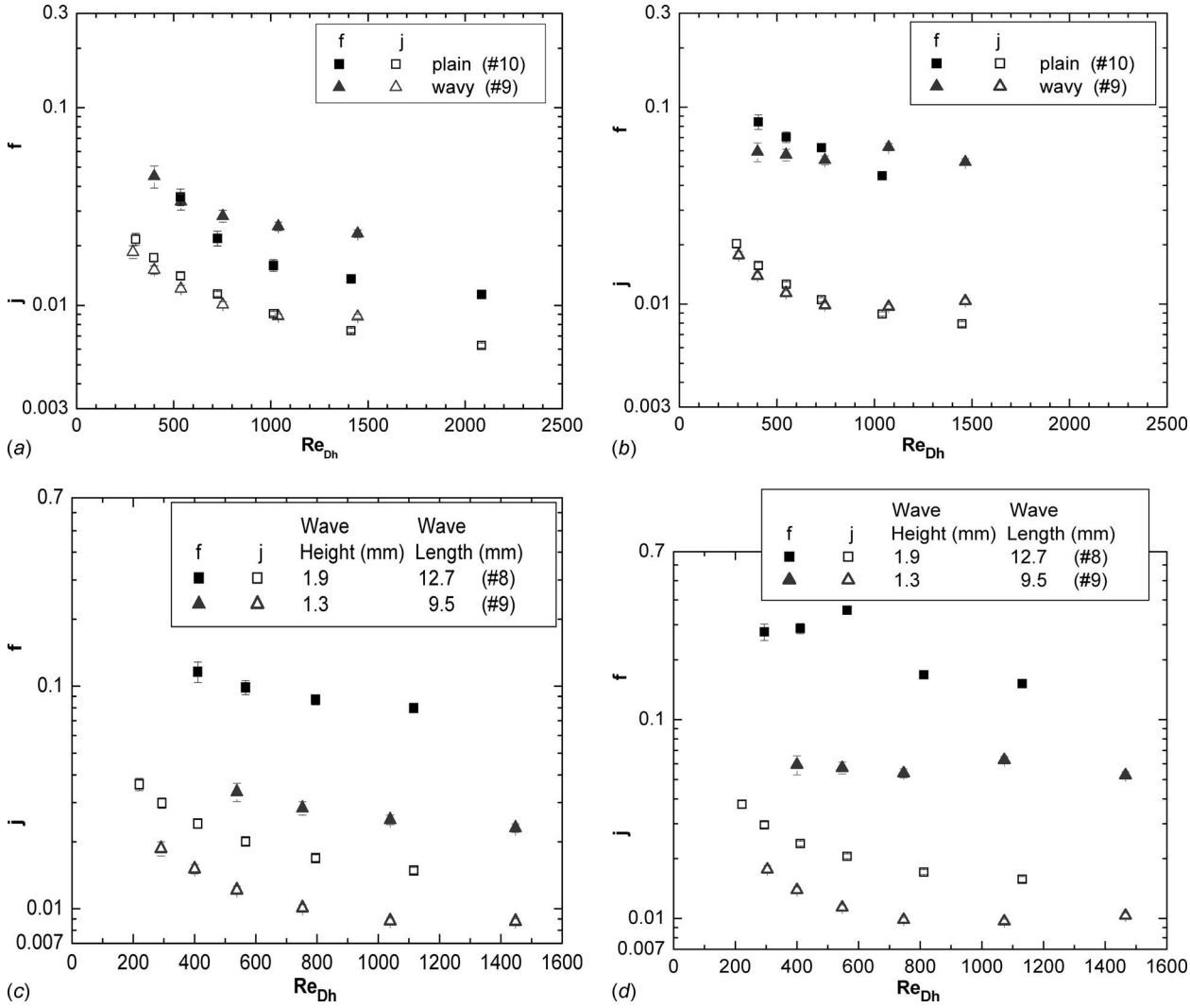

Fig. 4 Plain- and wavy-fin heat exchangers (Nos. 10 and 9): (*a*) dry condition and (*b*) wet condition. The effect of wavy fin and tube geometry (Nos. 8 and 9): (*c*) dry condition and (*d*) wet condition.

it can be concluded that the *f*-factor increases with wave height and wavelength. As for the difference in *j*-factor, specimen No. 9 has a larger flow depth and longer fins. Thus, the behavior reflected here is consistent with the general trends expected from earlier work. Figures 4(*a*) and 4(*b*) show that the effect of wave pattern alone is probably too small to explain the difference in *j*-factor in Figs. 4(*c*) and 4(*d*).

In order to assess the impact of operating temperature on the thermal-hydraulic performance under fully wet conditions, experiments were repeated at different thermal conditions as given in Table 2. For specimen Nos. 2–6, 9, and 10, the ratios of Colburn *j*-factors under "wet2" condition to those under "wet1" condition were calculated from the experimental data. Similar calculations were performed for *f*-factors. The mean values of *j* ratios and *f* ratios were 1.04 and 1.02 with standard deviations of 0.13 and 0.19, respectively. Over the range of this study, no effect of operating condition was discernable. This finding also provides further support to the data reduction scheme.

Wet-surface multipliers, as defined in Eq. (19), indicate the effect of surface conditions (i.e., dry or wet) on the performance. Figures 5 and 6 provide wet-surface multipliers of *j*- and *f*-factors for all ten specimens.

$$\phi_j = \frac{j_w}{j_0} \quad \text{and} \quad \phi_f = \frac{f_w}{f_0} \tag{19}$$

For the set of similar louver-fin heat exchangers in Fig. 5(*a*), the decrease in *f*-factor under wet condition is most significant for sample No. 5 (F_p=2.12 mm) and not as significant for sample No. 6 (F_p=1.41 mm). This may be due the presence of interlouver bridges and the absence of interfin bridges for the F_p =2.12 mm louver-fin heat exchanger. For a smaller fin spacing (1.41 mm), the formation of interfin bridges can increase the pressure drop, counteracting with the effect of interlouver bridges. The increased friction factor for F_p=1.41 mm at low Reynolds numbers is consistent with the formation of interfin bridges at low air velocities, especially for a small-fin spacing. Sample No. 4 (F_p =5.08 mm) shows negligible changes in *j*- and *f*-factors under wet conditions. Apparently, the air flow is duct-directed (as would be expected for such a large-fin spacing), and the flow pattern is not changed significantly by interlouver bridges. Figure 5(*a*) shows that the *j*-factor multiplier decreases with increasing Reynolds number and that it remains nearly constant for moderate to high Reynolds numbers, especially for small-fin-spacing heat exchangers. Because of the low flow efficiency at low Reynolds numbers under dry conditions, the heat transfer enhancement by boundary layer restarting is diminished under both dry and wet conditions.

Figure 5(*b*) presents another set of similar louver-fin heat exchangers (Nos. 1–3). In contrast to F_p=1.06 mm heat exchangers

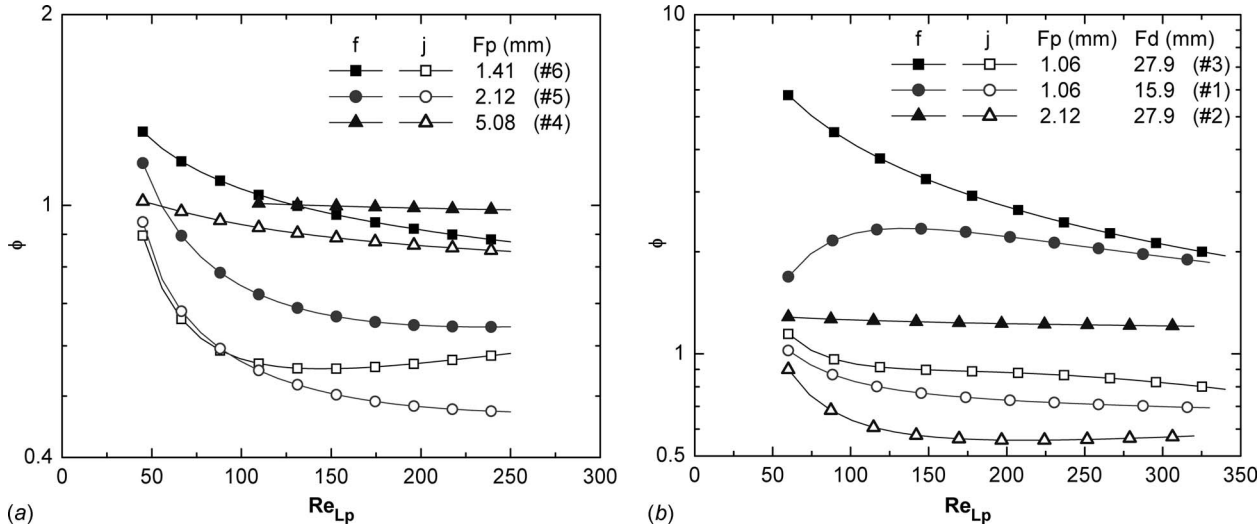

Fig. 5 Wet-surface multipliers of *f*- and *j*-factors for louver-fin heat exchangers: (*a*) effect of fin spacing (Nos. 6, 5, and 4) and (*b*) effect of fin spacing and flow depth (Nos. 3, 1, and 2). The symbols are used for distinction, not to indicate specific data points (also in Fig. 6).

(Nos. 1 and 3), where the *f*-factor increases two to five times under wet conditions, the difference in *f*-factor under dry and wet conditions is small for the $F_p=2.12$ mm heat exchanger. On the other hand, the *j*-factor is significantly decreased for the $F_p=2.12$ mm heat exchanger but not as much for the $F_p=1.06$ mm heat exchanger. In contrast to the other $F_p=2.12$ mm louver-fin heat exchanger (Fig. 5(*a*)), this heat exchanger shows an increased *f*-factor under wet conditions. Because this heat exchanger has a larger louver spacing, duct-directed flow may not be as easily induced by interlouver bridges. Furthermore, this heat exchanger has smaller tube spacing, which can be another disadvantage under wet conditions. In Figs. 5(*a*) and 5(*b*), louver-fin heat exchangers with a smaller fin spacing show less decrease in *j*-factor under wet conditions for moderate to high Reynolds numbers.

Wet-surface multipliers for uninterrupted wavy- and plain-fin heat exchangers (Nos. 7–10) are shown in Fig. 6. For a $F_p=2.12$ mm wavy-fin heat exchanger (No. 7) a significant increase in the *f*-factor over the entire Re range is observed under wet conditions. The *j*-factor is decreased at low Re, but the effect becomes negligible at high Re. Wet-surface multipliers for *j* and *f* approach unity with increasing Re for both wavy-fin heat exchangers with horizontal fins (Nos. 7 and 8). This behavior is congruent with the poor condensate drainage observed for this fin geometry; the retained condensate in the horizontal wavy fins leads to substantial fluctuations, especially for a small-fin spacing ($F_p=2.12$ mm). The literature is replete with reports of small increases in heat transfer for wet uninterrupted fins' high Reynolds numbers. The figure shows that the *f*-factor is noticeably increased and the *j*-factor is weakly affected under wet conditions for larger fin-spacing heat exchangers with wavy and plain fins (Nos. 8–10). Heat exchanger Nos. 9 and 10 have much better condensate drainage because the tubes are horizontal and the fins are vertical. The slightly increasing wet-surface multipliers for sample Nos. 9 and 10 contrast the decreasing trends for sample Nos. 7 and 8 and are probably because the forces associated with the air flow are so important for condensate removal for the horizontal fins. Figure 6 also indicates that, for the heat exchangers with vertical fins, the wavy fin (No. 9) has a lower wet-surface multiplier for the *f*-factor and a higher multiplier for the *j*-factor, and therefore is more preferable to the plain fin (No. 10) under wet-surface conditions than under dry conditions.

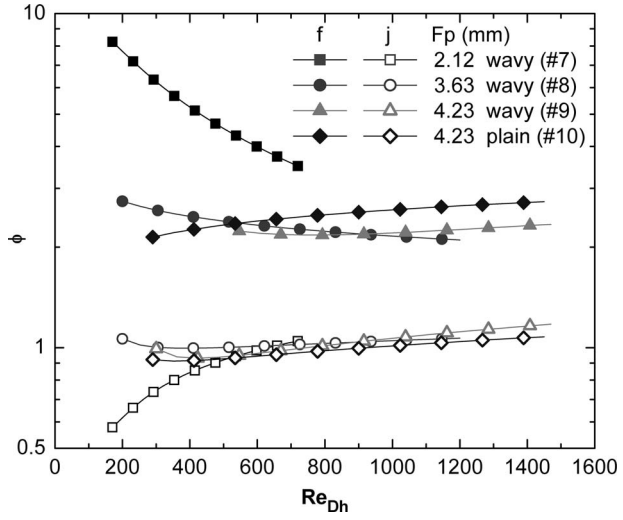

Fig. 6 Wet-surface multipliers of *f*- and *j*-factors for wavy- and plain-fin heat exchangers (Nos. 7–10)

The effect of heat exchanger inclination is shown in Fig. 7 for louver fins (Nos. 5 and 6) and wavy fins (Nos. 7 and 8). All four samples had the same configurations except for the fins. From experiments under dry and wet conditions, the ratios of *j*- and *f*-factors are obtained with an inclination of 27 deg (top toward the downstream direction) to those of the vertical heat exchanger. Under dry conditions, the *j*-factors were not changed by the inclination for louver fins. For wavy fins, the $F_p=3.6$ mm sample showed slightly increased *j*-factors by an inclination at high Reynolds numbers while the $F_p=2.1$ mm sample had nearly unaffected *j*-factors. The *f*-factors, on the other hand, were noticeably increased especially for a larger fin spacing, for high Reynolds numbers, and for wavy fins. This observation is expected for the present configuration where the ducts upstream and downstream of the test section remained horizontal and only the heat exchanger was inclined. Because the main change by the core inclination for the dry condition is caused by change in flow direction at the heat exchanger faces, samples with a higher sensitivity to the entrance/exit effects show more pronounced changes, especially in the *f*-factors.

Under wet conditions, core inclination is expected to assist drainage from the heat exchangers. Figure 7(*b*) shows that a core inclination increases *j*-factors of the louver-fin heat exchangers

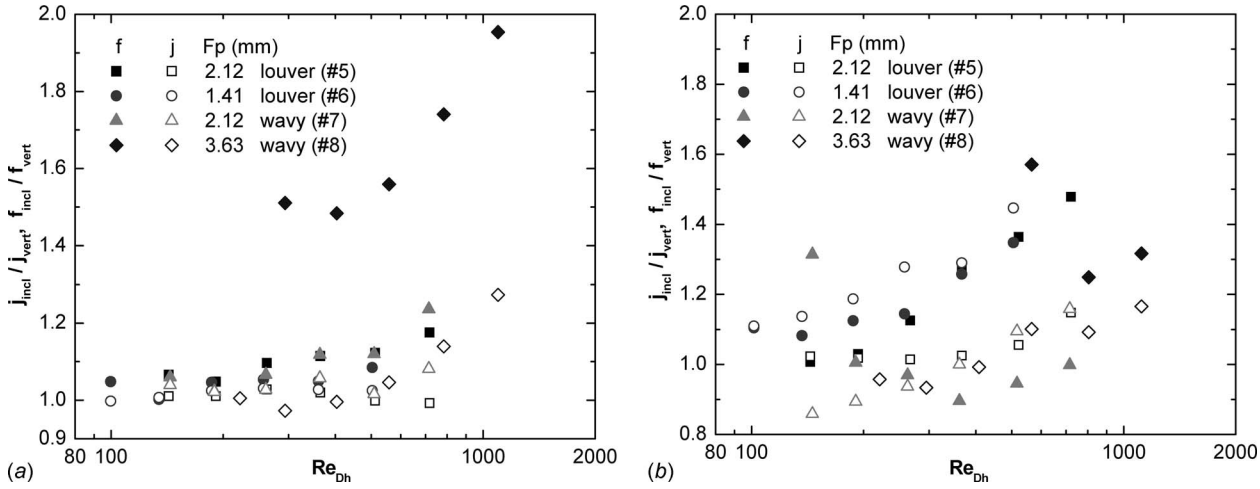

Fig. 7 Effect of inclination (27 deg) on *j*- and *f*-factors of louver- and wavy-fin heat exchangers: (*a*) dry condition and (*b*) wet condition

under wet conditions, especially for a smaller fin spacing and at high Reynolds numbers. It can be noticed that the *f*-factors of louver-fin heat exchangers under wet conditions were markedly increased by a core inclination—such an effect did not occur under dry conditions. As observed earlier, the louver-fin heat exchangers had decreased *f*-factors under dry conditions, likely due to interlouver bridges. Because the louver fins can behave like uninterrupted fins under wet conditions, a more pronounced entrance/exit effect may manifest, especially at high Reynolds number as appears in the figure. The effect of core inclination on *j*-factors of wavy-fin heat exchangers under wet conditions is generally insignificant, although a slight improvement at high Reynolds numbers appears. The fluctuations of condensate retention for wavy fins under wet conditions were not totally eliminated by the inclination. Consequently, the effect of core inclination on *f*-factors is overshadowed by a considerable scatter in the figure. However, considering the increased *f*-factor by inclination for wavy-fin heat exchangers under dry conditions, a reduced *f*-factor by core inclination under wet conditions can be noticed for moderate to high Reynolds numbers.

A comparison of the dry-surface data for louver-fin geometry obtained in these experiments to the work of Wang and coworkers [30,31] shows reasonable agreement, with 67% of the *j*-factor data and 48% of the *f*-factor data predicted to within $\pm 20\%$ by their well-known correlations. It should be noted that the new data extend the parameter space of these correlations. If only the data within the parametric space of the correlations were used in the comparison, 100% of the *j*-factor data and 28% of the *f*-factor data are predicted to within $\pm 20\%$. The *j*-factor correlation by Chang and Wang [31] consistently overpredicts the data at low Reynolds numbers, because the correlation is essentially a power-law function of selected parameters. The deviation of *j*-factors from a simple power-law relation at low Reynolds numbers has been noted in the present as well as previous studies. As discussed earlier, an optimal fin spacing for any given louver geometry is anticipated due to the thermal wake effect [11]; however, a power-law fit on fin spacing is unable to capture this behavior. Furthermore, the combined effects of geometrical and operational parameters can be more complicated than what can be best approximated using a simple power-law functional form.

4 Wet-Surface Performance Correlations for Louver Geometry

As reviewed earlier, several experimental studies of flat-tube louver-fin heat exchangers under wet conditions have been reported in literature [12,13,16–19,32]. In these studies, decreased sensible heat transfer and increased pressure drop frequently occurred under wet conditions. In some cases, however, increased sensible heat transfer and decreased pressure drop have been observed. The trends of experimental data in literature are often case-dependent and it is difficult to generalize the parametric effects. Because of the interdependence of parameters, different behaviors can manifest depending on the parametric configurations. Moreover, experimental errors can occur from the difficulties in experimentation and data reduction, or from failure to recognize important parametric effects. However, in general, literature suggests that the louver geometry has a strong impact on the wet air-side performance characteristics. Hydrophilic coatings can make noticeable changes in heat transfer and pressure drop, indicating that the wettability of air-side surface is an important parameter to wet-surface performance. The most critical parameters to the wet performance of flat-tube louver-fin heat exchangers identified in literature are louver spacing, louver angle, fin spacing, and surface wettability (or contact angles). Other important parameters may be unlouvered-fin length, air-flow depth, fin length, and tube pitch.

In this section, an empirical correlation is developed for wet air-side thermal-hydraulic performance of flat-tube louver-fin heat exchangers in terms of wet-surface multipliers, defined by Eq. (19). In order to improve general applicability of the correlations, the parameter space was expanded by compiling experimental data from independent studies. Based on Colburn *j*- and *f*-factor correlations under dry conditions, closed-form correlations of wet-surface *j*- and *f*-factors were obtained.

The experimental database for the air-side heat transfer and pressure drop has been compiled from literature. A total of 47 samples of flat-tube louver-fin heat exchangers with both dry and wet performance data were identified. The sources include studies by McLaughlin and Webb [16], Kaiser and Jacobi [17], Tang and Jacobi [18], Kim and Bullard [19], Kim et al. [32], and the present study. The heat exchangers in the wet-surface database are listed in Table 5, along with the geometrical parameters. All performance data were cast into the form of Colburn *j*-factor and Fanning friction factor. For consistency, friction factors were redefined as in Eq. (20). The entrance and exit pressure-loss coefficients, K_c and K_e, were evaluated according to Kays and London [33] with an assumption of highly interrupted fin geometry. For some friction data, the entrance and exit effects were not subtracted in the original data reduction. The difference in *f*-factors from this simplification is typically less than 5%, and the original *f* data were used without correction.

Table 5 Geometrical description of heat exchangers in wet-condition database

Source	L_p (mm)	F_p (mm)	F_1 (mm)	L_1 (mm)	α (deg)	F_d (mm)	T_p (mm)	δ_f (mm)	N_{LB}	θ_A (deg)	θ_R (deg)
Present No. 1	1.40	1.06	7.93	6.93	27	15.9	9.86	0.10	2	96	30
Present No. 2	1.40	2.12	7.93	6.93	27	27.9	9.86	0.10	2	96	30
Present No. 3	1.40	1.06	7.93	6.93	27	27.9	9.86	0.10	2	96	30
Present No. 4	1.14	5.08	12.43	11.15	29	25.4	14.26	0.11	2	72	10
Present No. 5	1.14	2.12	12.43	11.15	29	25.4	14.26	0.11	2	72	10
Present No. 6	1.14	1.41	12.43	11.15	29	25.4	14.26	0.11	2	72	10
KB[a] No. 1	1.7	1	8.15	6.4	15	20	10.15	0.1	2	70[b]	30[b]
KB[a] No. 2	1.7	1.2	8.15	6.4	15	20	10.15	0.1	2	70[b]	30[b]
KB[a] No. 3	1.7	1.4	8.15	6.4	15	20	10.15	0.1	2	70[b]	30[b]
KB[a] No. 4	1.7	1	8.15	6.4	27	20	10.15	0.1	2	70[b]	30[b]
KB[a] No. 5	1.7	1.2	8.15	6.4	27	20	10.15	0.1	2	70[b]	30[b]
KB[a] No. 6	1.7	1.4	8.15	6.4	27	20	10.15	0.1	2	70[b]	30[b]
KB[a] No. 7	1.7	1	8.15	6.4	23	16	11.15	0.1	2	70[b]	30[b]
KB[a] No. 8	1.7	1	8.15	6.4	23	20	10.15	0.1	2	70[b]	30[b]
KB[a] No. 9	1.7	1	8.15	6.4	23	24	10.15	0.1	2	70[b]	30[b]
KB[a] No. 10	1.7	1.4	8.15	6.4	23	16	11.15	0.1	2	70[b]	30[b]
KB[a] No. 11	1.7	1.4	8.15	6.4	23	20	10.15	0.1	2	70[b]	30[b]
KB[a] No. 12	1.7	1.4	8.15	6.4	23	24	10.15	0.1	2	70[b]	30[b]
KB[a] No. 13	1.7	1.4	8.15	6.4	25	16	11.15	0.1	2	70[b]	30[b]
KB[a] No. 14	1.7	1.4	8.15	6.4	27	16	11.15	0.1	2	70[b]	30[b]
KB[a] No. 15	1.7	1.4	8.15	6.4	29	16	11.15	0.1	2	70[b]	30[b]
KB[a] No. 16	1.7	1.4	8.15	6.4	19	20	10.15	0.1	2	70[b]	30[b]
KB[a] No. 17	1.7	1.4	8.15	6.4	25	24	10.15	0.1	2	70[b]	30[b]
KB[a] No. 18	1.7	1.4	8.15	6.4	27	24	10.15	0.1	2	70[b]	30[b]
KB[a] No. 19	1.7	1.4	8.15	6.4	29	24	10.15	0.1	2	70[b]	30[b]
KSB[c]	1.4	2.1	8.3	6.6	27	27.9	9.9	0.1	2	70[b]	30[b]
KJ[d] No. 1	1.2	1.81	8	6.35	30	58	10.1[e]	0.1	4[b]	68	44
KJ[d] No. 2	1	1.81	8	6.35	36	58	10.1[e]	0.1	4[b]	68	44
KJ[d] No. 3	1	1.81	8	6.35	42	58	10.1[e]	0.1	4[b]	68	44
TJ[f] No. 1	1.03	2.11	9	6.15	30	75	12.0[e]	0.08	4	82	25
TJ[f] No. 2	1.33	2.11	11.5	7.93	16	83	15.7[e]	0.13	4	76	44
TJ[f] No. 3	1.12	1.81	10	6.74	20	72	12.5[e]	0.09	4	110	48
TJ[f] No. 4	1.12	1.81	8	6.35	20	58	13.8[e]	0.1	4	64	44
TJ[f] No. 5	1.94	1.81	9	6.35	12	73	11.7[e]	0.13	4	79	18
TJ[f] No. 6	1.54	1.81	9.8	7.54	14	92	12.9[e]	0.15	4	86	45
TJ[f] No. 7	2.66	1.81	9	6.35	17	92	12.0[e]	0.1	4	60	34
TJ[f] No. 8	0.95	1.81	8	5.75	17	64	11.4[e]	0.09	4	83	25
MW[g] No. 1	1.1	1.6	8	7	30	50	9.7	0.1	4[b]	92	72
MW[g] No. 2	1.1	1.6	8	7	30	50	9.7	0.1	4[b]	51	17
MW[g] No. 3	1.3	1.6	8	7	30	50	9.7	0.1	4[b]	51	17
MW[g] No. 4	1.3	1.6	8	7	30	60	11	0.1	4[b]	51	17
MW[g] No. 5	1.3	2.4	8	7	30	60	11	0.1	4[b]	51	17

[a]Reference [19].
[b]Assumed.
[c]Reference [32].
[d]Reference [17].
[e]Estimated from original data.
[f]Reference [18].
[g]Reference [16].

$$f = \frac{A_c \rho_m}{A_{air} \rho_1} \left[\frac{2\rho_1 \Delta P}{G_c^2} - (K_c + 1 - \sigma^2) - 2\left(\frac{\rho_1}{\rho_2} - 1\right) + (1 - \sigma^2 - K_e)\frac{\rho_1}{\rho_2} \right] \tag{20}$$

Two databases of Colburn j- and f-factors were obtained, respectively, for dry and wet conditions. The dry data points of the individual heat exchanger samples were fitted by either a power-law or a third-order polynomial function of Reynolds number (the overall rms residual was less than 2%). The wet-surface multipliers were calculated from the ratios of wet-surface data points to dry curve-fits. The entire wet-surface multiplier database contains 166 data points for j and 196 data points for f.

The advantage of using wet-surface multipliers instead of independent wet j- and f-factor correlations lies in the handling of data with experimental uncertainties, unidentified errors, and inconsistent data reduction methods. The discrepancies in the experimental data among different studies are difficult to reconcile, whereas individual studies often show self-consistent data. The wet-surface multipliers can reduce biases from systematic errors in the experiments and inconsistent data interpretation methods. The correlations for wet-surface multipliers of Colburn j- and f-factors are given by Eqs. (21) and (23), respectively. Basic power-law functional forms were modified to capture detailed parametric effects. Note that all angles should be in radians. The constants are dimensionless and determined such that the rms relative residual of the entire database, defined by Eq. (22), is minimized. The regression constants and their confidence intervals are given in Table 6. These fits predict the entire database with rms errors of 21.1% for j and 24.4% for f. Figure 8(*a*) presents a comparison between the wet-surface multipliers from experiments and the predictions by correlations.

Table 6 Regression constants, along with 95% confidence intervals by linear approximation for wet-surface multiplier correlations

ϕ_j per Eq. (21), $\text{rms}_{\text{rel}}=21.1\%$			ϕ_f per Eq. (23), $\text{rms}_{\text{rel}}=24.4\%$		
Constant		Confidence interval	Constant		Confidence interval
C_1	−1.215	±6.394	D_1	0.7564	±0.1554
C_2	0.5782	±0.1165	D_2	0.2602	±0.2479
C_3	0.03590	±0.06021	D_3	−0.003949	±0.002563
C_4	0.4332	±0.6563	D_4	0.3532	±0.7692
C_5	0.2423	±0.1712	D_5	4.168	±1.501
C_6	0.04894	±0.1121	D_6	−0.07233	±0.5001
C_7	0.3659	±0.1918	D_7	−0.03771	±0.2059
C_8	−0.01426	±0.01013	D_8	−0.8744	±0.5045

$$\phi_j = \left(\text{Re}_{Lp}{}^{C_1} + \left(\frac{L_p}{F_p}\right)^{C2} \text{Re}_{Lp}{}^{C_3}\right)\left(\frac{L_1}{F_1}\right)^{C_4} \sin(\alpha + C_5) \times \left(\frac{F_d}{F_p}\right)^{C_6} (\cos(\theta_R))^{C_7}(1 - \phi_{j,\text{duct}}) + \phi_{j,\text{duct}} \quad (21a)$$

$$\phi_{j,\text{duct}} = 1 - \exp\left[C_8\left(\frac{F_p}{L_p}\right)^3\right] \quad (21b)$$

$$(\text{rms}_{\text{rel}}) = \left[\frac{1}{N}\sum\left(\frac{\phi_{j,\text{cor}}}{\phi_j} - 1\right)^2\right]^{1/2} \quad (22)$$

N = total number of data points

$$\phi_f = \left[D_1 + D_2 \exp(D_3 \text{Re}_{Lp})(\sin(\alpha))^{D_4}\left(\frac{L_p}{F_p}\right)^{D_5}\right] \times \left(\frac{F_1}{T_p}\right)^{D_6}\left(\frac{L_p}{F_p}\right)^{D_7}\left(\frac{L_1}{F_1}\right)^{D_8} \quad (23)$$

Colburn j- and f-factors under wet-surface conditions can be predicted by using the dry-surface correlations (or experimental data, if available) and the wet-surface multipliers. If information on dry-surface behavior is unavailable, or has large uncertainties, then use of a wet-surface multiplier is not desirable, because the uncertainty in the wet-surface multiplier is compounded with uncertainty in the dry-surface data. Therefore, alternative stand-alone Colburn j- and f-factor correlations can be useful. With the limited experimental database available, independent wet-surface j- and f-factor correlations were developed. The resulting correlations, given by Eqs. (24) and (25), predict the Colburn j- and f-factor data with rms relative residuals of 22.7% and 29.1%, respectively, for the entire data set. The regression constants and their confidence intervals are given in Table 7. A comparison of the wet-surface j and f data and the predictions by correlations is given in Fig. 8(*b*).

$$j_w = a_1 \text{Re}_{Lp}{}^{a_2}\left(\frac{L_p}{F_p}\right)^{a_3}(\sin(\alpha))^{a_4}\left(\frac{L_1}{F_1}\right)^{a_5}\left(\frac{F_d}{F_p}\right)^{a_6}\left(\frac{F_1}{T_p}\right)^{a_7} \quad (24)$$

$$f_w = b_1 + b_2 \text{Re}_{Lp}{}^{b_3}\left(\frac{L_p}{F_p}\right)^{b_4}(\sin(\alpha))^{b_5}\left(\frac{F_1}{T_p}\right)^{b_6} \quad (25)$$

The present wet-surface multiplier and stand-alone j and f correlations were obtained after repeated revision of the functional forms by examining the confidence intervals and the covariance matrices obtained from an approximated linear multiple regression model [34]. Reporting the confidence intervals for the con-

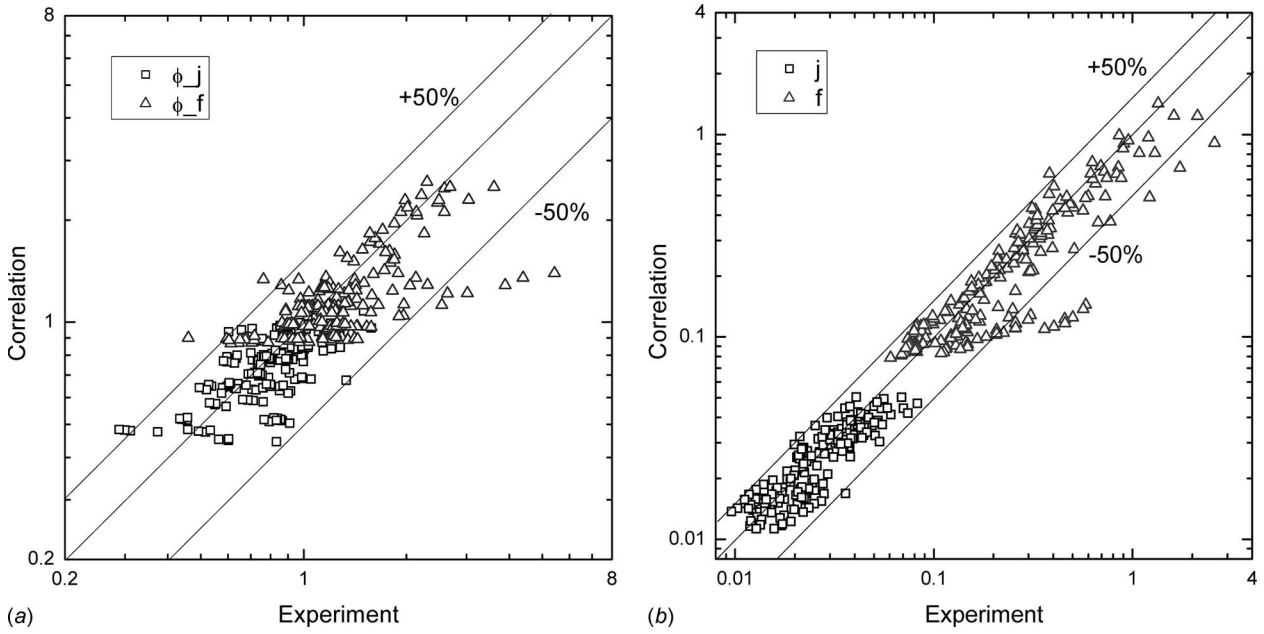

Fig. 8 Comparison of experimental data for louver-fin heat exchangers and predictions by correlations for (*a*) wet-surface multipliers and (*b*) stand-alone wet-surface *j*- and *f*-factors

Table 7 Regression constants, along with 95% confidence intervals by linear approximation for stand-alone wet-surface Colburn *j* and *f* correlations

j_w per Eq. (24), $rms_{rel}=22.7\%$			f_w per Eq. (25), $rms_{rel}=29.1\%$		
Constant	Confidence interval		Constant	Confidence interval	
a_1	0.4260	±0.1572	b_1	0.07400	±0.01326
a_2	−0.3149	±0.07526	b_2	152.7	±142.7
a_3	0.6705	±0.07928	b_3	−1.116	±0.1650
a_4	0.3489	±0.1889	b_4	2.242	±0.3880
a_5	0.5123	±0.6127	b_5	0.9680	±0.4011
a_6	−0.2698	±0.09366	b_6	1.716	±1.670
a_7	−0.2845	±0.5312			

stants in the curve-fits is useful, because they provide a measure of statistical significance for the regression constants. The covariance matrices were used to identify redundancies in the forms of fits, and although using more complex functional forms can further reduce the residuals we selected the present forms of the correlations based on statistical significance. Additional details of the correlation development process used in the present study can be found in a related study [20].

Several regression constants in Tables 6 and 7 have fairly large confidence intervals. This is consistent with a considerable scatter we found when the correlations were compared with the experimental data. Apparently, the accuracy of the present correlations is limited by the quality of the experimental data available from this study and prior work reported in literature. All data were evenly weighted in the development of the correlations. The wettability effect has not been well represented by the database and, consequently, by the correlations. Furthermore, due to the complex nature of condensate retention and drainage in these heat exchangers, small geometrical differences may cause significant changes in performance. Moreover, the current experimental database is fairly limited in size and parameter space, and it is not expected to fully represent the effects of all the relevant parameters. Despite the limitations posed by the available empirical data, the proposed correlations fulfill the need for general performance correlations for flat-tube louver-fin heat exchangers under wet conditions. In comparison to the only previous correlations by Kim and Bullard [19], the present correlations rely on a larger set of database with a wider parameter space. Furthermore, through a statistical assessment, we were able to identify important parameters and minimize overfitting during the regression process, therefore reaching more reliable and effective forms of fit.

5 Conclusions

Thermal-hydraulic performance data from wind-tunnel experiments confirm the expectation from literature that there is an optimal fin spacing for a given louver geometry. Under dry- and wet-surface conditions, the impact of fin spacing on *f* and *j* dominates the effects of other fin design parameters, especially at high Reynolds numbers. For louvered-fin heat exchangers with a small-fin spacing, the *j*-factor deviates from the commonly assumed power-law behavior at low Reynolds numbers, and the deviation depends on whether the fin is dry or wet. This deviation is consistent with the anticipated failure of flow-directing performance of the louvers at low Reynolds numbers. The impact of fin spacing on *f* for louvered-fin heat exchangers is larger under wet conditions than for dry conditions, probably due to condensate bridges forming at a small-fin spacing. Louver spacing has more impact on the performance under wet conditions than under dry conditions. Under wet conditions, *f* and *j* decrease with smaller louver spacing, while no such effect was found under dry conditions. This behavior is probably due to the formation of interlouver condensate bridges, which change the air flow from being louver-directed to duct-directed, decreasing both pressure drop and heat transfer. The experimental results show that the degradation of thermal performance under wet-surface conditions can be minimized by using a large louver spacing and a small-fin spacing.

Wavy-fin heat exchangers show higher *f* and *j* than plain-fin heat exchangers, especially at high air velocities. While the effect of fin spacing on thermal-hydraulic performance was not profound for wavy-fin heat exchangers, the wave pattern has a clear impact on *f*, and flow depth has an important effect on the *j*-factor. Under wet conditions, folded wavy-fin heat exchangers with horizontal fins perform poorly, due to retained condensate.

Inclining heat exchangers in a horizontal test section increases the entrance/exit pressure drop. Under dry conditions, a 27 deg inclination had an insignificant impact on the performance of louver-fin heat exchangers. Inclined wavy-fin heat exchangers had higher friction factors especially at high Reynolds numbers. Under wet conditions, core inclination improved condensate drainage for both louver and wavy-fin geometries. For louver-fin heat exchangers, both Colburn *j*- and *f*-factors were increased by core inclination. Inclined wavy-fin heat exchangers have reduced friction factors under wet conditions. For the heat exchangers in the present study, it was generally observed that the differences in thermal-hydraulic performance for the wet1 and wet2 conditions were very small.

In addition to providing novel data for the wet-surface behavior of louver- and wavy-fin heat exchangers, new empirical correlations for the *j*-factor and *f*-factor for flat-tube, louver-fin heat exchangers under wet conditions have been developed. Using the new data from this study and data available in literature, a total of 47 geometrical variants contributed to 362 measurements used to develop curve-fits, both in terms of wet-surface multipliers and stand-alone *j* and *f* correlations. Statistical methods were used to assess the significance and redundancy of the regression constants. The proposed correlations show reasonable agreement with the experimental data. Further improvement of the correlations requires more accurate experimental data spanning a larger parameter space.

Acknowledgment

This work was financially supported by the U.S. Department of Energy and the Air-Conditioning and Refrigeration Technology Institute (ARTI) under the 21-CR program.

Nomenclature

A_{air} = total air-side heat transfer surface area
A_c = minimum cross-sectional area for air flow
A_f = air-side heat transfer area due to fins
A_{fr} = frontal area of the heat exchanger
b = slope of saturated enthalpy line (see Eq. (15))
C = heat capacity rate, $C=\dot{m}c_p$
c_p = specific heat
D_{AB} = binary mass diffusivity
D_h = air-side hydraulic diameter, $D_h=4A_cF_d/A_{air}$

f = Fanning friction factor from data (see Eqs. (11*b*) and (20))
F_d = air-side flow depth, or fin width (see Fig. 1)
F_l = fin length (see Fig. 1)
F_p = fin spacing (see Fig. 1)
G_c = air mass flux at minimum cross-sectional area
h = heat transfer coefficient
i = enthalpy of saturated moist air
j = Colburn j-factor (see Eq. (11*a*))
K_c = entrance pressure-loss coefficient
K_e = exit pressure-loss coefficient
L_l = louver length (see Fig. 1)
L_p = louver spacing (sometimes called louver spacing) (see Fig. 1)
Le = Lewis number, $\mathrm{Le}=\alpha/D_{AB}$
$\dot{m}$ = mass flow rate
N_{LB} = number of louver banks
ΔP = air-side pressure drop across heat exchanger
P_f = fin perimeter
Pr = Prandtl number
Q = heat transfer rate to heat exchanger
Re_{Dh} = Reynolds number based on hydraulic diameter
Re_{Lp} = Reynolds number based on louver spacing
$\mathrm{rms}_{\mathrm{rel}}$ = root-mean-squared relative residuals (see Eq. (22))
T = temperature
T_p = tube spacing (see Fig. 1)

Greek Symbols

α = louver angle (see Fig. 1) or thermal diffusivity
δ_f = fin thickness
η = fin efficiency
η_o = overall surface efficiency
θ_A, θ_R = advancing, receding contact angles
ρ = density
σ = area contraction ratio, $\sigma=A_c/A_{\mathrm{fr}}$
ϕ_j, ϕ_f = wet-surface multipliers for Colburn j- and f-factors (see Eq. (19))

Subscripts

0 = dry surface
1 = inlet
2 = outlet
air = air-side
b = fin base
c = cross sectional
cool = coolant
dew = corresponding to the dew point
f = fin
m = mean
s = saturation
t = fin tip
tube = tube
w = wet-surface condition

References

[1] Davenport, C. J., 1983, "Correlations for Heat Transfer and Flow Friction Characteristics of Louvered Fin," AIChE Symp. Ser., **225**, pp. 19–27.
[2] Cowell, T. A., Heikal, M. R., and Achaichia, A., 1995, "Flow and Heat Transfer in Compact Louvered Fin Surfaces," Exp. Therm. Fluid Sci., **10**(2), pp. 192–199.
[3] Achaichia, A., and Cowell, T. A., 1988, "Heat Transfer and Pressure Drop Characteristics of Flat Tube and Louvered Plate Fin Surfaces," Exp. Therm. Fluid Sci., **1**(2), pp. 147–157.
[4] Webb, R. L., and Jung, S. H., 1992, "Air-Side Performance of Enhanced Brazed Aluminum Heat Exchangers," ASHRAE Trans., **98**, pp. 391–401.
[5] Rugh, J. P., Pearson, J. T., and Ramadhyani, S., 1992, "A Study of a Very Compact Heat Exchanger Used for Passenger Compartment Heating in Automobiles," ASME, New York, **HTD-201**, pp. 15–24.
[6] Kim, M. H., and Bullard, C. W., 2002, "Air-Side Thermal Hydraulic Performance of Multi-Louvered Fin Aluminum Heat Exchangers," Int. J. Refrig., **25**(3), pp. 390–400.
[7] Kim, J. H., Yun, J. H., and Lee, C. S., 2004, "Heat-Transfer and Friction Characteristics for the Louver-Fin Heat Exchanger," J. Thermophys. Heat Transfer, **18**(1), pp. 58–64.
[8] Achaichia, A., and Cowell, T. A., 1988, "A Finite Difference Analysis of Fully Developed Periodic Laminar Flow in Inclined Louver Arrays," *Proceedings of the Second UK National Conference on Heat Transfer*, Vol. 1, pp. 883–892.
[9] Webb, R. L., and Trauger, P., 1991, "Flow Structure in the Louvered Fin Heat Exchanger Geometry," Exp. Therm. Fluid Sci., **4**(2), pp. 205–217.
[10] Cui, J., and Tafti, D. K., 2002, "Computations of Flow and Heat Transfer in a Three-Dimensional Multilouvered Fin Geometry," Int. J. Heat Mass Transfer, **45**(25), pp. 5007–5023.
[11] Suga, K., and Aoki, H., 1991, "Numerical Study on Heat Transfer and Pressure Drop in Multilouvered Fins," *Proceedings of the ASME/JSME Thermal Engineering Joint Conference*, ASME, New York, pp. 361–368.
[12] Goodremote, C. E., and Hartfield, J. P., 1985, "The Effect of a Hydrophilic Surface on the Performance of a Serpentine Automotive Air Conditioning Evaporator," SAE Technical Paper Series 850036.
[13] Chiou, C. B., Wang, C. C., Chang, Y. J., and Lu, D. C., 1994, "Experimental Study of Heat Transfer and Flow Friction Characteristics of Automotive Evaporators," ASHRAE Trans., **100**(2), pp. 575–581.
[14] McQuiston, F. C., 1975, "Fin Efficiency With Combined Heat and Mass Transfer," ASHRAE Trans., **81**, pp. 350–355.
[15] Wu, G., and Bong, T. Y., 1994, "Overall Efficiency of a Straight Fin With Combined Heat and Mass Transfer," ASHRAE Trans., **100**(1), pp. 367–373.
[16] McLaughlin, W. J., and Webb, R. L., 2000, "Wet Air Side Performance of Louver Fin Automotive Evaporators," SAE Technical Paper Series 2000-01-0574.
[17] Kaiser, J. M., and Jacobi, A. M., 2000, "Condensate Retention Effects on the Air-Side Heat Transfer Performance of Automotive Evaporator Coils," ACRC, University of Illinois, Report No. CR-32.
[18] Tang, A. D., and Jacobi, A. M., 2001, "Air-Side Heat Transfer With Highly Interrupted Surfaces: An Experimental Study of Condensate Retention Effects," ACRC, University of Illinois, Report No. TR-185.
[19] Kim, M. H., and Bullard, C. W., 2002, "Air-Side Performance of Brazed Aluminum Heat Exchangers Under Dehumidifying Conditions," Int. J. Refrig., **25**(7), pp. 924–934.
[20] Park, Y., and Jacobi, A. M., 2009, "Air-Side Heat Transfer and Friction Correlations for Flat-Tube, Louver-Fin Heat Exchangers," ASME J. Heat Transfer, **131**(2), p. 021801.
[21] Shah, R. K., Aung, W., and Kakac, S., 1987, *Handbook of Single-Phase Convective Heat Transfer*, Wiley, New York.
[22] Rush, T. A., Newell, T. A., and Jacobi, A. M., 1999, "Experimental Study of Flow and Heat Transfer in Sinusoidal Wavy Passages," Int. J. Heat Mass Transfer, **42**(9), pp. 1541–1553.
[23] Zhang, J., Kundu, J., and Manglik, R. M., 2004, "Effect of Fin Waviness and Spacing on the Lateral Vortex Structure and Laminar Heat Transfer in Wavy-Plate-Fin Cores," Int. J. Heat Mass Transfer, **47**(8–9), pp. 1719–1730.
[24] Dong, J., Chen, J., Chen, Z., Zhou, Y., and Zhang, W., 2007, "Heat Transfer and Pressure Drop Correlations for the Wavy Fin and Flat Tube Heat Exchangers," Appl. Therm. Eng., **27**(11–12), pp. 2066–2073.
[25] Park, Y., 2007, "Predicting the Air-Side Thermal-Hydraulic Performance Characteristics of Flat-Tube Louver-Fin Heat Exchangers Under Dry and Wet Conditions," Ph.D. thesis, University of Illinois, Urbana, IL.
[26] Incropera, F. P., and DeWitt, D. P., 1996, *Fundamentals of Heat and Mass Transfer*, 4th ed., Wiley, New York.
[27] Shah, R. K., and London, A. L., 1978, *Laminar Flow Forced Convection in Ducts: A Source Book for Compact Heat Exchanger Analytical Data*, Academic, New York.
[28] Threlkeld, J. L., 1970, *Thermal Environmental Engineering*, 2nd ed., Prentice-Hall, Englewood Cliffs, NJ.
[29] Taylor, B. N., and Kuyatt, C. E., 1994, "Guidelines for Evaluating and Expressing the Uncertainty of NIST Measurement Results," National Institute of Standards and Technology Technical Note 1297.
[30] Chang, Y.-J., Hsu, K.-C., Lin, Y.-T., and Wang, C.-C., 2000, "A Generalized Friction Correlation for Louver Fin Geometry," Int. J. Heat Mass Transfer, **43**(12), pp. 2237–2243.
[31] Chang, Y.-J., and Wang, C.-C., 1997, "A Generalized Heat Transfer Correlation for Louver Fin Geometry," Int. J. Heat Mass Transfer, **40**(3), pp. 533–544.
[32] Kim, M.-H., Song, S., and Bullard, C. W., 2002, "Effect of Inlet Humidity Condition on the Air-Side Performance of an Inclined Brazed Aluminum Evaporator," Int. J. Refrig., **25**(5), pp. 611–620.
[33] Kays, W. M., and London, A. L., 1984, *Compact Heat Exchangers*, 3rd ed., McGraw-Hill, New York.
[34] Draper, N. R., and Smith, H., 1998, *Applied Regression Analysis*, 3rd ed., Wiley, New York.

Experimental Study and Genetic-Algorithm-Based Correlation on Pressure Drop and Heat Transfer Performances of a Cross-Corrugated Primary Surface Heat Exchanger

Qiu-Wang Wang[1]
e-mail: wangqw@mail.xjtu.edu.cn

Dong-Jie Zhang

Gong-Nan Xie

State Key Laboratory of Multiphase Flow in Power Engineering,
Xi'an Jiaotong University,
Xi'an, Shaanxi 710049, China

Heat transfer and pressure drop characteristics of a cross-corrugated (CC) primary surface heat exchanger with different CC passages ($P/H=2$, $\theta=60$ and 120 deg, called CC2-60 and CC2-120, respectively) in two air sides have been experimentally investigated in this study. It is shown that the corrugation angle (θ) and the ratio of the wavelength P to height H (P/H) are the two key parameters of CC passages to influence the heat transfer and flow friction performances. The heat transfer and friction factor correlations for these two configurations are also obtained with Reynolds numbers ranging from $Re=450-5500$(CC2-60) and $Re=570-6700$(CC2-120). At a certain P/H, the Nusselt number, Nu, and the friction factor, f, are affected by the corrugation angle, θ. The heat transfer performance of CC2-120 are much better than that of CC2-60 while the pressure drop of the former is higher than that of the latter, especially at high Reynolds numbers region. The critical Reynolds numbers at which the flow mode transits from laminar to turbulent in the two different passages are also estimated. Furthermore, in this study a genetic algorithm (GA) has been used to determine the coefficients of heat transfer correlations by separation of total heat transfer coefficient without any information of measured wall temperatures. It is concluded that the GA-based separated heat transfer Nusselt number provides a good agreement with the experimental data; the averaged relative deviation by GA (1.95%) is lower than that by regression analysis (2.84%). The inversely yielding wall temperatures agree well with the measured data in turn supporting the reliability of experimental system and measurements. It is recommended that GA techniques can be used to handle more complicated problems and to obtain both-side heat transfer correlations simultaneously, where the conventional Wilson-plot method cannot be applied. [DOI: 10.1115/1.3090716]

Keywords: heat transfer and friction factor, cross-corrugated primary surface, genetic algorithm, separated correlation, wall temperature

1 Introduction

As a kind of equipment of energy transfer, compact heat exchangers are widely used in many industrial fields. Their researches and developments are of great significance for energy utilization and conservation. The cross-corrugated primary surface (CCPS) heat exchanger is one of such promising equipment. The CCPS is developed from the CC duct, which is also called the herring bone pattern, and has been traditionally classified as a plate type heat transfer surfaces. At first, it has been used in the process industry with large hydraulic diameter. In the late of 1970s, the heat transfer tests of small hydraulic diameters (from 1.24 mm to 0.6 mm) CCPS were carried out for different applications but not commercialized [1]. Until in the recent years, McDonald [2] re-evaluated the CCPS for possible application in microturbine recuperator with which the electricity efficiency of a microturbine system may be improved up to 30%. The CCPS is probably one of the best surfaces for primary surface recuperators [3–5], whose higher compactness, lower pressure drop, and easier fabrication make it potential to give a smallest volume and weight. Also with these characteristics, the CCPS may be adopted as the heat exchanger in fresh-air ventilators. The volume is only 40% percent of the traditional plate-and-fin heat exchanger when cooling the same flow rate of fresh air, as well as less pressure drop [6,7].

Many efforts have been made to reveal the flow and heat transfer performances of CC geometry [8–21]. For example, Focke et al. [8] claimed that the inclination angle between the plate corrugations and the overall flow direction is a major parameter to decide the thermohydraulic performance of the herringbone type plate heat exchangers and demonstrated the flow patterns inside the passages of different corrugation inclination angles with the flow visualization technique. Slasiek et al. [9,10] reported an experimental and numerical study of flow and heat transfer in various cross-corrugated geometries. The local Nu distribution over the surface and the average Nu were given by the method of applying thermochromic liquid crystals and true-color image processing. Mehrabian et al. [16], and Corce and Agaro [18] simpli-

[1]Corresponding author.

Contributed by the Heat Transfer Division of ASME for publication in the JOURNAL OF HEAT TRANSFER. Manuscript received May 6, 2008; final manuscript received October 23, 2008; published online March 31, 2009. Review conducted by Gautam Biswas.

fied the CC plate into a single periodic element and numerically investigated the thermal performance and the frictional pressure losses of the CC plate at different Re, different corrugated inclination angle, and different ratio of the wavelength P to height H (P/H). However, the existing experimental studies were mostly contributed to flow and heat transfer characteristics of single passage, which is usually maintained a constant wall temperature. Very few reports of the performance investigation of both-side CCPS passages when two airs at different temperatures flow into each side were found yet. In fact, the flow pattern and boundary conditions in such situations are more close to those inside a heat exchanger. It is quite useful if we can obtain the heat transfer coefficients for both sides directly without measuring the wall temperatures. This is the main motivation of carrying out this work.

On the other hand, a common practice for engineering applications or further researches is to compress the experimental data into one or more compact correlations related to heat transfer or friction factor, e.g., $\mathrm{Nu}=c\,\mathrm{Re}^m\,\mathrm{Pr}^n$. The most conventional way of correlating data in the field of heat transfer is using the regression analysis (RA) technique. However, the recent studies showed that the predicted data through correlations obtained by RA are not so good to describe the experimental data than that obtained by computational intelligence techniques such as genetic algorithms (GAs) or artificial neural networks (ANNs) [22–25]. In recent years, application of GAs in thermal engineering has received much attention for solving real-world problems [26–28]. For example, the plate-fin heat exchangers were optimized by means of GA [26]; the idea of applying GA into thermal design process has been proposed for fin-and-tube heat exchangers design by Xie et al. [27,28]. Optimizations of the geometries of the cross-wavy and cross-corrugated primary surface recuperators were studied via a GA by Wang et al. [29]. Other applications in estimating the radiative properties and the surface emissivities [30] and in modeling phonon-phonon normal and Umklapp scattering processes [31] were presented. These reports suggested that GAs have a strong ability of evolutional search and combinational optimization, and GAs can successfully optimize and predict thermal problems. Cai et al. [32] described a methodology that uses symbolic regression to extract correlations from heat transfer measurements by searching for both the form of the correlation equation and the constants in it that enable the closest fit to experimental data. The advantage of using this technique is that no initial assumption on the form of the correlation is needed. The procedure is tested using two sets of published experimental data, one for a compact heat exchanger and the other for liquid flow in a circular pipe.

Returning to the present work, it is generally recognized that when determining the heat transfer Nusselt number, the wall temperature of CCPS plate should be measured before data reduction. Alternatively, due to the difficulty of installing thermocouples on the wall surfaces under special conditions, researchers in laboratories usually adopt the Wilson-plot technique to separate heat transfer coefficient indirectly. However, usually this separation method should satisfy two basic requirements; that is, the thermal resistant of one side should be kept constant and the exponent of Reynolds number in correlation is fixed. Actually in practical situations, keeping the constant heat transfer of one side will involve in many difficulties of experiments, and in most cases the exponential relation of heat transfer versus flow rate (that is, Nu versus Re) is not specific surely before conducting experiments. Based on this point, in the present study, an attempt is devoted to use a genetic algorithm to separate heat transfer coefficients of both hot and cold sides in the CCPS heat exchanger.

The purpose of the present paper is to experimentally study the heat transfer and flow performance of the CCPS heat exchanger with different CC passages ($P/H=2$, $\theta=60$ and 120 deg, hereafter we call CC2-60 and CC2-120, respectively), and to establish the heat transfer and friction factor correlations for these two configurations in a wide range of Reynolds numbers (from laminar to turbulent flow). Furthermore, a genetic algorithm is employed to obtain the new correlations by separating heat transfer coefficients in the total heat transfer equation.

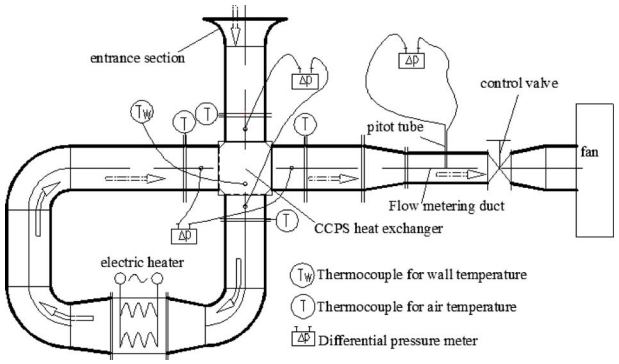

Fig. 1 Sketch of experimental system

2 Experimental Method

2.1 Experimental System. The experiments are conducted in an open wind tunnel, as schematically shown in Fig. 1. The cold air is absorbed from the entrance section and flows across the cold air side of the CCPS heat exchanger, then flows into the electric heater to be heated, and at last flows across the hot air side of the CCPS heat exchanger to exchange heat with the cold air through the thin CCPS plates.

On the inlet and outlet sections of the CCPS heat exchanger, thermocouples and pressure meters are mounted to measure the temperatures and pressure drops of the two sides. Also some thermocouples are welded on the surface of the plate to measure the wall temperature. The air velocity is measured by a Pitot tube, which is located in the flow metering duct far downstream of the CCPS heat exchanger. The Pitot tube is connected to the differential pressure meter. All the output signals of the above measurement apparatus are collected by a digital collector, which is connected with the computer.

During the test, the air flow rate can be changed by adjusting the control valve, and the power of the electric heater is correspondingly changed to maintain the inlet hot air temperature at 50°C or so. Before recording the data in the experiments, much attention is paid on the heat balance to ensure the steady state of heat exchange. In the data-acquisition procedure, each measured value is read 20 times in 1 min, and the arithmetic mean of the recorded data is used for checking the heat balance between the energy gain of cold air and the energy reduction in the hot air. In all tests, the heat balance between the two air sides is within 5%.

2.2 CCPS Heat Exchanger and Performance Parameters. The dimension of the CCPS heat exchanger is 260 mm(length) $\times$ 260 mm(width) $\times$ 320 mm(height). Figure 2 shows the exploded view of the CCPS heat exchanger. The CCPS plate is fabricated by 0.2 mm thick aluminum foil and is pressed with two different corrugations (plate-1 and plate-3 are the same but different with plate-2 and plate-4). The exchanger consists of plurality of CCPS plates, and plates with different corrugations are adjacent. As shown in Fig. 2, a pair of spacerbar-1 are inserted between plate-1 and plate-2, and welded with the adjacent plates inside, which is the hot air passage. A pair of spacerbar-2 is inserted between plate-2 and plate-3, and welded with the adjacent plates inside, which is the cold air passage. Thus the cold air and the hot air are in cross flow.

The geometry of the CCPS plate is shown in Fig. 3. P is the wavelength P, H is the corrugation height, and θ is the corrugation angle. Usually the ratio P/H and the corrugation θ are the two key parameters of CC passages to affect the heat transfer and flow performances. The dimensions of the tested heat exchanger

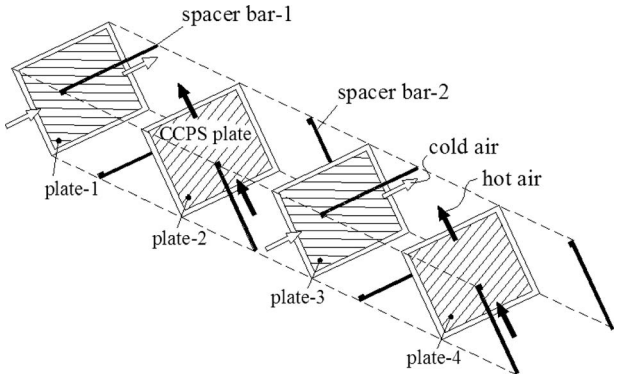

Fig. 2 Exploded view of CCPS heat exchanger

are as follows: $P=11$ mm, $H=5.5$ mm, $P/H=2$, the corrugation angle of hot air side is $\theta=60$ deg, and the corrugation angle of the cold air side is $\theta=120$ deg. The performance parameters of the heat exchanger are defined as below: If G (kg/s) is the mass flow rate crossing one wave, the mean velocity can be defined as

$$u = \frac{G}{\rho A_c} \tag{1}$$

where ρ is the density of air, kg/m^3; A_c is the flow cross section area, which is related to the corrugation angle, m^2:

$$A_c = 2PH \sin(\theta/2)/\sin\theta \tag{2}$$

The hydraulic diameter d_e, not like the common definition, is related to the corrugation angle:

$$d_e = \frac{4A_c}{C} \tag{3}$$

where C is the wetted perimeter of the cross section normal to the flow stream, which is also related to the corrugation angle, m:

$$C = 4\sqrt{H^2 + (P/2)^2/\cos^2(\theta/2)} \tag{4}$$

The hydraulic diameters in two sides are 8.2 mm for CC2-60 and 9.7 mm for CC2-120, respectively, while they are both 4.4 mm in common definition.

The Reynolds number can be based on the mean velocity and the hydraulic diameter:

$$\mathrm{Re} = \frac{u d_e}{\nu} \tag{5}$$

where ν is the kinematic viscosity of air, m/s^2.

2.3 Uncertainty Analysis. The uncertainty analysis was studied carefully with the method presented in Ref. [33]. Generally the uncertainty of the experimental measurements W is calculated based on the combination of the bias error limit B and precision error limit P,

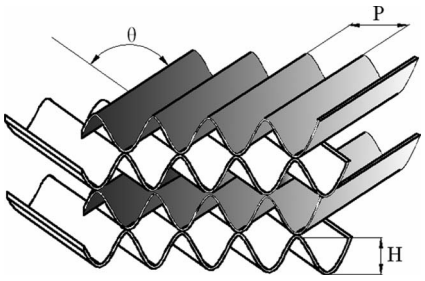

Fig. 3 Sketch of CCPS plate

Table 1 Summary of uncertainty analysis

Parameters	Uncertainties
G	1.27%
Q_1	4.05%
Q_2	4.69%
Re	2.38%
Nu_1	6.21%
Nu_2	5.22%
f_1	6.00%
f_2	5.61%

$$W = \sqrt{B^2 + P^2} \tag{6}$$

Since the data of the air temperature and the pressure are all collected with a digital collector and the number collection samples are over 30, the precision error limit for the measured parameters P is very small compared with the bias error limit B. Therefore, the uncertainty of the experimental measurements, W, is dominated by the bias error limit, B. The accuracy of the measurement system supplied by the manufacturer is used to calculate the bias error limit.

Given a variable R, which is a function of n independent variables $x_1, x_2 \ldots, x_n$,

$$R = f(x_1, x_2 \ldots, x_n) \tag{7}$$

The absolute uncertainty of R can be determined as

$$W_R = \sqrt{\left(\frac{\partial R}{\partial x_1} W_{x_1}\right)^2 + \left(\frac{\partial R}{\partial x_2} W_{x_2}\right)^2 + \cdots + \left(\frac{\partial R}{\partial x_n} W_{x_n}\right)^2} \tag{8}$$

where $W_{x1}, W_{x2}, \ldots, W_{xn}$ are the absolute uncertainties of $x_1, x_2, \ldots, x_n$. The precision of the differential pressure meters is $\pm 1\%$, and that of the thermocouples is 0.4%. Data of a typical experimental case are used to calculate the uncertainty of the parameters, and the summary is shown in Table 1.

3 Data Reduction

3.1 Pressure Drop. The pressure drop can be dimensionless by defining the equivalent Fanning friction coefficients [34]:

$$\text{hot air side: } f_1 = \frac{|\Delta p_1| d_{e1}}{2L\rho_1 u_1^2}$$
$$\text{cold air side: } f_2 = \frac{|\Delta p_2| d_{e2}}{2L\rho_2 u_2^2} \tag{9}$$

where Δp_1 and Δp_2 are the pressure differences between the air inlet and outlet of the two sides, Pa. L is the length along the main flow direction, m.

3.2 Heat Transfer. The main purpose of the data reduction is to determine the Nusselt number, Nu, of the heat exchangers from the experimental data, including the temperatures of the air and the wall temperature of the CCPS plate, which are recorded at steady state conditions during each test run, and to find out the corresponding correlations of Nu versus Re for each case. The mean value of the inlet and outlet temperatures is used to evaluate the physical properties of the hot air or the cold air.

Based on the hot air temperature difference Δt_1 and the mass flow rate G, the hot air heat transfer rate is given as

$$Q_1 = c_p G \Delta t_1 \tag{10}$$

where c_p is the specific heat of the air, kJ/kg K, which could be a constant of 1.005 at the test temperature range 26–50°C. In similar manner, with the cold air temperature difference Δt_2 and the mass flow rate G, the cold air heat transfer rate is given as

$$Q_2 = c_p G \Delta t_2 \tag{11}$$

In all tests, the heat balance between the two sides, $|Q_1 - Q_2|/Q_m$, is within 5%. Q_m is the average heat transfer rate:

$$Q_m = (Q_1 + Q_2)/2 \tag{12}$$

Thus the mean Nusselt number can be defined as [34]

$$\text{hot air side: } \mathrm{Nu}_1 = \frac{Q_m d_{e1}}{\lambda_1 A_d (t_{f1} - t_w)}$$
$$\text{cold air side: } \mathrm{Nu}_2 = \frac{Q_m d_{e2}}{\lambda_2 A_d (t_w - t_{f2})} \tag{13}$$

where λ is the thermal conductivity of air, W/m K; A_d is the heat exchange area, m^2; t_{f1} and t_{f2} are the average temperatures of the hot air and the cold air, respectively; t_w is the wall temperature of the CCPS plate. The thermal resistance of the CCPS plate was ignored due to its thin thickness (0.2 mm) and high thermal conductivity coefficient (236 W/m K) (the material of plate is aluminum). It is recognized from Eq. (13) that if we want to obtain the heat transfer coefficients, the wall surface temperature should be measured for data reduction. In this paper, we measured wall temperatures at several different points inside the heat exchangers in order to obtain the Nusselt numbers at both sides according to Eq. (13). It was found that the mean wall temperature is almost constant in each case and keeps at the range of 37.4–39.1°C according to the slightly change in the air inlet temperature.

On the other hand, the wall temperature is usually hard or even impossible to obtain for most heat exchangers, especially when they are operated at high pressure and high temperature. So a new alternative effective method should be used to obtain heat transfer coefficients at both sides when there is no any information on wall temperature. The GA technique may be suitable among the available methods.

The GA is maintained by a population of parent individuals that represent the latent solutions of a real-world problem. Each individual is assigned a fitness based on how well each individual fits in a given environment, evaluated by survival of the fittest. Fit individuals go through the process of survival selection, crossover, and mutation, creating a next generation, called child individuals. A new population is therefore formed by selection of good individuals from parent and child individuals. After some generations, the algorithm is converged to the best individual, which possibly represents the best solution of the given problem. More details about the description of the genetic algorithm can be found in many classic books [35,36].

The conventional GA determines the global maximum value in search spaces; however, the objective of the present correlation and prediction is to make the deviation minimum between the predicted and the experimental results. Thus, when searching the coefficients, a fitness function is developed as described in the following procedure.

In the present experiments, it is obvious that the area of each side is identical because of the same plate at different angles, the total heat transfer coefficient equation can be written as

$$\frac{1}{k} = \frac{1}{h_1} + \frac{\delta}{\lambda} + \frac{1}{h_2} \tag{14}$$

Assume the heat transfer correlations as

$$\mathrm{Nu} = c\ \mathrm{Re}^m \tag{15}$$

So for each side there are similar forms of heat transfer coefficients:

$$\text{hot air side: } h_1 = c_1 \frac{\lambda_1}{d_{e1}} \mathrm{Re}_1^{m_1} \tag{16a}$$

$$\text{cold air side: } h_2 = c_2 \frac{\lambda_2}{d_{e2}} \mathrm{Re}_2^{m_2} \tag{16b}$$

Incorporating Eq. (16) into Eq. (14) yields

$$k = \left(\frac{d_{e1}}{c_1 \lambda_1\ \mathrm{Re}_1^{m_1}} + \frac{\delta}{\lambda} + \frac{d_{e2}}{c_2 \lambda_2\ \mathrm{Re}_2^{m_2}} \right)^{-1} \tag{17}$$

The thermal resistance of plate wall is really very small because of thin thickness and high thermal conductivity of the CC plates, and it may be neglected or kept as a constant. Because the thermal properties and geometry are known, there are four coefficients, c_1, c_2, m_1, and m_2, to be obtained. Fortunately, these four coefficients can be found by GA-based separation. After collecting n sets of experimental points, the fitness function now is defined as [35,36]

$$\text{fitness} = \frac{10}{\frac{1}{n}\sum_i^n 100 \left| \frac{k - k_i}{k_i} \right|} \tag{18}$$

where k_i can be directly reduced from the experimental data. It is noted from above fitness function that its value of being less than unity results in the averaged relative deviation of being less than 10%.

A binary string is adopted for encoding the variables of a given model. Four coefficients of correlations were assigned to vary between 0 and 1. Considering the ability of computers to handle bit operations and engineering applications, the computational precision is set to four decimals 0.0001. Thus, a coefficient needs a 7-character binary, and an individual coefficient of a model needs a 28-character binary.

In the present study, the tournament selection, uniform crossover, and one-point mutation were selected. Niching and elitism were adopted [37–39]. The size of the population and maximum evolution generation were set to 20 and 1000, respectively. The probabilities of crossover and mutation were set to 0.5 and 0.005, respectively. The selection of genetic parameters was a trial-and-error process, and with the variation in these parameters, the corresponding results were not exactly identical but were very close to each other. On the other hand, in this study the selection of genetic parameters and operators was based on the previous recommendations [37].

4 Results and Discussion

4.1 Pressure Drop. The Re dependence of f Re is described by a power-law function:

$$f\ \mathrm{Re} = c'\ \mathrm{Re}^n \tag{19}$$

f Re results are reported as a function of Reynolds number for $P/H = 2$ and two tested corrugation angles θ (60 deg and 120 deg), as shown in Fig. 4. The average deviations are 1.3% and 1.1%, respectively, and the Reynolds numbers are in the range of 450–5500 (for CC2-60) and 570–6700 (for CC2-120), respectively.

The pressure drop of CC2-120 passages is much higher than that of CC2-60. As shown in Figs. 5 and 6, the friction factor data for the two configurations are presented from Re = 450–5500(CC2-60) and Re = 570–6700(CC2-120). It can be found that there is a change in slope in each curve of f. For CC2-60 passage, the change occurs near Re = 948, and for CC2–120 passage it occurs near Re = 1284. They may be the critical Reynolds numbers, at which the flow mode transits from laminar to turbulent in these two configurations.

4.2 Heat Transfer. As mentioned above, Nu versus Re correlation, as shown in Eq. (15), can be obtained by two different methods: One is obtained by the RA method using Eq. (13) based on the experimental data, including the wall temperatures of the CCPS plates; the other one is based on GA technique, by which the two-side heat transfer coefficients can be obtained without the

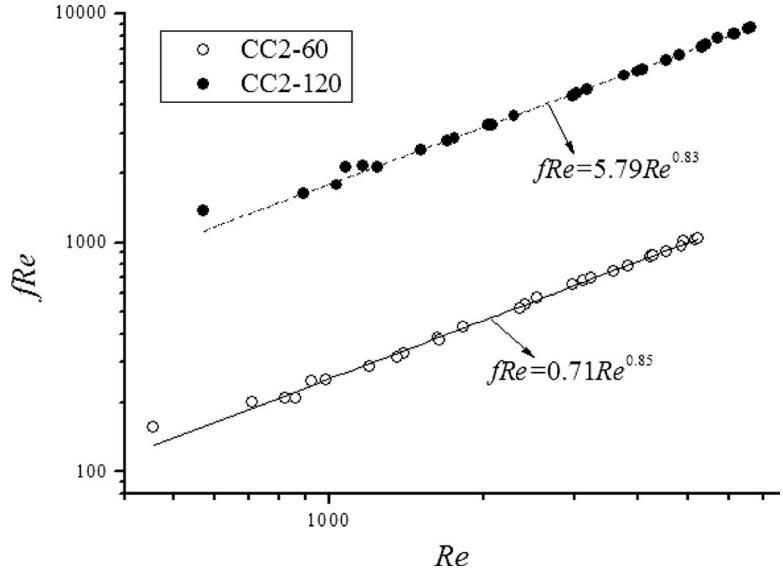

Fig. 4 *f* Re versus Re for two corrugation angles

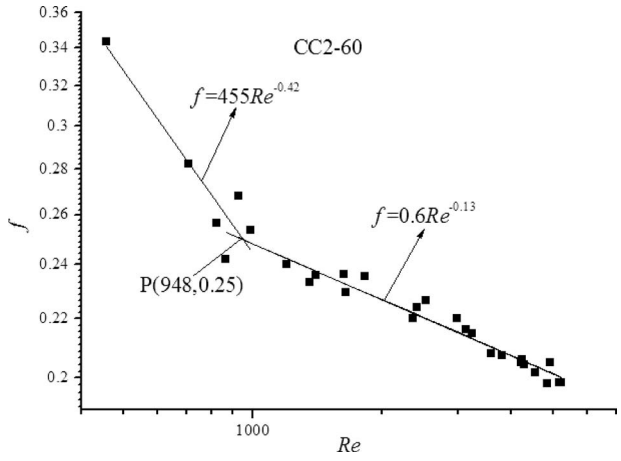

Fig. 5 *f* versus Re for corrugation angle θ=60 deg

information of wall temperature. The detailed process of GA method and the comparison between these two methods are shown as follows.

The evolution process for the fitness is shown in Fig. 7. At the beginning of evolution process (about less than 40 generations), the differences between every individual are relatively large, in turn leads to the individuals with low fitness being eliminated and individuals with higher fitness being saved. After certain generations (about larger than 100 generations), the variation in fitness for minimum deviation is small, finally approaching to a constant value.

The separated heat transfer Nusselt number for each side versus experimental data of the heat exchanger is shown in Fig. 8. In this figure, those data in *y*-coordinate refer to the results obtained by GA separation while those data in *x*-coordinate refer to the experimentally measured data. The middle straight line means that the GA results are similar to the experimental results. It can be seen that most of predicted results obtained by GA are much closer to the middle straight line, which means good agreements with the experimental data. The averaged relative deviations are 3.7% and 7.7%, respectively. On the other hand, the heat transfer rates de-

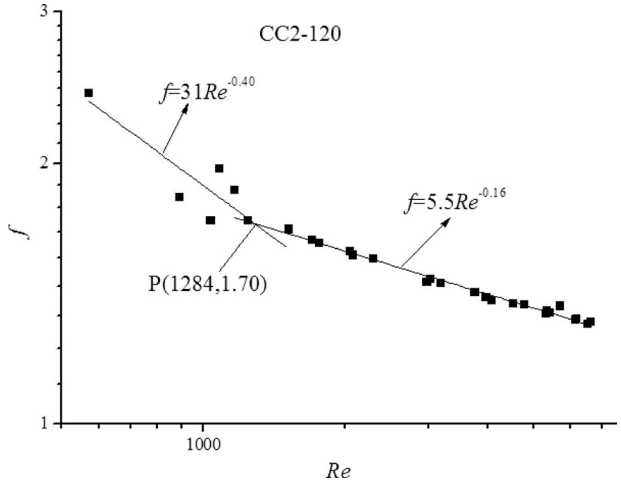

Fig. 6 *f* versus Re for corrugation angle θ=120 deg

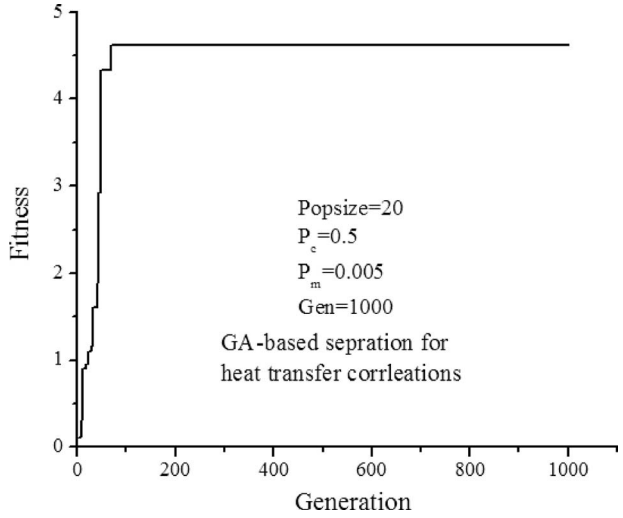

Fig. 7 Evolution process of maximizing fitness

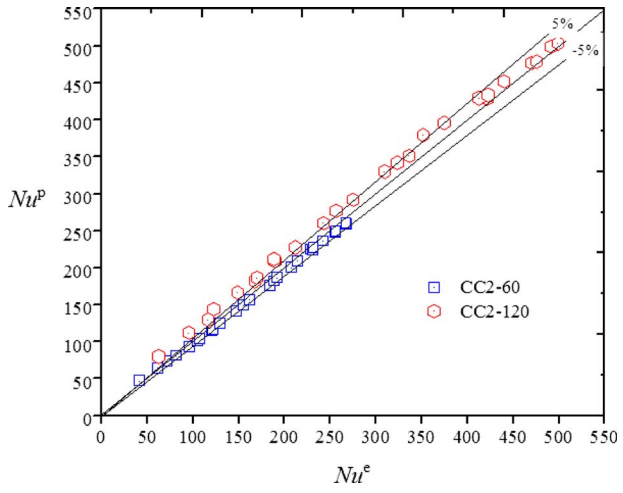

Fig. 8 Plot of separated Nusselt numbers against experimental data. (The variables in *x*-coordinate refer to the experimental measured data while the variables in *y*-coordinate stand for genetic algorithm separated data.)

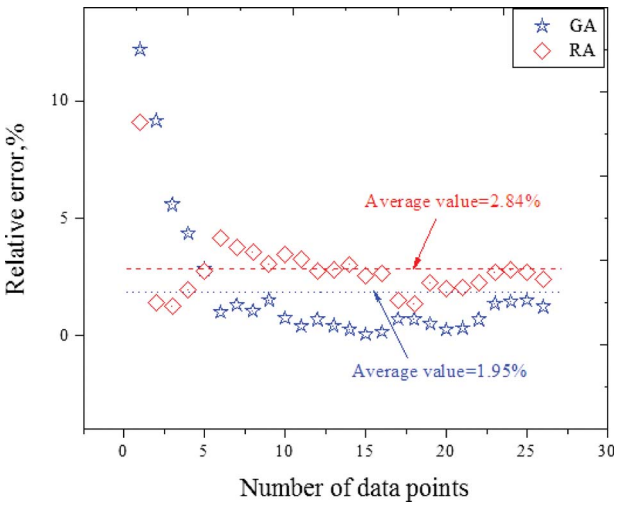

Fig. 10 Comparison of relative errors from genetic algorithm and regression analysis. (The relative error is produced from the deviation of the GA-separated or RA-obtained heat transfer rate and experimental heat transfer rate.)

termined from GA-based and RA-based two-side heat transfer coefficients are, respectively, plotted against experimental data, as shown in Fig. 9. By casual observation of this figure, it seems that both of heat transfer rates from RA based and GA based are close the experimental data; however, after careful examination of nearness of points to line, it is found that the points of GA based are closer to the line than those of RA based. In order to present such difference, the quantitative of comparison of relative deviations is shown in Fig. 10. It can be clearly seen that most of deviations from GA based are smaller than those from RA based, and their averaged deviations are 1.95% and 2.84%, respectively. Accordingly, the fact of the predicted results by GA being better than those by RA is revealed in the present study.

On the other hand, having obtained heat transfer coefficients of both sides by GA-based separation, the wall temperature can be inversely determined by the following relation:

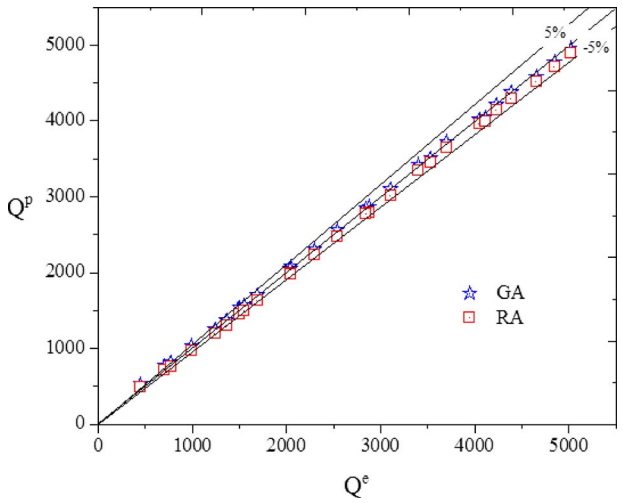

Fig. 9 Comparison of heat transfer rate from genetic algorithm and regression analysis. (The variables in *x*-coordinate refer to experimental measured heat transfer rate while the variables in *y*-coordinate stand for those data determined from heat transfer coefficients inserting total heat transfer coefficient equation, $Q=kA_d\Delta t_m$; "GA" means heat transfer coefficients are separated by genetic algorithm and "RA" means heat transfer coefficients are reduced from experimental data directly.)

$$t_w = \frac{h_1 t_{f1} + h_2 t_{f2}}{h_1 + h_2} \tag{20}$$

The comparison of wall temperatures and scatter plot of relative deviation is shown in Fig. 11. It is clearly shown that the wall temperatures by GA-based separation are close to experimentally measured data so well, and most of relative deviations between them are less than 1.5%. The good agreement between the separated wall temperature and measured data indicates that the experimental system and measurement are reliable enough.

So far the two-side heat transfer Nusselt number correlations based on GA separation can be then written as

$$\begin{aligned} \text{CC2-60:Nu}_1 &= 0.65\ \text{Re}_1^{0.7} \\ \text{CC2-120:Nu}_2 &= 0.69\ \text{Re}_2^{0.75} \end{aligned} \tag{21}$$

The average Nusselt number is reported for $P/H=2$ and two corrugation angles θ of 60 deg and 120 deg, as shown in Fig. 12. Generally better heat transfer is always at the cost of larger pressure drop. The experimental results proved this point. It can be seen from Fig. 12 that the heat transfer performance of CC2-120 passage is much better than that of CC2-60, and it becomes more

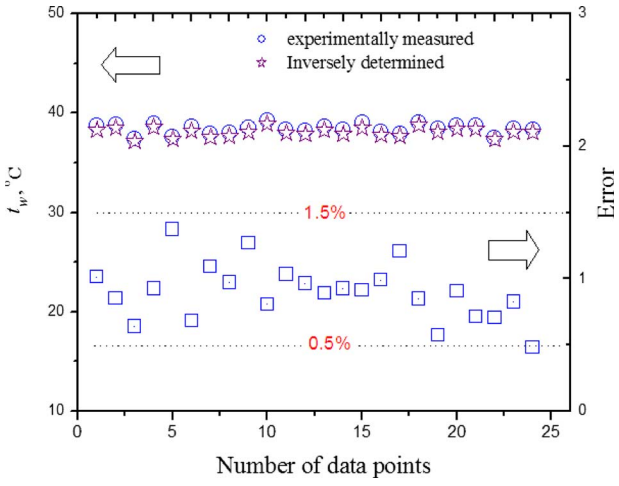

Fig. 11 Comparison wall temperature and its relative error

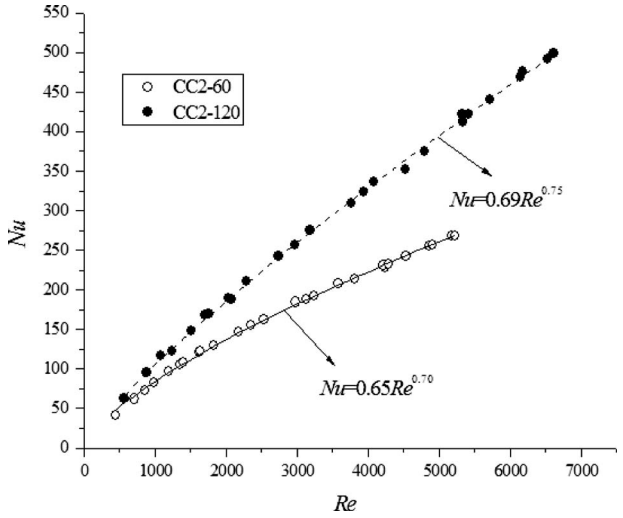

Fig. 12 Nu versus Re for two corrugation angles based on GA method

apparent with the increase in Reynolds number. Blomerius et al. [13] and Zhang [20,21] showed the numerical results inside the CC ducts and analyzed the flow phenomena in different Reynolds numbers. It was found that the major part of the flow followed the valleys of corrugations of upper and lower walls at an angle of 45 deg to the main flow direction while a minor part of the flow followed the main flow direction crossing the crests of the corrugations. And at the higher Reynolds number, an extensive vortex led to considerable mixing between these streams; interactions between the streams in the valleys led to stronger mixing of the flow. This can be used to explain our experimental results. The larger the corrugation angle, the stronger the mixing of the streams, and the better the heat transfer. Also the difference of the heat transfer performance between the CC2-60 and CC2-120 passages will increase with the increase in Reynolds number.

The current study indicates that genetic algorithm can reflect the real performance better and it has superiorities, such as searching and predicting. It is recommended that engineers use GAs to fit and predict the experimental results leading to further studies or engineering applications; what is more, GA might be employed to separate the heat transfer coefficient of both sides and predict the wall temperature instead of knowing the wall temperatures in advance. The present successful application of GA suggests a possible extension to other kinds of heat exchangers neglecting the thermal resistance of plate wall or not. As mentioned by Cai et al. [31], if we do not assume the specific form of heat transfer correlations for both sides, there should be a large number of correlation forms, and a penalty function to the usual fitness function may have to be added to prevent this from happening. We will try to use the method without initial assumption of the functional form for our further study.

5 Conclusions

This paper reports the experimental studies of heat transfer and flow performances for a CCPS heat exchanger with different CC passages ($P/H=2$, $\theta=60$ and 120 deg) in two air sides. The effects of two different corrugated angles and Reynolds number have been investigated. And the GA method is applied to obtain the two-side heat transfer correlations by separating coefficients in the total heat transfer equation. The main conclusions are summarized as follows.

(1) The performance of heat transfer and fluid flow is strongly dependent on the corrugation angle θ at the same ratio of the wavelength P to height H (P/H). Both the heat transfer and pressure drop will increase with the increase in corrugation angle. Nu and f of $\theta=120$ deg (CC2-120) are 49–86% higher and 5.5–6 times higher than those of $\theta=60$ deg (CC2-60), respectively.

(2) The correlations of heat transfer and flow performance are obtained at a wide range of Re (CC2-60: Re=450–5500, CC2–120: Re=570–6700), and there exist the critical Reynolds numbers from laminar to turbulent flow, especially for the flow transitions.

(3) The GA method has been used to separate the coefficients of heat transfer correlations in the hot and cold sides of the heat exchanger by separation of total heat transfer coefficient without experimentally knowing wall temperatures. The GA-based separated heat transfer Nusselt number, heat transfer rate, and the inversely yield wall temperatures provide a good close fit to experimental data than the RA based. This method provides a reliable way to obtain both-side heat transfer coefficient from the experimental data when the wall temperatures of a complex heat exchanger configuration cannot be easily measured during the test.

Acknowledgment

This work is supported by the National High Technology R&D Project of China (Grant No. 2007AA050501) and the National Natural Science Foundation of China (Grant No. 50776068).

Nomenclature

A_c = flow cross section area, m^2
A_d = heat exchange surface area, m^2
B = bias error limit
c, c' = coefficients of formulation, Eqs. (15) and (19)
c_1, c_2 = coefficients of formulation
c_p = specific heat at constant pressure, J/(kg K)
C = wetted perimeter of cross section normal to flow, m
d_e = hydraulic diameter, m
f_1 = Fanning friction coefficient for hot air side
f_2 = Fanning friction coefficient for cold air side
G = mass flow rate, kg/s
h_1 = heat transfer coefficient for hot air side, $W/(m^2 K)$
h_2 = heat transfer coefficient for cold air side, $W/(m^2 K)$
H = wave height, m
K = overall heat transfer coefficient, $W/(m^2 K)$
L = length along the main flow direction, m
m, n = coefficients of formulation, Eqs. (15) and (19)
n = sets of experimental points
Nu = Nusselt number
P = precision error limit; wavelength, m
Δp_1 = pressure drop of hot air side, Pa
Δp_2 = pressure drop of cold air side, Pa
Q_1 = heat transfer rate of hot air, W
Q_2 = heat transfer rate of cold air, W
Q_m = average heat transfer rate, W
Re = Reynolds number
t_{f1} = temperature of hot air, °C
t_{f2} = temperature of cold air, °C
t_w = temperature of plate wall, °C
Δt_1 = temperature difference of hot air, °C
Δt_2 = temperature difference of cold air, °C
Δt_m = logarithmic mean temperature difference, °C
u = air velocity, m/s
W = uncertainty of experimental measurements

Greek

ρ = air density, kg/m^3

λ = thermal conductivity, W/(m K)
δ = plate thickness, mm
ν = kinematic viscosity, m/s^2
θ = corrugation angle, deg

Subscripts

1 = hot air side
2 = cold air side

References

[1] Utriainen, E., and Sundén, B., 2001, "A Comparison of Some Heat Transfer Surfaces for Small Gas Turbine Recuperators," *Proceedings of the ASME Turbo Expo 2001*.

[2] McDonald, C. F., 2000, "Low-Cost Compact Primary Surface Recuperator Concept for Microturbines," Appl. Therm. Eng., **20**(5), pp. 471–497.

[3] Utriainen, E., and Sundén, B., 2002, "Evaluation of the Cross Corrugated and Some Other Candidate Heat Transfer Surfaces for Microturbine Recuperators," ASME J. Eng. Gas Turbines Power, **124**(3), pp. 550–560.

[4] Utriainen, E., and Sundén, B., 2000, "Recuperators and Regenerators in Gas Turbine Systems," *Heat Transfer in Gas Turbine Systems*, WIT, Southampton.

[5] Liang, H. X., Wang, Q. W., Peng, B. T., Luo, L. Q., and Feng, Z. P., 2004, "Comparison of Heat Transfer Surfaces for Microturbine Recuperators," J. Eng. Phys. Thermophys., **25**(4), pp. 688–690.

[6] Zhang, D. J., Zeng, M., Luo, L. Q., and Wang, Q. W., 2005, "Configuration and Thermal Design of a New Type Exchanger Used in Fresh Air Ventilator," *Proceedings of the Second Proseminar of Heat Transfer Technology*, pp. 112–115, in Chinese.

[7] Wang, Q. W., Zhang, D. J., Zeng, M., Luo, L. Q., and Wu, Y. N., 2005, "A New Type Primary Surface Heat Exchanger Used in Fresh Air Ventilator," Chinese Patent No. ZL200510042697.X.

[8] Focke, W. W., Zachariades, J., and Olivier, I., 1985, "The Effect of the Corrugation Inclination Angle on the Thermohydraulic Performance of Plate Heat Exchangers," Int. J. Heat Mass Transfer, **28**(8), pp. 1469–1479.

[9] Stasiek, J., Collins, M. W., and Ciofalo, M., 1996, "Investigation of Flow and Heat Transfer in Corrugated Passages—I. Experimental Results," Int. J. Heat Mass Transfer, **39**(1), pp. 149–164.

[10] Ciofalo, M., Stasiek, J., and Collins, M. W., 1996, "Investigation of Flow and Heat Transfer in Corrugated Passages—II. Numerical Simulations," Int. J. Heat Mass Transfer, **39**(1), pp. 165–192.

[11] Muley, A., and Manglik, R. M., 1997, "Enhanced Heat Transfer Characteristics of Single-Phase Flows in a Plate Heat Transfer With Mixed Chevron Plates," J. Enhanced Heat Transfer, **l4**, pp. 187–201.

[12] Muley, A., and Manglik, R. M., 1999, "Experimental Study of Turbulent Flow Heat Transfer and Pressure Drop in a Plate Heat Exchanger With Chevron Plates," ASME J. Heat Transfer, **121**(1), pp. 110–117.

[13] Sawyers, D. R., Sen, M., and Chang, H. C., 1998, "Heat Transfer Enhancement in Three-Dimensional Corrugated Channel Flow," Int. J. Heat Mass Transfer, **41**, pp. 3559–3573.

[14] Blomerius, H., Höisken, C., and Mitra, N. K., 1999, "Numerical Investigation of Flow Field and Heat Transfer in Cross-Corrugated Ducts," ASME J. Heat Transfer, **121**(2), pp. 314–321.

[15] Mehrabian, M. A., Poulter, R., and Quarini, G. L., 2000, "Hydrodynamic and Thermal Characteristics of Corrugated Channels: Experimental Approach," Exp. Heat Transfer, **13**, pp. 223–234.

[16] Mehrabian, M., and Poulter, R., 2000, "Hydrodynamics and Thermal Characteristics of Corrugated Channels: Computational Approach," Appl. Math. Model., **24**(5–6), pp. 343–364.

[17] Zimmerer, C., Gschwind, P., Gaiser, G., and Kottke, V., 2002, "Comparison of Heat and Mass Transfer in Different Heat Exchanger Geometries With Corrugated Walls," Exp. Therm. Fluid Sci., **26**, pp. 269–273.

[18] Croce, G., and Agaro, P., 2002, "Numerical Analysis of Forced Convection in Plate and Frame Heat Exchangers," Int. J. Numer. Methods Heat Fluid Flow, **12**(6), pp. 756–771.

[19] Metwally, H. M., and Manglik, R. M., 2004, "Enhanced Heat Transfer Due to Curvature-Induced Lateral Vortices in Laminar Flows in Sinusoidal Corrugated-Plate Channels," Int. J. Heat Mass Transfer, **47**(10–11), pp. 2283–2292.

[20] Zhang, L. Z., 2005, "Numerical Study of Periodically Fully Developed Flow and Heat Transfer in Cross-Corrugated Triangular Channels in Transitional Flow Regime," Numer. Heat Transfer, Part A, **48**(4), pp. 387–405.

[21] Zhang, L. Z., 2005, "Convective Mass Transport in Cross-Corrugated Membrane Exchangers," J. Membr. Sci., **260**, pp. 75–83.

[22] Pacheco-Vega, A., Diaz, G., Sen, M., Yang, K. T., and McClain, R. T., 2001, "Heat Rate Predictions in Humid Air-Water Heat Exchangers Using Correlations and Neural Networks," ASME J. Heat Transfer, **123**, pp. 348–354.

[23] Pacheco-Vega, A., Sen, M., and Yang, K. T., 2003, "Simultaneous Determination of In-and-Over-Tube Heat Transfer Correlations in Heat Exchangers by Global Regression," Int. J. Heat Mass Transfer, **46**, pp. 1029–1040.

[24] Wang, Q. W., Xie, G. N., Peng, B. T., and Zeng, M., 2007, "Experimental Study and Genetic-Algorithm-Based Correlation on Shell-Side Heat Transfer and Flow Performance of Three Different Types of Shell-and-Tube Heat Exchangers," ASME J. Heat Transfer, **129**, pp. 1277–1285.

[25] Xie, G. N., Wang, Q. W., Zeng, M., and Luo, L. Q., 2007, "Heat Transfer Analysis for Shell-and-Tube Heat Exchangers With Experimental Data by Artificial Neural Networks Approach," Appl. Therm. Eng., **27**, pp. 1096–1104.

[26] Xie, G. N., Sunden, B., and Wang, Q. W., 2008, "Optimization of Compact Heat Exchangers by a Genetic Algorithm," Appl. Therm. Eng., **28**, pp. 895–906.

[27] Xie, G. N., Wang, Q. W., and Sunden, B., 2008, "Application of a Genetic Algorithm for Thermal Design of Fin-and-Tube Heat Exchangers," Heat Transfer Eng., **29**(7), pp. 597–607.

[28] Xie, G. N., Wang, Q. W., and Zeng, M., 2007, "Genetic Algorithm Based Design and Optimization of Outer-Fins and Inner-Fins Tube Heat Exchangers," ASME Paper No. GT 2007-27889.

[29] Wang, Q. W., Liang, H. X., Xie, G. N., Luo, L. Q., and Feng, Z. P., 2007, "Genetic Algorithm Optimization for Primary Surfaces Recuperator of Microturbine," ASME J. Eng. Gas Turbines Power, **129**, pp. 436–442.

[30] Deiveegan, M., Balaji, C., and Venkateshan, S. P., 2006, "Comparison of Various Methods for Simultaneous Retrieval of Surface Emissivities and Gas Properties in Gray Participating Media," ASME J. Heat Transfer, **128**, pp. 829–837.

[31] Cai, W., Pacheco-Vega, A., Sen, M., and Yang, K. T., 2006, "Heat Transfer Correlations by Symbolic Regression," Int. J. Heat Mass Transfer, **49**, pp. 4352–4359.

[32] Chen, Y. F., Li, D. Y., Lukes, J. R., and Majumdar, A., 2005, "Monte Carlo Simulation of Silicon Nanowire Thermal Conductivity," ASME J. Heat Transfer, **127**, pp. 1129–1137.

[33] Wheeler, A. J., and Ganji, A. R., 2004, *Introduction to Engineering*, 2nd ed., Prentice-Hall, Englewood Cliffs, NJ.

[34] Yang, S. M., and Tao, W. Q., 2000, *Heat Transfer*, 3rd ed., Higher Education, Beijing.

[35] Goldberg, D. E., 1989, *Genetic Algorithms in Search, Optimization and Machine Learning*, Addison-Wesley, Reading, MA.

[36] Michalewicz, Z., and Fogel, D. B., 2000, *How to Solve It: Modern Heuristics*, Springer, New York.

[37] Carroll, D. L., 1996, "Chemical Laser Modeling With Genetic Algorithms," AIAA J., **34**, pp. 338–346.

[38] Carroll, D. L., 1996, "Genetic Algorithms and Optimizing Chemical Oxygen-Iodine Lasers," *Developments in Theoretical and Applied Mechanics*, Vol. XVIII, H. Wilson, R. Batra, C. Bert, A. Davis, B. Schapery, B. Stewart, and F. Swinson, eds., School of Engineering, The University of Alabama, Tuscaloosa, AL, pp. 411–424.

[39] Michalewicz, Z., Deb, K., Schmidt, M., and Stidsen, T., 2000, "Test-Case Generator for Constrained Parameter Optimization Techniques," IEEE Trans. Evol. Comput., **4**, pp. 197–215.

Film-Cooling Enhancement of the Mist Vertical Wall Jet on the Cylindrical Channel Surface With Heat Transfer

V. I. Terekhov
e-mail: terekhov@itp.nsc.ru

M. A. Pakhomov

Kutateladze Institute of Thermophysics,
Russian Academy of Sciences,
Siberian Branch,
1 Academician Lavrent'ev Avenue,
Novosibirsk 630090, Russia

*Results of a numerical study of heat and mass transfer in a gas-droplet wall jet developing over a surface with supplied heat flux are reported. The calculation model is based on an Eulerian/Eulerian approach using a turbulence model that allows for the dynamic and thermal interactions between the phases. This approach is based on using the kinetic equation of probability density function for the coordinates, velocities, and temperatures of droplets in the turbulent flow (Derevich, I. V., "The Hydrodynamics and Heat Transfer and Mass Transfer of Particles Under Conditions of Turbulent Flow of Gas Suspension in a Pipe and in an Axisymmetric Jet," 2002, High Temp., **40**, pp. 78–91). The effects due to many factors are traced, including the dispersed-phase concentration in the wall jet, the droplet diameter, the blowing ratio* $m = \rho_S U_S / \rho_1 U_1$*, the main-flow temperature, and the wall heat flux. A considerable enhancement of heat transfer at relatively low mass concentrations of droplets* M_{LS} *in the jet (more than twofold at* $M_{LS} \leq 0.05$*) has been revealed.* [DOI: 10.1115/1.3082404]

Keywords: gas-droplet wall jet, two-fluid model, droplet evaporation, nonadiabatic cylindrical channel wall

1 Introduction

The theory of single-phase film-cooling flows, both for relatively simple and complex dynamic conditions, is well established, with its fundamentals described in Refs. [1–6]. However, the potential of single-phase cooling seems to be nearly exhausted, and the development of new cooling techniques for surfaces acted upon by hot flows therefore becomes a challenging problem. A most efficient strategy in protecting channel walls against the action of high temperature gas flows is the addition of a liquid phase in the form of a finely dispersed mist to the cooling gas flow. The main mechanism underlying the enhanced protective properties of such gas-droplet systems is the use of the phase change energy in the vicinity of the wall.

To date, in spite of the complexity of the turbulent transport process in multicomponent systems, certain progress has been achieved in the development of calculation algorithms for two-component gas-droplet cooling jets [7–12]. Available integral approaches to the theoretical treatment of the problem, described in Refs. [7,8], use many simplifying assumptions still lacking a detailed substantiation. These articles use the integral approach to heat and mass transfer prediction in a gas-droplet wall jet with similarity between mass concentration of mixture species and total enthalpy of gas-vapor-droplet flow.

Models based on the use of differential boundary-layer equations or the Reynolds averaged Navier-Stokes (RANS) approach for a two-component mixture are free of most of these deficiencies [9–12,17]. Numerical models allow one to more adequately take into account specific features of heat and mass transfer processes in gas-droplet wall jets. In this statement, the problem on heat and mass transfer in a gas-droplet film flow over an adiabatic surface can be solved [9–12]. In the mentioned works, primary attention was focused on the influence of various factors (liquid-phase content, blowing ratio, nonisothermality, and droplet diameter) on the downstream evolution of the adiabatic wall temperature, which directly defines the adiabatic film-cooling effectiveness

$$\Theta = (T_1 - T_W^*)/(T_1 - T_S) \tag{1}$$

Here T_1, T_S, and T_W^* are, respectively, the main-flow temperature, the injected gas temperature, and the adiabatic wall temperature. The calculated data comply well with the experimental data in Refs. [7–9,14,15] in terms of Θ and adequately reproduce the distributions of flow quantities over the jet cross section. The numerical and experimental studies reported in Refs. [7–17] revealed a substantial increase in cooling efficiency (by a factor of 1.5–2) for gas-droplet film flows in comparison with single-phase film flows already at relatively low liquid-phase contents of the injected jet (less than 10 wt % of the secondary flow).

Situations, when film cooling is combined with heat supply or removal from the tube wall, are often for various engineering applications. There are few published works dealt with modeling of gas-droplet film cooling at heat transfer on a wall. Reference [18], investigating the near-wall gas-droplet screen with heat removal from the wall, is an exclusion.

In the present paper, we consider the flow structure and heat transfer in a gas flow with a two-phase wall mist jet injected cocurrently into the flow in the presence of heat transfer on the cylindrical channel surface with allowance for the interphase interaction, the stochastic motion of impurity, and turbophoresis. Both the wall jet and the main stream were assumed directed downward. The model for the gas flow and for the motion of the dispersed phase in it is developed within an Eulerian/Eulerian approach [19–23] that closely resembles, on the whole, the numerical models in Refs. [21–24]. An important advantage of Eulerian/Eulerian models over the Eulerian/Lagrangian method is the use of equations of one and the same type for both phases; these equations can therefore be solved using a uniform solution algorithm. The description of the dynamics of fine impurity also presents no difficulties here as the dispersed-phase size decreases.

In the present work, that continues our previous studies [11,25,26], we treat both the case of low blowing ratios ($m < 1$),

Contributed by the Heat Transfer Division of ASME for publication in the JOURNAL OF HEAT TRANSFER. Manuscript received March 25, 2007; final manuscript received October 10, 2008; published online March 30, 2009. Review conducted by S. A. Sherif.

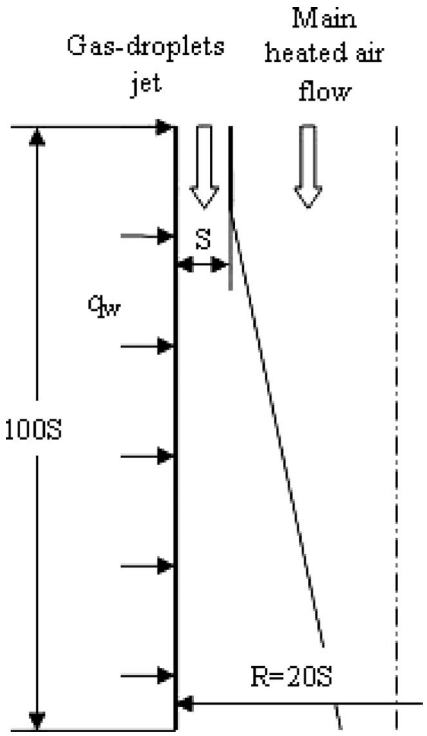

Fig. 1 Schematic of the gas-droplet wall jet propagating along the wall in the presence of heat flux: (1) air and water droplets and (2) main air flow

with wall turbulence regularities dominating the development of the wall jet [1], and the case of high blowing ratios ($m>1$), with prevalence of jet mixing [27].

2 Problem Statement

A schematic of the wall jet is shown in Fig. 1. The flow consists of two co-axial streams. The main heated air stream with a temperature T_1 is delivered into the central channel of diameter $2(R\text{-}S)$. The flow velocity in this stream is distributed uniformly, and the air may be either dry or humid with some humidity φ_1, also uniform over the cross section of the flow. Through the peripheral annular slot of height S, a gas-steam-droplet flow is supplied with a uniform distribution of all flow quantities both over the height of the slot. The steam-liquid mixture at the outlet from the slot can be either in an equilibrium state, with the steam and droplets being at the saturation curve, or in a nonequilibrium state, with temperatures of the two phases being different.

The volume concentration of the liquid phase is low ($\Phi<10^{-4}$), and the droplets are fine, the initial droplet diameter being $d_S<100$ μm. No coalescence occurs in the flow (because the amount of the dispersed phase is small), and droplets never undergo fractionation (the Weber number based on the droplet size and on the interphase velocity is much smaller than unity (We $\ll 1$), whereas the critical Weber number, according to the data reported in Ref. [28], is $\mathrm{We}_*=7$). According to the data in Ref. [22], in two-phase flows the effects due to interdroplet collisions are negligible in the indicated range of concentrations. We assume that the particles deposited on the wall from the two-phase flow undergo instantaneous evaporation, leaving the wall surface always dry; this assumption is quite valid for channels with heated walls. Indicative of that are the experimental data in Ref. [28] and the numerical data in Refs. [9–11,25,26]. This condition is valid if the wall temperature is 40°C superheated. The concentration of particles steadily decreases in the downstream direction due to their deposition onto the wall and due to wall jet expansion. The droplet size in the flow varies both over the cylindrical channel length and over the cylindrical channel cross section due to the nonuniform rate of evaporation, dependent on the local gas-flow temperature. The droplet temperature is assumed to be uniform over the droplet radius.

2.1 System of Equations for the Gas Phase. Under the adopted assumptions, the system of equations for the axisymmetric two-phase gas-droplet flow in the boundary-layer approximation has the form

$$\frac{\partial U}{\partial x}+\frac{1}{r}\frac{\partial (rV)}{\partial r}=\frac{6J\Phi}{\rho d}$$

$$\rho\left[U\frac{\partial U}{\partial x}+\frac{V}{r}\frac{\partial (rU)}{\partial r}\right]=-\frac{\partial P}{\partial x}+\frac{\rho}{r}\frac{\partial}{\partial r}\left[r(\mu+\mu_T)\frac{\partial U}{\partial r}\right]-\frac{3\Phi(U-U_L)}{4d}C_D\rho|\boldsymbol{U}-\boldsymbol{U}_L|+\rho g$$

$$\rho C_p\left[U\frac{\partial T}{\partial x}+\frac{V}{r}\frac{\partial (rT)}{\partial r}\right]=\frac{1}{r}\frac{\partial}{\partial r}\left[r\left(\frac{\mu}{\mathrm{Pr}}+\frac{\mu_T}{\mathrm{Pr}_T}\right)\frac{\partial T}{\partial r}\right]-\frac{\alpha}{d}(T-T_L)+\rho D\frac{\partial K_V}{\partial r}(C_{pV}-C_{pA})\frac{\partial T}{\partial r} \quad (2)$$

$$\rho\left[U\frac{\partial K_V}{\partial x}+\frac{V}{r}\frac{\partial (rK_V)}{\partial r}\right]=\frac{1}{r}\frac{\partial}{\partial r}\left[r\left(\frac{\mu}{\mathrm{Sc}}+\frac{\mu_T}{\mathrm{Sc}_T}\right)\frac{\partial K_V}{\partial r}\right]+\frac{J\Phi}{d}$$

$$\rho=P/(\Re T),\qquad \partial P/\partial r=0$$

The continuity, energy, and diffusion equations involve source and sink terms that model the influence of droplets on transport processes, and the equation of motion in axial direction contains an additional term that allows for the dynamic interaction between the phases. In the present study, the Prandtl and Schmidt numbers were assumed uniform both over the cylindrical channel length and radius; this numbers were set to $\mathrm{Pr}_T=\mathrm{Sc}_T=0.9$.

2.2 Two-Equation Turbulence Model. The equations for the turbulence kinetic energy k and for the dissipation rate $\tilde{\varepsilon}$ modified so that to allow for the presence of the dispersed phase have the form

$$\rho\left[U\frac{\partial k}{\partial x}+\frac{V}{r}\frac{\partial (rk)}{\partial r}\right]=\frac{\rho}{r}\frac{\partial}{\partial r}\left[r\left(\mu+\frac{\mu_T}{\sigma_k}\right)\frac{\partial k}{\partial r}\right]+\Pi-\rho\varepsilon+\Pi_k+S_k$$

$$\rho\left[U\frac{\partial \tilde{\varepsilon}}{\partial x}+\frac{V}{r}\frac{\partial (r\tilde{\varepsilon})}{\partial r}\right]=\frac{\rho}{r}\frac{\partial}{\partial r}\left[r\left(\mu+\frac{\mu_T}{\sigma_\varepsilon}\right)\frac{\partial \tilde{\varepsilon}}{\partial r}\right]+\frac{\tilde{\varepsilon}}{k}(C_{\varepsilon 1}f_1\Pi-C_{\varepsilon 2}\tilde{\varepsilon}\rho f_2)+\frac{0.79}{4}\frac{k^2}{\tilde{\varepsilon}}\frac{\partial U}{\partial x}\left(\frac{V}{r}\right)^2+\Pi_\varepsilon+S_\varepsilon \quad (3)$$

Here, $\mu_T=C_\mu f_\mu \rho k^2/\tilde{\varepsilon}$ and $\Pi=\mu_T(\partial U/\partial r)^2$. The constants and the damping functions are taken from Ref. [29].

The third term in the right-hand side of the equation for the dissipation of turbulent energy allows for the stretching of turbulent eddies in the internal flow. The terms S_k and S_ε, which characterize the excessive rate of gas-flow turbulence dissipation due to the presence of fine droplets and the energy exchange with the time-average flow, resulting from the mean slip between the phases in cases with nonuniform distribution of droplet concentration, and also the influence of evaporation on the gas-flow turbulence, are described in detail [11,25].

3 System of Equations for the Dispersed Phase

One way to construct the system of equations for the flow and heat transfer in the dispersed phase is the use of the kinetic equation for the probability density function (PDF) of particle coordinate, velocity, and temperature in the turbulent flow [24,26]. The

equation for PDF arises on the assumption that the velocity and temperature pulsations in the dispersed phase result from the interaction of the particles with turbulent gas-flow fluctuations, which can be represented with a Gaussian process. Modeling of a real turbulent flow with a Gaussian process, although an approximation, yields satisfactory results from the practical point of view. From the kinetic equation for PDF, a system of equations can be derived for modeling the dispersed-phase dynamics and heat transfer in the Eulerian approach.

Numerous recent studies [21–24] show that, for the conditions under the present consideration, the main forces acting on a droplet in a turbulent flow are the aerodynamic drag, the gravity force, and the force due to turbophoresis.

The system of equations for the dispersed phase consists of the continuity equation, the equations for the averaged momentum in axial (U_L) and radial (V_L) directions, and the energy equation in the axisymmetric case shown below

$$\frac{\partial(\Phi U_L)}{\partial x}+\frac{1}{r}\frac{\partial(r\Phi V_L)}{\partial r}=-\frac{6J\Phi}{\rho_L d}$$

$$U_L\frac{\partial U_L}{\partial x}+\frac{V_L}{r}\frac{\partial(rU_L)}{\partial r}+\frac{\partial\langle v_L^2\rangle}{\partial x}+\frac{1}{r\Phi}\frac{\partial}{\partial r}[r\Phi\langle u_L v_L\rangle]=\frac{U-U_L\pm\tau g}{\tau}-\frac{D_{xL}}{\tau}\frac{\partial\ln\Phi}{\partial r}$$

$$U_L\frac{\partial V_L}{\partial x}+\frac{V_L}{r}\frac{\partial(rV_L)}{\partial r}+\frac{\partial\langle v_L^2\rangle}{\partial r}=\frac{V-V_L}{\tau}-\frac{D_{rL}}{\tau}\frac{\partial\ln\Phi}{\partial r} \tag{4}$$

$$U_L\frac{\partial T_L}{\partial x}+\frac{V_L}{r}\frac{\partial(rT_L)}{\partial r}+\frac{1}{r\Phi}\frac{\partial}{\partial r}(r\Phi\langle\theta v_L\rangle)=\frac{6}{C_{pL}\rho_L d}\{\alpha(T-T_L)-J[L+C_{pV}(T-T_L)]\}$$

The equations for the fluctuating dispersed-phase velocity in the longitudinal and transverse directions, and the turbulent diffusion coefficients of droplets, were determined using the procedure in Ref. [24].

3.1 Heat Transfer Between the Channel Wall and the Deposited Droplets. As particles come in contact with the channel wall, part of the heat flux is required for their heat-up and evaporation. Like in Refs. [26,28], in the present study superposition of heat flows was assumed possible. The equation for the heat flux q_W supplied to the cylindrical channel surface involves the sum of the heat flux from the wall to the droplets (q_{WL}) and from the wall to the gas-steam-droplet mixture (q_{WF})

$$q_W=q_{WL}+q_{WF}$$

The heat flux from the wall to the droplets on the wall has the form [28]

$$q_{WL}=\exp[1-(T_W/T_L)^2]V_{LW}\rho_L L M_{Lm}$$

where $M_{Lm}=2/R^2\int_0^R M_L\cdot r\cdot dr$ is the concentration of droplets averaged over the cross section of the channel.

Equations (2)–(4) were supplemented with conservation equations for the mass concentration of the gas-steam-droplet mixture over the channel length.

3.2 The Modeling of Heat and Mass Transfer and Resistance for Single Evaporating Droplet. The vapor mass flux on the surface of an evaporating droplet can be written as

$$J=\underbrace{JK_V^{\text{sat}}}_{\text{I}}-\underbrace{\rho D\left(\frac{\partial K_V}{\partial r}\right)_{\text{droplet}}}_{\text{II}} \tag{5}$$

where K_V^{sat} is the vapor concentration at the droplet surface, which should be taken at saturation parameters for the droplet temperature T_L. (I) is the convective flux of the mass of vapor and (II) is the diffusional mass flow rate.

Taking into account that the diffusional Stanton number St_D has the form

$$\text{St}_D=-\rho D\frac{\partial K_V^{\text{sat}}}{\partial r}/\rho(U-U_L)(K_V^{\text{sat}}-K_V)$$

we can write Eq. (5) in the form

$$J=\text{St}_D\ \rho(U-U_L)B_{1D} \tag{6}$$

Considering the blowing and convection effects on heat and mass transfer, Haywood et al. [30] suggested the semi-empirical correlations for Nusselt and Sherwood numbers of evaporating droplet

$$\text{Nu}=\frac{\alpha d}{\lambda}=\frac{2+0.57\ \text{Re}_L^{1/2}\ \text{Pr}^{1/3}}{(1+B_{1T})^{0.7}},$$

$$\text{Sh}=\frac{\beta d}{D}=\frac{2+0.87\ \text{Re}_L^{1/2}\ \text{Sc}^{1/3}}{(1+B_{1D})^{0.7}}$$

where $B_{1T}=C_p(T-T_L)/L$ is the Spalding heat transfer number.

For evaporating droplets, a coefficient of resistance C_D is given by the following expression [28]:

$$C_D=\frac{C_{DP}}{1+C_p(T-T_L)/L}$$

Here C_{DP} is the coefficient of resistance of nonevaporating particles, which can be calculated from the relations presented by Volkov et al. [22],

$$C_{DP}=\begin{cases}24/\text{Re}_L, & \text{Re}_L\le 1\\ 24/\text{Re}_L(1+\text{Re}_L^{2/3}/6), & \text{Re}_L>1\end{cases}$$

4 Boundary Conditions

At the cylindrical channel axis, symmetry conditions were posed:

$$\frac{\partial T}{\partial r}=\frac{\partial K_V}{\partial r}=\frac{\partial U}{\partial r}=V=\frac{\partial U_L}{\partial r}=V_L=\frac{\partial\langle u_L^2\rangle}{\partial r}=\frac{\partial\langle v_L^2\rangle}{\partial r}=\frac{\partial T_L}{\partial r}=\frac{\partial k}{\partial r}=\frac{\partial\tilde{\varepsilon}}{\partial r}=0 \tag{7}$$

At the wall, no-slip and impermeability conditions for the gas-phase velocity are fulfilled, with the kinetic energy of the gas flow and the dissipation rate of this energy being both zero:

$$U=V=0,\quad \frac{\partial K_V}{\partial r}=0,\quad k=\tilde{\varepsilon}=0 \tag{8}$$

The heat flux was assumed uniform over the cylindrical channel length ($q_W=\text{const}$).

The conditions at the wall for rms fluctuations of the axial and radial velocities, and for the dispersed-phase temperature, are [24]

$$\langle v_L^2\rangle\frac{\partial U_L}{\partial r}=-\frac{2}{\tau}q_L\nu_T\left(\frac{\partial U}{\partial r}\right)_W,\quad V_{L,W}=\left(\frac{2}{\pi}\langle v_L^2\rangle\right)^{1/2}$$

$$\frac{\partial\langle u_L^2\rangle}{\partial r}=0,\quad \frac{\partial\langle v_L^2\rangle}{\partial r}=-V_{L,W}/\tau$$

$$\left(\frac{1}{\tau}-\frac{1}{\tau_\Theta}\right)^{-1}\langle v_L^2\rangle\frac{\partial T_L}{\partial r}=-f_{\theta v}\langle tv\rangle_W \tag{9}$$

where q_L and $f_{\theta v}$ are functions of droplet entrainment into the turbulent motion and heat transfer of the gas phase [24].

In the inlet cross section of the cylindrical channel, the distribution of all flow quantities across the main single-phase flow

$(0 \le r \le (R\text{-}S))$ is uniform. For the gas-droplet jet $((R\text{-}S) \le r \le R)$ supplied through the tangential slot, we assume that

$$U_S = U_{LS}, \quad T_S = T_{LS} \tag{10}$$

At the slot exit plane, the velocities and temperatures of the phases were assumed to be identical, and the distributions of all other initial parameters were assumed uniform. A similar approach was previously used in Refs. [9–11,25,26]. At the inlet, all droplets are of identical sizes and temperatures. In the present study, the turbulence intensity of the gas phase in the main flow at the inlet to the channel was taken to be $Tu_1 = 4\%$, and in the near-wall flow, $Tu_S = 7\%$. These values were selected in accordance with the experimental measurements in Refs. [13,14].

5 Numerical Algorithm

To numerically solve the transport equation for the gas phase and the equations for the kinetic energy and the dissipation rate of this energy, we used the method developed for boundary-layer flows in Ref. [31]. The finite difference scheme is of second order of accuracy along both directions. The system of finite difference equations (2)–(6) was supplemented with boundary conditions (7)–(10) to be subsequently solved by the sweep method [31].

The continuity equations for the gaseous and dispersed phases and the equation for the radial velocity of droplets were solved using the Keller cell method [32], which also has second order accuracy along both directions.

If the grid was logarithmically nonuniform in the transverse direction, the coordinate r could be conveniently transformed to solve the system in the computational domain on a uniform grid. Suitable for such a two-dimensional boundary-layer problem is the transformation of coordinates used in Ref. [32].

All calculations in the present study were performed on a grid that contained a total of 201 nodes in the axial and radial directions. The Stanton number is the most sensitive to the grid change. At the stage of testing, the effect of grid resolution on the Stanton number was studied for the case of the gas-droplet wall jet with the low Reynolds number (LRN) model in Ref. [29]. In addition, methodical calculations were performed on the finer nested grid that contained 301 nodes over the cylindrical channel length and 301 nodes over the cylindrical channel radius. Further increase in the number of nodes was found to yield no substantial changes in the calculated data.

Since the equations in the system of Eqs. (2)–(6) are nonlinear, their solutions were calculated in an iterative manner. The following convergence conditions were adopted: $|E_i - E_{i-1}| < 10^{-5}$ (i is the iteration number, E: U, k, $\tilde{\varepsilon}$, T, K_V, U_L, V_L, $\langle u_L^2 \rangle$, $\langle v_L^2 \rangle$, and T_L). The calculations were assumed completed on fulfillment of all the above criteria.

6 Testing of Calculation Data for Single-Phase Cooling Flow

At the first stage of the study, calculations of momentum thickness in the single-phase gas film flow were performed. The calculated data are shown in Fig. 2. For comparison, the same figure also shows the experimental data in Refs. [33–35] and the data calculated by the formula in Ref. [3], derived by solving the integral momentum equation

$$\delta^{**}/\delta_S^{**} = \left[1 + 0.016 \left(\frac{\Delta x}{\mathrm{Re}_{\Delta x}^{0.2} \ \delta_S^{**}} \right)^{1.25} \right]^{0.8} \tag{11}$$

where $\delta_S^{**} = \int_0^S \rho_S U_S / \rho_1 U_1 (1 - U_S/U_1) dy$ is the momentum thickness in the slot. It is widely used in the integral theory of film cooling [1–4]. In the limit case of uniform velocity distribution in the single-phase main flow and in the jet, as in the current work, this value is $\delta_S^{**} = m(1-m)S$. The numerical data are seen to comply well with the experimental data in Refs. [33–35] and with the data calculated by Eq. (11).

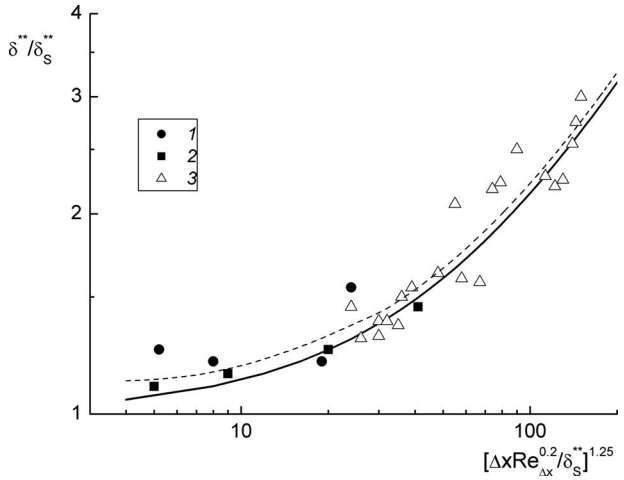

Fig. 2 Variation in momentum thickness at the injection of a single-phase jet; solid curve—calculation by formula (11), dashed line—calculation by this numerical model, and points—experimental data: (1) Ref. [33], (2) Ref. [34], and (3) Ref. [35]

Indicative of the possibility of using, as a characteristic temperature scale, the temperature difference between the wall with and without heat transfer are the calculated data in Fig. 3, presented in the form of the Stanton number St^* versus integral Reynolds number Re_t^{**}. Here, the numbers St^* and Re_t^{**} were calculated from the temperature difference $T_W - T_W^*$:

$$\mathrm{St}^* = \frac{q_W}{C_{p1}\rho_1 U_1 (T_W - T_W^*)} \tag{12}$$

$$\mathrm{Re}_t^{**} = \frac{\rho_1 U_1 \delta_t^{**}}{\mu_1} \tag{13}$$

It should be noted that the calculated data agree well with the formula for heat transfer in developed boundary-layer flow [1]

$$\mathrm{St}^* = 0.0128 (\mathrm{Re}_t^{**})^{-1/4} \ \mathrm{Pr}^{-3/4} \tag{14}$$

7 Calculation Data

All calculations were performed for a water/air mist in the following range of initial parameters: blowing ratio $m = 0.1-2$, mass concentration of droplets in the jet $M_{LS} = 0-0.05$, main-flow temperature $T_1 = 323-473$ K, main-flow velocity $U_1 = 20-50$ m/s,

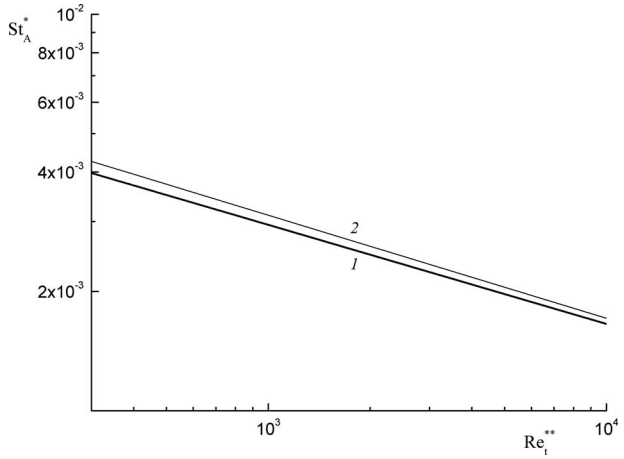

Fig. 3 Heat transfer in the cooling region: (1) calculation by the numerical model and (2) as predicted by Eq. (14)

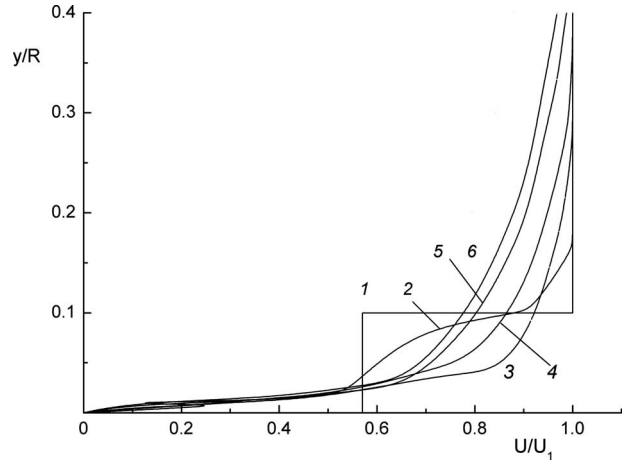

Fig. 4 Profiles of gaseous phase velocity at the injection of the gas-droplet wall jet: (1) $x/S=0$, (2) 25, (3) 50, (4) 100, (5) 150, and (6) 200 ($q_W=5$ kW/m^2, $T_1=373$ K, $T_S=T_{LS}=293$ K, $U_1=50$ m/s, $d_S=30$ μm, $m=0.8$, $M_{VS}=0.014$, $M_{LS}=0.05$)

and temperature of the two-phase flow at the slot exit plane $T_S=T_{L1}=293$ K. The channel diameter was $2R=0.1$ m, their length was 0.5 m, and the slot height was $S=5$ mm. The Reynolds number in the main flow was $\mathrm{Re}=\rho_1 U_1 2R/\mu_1=(1-3.5)\times 10^5$. The particle diameter was varied in the interval $d_S=0-100$ μm, and the droplet Reynolds number based on the interphase velocity in the flow and on the initial size of the dispersed phase is in the interval $\mathrm{Re}_L=0.01-4$, which refers to limiting values of the Oseen flow regime around a droplet. All calculations were performed assuming a uniform wall heat flux ($q_W=$const). The heat flux was varied in the range $q_W=5-20$ kW/m^2. The cylindrical channel surface was dry, that no liquid film from deposited droplets formed on the wall. This assumption for heated channels was allowable (see Ref. [28]).

Figures 4 and 5 illustrate the evolution of the velocity profiles for the gas and dispersed phases over the cylindrical channel length at a fixed blowing ratio of $m=0.8$. In the initial cross section ($x/S=0$), the stepwise velocity profile for either phase was set (line 1). The velocities of the phases at the exit from the tangential slot are identical. Further downstream, as the jet mixes with the main flow, the velocity profile for the gas phase levels out (curves

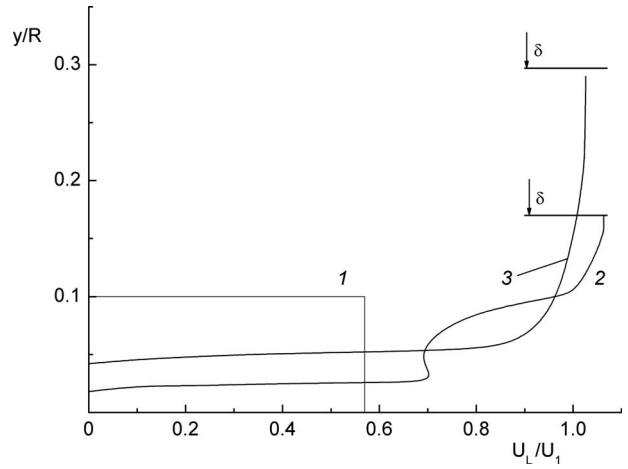

Fig. 5 Variation in droplet velocity in the two-phase jet over the channel length: (1) $x/S=0$, (2) 25, and (3) 50. Conditions adopted in the calculations are the same as in Fig. 4.

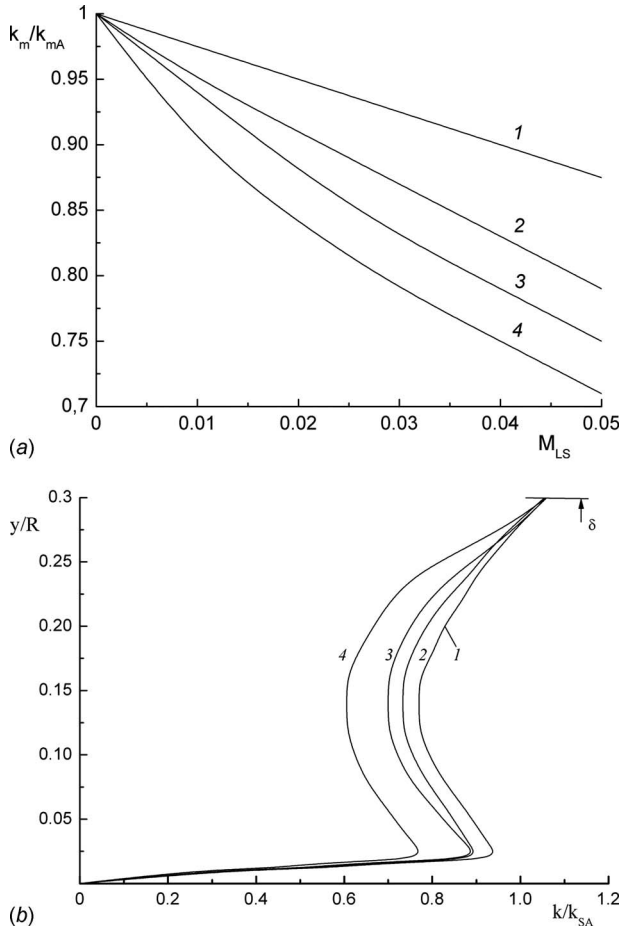

Fig. 6 Effect of droplet concentration M_{LS} (*a*) and droplet diameter (*b*) on the gas-flow turbulence in the wall jet: (1) $d_S=10$ μm, (2) 30 μm, (3) 50 μm, and (4) 100 μm ($q_W=5$ kW/m^2, $T_1=373$ K, $T_S=T_{LS}=293$ K, $U_1=50$ m/s, $m=0.8$, $M_{VS}=0.014$, $x/S=50$)

5 and 6), and the flow acquires regularities typical of a developed pipe flow [1]. The evaporation of liquid droplets acts to raise the local velocity of the gas flow due to additional influx of vapor mass and increased gradient of flow velocity in the wall zone. As liquid droplets move farther downstream, their velocity increases due to gravitation (curves 2 and 3). In the wall zone, the dispersed-phase velocity displays a local maximum of low amplitude. The formation of the maximum can be attributed to gas rarefaction in the heated wall region of the flow. The outer boundary for the particles is defined by the thickness of the boundary-layer flow.

Figure 6 shows the calculated turbulence kinetic energy profiles of the gas flow versus the droplet concentration in the two-phase jet and across the pipe. In Fig. 6, k_{mA} is the mean value of the gas-flow turbulence in the single-phase flow, and k_{SA} is the value of the gas-flow turbulence in the single-phase flow, with all other conditions being identical. The turbulence energy averaged over the cylindrical channel cross section was calculated from the relation

$$k_m=\frac{2}{R^2}\int_0^R k\cdot r\cdot dr$$

Larger particles ($d_S=100$ μm) act to make the flow less turbulent and decrease the gas turbulence energy. The decrease in the turbulence energy is related to the entrainment of droplets into the large-scale fluctuating motion of the gas flow. Here, part of the

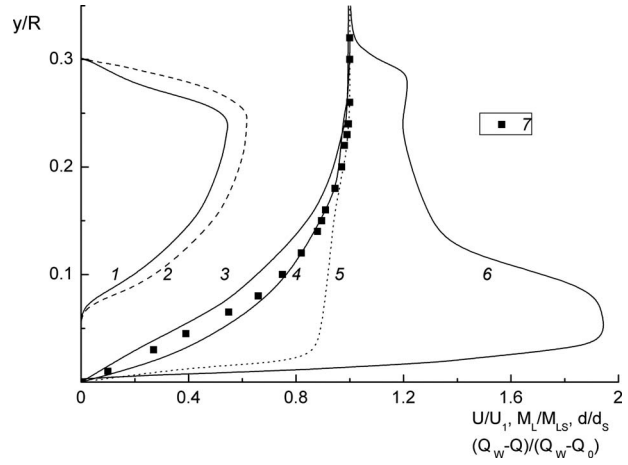

Fig. 7 Distribution of flow quantities in the two-phase film flow over the channel cross section: (1) M_L/M_{LS}, (2) d/d_S, (3) Θ, (4) Θ_H, (5) U/U_1, (6) $(M_{VW}-M_V)/(M_{VW}-M_0)$, and (7) profile of $\Theta=U/U_0=(y/\delta_t)^{1/7}$ (q_W=5 kW/m^2, T_1=373 K, $T_S=T_{LS}$=293 K, U_1=50 m/s, m=0.8, M_{VS}=0.014, M_{LS}=0.05, d_S=30 μm, x/S=50)

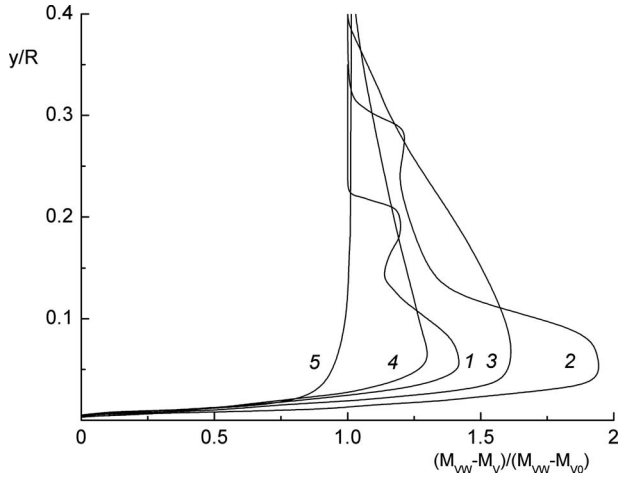

Fig. 8 Profiles of the mass concentration of steam over the transverse coordinate: (1) x/S=25, (2) 50, (3) 100, (4) 150, and (5) 200. Conditions adopted in the calculations are the same as in Fig. 4.

gas-phase turbulent energy is transferred to the dispersed phase. Particles are involved in the fluctuational motion of the gas phase because large eddy Stokes number Stk$=\tau/\tau_f \ll 1$, where τ is the particle relaxation time and $\tau_f=R/U_1$ is the typical time of the carrying phase in the averaged motion. Large eddy Stokes number is one of the main parameters, characterizing involvement of the disperse phase into the pulsation motion of gas. In our calculations Stk$=0.01-1$ for the studied range of applied parameters of the disperse phase.

The complex heat and mass transfer regularities that arise in gas-droplet wall jets can be figured out considering the local distributions of thermal and gas-dynamic quantities across the boundary layer. Relative profiles of droplet concentration (curve 1), droplet diameters (2), gas temperatures (3), total enthalpy (4), gas-flow velocity (5), and steam concentration (6) are shown in Fig. 7.

The total enthalpy of the gas-droplet mixture was calculated by the formula

$$H=\sum_{i=1}^{3} H_i M_i = H_A M_A + H_L M_L + H_V M_V$$

Here, $H_i=\int C_{pi}dT_i+h_i^0$ is the enthalpy of the ith component of the mixture with allowance for the formation energy of the component from elementary substances (h_i^0), and M_i is the mass concentration of the component.

The solid symbols (7) in Fig. 7 show the power law ($n=1/7$) of flow quantities across the boundary layer. As it is seen, no similarity is observed in the distributions of flow quantities across the boundary layer. This is just what would be expected because the flow, energy, and diffusion equations possess no similarity properties owing to the presence of source terms due to the evaporation of liquid droplets. It should be noted that a similar picture is also displayed by gas-droplet flows on adiabatic wall [7]. The distributions of the mass concentration of the liquid phase (1) and droplet diameter (2) are both domelike. The wall zone is free of particles, and the outer boundary coincides with the thickness of the boundary layer. The profiles of temperature (3) and total enthalpy (4) lie rather close to the power distributions. The profiles of gas-phase velocity (5) are less filled in the wall region due to intense steam release.

The profile of the mass concentration of steam (6) displays a distinct maximum, an evaporation front, occupying a position in the wall zone. In the presence of the heat flux, most intense evaporative processes proceed near the wall. In the outer zone of the boundary layer another local maximum of steam concentration is observed, resulting from steam release at the mixing boundary with the heated main flow.

The evolution of steam concentration profiles with the development of the wall jet flow over the cylindrical channel wall can be traced considering Fig. 8. At the inlet cross section, the profile was uniform. As the flow moves in the downstream direction, the concentration profiles deform with the emergence of two maxima. Then, as the role of diffusion and jet mixing processes becomes more pronounced, the large gradients of the steam concentration (1–3) smoothen. Here, with increasing distance from the inlet, the liquid-phase concentration decreases as well, and the concentration profiles start therefore displaying a boundary-layer type behavior.

Figure 9 demonstrates the distributions of wall temperature for various mass concentrations of liquid droplets in the jet. Lines 6 and 7 in the figure show the temperature of the jet and main flow at the inlet. These lines are the typical scales of the wall temperature distribution. With increasing concentration of the dispersed

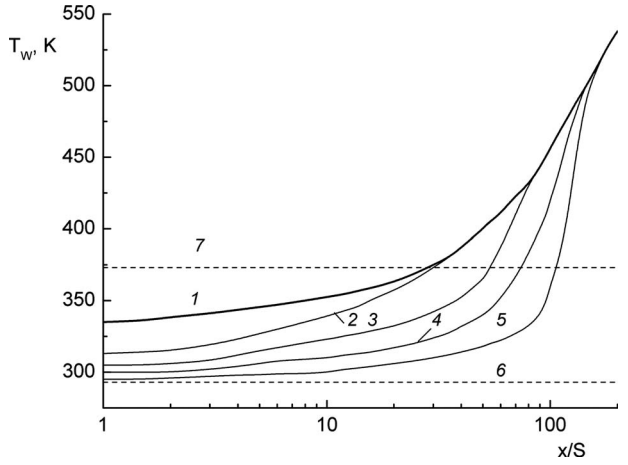

Fig. 9 Wall surface temperature versus the droplet concentration in the two-phase jet: (1) M_{LS}=0, (2) 0.005, (3) 0.01, (4) 0.025, (5) 0.05, (6) $T_S=T_{LS}$=293 K, and (7) T_1=373 K (q_W=5 kW/m^2, T_1=373 K, $T_S=T_{LS}$=293 K, U_1=50 m/s, m=0.8, M_{VS}=0.014, d_S=30 μm)

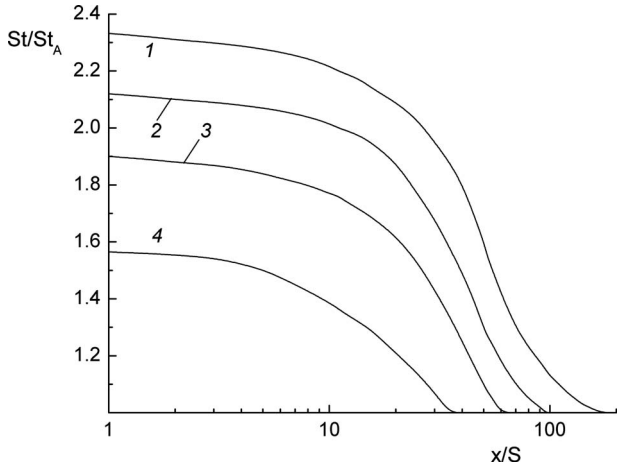

Fig. 10 Heat transfer intensification ratio versus axial coordinate for air main-flow temperature: (1) T_1=323 K, (2) 373 K, (3) 423 K, and (4) 473 K (q_W=5 kW/m^2, T_S=T_{LS}=293 K, U_1=50 m/s, m=0.8, d_S=30 μm, M_{VS}=0.014, M_{LS}=0.05)

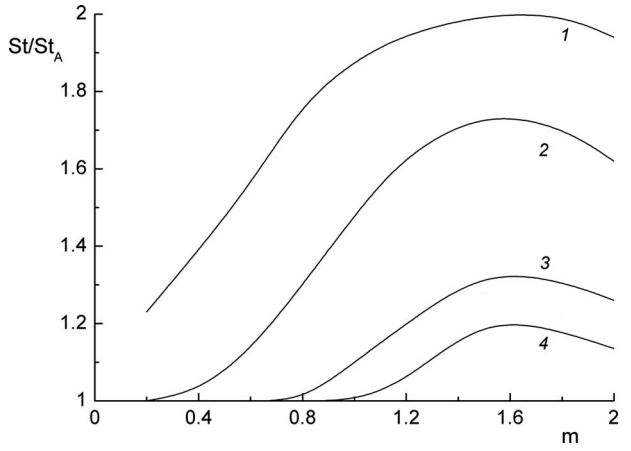

Fig. 12 Effect of blowing ratio m on heat transfer augmentation: (1) x/S=25, (2) 50, (3) 100, and (4) 200 (q_W=5 kW/m^2, T_1=373 K, T_S=T_{LS}=293 K, U_1=50 m/s, M_{VS}=0.014, M_{LS}=0.05, x/S=50)

phase, a decrease in the wall temperature is observed due to the use of the droplet evaporation phase change energy in the vicinity of the wall. As the flow moves farther downstream and the droplets undergo evaporation, the wall temperature increases to finally approach its value for the single-phase flow regime (1).

The influence of the main-flow temperature T_0 on the heat transfer between the cylindrical channel wall and the gas-droplet cooling flow is illustrated in Fig. 10. Here, St_A is the Stanton number for the single-phase flow, all other conditions being identical to those for the film flow with heat transfer. This representation makes the advantages of the two-phase coolant over a single-phase gas flow easy to reveal. Note that, like in the case of two-phase film flows on adiabatic surface, the experiments in Refs. [13–16] and the numerical studies in Refs. [9–11,15] demonstrate a strong effect of the main-flow temperature T_0 on the heat and mass transfer processes. An increase in the main-flow temperature leads to a substantial reduction in St/St_A. The latter effect can be understood as resulting from more pronounced influence of evaporation processes, which prevail at the outer boundary of the jet mixing layer rather than in the vicinity of the wall.

Figure 11 shows the distributions of the heat transfer enhancement ratio in gas-droplet jets for various values of the wall heat flux. An increase in the heat flux is seen to lead to a decrease in St/St_A due to more rapid evaporation of the liquid phase from the gas boundary layer near the wall, which leads to reduction in temperature gradients in the wall zone.

The effect of blowing ratio m on the heat transfer intensification ratio in the two-phase cooling flow is illustrated in Fig. 12. It is seen that, as we move farther from the injection place, the heat transfer augmentation becomes less pronounced owing to lower liquid-phase content of the flow. Like the relative temperature Θ [13–15], the ratio St/St_A displays a maximum. But, unlike the quantity Θ, whose maximum value corresponds to m=1, in the two-phase flow the heat transfer rate attains its highest at m =1.5–1.8.

The heat transfer enhancement ratio as a function of initial droplet diameter is shown in Fig. 13. As the particle diameter increases, the ratio St/St_A decreases due to a reduction in the interphase surface. The heating and evaporation of large drops proceed at a slower pace compared with fine droplets; yet, the zone with the two-phase regime of the cooling flow here is more extended in the downstream direction. For the conditions considered in this work, the range of droplet sizes of d_s=30–50 μm is probably optimal both by the length of the zone with the two-

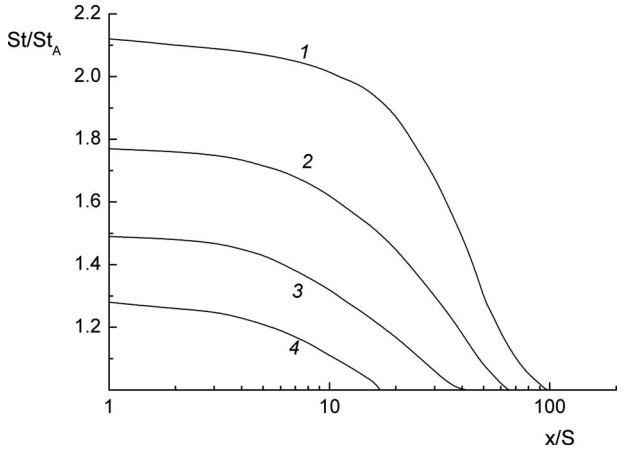

Fig. 11 Heat transfer in the gas-droplet flow for various values of the relative heat flux $\bar{q}\times10^3$: (1) 1.4, (2) 2, (3) 2.8, and (4) 5.5 (T_1=373 K, T_S=T_{LS}=293 K, U_1=50 m/s, m=0.8, M_{VS} =0.014, M_{LS}=0.05)

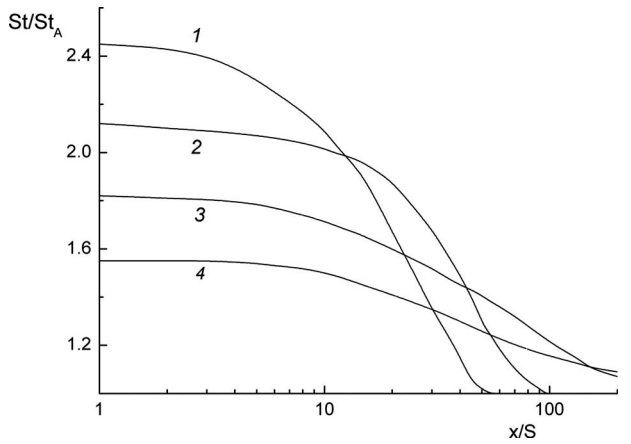

Fig. 13 Heat transfer in gas-droplet jets with different initial droplet diameters: d_S=10 μm, (2) 30 μm, (3) 50 μm, and (4) 100 μm

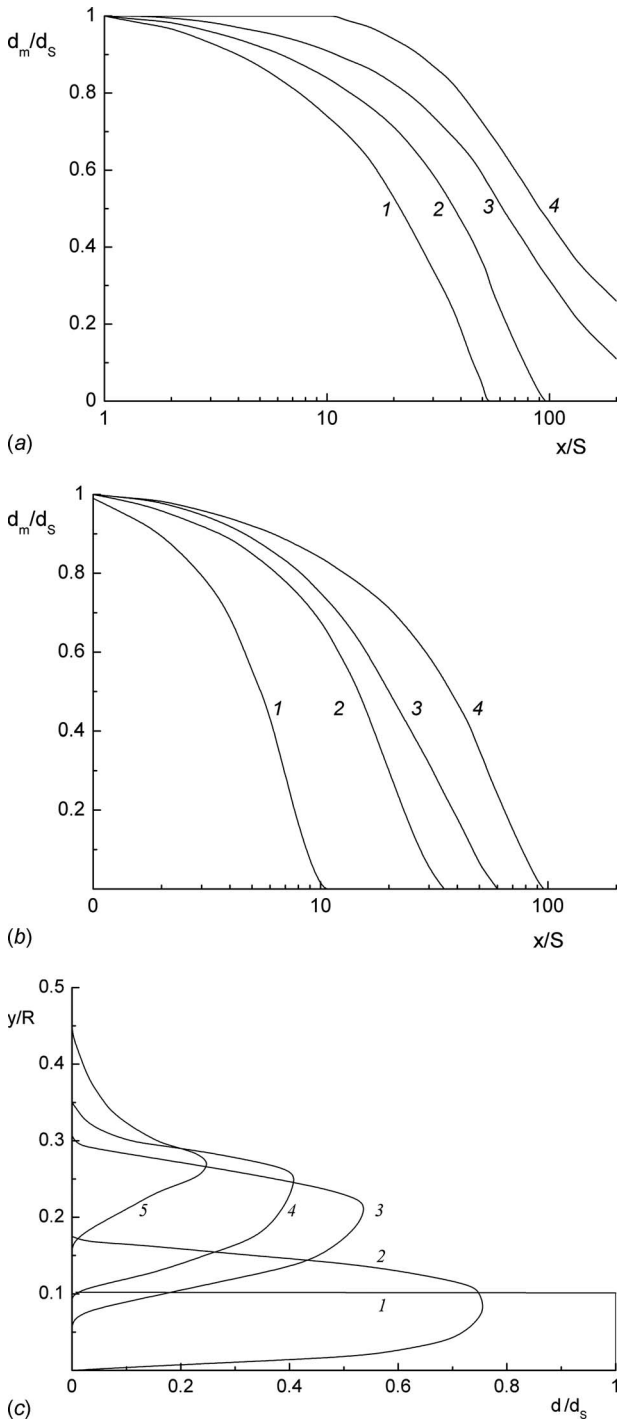

Fig. 14 Variation in the droplet size over the cylindrical channel length: (*a*) for various particle sizes: (1) d_S=10 μm, (2) 30 μm, (3) 50 μm, and (4) 100 μm (M_{LS}=0.05); (*b*) for various dispersed-phase mass concentrations: (1) M_{LS}=0.005, (2) 0.01, (3) 0.025, and (4) 0.05 (d_S=30 μm); (c) cross-section profiles of droplet diameter: (1) x/S=0, (2) 25, (3) 50, (4) 100, and (5) 200 (q_W=5 kW/m^2, T_1=373 K, T_S=T_{LS}=293 K, U_1=50 m/s, m=0.8, M_{VS}=0.014, M_{LS}=0.05)

phase flow and the value of enhancement ratio St/St_A. For other inlet conditions (ratio of phase velocities and thermal-physical properties of droplets) this optimum can change.

Figure 14 shows the calculated evolution of particle sizes for various initial particle diameters (Fig. 14(*a*)), for various mass concentrations M_{LS} of droplets in the flow (Fig. 14(*b*)), and droplet diameter distribution across the cylindrical channel (Fig. 14(*c*)). The mean droplet diameter was calculated from the relation

$$d_m = \frac{2}{R^2}\int_0^R d \cdot r \cdot dr$$

As it follows from the data in Fig. 14, the particle size monotonically decreases over the cylindrical channel length. An increase in the dispersed-phase size of the wall jet makes the length of the zone occupied by the two-phase gas-droplet jet longer due to slower evaporation of large drops and due to decreased contact surface between the phases. The data in Fig. 14 can be used to estimate the length of the evaporation zone as a function of different thermal and gas-dynamic parameters of the two-phase flow. The length of two-phase flow increases with increasing droplet concentration and droplet size.

8 Conclusions

The physical model has been developed for heat and mass transfer of a gas-droplet wall jet cocurrently injected into a turbulent gas flow moving through a cylindrical channel with heat flux supplied to the channel wall. In the model, the liquid phase acts as localized sink for heat and source of steam and interphase friction. Both the deposition of droplets onto the wall and the heat transfer due to the contact of droplets with the wall were taken into account. The droplets were assumed to undergo instantaneous evaporation on the wall, with no liquid film formed on it. To calculate the turbulent characteristics of the gas phase, the (k-$\tilde{\varepsilon}$) LRN model of turbulence was used.

For the first time, the numerical study of heat and mass transfer, and a study of the flow structure, was performed for a wall jet propagating in the channel with a heat flux supplied to the channel wall in a broad range of inlet thermal- and gas-dynamic parameters.

Addition of droplets to the wall jet intensifies heat transfer (by a factor of 2 or greater) due to an increase in the fraction of the heat consumed for the phase transition and for the heat transfer due to the direct contact of droplets with the wall. It is shown that, with an increase in the initial droplet diameter, the exchange with heat between the channel surface and the gas-droplet jet becomes less intense.

It is found that, with an increase in the main-flow temperature and in the wall heat flux density, the heat transfer intensification becomes less pronounced.

It is also shown that the method for calculating heat transfer in single-phase gas cooling flows based on using, as a determining temperature, the adiabatic wall temperature cannot be applied to two-phase gas-droplet film flows.

Acknowledgment

This work was partially supported by the Russian Foundation for Basic Research (Project Nos. 05-08-33586 and 06-08-00967) and Russian Federation's Presidential Foundation for Young Scientists (Grant No. MK-186.2007.8).

Nomenclature

B_{1D} = diffusional blowing parameter for the vapor $=(K_V^{sat}-K_V)/(1-K_V^{sat})$

B_{1T} = Spalding heat transfer number $=C_p(T-T_P)/L$

C_D = coefficient of droplet resistance

C_{DP} = coefficient of resistance of nonevaporating particles

C_p, C_{pA}, C_{pL}, and C_{pV} = heat capacities of mixture, air, liquid, and vapor (J/kg K)

D = vapor diffusion coefficient in air (m^2/s)

D_{xL} and D_{rL} = turbulent diffusivities of droplets in the axial and radial directions due to the stochastic motion of droplets and its entrainment into the gas flow by intense vortices (m^2/s)

d_S = droplet diameter (m)

H = enthalpy (J/kg)

h_i^0 = is the formation enthalpy of the ith component of the mixture from elementary substances (J/kg)

J = vapor mass flux from the surface of evaporating droplet (kg/m^2 s)

k = turbulent kinetic energy (m^2/s^2)

K_A and K_V = air and vapor mass concentrations in the binary air-vapor mixture, respectively

K_V^{sat} = vapor concentration at the droplet surface, which should be taken at saturation parameters for the droplet temperature T_L

L = heat of vaporization (J/kg)

m = blowing ratio $=\rho_S U_S/\rho_1 U_1$

M_A, M_V, and M_L = air, vapor, and droplet mass concentrations in the triple air-vapor-droplet mixture, respectively

M_{Lm} = mean concentration of droplets $=2/R^2\int_0^R M_L \cdot r \cdot dr$

Nu_L = droplet Nusselt number ($\alpha_L d_S/\lambda$)

P = pressure (N/m^2)

Pr = Prandtl number ($C_P\mu/\lambda$)

q_W = heat flux density (W/m^2)

$\bar{q}$ = nondimensional heat flux density $=q_W/\rho_1 C_{p1} U_1 (T_1 - T_S)$

$\Re$ = absolute gas constant (J/(kg K))

R = tube radius (m)

Re, Re_t^{**} = Reynolds numbers $\rho U 2R/\mu$, $U\delta_t^{**}\rho/\mu$

Re_L = Reynolds number of dispersed phase, $\rho d_S\sqrt{(U-U_L)^2+(V-V_L)^2}/\mu$

S = slot height (m)

Sc = Schmidt number ($\mu/\rho D$)

St = Stanton number ($q_W/\rho C_p U(T-T_W)$)

St^* = Stanton number ($q_W/C_{p1}\rho_1 U_1 (T_W - T_W^*)$)

Stk = large eddy Stokes number (τ/τ_f)

U and V = velocity components in axial and radial directions (m/s)

T = temperature (K)

T_W^* = adiabatic wall temperature (K)

Tu = turbulence intensity in the flow

$\langle tv\rangle$ = turbulent heat flux in gas phase $=-(\nu_T/\mathrm{Pr}_T)\times(\partial T/\partial r)$ (km/s)

W = correction factor for the Stokes law $=(1+\mathrm{Re}_L^{2/3}/6)$

We = Weber number ($\rho|\boldsymbol{U}-\boldsymbol{U}_L|d/\sigma$)

V_{LW} = droplet deposition velocity (m/s)

x and r = axial and radial coordinates (m)

Δx = longitudinal coordinate (m) $=x-x_0$

x_0 = initial region length of wall jet, where $\Theta_T=1$ (m)

Y = correction factor $=(1+0.3\ \mathrm{Re}_L^{1/2}\ \mathrm{Pr}^{1/3})$

y = distance from the wall (m)

y_+ = nondimensional distance from the wall $=u_* \rho y/\mu$

u_* = friction velocity $=\sqrt{\tau_W/\rho}$ (m/s)

$\langle uv\rangle$ = turbulent stresses in gas phase $=-(\mu_T/\rho)(\partial U/\partial r)$ (m^2/s^2)

$\langle u_L v_L\rangle$ = Reynolds stresses in the dispersed phase (m^2/s^2)

$\langle u^2\rangle$ and $\langle v^2\rangle$ = rms velocity fluctuations in axial and radial directions (m^2/s^2)

Greek

Φ = volume concentration of droplets

Θ = relative temperature $=(T_0-T_W)/(T_0-T_S)$

α = heat transfer coefficient ($W/(m^2\ K)$)

β = mass transfer coefficient (m/s)

δ, δ^{**}, and δ_t^{**} = thickness of the boundary layer, momentum thickness, and energy thickness (m)

δ_S^{**} = momentum thickness in the slot $=\int_0^S \rho_S U_S/\rho_1 U_1 (1-U_S/U_1)dy$ (m)

$\varepsilon=\tilde{\varepsilon}+\hat{\varepsilon}$ = dissipation rate (m^2/s^3)

$\tilde{\varepsilon}$ = dissipation rate (m^2/s^3)

$\hat{\varepsilon}$ = rate of energy dissipation in the wall zone ($y_+ \le 15$) $=2\mu/\rho[\partial(\sqrt{k})/\partial r]^2$ (m^2/s^3)

φ = humidity of the flow

λ = thermal conductivity (W/(m K))

μ = dynamic viscosity ((N s)/m^2)

$\langle \theta v_L\rangle$ = turbulent heat flux in the dispersed phase (Km/s)

ρ, ρ_L, and ρ_V = mixture, liquid, and vapor densities, respectively (kg/m^3)

σ = surface tension (N/m^2)

τ = particle relaxation time $=\rho_L d^2/18\ \mu$W (s)

τ_f = the typical time of the carrying phase in the mean motion (R/U_1)

τ_W = wall shear stress (Pa)

τ_Θ = particle thermal relaxation time $=C_{pL}\rho_L d^2/(12\lambda Y)$ (s)

Subscripts

0 = parameter at the cylindrical channel axis

1 = parameter at the entrance of the main flow

A = air

D = diffusional parameter

L = droplet

m = mean parameter

P = nonevaporating particle

S = parameter at the entrance of jet flow

T = turbulent parameter

V = vapor

W = parameter under condition at the wall

i = current calculation cross section along the axial direction

$i-1$ = previous calculation cross section along the axial direction

$*$ = critical parameter (for Weber number)

References

[1] Kutateladze, S. S., and Leontiev, A. I., 1989, *Heat Transfer, Mass Transfer and Friction in Turbulent Boundary Layer*, Hemisphere, New York, p. 305.

[2] Goldstein, R. J., 1971, "Film Cooling," *Advance in Heat Transfer*, Vol. 7, T. F. Irvine and J. P. Hartnett, eds., Academic, New York, pp. 321–379.

[3] Volchkov, E. P., 1983, *Film Cooling*, Nauka, Novosibirsk, p. 259, in Russian.

[4] Leontiev, A. I., 1999, "Heat and Mass Transfer Problems in Film Cooling," ASME J. Heat Transfer, **121**, pp. 509–527.

[5] Repukhov, V. M., 1980, *The Theory of Thermal Shielding of a Wall by Gas Injection*, Naukova Dumka, Kiev, p. 295 (in Russian).

[6] Ligrani, P. M., Wigle, J. M., and Jackson, S. W., 1994, "Film-Cooling From Holes With Compared Angle Orientations," ASME J. Heat Transfer, **116**, pp. 353–362.

[7] Vasiliev, A. A., 1988, "The Effectiveness of Gas-Steam and Liquid Thermal Screen Behind a Tangential Slot," Promyshlennya Teplotechnika, **10**, pp. 36–38 (in Russian).

[8] Repukhov, V. M., and Neduzhko, A. I., 1989, "The Effectiveness of Gas-Steam and Liquid Thermal Screen Behind a Tangential and Inclined Slots," Promyshlennya Teplotechnika, **11**, pp. 31–37 (in Russian).

[9] Terekhov, V. I., and Pakhomov, M. A., 2004, "The Study of Structure, Heat and Mass Transfer in the Gas-Droplet Near-Wall Jet in a Tube," *Proceedings of*

the Third International Symposium on Two-Phase Flow Modelling and Experimentation, Pisa, Italy, CD-ROM, Paper No. VEN 11.
[10] Terekhov, V. I., and Pakhomov, M. A., 2004, "The Modeling of a Tube Flow With Injection of Near-Wall Non-Isothermal Turbulent Gas-Droplets Jet," *Proceedings of the Fifth International Conference on Multiphase Flow ISMF-2004*, Yokohama, Japan, CD-ROM, Paper No. 135.
[11] Terekhov, V. I., and Pakhomov, M. A., 2005, "The Thermal Efficiency of Near-Wall Gas-Droplets Screens. I. Numerical Modeling," Int. J. Heat Mass Transfer, **48**, pp. 1747–1759.
[12] Li, X., and Wang, T., 2006, "Simulation of Film Cooling Enhancement With Mist Injection," ASME J. Heat Transfer, **128**, pp. 509–519.
[13] Terekhov, V. I., Sharov, K. A., and Shishkin, N. E., 1999, "An Experimental Study of Gas-Steam Mixing With a Near-Wall Gas-Drop Jet," Thermophys. Aeromechanics, **6**, pp. 331–339.
[14] Terekhov, V. I., Sharov, K. A., and Shishkin, N. E., 2003, "Heat Shielding Characteristics of Gas-Droplets Screens in a Vertical Channel," Izvestia Rossiyskoy Akademii Nauk., Ser. Energetika, pp. 111–119 (in Russian).
[15] Terekhov, V. I., Pakhomov, M. A., Sharov, K. A., and Shishkin, N. E., 2005, "The Thermal Efficiency of Near-Wall Gas-Droplets Screens. II. Experimental Study and Comparison With Numerical Results," Int. J. Heat Mass Transfer, **48**, pp. 1760–1771.
[16] Talmor, E., and Weber, N., 1970, "Foreign-Gas Film Cooling Along Nonconverging and Converging Walls at Various Free-Stream Turbulence Levels," *Proceedings of the Fourth International Heat Transfer Conference IHTC-4*, Paris, France, Paper No. FC-8.7, pp. 1–11.
[17] Li, X., and Wang, T., 2007, "Effects of Various Modeling Schemes on Mist Film Cooling Simulation," ASME J. Heat Transfer, **129**, pp. 472–482.
[18] Li, X., and Wang, T., 2006, "Two Phase Flow Simulation of Mist Film Cooling With Different Wall Heating Conditions," *Proceedings of the 13th International Heat Transfer Conference*, Sydney, Australia, Aug. 13–18, Paper No. MPH-46, p. 12.
[19] Ishii, M., 1975, *Thermo-Fluid Theory of Two-Phase Flows*, Eyrolles, Paris.
[20] Drew, D. A., 1983, "Mathematical Modeling of Two-Phase Flow," Annu. Rev. Fluid Mech., **15**, pp. 261–291.
[21] Shraiber, A. A., Gavin, L. B., Naumov, V. A., and Yatsenko, V. P., 1990, *Turbulent Flows of Gas Suspensions*, Hemisphere, New York.
[22] Volkov, E. P., Zaichik, L. I., and Pershukov, V. A., 1994, *Numerical Modeling of Combustion of Solid Fuels*, Nauka, Moscow (in Russian).
[23] Crowe, C. T., Sommerfeld, M., and Tsuji, T., *Fundamentals of Gas-Particle and Gas-Droplet Flows*, CRC, Boca Raton, FL.
[24] Derevich, I. V., 2002, "The Hydrodynamics and Heat Transfer and Mass Transfer of Particles Under Conditions of Turbulent Flow of Gas Suspension in a Pipe and in an Axisymmetric Jet," High Temp., **40**, pp. 78–91.
[25] Terekhov, V. I., and Pakhomov, M. A., 2004, "The Numerical Modeling of the Tube Turbulent Gas-Drop Flow With Phase Changes," Int. J. Therm. Sci., **43**, pp. 595–610.
[26] Terekhov, V. I., and Pakhomov, M. A., 2006, "Numerical Study of the Near-Wall Droplet Jet in a Tube With Heat Flux on the Surface," J. Appl. Mech. Tech. Phys., **47**, pp. 1–11.
[27] Abramovich, G. N., Girshovich, T. A., Krasheninnikov, S. Yu., Sekundov, A. N., and Smirnova, I. P., 1984, *The Theory of Turbulent Jets*, Nauka, Moscow (in Russian).
[28] Mastanaiah, K., and Ganic, E. N., 1981, "Heat Transfer in Two-Component Dispersed Flow," ASME J. Heat Transfer, **103**, pp. 300–306.
[29] Hwang, C. B., and Lin, C. A., 1998, "Improved Low-Reynolds-Number k-$\tilde{\varepsilon}$ Model Based on Direct Simulation Data," AIAA J., **36**, pp. 38–43.
[30] Haywood, R. J., Nafziger, R., and Renksizbulut, M., 1989, "A Detailed Examination of Gas and Liquid Phase Transient Processes in Convective Droplet Evaporation," ASME J. Heat Transfer, **111**, pp. 495–502.
[31] Brailovskaya, I. Yu., and Chudov, L. A., 1962, "Solving the Boundary Layer Equations With Using Finite-Difference Technique," Vychislitelnye Metody i Programmirovanie, pp. 167–182 (in Russian).
[32] Fletcher, C. A. J., 1988, *Computational Techniques for Fluid Dynamics*, Vol. 2, Springer, Berlin.
[33] Lebedev, A. V., and Shvaikovsky, Yu. V., 1965, "Experimental Study Velocity Distribution and Turbulence Characteristics in the Gas Screen," High Temp., **3**, pp. 569–576.
[34] Hartnett, J. P., Eckert, E. R. G., and Birkebak, R. C., 1961, "Velocity Distribution, Temperature Distributions, Effectiveness, and Heat Transfer for Air Injected Through Tangential Slot Into a Turbulent Boundary Layer," ASME J. Heat Transfer, **83**, pp. 293–306.
[35] Seban, R. A., and Back, L. H., 1962, "Velocity and Temperature Profiles in Turbulent Boundary Layers With Tangential Injection," ASME J. Heat Transfer, **84**, pp. 255–265.

Modeling Frost Growth for Subcooled Tube-Array Configurations

V. Yadav[1]
e-mail: v.yadav@auckland.ac.nz

C. G. Moon
e-mail: c.moon@auckland.ac.nz

Department of Mechanical Engineering,
The University of Auckland,
Auckland 1142, New Zealand

K. Kant
Former Professor
Department of Mechanical Engineering,
Indian Institute of Technology Kanpur,
Kanpur 208 016, India
e-mail: keshav@iitk.ac.in

Methodology for predicting frost growth trends on a subcooled cylindrical surface is developed and implemented for multitube array configuration. Extension of conventional analysis and a novel technique for understanding frost formation phenomenon on the cylindrical surfaces is proposed; later one takes into account the nonsteady temperature field, which affects the density and thermal conductivity at a local level in the growing frost mass, for more accurate prediction of thermal resistance. The influence of migration of liquid water due to tortuosity effect is also considered. The results due to new model are found to be in good agreement with the data in the open literature. Data for frost thickness ratio (FTR) versus time for a section of array with four (tube) rows in the airstream are presented and thoroughly analyzed. The trends of FTR noted are complex and considerably dependent on the tube location, temperature of subcooled surface (T_s), airflow velocity (U_a), and the relative humidity (RH_a) values. Approximate ranges for important parameters are $-30 \leq T_s \leq -5.0°C$, $1.0 \leq U_a \leq 5.0$ m/s, and $0.20 \leq RH_a \leq 0.80$. Presented analysis and the results are valuable in order to predict probable locations and precursors to partial or complete choking of airflow passages due to frost deposition in the evaporator coils. [DOI: 10.1115/1.3082424]

Keywords: frost thickness, cylindrical surface, multitube array, frost thickness ratio (FTR)

1 Introduction

Owing to the multitude of parameters involved, frost formation phenomenon is quite complex to study even for simple subcooled surface geometries. Literature reveals considerable amount of ongoing research to correlate some of the vital frost development characteristics such as thickness, temperature, mass, and heat flux with input parameters such as relative humidity of air and temperature of the cold plate/surface. There are two basic categories into which the major activities can be divided. The first category concerns with microlevel analysis of moisture/water deposition process primarily at simple (flat) subcooled surface including water mass diffusion within frost structure [1–4]. Second category extends analysis to realistic surface geometries and thermal and flow conditions occurring inside the heat transfer equipments [5–13]. A categorical review of literature is given below.

A simplified model for estimating thickness of frost deposition at a flat subcooled surface was proposed considering the square root of time and the temperature difference between the flat cold surface and the frost surface as major parameters [14]. The effect of relative humidity was incorporated based on the theory of crystal growth and the ratio of supersaturation. Storey and Jacobi [15] presented an experimental study to assess the influence of streamwise vortices on frost growth in a steady, developing, laminar channel flow. Lee et al. [16] developed the frost maps for surfaces with different hydrophilic characteristics. It was also observed that the hydrophilic surface with a lower dynamic contact angle (DCA) had a lower frost thickness and high density than hydrophobic surface having a higher DCA. Na and Web [17] proposed a mathematical relation for calculating the supersaturated water vapor density at the frost surface employing boundary-layer analysis. Tanda and Fossa [18] experimentally investigated frost growth on a plate in a vertical channel under free convection. A useful correlation was proposed accounting for important frost growth parameters. Kwon et al. [19] investigated a flat plate with cooling modules at the central region to determine the heat and mass transfer characteristics of the humid airflow under frosting conditions. Sherif et al. [20] developed a continuous differential model to estimate the temperature and thickness of the frost layer using a convective heat transfer correlation and the Lewis analogy to compute mass and enthalpy transfer coefficients. Abdel-Wahed et al. [21] determined the factors that influenced frost formation on a cold surface and correlated the Nusselt number and Sherwood number with these factors.

On the other hand, Raju and Sherif [22] proposed a transient model to predict the frosting process over a circular cylinder in a cross-flow of the humid air employing a numerical solution of the momentum, energy, and diffusion boundary-layer equations along with the continuity equation and using a finite difference scheme. Anderson and Reider [23] presented finite difference method for computing the solutions of the incompressible Navier–Stokes equations for flow around a circular cylinder in two dimensions. Comparison of the results is presented due to methods along with order of accuracy as well as effectiveness of the vorticity and far field boundary conditions. Ismail et al. [24] described numerical solution for a two-dimensional flow based on frost formation model, which permitted the evaluation of the local properties during the process. Heat and mass transfer coefficients were determined by solving the flow, temperature, and humidity fields. Sengupta et al. [25] carried out an experimental investigation and developed empirical correlation based on the frost thickness-time history and the heat transfer coefficient-time history for a cylinder in humid air cross-flow. Lee and Ro [26] carried out experimental investigation to understand frost formation process on a horizontal cylinder under cross-flow condition. It was observed that higher air temperature caused a thicker frost layer formation, which was also interpreted as a unique characteristic of the frost formation process under the low air humidity conditions. Szczepanik et al.

[1]Corresponding author.

Contributed by the Heat Transfer Division of ASME for publication in the JOURNAL OF HEAT TRANSFER. Manuscript received December 2, 2007; final manuscript received December 6, 2008; published online March 31, 2009. Review conducted by S. A. Sherif.

[27] reported numerical investigation to characterize heat transfer from a cylinder in cross-flow. The experimental data were compared with the results from standard k-ω turbulence model as well as k-ω model. Tso et al. [28] presented an analytical model to predict the dynamic behavior of an air-cooler both under nonfrost and frost conditions. The equations for finned tube heat exchanger were derived for non-steady-state manner and quasisteady state in the frost model. In order to evaluate the frost behavior of a fin-tube heat exchanger under frosting conditions, Yang et al. [29] proposed a mathematical model. The empirical correlations of the heat transfer coefficients for the plate and tube surfaces and a diffusion equation for the frost layer were used for this purpose.

Methodologies available for estimating frost deposition over cylindrical geometries invariably use computational fluid dynamics (CFD) based flow solving techniques to numerically obtain the flow, thermal, and psychrometric (such as humidity ratio) fields, which in conjunction with available empirical/semi-empirical frost property relationships are used to compute frost growth rate, etc. As far as multitube array geometries are concerned, an inherent problem with such a methodology is that CFD solutions are quite fumbling for real unsteady flow scenario requiring sequential multi-property-field evaluation while solid boundaries are constantly being altered. Furthermore, a careful review of models available brings out the fact that most of the constants and input parameters used during calculations for frost deposition process are dynamic variables when dealing with an array of subcooled surfaces.

The first and crucial objective is to explore available approaches for modeling frost formation phenomenon over a subcooled surface with flat as well as cylindrical surface geometries for suitability to handle multiple cylindrical surface geometries, which occur in a tube array with subcooled surfaces under the widest possible range of flow and thermal conditions. Second, it is necessary to develop an implementation scheme for evaluating frost thickness in an array of subcooled tube surfaces. An available conventional analysis is extended for determining frost layer thickness and deposition rate on flat plate/surfaces to the cylindrical/tube geometry and its efficacy is also determined using the literature data. A novel method for obtaining frost growth rate at the cylindrical surfaces is proposed, which takes into account the thermal resistance of developing frost layers and any variation into it because of change in local frost density and thermal conductivity due to nonsteady temperature field within the growing frost mass and apparent motion of water within the frost layer. Time varying local heat and mass transfer coefficients are estimated and, after incorporating the effect of tortuosity factor, they are subsequently used for evaluating the increment in frost thickness around the tube. Current work assumes axisymmetrical frost growth pattern. The results due to the new model were found to be in excellent agreement with the data in literature for a similar range of input parameters. The analysis has been extended to determine frost growth characteristics on a four-row tube array; trends in data are presented and thoroughly analyzed. The presented information is helpful in accurately understanding frosting phenomenon in the evaporator/chiller coils.

2 Common Modeling Propositions

The presented analysis is based on following propositions regarding frost formation and growth on a cold surface.

1. Inside the frost layer the temperature and pressure are in quasisteady state [22].
2. The air in the vicinity of the frost surface is under supersaturated condition [11,12].
3. Heat conduction and blackbody radiation through a very thin frost layer are one dimensional [1,3].
4. The heat flux by the radiation and forced air enthalpy transport are negligible as compared with the thermal conductivity of the air-ice structure and the latent heat release of water vapor [3,17].
5. Total heat transfer from moist air to the subcooled surface is via convection at the frost surface and conduction inside the frost layers.
6. The frost growth rate is dependent on cold surface temperature and psychometric properties of the humid air [26,18].
7. Density of the developing frost layer is found to be intemperately dependent on the flow velocity of the airstream [25].
8. Frost density and thermal conductivity at a location are functions of the frost temperature [30,31].

2.1 Single Tube With Subcooled Surface. Conventional analytical strategy formally providing an expression for time versus frost thickness relationship and subsequent corrective measures to include the effect of the temperature of the airstream is presented in Sec. 2.1.1. An inherent limitation is the consideration of only mean values for physiothermal properties for deposited frost bulk. A scope of further refinements in the analysis is explored in Sec. 2.1.2. The frost deposition at a given time is analyzed assuming variation in the local frost density and thermal conductivity. The technique potentially incorporates the influence of tortuosity in the evolving frost structure. A function is proposed based on the data from literature, to split up instantaneous heat transfer into latent and sensible heat transfer fractions; the former quantity is then used for evaluating alternations in frost structure including changes in thickness, etc.

Note that, during frosting process, the temperature distribution within the frost mass changes, which develops susceptibility for change in the frost density. The lower side frost temperature (toward the subcooled surface) results in a higher value of frost density, owing to physically rigid nature of frost structure. The mentioned susceptibility virtually leads to attraction of moisture from the layers above (at relatively higher temperature). The resulting increase in the structural density at the local level alters the thermal conductivity at the same level and the effect gets modulated due to variation in local temperature distribution occurring inside due to addition of frost layers at the top.

2.1.1 Conventional Basis With Mean Equivalent Thermal Resistance (Model-1). Let us assume a cylindrical tube surface of radius R with subzero temperature T_s, with a frost layer of uniform thickness X existing at the surface. Consider a conical needlelike portion of the frost suspending an angle $\Delta\theta$ at the center/axes of cylindrical surface as shown in Fig. 1. As the water vapor of mass ΔM_w sublimates at the top of the needle, this increases the frost needle height by ΔX. The amount of the heat delivered during condensation is [14]

$$\Delta Q_s = h_s \rho_l A_X \Delta X = h_s \rho_l \left(1 + \frac{X}{R}\right) A_s \Delta X \tag{1}$$

where h_s is the latent heat of sublimation and ρ_l is the density of ice water. The latent heat of sublimation was evaluated as

$$h_s = h_{fg} + h_{\text{vap}} \tag{2}$$

where h_{fg} and h_{vap} are the enthalpy of fusion and enthalpy of vaporization, respectively. Taking frost surface to be at temperature T_f, the amount of heat conducted through the needle, ΔQ_s, due to the temperature difference $(T_f - T_s)$ is

$$\Delta Q_s = \frac{T_f - T_s}{R_{\text{eq}}} A_X \Delta t \tag{3}$$

where A_X is the effective surface area at which moisture deposition occurs. Also, the equivalent thermal resistance for the entire bulk of cylindrical frost structure R_{eq} at a given instance (X being the frost layer thickness) can be written as

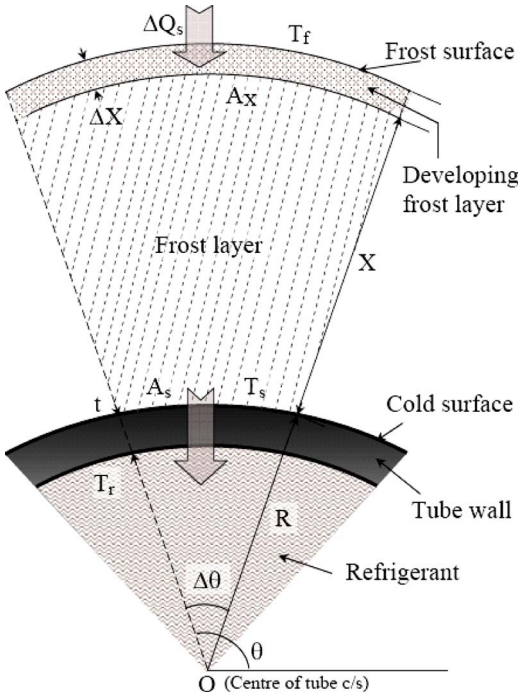

Fig. 1 Schematics for a conical needlelike portion

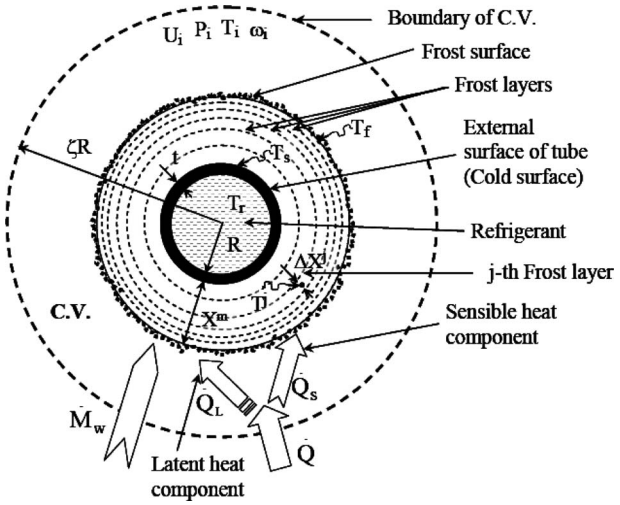

Fig. 2 Schematics of internal control volume

$$R_{eq} = \frac{X}{k}\ln\left(1+\frac{X}{R}\right) \tag{4}$$

The use of Eqs. (1) and (4) in Eq. (3) gives

$$\Delta Q_s = \frac{T_f - T_s}{\ln\left(1+\frac{X}{R}\right)}\left(\frac{R+X}{RX}\right)c_0 k_f A_s \Delta t \tag{5}$$

where $c_0 k_f$ represents thermal conductivity for ice water.

Equations (1) and (5) give

$$X\ln\left(1+\frac{X}{R}\right)\Delta X = \frac{c_0 k_f}{h_s \rho_l}(T_f - T_s)\Delta t \tag{6}$$

Application of limit $\Delta t \to 0$ gives

$$\frac{dX}{dt} = \frac{c_0 k_f (T_f - T_s)}{h_s \rho_l X \ln\left(1+\frac{X}{R}\right)} \tag{7}$$

Integration of Eq. (7) results in the following relation:

$$t = \frac{h_s \rho_l}{4c_1 k_f (T_f - T_s)}\left[2(X^2 - R^2)\ln\left(1+\frac{X}{R}\right) - X^2 + 2XR\right] \tag{8}$$

Note that coefficient c_1 can also incorporate the effect of flow velocity of airstream.

In order to incorporate the effect of air humidity to degree of supersaturation, the mass transfer rate $\dot{M}_w$ can be written based on a relation by McCabe and Smith [32] as follows:

$$\dot{M}_w = c_3(R_s - 1)^n \tag{9}$$

where R_s is the ratio of supersaturation.

The condensation rate of water vapor at the top of the frost (needle) cone is given as

$$\dot{M}_w = c_4\left(\frac{p - p_f'}{p_e'}\right)^n = c_5[X^2 + 2XR] \tag{10}$$

where p_f' is the pressure of saturated water vapor condensing at the temperature T_f at the frost surface. From the experimental data over a plain surface, it would be appropriate to take $n \simeq 0.25$ [14].

For the case of saturated air, pressure p is replaced with the pressure p' of the saturated vapor such that

$$\dot{M}_w = c_4\left(\frac{p' - p_f'}{p_f'}\right)^n = c_5[X'^2 + 2X'R] \tag{11}$$

Equations (10) and (11) give

$$X^2 + 2XR - \Pi = 0 \tag{12}$$

where

$$\Pi = \left[\frac{p - p_f'}{p' - p_f'}\right]^n [X'^2 + 2X'R] \tag{13}$$

Possible solution for Eq. (13) is

$$X = \sqrt{R^2 + \Pi} - R \tag{14}$$

In order to incorporate the effect of the temperature of airstream, T, Eq. (14) can be modified [14] as

$$X = [\sqrt{R^2 + \Pi} - R]\left[1 + 0.052\left(\frac{T - T_M}{T_M - T_w}\right)\right] \tag{15}$$

where T_M is the melting point of water-ice mixture. Under the condition $T \leq T_M$ Eq. (14) can be directly used.

2.1.2 Latent Heat-Ratio Model (Model-2). On one hand relative magnitudes of latent heat gain and sensible heat gain are considerably dependent on structural and physiothermal properties of the frost layer; and, on the other hand, the total thickness of the frost layer along with cumulative effect of inside physical structure dictates the magnitude of total heat gain to the cold surface from the surroundings [17,33].

Let us assume that the deposited frost structure (see Fig. 2) is constituted by j number of concentric sublayers with total thermal resistance

$$(R_{th})_{frost} = \sum_{k=1}^{j} R_{th}^k \tag{16}$$

where thermal resistance of the jth layer, R_{th}^k, can be written as

$$R_{th}^j = \frac{\Delta X^j}{2\pi W(R + X^{j-1})k^j} \tag{17}$$

The thermal conductivity of the jth sublayer, k^j, can be evaluated

Table 1 Details of property correlations used for model implementation purposes

Material	Property	Relation	Source
Dry air	Thermal conductivity	$k_{air}=(0.001968+8.15)\times10^{-5}T$, T in K	[1]
	Density	$\rho_{air}=\dfrac{344.9}{T}$, T in K	
Humid air	Humidity ratio	$\omega=0.6218\dfrac{p_{v,sat}}{p_{total}-p_{v,sat}}$	
	Vapor saturation pressure	$\ln(p_{v,sat})=\dfrac{C_1}{T}+C_2+C_3T+C_4T^2+C_5T^3+C_6T^4+C_7\ln(T)$ where T is in K and $C_1=-5674.5359$, $C_2=6.392547$, $C_3=-0.9677843\times10^{-2}$, $C_4=0.62215701\times10^{-6}$, $C_5=0.20747825\times10^{-8}$, $C_6=-0.9484024\times10^{-12}$, and $C_7=4.1635019$	[35]
	Specific heat	$c_{p\beta}=2116.56+7.2845T$, T in K	
	Density	$\rho_\beta=[1.0907\times10^{-3}+1.4635\times10^{-7}T]^{-1}$, T in K	
Porous frost layer	Thermal conductivity	$k_{eff}=(0.02422+7.214)\times10^{-4}\rho_f+1.1797\times10^{-6}\rho_f^2$, ρ_f is in kg m^{-3}	[33]
Properties used for nondimensionalization (at the start)	Frost density	$\rho_{fo}^*=92.84$ kg m^{-3}	[36]
	Thermal conductivity	$k_{eff}^*=0.245$ W m^{-1} K^{-1}	
	Specific heat	$C_{Pfo}^*=\dfrac{k_{eff}^*}{\alpha_{eff}^*\rho_{fo}^*}=912.28$ J kg^{-1} K^{-1}	
	Frost layer thickness	$\delta_0^*=0.0029$ m	

using appropriate expression from Table 1.

Total thermal resistance for the heat energy being transferred from moist air into the refrigerant flowing inside the tubes can be given as

$$(R_{th})_{total}=(R_{th})_{refrigerant}+(R_{th})_{tube\text{-}wall}+(R_{th})_{contact}+(R_{th})_{frost}+(R_{th})_{air} \tag{18}$$

The initial heat transfer rate from the tube under zero frost thickness is given by

$$\dot{Q}_0=\frac{T_a-T_r}{(R_{th})_0}$$

where

$$(R_{th})_0=(R_{th})_{refrigerant}+(R_{th})_{tube\text{-}wall}+(R_{th})_{air}$$

When there is a frost layer over the surface, heat transfer rate can be written as

$$\dot{Q}_t=\frac{T_a-T_r}{(R_{th})_{total}} \tag{19}$$

where T_a and T_r are the mean temperatures of air in control volume (C.V.) and that of refrigerant/coolant inside the tube. It is possible to evaluate frost surface and cold surface temperatures by using the following relations:

$$T_f=T_a-\dot{Q}_t(R_{th})_{air}=T_r+\dot{Q}_t[(R_{th})_{refrigerant}+(R_{th})_{tube\text{-}wall}+(R_{th})_{contact}+(R_{th})_{frost}]$$
$$T_s=T_r+\dot{Q}_t[(R_{th})_{refrigerant}+(R_{th})_{tube\text{-}wall}]=T_a-\dot{Q}_t[(R_{th})_{contact}+(R_{th})_{frost}+(R_{th})_{air}] \tag{20}$$

Consider maximum possible latent heat and sensible heat loads occurring for the tube as

$$(\dot{Q}_L)_{max}=\rho_a h_{fg}\omega_a\delta_t WU_a$$
$$(\dot{Q}_S)_{max}=\rho_a C_{p,a}(T_a-T_f)\delta_t WU_i \tag{21}$$

where ω_i is the humidity ratio, δ_t is the thickness of the thermal boundary layer, h_{fg} is the heat of condensation, $C_{p,a}$ is the specific heat of air, U_a is the airflow velocity, and W is the length of the tube.

Latent heat load ratio (ϕ_L) can be evaluated using Eq. (21) as

$$\phi_L=\frac{(\dot{Q}_L)_{max}}{(\dot{Q}_L)_{max}+(\dot{Q}_S)_{max}}=\frac{\omega_a h_{fg}}{\omega_a h_{fg}+C_{p,a}(T_a-T_f)} \tag{22}$$

A new parameter, latent load factor (Φ_L), is introduced as

$$\Phi_L=\Psi(\phi_L) \tag{23}$$

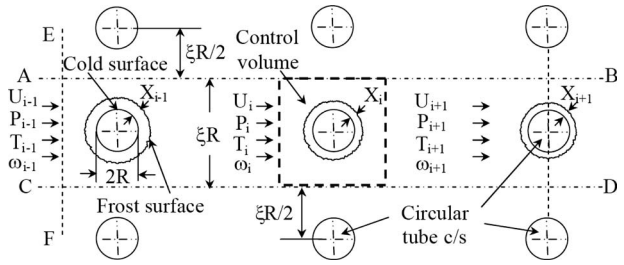

Fig. 3 Schematic of a tube-array section

where we propose function $\Psi = \phi_L^b$, $b = 2.7$.

The rate of frost mass deposition at any instant, $\dot{M}_w$, can be given by

$$\dot{M}_w = \frac{\dot{Q}_t}{h_{fg}} \Phi_L \tag{24}$$

Therefore, the thickness of the jth frost layer ΔX^j deposited over the cylindrical surface of the tube in small time interval Δt is

$$\Delta X^j = \frac{(T_a - T_r)\Phi_L \Phi_{TC} \Delta t}{(R_{th})_{total}^{j-1} h_{fg} \rho_f^{j-1/2} 2\pi (R + X^{j-1}) W} \tag{25}$$

where Φ_{TC} is a tortuosity correction factor, which we propose as

$$\Phi_{TC} = \Phi_0 \left[1 - \ln \left\{ 1 + \left(\frac{\delta_c + \delta_f}{X_f + \delta_f} \right)^3 \right\} \right] \exp(1 - \rho_f^{j-1/2}/\rho_{max})$$

$$\delta_c = \left(\phi_1 + \frac{\Phi_L - \phi_2}{\phi_3} \right) \cdot \phi_{Rt}, \quad \Phi_0 = 0.576, \quad \delta_f = 10^{-5}, \tag{26}$$

$$\phi_1 = 0.03, \quad \phi_2 = 0.20, \quad \phi_3 = 3.70$$

where ρ_{max} is the maximum possible density at frost surface temperature T_f, δ_c is a characteristic thickness of frost layer for which ϕ_1, ϕ_2, ϕ_3, and ϕ_{Rt} are to be determined experimentally, and factor ϕ_{Rt} is found to be numerically equal to the tube radius in meter.

Note that the mean density of the jth frost layer, $\rho_f^{j-1/2}$, can be evaluated as

$$\rho_f^{j-1/2} = a\rho_f^{j-1} + (1 - a)\rho_f^j \tag{27}$$

At the initial stage (i.e., $j = 1$) $a = 1$ is considered while for other stages, a suitable value is assumed such that $0 < a < 1$. Again, the values for ρ_f^j can be evaluated using appropriate expression from Table 1.

3 Implementing Single Tube Model to Multitube Array Configuration

For the fixed cylindrical geometry, both the proposed models essentially require four input parameters, i.e., pressure (P), dry bulb temperature (T), humidity ratio of the moist airstream (ω), and flow velocity (U). Tube arrangement in evaporator or chillers often follows a definite pattern [11], a symmetrical subdivision can be chosen for the analysis. Consider three tubes in succession out of an array of circular tubes as shown in Fig. 3. Although, parameters associated with geometries of each cylindrical surface occurring within the tube array are assumed unaltered; previously mentioned input parameters for single cylindrical geometry become dynamic variables when associated with an array of tubes. The steady cross-flow over the tubes is assumed considering an airflow path (shown between two horizontal lines AB and CD) of width ξR, each drawn midway between the two consecutive tube rows. Similarly, line EF passes midway between the two successive tube columns. Consider a square shape C.V. as shown in Fig. 4. Humid air enters the C.V. at velocity U_i and with properties P_i, T_i, ω_i and leaves at velocity U_{i+1} under state $P_{i+1}, T_{i+1}, \omega_{i+1}$.

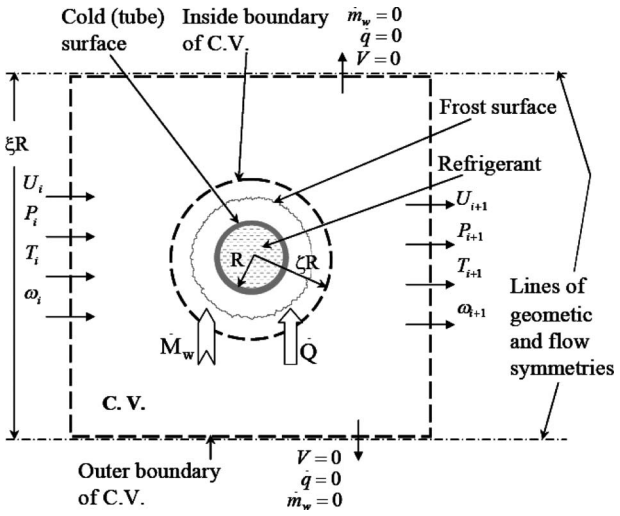

Fig. 4 Schematic of external control volume

Values for U_0, P_0, T_0, ω_0, at the array inlet (i.e., $i = 0$) are the same as for free airstream; however, subsequent values are obtained as

$$U_i = U_{i-1} \frac{(\xi R/2 - X_i)\rho_i}{(\xi R/2 - X_{i-1})\rho_{i-1}}, \quad T_i = T_{i-1} - \frac{(\dot{Q}_t)_{i-1}}{\rho_{i-1} U_{i-1} R \xi W}$$

$$\omega_i = \omega_{i-1} - \frac{(\dot{Q}_t \Phi_L)_{i-1}}{h_{fg} \rho_{i-1} U_{i-1} R \xi W}, \quad P_i = P_{i-1} - (\Delta P)_c \frac{U_{i-1}^2}{\rho_{i-1}} \tag{28}$$

where $(\Delta P)_c$ is the pressure drop coefficient for cross-flow across the a cylinder. Furthermore, Reynolds number and Nusselt number are evaluated using the following relations:

$$\mathrm{Re} = \frac{2 \cdot U_a \cdot (R + X_f)\rho_a}{\mu_a} \tag{29}$$

$$\mathrm{Nu} = c_a \ \mathrm{Re}^{c_0} \ \omega^{c_b} (T_M - T_f)^{c_c} \tag{30}$$

where c_0, c_a, c_b, and c_c are the constants with the values 0.70, 0.04, 0.294, and 0.05, respectively.

Algorithm used for implementing the simulation model and developing the computer code using engineering equation solver (EES) [34] are presented in flowcharts in Figs. 5 and 6, respectively. The complete calculation procedure involves time loop and nested spatial loop. Input to the calculation procedure are the parameters corresponding to ambient air conditions (T_a and ω_a), airflow velocity (U_a), geometrical parameters for the subcooled surface, i.e., tube radius (R) and tube wall thickness (t), tube separation parameter (ξ), and number of tubes (N); either of the refrigerant/coolant temperature (T_r) or outside tube surface temperature (T_s) can be considered as an input parameter.

4 Results and Discussion

4.1 Model Validation for a Single Tube. Comparison of results due to proposed models and data from literature for nearby the same set of input parameters (see Table 2) is presented in Figs. 7–9. Figure 7 presents the cases for the set of input parameters resulting to (final frost thickness) $X_f \leq 5.0$ mm for frost growth time duration, $t \leq 200$ min. The constant c_1 appearing in Model-1 is evaluated using relation $c_1 = \mathrm{Re}^{c_0}$. Each of the frost layers (with thickness) appearing in 1 min interval is used in Model-2 for evaluating thermal resistance and tortuosity effects. It can be observed that results due to Model-2 are in better agreement with the

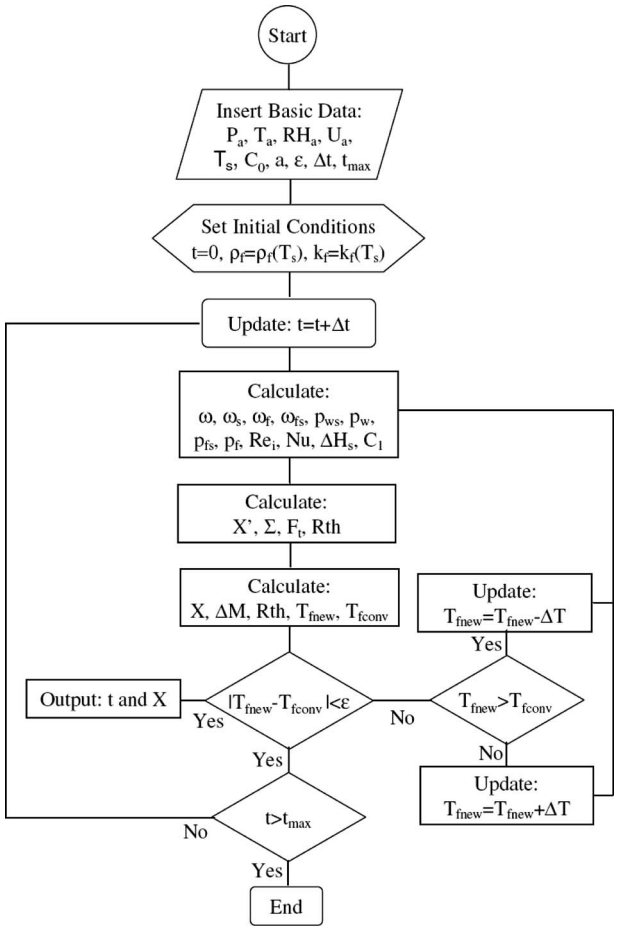

Fig. 5 Algorithm for implementing Model-1

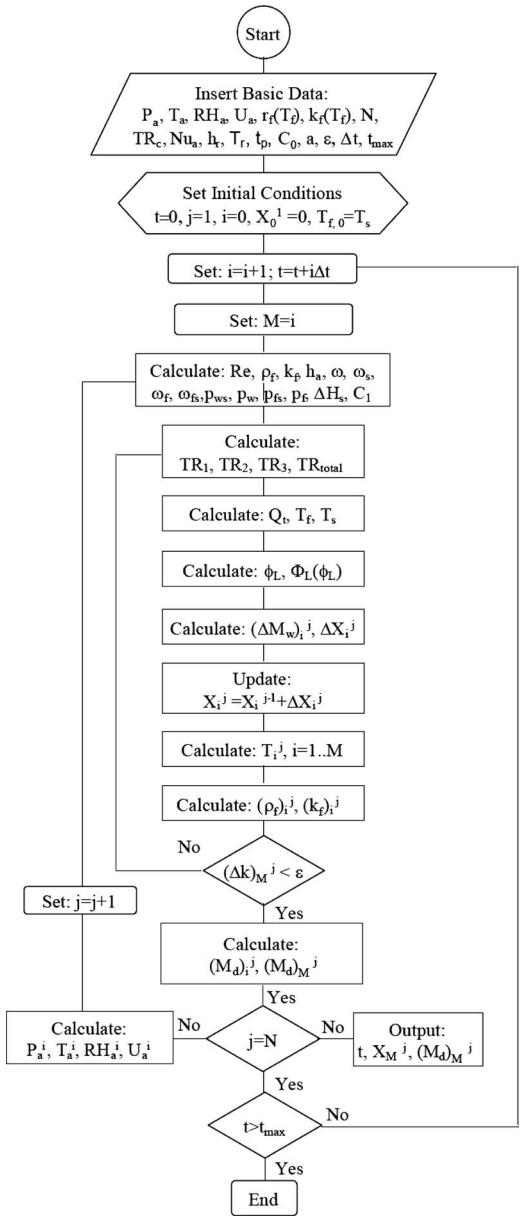

Fig. 6 Algorithm for implementing Model-2

experimental data due to Lee and Ro [26]; excellent agreement is found for the data corresponding to $RH_a=0.2$ (case C-1) typically during the frost deposition period of 30–150 min; agreement within 30% is found for cases C-2 and C-3 during the same time interval. Results due to Model-1 are at the lower side of the corresponding experimental values and maximum deviations are 20%, 30%, and 30% for cases C-1, C-2, and C-3, respectively.

Figure 8 presents the cases for the set of input parameters resulting in $X_f>5.0$ mm; as the deviation between literature and current Model-1 is considerably large (nearby 30%); Model-2 is only considered henceforth. In general, current results are in excellent agreement (within 10%) with the data due to Lee and Ro [26] (case C-5) and Raju and Sherif [22] (case C-6). Agreement is fair for case C-7 (within 8%), for $t>100$ min. For case C-4, comparison is possible for $t\leq 10$ min, where discrepancy in results is averaged around 25%.

Initial phase of frost growth is considered very critical [30]. Results due to the proposed model are closely examined and compared with literature for initial phase of frost growth in Fig. 9. For the first few tens of seconds after the frost accumulation begins, the current model overpredicts the frost thickness, which is unanimously true for all cases; a probable cause may be the underestimated influence of tortuosity. However, typically for $t>5.0$ min, results are in reasonable agreement within 3%, 4%, 12%, and 8% for cases C-8, C-9, C-10, and C-11, respectively, when compared with literature data.

4.2 Results for Leading-Tube in the Array. Results describing the influence of refrigerant/coolant temperature, T_r, relative humidity of air at the inlet, RH_a, and flow velocity of air, U_a, upon the frost thickness pattern at the leading-tube of the tube array are presented in Figs. 10 and 11. It can be observed from Fig. 10 that at $U_a=1.0$ m/s and $RH_a=0.40$, decrease in T_r from $-10°C$ to $-30°C$ results in more than 25% increase in frost thickness in the time interval ($10\leq t\leq 500$ min). Trends are nearby the same for $RH_a=0.80$ values; however, for the case when $RH_a=0.60$, for $t<300$ min, lower surface temperature results in only marginally increased value (less than 3%) of frost thickness and the trend is reversed for $t>300$ min when frost thickness is found to be more (greater than 10% in the considered time interval) for higher T_r value. A probable explanation for observed patterns is a complex interplay between the tortuosity factor and variable thermal resistance of the deposited layer (due to variation in frost thickness and density). It is also interesting to observe that for RH_a values on the lower side the trend in the time versus frost thickness curves is nearby parabolic for the entire time domain; however, for the larger RH values, the curves initially (for one-third of the considered time interval) follow a parabolic pattern typically; subsequently linearity dominates. Furthermore, slope for the linear portion of the curves is large at a lower T_r value.

Table 2 Parametric values used from literature

No.	Tube radius, R (m)	Inlet airflow velocity, U (ms^{-1})	Inlet air relative humidity (RH)	Surface temperature, T_s (°C)	Inlet air temperature, T_a (°C)	Source
C-1	0.07	1.137	0.2041	−17.0	20.3	[26]
C-2	0.07	1.111	0.2856	−17.0	16.5	[26]
C-3	0.07	1.852	0.3484	−17.0	9.2	[26]
C-4	0.0254	4.4	0.41	−15.0	29.0	[25]
C-5	0.07	1.853	0.4795	−17.0	9.6	[26]
C-6	0.0254	3.74	0.3653	−13.15	28.7	[22]
C-7	0.07	1.072	0.4211	−17.0	9.9	[26]
C-8	0.0254	3.74	0.5855	−13.15	28.7	[22]
C-9	0.0254	1.87	0.5855	−13.15	28.7	[22]
C-10	0.0254	3.74	0.5855	−7.54	28.7	[37,22]
C-11	0.0254	3.74	0.5859	−8.0	15.0	[24]

The trends for frost layer growth at the leading-tube of array for flow velocity of 5.0 m/s; RH_a=0.40, 0.60, and 0.80; and T_r= −10°C and −30°C are shown in Fig. 11. It can be observed that rate of increase in frost thickness increases with increase in air RH_a and/or decrease in refrigerant/coolant temperature; increment in frost thickness is found to be more than 50% as T_r decreases

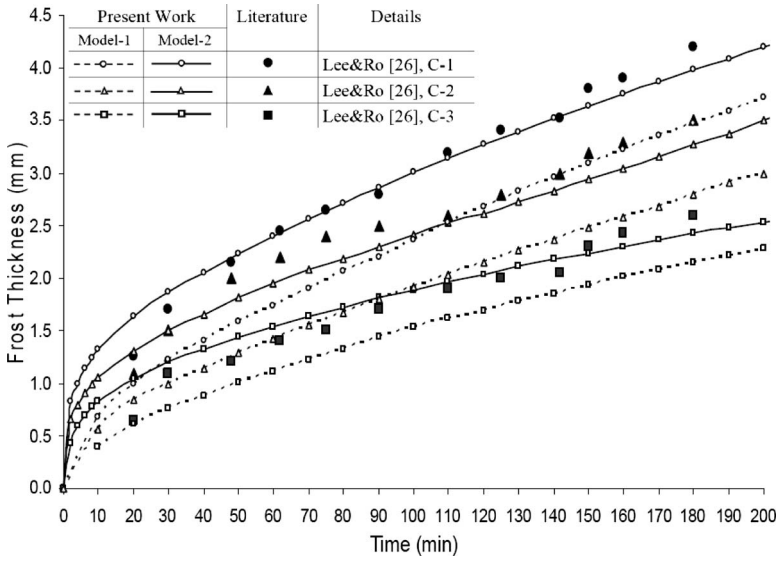

Fig. 7 Comparison of frost growth trends from Model-1 with literature

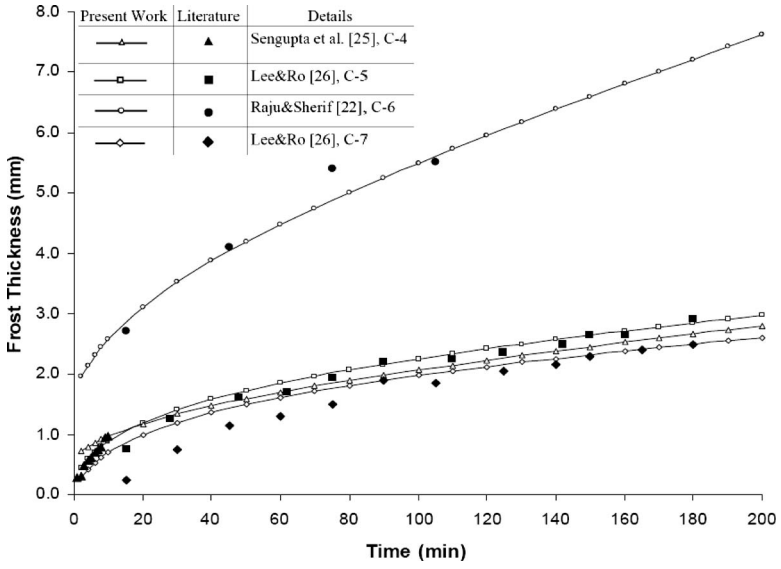

Fig. 8 Comparison of frost growth trends from Model-2 with literature

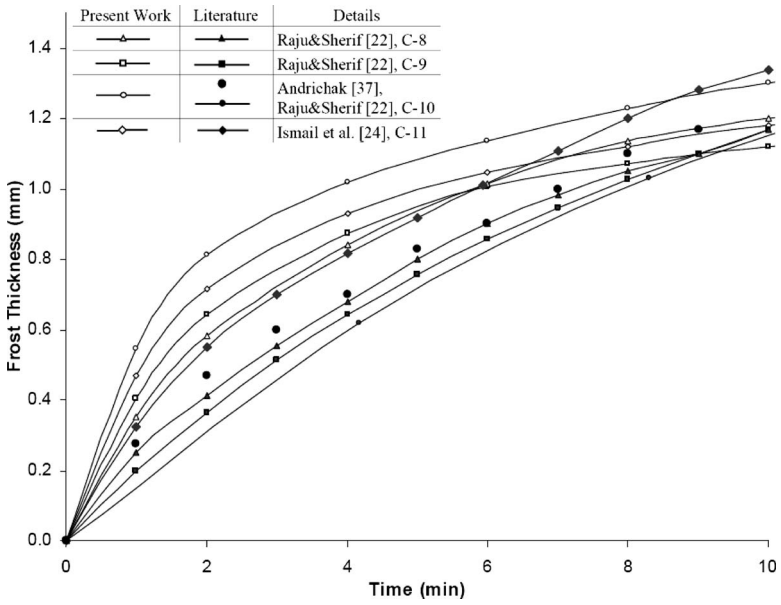

Fig. 9 Comparison of frost growth trends for initial period (from Model-2) with literature

from −10°C to −30°C; similarly growth in frost layer is rapid by as much as 300% as the RH_a for air increases from 0.40 to 0.80. Overpattern in the curve can be divided into paraboliclike and linear portions; however, as compared with the previous case of low flow velocity, in the current case parabolic trend occurs for a relatively shorter period typically less than a quarter of the total interval considered. The paraboliclike portion in the trend curves occurs for a shorter period as RH_a for air increases.

4.3 Results for Multitube Array. Representative trends for variation in ratio of instantaneous frost thickness at second, third, and fourth tube rows in the array to that at the leading-tube (i.e., FTR) are presented in Figs. 12–15 for the various values of temperature and velocity and $t_{max}=500$ min.

Figures 12(*a*)–12(*c*) show trends in the FTR values corresponding to $RH_a=0.40$, 0.60, and 0.80, respectively, and $U_a=1.0$ m/s, $T_r=-10°C$. In general, as FTR<1.0, the thickness of the frost layer deposited on the tubes located at the downstream side of airflow is less than that occurring at the leading-tube; possibly due to the fact that humidity ratio (ω_i) for the air at the downstream side reduces due to frost deposition on the upstream tube surfaces. Overall trends can generally be divided into two distinct phases; first or initial phase, which occurs for relatively short time period ($t\leq 100$ min) can be characterized with sharp rise in FTR; for instance, at $RH_a=0.40$, FTR increases by as much as 15%, 30%, and 45% for second, third, and fourth rows, respectively, toward the end. In the second phase only moderate rise in FTR is observed; (at $RH_a=0.40$) typically by 3%, 4%, and 7% for second, third, and fourth rows, respectively, in the time period $100<t\leq 500$ min. It is also observed that the relative order of FTR values for second, third, and fourth rows may not essentially be the same for the two phases. Note that in the first phase, the maximum and the minimum values for FTR correspond to second and fourth rows of tubes, respectively (irrespective of RH_a values); however, in the second phase, maximum and minimum FTR values occur for fourth and second rows, third and fourth rows, and second and fourth rows for $RH_a=0.40$, 0.60, and 0.80, respectively.

Figure 13 shows trends in the FTR values for $U_a=1.0$ m/s and

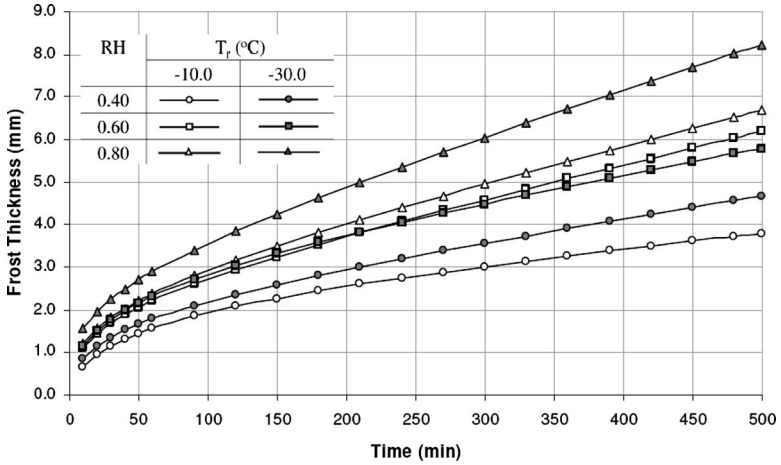

Fig. 10 Trends for frost layer development at leading-tube surfaces for flow velocity $U_a=1.0$ m/s

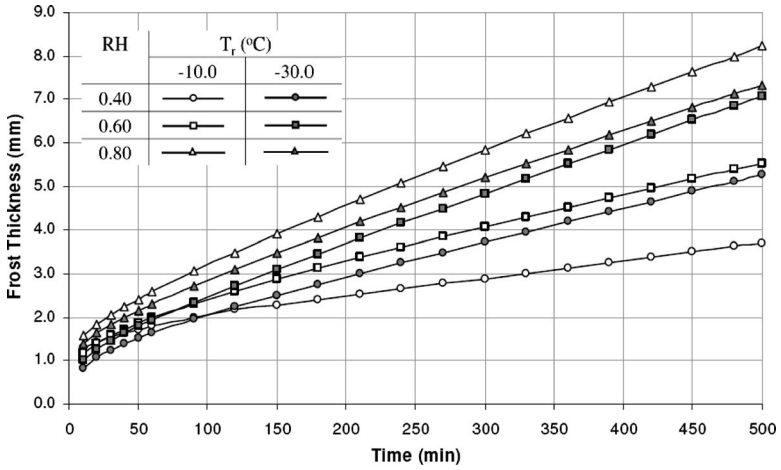

Fig. 11 Trends for frost layer development at leading-tube surface for flow velocity U_a=5.0 m/s

T_r=−30°C. Trends for the first phase are independent of RH_a and are nearby identical to that discussed previously; however, in the second phase, composite trend is followed by curves corresponding to the fourth row. For RH_a=0.40 and $t>200$ min, with the progress of frost deposition process, the curve representing the FTR pattern at the fourth row tube shifts toward and then overlaps with the FTR trend curve for the third row; as RH_a increases to 0.60, FTR curve for the fourth row tube shifts toward the second row curve; further increase in RH_a to 0.80 results in shift in the third row FTR curve toward that corresponding to the second row; toward the end of the considered time interval, the third row FTR value is about 0.5% higher than the second row FTR value.

Figure 14 shows FTR trends corresponding to U_a=5.0 m/s and T_r=−10°C. For RH_a=0.40, FTR patterns are considerably different from all previously discussed cases. In this particular case, minimum and maximum FTR values correspond to second and fourth rows, respectively; there is no crossover in the curves. FTR is found to gradually increase with time; toward the end of the considered time interval, there is nearby 18%, 43%, and 75% increase in FTR values for second, third, and fourth rows, respectively. At a given instance, change in FTR or strong deviation in FTR from unity for any particular row is indicative of a large difference in frost layer thickness as compared with that at the leading-tube. The FTR pattern as observed is an apparent stretching of the previously discussed first phase (occurring in Figs. 12 and 13 for $0<t<100$ min) for overall available time interval. The FTR pattern for RH_a=0.60 can again be divided into two phases as discussed in cases with U_a=1.0 m/s; when compared with the frost thickness value at the leading-tube toward the end of the time interval, the frost thickness value at all three tube rows is nearby 2% lower. For RH_a=0.80, frost thickness value for all three tube rows toward the end of the interval has less than 5% deviation when compared with that for the leading row; FTR values for the second row is maximum, closely followed by values for the third and fourth rows (within 5% difference).

Figure 15 shows FTR trends for U_a=5.0 m/s, T_r=−30°C. In general, within 1 h of the start of the frost deposition process, FTR values for all tubes at the downstream side approach the value very close to typically, within the difference of 5%, to the FTR

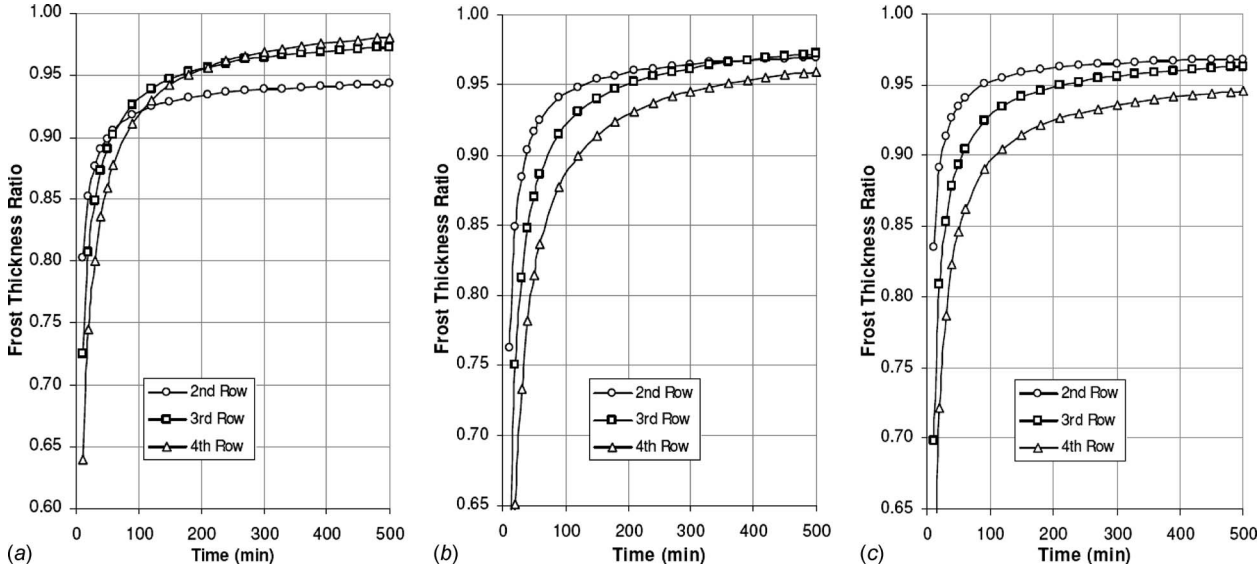

Fig. 12 Trends in frost thickness ratio for tubes in succession at U_a=1.0 m/s and T_r=−10.0°C for RH_a values of (*a*) 0.40, (*b*) 0.60, and (*c*) 0.80

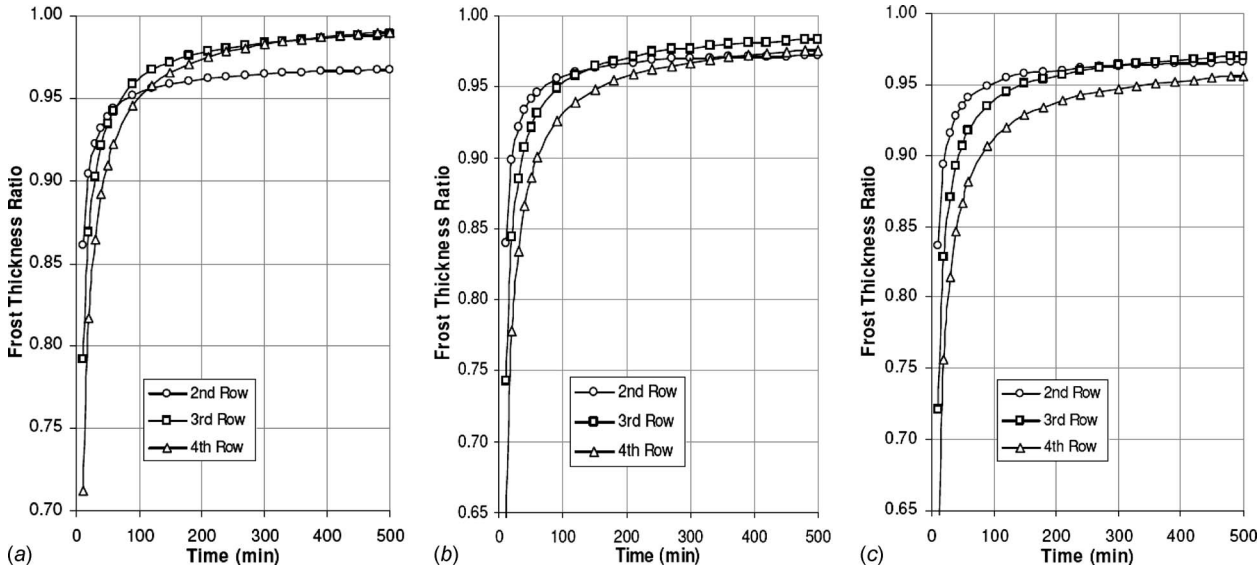

Fig. 13 Trends in frost thickness ratio for tubes in succession at U_a=1.0 m/s and T_r=−30.0°C for RH_a values of (*a*) 0.40, (*b*) 0.60, and (*c*) 0.80

values at the leading-tube; note that for the previous case of U_a = 1.0 m/s under similar parametric conditions, the corresponding difference was more than 10%.

5 Conclusions

Two new models for determining frost growth on the cylindrical surfaces have been developed. The first model (M-1) is an attempt to branch out existing analytical technique for determination of frost deposition on flat subcooled surfaces to cylindrical geometry; it basically deals with deposited frost mass using mean density and thermal conductivity and incorporates the effect of air temperature at a different stage of calculation. The second model (M-2) is a novel approach, which assumes overall frost layer as an aggregation of very thin layers each with time variable density and thermal conductivity; tortuosity factor has been introduced through tortuosity function.

When compared with the data from literature the performance of Model M-2 was found to be comparable with Model M-1. Subsequently, Model M-2 was implemented in order to determine frost growth pattern for a multitube array configuration resembling conventional evaporators and chillers. Frost thickness data for a four-row tube array were obtained and critically analyzed for a period of 500 min. Under identical thermal conditions at subcooled surfaces, the relative frost growth rate at tubes was found to be significantly dependent on the airflow velocity and inlet air RH value. Considerable variation in frost deposition rate (leading to as much as 40% difference in FTR values) occurred at the subcooled tube surfaces at the downstream location during the start of the frosting process. Furthermore, the frost layer thickness value for downstream rows approach around 90% and 95% close to the corresponding values at the leading-tube for airflow velocities of 1.0 m/s and 5.0 m/s, respectively. The frost formation mod-

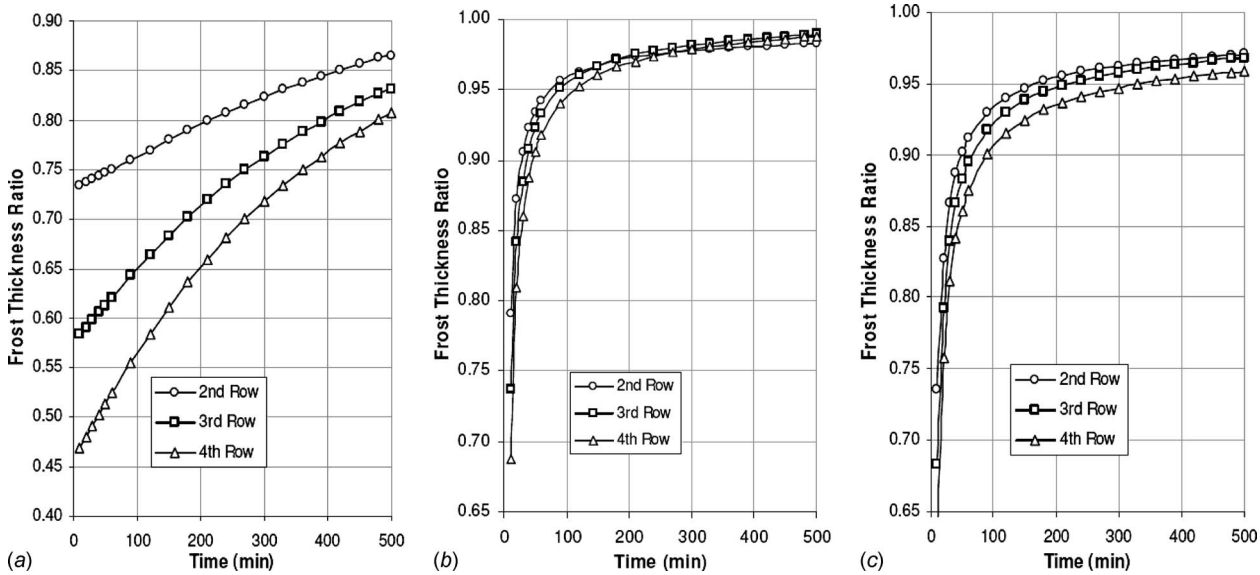

Fig. 14 Trends in frost thickness ratio for tubes in succession at U_a=5.0 m/s and T_r=−10.0°C for RH_a values of (*a*) 0.40, (*b*) 0.60, and (*c*) 0.80

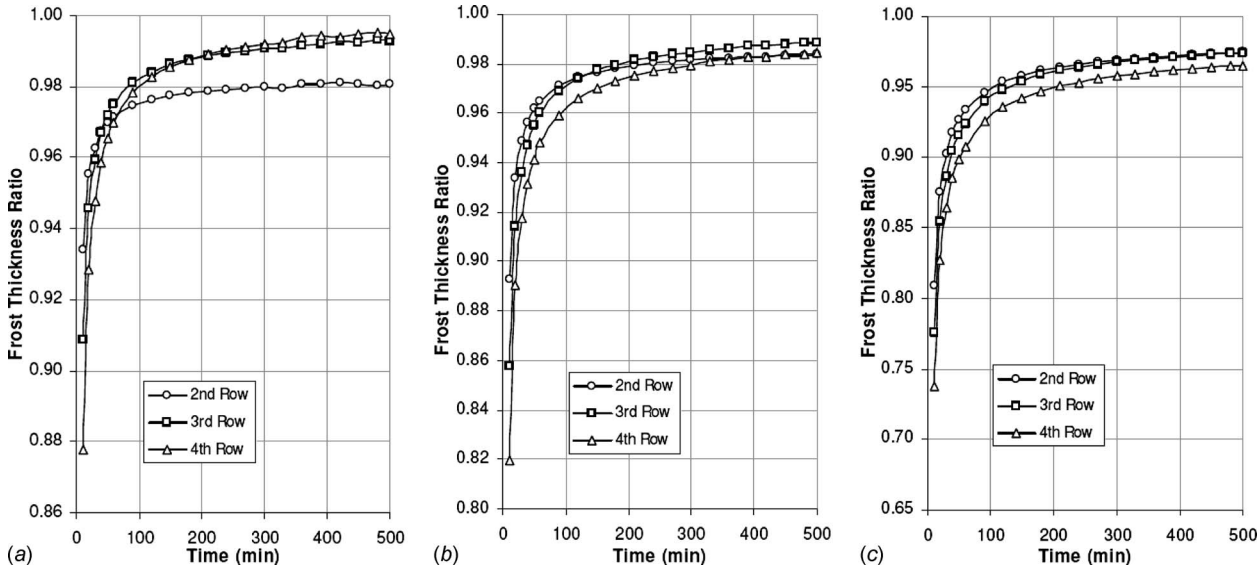

Fig. 15 Trends in frost thickness ratio for tubes in succession at U_a=5.0 m/s and T_r=−30.0°C for RH_a values of (*a*) 0.40, (*b*) 0.60, and (*c*) 0.80

els developed and employed for multitube array configuration assumed axially symmetric frost distribution over all cylindrical surfaces. Future investigations should therefore focus on extending the work considering the wake region and the turbulence effects.

Acknowledgment

The authors would like to express sincere thanks to Dr. Arun K. Saha, Department of Mechanical Engineering, Indian Institute of Technology, Kanpur for a notable suggestion regarding the matter presented in this work.

Nomenclature

A_s = area of conical needle base at subcooled surface, m^2
A_X = effective surface area at the top of the frost needles, m^2
c_0, c_1, c_2, c_3, c_4, c_5, C_1, C_a, C_b, and C_c = constants
C_{MD} = effective water vapor diffusion coefficient, $m\ s^{-1}$
$C_{p,a}$ = specific heat of air, $kJ\ kg^{-1}\ K^{-1}$
h_{fg} = enthalpy of fusion, $kJ\ kg^{-1}$
h_s = latent heat of sublimation, $kJ\ kg^{-1}$
h_{vap} = enthalpy of vaporization, $kJ\ kg^{-1}$
k = thermal conductivity, $W\ m^{-1}\ K^{-1}$
k_{air} = thermal conductivity of air, $W\ m^{-1}\ K^{-1}$
k_{eff} = effective thermal conductivity of porous layer of frost, $W\ m^{-1}\ K^{-1}$
k_f = thermal conductivity of frost, $W\ m^{-1}\ K^{-1}$
M_w = mass of sublimated water vapor, kg
$\dot{M}_w$ = mass transfer rate $\dot{M}_w$, $kg\ s^{-1}$
n = constant
N = total number of tube rows in the tube-array configuration
Nu = Nusselt number
p'_f = pressure of saturated water vapor, kPa
Q_s = heat delivered during condensation water vapor of mass, kJ
$\dot{Q}_t$ = heat transfer rate at the frost surface, W
$(\dot{Q}_L)_{max}$ = maximum possible latent load per unit tube length, $W\ m^{-1}$
$\dot{Q}_0$ = heat transfer rate from the tube under zero frost thickness, W
$(\dot{Q}_S)_{max}$ = maximum possible sensible load per unit tube length, $W\ m^{-1}$
R = radius of tube, m
R_{eq} = equivalent thermal resistance
R_s = ratio of supersaturation
Re = Reynolds number
RH = relativity humidity
t = time, min
t_w = thickness of tube wall, m
T_a = mean temperature of air in control volume, °C
T_f = temperature at the frost surface exposed to airstream, °C
T_M = melting point of water-ice mixture, °C
T_r = temperature of refrigerant/coolant inside the tube, °C
T_s = subcooled surface temperature, °C
U_a = airflow velocity, ms^{-1}
W = length of the tube in the array, m
X = frost layer thickness, m

Greek Symbols

δ_c = characteristic thickness of the frost layer, Eq. (26)
δ_f = constant
δ_t = thickness of the thermal boundary layer, m
ϕ_L = latent load ratio, Eq. (22)
Φ_L = latent load factor, Eq. (23)
Φ_{TC} = tortuosity correction factor
Π = as defined by Eq. (13)
ω_a = humidity ratio of airstream, kg of moisture/kg of dry air
ω_i = humidity ratio of airstream at the inlet, kg of moisture/kg of dry air
$\Delta\theta$ = angle suspended by conical needle at cylinder axes
ρ_a = density of air, $kg\ m^{-3}$

ρ_l = density of ice water, kg m^{-3}
ρ_{fo}^* = frost density, kg m^{-3}
ξ = factor used to affix the dimension of control volume in direction perpendicular to airflow direction

References

[1] Dietenberger, M. A., 1983, "Generalized Correlation of the Water Frost Thermal Conductivity," Int. J. Heat Mass Transfer, **26**, pp. 607–619.
[2] Tao, Y. X., Besant, R. W., and Rezkallah, K. S., 1993, "A Mathematical Model for Predicting the Densification and Growth of Frost on a Flat Plate," Int. J. Heat Mass Transfer, **36**, pp. 353–363.
[3] Na, B., and Webb, R. L., 2003, "A Fundamental Understanding of Factors Affecting Frost Nucleation," Int. J. Heat Mass Transfer, **46**, pp. 3797–3808.
[4] Hao, Y. L., Iragorry, J., and Tao, Y. X., 2005, "Frost-Air Interface Characterization Under Natural Convection," ASME J. Heat Transfer, **127**, pp. 1174–1180.
[5] Östin, R., and Andersson, S., 1991, "Frost Growth Parameters in a Forced Air Stream," Int. J. Heat Mass Transfer, **34**, pp. 1009–1017.
[6] Yun, R., Kim, Y., and Min, M. K., 2002, "Modelling of Frost Growth and Frost Properties With Airflow Over a Flat Plate," Int. J. Refrig., **25**, pp. 362–371.
[7] Cheng, C. H., and Wu, K. H., 2003, "Observation of Early-Stage Frost Formation on a Cold Plate in Atmospheric Air Flow," ASME J. Heat Transfer, **125**, pp. 95–102.
[8] Buyruk, E., 1999, "Heat Transfer and Flow Structures Around Circular Cylinders in Cross-Flow," Turk. J. Eng. Environ. Sci., **23**, pp. 299–315.
[9] Abu-Hijleh, Bassam A/K, 2001, "Laminar Forced Convection Heat Transfer From a Cylinder Covered With an Orthotropic Porous Layer in Cross-Flow," Int. J. Numer. Methods Heat Fluid Flow, **11**(2), pp. 106–120.
[10] Verma, P., Bullard, C. W., and Hrnjak, P. S., 2002, "Design Strategies for Reducing Performance Degradation Due to Frosting of Display Case Heat Exchangers," IIF-IIR–Commission D1/B1–Urbana, IL.
[11] Mago, P. J., and Sherif, S. A., 2002, "Modeling of the Cooling Process Path of a Dehumidifying Coil Under Frosting Conditions," ASME J. Heat Transfer, **124**, pp. 1182–1191.
[12] Mago, P. J., and Sherif, S. A., 2003, "Heat and Mass Transfer on a Cylinder Surface in Cross Flow Under Supersaturated Frosting Conditions," Int. J. Refrig., **26**, pp. 889–899.
[13] Sommers, A. D., and Jacobi, A. M., 2006, "An Exact Solution to Steady Heat Conduction in a Two-Dimensional Annulus on a One-Dimensional Fin: Application to Frosted Heat Exchangers With Round Tubes," ASME J. Heat Transfer, **128**, pp. 397–404.
[14] Schneider, H. W., 1978, "Equation of the Growth Rate of Frost Forming on Cooled Surfaces," Int. J. Heat Mass Transfer, **21**, pp. 1019–1024.
[15] Storey, B. D., and Jacobi, A. M., 1999, "The Effect of Streamwise Vortices on the Frost Growth Rate in Developing Laminar Channel Flows," Int. J. Heat Mass Transfer, **42**, pp. 3787–3802.
[16] Lee, H., Shin, J., Ha, S., Choi, B., and Lee, J., 2004, "Frost Formation on a Plate With Different Surface Hydrophilicity," Int. J. Heat Mass Transfer, **47**, pp. 4881–4893.
[17] Na, B., and Webb, R. L., 2004, "New Model for Frost Growth Rate," Int. J. Heat Mass Transfer, **47**, pp. 925–936.
[18] Tanda, G., and Fossa, M., 2006, "Free Convection Frost Growth in a Narrow Vertical Channel," Int. J. Heat Mass Transfer, **49**, pp. 1946–1957.
[19] Kwon, J. T., Lim, H. J., Kwon, Y. C., Koyama, S., Kim, D. H., and Kondou, C., 2006, "An Experimental Study on Frosting of Laminar Flow on a Cold Surface With Local Cooling," Int. J. Refrig., **29**, pp. 754–760.
[20] Sherif, S. A., Raju, S. P., Padki, M. M., and Chan, A. B., 1993, "A Semi-Empirical Transient Method for Modelling Frost Formation on a Flat Plate," Int. J. Refrig., **16**(5), pp. 321–329.
[21] Abdel-Wahed, R. M., Hifni, M. A., and Sherif, S. A., 1984, "Heat and Mass Transfer From a Laminar Humid Air Stream to a Plate at Subfreezing Temperature," Int. J. Refrig., **7**(1), pp. 49–55.
[22] Raju, S. P., and Sherif, S. A., 1993, "Frost Formation and Heat Transfer on Circular Cylinders in Cross-Flow," Int. J. Refrig., **16**, pp. 390–401.
[23] Anderson, C. R., and Reider, M. B., 1996, "High Order Explicit Method for the Computation of Flow About a Circular Cylinder," J. Comput. Phys., **125**, pp. 207–224.
[24] Ismail, K. A. R., Salinas, C., and Goncalves, M. M., 1997, "Frost Growth Around a Cylinder in a Wet Air Stream," Int. J. Refrig., **20**, pp. 106–119.
[25] Sengupta, S., Sherif, S. A., and Wong, K. V., 1998, "Empirical Heat Transfer and Frost Thickness Correlations During Frost Deposition on a Cylinder in Cross-Flow in the Transient Regime," Int. J. Energy Res., **22**, pp. 615–624.
[26] Lee, Y. B., and Ro, S. T., 2001, "An Experimental Study of Frost Formation on a Horizontal Cylinder Under Cross Flow," Int. J. Refrig., **24**, pp. 468–474.
[27] Szczepanik, K., Ooi1, A., Aye, L., and Rosengarten, G., 2004, "A Numerical Study of Heat Transfer From a Cylinder in Cross Flow," 15th Australasian Fluid Mechanics Conference, Dec. 13–17, University of Sydney, Sydney, Australia.
[28] Tso, C. P., Cheng, Y. C., and Lai, A. C. K., 2006, "An Improved Model for Predicting Performance Finned Tube Heat Exchanger Under Frosting Condition, With Frost Thickness Variation Along Fin," Appl. Therm. Eng., **26**, pp. 111–120.
[29] Yang, D. K., Lee, K. S., and Song, S., 2006, "Modeling for Predicting Frosting Behaviour of a Fin-Tube Heat Exchanger," Int. J. Heat Mass Transfer, **49**, pp. 1472–1479.
[30] Iragorry, J., Tao, Y. X., and Jia, S., 2004, "A Critical Review of Properties and Models for Frost Formation Analysis," HVAC&R Res., **10**(10), pp. 393–420.
[31] Iragorry, J., and Tao, Y. X., 2005, "Frost Temperature Relations for Defrosting Sensing System," ASME J. Heat Transfer, **127**, pp. 344–351.
[32] McCabe, W. L., and Smith, J. C., 1967, *Unit Operations of Chemical Engineering*, 2nd ed., McGraw-Hill, New York.
[33] Yonko, J. D., and Sepsy, C. F., 1967, "An Investigation of the Thermal Conductivity of Frost While Forming on a Flat Horizontal Plate," ASHRAE Trans., **73**, pp. 1.l.l–1.1.10.
[34] Klein, S., and Alvarado, F., 1995, Engineering Equation Solver, F-Chart software, Middleton, WI.
[35] ASHRAE, 2006, *ASHRAE Handbook-2006 Refrigeration*, The American Society of Heating, Refrigeration and Air-Conditioning Engineers, Atlanta, GA.
[36] Parish, H. C., and Sepsy, C. F., 1972, "A Numerical Analysis of the Frost Formation Under Forced Convection," ASHRAE Trans., **78**, pp. 236–251.
[37] Andrichak, S. M., 1962, "Formation of a Layer of Frost on a Cylinder in Crossflow of Air," MS thesis, Ohio State University, Columbus, OH.

Non-Newtonian Natural Convection Along a Vertical Flat Plate With Uniform Surface Temperature

S. Ghosh Moulic
Department of Mechanical Engineering,
Indian Institute of Technology,
Kharagpur,
Kharagpur 721302, India

L. S. Yao
Department of Mechanical and Aerospace Engineering,
Arizona State University,
Tempe, AZ 85287-6106

Natural-convection boundary-layer flow of a non-Newtonian fluid along a heated semi-infinite vertical flat plate with uniform surface temperature has been investigated using a four-parameter modified power-law viscosity model. In this model, there are no physically unrealistic limits of zero or infinite viscosity that are encountered in the boundary-layer formulation for two-parameter Ostwald–de Waele power-law fluids. The leading-edge singularity is removed using a coordinate transformation. The boundary-layer equations are solved by an implicit finite-difference marching technique. Numerical results are presented for the case of a shear-thinning fluid. The results indicate that a similarity solution exists locally in a region near the leading edge of the plate, where the shear rate is not large enough to induce non-Newtonian effects; this similarity solution is identical to the similarity solution for a Newtonian fluid. The size of this region depends on the Prandtl number. Downstream of this region, the solution of the boundary-layer equations is nonsimilar. As the shear rate increases beyond a threshold value, the viscosity of the shear-thinning fluid is reduced. This leads to a decrease in the wall shear stress compared with that for a Newtonian fluid. The reduction in the viscosity accelerates the fluid in the region close to the wall, resulting in an increase in the local heat transfer rate compared with the case of a Newtonian fluid. [DOI: 10.1115/1.3090810]

Keywords: non-Newtonian, natural convection, modified power law, heated semi-infinite vertical flat plate, uniform surface temperature, nonsimilar boundary layer, implicit finite-difference marching scheme

1 Introduction

The interest in thermal convection problems involving power-law non-Newtonian fluids has grown in the past half century. An excellent series of lectures on non-Newtonian fluids was given recently by Hinch [1]. It appears that Acrivos [2], a frequently cited paper, was the first to consider natural-convection boundary-layer flows of power-law fluids. Since then, a large number of papers on non-Newtonian power-law fluids have been published due to their wide relevance in chemical, food, polymer, molten plastics, and petroleum industry [3–13].

The popular two-parameter Ostwald–de Waele power-law model [14] yields a physically unrealistic prediction of the shear-rate-dependent viscosity in the limits of large or small shear rates. For shear-thinning fluids, the non-Newtonian viscosity predicted by the Ostwald–de Waele power-law model vanishes or becomes infinite in the limit of large or small shear rates, respectively; for shear-thickening fluids, the non-Newtonian viscosity vanishes or becomes unbounded in the limit of small or large shear rates, respectively. Small shear rates occur near the outer edge of boundary layers, where the boundary-layer solution matches with the outer inviscid flow and near the leading edge of the plate in the case of natural-convection boundary layers. Large shear rates occur near the leading edge of the plate in the case of forced-convection boundary layers. Thus, the Ostwald–de Waele power-law model introduces nonphysical singularities in the boundary-layer formulation at the leading edge and near the outer edge of the boundary layer. Without recognizing the cause of such unrealistic situations, a false starting procedure is frequently used to integrate the boundary-layer equations by specifying initial conditions slightly downstream of the leading edge in order to avoid the leading-edge region. Sometimes, complex multilayer structures are introduced to overcome the mathematical difficulties in order to obtain a solution using a physically unrealistic formulation [12,13].

Experimental data indicate that many non-Newtonian fluids, such as polymeric liquids, are Newtonian at very low and very high shear rates, with constant apparent viscosities referred to as zero-shear-rate viscosity and infinite-shear-rate viscosity, respectively; the apparent viscosity varies with the shear rate only in an intermediate range of shear rates [14]. Recently, Yao and Molla [15] proposed a modified power-law correlation in which the Ostwald–de Waele power law is used to determine the non-Newtonian viscosity for a certain range of shear rates; outside this range of shear rates, the viscosity is assumed to be constant. The values of the constant viscosities at small and large shear rates and the threshold shear rates, which determine the range of shear rates within which the two-parameter Ostwald–de Waele model is applicable, can be fixed from experimental data. The modified power-law correlation does not predict zero or infinite viscosity in the limits of small and large shear rates. Thus, the singularities introduced into the boundary-layer formulation by the popular two-parameter Ostwald–de Waele power-law model do not appear if the modified power-law correlation is used. The modified power law, in fact, fits data better. The power-law correlation introduces a length scale into the boundary-layer formulation. Consequently, simple self-similar solutions do not exist. Yao and Molla [15,16] and Molla and Yao [17,18] obtained numerical solutions of the boundary-layer equations for forced-convection boundary-layer flows of non-Newtonian fluids using a finite-difference marching

Contributed by the Heat Transfer Division of ASME for publication in the JOURNAL OF HEAT TRANSFER. Manuscript received May 23, 2008; final manuscript received December 14, 2008; published online April 7, 2009. Review conducted by Yogesh Jaluria.

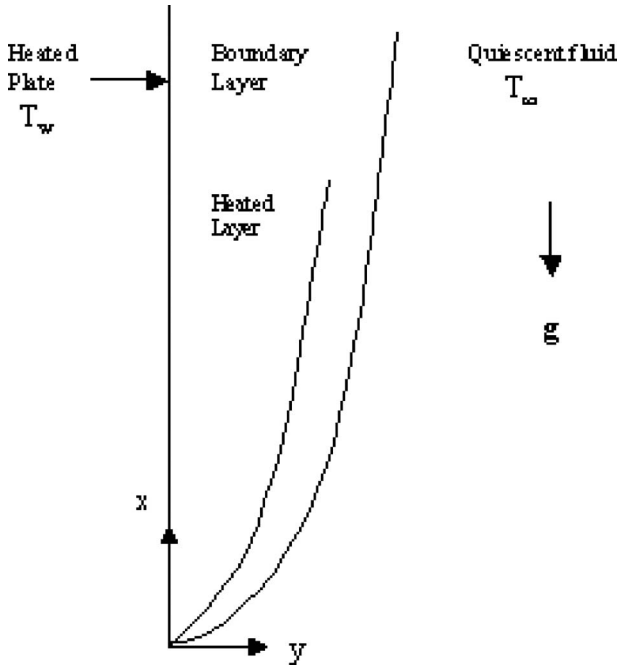

Fig. 1 Coordinates

technique similar to the numerical method used by Yao [19]. Molla and Yao [20] used the modified power-law correlations to obtain a prediction of non-Newtonian natural convection along a heated vertical wavy surface. Molla and Yao [21] obtained a numerical solution of non-Newtonian mixed convection along a heated vertical flat plate.

In the present investigation, the modified power-law correlation proposed by Yao and Molla [15] is used to study natural-convection boundary-layer flow of a generalized Newtonian fluid along a semi-infinite heated vertical plate. The boundary-layer equations, which are of parabolic type, are solved numerically by an implicit finite-difference marching procedure. Results are presented for a typical shear-thinning oil.

2 Problem Formulation

Natural-convection boundary-layer flow of a non-Newtonian fluid along a heated semi-infinite vertical flat plate has been studied. The temperature of the plate is held at a constant value, T_w, higher than the ambient temperature, T_∞. The coordinate system is shown in Fig. 1. The constitutive equations for a generalized Newtonian fluid, with a shear-rate-dependent viscosity, are used in the analysis. Following Yao and Molla [15], the shear-rate-dependent viscosity is approximated by the modified power law

$$\mu(\bar{\gamma}) = \begin{cases} \mu_1, & \bar{\gamma} < \bar{\gamma}_1 \\ K\bar{\gamma}^{n-1}, & \bar{\gamma}_1 \le \bar{\gamma} \le \bar{\gamma}_2 \\ \mu_2, & \bar{\gamma} > \bar{\gamma}_2 \end{cases} \tag{1}$$

where

$$\bar{\gamma} = \left| \frac{\partial \bar{u}}{\partial \bar{y}} \right| \tag{2}$$

is the magnitude of the shear rate, n is the power-law index, K is a dimensional constant, referred to as the fluid consistency, whose dimension depends on the power-law index, $\bar{\gamma}_1$ and $\bar{\gamma}_2$ are two threshold shear rates, and μ_1 and μ_2 are constants. The Ostwald–de Waele power law is used to determine the viscosity when the shear rate falls in the range of $\bar{\gamma}_1 \le \bar{\gamma} \le \bar{\gamma}_2$. The viscosity is assumed to be constant when the shear rate is outside the range of $\bar{\gamma}_1 \le \bar{\gamma} \le \bar{\gamma}_2$. The function defined by Eq. (1) is assumed to be a continuous function of $\bar{\gamma}$. If $\bar{\gamma}_1$ is set to zero and $\bar{\gamma}_2$ to infinity, the power law covers the entire range of shear rates, and the values of the constants μ_1 and μ_2 are not required. When $\bar{\gamma}_1$ is nonzero, the continuity of the function defined by Eq. (1), at $\bar{\gamma} = \bar{\gamma}_1$, requires that

$$\mu_1 = K\bar{\gamma}_1^{n-1} \tag{3}$$

Equation (3) gives a relation between μ_1 and $\bar{\gamma}_1$ when $\bar{\gamma}_1$ is nonzero. The model constant μ_1 may be identified as the zero-shear-rate viscosity and can be easily determined from experimental data. The value of the lower threshold shear rate $\bar{\gamma}_1$ can be determined using Eq. (3). When $\bar{\gamma}_2$ is finite, the continuity of the function defined by Eq. (1), at $\bar{\gamma} = \bar{\gamma}_2$, requires that

$$\mu_2 = K\bar{\gamma}_2^{n-1} \tag{4}$$

Equation (4) gives a relation between μ_2 and $\bar{\gamma}_2$ when $\bar{\gamma}_2$ is finite. The model constant μ_2 may be identified with the infinite-shear-rate viscosity, and its value can be readily obtained from experimental measurements. The value of the upper threshold shear rate $\bar{\gamma}_2$ can be calculated using the relation given by Eq. (4).

The modified power-law correlation, given by Eq. (1), involves six parameters: K, n, $\bar{\gamma}_1$, $\bar{\gamma}_2$, μ_1, and μ_2. Since μ_1 is related to $\bar{\gamma}_1$ by Eq. (3) and μ_2 is related to $\bar{\gamma}_2$ by Eq. (4), the modified power-law correlation involves four independent parameters: K, n, $\bar{\gamma}_1$, and $\bar{\gamma}_2$. It is worth noting that the Ostwald–de Waele power-law correlation involves only two parameters, K and n, and may be viewed as a special case of Eq. (1) when $\bar{\gamma}_1 = 0$ and $\bar{\gamma}_2$ is infinite. For this special case, when $\bar{\gamma}_1 = 0$ and $\bar{\gamma}_2$ is infinite, the values of μ_1 and μ_2 are not required.

The flow is considered to be steady, laminar, and two dimensional. The Boussinesq approximation is employed. The equations describing the flow inside the boundary layer may be written in nondimensional form as

$$\frac{\partial \hat{u}}{\partial x} + \frac{\partial \hat{v}}{\partial y} = 0 \tag{5a}$$

$$\frac{1}{\mathrm{Pr}}\left[\hat{u}\frac{\partial \hat{u}}{\partial x} + \hat{v}\frac{\partial \hat{u}}{\partial y}\right] = \frac{\partial}{\partial y}\left(D\frac{\partial \hat{u}}{\partial y}\right) + \hat{\theta} \tag{5b}$$

$$\hat{u}\frac{\partial \hat{\theta}}{\partial x} + \hat{v}\frac{\partial \hat{\theta}}{\partial y} = \frac{\partial^2 \hat{\theta}}{\partial y^2} \tag{5c}$$

where

$$x = \frac{\bar{x}}{l}, \quad y = \frac{\bar{y}}{l}\mathrm{Ra}^{1/4} \tag{6a}$$

$$\hat{u} = \frac{\bar{u}}{U_0}, \quad \hat{v} = \frac{\bar{v}}{U_0}\mathrm{Ra}^{1/4}, \quad \hat{\theta} = \frac{T - T_\infty}{T_w - T_\infty} \tag{6b}$$

$$D = \frac{\mu}{\mu_1}, \quad \mathrm{Pr} = \frac{\nu_1}{\alpha}, \quad \mathrm{Ra} = \frac{g\beta(T_w - T_\infty)l^3}{\nu_1 \alpha} \tag{6c}$$

$$U_0 = \sqrt{\frac{g\beta(T_w - T_\infty)l\alpha}{\nu_1}}, \quad \nu_1 = \frac{\mu_1}{\rho_0} \tag{6d}$$

The barred quantities in Eqs. (6*a*) and (6*b*) are dimensional variables, l is a reference length, U_0 is a reference velocity, ρ_0 is the reference density used in the Boussinesq approximation, β is the coefficient of thermal expansion, g is the gravitational acceleration, α is the thermal diffusivity, D is the nondimensional viscosity, Ra is the Rayleigh number, and Pr is the Prandtl number. The zero-shear-rate viscosity, μ_1, has been used as the reference viscosity. The scales used in the nondimensionalization have been obtained by balancing the order of magnitude of the conduction and convection terms in the energy equation and the order of

magnitude of the viscous and buoyancy forces inside the heated layer. The Rayleigh number has been assumed to be large in the order-of-magnitude analysis. The nondimensional variables x, y, $\hat{u}$, $\hat{v}$, $\hat{\theta}$, and D are variables of order 1 inside the heated layer. Equation (6*a*) indicates that the ratio of the length scales in the y and x directions is $O(\mathrm{Ra}^{-1/4})$. Equation (6*b*) shows that the ratio of the velocity components in the y and x directions is also $O(\mathrm{Ra}^{-1/4})$. The Prandtl numbers of typical non-Newtonian fluids are large. Equation (5*b*) reflects the fact that for large Prandtl number fluids, inertia forces are small compared with the buoyancy and viscous forces in the heated layer close to the wall.

The nondimensional viscosity, D, may be expressed in the form

$$D = \begin{cases} 1, & \gamma < \gamma_1 \\ C\gamma^{n-1}, & \gamma_1 \le \gamma \le \gamma_2 \\ \mu_R, & \gamma > \gamma_2 \end{cases} \tag{7}$$

where

$$\gamma = \left| \frac{\partial \hat{u}}{\partial y} \right| \tag{8}$$

is the nondimensional shear-rate magnitude,

$$\gamma_1 = \bar{\gamma}_1 \left[\frac{\mu_1^3}{(\rho_0 g \beta (T_w - T_\infty))^3 \alpha l} \right]^{1/4} \tag{9}$$

is the nondimensional lower threshold shear rate,

$$\gamma_2 = \bar{\gamma}_2 \left[\frac{\mu_1^3}{(\rho_0 g \beta (T_w - T_\infty))^3 \alpha l} \right]^{1/4} \tag{10}$$

is the nondimensional upper threshold shear rate,

$$\mu_R = \frac{\mu_2}{\mu_1} \tag{11}$$

is the ratio of the infinite-shear-rate viscosity to the zero-shear-rate viscosity, and

$$C = \frac{K}{\mu_1} \left[\frac{(\rho_0 g \beta (T_w - T_\infty))^3 \alpha l}{\mu_1^3} \right]^{(n-1)/4} \tag{12}$$

Equation (12) indicates that the length scale associated with the non-Newtonian power law is

$$l = \frac{\mu_1^3}{(\rho_0 g \beta (T_w - T_\infty))^3 \alpha} \left[\frac{K}{\mu_1} \right]^{4/(1-n)} C^{4/(n-1)} \tag{13}$$

It is well known that the length scale can be determined up to a constant factor of order 1. This is the reason why the forms of the similarity variables for many well-known similarity problems differ by constant factors of order 1, depending on the choice of the researchers. Thus, the value of γ_1 can be set to a convenient value. We will show below that once the value of γ_1 is set to some convenient value, the values of γ_2 and the other nondimensional variables follow accordingly.

If $\bar{\gamma}_1$ is nonzero, the continuity of the nondimensional viscosity function defined by Eq. (7), at $\gamma = \gamma_1$, implies that

$$\gamma_1 = \left[\frac{1}{C} \right]^{1/(n-1)} \tag{14}$$

By a similar argument, one can conclude that when $\bar{\gamma}_2$ is finite,

$$\gamma_2 = \left[\frac{\mu_R}{C} \right]^{1/(n-1)} \tag{15}$$

using the continuity of the function defined by Eq. (7), at $\gamma = \gamma_2$. Equations (14) and (15) relate γ_1 and γ_2 to the power-law parameter C. The ratio of the nondimensional threshold shear rates is equal to the ratio of the dimensional threshold shear rates and is given by

$$\frac{\gamma_2}{\gamma_1} = \frac{\bar{\gamma}_2}{\bar{\gamma}_1} = \left[\frac{\mu_2}{\mu_1} \right]^{1/(n-1)} \tag{16}$$

Equation (16) indicates that this ratio is a fluid property, which is independent of the parameter C. The relations given by Eqs. (14)–(16) are, however, not valid for the special case when $\bar{\gamma}_1 = 0$ and $\bar{\gamma}_2$ is infinite. For this special case, $\gamma_1 = 0$ and γ_2 is infinite, as indicated by Eqs. (9) and (10); the power law thus covers the entire range of shear rates, and the value of μ_R is not required.

The associated boundary conditions are as follows:

(i) on the surface of the plate ($y = 0$),

$$\hat{u} = \hat{v} = 0, \quad \hat{\theta} = 1 \tag{17a}$$

(ii) matching with the quiescent isothermal ambient freestream,

$$\hat{u} \to 0 \quad \text{and} \quad \hat{\theta} \to 0 \quad \text{as} \quad y \to \infty \tag{17b}$$

The boundary-layer equations are singular at the leading edge $x = 0$. In order to remove the singularity at the leading edge and to minimize the variation in the boundary-layer thickness with x, for computational convenience, the following transformation is used:

$$\xi = x, \quad \eta = \frac{y}{(4x)^{1/4}}, \quad \hat{u} = (4\xi)^{1/2} u(\xi, \eta), \quad \hat{v} = (4\xi)^{-1/4} v(\xi, \eta),$$

$$\hat{\theta} = \theta(\xi, \eta) \tag{18}$$

Equation (5) transforms to

$$4\xi \frac{\partial u}{\partial \xi} + \frac{\partial w}{\partial \eta} + 3u = 0 \tag{19a}$$

$$\frac{1}{\mathrm{Pr}} \left[4\xi u \frac{\partial u}{\partial \xi} + w \frac{\partial u}{\partial \eta} + 2u^2 \right] = \frac{\partial}{\partial \eta} \left(D \frac{\partial u}{\partial \eta} \right) + \theta \tag{19b}$$

$$4\xi u \frac{\partial \theta}{\partial \xi} + w \frac{\partial \theta}{\partial \eta} = \frac{\partial^2 \theta}{\partial \eta^2} \tag{19c}$$

where

$$w = v - \eta u \tag{20}$$

while Eq. (8) transforms to

$$\gamma = (4\xi)^{1/4} \left| \frac{\partial u}{\partial \eta} \right| \tag{21}$$

The boundary condition (17) transforms to

$$u = w = 0, \quad \theta = 1 \quad \text{at} \quad \eta = 0 \tag{22a}$$

$$u \to 0, \quad \theta \to 0 \quad \text{as} \quad \eta \to \infty \tag{22b}$$

Equation (19) represents a system of parabolic partial differential equations and can be solved numerically by marching downstream in the ξ-direction, starting from the leading edge ($\xi = 0$). The initial conditions for advancing the solution forward in ξ may be determined by considering the limit of Eq. (19) as $\xi \to 0$. Equation (21) indicates that the shear rate, γ, is zero at the leading edge ($\xi = 0$), assuming that $\partial u / \partial \eta$ is finite at $\xi = 0$. It follows from Eq. (7) that $D = 1$ at $\xi = 0$. It may be noted that all the partial derivatives with respect to ξ in Eq. (19) are multiplied by ξ. Putting $\xi = 0$ in Eq. (19) and assuming that all derivatives with respect to ξ remain bounded, the following differential equations are obtained:

$$\frac{\partial w}{\partial \eta} + 3u = 0 \tag{23a}$$

$$\frac{1}{\mathrm{Pr}} \left[w \frac{\partial u}{\partial \eta} + 2u^2 \right] = \frac{\partial^2 u}{\partial \eta^2} + \theta \tag{23b}$$

$$w\frac{\partial\theta}{\partial\eta}=\frac{\partial^2\theta}{\partial\eta^2} \tag{23c}$$

Equation (23) may be viewed as ordinary differential equations, with η as the independent variable and ξ as a parameter, with value $\xi=0$. These ordinary differential equations are solved, subject to the boundary condition (22), to obtain the initial condition for u and θ at $\xi=0$. This initial condition is identical to the similarity solution for a Newtonian fluid. If Eq. (19) is solved for a Newtonian fluid ($n=1$), with this initial condition and boundary conditions given by Eq. (22), the solution does not vary with ξ; the variables u, w, and θ depend only on the coordinate η when the power-law index $n=1$.

Equation (19) was discretized using a finite-difference method. Derivatives with respect to η in the momentum and energy equations were approximated by three-point difference approximations on a nonuniform grid. Derivatives with respect to ξ were approximated by a two-point backward difference scheme. Since the equations are nonlinear and coupled, the solution at each ξ-station was obtained iteratively. The iterations were continued until the difference of successive iterates became less than a specified tolerance. The space-marching implicit scheme is unconditionally stable. The discrete equations were solved using a FORTRAN computer code.

The infinite domain in the η-direction was truncated to a finite domain. The maximum value of η was fixed at $\eta_{\max}=160$. This was found to be adequate. The computational domain in the η-direction was divided into three zones: a uniform grid zone near the wall with $\Delta\eta=0.02$, from $\eta=0$ to $\eta=20$, a uniform grid zone near the outer edge of the boundary layer with $\Delta\eta=0.2$, and a middle zone where the grid spacing is slowly increased from $\Delta\eta=0.02$ to $\Delta\eta=0.2$. The ratio of successive grid sizes in the variable-grid middle zone was kept constant; the value of this ratio was fixed at 1.00997. After several test runs, the value of $\Delta\xi$ in the region near the leading edge was fixed at 5×10^{-6}. Far downstream of the leading edge, the step size $\Delta\xi$ can be increased without sacrificing accuracy, as the solution changes slowly with ξ. For $\xi>5\times10^{-4}$, a variable step size $\Delta\xi$ was used. The step size was determined using an adaptive marching strategy similar to that used by Ghosh Moulic [22] and Ghosh Moulic and Yao [23]. The solution was advanced from ξ to $\xi+2\Delta\xi$ first in two steps with step size $\Delta\xi$ and then in one step with step size $2\Delta\xi$. The differences in the wall heat transfer rates and the wall shear stresses predicted by the two-step integration and the one-step integration, at the location $\xi+2\Delta\xi$, were compared. If the difference was greater than 10^{-4}, the step size $\Delta\xi$ was halved and the process repeated; if the difference was less than 10^{-6}, the step size for the next step was doubled. The converged solution at $\xi+2\Delta\xi$ from the two-step integration was used as the initial guess for the single-step integration from ξ to $\xi+2\Delta\xi$. As a result, the iterations for the single-step integration converge rapidly. Using this strategy, the solution was advanced to $\xi=10^4$, with a reasonable accuracy, without using an excessive amount of computer time. The tolerance for the iterations at the leading edge was set to 10^{-12}. The tolerance for the iterations at other ξ-locations was taken to be 10^{-6}.

3 Results and Discussion

Results have been obtained for a shear-thinning oil with $n=0.95$. Computations have been done for $\gamma_1=0.1$ and $\gamma_2=10^5$. The nondimensional viscosity, D, given by the modified power-law correlation, is plotted in Fig. 2, as a function of the nondimensional shear-rate magnitude, γ. Results are presented for two values of the Prandtl number: Pr=100 and Pr=1000. The CPU time taken to march from $\xi=0$ to $\xi=10^4$, using the adaptive marching scheme, is about 5 min on a personal computer with a Pentium IV processor and a Redhat Linux operating system, for a typical run.

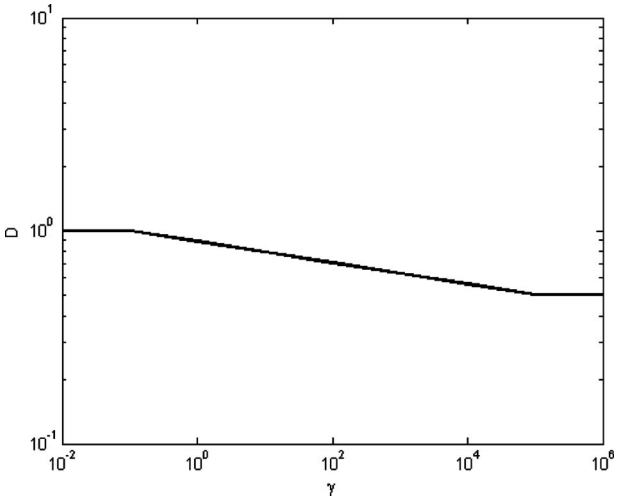

Fig. 2 Modified power-law correlation

At each ξ-location, the maximum value of the shear-rate magnitude, γ, was found to occur at the wall for all cases. The variation in the shear rate at the wall, γ_w, is shown in Fig. 3. This figure shows that the shear rate at the wall increases monotonically with ξ, from a zero value at the leading edge. The value of γ_w is less than the lower threshold shear rate over a region of $0\leq\xi\leq\xi_1$, where ξ_1 is the location where $\gamma_w=\gamma_1$. In this region, the value of the nondimensional viscosity, D, is 1 for all values of η. Since the viscosity is constant, the fluid behaves like a Newtonian fluid in this region.

The axial variation in the velocity gradient at the wall, $(\partial u/\partial\eta)_w$, is shown in Fig. 4. The figure indicates that $(\partial u/\partial\eta)_w$ is constant in the region of $0\leq\xi\leq\xi_1$, where $\gamma_w<\gamma_1$. The solution is self-similar in this region and is identical to the similarity solution for Newtonian fluids.

The variation in the wall viscosity, D_w, with distance from the leading edge is shown in Fig. 5. A glance at Fig. 5 reveals that $D_w=1$ in the region of $0\leq\xi\leq\xi_1$, where the shear rate is less than the lower threshold shear rate. In this region, the shear rate increases as $\xi^{1/4}$ and becomes equal to the lower threshold shear rate at $\xi=\xi_1$. Thereafter, the wall viscosity decreases with distance from the leading edge as the shear rate increases since the power-law index $n<1$. The reduction in the viscosity of the shear-

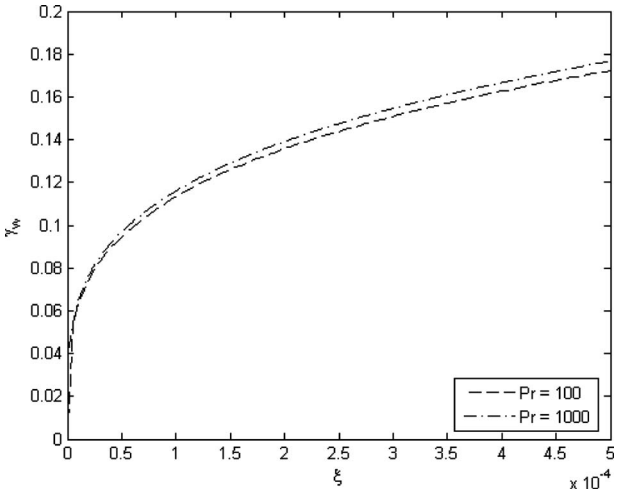

Fig. 3 Axial variation in the rate of shear strain at the wall

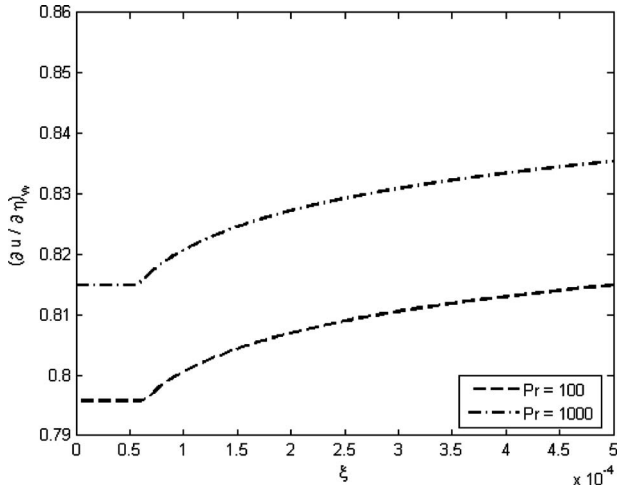

Fig. 4 Axial variation in velocity gradient, $\partial u/\partial \eta$, at the wall

thinning fluid accelerates the fluid, leading to an increase in the velocity gradient, $(\partial u/\partial \eta)_w$, at the wall, for $\xi > \xi_1$, as indicated by Fig. 4.

The distance from the leading edge where non-Newtonian effects start to develop may be predicted by noting that in the region of $0 \leq \xi \leq \xi_1$, the maximum shear-rate magnitude occurs at the wall and is given by

$$\gamma_w = (4\xi)^{1/4}\left(\frac{\partial u}{\partial \eta}(0,0)\right) \tag{24}$$

where $(\partial u/\partial \eta)(0,0)$ is the velocity gradient at the leading edge since $(\partial u/\partial \eta)_w$ is constant in this region, as indicated in Fig. 4, and the value of this constant is equal to the value of the velocity gradient at the leading edge. Setting $\gamma_w = \gamma_1$ in Eq. (24) yields

$$\xi_1 = \frac{1}{4}\frac{\gamma_1^4}{\left(\frac{\partial u}{\partial \eta}(0,0)\right)^4} \tag{25}$$

The values of ξ_1 for Pr=100 and Pr=1000 are given in Table 1. The velocity gradient, $(\partial u/\partial \eta)(0,0)$, increases with an increase in the value of the Prandtl number. This results in a decrease in the value of ξ_1.

Figures 6(*a*) and 6(*b*) show the profiles of the scaled axial velocity, u, at selected ξ-locations for Pr=100 and Pr=1000, respectively. The figures show that the velocity increases from a zero value at the wall to a maximum inside the boundary layer and then decreases in the outer part of the boundary layer to zero at large distances from the plate. The peak value of the velocity increases with distance from the leading edge for $\xi > \xi_1$. This acceleration may be attributed to the decrease in the non-Newtonian viscosity of the shear-thinning fluid caused by an increase in the shear rate. The acceleration of the fluid leads to an increase in the velocity gradients at the wall. A comparison of Figs. 6(*a*) and 6(*b*) indicates that the boundary layer is thicker for Pr=1000.

Table 1 Variation in ξ_1 with Pr

Pr	100	1000
ξ_1	0.6233×10^{-4}	0.5673×10^{-4}

The distribution of the nondimensional viscosity, D, as a function of η at selected ξ-locations is shown in Figs. 7(*a*) and 7(*b*) for Pr=100 and Pr=1000, respectively. Figure 7(*a*) shows that for Pr=100, there is only one region of variable viscosity at $\xi=0.01$ and $\xi=0.1$. This region occurs near the wall, where the shear rate is higher than the lower threshold shear rate. Figure 7(*a*) shows that there are two regions of variable viscosity at $\xi=10$ and $\xi=1000$: a variable-viscosity region near the wall and another variable-viscosity region in the outer part of the boundary layer. A region of constant viscosity, with $D=1$, occurs between these two

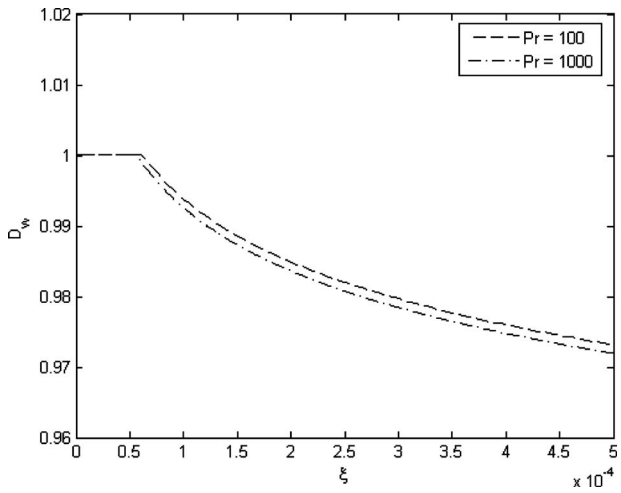

Fig. 5 Axial variation in nondimensional viscosity at the wall

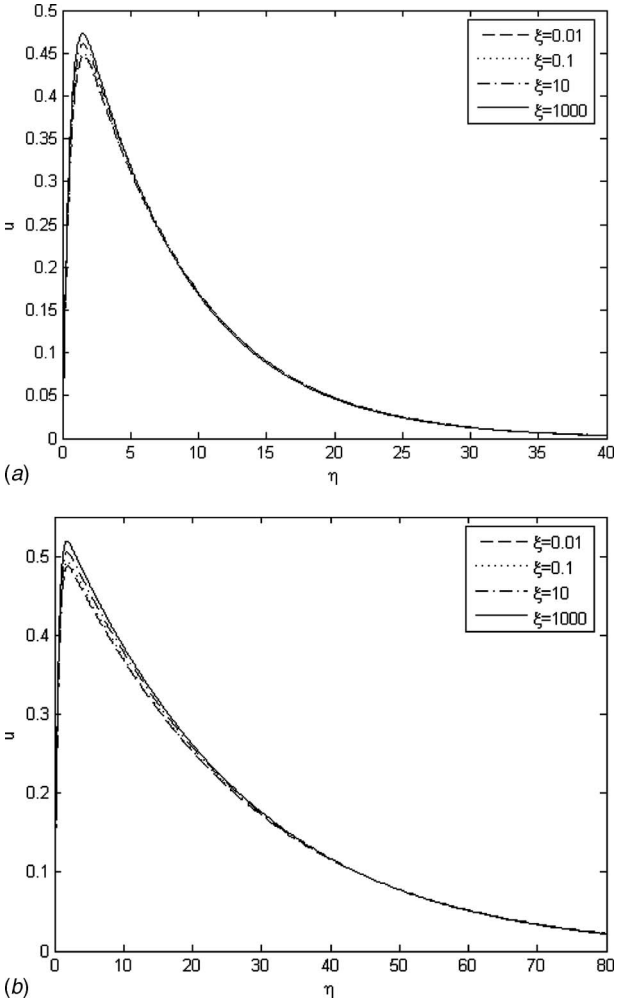

Fig. 6 Velocity distribution at selected ξ for (*a*) Pr=100 and (*b*) Pr=1000

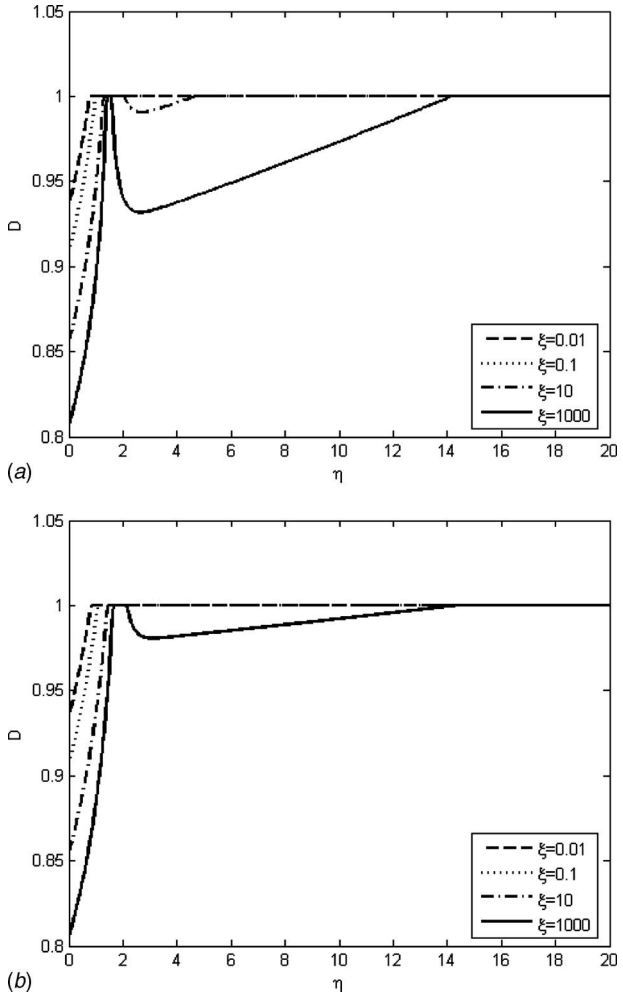

Fig. 7 Viscosity distribution at selected ξ for (*a*) Pr=100 and (*b*) Pr=1000

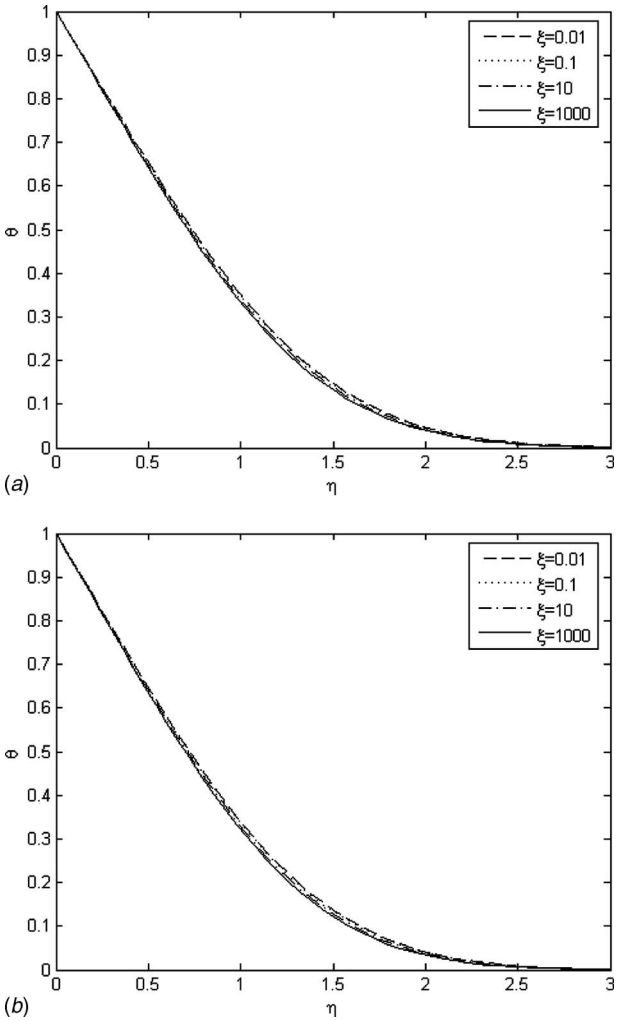

Fig. 8 Temperature distribution at selected ξ for (*a*) Pr=100 and (*b*) Pr=1000

zones of variable viscosity; this region includes the peak of the velocity profile where the shear rate is zero. Figure 7(*b*) indicates that at Pr=1000, there is only one region of variable viscosity at ξ=0.01, 0.1, and 10. The second region of variable viscosity appears further downstream. The delay in the appearance of the second region of non-Newtonian viscosity may be explained by the fact that the boundary-layer thickness is larger for Pr=1000; consequently, the velocity gradients in the outer part of the boundary layer for Pr=1000 are smaller than the velocity gradients at the same ξ-location for Pr=100. Thus, the ξ-location beyond which the shear rates in the outer part of the boundary layer exceed the lower threshold shear rate occurs further downstream for Pr=1000.

Temperature profiles at selected ξ-locations are plotted in Figs. 8(*a*) and 8(*b*) for Pr=100 and Pr=1000, respectively. The figures show that the temperature of the fluid approaches the ambient temperature at $\eta \approx 3$. The temperature gradients at the wall increase with distance from the leading edge for $\xi > \xi_1$. A comparison of Figs. 6 and 8 reveals that the thickness of the heated layer is a small fraction of the boundary-layer thickness. Buoyancy forces are negligible outside the heated layer. The fluid in the heated layer is driven by buoyancy forces, while the fluid in the outer part of the boundary layer is dragged by the fluid inside the heated layer by viscous action.

The local Nusselt number, based on distance from the leading edge, is given by

$$\mathrm{Nu}_x \mathrm{Ra}_x^{-1/4} = -\frac{1}{\sqrt{2}}\left(\frac{\partial \theta}{\partial \eta}\right)_{\eta=0} \tag{26}$$

where

$$\mathrm{Nu}_x = \frac{h\bar{x}}{k} \tag{27}$$

h is the local heat transfer coefficient, k is the thermal conductivity of the fluid, and Ra_x is the local Rayleigh number based on distance from the leading edge, defined by

$$\mathrm{Ra}_x = \frac{g\beta(T_w - T_\infty)\bar{x}^3}{\nu_1 \alpha} \tag{28}$$

The variation in $\mathrm{Nu}_x \mathrm{Ra}_x^{-1/4}$ with distance from the leading edge is displayed in Fig. 9. For the special case of a Newtonian fluid, $\mathrm{Nu}_x \mathrm{Ra}_x^{-1/4}$ does not vary with ξ. Figure 9 shows that the value of $\mathrm{Nu}_x \mathrm{Ra}_x^{-1/4}$ is constant in the region of $0 \leq \xi \leq \xi_1$. The value of this constant is the same as that for Newtonian fluids; it increases with an increase in the value of the Prandtl number. For $\xi > \xi_1$, the value of $\mathrm{Nu}_x \mathrm{Ra}_x^{-1/4}$ increases with distance from the leading edge due to an increase in the temperature gradient at the wall, as indicated in Figs. 8(*a*) and 8(*b*). The increase in the local heat transfer rate compared with the case of a Newtonian fluid is associated with the acceleration of the fluid in the region close to the

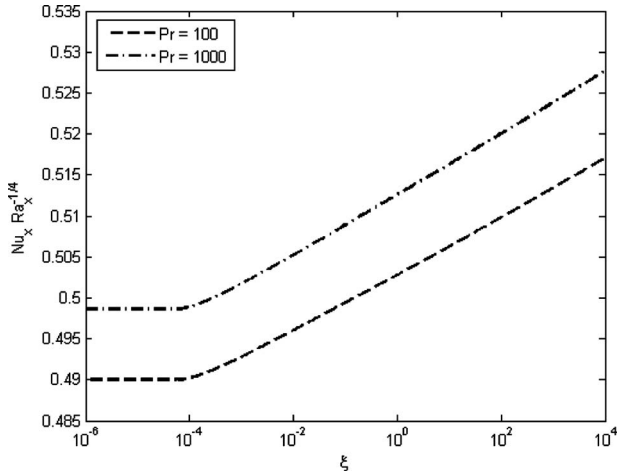

Fig. 9 Axial variation in $Nu_x Ra_x^{-1/4}$

wall caused by the reduction in the viscosity of the shear-thinning fluid due to an increase in the shear rate.

The local skin-friction factor defined by

$$c_{f_x} = \frac{\tau_w}{\frac{1}{2}\rho_0 U_0^2} \tag{29}$$

where τ_w is the wall shear stress, is given by

$$\frac{c_{f_x} \mathrm{Ra}_x^{1/4}}{\mathrm{Pr}\xi} = 2\sqrt{2}\left(D\frac{\partial u}{\partial \eta}\right)_{\eta=0} \tag{30}$$

The variation in $c_{f_x}\mathrm{Ra}_x^{1/4}/(\mathrm{Pr}\xi)$ with distance from the leading edge is displayed in Fig. 10. For the special case of a Newtonian fluid, $c_{f_x}\mathrm{Ra}_x^{1/4}/(\mathrm{Pr}\xi)$ does not vary with ξ. Figure 10 indicates that the value of $c_{f_x}\mathrm{Ra}_x^{1/4}/(\mathrm{Pr}\xi)$ is constant in the region of $0 \leq \xi \leq \xi_1$. The value of this constant is the same as that for Newtonian fluids; it increases with an increase in the value of the Prandtl number. For $\xi > \xi_1$, the value of $c_{f_x}\mathrm{Ra}_x^{1/4}/(\mathrm{Pr}\xi)$ decreases with distance from the leading edge; this decrease is due to the decrease in the viscosity of the shear-thinning fluid with an increase in shear rate.

4 Conclusions

The four-parameter modified power-law correlation for the non-Newtonian viscosity removes the physically unrealistic limits of zero and infinite viscosity introduced into the boundary-layer formulation by the popular two-parameter Ostwald–de Waele power-law model; consequently, it is a physically realistic model. The values of the four parameters in the modified power-law correlation can be determined from available experimental data. The numerical results indicate that a locally self-similar solution exists in a region close to the leading edge of the plate where the shear rate is smaller than the lower threshold shear rate. This self-similar solution is identical to the similarity solution for a Newtonian fluid. The size of the region near the leading edge where a self-similar solution exists locally depends on the Prandtl number. As the shear rate increases beyond the lower threshold shear rate, the solution of the boundary-layer equations becomes nonsimilar. The results obtained for a shear-thinning fluid indicate that in the downstream region, the wall shear stress decreases compared with the case of a Newtonian fluid, while the local heat transfer rate increases due to the reduction in viscosity caused by an increase in the shear rate.

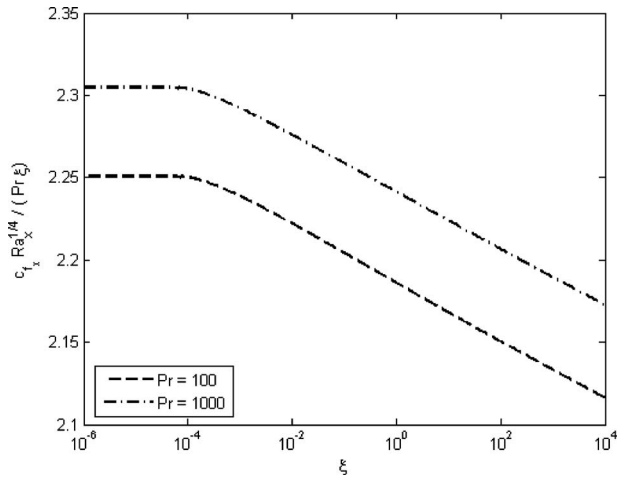

Fig. 10 Axial variation in $c_{f_x}\mathrm{Ra}_x^{1/4}/(\mathrm{Pr}\xi)$

Nomenclature

C = power-law parameter
c_f = skin-friction coefficient
D = nondimensional viscosity
g = gravitational acceleration
h = local heat transfer coefficient
k = thermal conductivity of the fluid
K = fluid consistency
l = reference length
n = non-Newtonian power-law index
Nu = Nusselt number
Pr = Prandtl number
Ra = Rayleigh number
T = dimensional temperature
T_w = surface temperature of the plate
T_∞ = Ambient temperature
u = velocity in the x-direction
U_0 = reference velocity
v = velocity in the y-direction
w = transformed velocity
x = coordinate along the plate
y = coordinate normal to the plate

Greek Symbols

α = thermal diffusivity of the fluid
β = coefficient of thermal expansion
γ = nondimensional shear rate
$\bar{\gamma}$ = dimensional shear rate
$\bar{\gamma}_1$ = lower threshold shear rate
$\bar{\gamma}_2$ = upper threshold shear rate
η = pseudosimilarity variable
μ = viscosity of the non-Newtonian fluid
μ_1 = zero-shear-rate viscosity
μ_2 = infinite-shear-rate viscosity
μ_R = ratio of infinite-shear-rate and zero-shear-rate viscosities
θ = nondimensional temperature
ρ_0 = reference density
τ_w = wall shear stress
ξ = axial coordinate along the plate
ξ_1 = location where non-Newtonian behavior starts

Superscripts

$-$ = dimensional quantities

Subscripts

w = surface
x = local value
∞ = freestream

References

[1] Hinch, J., 2003, "Non-Newtonian Geophysical Fluid Dynamics," 2003 Program in Geophysical Fluid Dynamics, Woods Hole Oceanographic Institution Woods Hole, MA.

[2] Acrivos, A., 1960, "A Theoretical Analysis of Laminar Natural Convection Heat Transfer to Non-Newtonian Fluids," AIChE J., **6**, pp. 584–590.

[3] Tien, C., 1967, "Laminar Natural Convection Heat Transfer to Non-Newtonian Fluids," Appl. Sci. Res., **17**, pp. 233–248.

[4] Chen, T. V. W., and Wollersheim, D. E., 1973, "Free Convection at a Vertical Plate With Uniform Flux Conditions in Non-Newtonian Power-Law Fluids," ASME J. Heat Transfer, **95**, pp. 123–124.

[5] Shulman, Z. P., Baikov, V. I., and Zaltsgendler, E. A., 1976, "An Approach to Prediction of Free Convection in Non-Newtonian Fluids," Int. J. Heat Mass Transfer, **19**, pp. 1003–1007.

[6] Som, A., and Chen, J. L. S., 1984, "Free Convection of Non-Newtonian Fluids Over Non-Isothermal Two-Dimensional Bodies," Int. J. Heat Mass Transfer, **27**, pp. 791–794.

[7] Haq, S., Kleinstreuer, C., and Mulligan, J. C., 1988, "Transient Free Convection of a Non-Newtonian Fluid Along a Vertical Wall," ASME J. Heat Transfer, **110**, pp. 604–607.

[8] Huang, M. J., Chung, J. S., Chou, Y. L., and Cheng, C. K., 1989, "Effects of Prandtl Number on Free Convection Heat Transfer From a Vertical Plate to a Non-Newtonian Fluid," ASME J. Heat Transfer, **111**, pp. 189–191.

[9] Huang, M. J., and Chen, C. K., 1990, "Local Similarity Solutions of Free-Convective Heat Transfer From a Vertical Plate to Non-Newtonian Power-Law Fluids," Int. J. Heat Mass Transfer, **33**, pp. 119–125.

[10] Kim, E., 1997, "Natural Convection Along a Wavy Vertical Plate to Non-Newtonian Fluids," Int. J. Heat Mass Transfer, **40**, pp. 3069–3078.

[11] Khan, W. A., Culham, J. R., and Yovanovich, M. M., 2006, "Fluid Flow and Heat Transfer in Power-Law Fluids Across Circular Cylinders: Analytical Study," ASME J. Heat Transfer, **128**, pp. 870–878.

[12] Denier, J. P., and Hewitt, R. E., 2004, "Asymptotic Matching Constraints for a Boundary-Layer Flow of a Power-Law Fluid," J. Fluid Mech., **518**, pp. 261–279.

[13] Denier, J. P., and Dabrowski, P. P., 2004, "On the Boundary-Layer Equations for Power-Law Fluids," Proc. R. Soc. London, Ser. A, **460**, pp. 3143–3158.

[14] Bird, R. B., Armstrong, R. C., and Hassager, O., 1987, *Fluid Mechanics* (Dynamics of Polymeric Liquids Vol. 1), 2nd ed., Wiley, New York.

[15] Yao, L. S., and Molla, M. M., 2008, "Non-Newtonian Fluid Flow on a Flat Plate Part 1: Boundary Layer," J. Thermophys. Heat Transfer, **22**, pp. 758–761.

[16] Yao, L. S., and Molla, M. M., 2008, "Forced Convection of Non-Newtonian Fluids on a Heated Flat Plate," Int. J. Heat Mass Transfer, **51**, pp. 5154–5159.

[17] Molla, M. M., and Yao, L. S., 2008, "Non-Newtonian Fluid Flow on a Flat Plate Part 2: Heat Transfer," J. Thermophys. Heat Transfer, **22**, pp. 762–765.

[18] Molla, M. M., and Yao, L. S., 2009, "The Flow of Non-Newtonian Fluids on a Flat Plate With a Uniform Heat Flux," ASME J. Heat Transfer, **131**, p. 011702.

[19] Yao, L. S., 1987, "Two-Dimensional Mixed Convection Along a Flat Plate," ASME J. Heat Transfer, **109**, pp. 440–445.

[20] Molla, M. M., and Yao, L. S., 2009, "Non-Newtonian Natural Convection Along a Vertical Heated Wavy Surface Using a Modified Power-Law Viscosity Model," ASME J. Heat Transfer, **131**, p. 012501.

[21] Molla, M. M., and Yao, L. S., 2008, "Non-Newtonian Mixed Convection Along a Vertical Flat Plate Heated With a Uniform Surface Temperature," Int. J. Heat Mass Transfer, (to be published).

[22] Ghosh Moulic, S., 1988, "Mixed Convection Along a Wavy Surface," MS thesis, Arizona State University, Tempe, AZ.

[23] Ghosh Moulic, S., and Yao, L. S., 1989, "Mixed Convection Along a Wavy Surface," ASME J. Heat Transfer, **111**, pp. 974–979.

The Impact of Normal Magnetic Fields on Instability of Thermocapillary Convection in a Two-Layer Fluid System

Hulin Huang[1]
e-mail: hlhuang@nuaa.edu.cn

Xiaoming Zhou

Academy of Frontier Science,
Nanjing University of Aeronautics and Astronautics,
Nanjing, 210016, P.R. China

When a temperature gradient is imposed along a liquid-liquid interface, thermocapillary convection is driven by the surface tension gradient. Such flow occurs in many application processes, such as thin-film coating, metal casting, and crystal growth. In this paper, the effect of a normal magnetic field, which is perpendicular to the interface, on the instability of thermocapillary convection in a rectangular cavity with differentially heated sidewalls, filled with two viscous, immiscible, incompressible fluids, is studied under the absence of gravity. In the two-layer fluid system, the upper layer fluid is electrically nonconducting encapsulant B_2O_3, while the underlayer fluid is electrically conducting molten InP. The interface between the two fluids is assumed to be flat and nondeformable. The results show that the two-layer fluid system still experiences a wavelike state when the magnetic field strength B_z is less than 0.04 T. The wave period increases and the amplitude decreases with the increasing of magnetic field strength. However, the convective flow pattern becomes complicated with a variable period, while the perturbation begins to fall into oblivion as the magnetic field intensity is larger than 0.05 T. When $B_z = 0.1$ T, the wavelike state does not occur, the thermocapillary convection instability is fully suppressed, and the unsteady convection is changed to a steady thermocapillary flow. [DOI: 10.1115/1.3084211]

Keywords: horizontal temperature gradient, thermocapillary convection, magnetohydrodynamics, wavelike state, magnetic fields, two-layer fluid system

1 Introduction

The study of two-layer fluid thermocapillary convection is of great importance in many engineering applications, including thin-film coating, metal casting, and crystal growth. In these types of flow, a nonuniform temperature distribution at the fluid interface induces interfacial tension gradients that, in turn, generate a driving force for thermocapillary convection (also known as Marangoni convection). The phenomena can cause adverse effects in several manufacturing processes, i.e., imperfections in crystal growth, and thus have attracted much interest. Smith and Davis [1] (S&D hereafter) performed a linear stability analysis on a thermocapillary flow in an infinite liquid layer with a constant-temperature gradient along a free surface. They predicted that the hydrothermal wave instability was a kind of new instability. Afterwards, the hydrothermal wave was confirmed by many reports. Riley and Neitzel [2] experimentally proved the existence of the hydrothermal wave, the characteristics of which were similar to the analysis by S&D. Xu and Zebib [3] made a numerical simulation on thermocapillary convection in a cavity including the influence of sidewalls, and they obtained a standing wave consisting of a pair of hydrothermal waves. Burguete et al. [4] reported experiments on buoyant-thermocapillary instabilities in differentially heated liquid layers. Depending on the height of liquid and on the aspect ratio, the two-dimensional basic flow destabilized into oblique traveling waves or longitudinal stationary rolls, respectively, for small and large fluid heights. The magnetic field has been motivated as one of the ways to further control free surface fluid flows. In particular, a magnetic field was applied to damp the flow in growing single crystals. Yang and Ma [5] investigated the impact of a magnetic field on the natural convection in a two-layer fluid system. Their results showed that the magnetic field provided an electromagnetic damping of the molten semiconductor in the lower layer fluid. Morthland and Walker [6] studied the effect of a magnetic field on the thermocapillary convection of the floating zone in a microgravity environment. The authors thought that a strong magnetic field parallel to the free surface of the floating zone could eliminate the unsteady convection associated with the hydrothermal rolls. Rao and Biswal [7] investigated the effect of a uniform magnetic field on the Benard–Marangoni convection in a shallow cavity. The results indicated that it was possible to control the convection in the lower layer by a suitable choice of the magnetic field.

Thermocapillary convection in a single fluid layer confined within a differentially heated rectangular cavity has been one of the most widely studied problems associated with the crystal growth process. Since encapsulation may be used to reduce the strength of steady thermocapillary convection, Liu et al. [8] extended their studies to the case of immiscible double liquid layers with the imposed temperature gradient parallel to the free surface. However, in comparison with the unencapsulated process, modeling of liquid-encapsulated crystal growth has received considerably less attention and the effect of magnetic fields on the stability of this flow remains an open question. Based on the fact that an applied external magnetic field does effectively suppress the thermocapillary convection instability, so, in this paper, we conducted a three-dimensional numerical simulation to investigate the effect of external magnetic fields on the instability of thermocapillary flow in a two-layer fluid system in a rectangular cavity under the absence of gravity.

[1]Corresponding author.

Contributed by the Heat Transfer Division of ASME for publication in the JOURNAL OF HEAT TRANSFER. Manuscript received January 29, 2008; final manuscript received November 9, 2008; published online April 7, 2009. Review conducted by Cholik Chan.

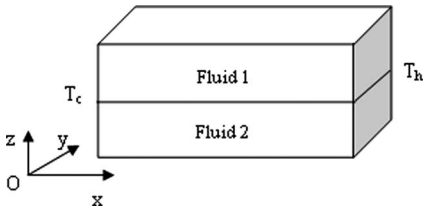

Fig. 1 Physical model

Table 1 Thermophysical properties of molten InP and B_2O_3

Property	Molten InP	B_2O_3
Viscosity (Pa s)	8.19×10^{-4}	3.9
Density (kg/m^3)	5050.0	1648.0
Specific heat (J/kg K)	424.0	1830.0
Thermal conductivity (W/m K)	22.0	2.0
Electrical conductivity (Ω^{-1} m^{-1})	7.0×10^5	0.0
Interfacial tension temperature coefficient (N/m K)	-1.2×10^{-3}	

2 Physical and Mathematical Models

The three-dimensional convective motion domain is a rectangular cavity as shown in Fig. 1 with a length (x) of 40 mm, a depth (y) of 20 mm, and a height (z) of 20 mm, respectively. The cavity is filled with two horizontal layers of immiscible fluids and each liquid layer height is 10 mm. The upper layer fluid is encapsulant boron oxide (B_2O_3) and the underlayer fluid is molten indium-phosphide (InP). The right wall is maintained at a constant-temperature T_h, while the left wall is at a lower temperature T_c ($T_h > T_c$). All the other walls are considered to be adiabatic. The temperature gradient is along the interface from right to left, the characteristic length is $L=40$ mm based on the interfacial length, which is significant for the wave traveling, and the aspect ratio Γ for each fluid is 4. The assumptions made in our model are as follows: (1) The two kinds of fluids are incompressible Newtonian fluids, (2) the flow is laminar flow, (3) the interface is flat and nondeformable, and (4) all the walls are electrically nonconducting. With the above assumptions, the momentum and energy equations are expressed as follows (subscript $i=1$ or 2, and 1 denotes the upper layer and 2 denotes the lower layer):

$$\nabla \cdot \boldsymbol{v}_i = 0 \tag{1}$$

$$\frac{\partial \boldsymbol{v}_i}{\partial t} + \boldsymbol{v}_i \cdot \nabla \boldsymbol{v}_i = -\frac{1}{\rho_i}\nabla p_i + \nu_i \nabla^2 \boldsymbol{v}_i + \frac{1}{\rho_i}\boldsymbol{f}_i \tag{2}$$

$$\frac{\partial T_i}{\partial t} + \boldsymbol{v}_i \cdot \nabla T_i = \alpha_i \nabla^2 T_i \tag{3}$$

where Lorentz force is expressed as $\boldsymbol{f}_i = \boldsymbol{J}\times\boldsymbol{B}$. $\boldsymbol{B}$ is the magnetic field intensity, which includes both the applied ($\boldsymbol{B}_z$) and induced magnetic field ($\boldsymbol{b}$) components. $\boldsymbol{J}$ is induced current density.

The induced magnetic field $\boldsymbol{b}$ can be derived from Maxwell's equations and Ohm's law as follows:

$$\frac{\partial \boldsymbol{b}}{\partial t} + (\boldsymbol{v}\cdot\nabla)\boldsymbol{b} = \frac{1}{\mu_m \sigma_m}\nabla^2 \boldsymbol{b} + (\boldsymbol{B}\cdot\nabla)\boldsymbol{v} \tag{4}$$

The induced current density is $\boldsymbol{J} = 1/\mu_m(\nabla\times\boldsymbol{B})$.

2.1 Boundary Conditions . All the walls are the no slip conditions and

$$T = T_c, \quad J_x = 0 \quad \text{at} \quad x = 0 \tag{5a}$$

$$T = T_h, \quad J_x = 0 \quad \text{at} \quad x = L \tag{5b}$$

$$\frac{\partial T}{\partial t} = 0, \quad J_z = 0 \quad \text{at} \quad z = 0 \quad \text{and} \quad L/2 \tag{5c}$$

$$\frac{\partial T}{\partial t} = 0, \quad J_y = 0 \quad \text{at} \quad y = 0 \quad \text{and} \quad L/2 \tag{5d}$$

The boundary conditions at the interface (at $z=L/4$)

$$u_1 = u_2, \quad v_1 = v_2, \quad w_1 = w_2 = 0 \tag{6a}$$

$$\mu_1\frac{\partial u_1}{\partial z} - \mu_2\frac{\partial u_2}{\partial z} = \frac{\partial \sigma_T}{\partial T}\frac{\partial T_2}{\partial x}, \quad \mu_1\frac{\partial v_1}{\partial z} - \mu_2\frac{\partial v_2}{\partial z} = \frac{\partial \sigma_T}{\partial T}\frac{\partial T_2}{\partial y} \tag{6b}$$

$$T_1 = T_2, \quad k_1\frac{\partial T_1}{\partial z} = k_2\frac{\partial T_2}{\partial z} \tag{6c}$$

$$\boldsymbol{J}_n = 0 \tag{6d}$$

To make sure that the oscillatory thermocapillary flow occurs in the two-layer fluid system in this paper, a $\Delta T = T_h - T_c = 15$ K corresponding to $\mathrm{Ma} = 8.79\times10^4$ was chosen; Ma represents the ratio of thermocapillary convection to conduction heat transfer. The physical properties of the fluids are the same as in Table 1.

3 Computational Method

The fundamental equations are discretized by the finite volume method. The central difference approximation is applied to the diffusion terms, while the second order upwind scheme is used for the convective terms. The discretized equations are solved by a fully implicit method in time marching. The pressure-implicit with splitting of operators (PISO) algorithm is used to handle the pressure-velocity coupling. The calculations are carried out on a nonuniform staggered grid system. Validation of the code for the oscillatory thermocapillary flow simulation was carefully done by comparing our simulation solutions with the experimental results by Schwabe and Benz [9]. Figure 2 shows the comparing of temperature oscillation frequency at a monitoring point. It indicates that the trend of simulation results is similar with the experimental results well.

The test cavity is discretized with a nonuniform mesh of $81^x \times 41^y \times 41^z$. A finer mesh gradation is utilized in regions where strong velocity and temperature gradients are anticipated. This includes regions near the solid boundaries, as well as the interface. This mesh is determined by refining the mesh size until convergence and constancy of temperature oscillatory frequency are achieved. In order to check the grid convergence, simulations with three sets of different meshes, as shown in Table 2, are performed at $\Delta T = 15$ K. Three sets of grids produced similar flow patterns

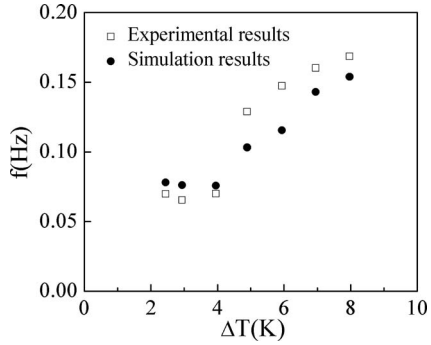

Fig. 2 Comparison of temperature oscillation frequency at a monitoring point

Table 2 Mesh dependency of temperature oscillation frequency at monitoring point *P*

Mesh	$81^x \times 41^y \times 41^z$	$91^x \times 46^y \times 46^z$	$101^x \times 51^y \times 51^z$
Frequency (Hz)	0.232511	0.232558	0.232603

and oscillation characteristics. However, the frequency of temperature oscillation at the monitoring point P of interface ($x=20$ mm, $y=10$ mm, and $z=10$ mm) showed small grid dependence. In addition, when magnetic field is applied, the calculations are repeated with a $101^x \times 51^y \times 51^z$ grid. The numerical solutions show for both grids the same qualitative behavior and differ quantitatively by less than 5%. Therefore, the mesh elected in this study is sufficient for accurate simulation. Based on Leboucher's [10] study, to achieve a stable numerical solution throughout the simulation the time step should be reduced when a magnetic field is applied. So the adaptive time step is used and varies between 1×10^{-4} and 1×10^{-2}. For each time step the quotient $Q=|\varphi^{n+1}-\varphi^n|/|\varphi^n_{\max}|$ is calculated for all dependent variables in all grid points. The index $n+1$ denotes a discrete point of time, which follows the point of time n after a time step Δt. If $Q\leq10^{-5}$ is valid for all variables in all grid points the solution is interpreted as converged.

4 Results and Discussions

Numerical simulations for the effect of normal magnetic field on the instability of thermocapillary convection were performed in the present work. The upper layer fluid is encapsulant and the underlayer fluid is molten semiconductor. Here, the convection in the underlayer fluid is our concern because of its role in practical engineering.

4.1 Thermocapillary Convection Instability Without Magnetic Field. Any temperature difference ($\Delta T>0$) produces a surface tension gradient at the interface between the molten liquid and the encapsulant and the Marangoni effect induces thermocapillary flows in two fluids. The thermocapillary flow of each fluid layer (aspect ratio $\Gamma=4$) appears as a steady flow with a single convective cell when ΔT is very small, which is called as the "basic flow." However, when ΔT exceeds a certain threshold value, this basic flow will change to oscillatory convection.

Figure 3 exhibits the streamlines' pattern of the oscillatory thermocapillary convection in one period at $\mathrm{Ma}=8.79\times10^4$. When $t=\tau_0$, it is an initial pattern of a periodical oscillatory flow in the two-layer fluids, where τ_0 is the starting time of temperature oscillation. The cell near the cold wall in the underlayer fluid begins to grow out and has the tendency to separate into two cells in the left. At $t=\tau_0+1/4\tau_p$, τ_p is the period of oscillation, the cell is divided into two small eddies. One (first eddy) locates at the vicinity of the cold wall, and the other (the second eddy) moves to the position at $x=0.01$ m. Moreover, there is a third eddy found underneath the interface. When $t=\tau_0+1/2\tau_p$, the second eddy travels to the center of the underlayer fluid, and almost occupies the whole domain. At the moment, both the first and third eddies disappear. Thereafter, the primary cell (the second eddy) still migrates continuously toward the right, but it will be drawn back toward the cold wall along the interface after it is fully developed. At $t=\tau_0+3/4\tau_p$, the center of the cell moves to the vicinity of the cold wall, and the peripheral streamlines' structures are separated into a few convective circulations again. It is obvious that there is another convective loop at the corner of the hot wall. Next, the cell near the cold wall will move down, restore back to the initial flow pattern of the τ_0, and start the next oscillatory convection. In the upper layer, the flow consists of a strong eddy attached to the hot wall, and embedded in the return flow is a small region of closed streamlines near the cold side, which is similar to the flow state of oscillatory instability for aspect ratio $\Gamma=4$ as reported by Kuhlmann and Albensoder [11]. From the streamlines' evolution, we know that these cells travel from the cold wall to the hot wall; however, the cell configurations are different from those of the underlayer fluid because the Pr number is different between the upper layer and the underlayer fluids.

That mentioned above is the developing process of the oscillatory wavelike state; it shows that a pair of wave traveling in the x direction formed the two-layer fluid system. This present oscillatory instability is similar with the hydrothermal wave in return flow as reported by S&D [1] due to the thermocapillary effect primarily, but the particular structure of the wave is strongly influenced by the underlying nonparallel basic flow. In order to observe the oscillatory flow much clearly and obtain the exact oscillatory period, we monitored the temperature fluctuation of point P ($x=0.02$ m, $y=0.01$ m, and $z=0.01$ m) with calculating time as shown in Fig. 4. From the figure we can find that the temperature fluctuation is a sinusoid, and the oscillatory period and amplitude become constant after 39.5 s. After that, a periodical temperature wave traveling occurs; it means that the oscillatory instability occurs. The period determined from the temperature oscillation at point P (Fig. 4) is 4.30 s, which is consistent with that found in the temperature wave evolution (Fig. 5).

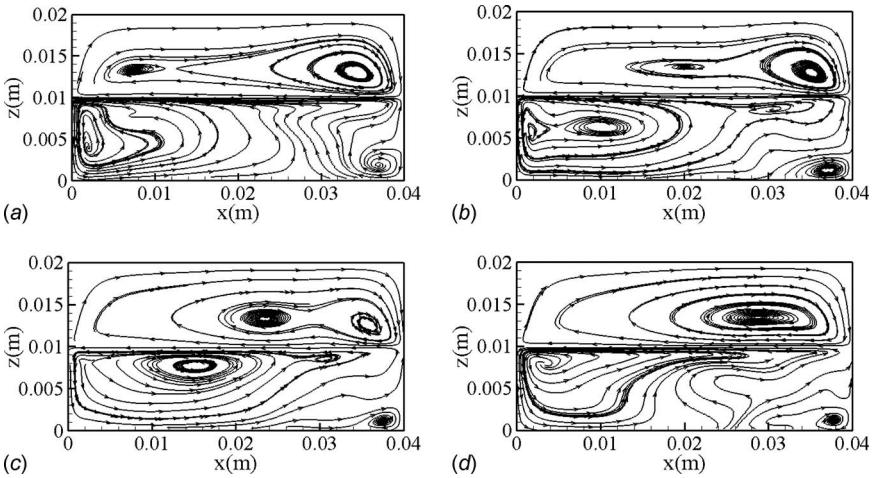

Fig. 3 Streamlines on $y=0.01$ m plane in one oscillation period (τ_p) without MHD: (*a*) $t=\tau_0$, (*b*) $t=\tau_0+1/4\tau_p$, (*c*) $t=\tau_0+1/2\tau_p$, and (*d*) $t=\tau_0+3/4\tau_p$

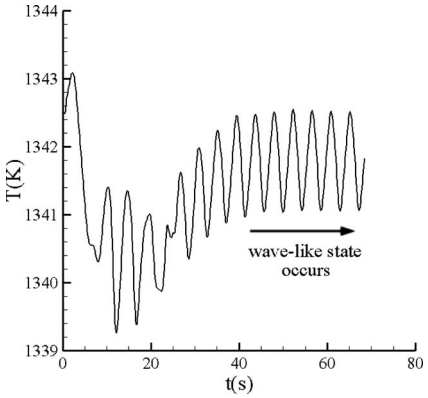

Fig. 4 Temperature fluctuation at the monitoring point *P* with time without MHD

Here, in order to clearly express temporal distributions of temperature disturbances, we introduce a temperature fluctuation function δT [12] for this case, where δT is the deviation of local temperature from time-averaged temperature at that point, defined as $\delta T = T - 1/\tau_p \int_{\tau_0}^{\tau_0+\tau_p} T dt$. Figure 5 indicates a variation of temperature temporal distributions on the $y = 0.01$ m plane in one period. The temperature perturbation periodically initiates near the cold wall and propagates from the cold wall to the hot wall, similar to a hydrothermal wave. Its intensity of the temperature perturbation is strengthening gradually during its traveling process. After the temperature wave crest arrives at the hot wall, they are then extruded and die away finally. The range of the temperature fluctuation is -1.0 K to 1.5 K.

4.2 The Impact of Magnetic Fields on Thermocapillary Convection Instability. In order to investigate the effect of a magnetic field on the thermocapillary convection instability, magnetic fields normal to the temperature gradient direction are applied to the system with an intensity of magnetic field varying from 0.01 T to 0.1 T. The corresponding Hartmann number, which represents the ratio of electromagnetic forces to viscous forces, is 11.7 to 117. For the sake of reducing the computation time, in all magnetohydrodynamics (MHD) calculations the magnetic field is applied after the oscillatory convection has formed.

For magnetic field intensity below 0.04 T, the analysis showed that the thermocapillary convection instability in the two-layer fluid system was not suppressed completely and the magnetic field just influenced the period and the amplitude of oscillation. Here, the effects of magnetic field on the wavelike state instability at $B_z = 0.04$ T are shown in Fig. 6. When $t = \tau_0$, the convective cell near the cold wall in the underlayer fluid begins to protrude to-

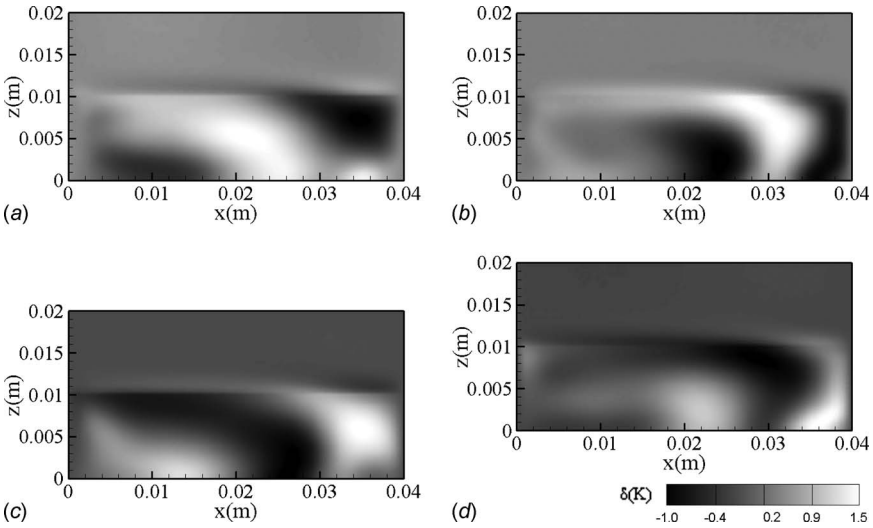

Fig. 5 Temperature temporal perturbation on $y = 0.01$ m plane in one period (τ_p) without MHD: (*a*) $t = \tau_0$, (*b*) $t = \tau_0 + 1/4\tau_p$, (*c*) $t = \tau_0 + 1/2\tau_p$, and (*d*) $t = \tau_0 + 3/4\tau_p$

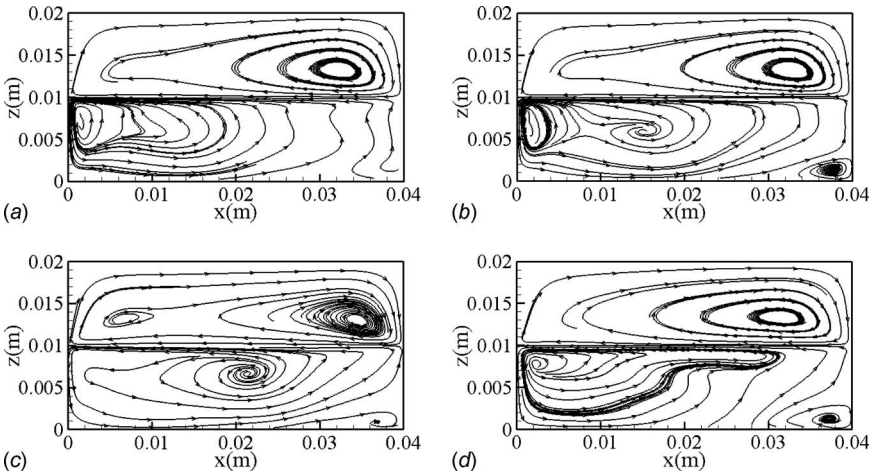

Fig. 6 Streamlines on $y = 0.01$ m plane in one oscillation period (τ_p) under $B_z = 0.04$ T: (*a*) $t = \tau_0$, (*b*) $t = \tau_0 + 1/4\tau_p$, (*c*) $t = \tau_0 + 1/2\tau_p$, and (*d*) $t = \tau_0 + 3/4\tau_p$

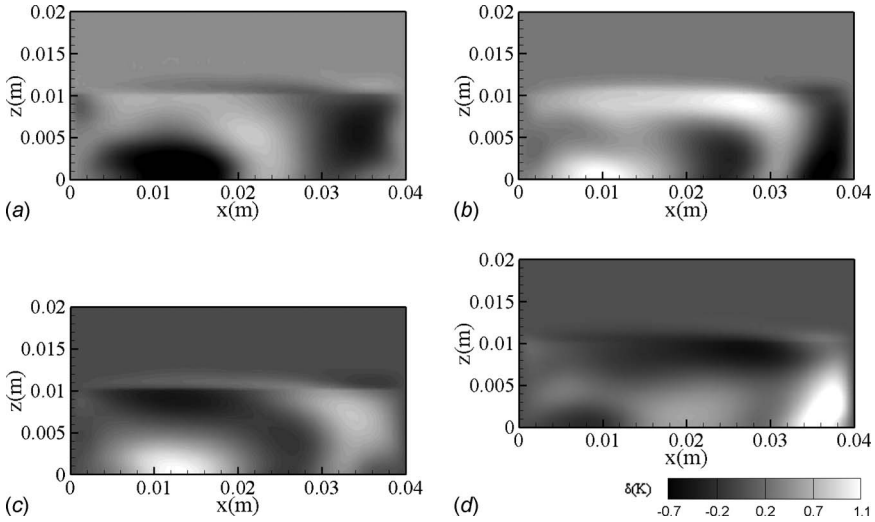

Fig. 7 Temperature perturbation on $y=0.01$ m plane in one period (τ_p) under $B_z=0.04$ T: (*a*) $t=\tau_0$, (*b*) $t=\tau_0+1/4\tau_p$, (*c*) $t=\tau_0+1/2\tau_p$, and (*d*) $t=\tau_0+3/4\tau_p$

ward the right, which makes as starting point of a traveling periodical cell. Comparing with that without a magnetic field, the length of protrusion is shorter, and the distortion of streamlines and the convective eddies are weaker. At $t=\tau_0+1/4\tau_p$, the cell is separated into two small cells. The new cell moves to the position at $x=0.015$ m and the periphery streamlines form an integrated convective circulation, which is faster than that without a magnetic field. At $t=\tau_0+1/2\tau_p$, the cell near the cold wall (old cell) disappears and the new cell becomes the primary convective cell in the underlayer fluid, whose center is closer to the center of the fluid domain compared with that without a magnetic field. The primary cell will contract toward the cold wall along the interface after fully developed and become a smaller cell. When $t=\tau_0+3/4\tau_p$, the cell moves back to the corner between the cold wall and the interface, and the integrated convective circulation is broken. Next, it will redisplay the flow structure of the τ_0 and become the incipience of next traveling after $1/4\tau_p$.

A variation of temperature perturbations on the $y=0.01$ m plane during one period shown in Fig. 7 reveals a similar pattern of temperature wave traveling that found in no magnetic field. The temperature perturbation initiates periodically near the cold wall and propagates toward the hot wall along the temperature gradient direction. However, it should be noticed that the range of temperature oscillation is reduced to −0.7 K to 1.1 K. The temperature perturbation at monitoring point *P* is shown in Fig. 8 under an applied magnetic field $B_z=0.04$ T. As shown, the period increases slightly to 4.62 s, while the oscillatory amplitude decreases to 1.38 K.

When the magnetic field intensity is increased to 0.05 T, the variation of temperature fluctuations at the monitoring point is not a complete sinusoid as shown in Fig. 9. The oscillatory period and amplitude do not keep constant (see the circle in Fig. 9) and the thermocapillary convection instability becomes more complicated. This means that the oscillation includes several oscillatory frequencies. The temperature fluctuation at the monitoring point under a magnetic field $B_z=0.08$ T is shown in Fig. 10, which displays that the oscillation begins to become irregular and the thermocapillary convection perturbation begins to be annihilated.

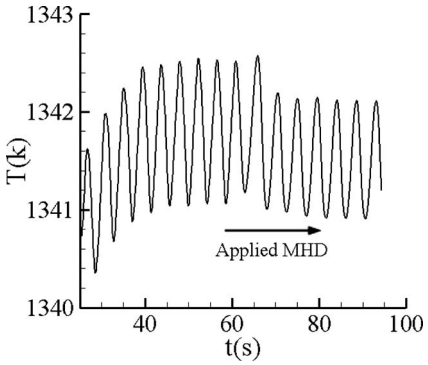

Fig. 8 Temperature fluctuation at monitoring point *P* under $B_z=0.04$ T

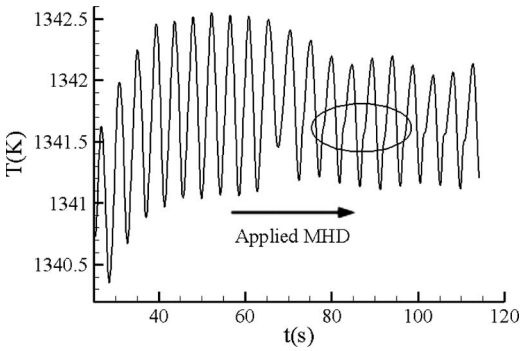

Fig. 9 Temperature fluctuation at point *P* under $B_z=0.05$ T

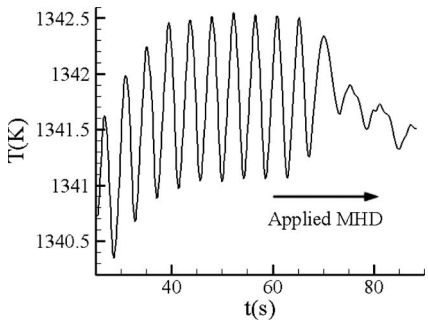

Fig. 10 Temperature fluctuation at point *P* under $B_z=0.08$ T

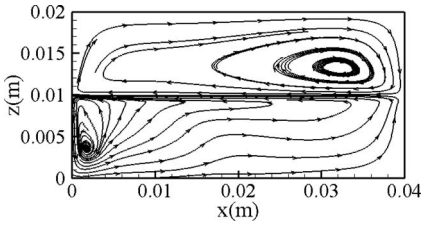

Fig. 11 Steady streamlines' pattern of thermocapillary convection under B_z=0.1 T

When a magnetic field B_z=0.1 T is applied to the two-layer fluid system, the computational results show that the thermocapillary convection does not follow the phenomenon of wavelike state anymore, and the convective configuration is a steady convection cell as shown in Fig. 11. This reveals that the unsteady flow is changed to a steady flow under the normal magnetic field B_z=0.1 T, because the effect of Lorentz forces is stronger than the perturbation effect of thermocapillary forces, then the wave traveling mechanism is suppressed. At the same time, the temperature at the monitoring point *P* becomes constant gradually, as shown in Fig. 12, which indicates that the oscillatory instability is fully suppressed and the fluid temperature at every point remains constant.

Figure 13 shows that the oscillatory period and oscillatory amplitude vary with Hartmann number at the monitoring point *P*. From this figure, we understand that the oscillatory period increases slightly with the Hartmann number under lower Hartmann number, but it increases sharply with the Hartmann number approaching 50 or more. Meanwhile, the amplitude of oscillation decreases gradually with the Hartmann number. It indicates that the oscillatory frequency of the wavelike state becomes very slow and the temperature fluctuation is very small under high Hartmann number conditions. Consequently, the unsteady flow is changed to steady flow under a high magnetic field.

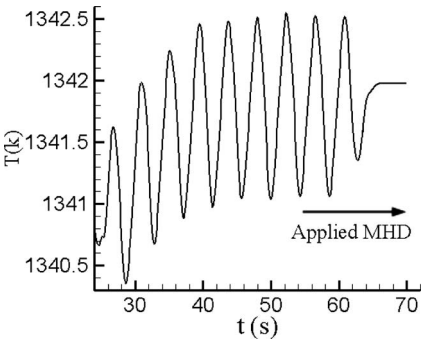

Fig. 12 Temperature fluctuation at monitoring point under B_z =0.1 T

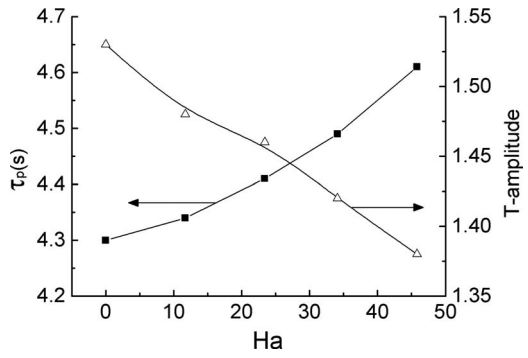

Fig. 13 Oscillatory period and amplitude vary with H_a

5 Conclusions

In this paper, the instability of thermocapillary convection driven by the surface tension gradient and the effects of uniform normal magnetic fields on the convection instability were investigated in the absence of gravity. From the simulation results, the following conclusions are drawn.

(1) In each layer of fluid, the flow cells originate near the cold wall and travel along the temperature gradient direction at $Ma=8.79\times10^4$. It is believed that these moving cells mean that an oscillatory, wavelike state is formed, and this wavelike state is similar with the hydrothermal wave.
(2) When the applied magnetic field B_z is below 0.04 T, the two-layer fluid system still demonstrates a periodic wavelike state, but the oscillatory period increases and the oscillatory amplitude decreases with the increasing of magnetic field intensity. Furthermore, the thermocapillary convection shows no periodic wavelike state instability when $B_z \geq 0.05$ T.
(3) When the intensity of the normal magnetic field is over 0.1 T, the oscillatory instability is fully suppressed, the wavelike state does not occur, and the unsteady thermocapillary convection is transformed into a steady convection flow.

Acknowledgment

The research was supported by the National Natural Science Foundation of China (Grant No. 50576036).

Nomenclature

$\boldsymbol{B}$ = magnetic field intensity (T)
$\boldsymbol{B_z}$ = applied magnetic field intensity (T)
$\boldsymbol{b}$ = induced magnetic field intensity (T)
$\boldsymbol{f}$ = Lorentz force (N m^{-3})
H_a = Hartmann number, $H_a=B_zL\sqrt{\sigma_m/\mu_2}$
$\boldsymbol{J}$ = induced current (A m^{-2})
k = thermal conductivity (W m^{-1} K^{-1})
L = cavity length
M_a = Marangoni number, $M_a=(\partial\sigma_T/\partial T)(T_h-T_c)L/\mu_2\alpha_2$
P = pressure (Pa)
Q = convergence criteria
t = time (s)
T = temperature (K)
u, v, w = velocity components in the (x,y,z) directions

Greek Symbols

α = thermal diffusivity (m^2 s^{-1})
Γ = aspect ratio (the ratio of length to high)
μ = dynamic viscosity (kg s^{-1} m^{-1})
μ_m = magnetic conductivity (henries per meter m^{-1})
ν = kinematic viscosity (m^2 s^{-1})
ρ = density (kg m^{-3})
σ_m = electrical conductivity (Ω^{-1} m^{-1})
σ_T = surface tension (N m^{-1})
τ_p = wave traveling period (s)

Subscripts

i = ith fluid layer (i=1,2)
m = magnetic field
n = normal to the interface

References

[1] Smith, M. K., and Davis, S. H., 1983, "Instabilities of Dynamic Thermocapillary Liquid Layers. Part 1. Convective Instabilities," J. Fluid Mech., **132**, pp. 119–144.
[2] Riley, R. J., and Neitzel, G. P., 1998, "Instability of Thermocapillary–Buoyancy Convection in Shallow Layers. Part 1. Characterization of Steady and Oscillatory Instabilities," J. Fluid Mech., **359**, pp. 143–164.

[3] Xu, J., and Zebib, A., 1998, "Oscillatory Two- and Three-Dimensional Thermocapillary Convection," J. Fluid Mech., **364**, pp. 187–209.
[4] Burguete, J., Mukolobwiez, N., and Daviaud, F., 2001, "Buoyant–Thermocapillary Instabilities in Extended Liquid Layers Subjected to a Horizontal Temperature Gradient," Phys. Fluids, **13**, pp. 2773–2787.
[5] Yang, M., and Ma, N., 2005, "A Computational Study of Natural Convection in a Liquid-Encapsulated Molten Semiconductor With a Horizontal Magnetic Field," Int. J. Heat Fluid Flow, **26**, pp. 810–816.
[6] Morthland, T. E., and Walker, J. S., 1998, "Magnetically Damped Thermocapillary Convections in Fluid Layers in Microgravity," AIAA 98-0653.
[7] Rao, A. R., and Biswal, P. C., 2001, "Benard-Marangoni Convection in Two Thin Immiscible Liquid Layers With a Uniform Magnetic Field," Acta Mech., **151**, pp. 61–73.
[8] Liu, Q. S., Roux, B., and Velarde, M. G., 1998, "Thermocapillary Convection in Two-Layer Systems," Int. J. Heat Mass Transfer, **41**, pp. 1499–1511.
[9] Schwabe, D., and Benz, S., 2002, "Thermocapillary Flow Instabilities in an Annulus Under Microgravity—Results of the Experiment MAGIA," Adv. Space Res., **29**, pp. 629–638.
[10] Leboucher, L., 1999, "Monotone Scheme and Boundary Conditions for Finite Volume Simulation of Magnetohydrodynamic Internal Flows at High Hartmann Number," J. Comput. Phys., **150**, pp. 181–198.
[11] Kuhlmann, H. C., and Albensoder, S., 2008, "Three-Dimensional Flow Instability in a Thermocapillary Driven Cavity," Phys. Rev. E, **77**, p. 036303.
[12] Shi, W. Y., and Nobuyuki, I., 2006, "Hydrothermal Waves in Differentially Heated Shallow Annular Pools of Silicone Oil," J. Cryst. Growth, **290**, pp. 280–291.

Experimental Investigation of Radiation Effects on Natural Convection in Horizontal Channels Heated From Above

Oronzio Manca
e-mail: oronzio.manca@unina2.it

Sergio Nardini

Dipartimento di Ingegneria Aerospaziale e Meccanica,
Seconda Università degli Studi di Napoli,
Real Casa dell'Annunziata via Roma 29,
81031 Aversa Caserta (CE), Italy

Radiation heat transfer affects natural convection of air inside an open-ended cavity with a heated horizontal upper plate and an unheated lower parallel plate. Its effect is the heating of the lower plate, which heats the adjacent fluid layer and could determine secondary motions. In this paper, an experimental study is carried out to describe the effect of high value of surface emissivity on air flow in an open-ended cavity. The investigation is performed by means of wall temperature profiles, smoke visualization, and air temperature measurements. Results are obtained for an emissivity of the horizontal plates equal to 0.8, for aspect ratios between 10.0 and 20.0. By means of flow visualization and local air temperature measurements in the cavity as a function of time, remarkable secondary motions in the cavity are observed for the highest considered surface heat flux ($Ra=8.91\times10^3$, 6.45×10^4, and 1.92×10^5). Measurement of the air temperature in the cavity also shows that radiation causes and damps secondary motions at the same time. Mean air temperature profiles as a function of the vertical coordinate, at different locations along the longitudinal axis, confirm both the main flow path inside the cavity and radiation effect on convective heat transfer. Finally, correlations for average Nusselt numbers and dimensionless maximum wall temperatures, in terms of Rayleigh number and channel aspect ratio, are proposed for natural convection with or without radiative heat transfer contribution for $2.26\times10^3\leq Ra\leq1.92\times10^5$ and $10\leq 2L/b\leq20$. [DOI: 10.1115/1.3084212]

Keywords: natural convection, radiative effect, open-ended cavity, electronic cooling

1 Introduction

Natural convection in open-ended cavities has particular importance in natural phenomena as well as in several applications, such as thermal control of electronic systems, chemical vapor deposition reactors, solar collectors, and nuclear reactors. According to Vafai and Etthefagh [1], if a cavity has one permeable vertical surface, it is called open cavity. Whenever a cavity has two parallel permeable vertical surfaces, it is called open-ended cavity. In these configurations, there is a continuous intake of fresh air from the ambient and exhaust of heated air back to the ambient and hence stratification effects are reduced. The horizontal plates in the open-ended cavities can be both heated or one heated and the other one unheated. If the lower plate is heated or both the plates are heated, secondary motions may occur in the cavity [2]. When only the upper plate is heated instead, there are no secondary motions in the air flow for Grashof number values less than 6.0×10^5, as shown in Ref. [3]. Surface thermal radiation always exists and in natural convection, even moderate temperature differences determine significant effects. Therefore, the radiative and convective contributions may be comparable and influence the total heat transfer rate, the surface temperature, and the flow fields. Thermal radiation effects on the natural convection of air in open cavities and open-ended cavities may be meaningful whenever the heating process does not take place symmetrically, as shown in Ref. [4] for open top cavities.

Several investigations have been carried out on natural convection in horizontal open cavities [5–14] and open-ended cavities [1–3,15–22] both experimentally and numerically, as recently reviewed in Refs. [3,22]. These studies describe the effect on fluid flow and heat transfer of Rayleigh number and geometrical parameters. Moreover, the occurrence of transition and turbulence and interaction between the cavity and the external ambient are considered. Few papers have investigated the combined heat transfer by natural convection and thermal radiation in open cavities, as recently remarked in Ref. [23].

One of the first studies on the effect of surface radiation heat transfer in open cavity was accomplished by Lage et al. [4]. They studied numerically a two dimensional open top cavity in steady state condition, where one vertical wall was heated and the bottom and the other vertical wall were insulated. As far as the "C" shaped open cavity, Lin and Ko [24] showed that radiation increases the turbulent buoyancy-drive effect and the overall heat transfer of the cavity was enhanced significantly. Yu and Joshi [25] numerically and experimentally achieved results on combined conduction, natural convection, and radiation in a three-dimensional side-vented enclosure. Their results showed that in side-vented arrangement, natural convection was weakened by radiation, but the overall heat transfer was enhanced. Numerical investigations on transient combined natural convection and radiation were carried out by Hinojosa et al. [23,26] in square open cavities. The results for the horizontal open cavities [26] showed that the radiative heat transfer, between the walls and the aperture, considerably increases the total average Nusselt number. For tilted open cavities [23], it was observed that the Nusselt numbers increased with the Rayleigh number except the convective Nusselt number for 180°.

Radiation heightens the temperature on the lower plate in an open-ended cavity, where the upper plate is heated and the horizontal plate surfaces are gray. Lower plate heating may determine

Contributed by the Heat Transfer Division of ASME for publication in the JOURNAL OF HEAT TRANSFER. Manuscript received February 2, 2008; final manuscript received October 4, 2008; published online April 9, 2009. Review conducted by Yogesh Jaluria.

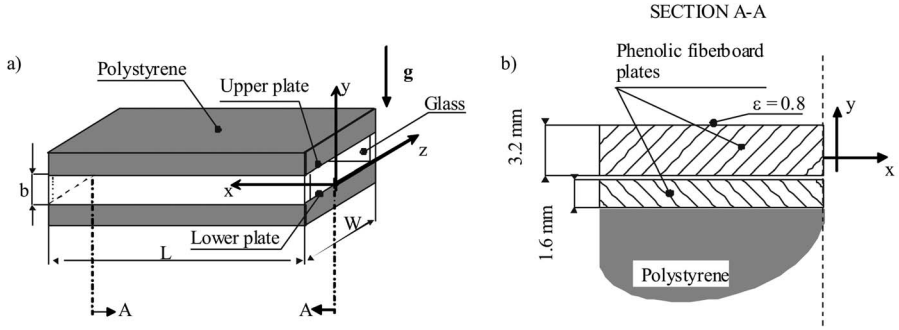

Fig. 1 (*a*) **View of the test section;** (*b*) **sketch of the heated sandwiched plate**

the onset of secondary motion that makes the main flow inside the cavity unstable and improves the buoyancy-drive effect. In the case of the presence of instability, the flow motion becomes three dimensional. To the authors' knowledge, no experimental investigation has been carried out on the radiation effects in open-ended cavities. This geometry is important in electronic cooling [20], in chemical vapor deposition processes [27], and in the study of smoke diffusion in a fire outbreak in building [14], as also underlined in Refs. [3,22].

This paper presents an experimental investigation for the natural convection of air between high emissivity horizontal walls with the upper plate exhibiting uniform heat flux and the lower plate unheated, by means of flow visualization and air temperature measurements. The wall length and width, and the distance between the horizontal wall, the wall heat flux, the ambient temperature, and the surface emissivity are the geometrical and thermal independent variables. These variables affect the wall temperature value, the convective and radiative heat transfer, and the main and secondary motions inside the open-ended cavity (horizontal channel), i.e., air velocity and temperature values. The experiments are carried out for two values of the wall distance, several values of heat flux and one value of wall emissivity equal to 0.8 in order to investigate mainly the influence of radiative heat transfer and the longitudinal aspect ratio. Flow visualization is performed to detect the flow patterns that can develop inside the channel. Air flow temperature measurements are carried out to furnish a thermal map inside the channel for the investigated configurations, and correlations are proposed for the evaluation of dimensionless heat transfer coefficients and maximum dimensionless wall temperatures in terms of Rayleigh number and longitudinal aspect ratio with and without radiative heat transfer contribution.

2 Experimental Apparatus

The experimental test section was composed of two horizontal principal plates: the upper one at uniform heat flux, the lower one adiabatic and two unheated side walls. The horizontal heated and unheated walls were made of two sandwiched phenolic fiberboard plates, each of them being 400 mm high and 530 mm wide. The side walls were made of glass rectangular rods, machined to an accuracy of ± 0.03 mm. The distance between the horizontal walls was measured to an accuracy of ± 0.25 mm by a dial-gauge equipped caliper.

The open-ended cavity was 400 mm long, $2L$, the distances between the plates, b, were 20.0 mm, 32.3 mm, 40.0 mm, and the width, W, was 450 mm. The cavity was open to ambient conditions along its right and left edges, Fig. 1(*a*). A 150 mm polystyrene block was affixed to the rear face of each plate to reduce conductive heat losses. The emissivity of the bare phenolic fiberboard was 0.8.

The rear plate was 1.6 mm thick. Its back surface was coated with a 17.5 μm thick copper layer, which was a serpentine shape heater. Its runs were 19.6 mm wide with a gap of nearly 0.5 mm between each one, giving a total length of 9.0 m. Its expected electrical resistance was 0.50 Ω. The narrow gaps between the runs, together with the relatively high thickness, 4.8 mm, of the resulting low-conductivity fiberglass, were suitable to maintain a nearly uniform heat flux at the plate surface [28]. The upper plate was heated by passing a direct electrical current through the heaters. This was accomplished by using a Hewlett-Packard 6260B dc power supply. The electrical power was evaluated by measuring the voltage drop across the upper plate and the current passing through it. An HP-3465A digital multimeter measured the voltage drop, while the current was calculated by a reference resistance and the measured voltage drop across it. To avoid electrical contact resistances, thick copper bars, soldered both to the electric supply cable and to the ends of the heater, were bolted together. A maximum variation of $\pm 10\%$ in the electrical resistivity of the copper was evaluated in the worst conditions, when the maximum wall temperature difference was 30 K. Therefore, a uniform wall heat flux was assumed, with a $\pm 5\%$ maximum deviation from its average value. The dissipated heat flux was evaluated to an accuracy of $\pm 2\%$. The entire apparatus was located within a room sealed to eliminate extraneous air currents.

Wall temperatures were measured by 24 0.50 mm outside diameter (OD) ungrounded iron-Constantan (J-type) thermocouples, embedded in each fiberboard plate and in contact with the outer layer. They were located at 12 longitudinal stations and three different z values. Seven thermocouples were affixed to the rear surface of the plates and embedded in the polystyrene to enable the evaluation of conductive heat losses.

The ambient air temperature was measured by a shielded thermocouple placed near one of the leading edges of the channel. An ISOTECH instrument D/J type J T/C Ice-Point was employed as a reference for cold thermocouple junctions. Their voltages were recorded to 1 μV by an NI SCXI Module Data Acquisition System unit connected to a personal computer. The recorded data were elaborated by the LABVIEW™ version 7.0 program [29]. The calibration of the temperature measuring system showed an estimated precision of the thermocouple-readout system of $\pm 0.1°C$. The entire apparatus was located in an enclosed room, accurately sealed in order to eliminate extraneous air currents, and air drafts were further reduced by vertical screens, 2.5 m high. A large fraction of the lower part of the screens was made up by a 0.20 m high mesh. The range of ambient temperature varied from 21°C to 22°C during the experiments.

The temperature of the air in the open-ended cavity was measured by a Dantec 5600 hot-wire system. The measurements were carried out using a subminiature 5 μm wire diameter probe connected to a 56C01–56C20 constant current bridge. The probe was calibrated in air in the 15–80°C temperature range. The maximum uncertainty was $\pm 0.1°C$. The probe could be manually positioned anywhere inside the cavity using a micrometer traversing mechanism supported on one side of the frame. The measurement locations in the $z=0$ longitudinal plane are indicated in Fig. 2 for

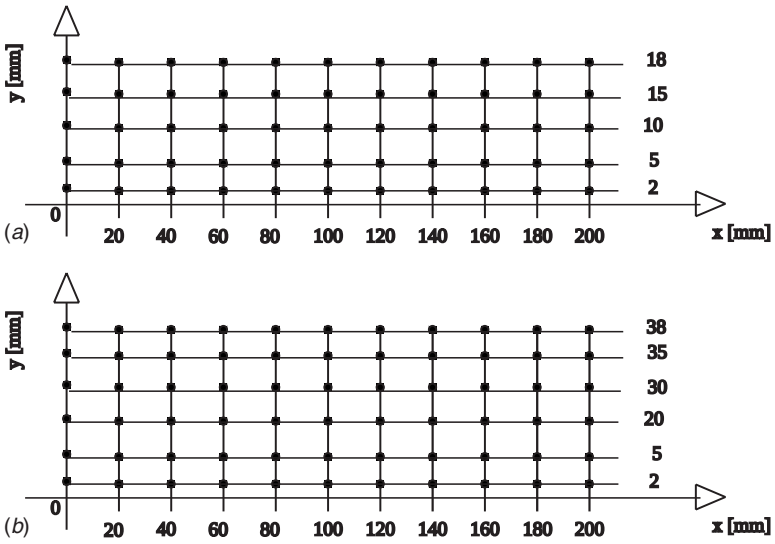

Fig. 2 Air temperature measurement grid in the longitudinal section: (*a*) *b*=20.0 mm; (*b*) *b*=40.0 mm

$b=20.0$ and 40.0 mm. This allowed positioning of the probe along the x and y axes to a maximum accuracy of 0.03 mm. The anemometer signal was acquired and recorded by the data acquisition system NI4351-DAQ along with the accessory TBX-68, and reduced by means of a personal computer through the VIRTUALBENCH-LOGGER software.

Each set of measurements was carried out for 8–9 h after modification of the configuration. This time interval was estimated to be long enough for the eventual wall temperature fluctuations to decrease and attain a quasisteady state, as regards time average values becoming constant.

Smoke for flow visualization was generated by burning incense sticks in a steel tube, connected to a compressor. The smoke was injected through a glass heat exchanger to reduce the temperature of the smoke and then passed into a plenum. The smoke temperature, measured by a thermocouple, turned out to be close to that of the ambient air entering the cavity. The smoke was then driven into the test section through a small slot situated under the leading edge of the bottom plate along the plate width. A sketch of the apparatus is shown in Fig. 3. A longitudinal view of the arrangement for the air temperature measurement is shown in Fig. 3(*a*), while a sketch of the visualization setup is shown in Fig. 3(*b*). Preliminary tests were carried out to determine the best plenum location in order not to interfere with the air flow at the inlet section. Visualization was made possible by means of a laser sheet, generated by a He–Ne laser source, Fig. 3(*b*). The laser sheet was produced by a cylindrical lens, which enlarged the beam as needed. Small adjustments were allowed by means of a micrometer screw system, in order to take photographs at different locations along the z axis. The same arrangement was used to obtain pictures in the y-z plane at several x locations. The still camera was a programmable Nikon F9X, and the film was high sensitivity Kodak TMAX™ 3200.

3 Data Reduction

The heating mode, taken into account, was the heated upper plate and the unheated lower one.

The Grashof and Rayleigh numbers were defined as

$$\mathrm{Gr}=\frac{g\beta q_c b^4}{\nu^2 k},\quad \mathrm{Ra}=\mathrm{Gr}\ \mathrm{Pr} \tag{1}$$

In addition, the Grashof and Rayleigh numbers can be defined in order to take into account both the convective and radiative heat transfer as:

$$\mathrm{Gr}^*=\frac{g\beta(q_c+q_r)b^4}{\nu^2 k},\quad \mathrm{Ra}^*=\mathrm{Gr}^*\ \mathrm{Pr} \tag{2}$$

where q_c and q_r are the average convective and radiative heat fluxes, respectively, defined as follows:

$$q_c=\frac{1}{2}\frac{1}{2L}\left[\int_0^{2L} q_{c,u}(x)dx+\int_0^{2L} q_{c,l}(x)dx\right] \tag{3a}$$

$$q_r=\frac{1}{2}\frac{1}{2L}\left[\int_0^{2L} q_{r,u}(x)dx+\int_0^{2L} q_{r,l}(x)dx\right] \tag{3b}$$

The Nusselt numbers were based on the difference between wall and inlet fluid temperatures rather than on that between wall and bulk fluid temperatures, since the latter is usually not available in practice. Two average Nusselt numbers can be defined. One accounts for the convective heat transfer from the walls and the other for the convective and radiative heat transfer. Thus we have

$$\mathrm{Nu}=\frac{q_c}{T_w-T_0}\frac{b}{k},\quad \mathrm{Nu}^*=\frac{q_c+q_r}{T_w-T_0}\frac{b}{k} \tag{4}$$

where the average wall temperature is

$$T_w=\frac{1}{2}\frac{1}{2L}\left[\int_0^{2L} T_{w,u}(x)dx+\int_0^{2L} T_{w,l}(x)dx\right] \tag{5}$$

The thermophysical properties were evaluated at the reference temperature $T_r=(T_w+T_0)/2$. The dimensionless temperatures are

$$T^+=\frac{T-T_0}{q_c b/k},\quad T^{+*}=\frac{T-T_0}{(q_c+q_r)b/k} \tag{6}$$

The local convective heat flux, $q_c(x)$, is not uniform because of radiation and conduction losses. Experimental data were reduced by introducing in Eqs. (3) and (5) the local convective heat flux:

$$q_c(x)=q_\Omega(x)-q_k(x)-q_r(x) \tag{7}$$

where $q_\Omega(x)$ is the local heat flux due to Ohmic dissipation, assumed to be uniform along the plate, $q_k(x)$ denotes the local conductive heat losses from the plate, and $q_r(x)$ is the local radiative heat flux from the plate. For each run, the term $q_k(x)$ was calculated by means of a numerical procedure, a three-dimensional distribution of the temperature being assumed in the polystyrene.

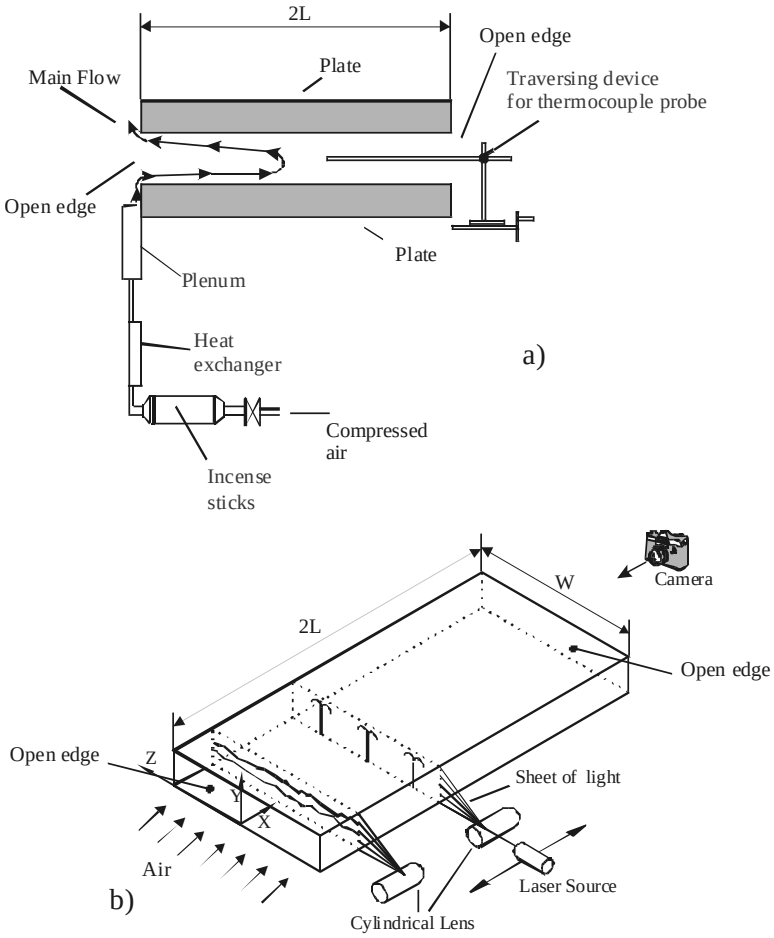

Fig. 3 Sketch of the test section with visualization and air temperature measurement arrangements: (*a*) longitudinal section; (*b*) three dimensional view

The numerical procedure employed the finite volume method and the wall temperatures, measured by 24 thermocouples, represented the input data. In order to check the accuracy of the numerical procedure, for some configurations, the temperatures of the numerical procedure, located in an x-z polystyrene plane very close to the heated plate, were compared with those measured by thermocouples, embedded in the polystyrene at the same plane location. The relationship was very good, the maximum deviation being 3%.

A two-dimensional radiative cavity was made of the two plates, considered as diffuse-gray surfaces and the two black edge sections at room temperature. The $q_r(x)$ terms were calculated for each temperature distribution of the wall, ambient temperature, and plate spacing, dividing each plate into 16 strips along its length. The value of the radiative heat losses was from 45% to 55% of the Ohmic dissipated rate from $b=20.0$ mm to $b=40.0$ mm, respectively.

A set of 1024 data samples was recorded for each run to measure the time-averaged temperatures and the fluctuations of the air temperature. The response of the subminiature probe was about 1 kHz [30], and, according to the procedure suggested by Bruun [31], the signal was sampled every 0.1 s.

3.1 Uncertainty Analysis. The uncertainty of the values of Gr and Nu was evaluated following the procedure suggested in Refs. [32,33]. Accordingly, the uncertainty of the dependent variable R, as a function of the uncertainties of the independent variables X_i, is given by the relation

$$U_R^2 = \left(\frac{\partial R}{\partial X_1}U_{X_1}\right)^2 + \left(\frac{\partial R}{\partial X_2}U_{X_2}\right)^2 + \cdots + \left(\frac{\partial R}{\partial X_j}U_{X_j}\right)^2 \quad (8)$$

Therefore, on the basis of Eqs. (1), (2), and (4) and of the non-negligible uncertainties of the values of the independent variables reported in Table 1, the uncertainties of Ra, Ra*, Nu, and Nu* were 8%, 6%, 7%, and 5%, respectively.

4 Results

Results were obtained for a cavity gap equal to 20.0 mm, 32.3 mm, and 40.0 mm. The Ohmic heat fluxes were set equal to 26 W/m^2, 60 W/m^2, and 120 W/m^2. The aforementioned parameters yield Rayleigh numbers in the 2.26×10^3–1.92×10^5 range.

A flow penetration inside the cavity was detected, for any considered Rayleigh number, as described in Refs. [2,3,22]. A sketch of the main flow patterns in the longitudinal section at $z=0$ is shown in Fig. 4. Subsequently, the above described flow will be referred to as C-loop, and the penetration length is the distance along the x axis from the leading edge to the section where the

Table 1 Percentage uncertainty values ($U_{Xi}|X_i100$)

Variable	T_0	T_w-T_0	q_c	q_r	q_c+q_r	q_Ω	q_k	b
Uncertainty	0.068	4.0	5.7	5.0	2.5	2.0	4.2	1.3

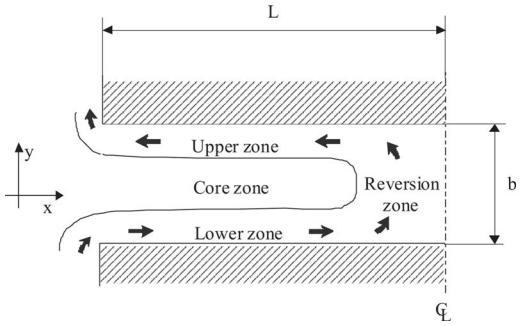

Fig. 4 Sketch of the main flow in the cavity

reversion zone is evident, according to Refs. [2,3,5,22]. Four zones are identified in the main flow: a lower boundary layer, where the fluid flows adjacent to the lower plate from the leading edge to the middle plane of the open-ended cavity; a reversion zone, where the main flow reverses its motion; an upper boundary layer, where the fluid flows adjacent to the upper plate from the reversion zone to the trailing edge; and a core zone separating the lower and the upper boundary layers.

4.1 Wall Temperatures. Figure 5 shows the profiles of the temperature rise as related to the ambient temperature T_0 in the $z=0$ mm plane over the heated upper and the unheated lower plates. In Figs. 5(*a*)–5(*c*), the profiles are reported for *b* values equal to 20.0 mm, 32.3 mm, and 40.0 mm, respectively, and heat flux values: $q_\Omega=26$, 60, and 120 W/m^2; hence Ra ranges between 2.26×10^3 and 1.92×10^5. For all configurations, the profiles along the *x*-direction are symmetric with respect to middle plane, the $x=200$ mm plane, as expected. Surface temperature decreases from the centerline to the leading edge due to edge effects. Enhancement of heat transfer, close to the edges, is caused both by radiation to the ambient and natural convection inside the open-ended cavity. Furthermore, for $q_\Omega=26$ W/m^2 (Ra$=2.26\times10^3$, 1.64×10^4, and 3.71×10^4), the temperature difference between the plates is the lowest for all *b* and, for $x=200$ mm, it is about 1.5°C, 2.2°C, and 2.6°C for $b=20.0$, 32.3, and 40.0 mm, respectively. As the heat flux rises, the surface temperatures and temperature gradients, along the plate, assume higher values. For $q_\Omega=120$ W/m^2 and $b=20.0$ and 32.3 mm (Ra$=8.91\times10^3$, 6.45×10^4), the slope is higher for the lower plate than for the upper one close to the cavity edges because the air temperature coming from the ambient and flowing adjacent to the lower plate is lower than the air temperature flowing nearby the upper heated plate edge and coming from the inner part of the cavity, where air has reverted its motion. This pattern is called C-loop, as previously described. In the Fig. 5(*b*), for $b=32.3$ mm (Ra$=1.64\times10^4$, 3.86×10^4, 6.45×10^4), the temperature profiles close to the edges have a lower slope than those for $b=20.0$ mm (Ra$=2.26\times10^3$, 5.38×10^3, 8.91×10^3), whereas in the plate central zone, they present lower gradients and magnitudes. The main flow does not penetrate up to the middle section and determines transversal vortex cells in this zone. The temperature difference between the two plates is greater than for $b=20.0$ mm. The higher value of this difference is attained at $x=60$ mm and its maximum value, which is attained for $b=32.3$ mm and $q_\Omega=120$ W/m^2 (Ra$=6.45\times10^4$), is about 13°C. This is explained with a higher air mass flow rate induced inside the open-ended cavity and a greater penetration depth. This trend is also present for $b=40.0$ mm. For $b=40.0$ mm and $q_\Omega=120$ W/m^2 (Ra$=1.92\times10^5$), Fig. 5(*c*), it is worth noting that the temperature decrease at $x=200$ mm is caused by the air motion due to the transversal vortex cells present in the reversion zone.

4.2 Flow Visualization. The pictures for longitudinal, *z*

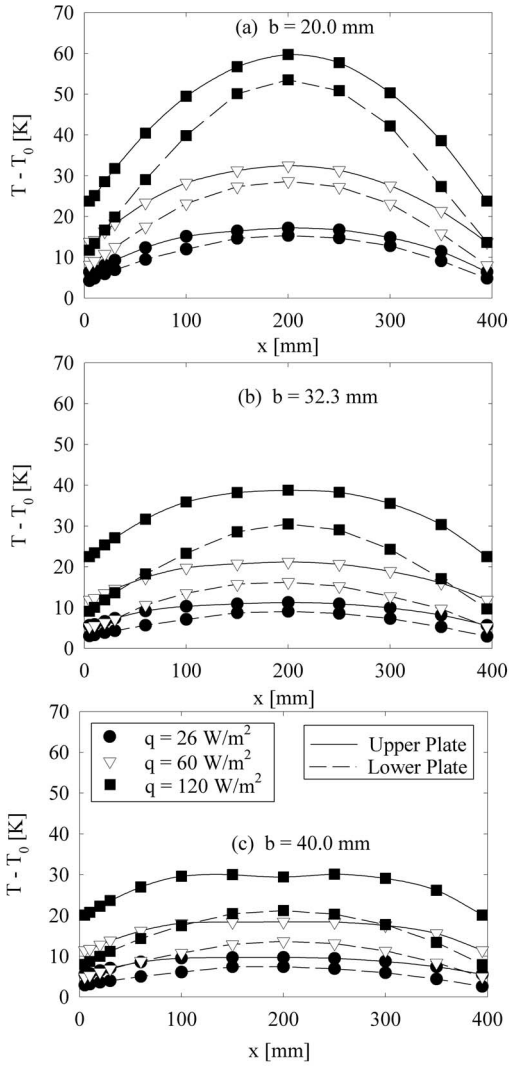

Fig. 5 Surface temperature versus longitudinal *x*-coordinate for three Ohmic wall heat fluxes: (*a*) $b=20.0$ mm (Ra = (●) 2.26×10^3, (▽) 5.38×10, (■) 8.91×10^3); (*b*) $b=32.3$ mm (Ra= (●) 1.64×10^4, (▽) 3.86×10^4, (■) 6.45×10^4); (*c*) $b=40.0$ mm (Ra= (●) 3.71×10^4, (▽) 8.92×10^4, (■) 1.92×10^5)

$=0$ mm, and transversal sections, $x=20$, 100, 150, and 200 mm, with a cavity gap of $b=20.0$ mm and an Ohmic wall heat flux of 60 W/m^2 (Ra$=5.38\times10^3$), are reported in Fig. 6. The longitudinal section, Fig. 6(*a*), shows the typical C-shaped main motion, in agreement with the wall temperature measurements and the results presented in Refs. [2,3,5]. It is clearly observed in Fig. 6(*a*) that the fluid enters the cavity flowing along the lower plate, then it reverses its motion flowing upward, and, finally, it exits the cavity flowing along the upper plate. For this configuration, $b=20.0$ mm, the flow has a penetration depth inside the cavity of about 140 mm, and the smoke does not totally fill the cavity gap. This confirms the described path of the main flow, as shown in Fig. 4, and agrees with the results given in Ref. [3]. The cross-stream sections are reported in Figs. 6(*b*)–6(*e*) at $x=20$, 100, 150, and 200 mm from the leading edge of the cavity. At $x=20$ mm (Fig. 6(*b*)), the flow is laminar and no disturbances induced by secondary motion are observed. At $x=100$ mm (Fig. 6(*c*)), two vortex structures with longitudinal axes are observed near the side vertical walls. Also, in the central part of the cross section, some vortex structures are observed. These structures become more evi-

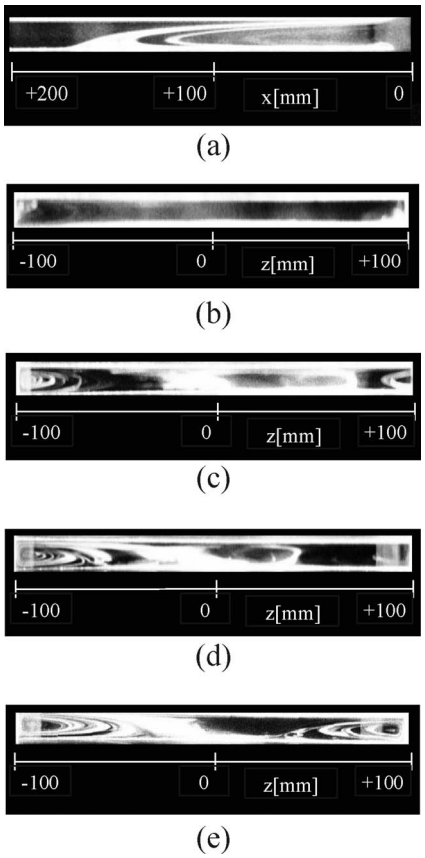

Fig. 6 Flow visualization for $b=20.0$ mm and $q_\Omega=60$ W/m^2 (Ra$=5.38\times10^3$). Longitudinal section at (*a*) $z=0$ mm; transversal sections at (*b*) $x=20$ mm, (*c*) $x=100$ mm, (*d*) $x=150$ mm, and (*e*) $x=200$ mm.

dent further inside the cavity. Figure 6(*d*) shows that the main flow reverses its motion at $x=150$ mm. The visualization at $x=200$ mm, in Fig. 6(*e*), is similar to the one at $x=150$ mm. This suggests that a fluid stagnation is present in this zone.

The configuration with $b=40.0$ mm and $q_\Omega=60$ W/m^2 (Ra $=8.92\times10^4$) is reported in Fig. 7. The longitudinal section, in Fig. 7(*a*), shows a greater penetration depth than the case of $b=20.0$ mm, and the reversion zone starts at $x\approx160$ mm. In addition, the motion reversal is perpendicular to the horizontal plates, clearly different from what was observed in the configuration with $b=20.0$ mm and Ra$=5.38\times10^3$. This indicates that the vortex cells are present in the reversion zone. Moreover, a thicker fluid layer is observed in the zone close to the upper plate. The cross-stream sections at $x=20$, 100, 150, and 200 mm are shown in Figs. 7(*b*)–7(*e*). These sections show that, close to the lower plate, weak secondary motions are present and there are small disturbances near the lateral walls. In the upper zone, the flow seems to be slightly chaotic due to the outflow branch of the C-loop. At $x=20$ mm, in Fig. 7(*b*), no secondary motions in the lower part of the cavity are detected. At $x=100$ mm, in Fig. 7(*c*), secondary motion in the central part of the section is observed going upward. Stronger secondary motions are shown in the sections at $x=150$ and 200 mm, Figs. 7(*d*) and 7(*e*).

The pictures of the configuration with $b=40.0$ mm and $q_\Omega=120$ W/m^2 (Ra$=1.92\times10^5$) are reported in Fig. 8, at the same locations. In the longitudinal section, in Fig. 8(*a*), the boundary layer on the lower plate has a thickness thinner than the one for $b=40.0$ mm and $q_\Omega=60$ W/m^2 (Ra$=8.92\times10^4$), in Fig. 7(*a*), but the C-loop paths are very similar. The cross-stream sections show more vigorous secondary motions than the case with $b=40.0$ mm and $q_\Omega=60$ W/m^2 (Ra$=8.92\times10^4$). At $x=20$ mm,

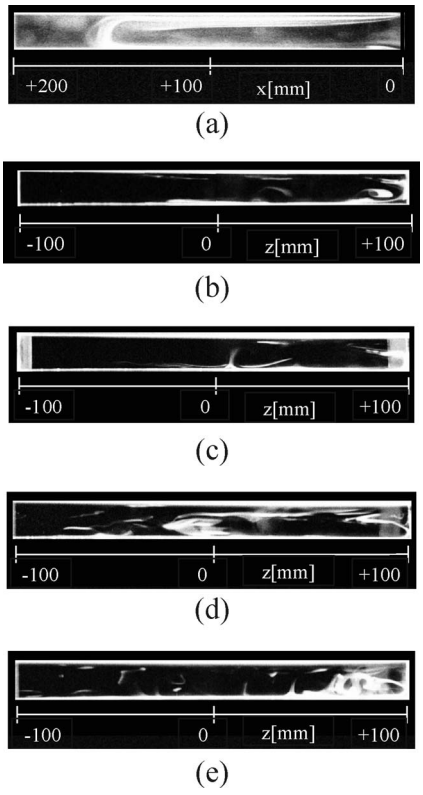

Fig. 7 Flow visualization for $b=40.0$ mm and $q_\Omega=60$ W/m^2 (Ra$=8.92\times10^4$). Longitudinal section at (*a*) $z=0$ mm; transversal sections at (*b*) $x=20$ mm, (*c*) $x=100$ mm, (*d*) $x=150$ mm, and (*e*) $x=200$ mm.

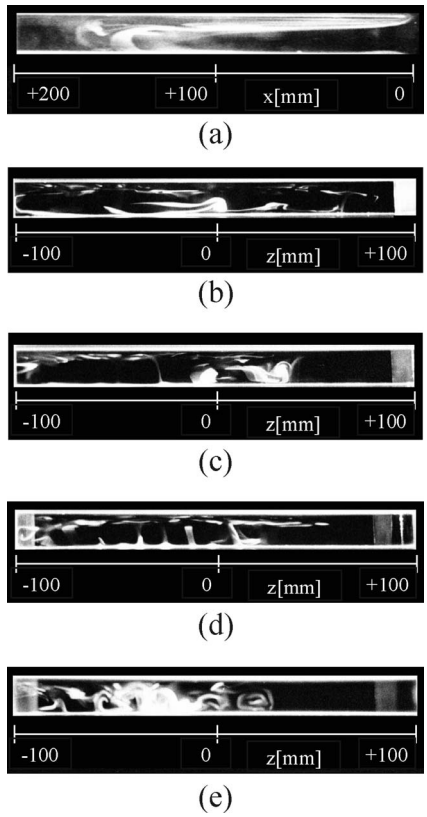

Fig. 8 Flow visualization for $b=40.0$ mm and $q_\Omega=120$ W/m^2 (Ra$=1.92\times10^5$). Longitudinal section at (*a*) $z=0$ mm; transversal sections at (*b*) $x=20$ mm, (*c*) $x=100$ mm, (*d*) $x=150$ mm, and (*e*) $x=200$ mm.

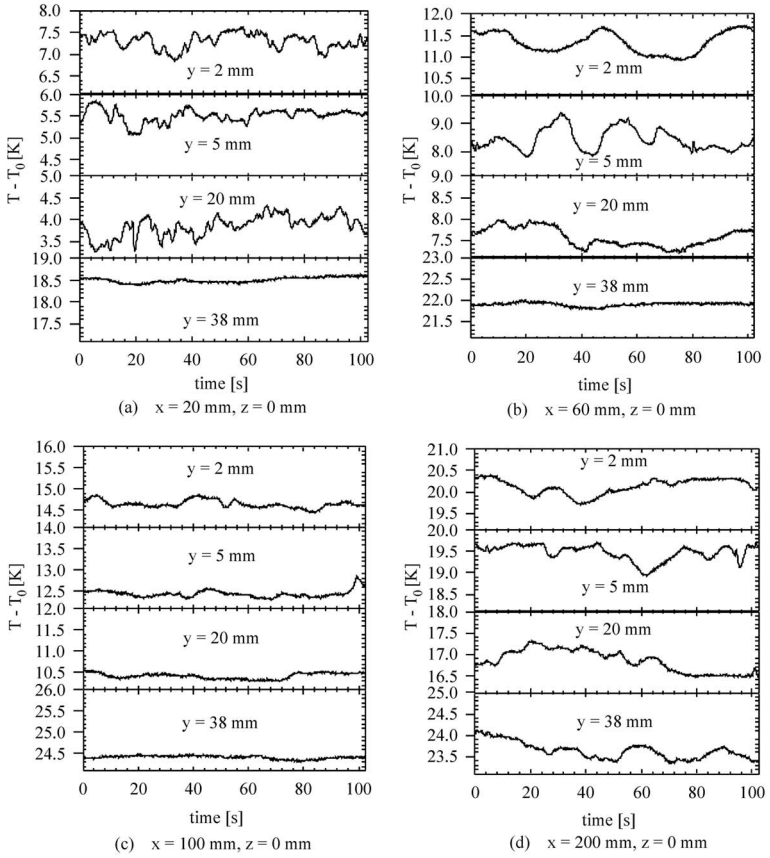

Fig. 9 Air temperatures versus time for $b=40.0$ mm, $z=0$ mm, and $q_\Omega=120$ W/m^2 (Ra$=1.92\times10^5$) at several y locations and four axial coordinates: (*a*) $x=20$ mm, (*b*) $x=60$ mm, (*c*) $x=100$ mm, and (*d*) $x=200$ mm

thermal plumes departing from the lower plate are detected in Fig. 8(*b*). As x increases, the motion in the cross-stream section near the upper plate is more chaotic and the secondary motions, occurring close to the lower plate, are stronger, Figs. 8(*c*)–8(*e*). In detail, at $x=150$ mm, in Fig. 8(*d*), several plumes depart from the lower plate, then they turn into vortices along the longitudinal axis at $x=200$ mm, in Fig. 8(*e*).

4.3 Air Temperature Measurements. The presence of secondary motions determines air temperature fluctuations in the open-ended cavity. As example, profiles of the local air temperature in the cavity, referred to the ambient temperature, as a function of time, in the $z=0$ plane, are reported in Fig. 9. This figure shows air temperature values for $b=40.0$ mm and $q_\Omega=120$ W/m^2 (Ra$=1.92\times10^5$) at $x=20$ mm (Fig. 9(*a*)); at $y=2$, 5, and 20 mm, temperature fluctuations show the presence of secondary motions, whereas they are not present near the upper plate, as shown in the temperature diagram for $y=38$ mm. This latter behavior, for $y=38$ mm, is also observed at $x=60$ and 100 mm, Figs. 9(*b*) and 9(*c*). At $y=2$ mm and $x=60$ mm, the oscillations amplitude are greater than those at $x=20$ mm, in Fig. 9(*a*). This is due to the viscous effect, which is present inside the boundary layer, where the point at $y=2$ mm is located. This implies an increment of the shear stress that locally damps secondary motions. A similar effect is noticed when the y value rises as well, even though it is weaker. At $x=100$ mm, in Fig. 9(*c*), and in the lower zone, $y=2$ and 5 mm, the amplitude fluctuations are lower, whereas the periodicity is similar to the one at $x=60$ mm, in Fig. 9(*b*). At $y=20$ mm and $x=100$ mm, the fluctuations are even weaker, showing that secondary motions are very weak in the central zone. In the section at $x=200$ mm, Fig. 9(*d*), the fluctuations are more emphasized when y increases due to the interaction between the vortex structures in the central zone of the cavity.

In Fig. 10, the average air temperature along the y-coordinate at various x-values is shown. For $b=20.0$ mm and $q_\Omega=60$ W/m^2 (Ra$=5.38\times10^3$), Fig. 10(*a*), at $x=0$ mm, the air temperature decreases from the zone near the lower plate to the central zone ($y=10$ mm) and it rises from the central zone to the upper plate. When x increases, temperature gradients decrease in the central zone, for $2<y<15$ mm, until they attain nearly uniform temperature values. This is due to the diffusive effects, which prevail over convection for low values of the Rayleigh number. In addition, radiation heats the lower plate, which directly contributes to the heat transfer inside the cavity. In the zone adjacent the upper plate ($y>15$ mm), a change in the profile slope, as a function of x, is noticed. Temperature gradients along the y-coordinate are present in the zone close to the exit section and in the central zone ($160<x\leq200$ mm), whereas air temperature is nearly uniform for $60\leq x\leq160$ mm. For $b=40.0$ mm and $q_\Omega=60$ W/m^2 (Ra$=8.92\times10^4$), in Fig. 10(*b*), the temperature profiles along the y-direction show lower values than for the previous configuration in Fig. 10(*a*), and the gradients, close to the two horizontal surfaces, are greater. The heat transfer, close to the lower plate, is enhanced by more vigorous convective effects. Three zones can be identified as lower, central, and upper. The first zone is adjacent to the lower surface, where the air entering the cavity is at the ambient temperature, and hence it efficiently exchanges thermal energy with the lower plate heated by radiation from the upper one. The second zone is where the air temperature profile reverses

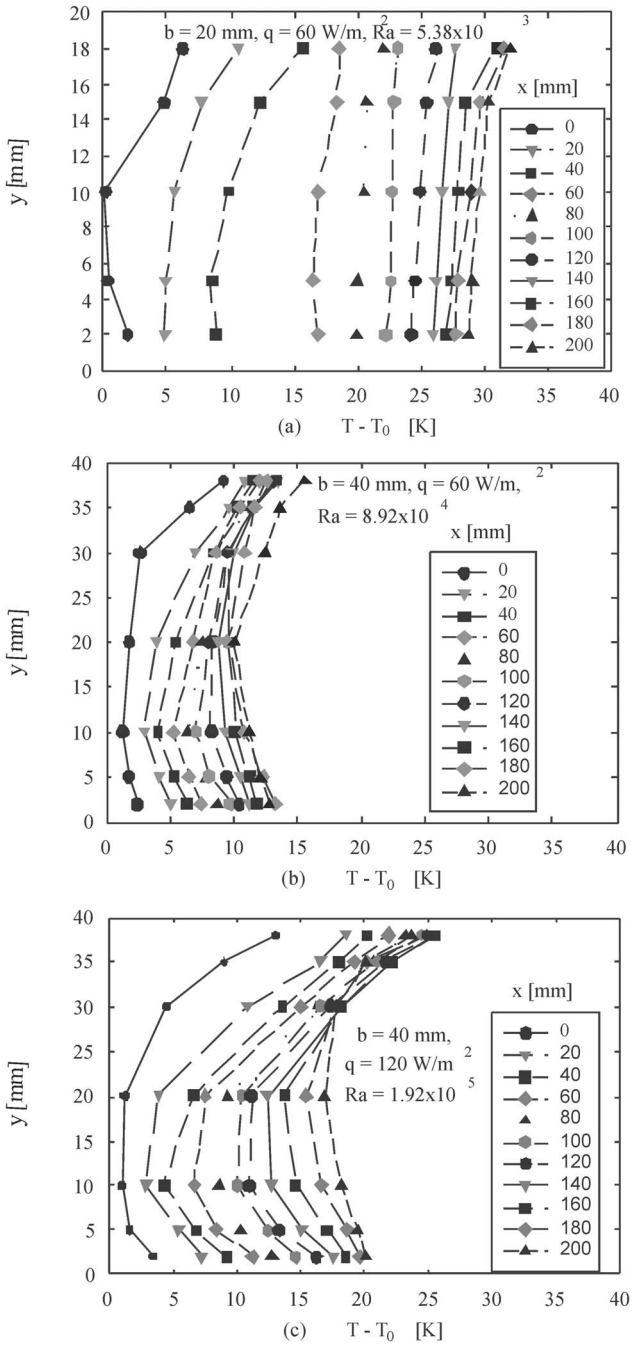

Fig. 10 Time averaged air temperature versus *y*-coordinate at several *x* locations and *z*=0 mm

and increases with the y-value. The heat transfer by convection is weaker than for the zone close to the lower surface. In the third zone ($y>30$ mm), convection is weak because the fluid flowing near the upper plate is warmer than the one near the lower plate. Similar trends are observed in Fig. 10(c) for $b=40$ mm and $q_\Omega=120$ W/m^2 ($\mathrm{Ra}=1.92\times10^5$), where the temperature values are higher, particularly near the horizontal surfaces.

4.4 Correlations for Average Nusselt Number and Maximum Wall Dimensionless Temperature. The Nusselt numbers, both convective, Nu, and convective and radiative heat transfer, Nu*, as well as the corresponding Rayleigh numbers, Ra and Ra*, were obtained by means of the experimental results using Eqs. (1), (2), and (4). Monomial correlations in the form $\mathrm{Nu}=a(\mathrm{Ra})^b$ and

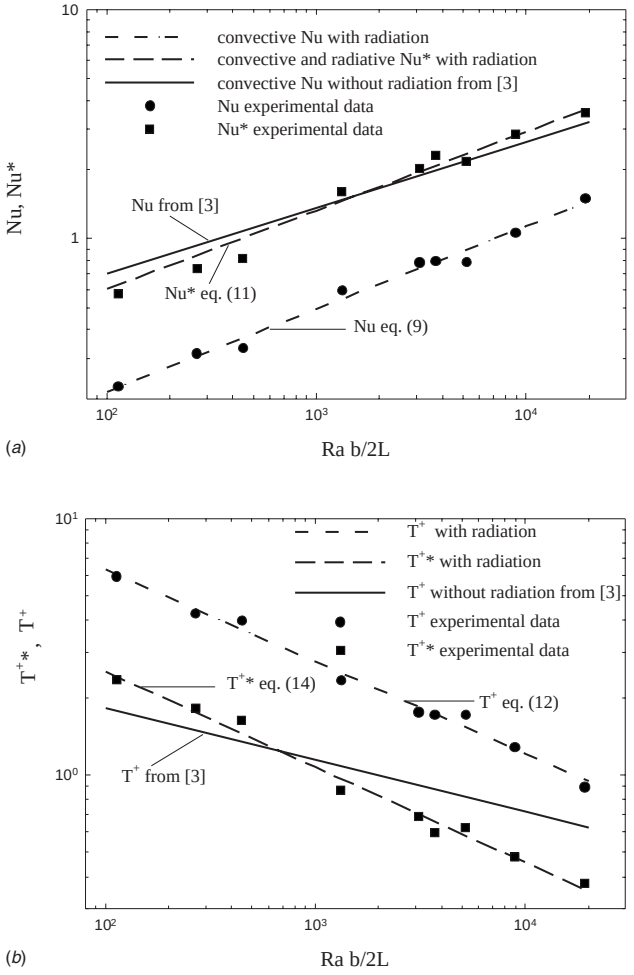

Fig. 11 Comparison between different correlations: (*a*) average Nusselt numbers, Nu and Nu*, versus average Rayleigh number and aspect ratio, Ra ($b/2L$); (*b*) dimensionless maximum wall temperatures, T^+ and T^{+*} versus average Rayleigh number and aspect ratio, Ra ($b/2L$).

$\mathrm{Nu}^*=a(\mathrm{Ra}^*)^b$ are used. The least-squares regression method is employed to evaluate the coefficients a and b. It is obtained as

$$\mathrm{Nu}=0.0407\left(\mathrm{Ra}\frac{b}{2L}\right)^{0.361} \tag{9}$$

with $r^2=0.987$ and valid for $2.26\times10^3\le\mathrm{Ra}\le1.92\times10^5$ and $10\le2L/b\le20$, and

$$\mathrm{Nu}^*=0.0692\left(\mathrm{Ra}^*\frac{b}{2L}\right)^{0.370} \tag{10}$$

with $r^2=0.987$, and valid for $5.71\times10^3\le\mathrm{Ra}^*\le4.55\times10^5$ and $10\le2L/b\le20$.

In order to compare the dimensionless heat transfer coefficients, a monomial correlation between Ra and Nu* is also estimated. The correlation equation is

$$\mathrm{Nu}^*=0.124\left(\mathrm{Ra}\frac{b}{2L}\right)^{0.343} \tag{11}$$

with $r^2=0.980$ and valid for $2.26\times10^3\le\mathrm{Ra}\le1.92\times10^5$ and $10\le2L/b\le20$.

A comparison between the proposed correlations, Eqs. (9) and (11), and the experimental data is given in Fig. 11(a). The figure shows that the proposed equations fit the experimental results very well. Moreover, the correlation curve given in Ref. [3], Nu

$=0.186(\mathrm{Ra}(b/2L))^{0.288}$, valid for negligible radiative heat transfer is also reported in this figure. It is observed that, for $\varepsilon=0.8$, the radiative heat transfer is more efficient for Ra $b/2L$ greater than 2.0×10^3.

The dimensionless maximum wall temperatures, referred to convective heat flux ($T^+_{w,\max}$) and convective and radiative heat flux ($T^{+*}_{w,\max}$), are correlated with Rayleigh numbers, Ra and Ra*. All monomial equations are proposed and the coefficients are evaluated by means of the least-squares regression method:

$$T^+_{w,\max}=33.0\left(\mathrm{Ra}\frac{b}{2L}\right)^{-0.359} \tag{12}$$

with $r^2=0.990$ and valid for $2.26\times10^3\le\mathrm{Ra}\le1.92\times10^5$ and $10\le2L/b\le20$.

The correlation in terms of Ra* and $T^{+*}_{w,\max}$ is

$$T^{+*}_{w,\max}=19.4\left(\mathrm{Ra}^*\frac{b}{2L}\right)^{-0.368} \tag{13}$$

with $r^2=0.990$, and valid for $5.71\times10^3\le\mathrm{Ra}^*\le4.55\times10^5$ and $10\le2L/b\le20$.

Also, a correlation between Ra and $T^{+*}_{w,\max}$ is given:

$$T^{+*}_{w,\max}=14.1\left(\mathrm{Ra}\frac{b}{2L}\right)^{-0.373} \tag{14}$$

with $r^2=0.986$ and valid for $2.26\times10^3\le\mathrm{Ra}\le1.92\times10^5$ and $10\le2L/b\le20$.

A comparison between the proposed correlations, Eqs. (12) and (14), and the experimental data is given in Fig. 11(*b*). Also for dimensionless maximum wall temperatures, the proposed correlations fit well the experimental results. Moreover, in the same figure the curve given in Ref. [3], $T^+_{w,\max}=4.66(\mathrm{Ra}(b/2L))^{-0.203}$, valid for negligible radiative heat transfer is also reported. It confirms that, for $\varepsilon=0.8$, the radiative heat transfer is convenient for Ra $b/2L$ greater than 7.0×10^2.

5 Conclusions

Natural convection for air inside an open-ended cavity was experimentally examined when the surface emissivity of the horizontal walls was high, $\varepsilon=0.8$. The open-ended cavity had the horizontal upper plate heated and the horizontal lower plate unheated. Wall temperature profiles, smoke visualization, and air temperature measurements were employed to describe and to detect the influence of surface radiation on air motion and average heat transfer coefficients inside the cavity.

Radiation heat transfer caused a temperature increase in the unheated lower plate, which could give secondary motions. This was different to what occurred for low surface emissivity of the horizontal walls, where no secondary motions where detected [3]. In the present paper, flow visualization in the transversal sections showed secondary motions due to plumes inside the cavity, close to the lower plate at $\mathrm{Ra}=1.92\times10^5$. Furthermore, flow visualization showed that the vertical side walls generated vortices with longitudinal axes along *x* direction. Time air temperature measurements confirmed the remarks from visualization. Fluctuations were noticed in some zones inside the cavity. In addition, for the lowest investigated value of the distance between the horizontal plates, $b=20.0$ mm and $\mathrm{Ra}=2.26\times10^3$, secondary motions were not detected, and the diffusive effects prevailed over the convective effects. In accordance with previous experimental investigation [2,3,5], it was observed that the main flow penetrates more inside the open-ended cavity when Rayleigh number increases. The average temperature profiles confirmed both the main flow pattern inside the cavity and radiation effect on convective heat transfer, which also occurred on the unheated lower plate due to the temperature rise caused by thermal radiation. Correlations for average Nusselt numbers and dimensionless maximum wall temperatures, in terms of Rayleigh numbers and aspect ratio, were proposed taking into account either the convection or the total heat transfer in the cavity, convection and radiation together, in the ranges $2.26\times10^3\le\mathrm{Ra}\le1.92\times10^5$, $5.71\times10^3\le\mathrm{Ra}^*\le4.55\times10^5$, and $10\le2L/b\le20$.

Acknowledgment

This work was supported by MIUR with Articolo No. 12D.M.593/2000 Grandi Laboratori "EliosLab" and SUN 2005 and 2007 grant research programs.

Nomenclature

- b = channel spacing, m
- g = acceleration of gravity, m s^{-2}
- Gr = Grashof number, Eq. (1)
- Gr* = Grashof number with convective and radiative heat fluxes, Eq. (2)
- h = heat transfer coefficient, W m^{-2} K^{-1}
- k = thermal conductivity, W m^{-1} K^{-1}
- L = half length of the plate, m
- Nu = average Nusselt number, Eq. (4)
- Nu* = average Nusselt number with convective and radiative heat fluxes, Eq. (4)
- q = heat flux, W m^{-2}
- r^2 = regression coefficient, dimensionless
- Ra = Rayleigh number, Eq. (1)
- Ra* = Rayleigh number with convective and radiative heat fluxes, Eq. (2)
- T = temperature, K
- T^+ = dimensionless temperature, Eq. (2)
- T^{+*} = dimensionless temperature with convective and radiative heat fluxes, Eq. (2)
- x = coordinate along the length of the plates, m
- y = coordinate along the spacing between the plates, m
- z = coordinate along the width of the plates, m
- W = width of the plates, m

Greek Symbols

- β = volumetric coefficient of expansion, K^{-1}
- ν = kinematic viscosity, m^2 s^{-1}

Subscripts

- c = convective
- k = conductive
- l = lower
- 0 = ambient air
- r = radiative, reference
- u = upper
- w = wall
- Ω = Ohmic dissipation

References

[1] Vafai, K., and Ettefagh, J., 1990, "The Effects of Sharp Corners on Buoyancy-Driven Flows With Particular Emphasis on Outer Boundaries," Int. J. Heat Mass Transfer, **33**, pp. 2311–2328.

[2] Manca, O., Morrone, B., and Nardini, S., 2000, "Experimental Analysis of Thermal Instability in Natural Convection Between Horizontal Parallel Plates Uniformly Heated," ASME J. Heat Transfer, **122**, pp. 50–57.

[3] Manca, O., and Nardini, S., 2007, "Experimental Investigation on Natural Convection in Horizontal Channels With Upper Wall at Uniform Heat Flux," Int. J. Heat Mass Transfer, **50**, pp. 1075–1086.

[4] Lage, J. L., Lim, J. S., and Bejan, A., 1992, "Natural Convection With Radiation in Cavity With Open Top End," ASME J. Heat Transfer, **114**, pp. 479–486.

[5] Bejan, A., and Kimura, S., 1981, "Penetration of Free Convection Into a Lateral Cavity," J. Fluid Mech., **103**, pp. 465–478.

[6] LeQuere, O., Humphery, J. A. C., and Sherman, F. S., 1981, "Numerical Calculation of Thermally Driven Two-Dimensional Unsteady Laminar Flow in Cavities of Rectangular Cross Section," Numer. Heat Transfer, **4**, pp. 249–283.

[7] Penot, F., 1982, "Numerical Calculation of Two-Dimensional Natural Convection in Isothermal Open Cavities," Numer. Heat Transfer, **5**, pp. 421–437.

[8] Hess, C. F., and Henze, R. H., 1984, "Experimental Investigation of Natural Convection Losses From Open Cavities," ASME J. Heat Transfer, **106**, pp. 333–338.
[9] Chan, Y. L., and Tien, C. L., 1985, "A Numerical Study of Two-Dimensional Natural Convection in Square Open Cavities," Numer. Heat Transfer, **8**, pp. 65–80.
[10] Chan, Y. L., and Tien, C. L., 1985, "A Numerical Study of Two-Dimensional Natural Convection in Shallow Open Cavities," Int. J. Heat Mass Transfer, **28**, pp. 603–612.
[11] Chan, Y. L., and Tien, C. L., 1986, "Laminar Natural Convection in Shallow Open Cavities," ASME J. Heat Transfer, **108**, pp. 305–309.
[12] Angirasa, D., Pourquié, M. J., and Nieuwstadt, F. T., 1992, "Numerical Study of Transient and Steady Laminar Bouyancy-Driven Flows and Heat Transfer in a Square Open Cavity," Numer. Heat Transfer, Part A, **22**, pp. 223–239.
[13] Angirasa, D., Eggels, J. G., and Nieuwstadt, F. T., 1995, "Numerical Simulation of Transient Natural Convection from an Isothermal Cavity Open on a Side," Numer. Heat Transfer, Part A, **28**, pp. 755–768.
[14] Abib, A. H., and Jaluria, Y., 1995, "Penetrative Convection in a Stably Stratified Enclosure," Int. J. Heat Mass Transfer, **38**(13), pp. 2489–2500.
[15] Vafai, K., and Ettfagh, J., 1990, "Thermal and Fluid Flow Instabilities in Buoyancy-Driven Flows in Open-Ended Cavities," Int. J. Heat Mass Transfer, **33**, pp. 2329–2344.
[16] Manca, O., Morrone, B., and Nardini, S., 2000, "Visualization of Flow Structures in Natural Convection Between Horizontal Uniformly Heated Parallel Plates," J. Flow Visualization Image Process., **7**, pp. 159–171.
[17] Khanafer, K., and Vafai, K., 2000, "Buoyancy-Driven Flows and Heat Transfer in Open-Ended Enclosures: Elimination of the Extended Boundaries," Int. J. Heat Mass Transfer, **43**, pp. 4087–4100.
[18] Khanafer, K., and Vafai, K., 2002, "Effective Boundary Conditions for Buoyancy-Driven Flows and Heat Transfer in Fully Open-Ended Two-Dimensional Enclosure," Int. J. Heat Mass Transfer, **45**, pp. 2527–2538.
[19] Baskaya, S., and Kauli, H., 2004, "Effects of Plate Separation, Plate Length and Temperature Difference on Buoyancy Driven Heat Transfer in Finite Horizontal Parallel Plates," Heat Mass Transfer, **40**, pp. 293–330.
[20] Icoz, T., and Jaluria, Y., 2005, "Numerical Simulation of Boundary Conditions and the Onset of Instability in Natural Convection Due to Protruding Thermal Sources in an Open Rectangular Channel," Numer. Heat Transfer, **48**, pp. 831–847.
[21] Turgut, O., and Onur, N., 2007, "An Experimental and Three-Dimensional Numerical Study of Natural Convection Heat Transfer Between Two Horizontal Parallel Plates," Int. Commun. Heat Mass Transfer, **34**, pp. 644–652.
[22] Andreozzi, A., Jaluria, Y., and Manca, O., 2007, "Numerical Investigation on Transient Natural Convection in a Horizontal Channel Heated From Upper Wall," Numer. Heat Transf., **51**, pp. 815–842.
[23] Hinojosa, J. F., Cabanillas, R. E., Alvarez, G., and Estrada, C. E., 2005, "Nusselt Number for the Natural Convection and Surface Thermal Radiation in a Square Tilted Open Cavity," Int. Commun. Heat Mass Transfer, **32**, pp. 1184–1192.
[24] Lin, C. X., and Ko, S. Y., 1994, "Effect of Surface Radiation on Turbulent Free Convection in an Open-Ended Cavity," Int. Commun. Heat Mass Transfer, **21**, pp. 117–129.
[25] Yu, E., and Joshi, Y. K., 1999, "Heat Transfer in Discretely Heated Side-Vented Compact Enclosures by Combined Conduction, Natural Convection, and Radiation," ASME J. Heat Transfer, **121**, pp. 1002–1010.
[26] Hinojosa, J. F., Estrada, C. A., Cabanillas, R. E., and Alvarez, G., 2005, "Numerical Study of Transient and Steady-State Natural Convection and Surface Thermal Radiation in a Horizontal Square Open Cavity," Numer. Heat Transfer, **48**, pp. 179–196.
[27] Chiu, W. K. S., Richards, C. J., and Jaluria, Y., 2000, "Flow Structure and Heat Transfer in a Horizontal Channel Heated From Below," Phys. Fluids, **12**(8), pp. 2128–2136.
[28] Chyu, M. C., 1987, "On the Boundary Condition and Data Reduction of Heat Transfer Experiment," Int. Commun. Heat Mass Transfer, **14**, pp. 543–550.
[29] 2005, LABVIEW, Reference Manual, National Instruments, Austin, TX.
[30] Dantec, 1996, "Probes for Hot-Wire Anemometry," Dantec Measurement Technology Publication No. 196-105-01.
[31] Bruun, H. H., 1995, *Hot-Wire Anemometry: Principles and Signal Analysis*, Oxford University Press, New York.
[32] Kline, S. J., and McClintock, F. A., 1953, "Describing Uncertainty in Single Sample Experiments," Mech. Eng. (Am. Soc. Mech. Eng.), **75**, pp. 3–12.
[33] Moffat, R. J., 1988, "Describing the Uncertainties in Experimental Results," Exp. Therm. Fluid Sci., **1**, pp. 3–17.

Chebyshev Collocation Spectral Methods for Coupled Radiation and Conduction in a Concentric Spherical Participating Medium

Ben-Wen Li[1]
e-mail: heatli@hotmail.com
e-mail: heatli@epm.neu.edu.cn

Ya-Song Sun

Da-Wei Zhang

Key Laboratory of National Education Ministry for Electromagnetic Processing of Materials,
Northeastern University,
P.O. Box 314,
Shenyang 110004, China

The Chebyshev collocation spectral method for coupled radiative and conductive heat transfer in concentric spherical participating medium is introduced and formulated. The angular dependence of the problem is discretized by conventional discrete ordinates method, and the space dependence is expressed by Chebyshev polynomial and discretized by collocation spectral method. Due to the exponential convergence of the spectral methods, very high accuracy can be obtained even using a small resolution (i.e., number of collocation points) for present problems. Comparisons between the solutions from Chebyshev collocation spectral–discrete ordinates method (SP-DOM) with available numerical or exact solutions in references indicate that the SP-DOM for the combination of radiation and conduction in concentric spherical participating medium is accurate and efficient. [DOI: 10.1115/1.3090617]

Keywords: radiation, conduction, combined heat transfer, participating medium, discrete ordinates method, Chebyshev collocation spectral methods

1 Introduction

Coupled radiative and conductive heat transfer in participating media exists in many engineering applications. Various approximate or numerical methods have been developed for this problem. The formulations, methods, and some results for combined radiation and conduction with participating media can be found in Ref. [1]. More recent review on methods for coupled radiative and conductive heat transfer can be found in Ref. [2]. The integrodifferential radiative transfer equation (RTE) with or without participating media can be solved by many numerical methods [1,3], say, zonal method, Monte Carlo method, discrete ordinates method (DOM), finite volume method (FVM), finite element method (FEM), etc. After the determination of spatial distributions of radiative intensities, or further the radiative energy sources, the diffusion equation for energy conservation can be solved by using finite difference method (FDM) or finite element method.

As for coupled radiative and conductive heat transfer special in spherical or in concentric spherical media, Viskanta and Crosbie [4] and Viskanta and Merriam [5] gave the rigorous formulations using exact radiative transfer methods, and the resulting equations were numerically solved by successive approximation. Siewert and Thomas [6] used the spherical harmonic method together with a sphere-to-plane transformation technique to solve this kind of problem, while Jia et al. [7] used Galerkin method, and Sghaier et al. [8] and Trabelsi et al. [9] developed a discrete ordinates method associated with the finite Legendre transform. Recently, Aouled-Dlala et al. [10] used the finite Chebyshev transform (FCT) to treat the angular derivative term of the discretized one-dimensional RTE, and finally the resulting equations were solved simultaneously using boundary value problem with finite difference (BVPFD). Kim et al. [11] used the combined finite volume and discrete ordinates method to investigate radiative heat transfer between two concentric spheres.

In the community of computational mechanics or numerical simulations, spectral methods can provide exponential convergence (in other words, spectral accuracy) [12] and have been widely used to solve Navier–Stokes equations in computational fluid dynamics (CFD) [13,14], Maxwell equations in electrodynamics [15], magnetohydrodynamics (MHD) equations in magnetofluids mechanics [16,17], and so on. Early in 1992, Zenouzi and Yener [18,19] used the Galerkin method to solve the radiative part of a radiation and natural convection combined problem. Later Kuo et al. [20,21] made a numerical comparison for spectral methods and finite volume method to solve the radiation and natural convection combined problem, and they concluded that the spectral methods are more accurate. Ganz et al. [22] used spectral methods for radiative heat transfer in a reacting flow. De Oliveira et al. [23] made a combination of spectral method and Laplace transform to solve radiative heat transfer in isotropic scattering media. Last year, the collocation spectral method for radiative part in stellar modeling was carried out [24]. Very recently, in Modest and Singh's work [25], the spherical harmonics method (P_N method so called, from mathematical view, the P_N method belongs to the category of spectral methods) was further developed to reduce the number of first-order partial differential equations. Other works regarding radiative transfer may be Refs. [26–30]. However, all these five works are not really correlated with "heat transfer" by thermal radiation but with quantum physics [26], electromagnetic wave [27,28], beam wave [29] propagation and scattering, and neutron transport [30]. Besides this fact, the final resultant algebraic equations in Refs. [26–29] need to be solved in coefficient space; in other words, spectral equations. Very recently, we have successfully developed the Chebyshev collocation method for one-dimensional radiative heat transfer even with anisotropic scattering media [31] and for one-dimensional radiative heat transfer in graded index medium [32]. As an expansion of our work [31,32], we developed the Chebyshev collocation method for coupled radiation and conduction in concentric spherical participating medium.

In the following of this paper, the physical model and governing equation will be presented in Sec. 2. The Chebyshev collocation methods for both RTE and diffusion equation for concentric

[1]Corresponding author.

Contributed by the Heat Transfer Division of ASME for publication in the JOURNAL OF HEAT TRANSFER. Manuscript received April 30, 2008; final manuscript received November 24, 2008; published online March 31, 2009. Review conducted by Walter W. Yuen.

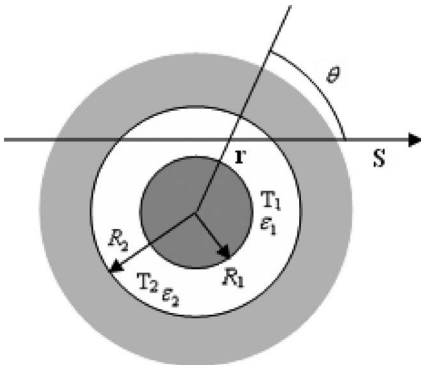

Fig. 1 Physical model and notations

spherical media will be presented in detail in Sec. 3. The discretized equations, for radiation and conduction separately, will be simultaneously solved iteratively, and the processes will be described in Sec. 4. Validations by typical cases with available numerical or exact results are stated in Sec. 5. Finally Sec. 6 gives the conclusions.

2 Physical Model and Governing Equations

Physical model and its governing equations for coupled radiative and conductive heat transfer in concentric spherical participating medium have been described in Refs. [4,5,7,9,10]. For continuity in understanding, it is necessary to present again. The physical model (see Fig. 1) consists of two opaque, gray, diffuse emitting, and scattering spheres. In the space, there exists a medium that conducts heat as well as absorbs, emits, and isotropically scatters radiant energy.

The equation for radiative transfer in the medium is

$$\frac{\mu}{r^2}\frac{\partial}{\partial r}[r^2 I(r,\mu)] + \frac{1}{r}\frac{\partial}{\partial \mu}[(1-\mu^2)I(r,\mu)] + \beta I(r,\mu) = K_a I_b(r) + \frac{K_s}{2}\int_{-1}^{1} I(r,\mu')d\mu' \quad \text{in } [R_1,R_2]\times[-1,1] \tag{1}$$

with boundary conditions

$$I(R_1,\mu) = \varepsilon_1 I_b(R_1) + 2(1-\varepsilon_1)\int_{-1}^{0} I(R_1,\mu')|\mu'|d\mu', \quad \mu > 0 \tag{2a}$$

$$I(R_2,\mu) = \varepsilon_2 I_b(R_2) + 2(1-\varepsilon_2)\int_{0}^{1} I(R_2,\mu')\mu' d\mu', \quad \mu < 0 \tag{2b}$$

In the above equations, $I(r,\mu)$ is the radiative intensity at position r and in direction denoted by the direction cosine μ; K_a, K_s, and β are the absorption, scattering, and extinction coefficients, respectively; and there is a relation between them $\beta=K_a+K_s$; and ε is the isotropic emissivity of the surface. The subscripts 1, 2, and b refer to the boundaries at $r=R_1$, $r=R_2$, and blackbody, respectively. The term $I_b(r)$ of blackbody radiation in Eq. (1) is related to the absolute temperature $T(r)$ at position r through $I_b(r)=n^2\sigma T^4(r)/\pi$. Here n denotes the refractive index and σ the Stefan–Boltzmann constant.

From the view of energy conservation, the simplified steady-state energy equation in the system reads [10]

$$\kappa\left(\frac{d^2T(r)}{dr^2} + \frac{2}{r}\frac{dT(r)}{dr}\right) = \frac{dq_r(r)}{dr} + \frac{2}{r}q_r(r) \quad \text{in } [R_1,R_2] \tag{3}$$

with boundary conditions

$$T(R_1) = T_1, \qquad T(R_2) = T_2 \tag{4}$$

where $q_r(r)$ and κ are the radiative heat flux at position r and the thermal conductivity of the medium, respectively.

The divergence of the radiative flux vector in Eq. (3) can be expressed as

$$\frac{dq_r(r)}{dr} + \frac{2}{r}q_r(r) = 4\pi K_a\left[I_b(r) - \frac{G(r)}{4\pi}\right] \tag{5}$$

Substituting Eq. (5) into Eq. (3), one obtains

$$\frac{d^2T(r)}{dr^2} + \frac{2}{r}\frac{dT(r)}{dr} = \frac{4\pi K_a}{\kappa}\left[I_b(r) - \frac{G(r)}{4\pi}\right] \tag{6}$$

$G(r)$ in Eqs. (5) and (6) is the incident radiative energy at position r, and $q_r(r)$ and $G(r)$ come from RTE (1).

Similar to Ref. [10], employing the reference absolute temperature, $T_{\text{ref}}=T_1$, and the other dimensionless variables, namely, dimensionless temperature $\theta=T/T_1$, dimensionless radius $r^*=r/R_2$, dimensionless radiation intensity $\psi=\pi I/\sigma n^2 T_1^4$, dimensionless radiation flux $q_r^*=q_r/n^2\sigma T_1^4$, conduction-radiation parameter $N_{cr}=\kappa\beta/4n^2\sigma T_1^3$, single scattering albedo $\omega=K_s/\beta$, and optical thickness $\tau_2=\beta R_2$, the set of dimensionless coupled equations governing the combined radiation and conduction problems in spherical medium can be expressed as

$$\frac{\mu}{\tau_2(r^*)^2}\frac{\partial}{\partial r^*}[(r^*)^2\psi] + \frac{1}{\tau_2(r^*)}\frac{\partial}{\partial \mu}[(1-\mu^2)\psi] + \psi = (1-\omega)\theta^4(r^*) + \frac{\omega}{2}\int_{-1}^{1}\psi(r^*,\mu')d\mu' \tag{7}$$

with the boundary conditions

$$\psi(R_1^*,\mu) = \varepsilon_1\theta_1^4 + 2(1-\varepsilon_1)\int_{-1}^{0}\psi(R_1^*,\mu')|\mu'|d\mu', \quad \mu > 0 \tag{8a}$$

$$\psi(R_2^*,\mu) = \varepsilon_2\theta_2^4 + 2(1-\varepsilon_2)\int_{0}^{1}\psi(R_2^*,\mu')|\mu'|d\mu', \quad \mu < 0 \tag{8b}$$

and

$$\frac{d^2\theta}{dr^{*2}} + \frac{2}{r^*}\frac{d\theta}{dr^*} = \frac{(1-\omega)}{N_{cr}}\tau_2^2\left(\theta^4 - \frac{G(r^*)}{4\pi}\right) \tag{9}$$

with the boundary conditions

$$\theta(R_1^*) = 1, \qquad \theta(R_2^*) = \theta_2 \tag{10}$$

3 Discretization of Governing Equations and Boundary Conditions Import

3.1 Formulations of Radiative Transfer Equation. For the sake of simplicity, the superscript " * " on the radius will be canceled hereafter. The discretization of dimensionless RTE (7) includes two aspects, i.e., space and angle. In our work, the DOM is used to treat the angular dependence of the RTE, and M points, $\{\mu^1,\mu^2,\ldots,\mu^M\}$, in the angular domain, $[-1,1]$, together with the

corresponding weights w_m, $m=1,2,\ldots,M$, are selected. The integral term on the right hand side of Eq. (7) is replaced by numerical quadrature. After that, Eq. (7) becomes

$$\frac{\mu^m}{\tau_2 r^2}\frac{\partial}{\partial r}(r^2\psi^m)+\frac{1}{\tau_2 r}\left\{\frac{\partial}{\partial\mu}[(1-\mu^2)\psi^m]\right\}_{\mu=\mu^m}+\psi^m = (1-\omega)\theta^4(r)+\frac{\omega}{2}\sum_{m'=1}^{M} w^{m'}\psi^{m'} \tag{11}$$

and the corresponding boundary conditions become

$$\psi^m(R_1)=\varepsilon_1\theta_1^4+2(1-\varepsilon_1)\sum_{\substack{m'=1\\ \mu^{m'}<0}}^{M} w^{m'}\psi^{m'}(R_1)|\mu^{m'}|,\quad \mu^m>0 \tag{12a}$$

$$\psi^m(R_2)=\varepsilon_2\theta_2^4+2(1-\varepsilon_2)\sum_{\substack{m'=1\\ \mu^{m'}>0}}^{M} w^{m'}\psi^{m'}(R_2)\mu^{m'},\quad \mu^m<0 \tag{12b}$$

For each direction $\mu=\mu^m$ in Eq. (11), the angular derivative term is discretized by central difference scheme [3], namely,

$$\left\{\frac{\partial}{\partial\mu}[(1-\mu^2)\psi^m]\right\}_{\mu=\mu^m}\approx\frac{\alpha^{m+1/2}\psi^{m+1/2}-\alpha^{m-1/2}\psi^{m-1/2}}{w^m} \tag{13}$$

where $\psi^{m+1/2}$ and $\psi^{m-1/2}$ are the angular intensities in the directions $m+1/2$ and $m-1/2$, and the central difference scheme is adopted to correlate them to the unknown ψ^m, i.e., $\psi^m=\frac{1}{2}(\psi^{m+1/2}+\psi^{m-1/2})$. The constants $\alpha^{m+1/2}$ and $\alpha^{m-1/2}$ only depend on the difference scheme and can be determined by the following recurrence relations, which satisfy the case of an isotropic intensity field as described in Ref. [3]:

$$\alpha^{m+1/2}-\alpha^{m-1/2}=-2w^m\mu^m,\qquad \alpha^{1/2}=\alpha^{M+1/2}=0 \tag{14}$$

Now Eq. (11) can be rewritten as

$$\frac{\mu^m}{\tau_2 r^2}\frac{\partial}{\partial r}(r^2\psi^m)+\frac{1}{\tau_2 r w^m}[\max(\alpha^{m+1/2},0)+\max(-\alpha^{m-1/2},0)]\psi^m+\psi^m = (1-\omega)\theta^4(r)+\frac{\omega}{2}\sum_{m'=1}^{M} w^{m'}\psi^{m'}+\frac{1}{\tau_2 r w^m}[\max(-\alpha^{m+1/2},0)\psi^{m+1}+\max(\alpha^{m-1/2},0)\psi^{m-1}] \tag{15}$$

The above equation group (15) for $m=1,2,\ldots,M$ will not be iteratively solved based on finite volume method as the conventional way in Refs. [33–35]. In our work, the Chebyshev collocation spectral method will be used for the spatial discretization. Similar to Ref. [36], the strategy of the RTE discretization in this article belongs to the category of so called space-angle decoupling.

First, the mapping of arbitrary interval $r\in[R_1,R_2]$ to standard interval $s\in[-1,1]$ is needed to fit the requirement of Chebyshev polynomial

$$s=\frac{2r-(R_2+R_1)}{R_2-R_1},\quad r=\frac{s(R_2-R_1)+(R_2+R_1)}{2} \tag{16}$$

After mapping, Eq. (15) becomes

$$\frac{\mu^m}{\tau_2 r^2}\left(\frac{2}{R_2-R_1}\right)\frac{\partial}{\partial s}(r^2\psi^m)+\frac{1}{\tau_2 r w^m}[\max(\alpha^{m+1/2},0)+\max(-\alpha^{m-1/2},0)]\psi^m+\psi^m = (1-\omega)\theta^4(r)+\frac{\omega}{2}\sum_{m'=1}^{M} w^{m'}\psi^{m'}+\frac{1}{\tau_2 r w^m}[\max(-\alpha^{m+1/2},0)\psi^{m+1}+\max(\alpha^{m-1/2},0)\psi^{m-1}] \tag{17}$$

Rearranging Eq. (17), one gets

$$\left\{\frac{\mu^m}{\tau_2}\left[\left(\frac{2}{R_2-R_1}\right)\frac{\partial}{\partial s}+\frac{2}{r}\right]+\frac{1}{\tau_2 r w^m}[\max(\alpha^{m+1/2},0)+\max(-\alpha^{m-1/2},0)+1]\right\}\psi^m = (1-\omega)\theta^4(r)+\frac{\omega}{2}\sum_{m'=1}^{M} w^{m'}\psi^{m'}+\frac{1}{\tau_2 r w^m}[\max(-\alpha^{m+1/2},0)\psi^{m+1}+\max(\alpha^{m-1/2},0)\psi^{m-1}] \tag{18}$$

The Gauss–Lobatto collocation points [12–14] are used for spatial discretization

$$s_i=-\cos\frac{\pi i}{N},\quad i=0,1,\ldots,N \tag{19}$$

The Chebyshev approximation of radiative intensity reads

$$\psi_N^m(s)=\sum_{k=0}^{N}\hat{\psi}_k^m T_k(s) \tag{20}$$

where the $T_k(s)$ is the first kind Chebyshev polynomial, and the coefficients $\hat{\psi}_k^m$, $k=0,1,\ldots,N$, are determined by requiring $\psi_N^m(s)$ to coincide with $\psi^m(s)$ at the collocation points s_i, $i=0,1,\ldots,N$. Therefore, the polynomial of degree N defined by Eq. (20) is nothing other than the Lagrange interpolation polynomial based on the set $\{s_i\}$ like

$$\psi_N^m(s)=\sum_{j=0}^{N} h_j(s)\psi^m(s_j) \tag{21}$$

with $\psi_N^m(s)=\psi^m(s_j)$, and $h_j(s)$ is the polynomial of degree N defined by

$$h_j(s)=\frac{(-1)^{j+1}(1-s^2)T_N'(s)}{\bar{c}_j N^2(s-s_j)}\quad\text{with}\quad \bar{c}_j=\begin{cases}2 & \text{if } j=0 \text{ and } N\\ 1 & \text{if } j<0<N\end{cases} \tag{22}$$

which is a function of the first-order derivative of Chebyshev polynomial. The representation (20) is equivalent to Eq. (21). Thus if expression (21) is substituted into the governing equation one will get the new form whose unknowns are the grid values, and the pth derivative of $\psi_N^m(s)$ with respect to s can be executed through differentiating p times directly to the interpolation polynomial (22), namely,

$$[\psi_N^m(s)]^{(p)}=\sum_{j=0}^{N} h_j^{(p)}(s)\psi_N^m(s_j)=\sum_{j=0}^{N} d_{i,j}^{(p)}\psi_N^m(s_j) \tag{23}$$

where $d_{i,j}^{(p)}$ are entries of pth derivative coefficients, which are functions of collocation points only.

For Gauss–Lobatto collocation points (19), the first-order derivative for $d_{i,j}^{(p)}$ reads

$$d_{i,j}^{(1)}=\frac{\bar{c}_i}{\bar{c}_j}\frac{(-1)^{i+j}}{(s_i-s_j)},\quad 0\le i,j\le N,\quad i\ne j$$

$$d_{i,i}^{(1)} = -\frac{s_i}{2(1-s_i^2)}, \quad 1 \le i \le N-1$$

$$d_{0,0}^{(1)} = -d_{N,N}^{(1)} = \frac{2N^2+1}{6} \tag{24}$$

and the second-order derivative reads

$$d_{i,j}^{(2)} = \frac{(-1)^{i+j}}{\bar{c}_j}\frac{s_i^2 + s_i s_j - 2}{(1-s_i^2)(s_i - s_j)^2}, \quad \begin{matrix} 1 \le i \le N-1 \\ 0 \le j \le N, \quad i \ne j \end{matrix}$$

$$d_{i,i}^{(2)} = -\frac{(N^2-1)(1-s_i^2)+3}{3(1-s_i^2)^2}, \quad 1 \le i \le N-1$$

$$d_{0,j}^{(2)} = \frac{2}{3}\frac{(-1)^j}{\bar{c}_j}\frac{(2N^2+1)(1-s_j)-6}{(1-s_j)^2}, \quad 1 \le j \le N \tag{25}$$

$$d_{N,j}^{(2)} = \frac{2}{3}\frac{(-1)^{j+N}}{\bar{c}_j}\frac{(2N^2+1)(1+s_j)-6}{(1+s_j)^2}, \quad 0 \le j \le N-1$$

$$d_{0,0}^{(2)} = d_{N,N}^{(2)} = \frac{N^4-1}{15}$$

The second-order derivative matrix $\mathbf{D}_s^{(2)}$ can also be computed by $\mathbf{D}_s^{(2)} = \mathbf{D}_s^{(1)} * \mathbf{D}_s^{(1)}$ directly. Whether for $\mathbf{D}_s^{(1)}$ or $\mathbf{D}_s^{(2)}$, they are needed to be computed once for all in the preparing computation.

After substitution of the above derivative matrices, the final discretized form of Eq. (18) reads

$$\sum_{k=0}^{N} A_{ik}^m \psi_k^m + \sum_{k=0}^{N} B_{ik}^m \psi_k^m = f_i^m, \quad m = 1,2,\ldots,M \tag{26}$$

where

$$A_{ik}^m = \begin{cases} \dfrac{\mu^m}{\tau_2}\left[\left(\dfrac{2}{R_2-R_1}\right)D_{s,ik}^{(1)} + \dfrac{2}{r_i}\right], & i = k \\ \dfrac{\mu^m}{\tau_2}\left[\left(\dfrac{2}{R_2-R_1}\right)D_{s,ik}^{(1)}\right] & \text{otherwise} \end{cases} \tag{27}$$

$$B_{ik}^m = \begin{cases} \dfrac{1}{\tau_2 r_i w^m}[\max(\alpha^{m+1/2},0) + \max(-\alpha^{m-1/2},0)] + 1, & i = k \\ 0 & \text{otherwise} \end{cases} \tag{28}$$

$$f_i^m = (1-\omega)\theta^4(r_i) + \frac{\omega}{2}\sum_{m'=1}^{M} w^{m'}\psi^{m'}(r_i) + \frac{1}{\tau_2 r_i w^m}[\max(-\alpha^{m+1/2},0)\psi^{m+1}(r_i) + \max(\alpha^{m-1/2},0)\psi^{m-1}(r_i)] \tag{29}$$

Equation (26) is valid for all directions, and for each direction m, the matrices $\mathbf{A}$ and $\mathbf{B}$ have the same size $(0{:}N, 0{:}N)$ corresponding to the point number $\{r_i, i=0,1,\ldots,N\}$ and can be incorporated into one matrix. Thus Eq. (26) can be rewritten as

$$\sum_{k=0}^{N} C_{ik}^m \psi_k^m = f_i^m, \quad m = 1,2,\ldots,M \tag{30}$$

where $C_{ik}^m = A_{ik}^m + B_{ik}^m$.

Equation (30) has to be solved with appropriate boundary conditions. One can rewrite Eq. (30) as the following in which the boundary conditions (12*a*) and (12*b*) are imported:

$$\tilde{\mathbf{C}}^m \tilde{\boldsymbol{\psi}}^m = \tilde{\mathbf{f}}^m, \quad m = 1,2,\ldots,M \tag{31}$$

where

$$\tilde{\mathbf{C}}^m = \begin{cases} \mathbf{C}^m(1{:}N, 1{:}N), & \mu^m > 0 \\ \mathbf{C}^m(0{:}N-1, 0{:}N-1), & \mu^m < 0 \end{cases} \tag{32}$$

$$\tilde{\boldsymbol{\psi}}^m = \begin{cases} \boldsymbol{\psi}^m(1{:}N), & \mu^m > 0 \\ \boldsymbol{\psi}^m(0{:}N-1), & \mu^m < 0 \end{cases} \tag{33}$$

$$\tilde{\mathbf{f}}^m = \begin{cases} \mathbf{f}^m(1{:}N) - \mathbf{C}^m(1{:}N, 0)\psi^m(0), & \mu^m > 0 \\ \mathbf{f}^m(0{:}N-1) - \mathbf{C}^m(0{:}N-1, N)\psi^m(N), & \mu^m < 0 \end{cases} \tag{34}$$

From the above equations the physical means of the problem should be clearly understood. For positive direction $\mu^m > 0$, the radiative intensities on the outer surface of inner sphere $\psi^m(R_1)$, corresponding to the above vector element $\tilde{\psi}^m(0)$, are computed by Eq. (12*a*) and should be imported through Eq. (34), but the radiative intensities on the inner surface of outer sphere $\psi^m(R_2)$, corresponding to the above vector element $\tilde{\psi}^m(N)$, are unknowns. For this situation, a subsquare matrix $\tilde{\mathbf{C}}^m$ with deletion of its first row and first column times the unknown vector $\tilde{\boldsymbol{\psi}}^m$ with its first element canceled constitutes the left hand side of matrix equation (31). For negative direction $\mu^m < 0$, the situation is just reverse.

3.2 Formulations of Diffuse Equation. The discretization of diffuse equation (9) is needed only in space domain $[R_1, R_2]$. After the mapping of $[R_1, R_2]$ to $[-1,1]$, Eq. (9) becomes

$$\left(\frac{2}{R_2-R_1}\right)^2 \frac{d^2\theta}{ds^2} + \frac{2}{r}\left(\frac{2}{R_2-R_1}\right)\frac{d\theta}{ds} = \frac{(1-\omega)}{N_{cr}}\tau_2^2\left(\theta^4 - \frac{1}{2}\sum_{m=1}^{M} w^m \psi^m\right) \tag{35}$$

in which the incident radiation $G(r)$ is replaced by numerical quadrature.

Employing the Chebyshev collocation method for Eq. (35) in the same way as it is for RTE, we obtain the following matrix equation:

$$\sum_{k=1}^{N} P_{ik}\theta_k = V_i \tag{36}$$

where

$$P_{ik} = \begin{cases} \left(\dfrac{2}{R_2-R_1}\right)^2 D_{s,ik}^{(2)} + \left(\dfrac{2}{R_2-R_1}\right)\dfrac{2}{r_i}D_{s,ik}^{(1)}, & i = k \\ \left(\dfrac{2}{R_2-R_1}\right)^2 D_{s,ik}^{(2)} + \left(\dfrac{2}{R_2-R_1}\right)D_{s,ik}^{(1)} & \text{otherwise} \end{cases} \tag{37}$$

$$V_i = \frac{(1-\omega)\tau_2^2}{N_{cr}}\left[\theta^4(r_i) - \frac{1}{2}\sum_{m=1}^{M} w^m \psi^m(r_i)\right] \tag{38}$$

After the Dirichlet boundary conditions (10) import, Eq. (36) becomes

$$\tilde{\mathbf{P}}\tilde{\boldsymbol{\theta}} = \tilde{\mathbf{V}} \tag{39}$$

where

$$\tilde{\mathbf{P}} = \mathbf{P}(1{:}N-1, 1{:}N-1) \tag{40}$$

$$\tilde{\boldsymbol{\theta}} = \boldsymbol{\theta}(1{:}N-1) \tag{41}$$

$$\tilde{\mathbf{V}} = \mathbf{V}(1{:}N-1) - \mathbf{P}(1{:}N-1,0)\theta(0) - \mathbf{P}(1{:}N-1,N)\theta(N) \tag{42}$$

4 Simultaneous Solution Procedure

From the above formulations we know that the matrix $\tilde{\mathbf{C}}^m$ in Eq. (31) is a function of direction cosine μ, node coordinate r, and angular difference constant α. If the direction cosine $\{\mu^1, \mu^2, \ldots, \mu^M\}$ and their corresponding weights w^m, as well as the collocation points $\{r_i,\ i=0,1,\ldots,N\}$, are determined, matrix $\tilde{\mathbf{C}}^m$ needs to be computed once for all in the preparing computation before iteration. Similarly, the matrix $\tilde{\mathbf{P}}$ in Eq. (39) needs to be computed only once.

Because the final matrix equation (31) corresponding to radiative heat transfer contains unknown dimensionless temperature, and the final matrix equation (39) corresponding to conductive heat transfer contains unknown dimensionless radiative intensity, they must be solved iteratively. Finally, the implementation of Chebyshev collocation spectral method for solving coupled radiative and conductive heat transfer can be executed through the following routine.

Step 1. Choose the resolution N and compute the coordinate values of nodes. Choose the direction number M and the corresponding direction cosine $\{\mu^1, \mu^2, \ldots, \mu^M\}$, as well as the weights w^m, hence to compute the angular difference constants α.

Step 2. Preparing compute matrices $\mathbf{D}_s$, $\tilde{\mathbf{C}}^m$, and $\tilde{\mathbf{P}}$ once for all.

Step 3. Give $\boldsymbol{\psi}^m$ and $\boldsymbol{\theta}$ an initial assumption (zero, for example) in the domain of the problem except for boundaries.

Step 4. Using the former solved or initial $\boldsymbol{\psi}^m$ and $\boldsymbol{\theta}$ to compute $\tilde{\mathbf{f}}^m$ according to Eq. (29) and compute $\psi^m(R_1)$ and $\psi^m(R_2)$ on the boundaries according to Eq. (12) and import the radiative intensity boundary conditions through formula (34).

Step 5. Directly solve Eq. (31) by $\tilde{\boldsymbol{\psi}}^m = (\tilde{\mathbf{C}}^m)^{-1}\tilde{\mathbf{f}}^m$ for all m.

Step 6. Using the immediately solved $\boldsymbol{\psi}^m$ and former solved $\boldsymbol{\theta}$ to compute $\tilde{\mathbf{V}}$ according to Eq. (38), import the temperature boundary conditions through formula (42).

Step 7. Directly solve Eq. (39) by $\tilde{\boldsymbol{\theta}} = (\tilde{\mathbf{P}})^{-1}\tilde{\mathbf{V}}$.

Step 8. Terminate the iteration if the relative maximum absolute difference of dimensionless radiative intensities or temperature, say, $\max\{|(\psi^m)^{\text{new}} - (\psi^m)^{\text{old}}|/(\psi^m)^{\text{old}}\}$ for all nodes and directions, is less than the tolerance (10^{-12} in our work, for example); otherwise, go back to Step 4.

From the formulations and above steps, the computation tasks mainly exit in the category of linear algebra. The most important two steps special for the matrix equation solution, Steps 5 and 7, can be executed directly and efficiently, while the other steps are concerned with the assembling of matrices only. The inverses $(\tilde{\mathbf{C}}^m)^{-1}$ and $(\tilde{\mathbf{P}})^{-1}$, which appear in Steps 5 and 7, are computed using the $\boldsymbol{LU}$ factorization [37]. In code design, if $\mathbf{A}$ is the inverse of $\mathbf{B}$, only one code like $\mathbf{A}=$**.i.**$\mathbf{B}$ is needed for the VISUAL FORTRAN system, and $\mathbf{A}=$**inv**$(\mathbf{B})$ is needed for the MATLAB system; otherwise, a small routine is necessary but still efficient.

After solving $\boldsymbol{\psi}^m$ and $\boldsymbol{\theta}$, the dimensionless conductive heat flux Q_c, the radiative heat flux q_r, and the total heat flux Q_t are determined by the following relations:

$$Q_c(r) = -\frac{d\theta}{dr}, \quad q_r = 2\sum_{m=1}^{M} \mu^m w^m \psi^m$$
$$Q_t(r) = -\frac{d\theta}{dr} + \frac{\tau_2}{2N_{cr}}\sum_{m=1}^{M} \mu^m w^m \psi^m \tag{43}$$

Table 1 Different orders of ordinate directions and the corresponding weights (positive only)

	S_N				
	S_4	S_6	S_8	S_{10}	S_{12}
w_m	1/2	1/3	1/4	1/5	1/6
μ_m	0.211325	0.146446	0.102672	0.083752	0.066877
	0.788675	0.500000	0.406205	0.312729	0.366693
		0.853354	0.593795	0.500000	0.288732
			0.897327	0.68727	0.711267
				0.916248	0.633307
					0.933123

From Eq. (7) one knows that, if the single scattering albedo ω is set to be 1, it becomes a pure RTE. As to this situation, one can design a switch in the codes to skip Steps 6 and 7 to solve a radiative heat transfer problem alone.

5 Results and Discussions

In the numerical community, the main superiorities of spectral methods over others like FVM, FEM, and FDM are exponential convergence and high accuracy. In our former work [31,32], the exponential convergence of spectral method for RTE, as well as the ability to capture large oscillations of variables, is confirmed and will not be illustrated again. For example, Fig. 4 in Ref. [32] shows that the accuracy almost keeps the same when the resolution was increased from 5 up to 99 and the direction number from 4 up to 12. For all cases in the present study, we found that the resolution of 11 is enough, and the increase in resolution will not lead to more accurate results obviously. Therefore we used a resolution of 11 for all our computations.

In our present work, the numerical results are presented for two aspects: pure radiation and coupled radiation and conduction, but all in a concentric spherical participating medium.

First, the different order of ordinate directions S_N for positive direction cosines and the corresponding weights, which are adopted in our computation, are listed in Table 1.

Similar to Ref. [10], the numerical values of $(r)^2 q_r$ for pure radiation under various combinations of ε_1 and ε_2 are given in Table 2. The symbols SP-DOM, DOM, and FCT in the table mean the results from spectral discrete ordinates method, standard discrete ordinates method, and finite Chebyshev transform, respectively, while the results from DOM and FCT are copied from Ref. [10]. The values in the last column of Table 2 are copied from Ref. [7], which is evaluated by Galerkin method. Comparisons are made for different order of S_N quadrature ($N=4,6,8,10,12$) also. Table 2 clearly shows that our SP-DOM can provide more accurate results than DOM and FCT as a whole. Those numbers in parentheses are relative percentage errors compared with the results from Galerkin method in Ref. [7]. In Table 2, the largest relative error from DOM is 14.55%, from FCT is 13.98%, and from SP-DOM is -2.58%.

In Fig. 2, the effect of the order of the S_N quadrature on the radiative heat flux for pure radiation problem is illustrated. Different from FCT in Ref. [10], the S_N quadrature gives very slight effect on the radiative heat flux in SP-DOM, and the results from S_4 up to S_{12} almost show no differences and agree excellently well with those of Ref. [7]. In Fig. 2 only the results from S_4 and S_{12} are presented.

In order to show the accuracy of the SP-DOM method, similar to the comparisons in Ref. [10], both nonscattering and scattering solutions are performed for a combined conduction and radiation between two concentric black spherical boundaries. In Table 3, the numerical solutions for the dimensionless total heat flux $Q_t(r)$ at the boundaries are listed for conduction-radiation parameter $N_{cr}=0.1$ and for various combinations of the optical thickness τ_2, the

Table 2 Comparisons of values of $(r)^2q_r$ for various combinations of ε_1 and ε_2 with R_1=0.5, θ_2=0.5, and τ_2=1 (numbers in parentheses are relative errors compared with Ref. [7], in percent)

		$(r)^2q_r$			
ε_1	ε_2	SP-DOM (N=4,6,8,10,12)	DOM [10] (N=4,6,8,10,12)	FCT [10] (N=4,6,8,10,12)	Ref. [7]
1	1	0.20496(−2.58)	0.24100(14.55)	0.23980(13.98)	0.21038
		0.20680(−1.70)	0.22890(8.80)	0.22634(7.59)	
		0.20762(−1.31)	0.21317(1.33)	0.22289(5.95)	
		0.20823(−1.02)	0.21997(4.56)	0.21938(4.28)	
		0.20846(−0.91)	0.21733(3.30)	0.21656(2.94)	
0.5	1	0.10934(−1.38)	0.12208(10.11)	0.12148(9.57)	0.11087
		0.10986(−0.91)	0.11715(5.66)	0.11647(5.05)	
		0.11010(−0.69)	0.11587(4.51)	0.11501(3.73)	
		0.11027(−0.54)	0.11397(2.80)	0.11385(2.69)	
		0.11035(−0.47)	0.11312(2.03)	0.11282(1.76)	
1	0.5	0.16819(−2.12)	0.18942(10.24)	0.18868(9.81)	0.17183
		0.16943(−1.40)	0.18304(6.52)	0.18130(5.51)	
		0.16999(−1.07)	0.17993(4.71)	0.17953(4.48)	
		0.17038(−0.84)	0.17782(3.49)	0.17743(3.26)	
		0.17054(−0.75)	0.17281(0.57)	0.17575(2.28)	
0.5	0.5	0.09792(−1.23)	0.10774(8.67)	0.10722(8.15)	0.09914
		0.09834(−0.81)	0.10401(4.91)	0.10312(4.01)	
		0.09853(−0.62)	0.10325(4.15)	0.10237(3.26)	
		0.09867(−0.47)	0.10157(2.45)	0.10152(2.40)	
		0.09873(−0.41)	0.09977(0.64)	0.10090(1.78)	

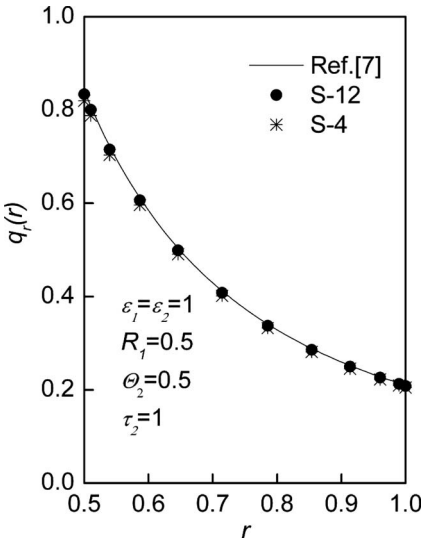

Fig. 2 SP-DOM results: Effect of angular quadrature on the radiative flux for pure radiation problem

ratio R_1/R_2, and the ratio of boundary temperature θ_2. The results indicate that our SP-DOM solutions with S_{12} quadrature also agree well with those of Viskanta and Merriam [5] and better than those of DOM and FCT. Compared with the results from Ref. [5], as to the total heat flux $Q_t(R_1)$, the largest relative error from DOM is 2.21%, from FCT is 3.10%, and from SP-DOM is −1.71%; as to $Q_t(R_1)$, the largest relative error from DOM is 6.47%, from FCT is 6.13%, and from SP-DOM is 5.11%.

The numerical values of dimensionless conductive $Q_c(r)$ and total heat flux $Q_t(r)$ at the boundaries for scattering medium are listed in Table 4. The results in Table 4 show that the SP-DOM can give very good solutions referring to those of Jia et al. [7]. This time, the largest relative error from DOM is 2.46%, from FCT is −1.53%, but from SP-DOM is up to 2.51%. However, all these three largest errors are less than 3%.

To further prove the accuracy of the SP-DOM method, more comparisons between our results with those available in Ref. [5] are made. In Table 5, the dimensionless conductive heat flux Q_c, total heat flux Q_t, and radiative heat flux q_r at the inner and outer spheres for various temperature ratios with θ_1=1.0, τ_2=2, R_1=0.5, $\varepsilon_1=\varepsilon_2$=1, and N_{cr}=0.1 are listed for SP-DOM and Ref. [5]. In Table 6, predictions of dimensionless total heat flux at the inner sphere with θ_1=1.0 and θ_2=0.5 by SP-DOM and Ref. [5] are

Table 3 Comparisons of dimensionless total heat flux Q_t at the inner and outer spheres for various combinations of θ_2, R_1, and τ_2 with ω=0, $\varepsilon_1=\varepsilon_2$=1, and N_{cr}=0.1 (numbers in parentheses are relative errors compared with Ref. [5], in percent)

			$Q_t(R_1)$				$Q_t(R_2)$			
θ_2	R_1	τ_2	SP-DOM	DOM [10]	FCT [10]	Ref. [5]	SP-DOM	DOM [10]	FCT [10]	Ref. [5]
0.1	0.5	2	7.603(−1.02)	7.742(0.79)	7.720(0.51)	7.681	1.901(−0.99)	1.935(0.78)	1.930(0.52)	1.920
0.5	0.5	2	5.994(−1.37)	6.131(0.89)	6.111(0.56)	6.077	1.499(−1.32)	1.532(0.86)	1.528(0.59)	1.519
0.5	0.9	2	9.866(−0.33)	9.945(0.46)	9.921(0.22)	9.899	7.991(−0.27)	8.055(0.52)	8.036(0.29)	8.013
0.5	0.5	10	11.259(−1.71)	11.475(0.17)	11.462(0.06)	11.455	2.832(−1.12)	2.868(0.14)	2.865(0.03)	2.864
0.5	0.5	0.2	2.468(−0.08)	2.498(1.13)	2.493(0.93)	2.470	0.617(5.11)	0.625(6.47)	0.623(6.13)	0.587
0.9	0.5	2	1.914(−1.59)	1.965(1.03)	1.958(0.67)	1.945	0.478(−1.65)	0.492(1.23)	0.489(0.62)	0.486
0.5	0.1	2	10.614(−0.85)	10.942(2.21)	11.037(3.10)	10.705	0.106(−0.93)	0.109(1.87)	0.110(2.80)	0.107

Table 4 Comparisons of dimensionless conductive heat flux Q_c and total heat flux Q_t at the inner and outer spheres for various combinations of N_{cr} and ω with $R_1=0.5$, $\varepsilon_1=\varepsilon_2=1$, $\theta_2=0.5$, and $\tau_2=2$ (numbers in parentheses are relative errors compared with Ref. [7], in percent)

N_{cr} (SP-DOM, DOM [10], FCT [10], Ref. [7])	ω	$Q_c(R_1)$	$Q_c(R_2)$	$Q_t(R_1)$	$Q_t(R_2)$
1	0.9	2.0062(−0.05)	0.5042(−0.14)	2.3735(−0.26)	0.5934(−0.25)
		2.0062(−0.05)	0.5040(−0.18)	2.3892(0.40)	0.5973(0.40)
		2.0064(−0.04)	0.5041(−0.16)	2.3851(0.23)	0.5963(0.24)
		2.0073	0.5049	2.3797	0.5949
	0.5	2.0303(−0.18)	0.5165(0.17)	2.3877(−0.32)	0.5969(−0.32)
		2.0606(1.31)	0.5161(0.10)	2.4032(0.33)	0.6008(0.33)
		2.0312(−0.13)	0.5160(0.08)	2.3994(0.17)	0.5998(0.17)
		2.0339	0.5156	2.3954	0.5988
	0.1	2.0511(−0.24)	0.5248(0.19)	2.3994(−0.36)	0.5999(−0.35)
		2.0629(0.34)	0.5243(0.10)	2.4149(0.29)	0.6037(0.28)
		2.0527(−0.16)	0.5243(0.10)	2.4112(0.13)	0.6028(0.13)
		2.0560	0.5238	2.4080	0.6020
0.1	0.9	2.0628(−0.48)	0.5406(0.52)	5.7350(−1.07)	1.4338(−1.07)
		2.0629(−0.48)	0.5395(0.32)	5.8924(1.65)	1.4731(1.64)
		2.0647(−0.39)	0.5393(0.28)	5.8507(0.93)	1.4627(0.92)
		2.0728	0.5378	5.7970	1.4493
	0.5	2.2963(−1.16)	0.6492(1.03)	5.8706(−1.22)	1.4676(−1.22)
		2.2978(−1.10)	0.6462(0.56)	6.0258(1.39)	1.5064(1.39)
		2.3022(−0.91)	0.6457(0.48)	5.9862(0.72)	1.4966(0.73)
		2.3233	0.6426	5.9433	1.4858
	0.1	2.4809(−1.42)	0.7178(1.10)	5.9727(−1.31)	1.4932(−1.31)
		2.4862(−1.21)	0.7142(0.59)	6.1279(1.26)	1.5319(1.25)
		2.4905(−1.04)	0.7135(0.49)	6.0889(0.61)	1.5222(0.61)
		2.5166	0.7100	6.0519	1.5130
0.01	0.9	2.6089(−1.72)	0.8211(1.87)	39.3144(−1.51)	9.8330(−1.46)
		2.6041(−1.90)	0.8147(1.08)	40.8963(2.45)	10.2240(2.46)
		2.6141(−1.53)	0.8135(0.93)	40.4739(1.39)	10.1185(1.40)
		2.6546	0.8060	39.9189	9.9789
	0.5	4.0757(−0.09)	1.4072(0.99)	40.1342(−1.50)	10.0368(−1.47)
		4.0765(−0.07)	1.3984(0.36)	41.708(2.36)	10.4271(2.36)
		4.0868(0.19)	1.3929(−0.04)	40.2866(−1.13)	10.3217(1.33)
		4.0792	1.3934	40.7451	10.1863
	0.1	4.9497(−0.10)	1.7256(2.51)	40.5990(−1.51)	10.1599(−1.41)
		4.9739(0.39)	1.7110(1.65)	41.8609(1.55)	10.4667(1.57)
		4.9861(0.63)	1.7075(1.44)	41.7625(1.31)	10.4406(1.32)
		4.9547	1.6833	41.2209	10.3050

listed and compared with those exact values. The results in these two comparable tables illustrate the good accuracy of SP-DOM again.

The authors would like to declare that Eq. (39), which is originally discretized from Eq. (35), cannot provide smooth solutions for all cases listed in Tables 3–5. The main reason may be the characteristic of the strong nonlinearity of Eq. (35).

To reduce the nonlinearity of Eq. (35), we first rewrite it to a new equivalent form

$$\frac{d^2\theta}{dr^2}+\frac{2}{r}\frac{d\theta}{dr}-\frac{2(1-\omega)\tau_2^2}{N_{cr}}\theta^4=-\frac{(1-\omega)\tau_2^2}{2N_{cr}}\sum_{m=1}^{M}w^m\psi^m-\frac{(1-\omega)\tau_2^2}{N_{cr}}\theta^4 \tag{44}$$

and then arrange Eq. (44) as

Table 5 Comparisons of dimensionless conductive heat flux Q_c, total heat flux Q_t, and radiative heat flux q_r at the inner and outer spheres for various temperature ratios with $\theta_1=1.0$, $\tau_2=2$, $R_1=0.5$, $\varepsilon_1=\varepsilon_2=1$, and $N_{cr}=0.1$

θ_2 (SP-DOM, Ref. [5])	$Q_c(R_1)$	$Q_t(R_1)$	$q_r(R_1)$	$Q_c(R_2)$	$Q_t(R_2)$	$q_r(R_2)$
0.1	3.565	7.603	0.808	1.327	1.901	0.115
	3.607	7.679	0.814	1.319	1.920	0.120
0.25	3.191	7.090	0.780	1.122	1.772	0.130
	3.233	7.170	0.787	1.114	1.792	0.136
0.5	2.521	5.994	0.695	0.731	1.498	0.153
	2.559	6.076	0.733	0.724	1.519	0.159
0.75	1.559	3.984	0.485	0.341	0.996	0.131
	1.585	4.046	0.492	0.337	1.012	0.135
0.9	0.713	1.914	0.240	0.131	0.479	0.070
	0.726	1.945	0.244	0.129	0.486	0.071

Table 6 Comparisons of approximate and exact dimensionless total heat flux at the inner sphere with $\theta_1=1.0$ and $\theta_2=0.5$

				$Q_t(R_1)$		
R_1	τ_2	N_{cr}	$\varepsilon_1=\varepsilon_2$	SP-DOM	Exact	Ref. [5]
0.5	1.1	1.0	1.0	2.243	2.047	2.09
0.5	1.1	0.1	1.0	4.419	2.470	2.88
0.167	2.0	0.1	1.0	8.296	6.612	11.2
0.333	2.0	0.1	1.0	6.458	5.635	8.99
0.5	2.0	1.0	1.0	2.402	2.411	2.60
0.5	2.0	0.1	1.0	5.994	6.076	7.98
0.5	2.0	0.1	0.1	3.469	3.482	3.93
0.5	11.0	10.0	1.0	2.095	2.108	2.11
0.5	11.0	1.0	1.0	2.956	3.088	3.15

$$\left[\frac{d^2}{dr^2}+\frac{2}{r}\frac{d}{dr}-\frac{2(1-\omega)\tau_2^2}{N_{cr}}(\theta^*)^3\right]\theta = -\frac{(1-\omega)\tau_2^2}{2N_{cr}}\sum_{m=1}^{M}w^m\psi^m-\frac{(1-\omega)\tau_2^2}{N_{cr}}(\theta^*)^4 \quad (45)$$

where the superscript * of dimensionless temperature θ denotes the last iterative value. To do so, the corresponding exchanges for matrix equation (39) must be made, and the matrices $\tilde{\mathbf{P}}$ and $\tilde{\mathbf{V}}$ in Eq. (39) need to be updated for each iteration. Now Eq. (39) can provide convergent results for all cases listed in Tables 3–5 after this treatment.

We briefly give explanation for the reason why Eq. (45) can provide smooth solutions for all our cases, even for some limited cases with limiting parameters or ratios, for example, the dimensionless temperature $\theta_2=0.9$ in Tables 4 and 5 and the radiation-conduction interaction parameter $N_{cr}=0.01$ in Table 4. The term $(d^2/dr^2)+(2/r)(d/dr)$ in Eq. (45) will give negative values in the main diagonal of $\tilde{\mathbf{P}}$ after boundary conditions import, and the term $-[2(1-\omega)\tau_2^2/N_{cr}](\theta^*)^3$ in Eq. (45) will only increase the main diagonal dominance of $\tilde{\mathbf{P}}$.

The detailed discussions and method introduction to improve the mathematical characteristics of matrices and further to let the matrix equations give smooth solutions are beyond the topic of this article.

6 Conclusions

In this work, the Chebyshev collocation method is successfully applied to solve the pure radiative heat transfer problem and coupled radiative and conductive heat transfer problem in concentric spherical participating medium. The spatial dependent variables, radiative intensity and temperature, are expressed by Chebyshev polynomials, and the governing equations are discretized using Chebyshev collocation points in space. The formulations and execution of Chebyshev collocation spectral method for the present problems are simple and efficient. The comparisons with available numerical or exact solutions indicate that the Chebyshev collocation spectral method for pure radiative heat transfer problem or for coupled radiative and conductive heat transfer problem in concentric spherical systems with participating medium can provide good accuracy.

Acknowledgment

This work was supported by the National Fundamental Research Programme of China (Contract No. 2006CB601203).

References

[1] Siegel, R., and Howell, J. R., 2002, *Thermal Radiation Heat Transfer*, 4th ed., Taylor & Francis, Washington, DC.
[2] Liu, L. H., and Tan, J. Y., 2007, "Meshless Local Petrov–Galerkin Approach for Coupled Radiative and Conductive Heat Transfer," Int. J. Therm. Sci., **46**, pp. 672–681.
[3] Modest, M. F., 2003, *Radiative Heat Transfer*, 2nd ed., Academic, San Diego, CA.
[4] Viskanta, R., and Crosbie, A. L., 1967, "Radiative Transfer Through a Spherical Shell of an Absorbing-Emitting Gray Medium," J. Quant. Spectrosc. Radiat. Transf., **7**, pp. 871–889.
[5] Viskanta, R., and Merriam, R. L., 1968, "Heat Transfer by Combined Conduction and Radiation Between Concentric Spheres Separated by Radiating Medium," ASME J. Heat Transfer, **90**, pp. 248–255.
[6] Siewert, C. E., and Thomas, J. R., Jr., 1991, "On Coupled Conductive-Radiative Heat-Transfer Problems in a Sphere," J. Quant. Spectrosc. Radiat. Transf., **46**, pp. 63–72.
[7] Jia, G., Yener, Y., and Cipolla, J. W., 1991, "Radiation Between Two Concentric Spheres Separated by a Participating Medium," J. Quant. Spectrosc. Radiat. Transf., **46**, pp. 11–19.
[8] Sghaier, T., Sifaoui, M. S., and Soufiani, A., 2000, "Study of Radiation in Spherical Media Using Discrete Ordinates Method Associated With the Finite Legendre Transform," J. Quant. Spectrosc. Radiat. Transf., **64**, pp. 339–351.
[9] Trabelsi, H., Sghaier, T., and Sifaoui, M. S., 2005, "A Theoretical Study of Radiation Between Two Concentric Spheres Using a Modified Discrete Ordinates Method Associated With Legendre Transform," J. Quant. Spectrosc. Radiat. Transf., **93**, pp. 415–428.
[10] Aouled-Dlala, N., Sghaier, T., and Seddiki, E., 2007, "Numerical Solution of Radiative and Conductive Heat Transfer in Concentric Spherical and Cylindrical Media," J. Quant. Spectrosc. Radiat. Transf., **107**, pp. 443–457.
[11] Kim, M. Y., Cho, J. H., and Baek, S. W., 2008, "Radiative Heat Transfer Between Two Concentric Spheres Separated by a Two-Phase Mixture of Non-Gray and Particles Using the Modified Discrete-Ordinates Method," J. Quant. Spectrosc. Radiat. Transf., **109**, pp. 1607–1621.
[12] Gottlieb, D., and Orszag, S. A., 1977, *Numerical Analysis of Spectral Methods: Theory and Applications* (Regional Conference Series in Applied Mathematics Vol. 28), SIAM, Philadelphia, PA.
[13] Canuto, C., Hussaini, M. Y., Quarteroni, A., and Zang, T. A., 1989, *Spectral Methods in Fluid Dynamics*, Springer-Verlag, Berlin.
[14] Peyret, R., 2002, *Spectral Methods for Incompressible Viscous Flow*, Springer-Verlag, New York.
[15] Ben Belgacem, F., and Grundmann, M., 1998, "Approximation of the Wave and Electromagnetic Diffusion Equations by Spectral Methods," SIAM J. Sci. Comput. (USA), **20**, pp. 13–32.
[16] Shan, X. W., Montgomery, D., and Chen, H. D., 1991, "Nonlinear Magnetohydrodynamics by Galerkin-Method Computation," Phys. Rev. A, **44**, pp. 6800–6818.
[17] Shan, X. W., 1994, "Magnetohydrodynamic Stabilization Through Rotation," Phys. Rev. Lett., **73**, pp. 1624–1627.
[18] Zenouzi, M., and Yener, Y., 1992, "Simultaneous Radiation and Natural Convection in Vertical Slots," ASME **HTD-203**, pp. 179–186.
[19] Zenouzi, M., and Yener, Y., 1992, "Thermal Stability of a Radiating Fluid in a Vertical Narrow Slot," ASME **HTD-219**, pp. 1–7.
[20] Kuo, D. C., and Morales, J. C., 1996, "Combined Natural Convection and Volumetric Radiation in a Horizontal Annulus: Spectral and Finite Volume Predictions," ASME **HTD-324**, pp. 29–36.
[21] Kuo, D. C., and Morales, J. C., 1999, "Combined Natural Convection and Volumetric Radiation in a Horizontal Annulus: Spectral and Finite Volume Predictions," ASME J. Heat Transfer, **121**, pp. 610–615.
[22] Ganz, B., Schmittel, P., Koch, R., and Wittig, S., 1998, "Validation of Numerical Methods at a Confined Turbulent Natural Gas Diffusion Flame Considering Detailed Radiative Transfer," ASME Paper No. GT 9.
[23] De Oliveira, J. V. P., Cardona, A. V., Vilhena, M. T., and Barros, R. C., 2002, "A Semi-Analytical Numerical Method for Time-Dependent Radiative Transfer Problems in Slab Geometry With Coherent Isotropic Scattering," J. Quant. Spectrosc. Radiat. Transf., **73**, pp. 55–62.
[24] Espinosa Lara, F., and Rieutord, M., 2007, "The Dynamics of a Fully Radiative Rapidly Rotating Star Enclosed Within a Spherical Box," Astron. Astrophys., **470**, pp. 1013–1022.
[25] Modest, M. F., and Yang, J., 2008, "Elliptic PDE Formulation and Boundary Conditions of the Spherical Harmonics Method of Arbitrary Order for General Three-Dimensional Geometries," J. Quant. Spectrosc. Radiat. Transf., **109**, pp. 1641–1666.
[26] Ritchie, B., Dykema, P. G., and Braddy, D., 1997, "Use of Fast-Fourier-Transform Computational Methods in Radiation Transport," Phys. Rev. E, **56**, pp. 2217–2227.
[27] Kim, A. D., and Ishimaru, A., 1999, "A Chebyshev Spectral Method for Radiative Transfer Equations Applied to Electromagnetic Wave Propagation and Scattering in a Discrete Random Medium," J. Comput. Phys., **152**, pp. 264–280.
[28] Kim, A. D., and Moscoso, M., 2002, "Chebyshev Spectral Methods for Radiative Transfer," SIAM J. Sci. Comput. (USA), **23**, pp. 2075–2095.
[29] Kim, A. D., and Moscoso, M., 2003, "Radiative Transfer Computations for Optical Beams," J. Comput. Phys., **185**, pp. 50–60.
[30] Asadzadeh, M., and Kadem, A., 2006, "Chebyshev Spectral-SN Method for the Neutron Transport Equation," Comput. Math. Appl., **52**, pp. 509–524.
[31] Li, B.-W., Sun, Y.-S., and Yu, Y., 2008, "Iterative and Direct Chebyshev Collocation Spectral Methods for One-Dimensional Radiative Heat Transfer," Int. J. Heat Mass Transfer, **51**, pp. 5887–5894.
[32] Sun, Y.-S., and Li, B.-W., 2009, "Chebyshev Collocation Spectral Method for One-Dimensional Radiative Heat Transfer in Graded Index Medium," Int. J.

Therm. Sci., **48**, pp. 691–698.
[33] Fiveland, W. A., 1984, "Discrete-Ordinates Solutions of the Radiative Transport Equation for Rectangular Enclosures," ASME J. Heat Transfer, **106**, pp. 699–706.
[34] Fiveland, W. A., 1987, "Discrete Ordinates Methods for Radiative Heat Transfer in Isotropically and Anisotropically Scattering Media," ASME J. Heat Transfer, **109**, pp. 809–812.
[35] Fiveland, W. A., 1988, "Three-Dimensional Radiative Heat-Transfer Solutions by the Discrete-Ordinates Method," J. Thermophys. Heat Transfer, **2**, pp. 309–316.
[36] Pontaza, J. P., and Reddy, J. N., 2005, "Least-Squares Finite Element Formulations for One-Dimensional Radiative Transfer," J. Quant. Spectrosc. Radiat. Transf., **95**, pp. 387–406.
[37] Anderson, E., Bai, Z., Bischof, C., Blackford, S., Demmel, J., Dongarra, J., Du Croz, J., Greenbaum, A., Hammarling, S., McKenney, A., and Sorensen, D., 1999, LAPACK Users' Guide, 3rd ed., http://www.netlib.org/lapack/lug/.

Numerical Investigation of Flow and Heat Transfer Performance of Nano-Encapsulated Phase Change Material Slurry in Microchannels

Sarada Kuravi
Krishna M. Kota
Jianhua Du
Louis C. Chow

Department of Mechanical, Materials and Aerospace Engineering, University of Central Florida, Orlando, FL 32816-2450

Microchannels are used in applications where large amount of heat is produced. Phase change material (PCM) slurries can be used as a heat transfer fluid in microchannels as they provide increased heat capacity during the melting of phase change material. For the present numerical investigation, performance of a nano-encapsulated phase change material slurry in a manifold microchannel heat sink was analyzed. The slurry was modeled as a bulk fluid with varying specific heat. The temperature field inside the channel wall is solved three dimensionally and is coupled with the three dimensional velocity and temperature fields of the fluid. The model includes the microchannel fin or wall effect, axial conduction along the length of the channel, developing flow of the fluid and not all these features were included in previous numerical investigations. Influence of parameters such as particle concentration, inlet temperature, melting range of the PCM, and heat flux is investigated, and the results are compared with the pure single phase fluid. [DOI: 10.1115/1.3084123]

Keywords: phase change material, microchannels, slurry flow

1 Introduction

Microchannel heat sinks, first demonstrated by Tuckerman and Pease [1], are predicted to be capable of cooling for circuit power densities of more than 1000 W/cm^2. The compact design enables the heat to be efficiently carried from the substrate into the coolant because of its inherently small passageways and a very large surface-to-volume ratio. However, due to high heat flux conditions, the temperature variation along the heat source may be large. In order to maintain isothermality, the mass flow rates are increased, which leads to considerable pressure drop. In applications where high temperature variation and large pressure drop are unacceptable, manifold microchannel (MMC) heat sink [2,3] is shown to be an effective way in reducing the pressure drop and significantly reducing the temperature variation. The MMC heat sink (Fig. 1 shows the geometry and flow domain inside the single microchannel) features many inlet and outlet channels alternating at a periodic distance ($\sim$1 mm) along the length of the MMC. The flow enters the microchannels from the manifold inlet channel, splits and flows through the microchannels, then exits to the manifold outlet channel. This pattern is repeated along the length of the MMC.

Nano-encapsulated phase change material (NEPCM) slurry is a two-phase fluid with a base fluid and nanosized particles (comprising of phase change material encapsulated in a polymer shell). A sample of NEPCM slurry was made at University of Central Florida with water as base fluid and octadecane as PCM (particle size of $\sim$100 nm and shell thickness of $\sim$5 nm). It is prepared by emulsification process where a surfactant (shell material) is first dissolved in the base fluid and is then heated to a temperature greater than the melting point of PCM while stirring continuously. Later the PCM is added to the mixture to carry out the emulsification. The formation of the nano-PCM was confirmed using Tyndall's effect. This involves the scattering of a laser beam as it passes through the emulsion due to the presence of nanosized particles. Pure water itself cannot scatter the laser beam. Figure 2 shows the measured size distribution of the sample with a diameter distribution at around 60–125 nm. Figure 3 shows the differential scanning calorimetry (DSC) curve of the sample. For the DSC measurement, 5 mg of the sample was heated at a rate of 2°C/min. A slightly broader peak at around 20°C is due to the phase change in PCM. It can be observed that the phase change peak is around 20°C and not between 28°C and 30°C, typical to octadecane, which is probably induced by the small size at nanoscale, where the surface effect is much more significant than that at the microscale. The estimated latent heat of the PCM has a high degree of uncertainty and was found to be between 100 kJ/kg and 240 kJ/kg (243.5 kJ/kg [4]).

Due to the presence of PCM in the slurry, the specific heat of the fluid increases when operating in the melting range. A numerical investigation was performed to analyze the performance of NEPCM slurry with polyalphaolefin (PAO) as the base fluid and compared with that of the single phase liquid. PAO is a dielectric oil used in cooling of military avionics systems and is inexpensive and stable.

Many researchers have studied both experimentally and numerically the heat transfer capability of PCM slurry with different base fluids. Some of the references are Refs. [5–21]. Numerical analysis of PCM slurries in regular channels was carried out by various researchers [13–19]. Most of these analyses assume homogeneous and hydrodynamically fully developed flow. Tao and co-workers [18,19] extended their numerical analysis for the slurry flow in a traditional microchannel. In any of the previous analyses, the three dimensional fin effects of the walls that become important in the case of microchannels were not considered. Due to the very short length of each channel and rectangular cross section that are typical of MMC heat sinks, the flow is never fully

Contributed by the Heat Transfer Division of ASME for publication in the JOURNAL OF HEAT TRANSFER. Manuscript received December 31, 2007; final manuscript received October 13, 2008; published online March 31, 2009. Review conducted by Anthony M. Jacobi.

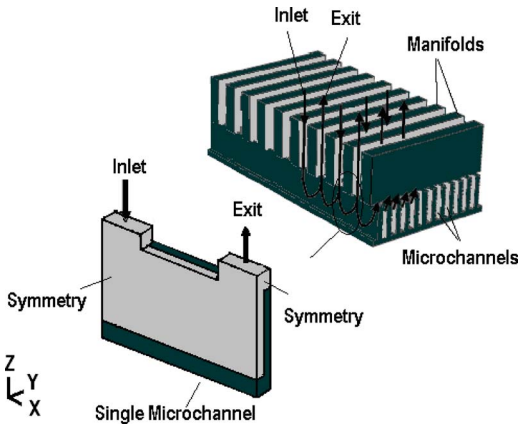

Fig. 1 MMC heat sink

developed, and the wall axial conduction becomes important. The current paper presents a fully three dimensional numerical analysis of NEPCM slurry flows inside a MMC heat sink considering the wall fin effect and axial conduction both in the developing flow regime. The main aim of this work is to look at fluid and heat transfer behavior of NEPCM slurry in a MMC heat sink compared with the single phase base fluid.

2 Numerical Model

The schematic of the flow domain considered is shown in Fig. 4. The walls represent microchannel walls, and the fluid that enters into the channel from the inlet leaves from the exit. The inlet and outlet are separated by the dividers or manifolds (as shown in Fig. 1) and are not part of the simulation domain. The inlet and outlet manifolds are 200 μm wide (y-direction), 50 μm high (z-direction), and 250 μm long (x-direction). The assumed dimensions for the microchannel are 100 μm width (y-direction), 500 μm height (z-direction), and 1000 μm length (x-direction). The wall and base thickness used are 50 μm and 100 μm, respectively. Only half of the channel was considered for simulation because of symmetry.

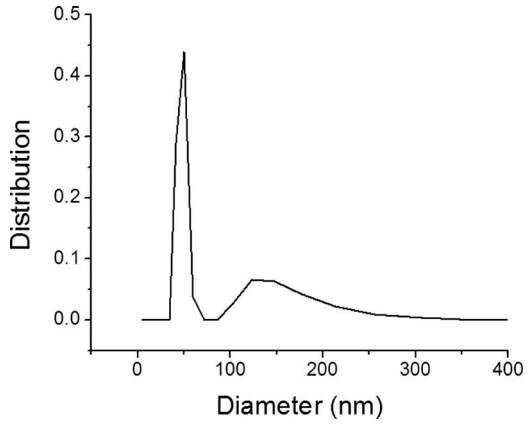

Fig. 2 Size distribution of NEPCM particles in the slurry sample

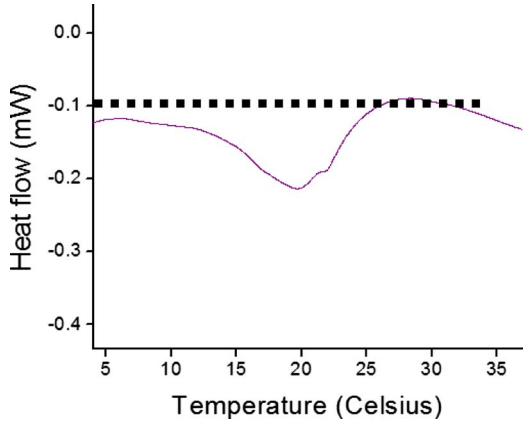

Fig. 3 DSC curve of the NEPCM slurry

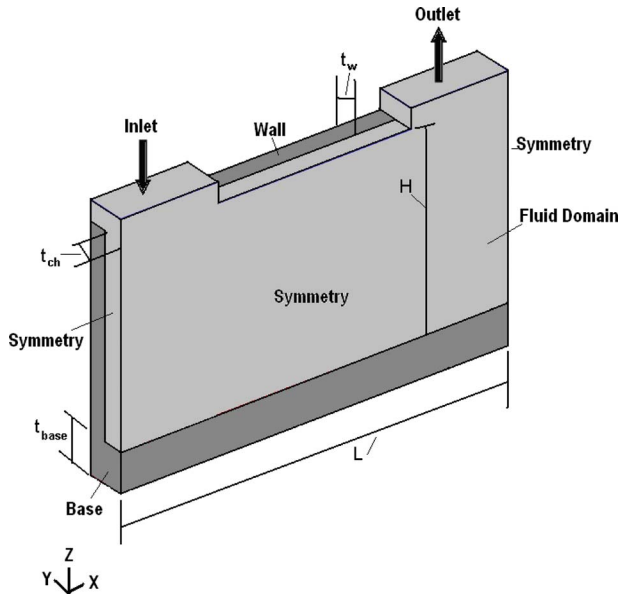

Fig. 4 Schematic of flow domain

2.1 Assumptions. The problem was solved using the following assumptions.

(1) The flow is steady and laminar.
(2) The fluid is Newtonian (valid up to a particle concentration of 0.3 [14]).
(3) The melting inside NEPCM particles takes place over a range of temperatures, between T_1 and T_2.
(4) The particles follow the fluid without any lag, i.e., the difference in the particle and fluid velocities is negligible.
(5) The particle distribution is homogeneous so that the bulk properties are assumed constant except for thermal conductivity and the heat capacity, which are functions of space and temperature, respectively.
(6) There is no temperature gradient inside the particle or the particle melts instantaneously.
(7) The effect of the particle depletion layer is negligible. The particle depletion layer is of the order of the particle radius if the channel size to particle size is large [22,23].
(8) The shape of the encapsulated particles is spherical. The effect of the shell material is neglected as it is thin.

2.2 Validation of Assumptions 4–6. *Assumption 4: No velocity difference between the particle and the fluid.* For validating this assumption, the time required by the particle to reach the base fluid velocity is evaluated and is shown to be very small. When the velocity of the fluid inside the channel is 0.6 m/s, the residence time of the fluid in a 1 mm length channel is 1.67 ms. If the particle diameter is 100 nm, the amount of time taken by the particle to reach the fluid velocity can be calculated using Eq. (1) [24].

Using the drag force on the particle (Fig. 5)

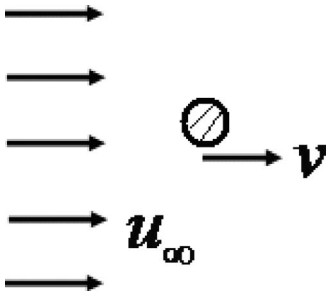

Fig. 5 Drag on a spherical particle in a fluid field

$$F_D = m\frac{dv}{dt} = 6\pi\mu_f R_p(u_\infty - v) \tag{1}$$

Integrating the equation and using $v=0$ at $t=0$ to find the integration constant, Eq. (1) becomes

$$t = \frac{2}{9}\frac{\rho_p {R_p}^2}{\mu_f}\ln\left(\frac{u_\infty}{(u_\infty - v)}\right) \tag{2}$$

Defining the time constant as in Eq. (3), the above equation becomes Eq. (4).

$$\tau = \frac{2}{9}\frac{\rho_p {R_p}^2}{\mu_f} \tag{3}$$

$$\frac{u_\infty - v}{u_\infty} = e^{-t/\tau} \tag{4}$$

At $t=\tau$, $v=0.63u_\infty$. This implies that the particle reaches 63% of fluid velocity in τ (in seconds). Using the appropriate property values, the value of the time constant is calculated as approximately 0.1 ns. Since the residence time of the fluid is 1.67 ms, it can be assumed that the particle reaches the fluid velocity almost instantly.

Assumption 5: Homogeneous Distribution. For checking this, the maximum lateral distance traveled by the particle within the residence time at different Re is calculated. When a suspension enters a channel or a pipe, the particles tend to migrate toward an equilibrium position known as Siegre and Silberberg position. Asmolov [25] asymptotically calculated the nondimensional force F' on a particle at different locations in a channel at different Re (Fig. 6). The Re is based on the channel width or the shortest dimension of the channel. Matas et al. [26] used this result to find the length at which the particle would reach its equilibrium state. They balanced the radial force F_l and the lateral drag force F_s at the equilibrium position. These forces are defined as

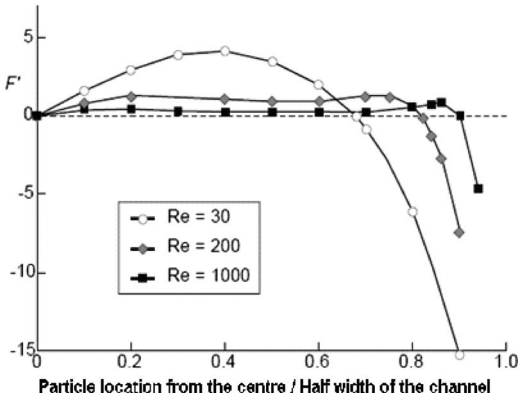

Fig. 6 Nondimensionalized force F' calculated using asymptotic analysis [25]

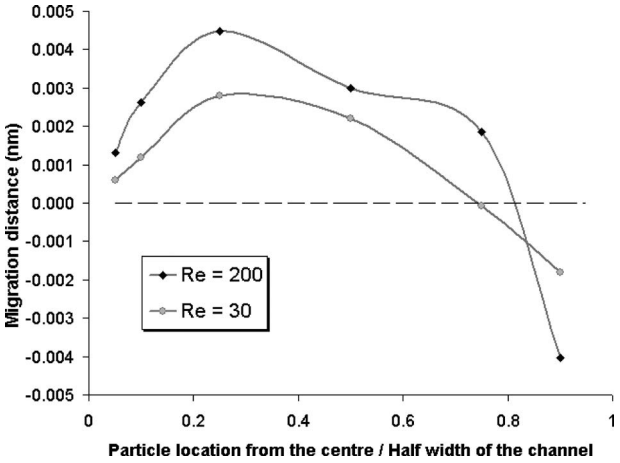

Fig. 7 Migration distance of a 100 nm particle in a 100 μm channel

$$F_l = F'(d_p/H)^4\rho_f U^2 H^2/4 \tag{5}$$

$$F_s = 6\pi\mu(d_p/2)V_{\text{migr}} \tag{6}$$

Using this definition, the migration velocity of a particle in a channel at different Re can be estimated when $\text{Re}_p \ll 1$. If the migration velocity is known, the lateral distance traveled by the particle can be calculated as

$$L_p = V_{\text{migr}}/t_{\text{res}} \tag{7}$$

Assuming the parabolic velocity inside the channel, the residence time of the particle is given by

$$t_{\text{res}} = L/U_p = L/U(1 - (d_p/H)^2) \tag{8}$$

Figure 7 shows the lateral migration of a 100 nm particle at different locations in a 100 μm channel when traveled a distance of 1 mm axially. It can be observed that if the particle is near the center or near the wall, the migration distance is large. This maximum migration distance traveled by the particle is less than 0.005 nm even for a Re of 200, which implies that it can be assumed that the particles will follow the fluid path and hence the flow can be considered homogeneous if it is true at the inlet.

Assumption 6: No temperature gradient inside the particle. Since the length of the channel is short for the MMC channel, it is important that the PCM particle completely melts within its residence time. Charunyakorn et al. [13] applied the method proposed by Tao [27] to calculate the solid-liquid or melt interface r_p (Fig. 8) in a sphere for calculating the source term in their model. Assuming that the particle has to melt 99% by the time it exits the channel, the required temperature difference between the surrounding fluid T_f and the melting temperature T_m of the PCM was calculated (Eq. (7)) using the same analogy.

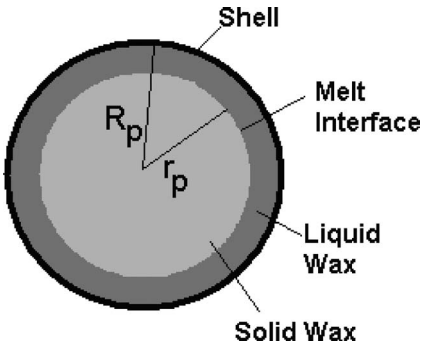

Fig. 8 Particle melting process

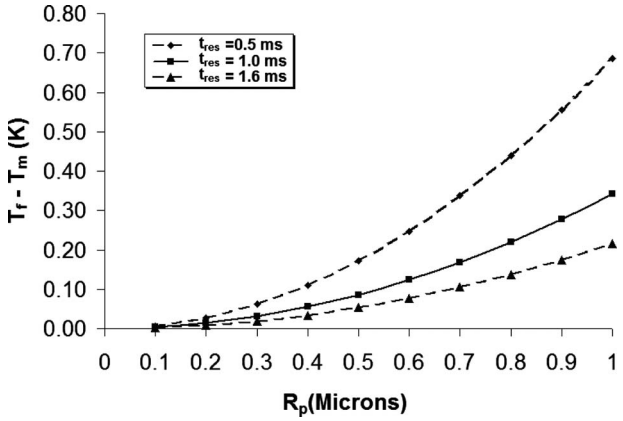

Fig. 9 T_{fm} **versus** R_p **to melt 99% of the particle at different residence times**

$$T_{fm} = T_f - T_m = \left[\frac{1}{2}\left[1 - \left(\frac{r_p}{R_p}\right)^2\right] + \frac{1}{3}\left[1 - \left(\frac{r_p}{R_p}\right)^3\right]\left(\frac{1}{\mathrm{Bi}_p} - 1\right)\right] \cdot \frac{h_{sf} \cdot R_p{}^2}{t \cdot \alpha \cdot c_p} \tag{9}$$

where the Biot number of the particle is given by

$$\mathrm{Bi}_p = \frac{k_{\mathrm{eff}}}{k_{\mathrm{pcm}}} \cdot \frac{2(1-c)}{2 - 3c^{1/3} + c} \tag{10}$$

Figure 9 shows the required temperature difference between the fluid and the particle melting temperature as a function of the particle radius for different residence times. It can be observed that the required T_{fm} increases with the increase in particle radius. For the present case where the particle diameter is 100 nm, the residence time is around 1.6 ms and it can be confirmed that the particle almost melts instantaneously for a very small temperature difference.

2.3 Governing Equations. With the assumptions mentioned above, the mass and momentum equations for slurry can be written as

$$\frac{\partial u}{\partial x} + \frac{\partial v}{\partial y} + \frac{\partial w}{\partial z} = 0 \tag{11}$$

$$\rho\left(u\frac{\partial u}{\partial x} + v\frac{\partial u}{\partial y} + w\frac{\partial u}{\partial z}\right) = -\frac{\partial p}{\partial x} + \mu\frac{\partial^2 u}{\partial x^2} + \mu\frac{\partial^2 v}{\partial y^2} + \mu\frac{\partial^2 w}{\partial z^2} \tag{12}$$

$$\rho\left(u\frac{\partial v}{\partial x} + v\frac{\partial v}{\partial y} + w\frac{\partial v}{\partial z}\right) = -\frac{\partial p}{\partial y} + \mu\frac{\partial^2 u}{\partial x^2} + \mu\frac{\partial^2 v}{\partial y^2} + \mu\frac{\partial^2 w}{\partial z^2} \tag{13}$$

$$\rho\left(u\frac{\partial w}{\partial x} + v\frac{\partial w}{\partial y} + w\frac{\partial w}{\partial z}\right) = -\frac{\partial p}{\partial z} + \mu\frac{\partial^2 u}{\partial x^2} + \mu\frac{\partial^2 v}{\partial y^2} + \mu\frac{\partial^2 w}{\partial z^2} \tag{14}$$

The energy equation for the slurry is

$$\rho c_p\left(u\frac{\partial T}{\partial x} + v\frac{\partial T}{\partial y} + w\frac{\partial T}{\partial z}\right) = \frac{\partial}{\partial x}\left(k\frac{\partial T}{\partial x}\right) + \frac{\partial}{\partial y}\left(k\frac{\partial T}{\partial y}\right) + \frac{\partial}{\partial z}\left(k\frac{\partial T}{\partial z}\right) \tag{15}$$

Energy equation for the microchannel wall/fin is

$$\frac{\partial^2 T_w}{\partial x^2} + \frac{\partial^2 T_w}{\partial y^2} + \frac{\partial^2 T_w}{\partial z^2} = 0 \tag{16}$$

2.4 Boundary Conditions. For flow inside the channels,

$\mathbf{u} = 0$ at the microchannel and manifold walls (17)

$p = p_0$ atmospheric pressure at the outlet (18)

$\mathbf{u} = (0,0,|w|)$ at the inlet (19)

For wall,

$q \cdot n = q_w$ constant heat flux at the base of the fin (20)

$q \cdot n = 0$ adiabatic on all other outer walls (21)

For fluid,

$T = T_{\mathrm{in}}$ at the inlet (22)

$q \cdot n = (\rho c_p \mathbf{u} T) \cdot n$ which is the convective heat flux boundary condition at the outlet/exit (23)

For wall and liquid interface,

$T_w = T$ continuity of temperature (24)

$$-k_w\frac{\partial T_w}{\partial n} = -k_f\frac{\partial T_f}{\partial n}$$ which is the continuity of heat flux (25)

A computational finite element method (FEM) software COMSOL® [28] is used to solve the above set of equations.

2.5 Bulk Properties of Slurry

2.5.1 Effective Thermal Conductivity. Bulk thermal conductivity of the suspension can be defined as [14]

$$k_b = k_f \cdot \frac{2 + \frac{k_p}{k_f} + 2c\left(\frac{k_p}{k_f} - 1\right)}{2 + \frac{k_p}{k_f} - c\left(\frac{k_p}{k_f} - 1\right)} \tag{26}$$

The effective thermal conductivity of slurries in the flow is enhanced due to the particle motions and particle-fluid interactions. It can be evaluated as follows [13]:

$$k_{\mathrm{eff}} = f \cdot k_b$$

$$f = 1 + Bc\ \mathrm{Pe}_p^m$$

$$B = 0, \quad m = 1.5, \quad \mathrm{Pe}_p < 0.67$$

$$B = 1.8, \quad m = 0.18, \quad 0.67 \le \mathrm{Pe}_p \le 250 \tag{27}$$

$$B = 3.0, \quad m = \tfrac{1}{11}, \quad \mathrm{Pe}_p > 250$$

The particle Peclet number is defined as

$$\mathrm{Pe}_p = \frac{e d_p{}^2}{\alpha_f} \tag{28}$$

Since the velocity is not fully developed in the current analysis, the shear rate is a function of all the spatial coordinates and corresponding velocities. The magnitude of the shear rate e can be calculated using the following equation:

$$e = \left(\frac{1}{2}\sum_i \sum_j \gamma_{ij}\gamma_{ji}\right)^{1/2} \tag{29}$$

where γ is the shear rate.

2.5.2 Dynamic Viscosity. Slurry viscosity is calculated using Vand's viscosity correlation [29,30]

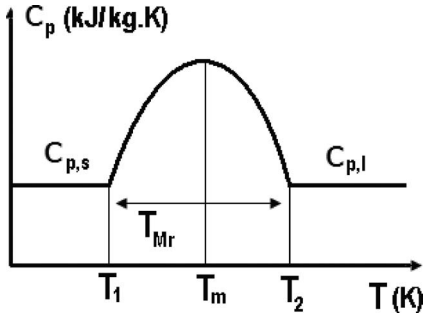

Fig. 10 Specific heat of NEPCM as a function of temperature

$$\frac{\mu_b}{\mu_f} = (1 - c - 1.16c^2)^{-2.5} \tag{30}$$

This correlation is derived for spherical particles and is valid for both small and large particle concentrations. In reality, the shape of the encapsulated particles might not be perfectly spherical and hence the viscosity can be different. It can be observed that from Table 1 of Ref. [20], the measured experimental viscosity values deviate from the values obtained using Vand's correlation. This difference increases with an increase in particle concentration.

2.5.3 Effective Specific Heat. Alisetti and Roy [16] used various profiles for the specific heat of PCM for calculating the effective specific heat and showed that the difference between the solutions is less than 4%. Hence the sine profile (Fig. 10) has been used to represent the NEPCM particle specific heat. As there is not much variation, the specific heat of solid and liquid phases of PCM is assumed to be equal.

$$c_{p,p} = c_{p,\text{pcm}} + \left\{ \frac{\pi}{2} \cdot \left(\frac{h_{sf}}{T_{Mr}} - c_{p,\text{pcm}} \right) \cdot \sin \pi \left[\frac{(T - T_1)}{T_{Mr}} \right] \right\} \tag{31}$$

The effective specific heat of the slurry can be calculated as [14]

$$c_{p,b} = c_m c_{p,p} + (1 - c_m) c_{p,f} \tag{32}$$

The value of specific heat of the particle in Eq. (32) is equal to $c_{p,\text{pcm}}$ when the temperature of the particle is outside the melting range and is given by Eq. (31) when the particle temperature is within the melting range.

Table 1 Thermophysical properties used for simulation of experiments in Ref. [12]

Property	Water	Eicosane
Density (kg/m^3)	997.07	778 (liquid) 856 (solid)
Viscosity (Pa s)	8.904×10^{-4}	-
Specific heat (J/kg K)	4179.6	2250 (liquid) 1773 (solid)
Thermal conductivity (W/m K)	0.606	0.15 (liquid) 0.2583 (solid)
Latent heat (J/kg)	-	247×10^3

3 Results and Discussion

The current numerical analysis mainly models the slurry with bulk properties using the effective specific heat method mentioned in Ref. [16]. Since there are no experiments performed inside the MMC channels using PCM slurries, the results could not be validated directly. However, the effective specific heat method was first used to simulate the experiments performed in Ref. [12] where the slurry is passed through a tube with an inner diameter of 3.14 mm and a length of 0.3 m. Figure 11 shows the comparison of the current model (effective specific heat method) with that of the experimental results in Ref. [12]. A two dimensional axisymmetric computational domain was used for solving the temperature along the tube. Boundary conditions used are constant inlet temperature, axial symmetry along the axis, constant heat flux along the tube radius or wall, and convective heat flux at the outlet. A fully developed parabolic profile was assumed at the inlet. Parameters used for the simulation are 100 μm particle diameter, 0.1 particle concentration, a Reynolds number of 200, and a Stefan number of 3.0. The thermophysical properties used are shown in Table 1. Different melting ranges of 1.8 K, 2 K, 2.4 K, and 3 K were used for the simulation. In Ref. [12], the melting range and the inlet temperature of the slurry were not specified. Hence the inlet temperature equal to T_1 was used for simulations to take maximum advantage of latent heat. There was a slight difference in the results for all the melting ranges used. The figure shows the plot of temperature when the melting range was 1.8 K with an inlet temperature equal to 308.95 K. It can be observed that the current numerical model predicts the behavior well.

For simulations in MMC heat sink, the slurry is assumed to consist of PAO and NEPCM with octadecane as the phase change material (melting point of 301.9 K). The properties used are shown in Table 2 and are evaluated based on the equations in Ref.

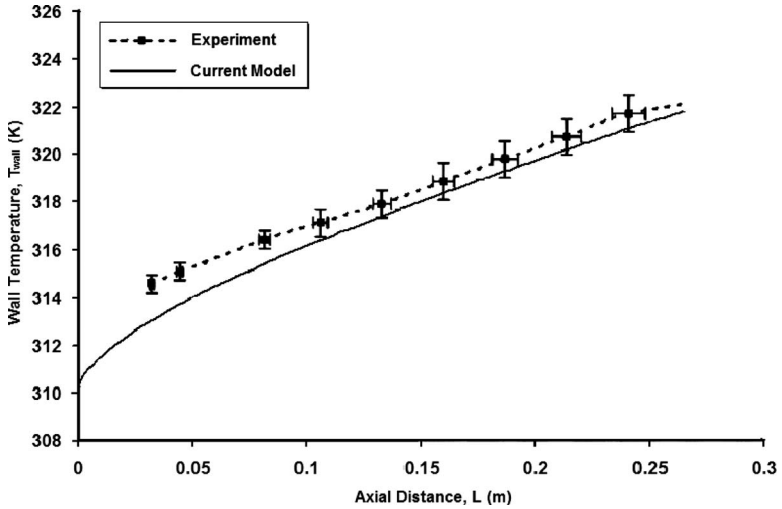

Fig. 11 Comparison of results using current model with experiments in Ref. [12]

Table 2 Thermophysical properties used

Property	Copper	PAO	Octadecane
Density (kg/m^3)	8700	784	774
Viscosity (Pa s)	-	4.45×10^{-3}	-
Specific heat (J/kg K)	385	2242	2180
Thermal conductivity (W/m K)	400	143×10^{-3}	0.15
Latent heat (J/kg)	-	-	244×10^3

[31]. Copper is used as wall material. The average pressure at the inlet and the bulk mean temperature of the fluid at the exit are calculated (from assumption 5, density is a constant) as

$$p_{\text{in}} = \frac{\int pds}{\int ds} \tag{33}$$

$$T_{\text{exit}} = \frac{\int T * c_{p,\text{eff}} * (n \cdot \boldsymbol{u}) ds}{\int c_{p,\text{eff}} * (n \cdot \boldsymbol{u}) ds} \tag{34}$$

where ds is the surface area at the corresponding boundary (inlet for Eq. (33) and outlet for Eq. (34)).

The pressure drop values obtained were found to match with theoretical predictions presented in Ref. [32]. The results were checked for global energy balance. The bulk mean temperature rise value in the case of pure PAO was found to be within 0.1 K of theoretical prediction. For slurry the temperature rise was found to be greater than the theoretical value assuming all the latent heat used and less than theoretical value assuming no latent heat was used at all.

Since the properties of PAO are function of temperature, the pure case of PAO was first run using varying properties and then with average properties for a mass flow rate of 20.8×10^{-6} kg/s and a heat flux of 100 W/cm^2. Table 3 shows the results with varying properties and constant average properties. As can be seen from the table, the difference between the heat transfer results for both cases is about 1%. The difference in the pressure drop results is less than 5%. Hence average properties of PAO were used for the simulation. For the numerical investigation, the parameters varied are the inlet temperature, PCM concentration, heat flux, and melting range of PCM, and a mass flow rate of 10.4×10^{-6} kg/s was used.

Unstructured grid consisting of 17,270 tetrahedral elements was generated using the free mesh option in COMSOL that was used for simulations. For checking grid independency, two meshes consisting of 61,641 and 203,954 elements were used. The maximum temperature difference in the results with refined mesh was around 0.15 K and there was no difference in velocity gradients. In the case of slurry, thermal conductivity enhancement was calculated using Eqs. (22)–(25). The flow field was first solved and the velocity gradients were exported to MATLAB® [33] to calculate the effective thermal conductivity. These data were then used to solve

Table 3 Comparison of results for pure PAO with varying properties and average properties

PAO properties	ΔT_{bulk} (K)	Nu_m	ΔP (Pa)
Varying properties	4.10	51.0	5585
Constant properties (evaluated at 28.8 °C)	4.14	50.5	5861

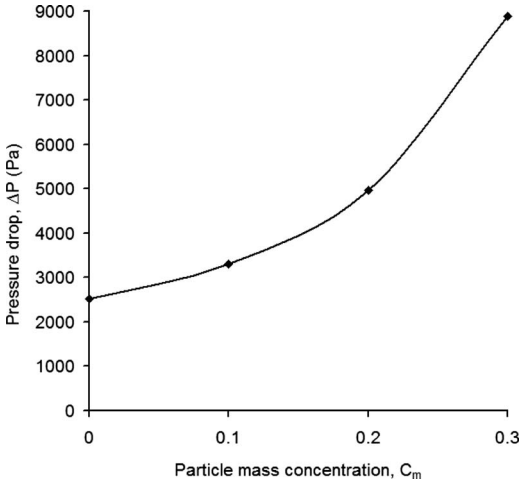

Fig. 12 Pressure drop inside the channel as a function of particle mass concentration

the temperature field. The enhancement in the thermal conductivity was found to be negligible for the current simulation cases since the particle diameter is small. However, for large particle diameters, this enhancement in thermal conductivity is large and it is important to consider while solving the problem [34].

3.1 Effect of Particle Concentration. For investigating the effect of particle mass concentration, the melting range used is 10 K, heat flux used is 100 W/cm^2, and $T_{\text{in}}=T_m$. The pressure drop from the inlet to the outlet increases with an increase in concentration (Fig. 12). The simulations show that the bulk mean temperature rise of the slurry lower than the pure fluid decreases with an increase in mass concentration (Fig. 13). The summary of results for cases considered is shown in Table 4. From the table it can be observed that if the bulk mean temperature rise for pure PAO is desired to be 0.65 K (which is the rise for the slurry with $c_m=0.3$), the mass flow rate must be increased around 12.7 times and the resulting pressure drop increases by 28.5 times. The Nusselt number is found to increase with an increase in concentration (Fig. 14).

3.2 Effect of Inlet Temperature and Melting Range. Since the PCM is assumed to have a melting range, it is interesting to observe the best case where the heat transfer enhancement is

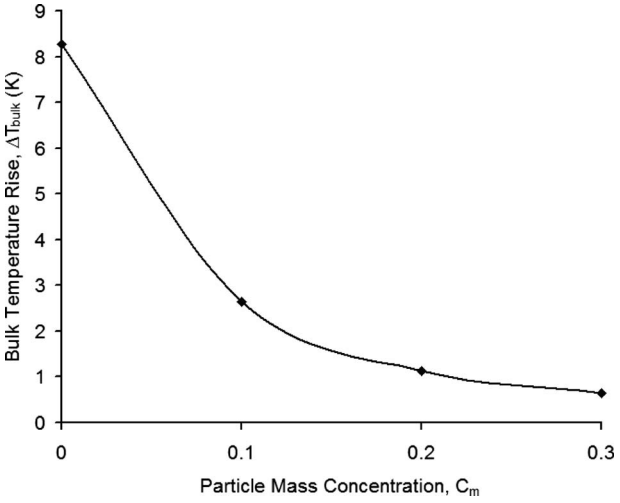

Fig. 13 Bulk mean temperature rise as a function of particle mass concentration

Table 4 Effect of mass concentration

Fluid (c_m)	$\dot{m}(\times 10^6)$ (kg/s)	ΔP (Pa)	ΔT_{bulk} (K)
PAO (0)	10.4	2,517	8.28
Slurry (0.1)	10.4	3,310	2.64
Slurry (0.2)	10.4	4,964	1.13
Slurry (0.3)	10.4	8,894	0.63
PAO (0)	132.0	71,706	0.63

$q=100$ W/cm^2, $T_{\text{in}}=T_m$, and $T_{Mr}=10$ K.

maximum and bulk mean temperature rise is minimum. Thus for a concentration of 0.3, at a heat flux of 100 W/cm^2, the inlet temperature was varied in order to calculate the best case. Figure 15 shows the bulk mean temperature rise of the fluid and Fig. 16 shows the Nusselt number as a function of nondimensional inlet temperature for different melting ranges. The results presented were run for varying melting ranges. As can be seen from the figures, if the nondimensional inlet temperature of the fluid is 0.5 ($T_{\text{in}}=T_m$), the bulk mean temperature rise of the slurry is better for both cases of melting range considered. But if the Nusselt number is considered, it depends on the melting range. Also if the melting ranges are observed the narrower the melting range is, the better the heat transfer enhancement is. As the melting range depends on the purity of PCM, it can be concluded that the purity of PCM helps in increasing the heat absorbing capacity of the bulk fluid and also the heat transfer.

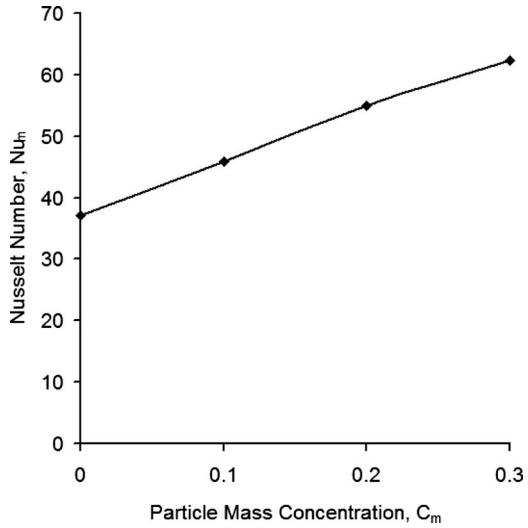

Fig. 14 Nusselt number as a function of particle mass concentration

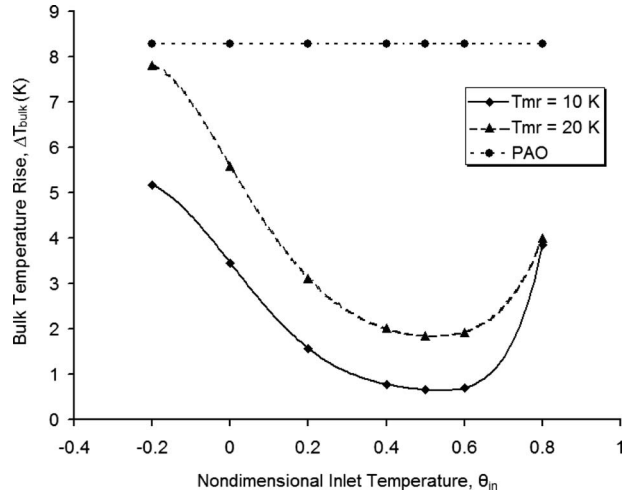

Fig. 15 Bulk temperature rise with varying inlet temperatures and melting ranges of PCM

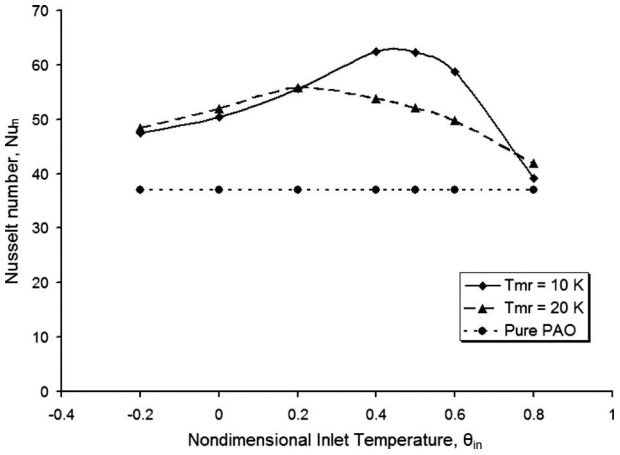

Fig. 16 Nusselt number with varying inlet temperatures and melting ranges of PCM

3.3 Effect of Heat Flux. The simulations were run for pure PAO and 0.3 concentration slurry for different heat fluxes at a nondimensional inlet temperature of 0.5. It can be observed that for high heat fluxes (Figs. 17(*F*), 17(*i*), 17(*g*), and 18), the performance of the slurry improves compared with PAO. The difference in the bulk temperature rise between pure PAO and slurry increases with an increase in heat flux whereas the Nusselt number is always high for the slurry for any case.

From the results for all the cases considered above, it can be concluded that the slurry performs better compared with single phase PAO. Since the flow is not fully developed, the thermal performance depends on both the specific heat capacity and thermal conductivity of the base fluid and slurry [21]. It can be observed from Table 2 that the only property that varies largely between PAO and the PCM is the latent heat of the PCM, and the thermal conductivity variation is negligible. Thus the slurry always performed better in all the cases considered. Even though these results are obtained in MMC channels, this behavior is ex-

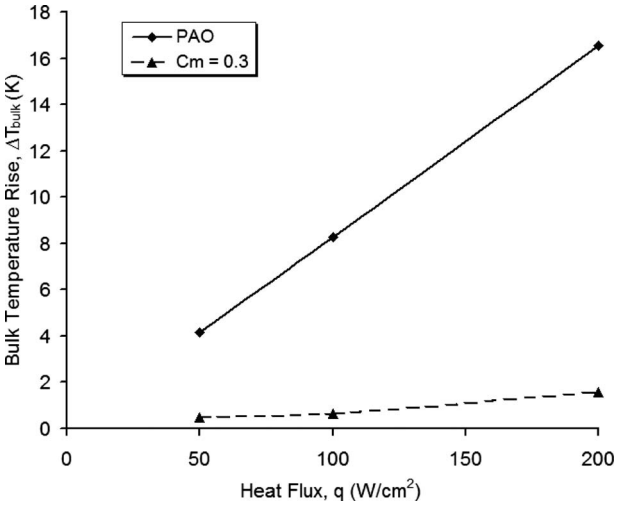

Fig. 17 Bulk temperature rise for pure PAO and slurry at varying heat fluxes

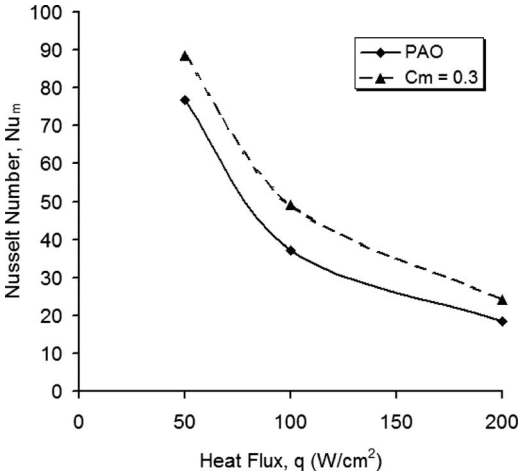

Fig. 18 Nusselt number for pure PAO and slurry at varying heat fluxes

pected in traditional microchannels too since the increase in length of the microchannel always increases the residence time. However, the optimum inlet temperature depends on the dimensions of the flow channel and hence on other parameters that depend on the channel geometry like the velocity field, residence time, etc.

4 Conclusion

The performance of the NEPCM slurry was compared with that of a single phase fluid in a MMC channel. Numerical results predict that the presence of NEPCM particles inside the fluid helps in increasing the Nusselt number and decreases the bulk mean temperature of the fluid. For the mass flow rates considered, an increase in mass concentrations of PCM aids in the improvement of heat transfer performance. However, the pressure drop inside the channel rises due to the increase in the effective viscosity of the fluid in the case of the slurry. The effect of inlet temperature on the fluid for different melting ranges of PCM was investigated and it was found that the performance of the slurry highly depends on the inlet temperature. It was found that if the melting range is narrow it is good to have the inlet temperature near the peak of the melting curve of the PCM. These results are expected to be dependent on the channel dimensions. Also, it was found that the difference in the performance of the slurry and PAO increases with an increase in heat flux. The analysis would help in designing and optimizing future designs of NEPCM slurry flows in MMC heat sinks.

Acknowledgment

The authors wish to acknowledge Dr. Mark Spector, program manager at Office of Naval Research (ONR), for funding this work. The authors would like to thank Dr. Ming Su of University of Central Florida for providing the technical information about NEPCM particles.

Nomenclature

Bi = Biot number
C = volume concentration of slurry
c_m = mass concentration of slurry or loading fraction
c_p = specific heat (J/kg K)
d_p = particle diameter (m)
D_h = hydraulic diameter (m)
e = magnitude of shear rate (1/s)
F' = nondimensionalized force
F_D = drag force on a particle (N)
h_{sf} = latent heat of fusion of PCM (J/kg)
H = height of the channel or tube diameter (m)
k = thermal conductivity (W/m K)
L = length of the channel or tube (m)
L_h = half of the channel height (m)
L_p = lateral particle position from the center of the axis (m)
m = mass of particle (kg)
$\dot{m}$ = mass flow rate (kg/s)
Nu = Nusselt number
Nu_m = Nusselt number $= q_w D_h/(k_{\mathrm{bulk}}*(T_{w,\max}-T_{\mathrm{in}}))$
p = Pressure (Pa)
Pe = Peclet number
Pr = Prandtl number
q = heat flux ($\mathrm{W/cm^2}$)
r_p = solid-liquid interface radius (m)
R = radius (m)
Re = Reynolds number
Re_p = particle Reynolds number, $=\mathrm{Re}(R_p/L_h)^2$
Ste = Stefan number $= c_{p,b}(q_w R_d \rho_b)/(c\rho_{\mathrm{pcm}} h_{sf} k_b)$
t = time (s), thickness (m)
t_{base} = thickness of the base (m)
t_{res} = residence time of the particle (s)
T = temperature (K)
T_1 = lower melting temperature (K)
T_2 = higher melting temperature (K)
T_m = melting temperature or average melting temperature $=(T_1+T_2)/2$ (K)
T_{Mr} = melting range $=T_2-T_1$ (K)
u = velocity in the x direction (m/s)
u_∞ = fluid velocity (m/s)
U = maximum velocity of fluid in the channel (m/s)
U_{av} = magnitude of average velocity (m/s)
U_p = particle axial velocity (m/s)
v = velocity in the y direction, particle velocity (m/s)
V_{migr} = migration velocity or lateral velocity of the particle (m/s)
w = velocity in the z direction (m/s)
x,y,z = spatial coordinates
ΔP = MMC inlet to outlet pressure drop (Pa)
ΔT_{bulk} = microchannel inlet to outlet temperature difference or bulk temperature rise (K)

Greek Symbols

α = thermal diffusivity ($\mathrm{m^2/s}$)
γ = shear rate (1/s)
ρ = density ($\mathrm{kg/m^3}$)
μ = dynamic viscosity (Pa s)
θ_{in} = nondimensional temperature at the inlet $(T_{\mathrm{in}}-T_1)/T_{Mr}$
ν = kinematic viscosity ($\mathrm{m^2/s}$)
τ = time constant (s)

Subscripts

b = bulk
ch = channel
d = duct
e, eff = effective
exit = exit/outlet
eq = equilibrium
f = fluid
i = index
in = inlet
l = liquid phase
m = mean
max = maximum
p = particle

pcm = PCM
s = solid phase
w = wall

References

[1] Tuckerman, D. B., and Pease, R. F. W., 1981, "High-Performance Heat Sinking for VLSI," IEEE Electron Device Lett., **2**, pp. 126–129.
[2] Harpole, G. M., and Eninger, J. E., 1991, "Microchannel Heat Exchanger Optimization," *Proceedings of the Seventh IEEE Semi-Therm Symposium*, pp. 59–63.
[3] Copeland, D., Behnia, B., and Nakayama, W., 1997, "Manifold Microchannel Heat Sinks: Isothermal Analysis," IEEE Trans. Compon., Packag. Manuf. Technol., Part A, **20**, pp. 96–102.
[4] Gokel, G. W., 2000, *Dean's Handbook of Organic Chemistry*, 2nd ed., McGraw-Hill, New York.
[5] Colvin, D. P., and Mulligan, J. C., 1987, "Microencapsulated Phase Change for Storage of Heat," NASA Technical Report No. MFSA-27198.
[6] Colvin, D. P., and Mulligan, J. C., 1986, "Spacecraft Heat Rejection Methods: Active and Passive Heat Transfer for Electronic Systems—Phase I," Air Force Wright Aeronautical Laboratories, Report No. AFWAL-TR-3074.
[7] Chen, K., and Chen, M. M., 1987, *An Analytical and Experimental Investigation of the Convective Heat Transfer of Phase Change Slurry Flows*, Vol. 2, Ziejiang University Press, Ziejiang, China, pp. 496–501.
[8] Charunyakorn, P., Sengupta, S., and Roy, S. K., 1990, "Forced Convection Heat Transfer in Microencapsulated Phase Change Material Slurries: Flow Between Parallel Plates," *General Papers: Phase Change and Convective Heat Transfer*, ASME HTD, Vol. 129, pp. 55–62.
[9] Colvin, D. P., Bryant, Y. B., Mulligan, J. C., and Duncan, J. D., 1989, "Microencapsulated Phase Change Heat Transfer System," U.S. Air Force Wright R & D Center, Report No. WRDC-TR-89-3072.
[10] Kasza, K. E., and Chen, M. M., 1985, "Improvement of the Performance of Solar Energy or Waste Heat Utilization Systems by Using Phase-Change Slurry as an Enhanced Heat Transfer Storage Fluid," ASME J. Sol. Energy Eng., **107**, pp. 229–236.
[11] Roy, S. K., and Sengupta, S., 1991, "An Evaluation of Phase Change Microcapsules for Use in Enhanced Heat Transfer Fluids," Int. Commun. Heat Mass Transfer, **18**(4), pp. 495–507.
[12] Goel, M., Roy, S. K., and Sengupta, S., 1994, "Laminar Forced Convection Heat Transfer in Microcapsulated Phase Change Material Suspension," Int. J. Heat Mass Transfer, **37**, pp. 593–604.
[13] Charunyakorn, P., Sengupta, S., and Roy, S. K., 1991, "Forced Convection Heat Transfer in Microencapsulated Phase Change Material Slurry: Flow in Circular Ducts," Int. J. Heat Mass Transfer, **34**, pp. 819–833.
[14] Zhang, Y. W., and Faghri, A., 1995, "Analysis of Forced Convection Heat Transfer in Microcapsulated Phase Change Material Suspensions," J. Thermophys. Heat Transfer, **9**(4), pp. 727–732.
[15] Yamagishi, Y., Tahkeuchi, H., Pyatenko, A., and Kayukawa, N., 1999, "A Technical Evaluation of a Microencapsulated PCM Slurry as a Heat Transfer Fluid," AIChE J., **45**(4), pp. 696–707.
[16] Alisetti, E. L., and Roy, S. K., 2000, "Forced Convection Heat Transfer to Phase Change Material Slurries in Circular Ducts," J. Thermophys. Heat Transfer, **14**, pp. 115–118.
[17] Zhang, Y., Hu, X., and Wang, X., 2003, "Theoretical Analysis of Convective Heat Transfer Enhancement of Microencapsulated Phase Change Material Slurries," Heat Mass Transfer, **40**, pp. 59–66.
[18] Hao, Y. L., and Tao, Y.-X., 2004, "A Numerical Model for Phase-Change Suspension Flow in Microchannels," Numer. Heat Transfer, Part A, **46**, pp. 55–77.
[19] Xing, K. Q., Tao, Y.-X., and Hao, Y. L., 2005, "Performance Evaluation of Liquid Flow With PCM Particles in Microchannels," ASME J. Heat Transfer, **127**, pp. 931–940.
[20] Rao, Y., Dammel, F., and Stephan, P., 2007, "Experiments on Microencapsulated Phase Change Material Suspensions Flow in Rectangular Minichannels," ASME-JSME Thermal Engineering Summer Heat Transfer Conference.
[21] Rao, Y., Dammel, F., and Stephan, P., 2007, "Experiments on Cooling Performance of Microencapsulated Phase Change Material Suspension Flow in Rectangular Minichannels," ASME-JSME Thermal Engineering Summer Heat Transfer Conference.
[22] Karnis, A., Goldsmith, H. L., and Mason, S. G., 1966, "The Kinetics of Flowing Dispersions. I. Concentrated Suspensions of Rigid Particles," J. Colloid Interface Sci., **22**, pp. 531–553.
[23] Watkins, R. W., Robertson, C. R., and Acrivos, A., 1976, "Entrance Region Heat Transfer in Flowing Suspensions," Int. J. Heat Mass Transfer, **19**, pp. 693–695.
[24] Schlichting, H., Gersten, K., Krause, E., and Oertel, H., Jr., 2000, *Boundary Layer Theory*, 8th ed., Springer, New York.
[25] Asmolov, E. S., 1999, "The Inertial Lift on a Spherical Particle in a Plane Poiseuille Flow at Large Channel Reynolds Number," J. Fluid Mech., **381**, pp. 63–87.
[26] Matas, J. P., Morris, J. F., and Guazzelli, E., 2004, "Inertial Migration of Rigid Spherical Particles in Poiseuille Flow," J. Fluid Mech., **515**, pp. 171–195.
[27] Tao, L. C., 1967, "Generalized Numerical Solutions of Freezing a Saturated Liquid in Cylinders and Spheres," AIChE J., **13**(1), pp. 165–169.
[28] www.comsol.com.
[29] Vand, V., 1945, "Theory of Viscosity of Concentrated Suspensions," Nature (London), **155**, pp. 364–365.
[30] Vand, V., 1948, "Viscosity of Solutions and Suspensions," J. Phys. Colloid Chem., **52**, pp. 300–321.
[31] Gu, C. B., Su, G. S., Chow, L. C., and Pais, M. R., 1993, "Comparison of Spray and Jet Impingement Cooling," National Heat Transfer Conference.
[32] Duan, Z., and Muzychka, Y. S., 2004, "Impingement Air Cooled Plate Fin Heat Sinks, Part-I, Pressure Drop Model," Intersociety Conference on Thermal Phenomena, pp. 429–435.
[33] www.matlab.com.
[34] Alisetti, E., 1998, "Forced Convection Heat Transfer to Phase Change Material Slurries in Circular Ducts," MS thesis, University of Miami, Miami, FL.

Vertical Movement of Isothermal Lines in Water

William R. Gorman

Gregory J. Parks

James D. Brownridge[1]
e-mail: jdbjdb@binghamton.edu

Department of Physics, Applied Physics, and Astronomy,
State University of New York at Binghamton,
Binghamton, NY 13902-6000

We experimentally investigated the development and vertical movement of isothermal lines in cooling columns of confined water. The isothermal line develops spontaneously whenever the bottom of the column cools to ~4°C before the top. The width of these lines was typically less than 1 cm, with up to a 3°C thermal gradient across these lines. The velocity was inversely proportional to the diameter of the column. The velocity was 1.4±0.1 cm/min when the column diameter was 2.2 cm, and decreases to 0.4±0.1 cm/min when the diameter was increased to 12.5 cm. Data presented here also raise serious questions about the claim of new phase transitions in water made by Esposito et al. (2008, "Mpemba Effect and Phase Transitions in the Adiabatic Cooling of Water Before Freezing," Physica A, ***387****, pp. 757–763).* [DOI: 10.1115/1.3084120]

Keywords: isothermal lines, cooling confined water, heavy water in light water, phase transition, thermal gradient, cooling curves of water, maximum density

1 Introduction

While investigating the effect that heavy water (D_2O) had on heat transfer in light water (H_2O), we occasionally observed that the shape of the cooling curves was dramatically changed after we added heavy water to light water (<0.03%) [1].Upon further investigations, it was determined that the shape of the cooling curves depended primarily on two factors: the location of the temperature probe in the water and whether or not heavy water had been added and not stirred. After a search of the literature [2–18] failed to produce information that explained these phenomena, we undertook an investigation to determine why. This technical brief is a report of our findings. Here we answered the following questions: Why does the shape of the cooling curve for still water depend on the location of the temperature probe in the water, and how does added heavy water affect the cooling curve? Data presented here also raise serious questions about the claim of new phase transitions in water by Esposito et al. [19].

2 Experimental Setup

The most important part of the experimental setup is shown schematically in the inset in Fig. 1. The thermocouples (TCs) were connected to an Omega OMB-DAQ-3000 data acquisition module with eight TC inputs. The TCs were Type T bare wire (AWG No. 36). They were evenly spaced down the length of the container with the tip of each extending to the center of the container. The response time of the Omega Type T SPCH-005 thermocouple was less than 0.25 s. An ice bath was used as a 0°C reference. A 15 point adjacent averaging was used to smooth all figures of temperature versus time presented here.

3 Experiments and Results

De-ionized water was cooled in three cooling environments: a freezer, an ice bath, and outside on cold days. In each case, after water was added to a container we waited for several minutes for turbulence to subside before we started the data acquisition system. We show in Fig. 1 how externally induced turbulence can change the shape of a cooling curve. We have also determined that the isothermal lines that we discuss here will not develop if the water is stirred while cooling. Although stirring is an extreme case of turbulence, less dramatic forms of turbulence will also effect the development of isothermal lines. The kink at ~4°C in the still water cooling curve in Fig. 1 was produced spontaneously when the water surrounding the tip of the TC passed through maximum density. This also marks the time when the isothermal line passed the position of the TC in the column of water; see the insets in Figs. 2 and 3.

In Fig. 2 we show the cooling curves for seven TCs in a 6 cm diameter Nalgene container that was 15 cm tall. Here we cooled water from ~70°C to ~1°C by inserting the container into an ice bath. Notice that the cooling curve for each TC is quite smooth and that they decrease in temperature in descending order (bottom TC the coolest) until the temperature of TC 1 reaches ~4°C, see the inset. At this time, approximately 22 min into cooling, the temperature of the water around TC 1 essentially stopped decreasing, while the temperatures of the water around the other thermocouples continue to decrease, each falling below ~4°C in ascending order. When the temperature of the water at the top of the container fell below ~4°C, the water at the bottom resumed cooling. It took about 12 min for the isothermal line to travel to the top of the container. The point in time when each TC registers the temperature falling below ~4°C marks the time when the isothermal line moving from the bottom of the container reaches the height of that TC in the container. We use these types of data to calculate the vertical velocity of isothermal lines in each size container. Our experiments have shown that the velocity is inversely proportional to the diameter of the column of water within the range of diameters that we studied; see Fig. 4.

In Fig. 3 we show the effect of the diameter of the column of water on the formation of an isothermal line and the ability to accurately determine when it reaches a specific point in the column. Here we use two TCs to measure the temperature near the top and the bottom of the column. Notice that when the diameter was 40 mm, it was quite clear when the temperature of the water near the top of the column fell below that of the water near the bottom of the column. However, when the diameter was reduced to 4 mm, it is not apparent that the temperature of the water at the top of the column ever falls below that of the water near the bottom of the column. These data were obtained by placing the containers inside a freezer (−17°C).

To obtain the data shown in the inset in Fig. 3, we modified our standard setup by placing six TCs near the top of a container that was 6 cm in diameter and 21 cm tall. The vertical distance between each TC was 1 cm, and the lower one (TC 1) was 14 cm above the bottom of the container. In the standard setup the bottom TC was within ~1 cm of the bottom. In this modified setup the pause in cooling of the water surrounding the bottom TC occurred at ~3°C rather than at ~4°C, as shown in the inset in Fig. 2. The exact temperature at which this phenomenon occurs depends primarily on three factors: the geometry of the container, the position of the thermocouples in the container, and the rate of temperature change in the water. We determined that cooling at <0.1°C/min causes the entire volume of water to cool uniformly.

[1]Corresponding author.

Contributed by the Heat Transfer Division of ASME for publication in the JOURNAL OF HEAT TRANSFER. Manuscript received January 10, 2008; final manuscript received December 3, 2008; published online April 2, 2009. Review conducted by S. A. Sherif.

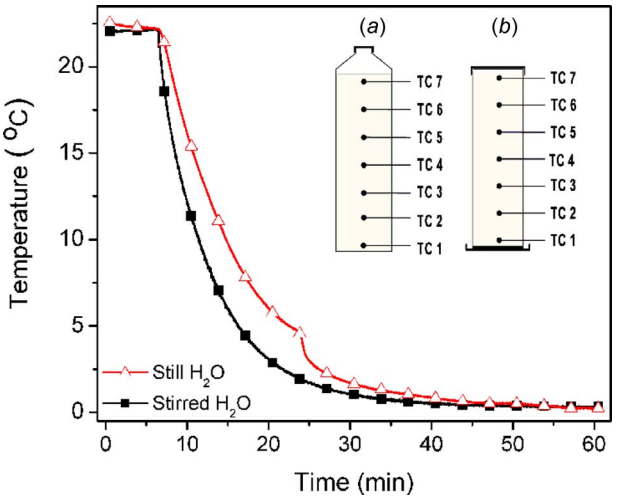

Fig. 1 Temperature versus time showing the difference between stirred and nonstirred water. The thermocouple is at the same location for each curve, and the error bars are smaller than the symbols. Inset: schematic of the water containers used to measure the vertical velocity of isothermal lines; (*a*) container for ice bath cooling and (*b*) container for freezer cooling. TCs 1–7 are seven thermocouples positioned axially in the center of each container with TC 1 at the bottom.

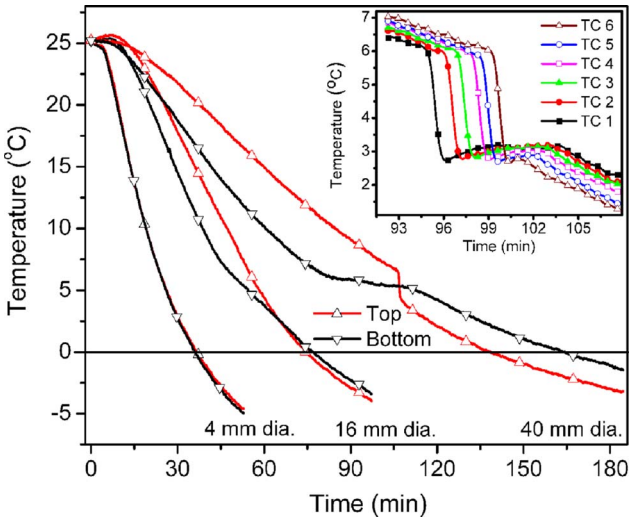

Fig. 3 Temperature versus time of a 4 mm, 16 mm, and 40 mm diameter cylinder with thermocouples placed at the top and bottom. Inset: movement of cold front monitored by six thermocouples in a 6 cm diameter cylinder, 21 cm tall, with the thermocouples 2 cm from the top and spaced 1 cm apart. TC 1 was 14 cm from the bottom.

In this case the entire column of water passes through maximum density at the same time, and no isothermal line develops.

Using data presented in the insets of Fig. 3, we were able to determine the maximum width of the isothermal for that cooling cycle. It was less than 1 cm wide with a 3°C gradient across the line. The sudden drop in temperature from ~6°C to ~3°C was the indication that the isothermal line was passing a TC, and that its width was less than the distance between that TC and the next TC because the temperature of the water surrounding the next TC had not begun the sudden drop characteristic of the arrival of colder water. This is clearly shown in the inset in Fig. 3. The velocity was 1.4 ± 0.1 cm/min when the column diameter was 2.2 cm, and decreases to 0.4 ± 0.1 cm/min when the diameter was increased to 12.5 cm.

We confirmed by experiments that isothermal lines also developed in heavy water by placing 99.9% pure D_2O in a container and cooling it through its maximum density at ~11°C. The result is presented in the inset in Fig. 4 alone with a typical cooling curve for light water as it is cooled through its maximum density at ~4°C.

4 Conclusions

We have measured for the first time the velocity of isothermal lines moving vertically through columns of confined still water. It was shown experimentally that the velocity was inversely propor-

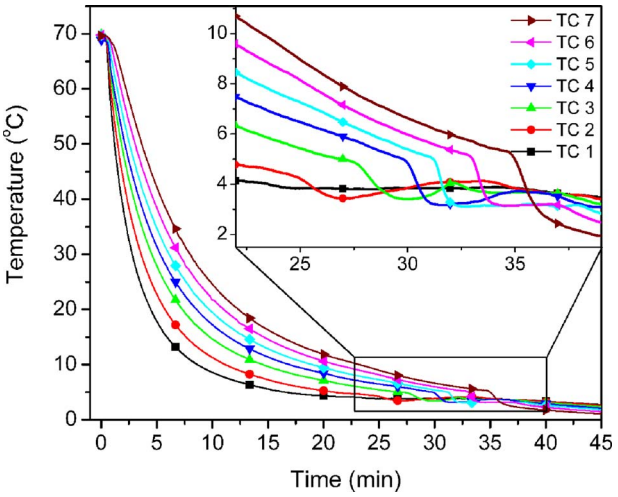

Fig. 2 Temperature versus time of warm water cooled in an ice bath in a container with a 6.0 cm diameter and 15 cm length. Inset: closeup of the movement of the isothermal line from that same run. TC 1 is ~0.3 cm from the bottom of the container, and TC 7 is ~0.3 cm from the top of the container. Notice the sudden change in the rate of cooling. This marks the time when the isothermal line arrives at each TC as it moves up the column.

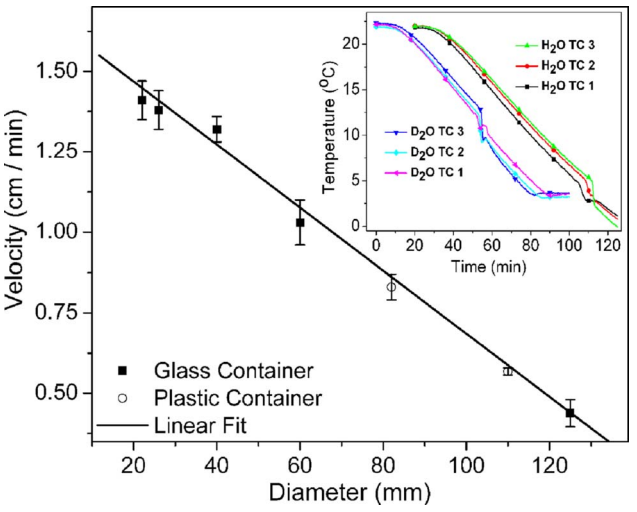

Fig. 4 Velocity of isothermal lines versus diameter of the column of water. Inset: temperature versus time for H_2O and D_2O placed in identical containers. The starting time of the H_2O curve was offset by 20 min for display purposes. TC 1 is 4.5 cm from the bottom of a 10 cm tall container.

tional to the diameter of the column of water. The width of the isothermal lines was determined to be less than 1 cm with a thermal gradient across the line, often as large as 3 °C.

Finally we believe that the data presented here call into question the claim in Ref. [19] that "phase transitions which take place at 6 ± 1 °C, 3.5 ± 0.5 °C and 1.3 ± 0.6 °C." are new phase transitions in water. They claimed that the one at 1.3 ± 0.6 °C "has not been detected earlier." The "transitions between different phases" that they refer to in their Fig. 2 (where the rate of change in temperature abruptly changes) are clearly seen in our data. We have demonstrated by experiments that what they refer to as a phase transition can be produced at any temperature between ~6 °C and ~1 °C by simply varying the geometry of the system, as we showed in Fig. 3. They can also be prevented from appearing in the cooling curve by stirring or adding a small amount of heavy water (~0.2% or less) to light water.

Acknowledgment

We would like to thank S. M. Shafroth, M. Stephens, and B. Poliks for their valuable conversations and help.

References

[1] Gorman, W. R., and Brownridge, J. D., 2008, "Reduced Heat Flow in Light Water (H_2O) Due to Heavy Water (H_2O)," Appl. Phys. Lett., **93**, p. 034101.
[2] 1972, *Water: A Comprehensive Treatise*, F. Franks, ed., Plenum, New York, Vol. 1, pp. 1–13.
[3] Jamin, Y. L., and Mohamad, A. A., 2008, "Natural Convection Heat Transfer Enhancements From a Cylinder Using Porous Carbon Foam: Experimental Study," ASME J. Heat Transfer, **130**(12), p. 122502.
[4] Murray, M. M., 2008, "Demonstration of Heat Transfer Enhancement Using Ferromagnetic Particle Laden Fluid and Switched Magnetic Fields," ASME J. Heat Transfer, **130**(11), p. 114508.
[5] Abu-Nada, E., Ziyad, K., Saleh, M., and Ali, Y., 2008, "Heat Transfer Enhancement in Combined Convection Around a Horizontal Cylinder Using Nanofluids," ASME J. Heat Transfer, **130**(8), p. 084505.
[6] Ben-Nakhi, A., Eftekhari, M. M., and Loveday, D. I., 2008, "Natural Convection Heat Transfer in a Partially Open Square Cavity With a Thin Fin Attached to the Hot Wall," ASME J. Heat Transfer, **130**(5), p. 052502.
[7] Dalal, A., and Das, M. K., 2006, "Natural Convection in a Cavity With a Wavy Wall Heated From Below and Uniformly Cooled From the Top and Both Sides," ASME J. Heat Transfer, **128**(7), pp. 717–725.
[8] Das, S. K., Putra, N., Thiesen, P., and Roetzel, W., 2003, "Temperature Dependence of Thermal Conductivity Enhancement for Nanofluids," ASME J. Heat Transfer, **125**(4), pp. 567–574.
[9] Maiti, D. K., Gupta, A. S., and Bhattacharyya, S., 2008, "Stable/Unstable Stratification in Thermosolutal Convection in a Square Cavity," ASME J. Heat Transfer, **130**(12), p. 122001.
[10] Cho, C. H., Singh, S., and Robinson, G. W., 1996, "An Explanation of the Density Maximum in Water," Phys. Rev. Lett., **76**, pp. 1651–1654.
[11] Cho, C. H., Singh, S., and Robinson, G. W., 1997, "Understanding All of Water's Anomalies With a Nonlocal Potential," J. Chem. Phys., **107**, pp. 7979–7988.
[12] Ivey, G. N., 1984, "Experiments on Transient Natural Convection in a Cavity," J. Fluid Mech., **144**, pp. 389–401.
[13] Robillard, L., and Vasseur, P., 1982, "Convection Response of a Mass of Water Near 4 °C at a Constant Cooling Rate Applied on Its Boundaries," J. Fluid Mech., **118**, pp. 123–141.
[14] Vedamuthu, M., Singh, S., and Robinson, G. W., 1994, "Properties of Liquid Water: Origin of the Density Anomalies," J. Phys. Chem., **98**, pp. 2222–2230.
[15] Chaplin, M. F., 2000, "A Proposal for the Structuring of Water," Biophys. Chem., **83**, pp. 211–221.
[16] Yen, Y. C., 1990, *Natural Convection Heat Transfer in Water Near Its Density Maximum*, U.S. Army Cold Regions Research and Engineering Laboratory, Hanover, NH.
[17] Lankford, K. E., and Bejan, A., 1986, "Natural Convection in a Vertical Enclosure Filled With Water Near 4 °C," ASME J. Heat Transfer, **108**, pp. 755–763.
[18] Arpaci, V. S., Selamet, A., and Kao, S. H., 2000, *Introduction to Heat Transfer*, Prentice-Hall, Upper Saddle River, NJ.
[19] Esposito, S., De Risi, R., and Somma, L., 2008, "Mpemba Effect and Phase Transitions in the Adiabatic Cooling of Water Before Freezing," Physica A, **387**, pp. 757–763.

Comparative Radial Heat Flow Method for Thermal Conductivity Measurement of Liquids

Ananth S. Iyengar
e-mail: ananth.iyengar@case.edu

Alexis R. Abramson[1]
e-mail: alexis.abramson@case.edu

Department of Mechanical and Aerospace Engineering,
Case Western Reserve University,
10900 Euclid Avenue,
Cleveland, OH 44106-7222

A steady state thermal conductivity measuring setup based on the comparative radial heat flow method is presented. The setup consists of a pair of coaxial cylinders as its main components, with test fluid placed in the annular space between these cylinders with water tight cover plates at the top and bottom of the cylinders. Experiment involves heating the coil at the concentric-center of the inner cylinder; steady state data are acquired for the calculation of the thermal conductivity. Thermal conductivity is calculated by comparing the radial heat flow between the cylinders and the test fluid (comparative method). Thermal conductivity of water, glycerol, and ethylene glycol was measured for varying temperatures and is in good agreement with the published thermal conductivity values in literature. [DOI: 10.1115/1.3084124]

Keywords: thermal conductivity, liquids, cylindrical

1 Introduction

Research and development of various technologies in fields such as food engineering, bioengineering, heat exchanger design, and agriculture/soil often requires highly accurate thermal conductivity data for liquids. A variety of methods have been employed for the thermal conductivity measurement of these materials, and techniques used may be broadly divided into transient and steady state measurement approaches. While each of these techniques has its own benefits and drawbacks, transient thermal methods are commonly preferred for measurements of liquids since quick results may be obtained, and convection effects are generally negligible in the short time interval of the experiment. Nonetheless, transient thermal conductivity measurement apparatus and relevant analysis techniques can be more complicated than using a steady state approach. Employed for their simplicity, common steady state methods such as the "cut bar" approach [1], the "hot plate" technique [2], and coaxial cylindrical apparatus [3–5], which can be used for the thermal conductivity measurement of liquids, do have drawbacks including difficulties in accounting for extraneous heat loss and natural convection effects.

Thermal conductivity measurement techniques can be further classified as direct or comparative depending on whether quantitative knowledge of the power dissipated from the heating element in the instrument is required. For example, using a direct method approach, the quantity of heat produced from a metal coil used in a typical thermal probe technique is calculated from the electrical power, and thermal conductivity is determined from either Fourier law at steady state or using a form of the transient heat flow equation [6,7]. Requiring knowledge of the exact heat output of the source imposes a limitation to the accuracy of the method since there is experimental uncertainty in the measurement of voltage and current output as well as unknowns regarding extraneous heat losses. Nonetheless, in a comparative measurement, a material of known thermal conductivity (the reference) is in contact with the sample, temperature measurements are taken at each surface, and the sample's thermal conductivity is calculated from temperature data and by determining the heat flux through the reference material (which must also pass through the adjacent sample).

The aim of this work is to demonstrate a novel steady state technique for measurement of thermal conductivity of liquids that combines some of the benefits of various previously demonstrated methods. The experimental setup is a coaxial type arrangement to impose heat flow along the radial direction away from the central axis, and the analysis method involves a comparative technique. Radial heat flow ensures that losses are minimized, and heat guards commonly found in other techniques [2] are not required. Moreover, the comparative approach eliminates the necessity of exact knowledge of the heat flux from the source. These factors help reduce uncertainty, and a simple steady state apparatus may be constructed for this purpose. The technique is referred to as the comparative radial heat flow method. To validate the technique, water, glycerol, ethylene, and glycol were tested, and results were compared to existing literature values [8].

2 Experimental Setup and Procedure

The experimental apparatus for this technique, as shown in Fig. 1, included a heating coil, which was placed at the central axis of an inner cylinder and which was made by coiling a nichrome wire of American wire gauge (AWG) 30 with a coil diameter of 2.5 mm. The test liquid was sandwiched in the 2.5 mm of annular space between inner and outer concentric cylinders, each composed of high density polyethylene (HDPE). HDPE was chosen since it could be easily machined, is inexpensive, and shows good chemical resistance to common liquids. The thermal conductivity of the HDPE material was measured at our laboratory facility at Case Western Reserve University using a proven axial flow method [9] and was found to be 0.39 ± 0.02 W/m K. The outer cylinder inner diameter was 44 mm and its outer diameter was 64 mm; the inner cylinder had an inner diameter of 5 mm and an outer diameter of 39 mm. The heater was held in place by stoppers that fit into the space inside the inner cylinder.

Grooves slightly larger in size than the thickness of the cylinder walls and small circular locator-holes were made in the apparatus' top and bottom caps, and small locator pins (cylindrical protrusions from the flat face of the cylinders) were fabricated during the machining of HDPE to enable the cylinders to secure into place for repeated measurements. These caps were composed of chlorinated polyvinyl chloride (CPVC) and possessed a thermal conductivity of 0.14 W/m K, as reported by the manufacturer. Additionally, small grooves were drilled at specific locations in and along the cylinder walls for thermocouple placement.

Figure 1(*b*) shows a top-down view of the cylinders in the assembly. The T-type thermocouples were positioned at the radial locations as indicated, namely, r_1, r_2, r_3, and r_4. The thermocouple wires were run along the walls until reaching a location at approximately half the cylinders' length. Additionally, a cylindrical aluminum heat sink was employed at the outer surface of the outer cylinder to enhance the radial heat transfer. Similarly, insulation was provided at the top and bottom of the setup to decrease the axial heat loss. The entire assembly was placed in an insulating box to restrict ambient air contact, thereby reducing temperature fluctuations.

To facilitate the measurement, electrical connections were made between the heating coil and power source, and the thermocouples

[1]Corresponding author.

Contributed by the Heat Transfer Division of ASME for publication in the JOURNAL OF HEAT TRANSFER. Manuscript received February 12, 2008; final manuscript received January 8, 2009; published online April 9, 2009. Review conducted by Minking Chyu.

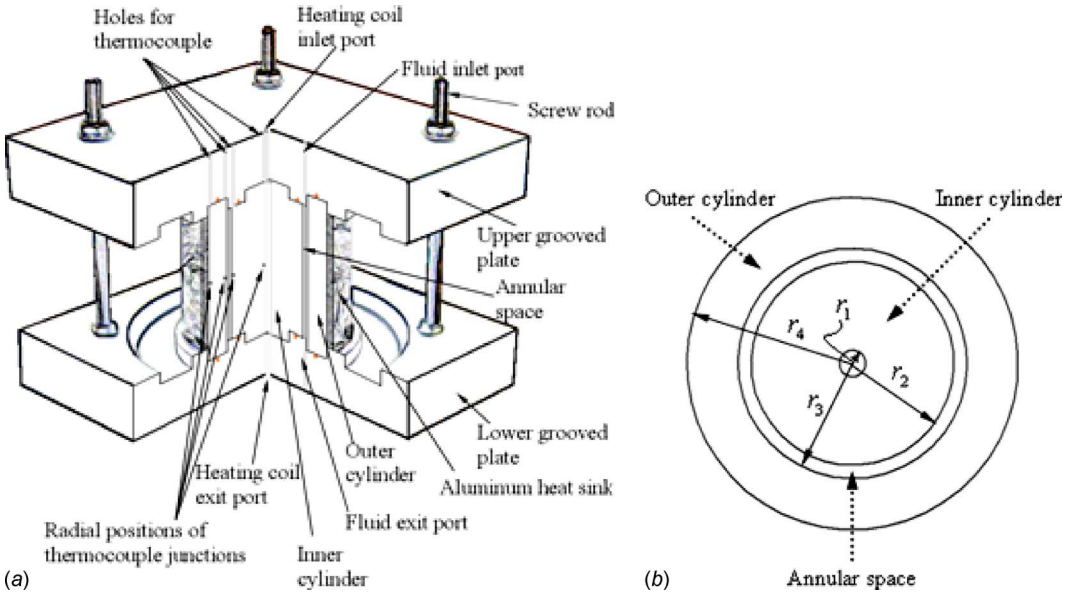

Fig. 1 Experimental setup: (*a*) a schematic cut section illustrating various parts and (*b*) a schematic of a top-down midsection view of the cylindrical setup; the *r* labels indicate the radial location of the four thermocouples used

and data acquisition instrumentation. The test liquid was injected into the annular space between the cylinders with a syringe. Note that to speed up the time period for data collection, the setup was typically preheated prior to the injection of the fluid to ensure that time to reach steady state was minimized. Additionally, the fluid itself was preheated on a hot plate (domestic electric heater) to a designated temperature to further accelerate the data collection period. Since settling may occur in a nanofluid, it was particularly important to minimize the time of the experimentation. After the data were acquired, the test liquid was drained through a hole at the bottom plate of the setup.

The thermal conductivity was calculated using a formula derived from the steady state cylindrical heat equation. By equating the heat flow rate from a reference cylinder and the test fluid annulus, the following equality is obtained:

$$\dot{q} = \frac{2\pi L \cdot k_r \cdot (T_1 - T_2)}{\ln\left(\frac{r_2}{r_1}\right)} = \frac{2\pi L \cdot k_f \cdot (T_2 - T_3)}{\ln\left(\frac{r_3}{r_2}\right)} = \frac{2\pi L \cdot k_r \cdot (T_3 - T_4)}{\ln\left(\frac{r_4}{r_3}\right)} \tag{1}$$

where $\dot{q}$ is the radial heat flow rate, k_f and k_r are the thermal conductivities of test fluid and reference material (HDPE), respectively, L is the vertical length of the cylinder, r_1, r_2, r_3, and r_4 refer to the radial locations of the thermocouples, respectively, and T_1, T_2, T_3, and T_4 are the temperatures measured with thermocouples at radial locations of r_1, r_2, r_3, and r_4, respectively. While either the inner or outer reference cylinders (or a weighted average of the two) may be employed to determine the unknown conductivity of the fluid, for data presented in this paper, the temperature values from the inner cylinder were used in the analysis because they exhibited a lower noise level. Alternatively, Eq. (1) may be written to easily facilitate the calculation of thermal conductivity of the test fluid, k_f, as

$$\frac{k_f}{k_r} = \frac{T_1 - T_2}{T_2 - T_3} \times \frac{\ln(r_3/r_2)}{\ln(r_2/r_1)} \tag{2}$$

3 Onset of Natural Convection

It is implicit in Eqs. (1) and (2) that the heat flow direction must be radial with respect to the central axis of the cylinder. Moreover, natural convection must be negligible, and heat conduction must be the only mechanism of heat transfer from the heater to the outer heat sink. Nonetheless, the onset of natural convection depends on the dimension of and the temperature difference across the test fluid layer as well as its thermophysical properties. The critical value of the dimensionless parameter, the Rayleigh number, determines the onset of the natural convection such that

$$\mathrm{Ra} = \frac{g \cdot \beta \cdot \Delta T \cdot x^3}{\alpha \cdot \nu} \tag{3}$$

where g is the acceleration due to gravity, β is the volumetric thermal expansion coefficient of the fluid, ΔT is the temperature difference across the test fluid, x is the characteristic length of the cylindrical test fluid sample, which for the described apparatus is the thickness of the annulus, and α and ν are the thermal diffusivity and kinematic viscosity of the test fluid, respectively. The criterion used for neglecting natural convection for similar cylindrical experimental setups includes assuring that the Rayleigh number is maintained less than 1000 [3]. Therefore, the design of experimental apparatus must ensure that natural convection is negligible through analysis of the variables in the expression of the Rayleigh number. For example, assuming water as the test fluid at 30 °C, $\beta/\alpha\cdot\nu$ was calculated to be 2.56×10^{10} m^{-4} s K^{-1}. Taking 1000, the maximum allowable Rayleigh number, and dividing by $g = 9.8$ m s^{-2} and $\beta/\alpha\cdot\nu$ for water requires that $\Delta T\cdot(x)^3 < 3.99\times10^{-9}$ m^3 s^{-3} K. Therefore, the apparatus was designed such that a maximum temperature difference of 2 °C would be maintained across the test fluid annulus of 2.5 mm to give $\Delta T\cdot(x)^3$ of 3.13×10^{-8} m^3 K. Therefore, this specific setup was appropriate for a liquid with $\beta/\alpha\cdot\nu$ less than 2.56×10^{10} m^{-4} s K^{-1} to ensure that natural convection effects are minimized. However, if the test fluid were to exhibit a $\beta/\alpha\cdot\nu$ much lower than 2.56×10^{10} m^{-4} s K^{-1}, or ΔT much smaller than 2 °C, then the outside cylinder could be replaced by an alternate cylinder with larger diameters to accommodate a larger volume of fluid for the measurement. For this particular setup, we built the apparatus to accommodate two different outer cylinders such that the alternate cylinder had an inner diameter of 80 mm and an outer diameter of 120 mm, resulting in an annulus of 20 mm, thus increasing the value of $\Delta T\cdot(x)^3$ for the same temperature difference to 1.6×10^{-5} m^3 K.

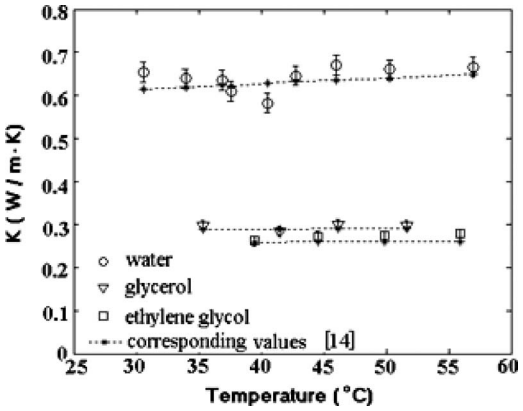

Fig. 2 Comparison of the measured thermal conductivity of water, glycerol, and ethylene glycol with literature values [8]

4 Error Analysis of the Method

The uncertainties in the thermal conductivity measurement of the experimental setup are dependent on the accuracy of the temperature measurements, knowledge of the exact location of the thermocouples, and the error associated with the thermal conductivity measurement of the reference material (HDPE). Therefore, the fluid thermal conductivity is a function of various parameters such that

$$k_{\text{fluid}} = f(k_{\text{ref}}, T_1, T_2, T_3, r_1, r_2, r_3) \tag{4}$$

The uncertainty in the thermocouples was specified by the manufacturer (Omega Engineering, Stamford, CT) to be $\pm 0.1\,^{\circ}\text{C}$; the uncertainty in the location of thermocouples was estimated to be within 0.3 mm. As stated previously, the thermal conductivity of the HDPE reference material was measured to be 0.39 ± 0.02 W m^{-1} K^{-1} by the method reported by Hostler et al. [9]. Using a data reduction method, the combined uncertainty for a typical experiment under ideal conditions was calculated to be no greater than 3.6%, thereby demonstrating the accuracy of this experimental setup. Note that there could be additional error if significant axial heat losses occurred such that the radial heat flux through the inner reference cylinder (which was used for the calculation) was not equivalent to that flowing through the fluid annulus. To estimate the heat loss, the heat fluxes through both the inner and outer reference cylinders were compared. The disparity between the heat fluxes was at maximum approximately 3%, but more typically between 1% and 2%.

A comparison of measured thermal conductivity of water, glycerol, and ethylene glycol with that reported in literature [8] is shown in Fig. 2. From the thermal conductivity curve for water in Fig. 2, we can see that the maximum deviation from the reported thermal conductivity to that of the measured thermal conductivity is 7%, and the average deviation is about 4%, similar observation made for glycerol shows the maximum deviation of 4%, and an average deviation of 3%, and thermal conductivity comparison for ethylene glycol shows maximum deviation of 7%, and average of 4% variation. These results demonstrate that the uncertainty in the apparatus can explain the average deviation of the results from the values reported in literature [8].

5 Results and Discussion

The thermal conductivity of three different liquids of known thermal conductivity was measured. As shown in Fig. 2, water, glycerol, and ethylene glycol were used as the test liquids, and the measured thermal conductivity values were compared with the data found in literature [8], and majority of the points matched the literature values within the limits of experimental uncertainty. Moreover, the linear curve fit lines associated with the measured points lie within $\pm 1\%$ for the literature values corresponding to the water, glycerol, and ethylene glycol for the entire temperature range. The curve fit line for all the conventional fluids follows the trend of the thermal conductivity with temperature that is reported in literature for the measured range of temperatures. From these measurements, the experimental setup and procedure were validated to an acceptable degree.

6 Conclusion

A simple setup using a radial heat flow method for thermal conductivity measurement is reported; its comparative technique ensures that the measurement does not require the estimation of electrical energy supplied to the heater. The error estimate (uncertainty calculation) shows that the reported thermal conductivity measuring system is accurate to 3.6%. The above mentioned system was validated for its accuracy by measuring the thermal conductivity of liquids of known thermal conductivity values, namely, water, glycerol, and ethylene glycol. The curve fit line for the measured data points for the above mentioned liquids fell within $\pm 1\%$ from the curve fit generated by the literature values.

Nomenclature

$\dot{q}$ = rate of heat flow
L = axial length of the cylinders
$k_r = k_{\text{ref}}$ = thermal conductivity of reference material
$k_f = k_{\text{fluid}}$ = thermal conductivity of fluid
T_1 = temperature, with subscripts having usual meaning
r_2 = radial distance from the center of the setup, with subscripts having usual meaning
Ra = Rayleigh number
g = acceleration due to gravity
β = volumetric expansion coefficient
ΔT = temperature difference
x = annular space between concentric cylinders (the thickness of the fluid layer)
α = thermal diffusivity
ν = kinematic viscosity

Subscripts

1,2,3, and 4 = properties at points 1, 2, 3, and 4 as indicated in Fig. 1(*b*)
r, ref = properties of reference
f, fluid = properties of fluid

References

[1] Li, C. H., and Peterson, G. P., 2006, "Experimental Investigation of Temperature and Volume Fraction Variations on the Effective Thermal Conductivity of Nanoparticle Suspensions (Nanofluids)," J. Appl. Phys., **99**, p. 084314.
[2] Wang, X., Xu, X., and Choi, S. U. S., 1999, "Thermal Conductivity of Nanoparticle-Fluid Mixture," J. Thermophys. Heat Transfer, **13**(4), pp. 474–480.
[3] Sklyarchuk, V., and Plevachuk, Y., 2005, "A Modified Steady State Apparatus for Thermal Conductivity Measurements of Liquid Metals and Semiconductors," Meas. Sci. Technol., **16**, pp. 467–471.
[4] Frezzotti, D., Goffredi, G., and Bencini, E., 1995, "Thermal Conductivity Measurements of Cis- and Trans-Decahydronaphthalene Isomers Using Steady State Coaxial Cylinders Method," Thermochim. Acta, **265**, pp. 119–128.
[5] Guildner, L. A., 1962, "Thermal Conductivity of Gases–I. The Coaxial Cylinder Cell," J. Res. Natl. Bur. Stand., Sect. A, **66A**(4), pp. 333–340.
[6] Zhang, H., Zhao, G., Ye, H., and Cheng, S., 2005, "An Improved Hot Probe for Measuring Thermal Conductivity of Liquids," Meas. Sci. Technol., **16**, pp. 1430–1435.
[7] Nagai, H., Rossignol, F., Nataka, Y., Tsurue, T., Suzuki, M., and Okutani, T., 2000, "Thermal Conductivity Measurement of Liquid Materials by a Hot-Disk Method in Short-Duration Microgravity Environments," Mater. Sci. Eng., A, **276**, pp. 117–123.
[8] Touloukian, Y. S., Powell, R. W., Ho, C. Y., and Klemens, P. G., 1970, *Thermal Conductivity—Non-Metallic Fluids and Gasses* (Thermophysical Properties of Matter Vol. 3), IFI/Plenum, New York.
[9] Hostler, S. R., Abramson, A. R., Gawryla, M. D., Bandi, S. A., and Schiraldi, D. A., 2008, "Thermal Conductivity of Clay Based Aero Gel," Int. J. Heat Mass Transfer, **52**(3–4), pp. 665–669.

Analysis of Instantaneous Turbulent Velocity Vector and Temperature Profiles in Transitional Rough Channel Flow

Noor Afzal
Faculty of Engineering,
Aligarh Muslim University,
Aligarh 202002, India

The instantaneous velocity vector and instantaneous temperature in a turbulent flow in a transitionally rough channel have been analyzed from unsteady Navier–Stokes equations and unsteady thermal energy equation for large Reynolds numbers. The inner and outer layers asymptotic expansions for the instantaneous velocity vector and instantaneous temperature have been matched in the overlap region by the Izakson–Millikan–Kolmogorov hypothesis. The higher order effects and implications of the intermediate (or meso) layer are analyzed for the instantaneous velocity vector and instantaneous temperature. Uniformly valid solutions for instantaneous velocity vector have been decomposed into the mean velocity vector, and fluctuations in velocity vector, as well as the instantaneous temperature, have been decomposed into mean temperature and fluctuations in temperature. It is shown in the present work that if the mean velocity vector in the work of Afzal (1976, "Millikan Argument at Moderately Large Reynolds Numbers," Phys. Fluids, ***16****, pp. 600–602) is replaced by instantaneous velocity vector, we get the results of Lundgren (2007, "Asymptotic Analysis of the Constant Pressure Turbulent Boundary Layer," Phys. Fluids,* ***19****, pp. 055105) for instantaneous velocity vector. The comparison of the predictions for momentum and thermal mesolayers is supported by direct numerical simulation (DNS) and experimental data.* [DOI: 10.1115/1.3085827]

Keywords: instantaneous velocity vector, instantaneous temperature, intermediate layer, mesolayer, Reynolds shear stress, Reynolds heat flux, pipe and channel, wall roughness, universal relations

1 Introduction

The experimental investigation of instantaneous velocity profiles in turbulent flow has been carried out by Robinson [1]. The experimental evidence for an instantaneous log law in which the additive function fluctuates but is independent of y is generally supportive, but not perfect. Nakayama et al. [2] also studied the similarity of instantaneous and filtered turbulent velocity fields in the near wall region of zero pressure turbulent boundary layer. In a turbulent boundary layer, the instantaneous velocity vector was analyzed by Lundgren [3] on a fully smooth surface in traditional two (inner and outer) layers, and without citation adopted earlier work, namely (i) Firstly, Afzal [4] and Afzal and Yajnik [5] work related to additional terms $1/y_+$ in inner layer log law and Y in outer layer log law. (ii) Secondly, Afzal [6–9] and Afzal and Bush [10] work related to intermediate/meso layer of order $R_\tau^{-1/2}$; (iii) Thirdly, Afzal [11,12] work related to power law velocity profile and its equivalence with log law for large Reynolds numbers (see Ref. [13]) zeroth order. Furthermore, if the mean velocity vector in the work of Afzal [4] is replaced by instantaneous velocity vector, we get the results of Lundgren [3] for instantaneous velocity vector also.

Wei et al. [14] pointed out that the existence and scaling of a third (intermediate, meso) layer was first found by Afzal [6] (see also Ref. [15]). Afzal [6–8,10], in 1982–1985, showed that the intermediate length scale is proportional to the geometric mean of the inner and outer length scales (see also Refs. [12,15]), and Afzal [9], in 1984, showed that the bursting time period scales with intermediate layer time period is proportional to the geometric mean of the inner and outer time scales. Gad-el-Hak's [16] book (Section 5.7.1, Bursting Period, p. 91) published during year 2000 stated the following: "Johansson and Alferdsson (1982) have suggested that the bursting period scale with intermediate scaling proportional to the geometric mean on the inner and outer scales," and earlier Sreenivasan [17] (p. 198), in the monograph edited by Gad-el-Hak during 1989, stated the following: "Mixed scaling consists of the geometric mean on the inner and outer scales has also been proposed Johansson and Alferdsson (1982)." These statements in Gad-el-Hak [16] and Sreenivasan [17] are totally erroneous, which would misguide the research community. This is because Johansson and Alferdsson [18] have neither made any statement about the intermediate (mixed or meso) scaling of bursting time period nor the intermediate (or mixed or meso) length scale. Further, Sreenivasan [19] during 1987 proposed a critical layer (equivalent to the mesolayer/intermediate layer) but has neither cited the mesolayer of Long and Chen [20] nor the intermediate layer of Afzal [6–10]. Procaccia and Sreenivasan [21] while describing the state of the art in hydrodynamic turbulence, past successes and future challenges, cited Sreenivasan and Bershadskii [22] involving mesolayer but completely ignored the pioneering work on mesolayer by Afzal (see Ref. [15]) as well as the power law velocity profile theory of Afzal (reviewed in Ref. [13]).

Zagarola and Smits [23] (Eqs. (42) and (43)), Gad-el-Hak [16] (p. 89, Eqs. (5.29 and 5.30) and Eyink [24] (p. 125101–5) stated the expressions of the Reynolds shear stress and occurrence of the peak value, in a turbulent channel and pipe flows, without citation to the original work of Afzal [6,8] (see also Refs. [25,26]). Metzger et al. [27] also presented the mesolayer approach in mean momentum balance in moderately favorable pressure gradient turbulent boundary layers, but the pertinent work of Afzal [6,25] have not been cited. Thus, it seems that Gad-el-Hak [16], Sreenivasan [17,19,21,22], Lundgren [3], Zagarola and Smits [23], Eynik [34], Metzger et al. [27], Klewicki group (see Ref. [15]), etc. have willfully ignored the primary work of Afzal [6,9] and Afzal and Bush [10], which infringes on to the intellectual property rights on the scientific findings (see also Seena et al. [15]).

The present work deals with the instantaneous turbulent velocity vector and instantaneous temperature on transitional surface roughness based on Navier–Stokes and energy equations for large Reynolds numbers, as the traditional Reynolds equations have been handicapped by the well known closure problem.

2 Momentum Transfer

The instantaneous velocity vector in a boundary layer with pressure turbulent gradient has been considered. The continuity and Navier–Stokes equations are

$$\frac{\partial \mathbf{u}}{\partial t} + \mathbf{u}\cdot\nabla\mathbf{u} = -\frac{1}{\rho}\nabla p + \nu\nabla^2\mathbf{u}, \quad \nabla\cdot\mathbf{u} = 0 \tag{1}$$

Here $\mathbf{u}$ is the instantaneous velocity vector in the direction of space vector $\mathbf{X}$, t is the time, and velocity components (u,v,w) in (x,y,z) directions, p is the static pressure, ρ is the density of fluid, and ν is the molecular kinematic viscosity of the fluid. The outer variables are $\mathbf{U}=\mathbf{u}/U_c$, $P=p/\rho U_c^2$, $X=x/\delta$, $Y=y/\delta$, $Z=z/\delta$, and $\hat{t}=tU_c/\delta$. Here δ is the semidepth of channel, pipe radius, and boundary layer thickness as appropriate, and $\mathbf{i}$ is the unit vector in

Contributed by the Heat Transfer Division of ASME publication in the JOURNAL OF HEAT TRANSFER DIVISION. Manuscript received February 23, 2008; final manuscript received December 16, 2008; published online April 10, 2009. Review conducted by Sai C. Lau.

the x-direction in which U_c is the streamwise velocity at $y=\delta$. The flow parameter is $\epsilon=u_\tau/U_c$ where u_τ is the appropriate friction velocity. The outer layer perturbation velocity gives

$$\mathbf{U} = \mathbf{i} + \epsilon \mathbf{U_0}(X,Y,Z,t_o) \tag{2}$$

$$\frac{\partial \mathbf{U_0}}{\partial t_o} + \mathbf{U_0}\cdot\nabla\mathbf{U_0} = -\nabla P_o + (\phi \mathrm{R}_\phi)^{-1}\nabla^2\mathbf{U_0} \tag{3}$$

where various Reynolds numbers are $\mathrm{R}_\phi=\mathrm{R}_\tau/\phi$, $\mathrm{R}_\tau=u_\tau\delta/\nu$, $\mathrm{Re}_\phi=\mathrm{Re}/\phi$, and $\mathrm{Re}=U_c\delta/\nu$, and $P_o=P-\rho U_o^2/2$. Lundgren [3] adopted a coordinate system frame moving with the freestream with time scale t_o in this frame, where $\mathbf{U_0}=\mathbf{U_0}(X-t_o,Y,Z)$ without explicit dependence on time $t_o=\epsilon\hat{t}$. The external stream frozen due to a slow turnover described by ϵt is negligible compared with the rapid convection. At fixed $\mathbf{X}$ the velocity would be seen as a fluctuating function of time as vortical structures are convected past the observer. The inner variables are $\mathbf{u}_+=\mathbf{u}/u_\tau$, $p_+=p/(\rho u_\tau^2)$, $x_{\phi+}=\mathrm{R}_\phi X$, $y_{\phi+}=\mathrm{R}_\phi Y$, $z_{\phi+}=\mathrm{R}_\phi Z$, and $t_{\phi+}=\hat{t}\epsilon\mathrm{R}_\phi$. The inner variables, the inner velocity vector, and the Navier–Stokes equations become

$$\mathbf{U} = \epsilon\mathbf{u}_+(x_{\phi+},y_{\phi+},z_{\phi+},t_{\phi+}) \tag{4}$$

$$\frac{\partial \mathbf{u}_+}{\partial t_{\phi+}} + \mathbf{u}_+\cdot\nabla_+\mathbf{u}_+ = -\nabla_+ p_+ + \phi^{-1}\nabla_+^2\mathbf{u}_+ \tag{5}$$

Matching by Izakson–Millikan–Kolmogorov (IMK) hypothesis. Between the viscous and the energetic scales in any turbulent flow exists an overlap domain over which the solutions characterizing the flow in the two corresponding limits must match as the Reynolds number tends to infinity. The matching condition for velocity vector in the inner and outer layers, for large Reynolds numbers, yields a functional equation and its derivative as

$$\mathbf{u}_+(x_{\phi+},y_{\phi+},z_{\phi+},t_{\phi+}) = \mathbf{i}U_{c+}(\mathrm{R}_\phi,\cdots) + \mathbf{U_0}(X,Y,Z,t_o) \tag{6}$$

$$y_{\phi+}\frac{\partial \mathbf{u}_+}{\partial y_{\phi+}}(x_{\phi+},y_{\phi+},z_{\phi+},t_{\phi+}) = Y\frac{\partial \mathbf{U_0}}{\partial Y}(X,Y,Z,t_o) = \mathbf{i}\mathrm{R}_\phi\frac{\partial U_{c+}}{\partial \mathrm{R}_\phi}(\mathrm{R}_\phi,\cdots) \tag{7}$$

where $U_{c+}(\mathrm{R}_\phi,\cdots)=\epsilon^{-1}$. The integration of relation (7) along with relation (6) in the x-direction yields the streamwise velocity vector in the inner and outer layers, as well as the skin friction law, as

$$u_+ = A\ln y_{\phi+} + b(x_{\phi+},z_{\phi+},t_{\phi+}) \tag{8a}$$

$$U = 1 + \epsilon[A\ln Y + B(X,Z,t_o)] \tag{8b}$$

$$U_{c+} = A\ln R_\phi + b(x_{\phi+},z_{\phi+},t_{\phi+}) - B(X,Z,t_o) \tag{9}$$

where $A=k^{-1}$. The extension of Izakson–Millikan argument for moderately large Reynolds numbers demanded the order of the higher order effect. However, the domain of validity of the Izakson–Millikan–Kolmogorov hypothesis is not known. Afzal [4] and Afzal and Yajnik [5] postulated that in a fully developed turbulent flow in a pipe or channel, the higher order effect is of order R_ϕ^{-1}. Consequently, the additional term of order $1/y_{\phi+}$ in Eq. (8*a*) and term of order Y in Eq. (8*b*) would arise due to higher order effect as

$$\text{Inner:}\quad u_+ = A\ln y_{\phi+} + b + \sum_{n=1}^{\infty}\frac{b_n}{y_{\phi+}^n} \tag{10}$$

$$\text{Outer:}\quad U = 1 + \epsilon\left(A\ln Y + B + \sum_{n=1}^{\infty}B_nY^n\right) \tag{11}$$

where the parameters $b_n=b_n(x_{\phi+},z_{\phi+},t_{\phi+})$ and $B_n=B_n(X,Z,t_o)$ are functions of order 1. The mesolayer variable is the geometric mean of inner and outer scales (Refs. [6,9]) $\eta=y_{\phi+}/\sqrt{\mathrm{R}_\phi}=Y\sqrt{\mathrm{R}_\phi}$, and the velocity in the mesolayer yields

$$u_+ - \frac{1}{2}U_{c+} = A\ln\eta + \frac{1}{2}(b+B) + \sum_{n=1}^{\infty}\mathrm{R}_\phi^{-n/2}\left(\frac{b_n}{\eta^n} + B_n\eta^n\right) \tag{12}$$

which for mean turbulent flow was first proposed by Afzal and Bush [10], vide Eqs. (22), (24*a*), and (26). The relation (12) in the mixed variables becomes

$$u_+ = A\ln y_{\phi+} + b + \sum_{n=1}^{\infty}\left(\frac{b_n}{y_{\phi+}} + B_bY^n\right) \tag{13}$$

The average velocity $\langle u_+\rangle$ from relation (13) yields

$$\frac{\langle u\rangle}{u_\tau} = A\ln y_{\phi+} + \langle b\rangle + \sum_{n=1}^{\infty}\left(\frac{\langle b_n\rangle}{y_{\phi+}^n} + \langle B_n\rangle Y^n\right) \tag{14a}$$

and the velocity fluctuating part $u_+'=u_+-\langle u_+\rangle$ yields

$$u_+' = b' + \sum_{n=1}^{\infty}\left(\frac{b_n'}{y_{\phi+}^n} + B_n'Y^n\right) \tag{14b}$$

In the mesolayer, the average velocity $\langle u_+\rangle$ yields

$$\frac{\langle u\rangle - 0.5U_c}{u_\tau} = A\ln\eta + \frac{1}{2}(\langle b\rangle + \langle B\rangle) + \sum_{n=1}^{\infty}\mathrm{R}_\phi^{-n/2}\left(\frac{\langle b_n\rangle}{\eta^n} + \langle B_n\rangle\eta^n\right) \tag{15}$$

and the velocity fluctuating part $u_+'=u_+-\langle u_+\rangle$ yields

$$u_+' = b' + \sum_{n=1}^{\infty}\mathrm{R}_\tau^{-n/2}\left(\frac{b_n'}{\eta^n} + B_n'\eta^n\right) \tag{16}$$

The instantaneous velocity normal and transverse components of velocities to lowest order $v_+=V_+=c$ and $w_+=W_+=d$ and higher order effects yield

$$v_+ = c + \sum_{n=1}^{\infty}\left(\frac{c_n}{y_{\phi+}^n} + C_nY^n\right),\quad w_+ = d + \sum_{n=1}^{\infty}\left(\frac{d_n}{y_{\phi+}^n} + D_nY^n\right) \tag{17}$$

The mean and turbulence intensities in normal and transverse components $v_+'=v_+-\langle v_+\rangle$ and $w_+'=w_+-\langle w_+\rangle$ yield

$$\langle v_+\rangle = \langle c\rangle + \sum_{n=1}^{\infty}\left(\frac{\langle c_n\rangle}{y_{\phi+}^n} + \langle C_n\rangle Y^n\right),\quad \langle w_+\rangle = \langle d\rangle + \sum_{n=1}^{\infty}\left(\frac{\langle d_n\rangle}{y_{\phi+}^n} + \langle D_n\rangle Y^n\right) \tag{18}$$

$$v_+' = c' + \sum_{n=1}^{\infty}\left(\frac{c_n'}{y_{\phi+}^n} + C_n'Y^n\right) \tag{19a}$$

$$w_+' = d' + \sum_{n=1}^{\infty}\left(\frac{d_n'}{y_{\phi+}} + D_n'Y^n\right) \tag{19b}$$

In terms of mesolayer variables, we get

$$v_+' = c' + \sum_{n=1}^{\infty}\mathrm{R}_\phi^{-n/2}\left(\frac{c_n'}{\eta^n} + C_n'\eta^n\right),\quad w_+' = d' + \sum_{n=1}^{\infty}\mathrm{R}_\phi^{-n/2}\left(\frac{d_n'}{\eta^n} + D_n'\eta^n\right) \tag{20}$$

The zeroth order terms in Eq. (15) for u_+' the velocity fluctuation has a peak value u_{p+}' at location η_{pu} are

$$\eta_{\rm pu}=\left(\frac{b_1'}{B_1'}\right)^{1/2},\quad u_{p+}'=b'+2(b_1'B_1')^{1/2}{\rm R}_\phi^{-1/2} \tag{21}$$

along with analogous expressions from Eq. (19). The Reynolds shear stress becomes

$$\langle u'v'\rangle_+=\left\langle\left[b'+\sum_{n=1}^{\infty}(b_n'y_{\phi+}^{-n}+B_n'Y^n)\right]\left[c'+\sum_{n=1}^{\infty}(c_n'y_{\phi+}^{-n}+C_n'Y^n)\right]\right\rangle \tag{22}$$

The implications of terms $1/y_{\phi+}$ and Y on mean velocity, Eq. (15), have considered for smooth wall ($\phi=1$, $y_{\phi+}=y_+$) by several works. Afzal and Bush [10], by using the eddy viscosity closure model of Bush and Fendell [28], showed $A=2.5$, $\langle b\rangle=5$, $\langle b_1\rangle=1/k^2$, and $\langle B_1\rangle=-1/k$. Buschmann and Gad-el-Hak [13] for boundary layer experimental data predicted Reynolds number dependence on constants A, $\langle b\rangle$, $\langle b_1\rangle$, and $\langle B_1\rangle$. Lundgren [3] for mean velocity $\langle u\rangle$ adopted the constants $A=2.5$, $\langle b\rangle=5$, $\langle b_1\rangle=20$, $\langle b_2\rangle=-300$, and $\langle B_1\rangle=1$, for velocity fluctuation u_+' adopted $b_1'/b'=15$, $b_1'/b'=-150$, and $B_1'/b'=-1$, and for v_+' (Eq. (19*a*)) adopted $c_1'/c'=-4$ and $C_1'/c'=-1/4$. The lower roughness Reynolds number effects are of order ${\rm R}_\phi^{-1}$ and are described by the relations $A=\Sigma_{r=0}^{\infty}A_r{\rm R}_\phi^{-r}$, $b=\Sigma_{r=0}^{\infty}b_r{\rm R}_\phi^{-r},\ldots$, and $B_n=\Sigma_{r=0}^{\infty}B_{r,n}{\rm R}_\phi^{-r},\ldots$, provided the corresponding zeroth order constants, respectively, are A_0, $b_0,\ldots$, and $B_{0,1},\ldots$.

3 Convective Heat Transfer

The heat transfer equation [25,26] is

$$\frac{\partial T}{\partial t}+\mathbf{u}\cdot\nabla T=\nu\sigma^{-1}\nabla^2T \tag{23}$$

where T is the temperature distribution and σ is the molecular Prandtl number. The inner and outer expansions for σ of order unity are as follows.

For the inner wall layer,

$$T=T_w+T_\tau T_+(x_{\phi+},y_{\phi+},z_{\phi+},t_{\phi+},\sigma) \tag{24a}$$

$$\frac{\partial T_+}{\partial t_{\phi+}}+\mathbf{u}_+\cdot\nabla T_+=(\phi\sigma{\rm R}_\phi)^{-1}\nabla^2T_+ \tag{24b}$$

For the outer defect layer,

$$T=T_c+T_\tau T_o(X,Y,Z,T_o) \tag{25a}$$

$$\frac{\partial \mathbf{T_o}}{\partial t_o}+\mathbf{U_o}\cdot\nabla\mathbf{T_o}=(\phi\sigma{\rm R}_\phi)^{-1}\nabla^2\mathbf{T_o} \tag{25b}$$

where $T_\tau=q_w/(\rho C_pu_\tau)$ is the friction temperature. The matching of two layers in the overlap region for large Reynolds numbers ${\rm R}_\phi\to\infty$ through Izakson–Millikan–Kolmogorov hypotheses, giving the functional equations for velocity and temperature profiles as described below:

$$T_+(x_{\phi+},y_{\phi+},z_{\phi+},t_{\phi+},\sigma)=T_{c+}({\rm R}_\phi,\sigma,\cdots)+T_o(X\,.\,Y,Z,t_o) \tag{26}$$

$$y_{\phi+}\frac{dT_+}{dy_{\phi+}}=Y\frac{dT_o}{dY}={\rm R}_\phi\frac{dT_{c+}}{d{\rm R}_\phi} \tag{27}$$

where $T_{c+}({\rm R}_\phi,\sigma,\ldots)=(T_c-T_w)/T_\tau$. The temperature profile in the inner and outer layers and heat transfer law become

$$\frac{T-T_w}{T_\tau}=A_t\ln y_{\phi+}+b_t(x_{\phi+},z_{\phi+},t_{\phi+},\sigma) \tag{28a}$$

$$\frac{T-T_c}{T_\tau}=A_t\ln Y+B_t(X,Z,t_o) \tag{28b}$$

$$\frac{T_c-T_w}{T_\tau}=A_t\ln R_\phi+b_t(x_{\phi+},z_{\phi+},t_{\phi+},\sigma)-B_t(X,Z,t_o) \tag{29}$$

where $A_t=k_t^{-1}$. Afzal [4] postulated that in a fully developed turbulent flow in a pipe or channel, the higher order effect is of the order ${\rm R}_\phi^{-1}$. Consequently, the additional terms of order $1/y_{\phi+}$ in Eq. (28*a*) and of order Y in Eq. (28*b*) arise due to a higher order effect of order ${\rm R}_\phi^{-1}$. Following the momentum analysis, the inner and outer layer relations become

$$\frac{T-T_w}{T_\tau}=A_t\ln y_{\phi+}+b_t+\sum_{n=1}^{\infty}\frac{b_{tn}}{y_{\phi+}^n} \tag{30}$$

$$\frac{T-T_c}{T_\tau}=A_t\ln Y+B_t+\sum_{n=1}^{\infty}B_{tn}Y^n \tag{31}$$

In the mesolayer variable η, the temperature profile becomes (Ref. [25])

$$\frac{T-T_m}{T_\tau}=A_t\ln\eta+\frac{1}{2}(b_t+B_t)+\sum_{n=1}^{\infty}{\rm R}_\phi^{-n/2}\left(\frac{b_{tn}}{\eta^n}+B_{tn}\eta^n\right) \tag{32}$$

where thermal mesolayer length scale is $\eta=y_{\phi+}/\sqrt{{\rm R}_\phi}=Y\sqrt{{\rm R}_\phi}$ for molecular Prandtl σ of order unity, and $T_m=(T_c+T_w)/2$ is the scale of mesolayer temperature [25]. This thermal mesolayer scale, even for fully smooth surface ($\phi=1$, $\eta=y_+/\sqrt{{\rm R}_\tau}$, ${\rm R}_\phi={\rm R}_\tau$), differs from the proposal of Wei et al. [29], which has not cited the momentum mesolayer proposed by Afzal [6–10,15]. The temperature distribution, Eq. (32), in mixed variables may also be expressed as

$$\frac{T-T_w}{T_\tau}=A_t\ln y_{\phi+}+\sum_{n=1}^{\infty}\left(\frac{b_{tn}}{y_{\phi+}^n}+B_{tn}Y^n\right) \tag{33}$$

The average velocity $\langle T_+\rangle$ and fluctuating temperature $t_+'=T_+-\langle T_+\rangle$ yield

$$\frac{T-T_w}{T_\tau}=A_t\ln y_{\phi+}+\langle B_t\rangle+\sum_{n=1}^{\infty}\left(\frac{\langle B_{tn}\rangle}{y_{\phi+}^n}+\langle D_{tn}\rangle Y^n\right) \tag{34}$$

$$t_+'=b_t'+\sum_{n=1}^{\infty}\left(\frac{b_{tn}'}{y_{\phi+}^n}+B_{tn}'Y^n\right) \tag{35}$$

In the mesolayer, the temperature profile $\langle T_+\rangle$ yields

$$\langle T_+\rangle-0.5T_{m+}=A_t\ln\eta+\frac{1}{2}(\langle b_t\rangle+\langle B_t\rangle)+\sum_{n=1}^{\infty}{\rm R}_\phi^{-n/2}\left(\frac{\langle b_{tn}\rangle}{\eta^n}+\langle B_{tn}\rangle\eta^n\right) \tag{36}$$

and the velocity fluctuating part $t_+'=T_+-\langle T_+\rangle$ yields

$$t_+'=b_t'+\sum_{n=1}^{\infty}{\rm R}_\phi^{-n/2}\left(\frac{b_{tn}'}{\eta^n}+B_{tn}'\eta^n\right) \tag{37}$$

The lowest order temperature fluctuation peak value t_{p+}' at location $\eta_{\rm tp}$ from Eq. (37) yields

$$\eta_{\rm tp}=\left(\frac{b_{t1}'}{B_{t1}'}\right)^{1/2},\quad t_{p+}'=b_t'+2(b_{t1}'B_{t1}')^{1/2}{\rm R}_\phi^{-1/2} \tag{38}$$

The proposed equilibrium relations for mean velocity $\langle T_+\rangle-T_{m+}=f_t(\eta)$ where $T_m=(T_w+T_\infty)/2$ and velocity fluctuation $(t_+'-t_{p+}'){\rm R}_\phi^{1/2}=t_{m+}'(\eta)$ in the mesolayer are tested later from the DNS data. The Reynolds heat flux becomes

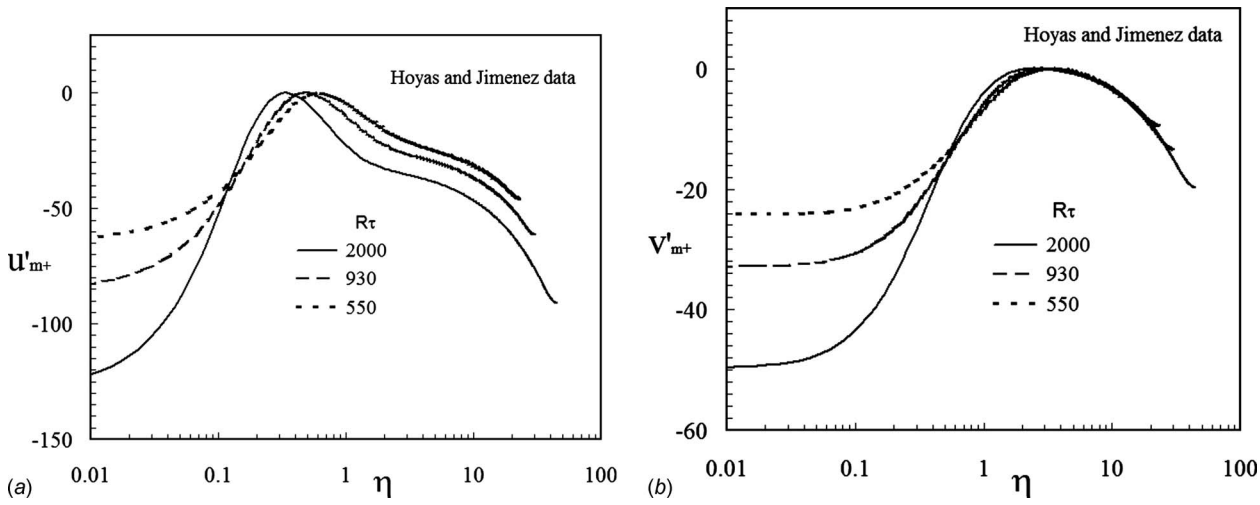

Fig. 1 Velocity fluctuations (u'_{m+}, v'_{m+}) versus η in the mesolayer from DNS data of Hoyas and Jimenez [30]

$$\langle v't'\rangle_+ = \left\langle \left[b'_t + \sum_{n=1}^{\infty} (b'_{tn} y_{\phi+}^{-n} + B'_{tn} Y^n) \right] \left[c' + \sum_{n=1}^{\infty} (c'_n y_{\phi+}^{-n} + C'_n Y^n) \right] \right\rangle \tag{39}$$

The low Reynolds number effects are of order R_ϕ^{-1} and are described by the relations $A_t = \Sigma_{r=0}^{\infty} A_{\mathrm{tr}}\ R_\phi^{-r}$, $b_t = \Sigma_{r=0}^{\infty} b_{\mathrm{tr}}\ R_\phi^{-r}, \cdots$, and $B_{\mathrm{tn}} = \Sigma_{r=0}^{\infty} B_{\mathrm{tr},n}\ R_\phi^{-r}, \cdots$ provided the corresponding zeroth order constants, respectively, are A_{t0}, $b_{t0}, \ldots$, and $B_{t0,1}, \ldots$.

4 Results and Discussion

The velocity fluctuations vector on fully smooth surface ($\phi = 1$, $R_\phi = R_\tau$) has been analyzed in terms of the mesolayer variables $u'_{m+} = (u'_+ - u'_{p+}) R_\tau^{1/2}$, $v'_{m+} = (v'_+ - v'_{p+}) R_\tau^{1/2}$, $w'_{m+} = (w'_+ - w'_{p+}) R_\tau^{1/2}$, where u'_{p+}, v'_{p+}, and w'_{p+} are the peak values. The velocity fluctuation vector in the mesolayer u'_{m+} and v'_{m+} versus η are shown in Figs. 1(*a*) and 1(*b*) from fully smooth channel DNS data of Hoyas and Jimenez [30] for $R_\tau = 2000$, 980, and 550. The figures show the similarity of the data in the mesolayer. Morrison et al. [31] proposed that a maximum of $\langle u'^2_+ \rangle$ occurs at $\eta_{\mathrm{mu}+} = y_{\mathrm{mu}+}/R_\tau^{1/2} = 1.8\ R_\tau^{0.02}$, which weakly depends on the Reynolds number. The mesolayer velocity w'_{m+} and temperature t'_+ versus η, not displayed here, also show the similarity from data of Hoyas and Jimenez [30] and Abe et al. [32] in the mesolayer.

In the mesolayer, the half-velocity defect law for mean velocity profile has logarithmic region as shown in Figs. 1–3 of Ref. [25] for fully smooth channel DNS data of Hoyas and Jimenez, Abe et al., and Iwamoto et al. The expression in Eq. (22) for Reynolds shear stress has to be simplified for fully developed turbulent pipe and channel flows. Alternately, we consider Reynolds mean momentum equation [4–6] in a fully developed turbulent pipe or channel flow,

$$\phi^{-1} \frac{\partial}{dy_{\phi+}} d\langle u\rangle + \tau_+ = 1 - R_\phi^{-1} y_{\phi+} \tag{40}$$

where $\tau = -\rho\langle u'v'\rangle$ is the appropriate Reynolds shear stress. The Reynolds shear stress is estimated from the momentum Reynolds equation, by using the lowest order velocity distribution (8*a*) in the mesolayer yields

$$\tau_+ = 1 - R_\phi^{-1/2}\left(\frac{1}{\phi k \eta} + \eta\right), \quad \tau_+ = 1 - \frac{1}{\phi k y_{\phi+}} - Y \tag{41}$$

The general expression for Reynolds shear stress distribution (40) may be obtained from Reynolds equation and velocity distribution in Eq. (14*a*). The Reynolds shear stress peak location $y_{\phi+m}$ and peak value τ_{+m} have been estimated. The first order result predictions $y_{\phi+m} = (R_\phi/k\phi)^{1/2}$ and $\tau_{+m} = 1 - 2(k\phi R_\phi)^{-1/2}$ for a fully smooth channel ($\phi = 1$, $y_{\phi+m} = y_{+m}$) have been presented in Figs. 4(a) and 4(b) of Ref. [25] and the higher order prediction by Afzal and Bush [10]. The constants in the third order predictions of y_{+m} and τ_{+m} for a fully smooth channel and pipe have been estimated from DNS and experimental data, which yields

$$y_{+m} = 1.58\ R_\tau^{1/2} + 6 + 48\ R_\tau^{-1/2} + O(R_\tau^{-1}) \tag{42}$$

$$\tau_{+m} = 1 - [3.16\ R_\tau^{-1/2} + 5\ R_\tau^{-1} + 62\ R_\tau^{-3/2} + O(R_\tau^{-2})] \tag{43}$$

The first, second, and third order effects based on higher order log law velocity profile perturbations are shown in Figs. 2(*a*) and 2(*b*). The third order predictions (Eqs. (42) and (43)) compare very well with the extensive DNS and experimental data in turbulent pipe and channel flows. The higher order theory of Afzal [4] was extended by Buschmann and Gad-el-Hak [33,34] for nonzero offset velocity (proposed by Squire [35]) for estimation of third order effects for location and peak value of Reynolds shear stress. Their higher order velocity profile prediction [33,34] for non-zero origin offset does not obey the Prandtl transposition theorem, and thus is not a rational solution (see Afzal [36]). Further, Gad-el-Hak [16], Buschmann and Gad-el-Hak [33,34], Klewicki et al. [37–40], Morris et al. [41], Faraz et al. [42], Priyadarshana et al. [43], Phuong and Papavassiliou [44] and others mentioned in Ref. [15] have not cited the pioneering primary work of Afzal [6–9] and Afzal and Bush [10] in the mesolayer.

In the mesolayer, the half-temperature defect law for mean temperature profile shows logarithmic behavior, which is supported by DNS data of channel of Abe et al. [32] and shown in Fig. 6 of Ref. [23]. Reynolds heat flux expression (39) has to be simplified for fully developed turbulent pipe and channel flows. Alternately, we consider thermal Reynolds mean energy equation [25] in a fully developed turbulent pipe or channel flow

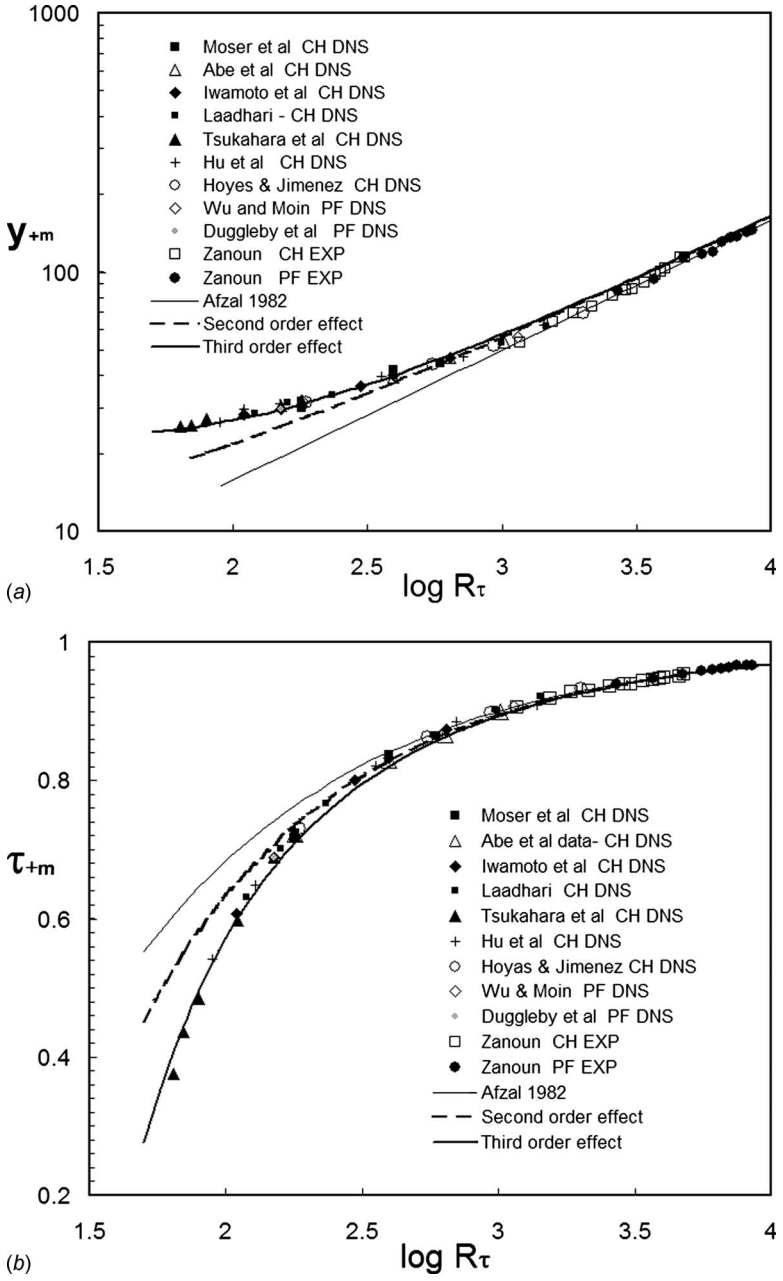

Fig. 2 Comparison of the Reynolds shear stress peak location y_{+m} and peak value τ_{+m} with the DNS and experimental data for fully developed flow in a fully smooth channel and pipe. The first, second, and third order predictions based on higher order logarithmic law velocity profile.

$$(\phi\sigma)^{-1}\frac{d}{dy_{\phi+}}(\langle T+\rangle - T_{w+}) + \tau_{t+} = 1 - \mathrm{R}_{\phi}^{-1}\frac{u_\tau}{U_b}\int_0^{y_+}(\langle T_+\rangle - T_{w+})dy_{\phi+} \tag{44}$$

where $\tau_t = -\rho c_p\langle v't'\rangle$ is the appropriate thermal Reynolds heat flux, U_b is depth averaged mean velocity. The thermal Reynolds heat flux has been estimated from mean energy (Eq. (44)) by using the lowest order temperature distribution (28) in the meso-layer yields

$$\tau_{t+} = 1 - \mathrm{R}_{\phi}^{-1/2}\left(\frac{A_t}{\sigma\phi\eta} + \frac{U_c}{2U_b}\eta\right), \quad \tau_{t+} = 1 - \frac{A_t}{\sigma\phi y_{\phi+}} - \frac{U_c}{2U_b}Y \tag{45}$$

The general expression for thermal Reynolds heat flux may be obtained from thermal Reynolds (Eq. (44)) and mean temperature distribution (36). The Reynolds heat flux peak location y_{t+m} and peak value τ_{t+m} from the first order predictions (Eq. (45)) yield

$$y_{t\phi+m} = \left(\frac{2U_b}{U_c}\frac{\mathrm{R}_\phi}{\sigma\phi k_t}\right)^{1/2} \tag{46a}$$

$$\tau_{t+m} = 1 - \left(\frac{2U_c}{U_b}\right)^{1/2}(k_t\sigma\phi\ \mathrm{R}_\phi)^{-1/2} \tag{46b}$$

have been compared for a fully smooth channel ($\phi=1$, $y_{t\phi+m}=y_{t+m}$) data in Figs. 7(a) and 7(b) of Ref. [26]. The constants in the third order predictions have been estimated from fully smooth channel ($\phi=1$, $y_{\phi+m}=y_{+m}$) DNS data of Abe et al. [32] for $\sigma=0.71$, which yield

$$y_{t+m} = 1.88\ \mathrm{R}_\tau^{1/2} + 7.1 + 59\ \mathrm{R}_\tau^{-1/2} + O(\mathrm{R}_\tau^{-1}) \tag{47}$$

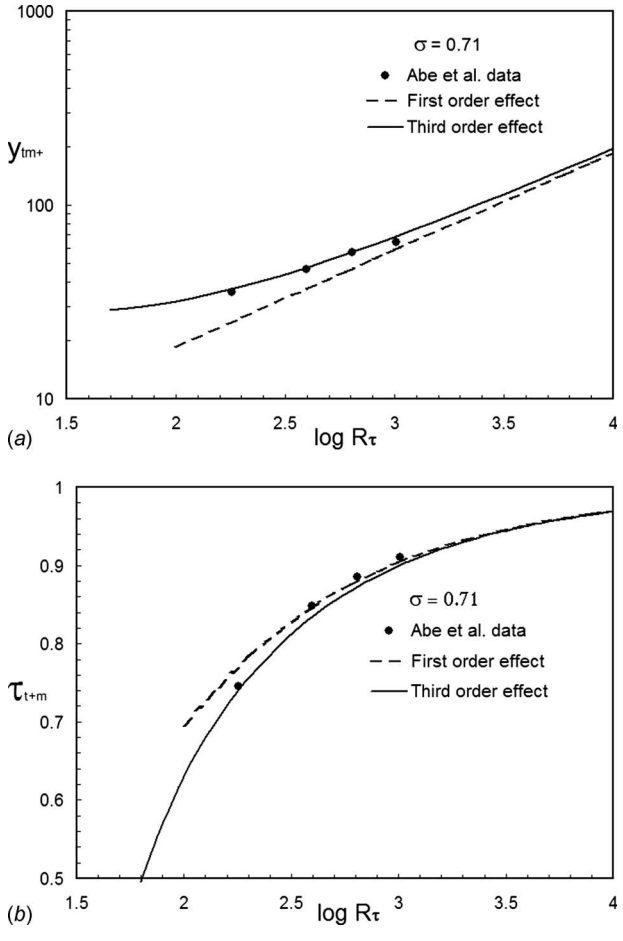

Fig. 3 Comparison of the thermal Reynolds heat flux peak location y_{t+m} and peak value τ_{t+m} with the DNS data of Abe et al. [32] for molecular Prandtl number $\sigma=0.71$ for fully developed flow in a fully smooth channel and pipe. The first and third order predictions based on higher order logarithmic law for temperature profile.

$$\tau_{t+m} = 1 - [3.05\ \mathrm{R}_\tau^{-1/2} + 5\ \mathrm{R}_\tau^{-1} + 33.2\ \mathrm{R}_\tau^{-3/2} + O(\mathrm{R}_\tau^{-2})] \quad (48)$$

The first and the third order results for log law for temperature profile theory are also shown in Figs. 3(*a*) and 3(*b*). The predictions in Eqs. (47) and (48) compare well with the DNS data of Abe et al. [32] in turbulent channel flows.

The matching of the two layers in the overlap region by the application of Izakson–Millikan–Kolmogorov hypothesis in addition of log law also leads to power law velocity profile [11,12,26]. A good review of the power law velocity for mean turbulent flow has been presented for fully smooth surfaces by Buschmann and Gad-el-Hak [13], and for transitional rough surfaces of the power law velocity and temperature profiles by Seena and Afzal [26].

Acknowledgment

N.A. is grateful for the support of All India Council of Technical Education, New Delhi.

References

[1] Robinson, S. K., 1986, "Instantaneous Velocity Profile Measurements in a Turbulent Boundary Layer," Chem. Eng. Commun., **43**, pp. 347–369.
[2] Nakayama, A., Noda, H., and Maeda, K., 2004, "Similarity of Instantaneous and Filtered Velocity in the Near Wall Region of Zero Pressure Gradient Boundary Layer," Fluid Dyn. Res., **35**, pp. 299–321.
[3] Lundgren, T. S., 2007, "Asymptotic Analysis of the Constant Pressure Turbulent Boundary Layer," Phys. Fluids, **19**, p. 055105.
[4] Afzal, N., 1976, "Millikan Argument at Moderately Large Reynolds Numbers," Phys. Fluids, **19**, pp. 600–602.
[5] Afzal, N., and Yajnik, K., 1973, "Analysis of Turbulent Pipe and Channel Flows at Moderately Large Reynolds Number," J. Fluid Mech., **57**, pp 23–32.
[6] Afzal, N., 1982, "Fully Developed Turbulent Flow in a Pipe: An Intermediate Layer," Ing.-Arch., **53**, pp. 355–377.
[7] Afzal, N., 1982, "A Sub-Boundary Layer With a Two Dimensional Turbulent Boundary Layer," J. Mec. Theor. Appl., **1**, pp. 963–973.
[8] Afzal, N., 1984, "The Mesolayer Theory of Turbulent Flows," AIAA J., **22**, pp. 437–439.
[9] Afzal, N., 1984, "Period Between Bursting in Turbulent Shear Flow: Intermediate Scaling," Curr. Sci., **53**(12), pp. 640–642.
[10] Afzal, N. and Bush, W. B., 1985, "A Three Layer Asymptotic Analysis of Turbulent Channel Flows," Proc. Indian Acad. Sci., Math. Sci., **94**, pp. 135–148.
[11] Afzal, N., 2005, "Analysis of Power Law and Log Law Velocity Profiles in Overlap Region of a Turbulent Wall Jet," Proc. R. Soc. London, Ser. A, **461**, pp, 1889–1910.
[12] Afzal, N., Seena, A., and Bushra, A., 2006, "Power Law Turbulent Velocity Profile in Transitional Rough Pipes," ASME Trans. J. Fluids Eng., **128**, pp. 548–558.
[13] Buschmann, M. H., and Gad-el-Hak, M., 2006, "Recent Developments in Scaling of Wall-Bounded Flows," Prog. Aerosp. Sci., **42**, pp. 419–467.
[14] Wei, T., Fife, P., Klewicki, J., and McMurtry, P., 2005, "Properties of the Mean Momentum Balance in Turbulent Boundary Layer, Pipe and Channel Flows," J. Fluid Mech., **522**, pp. 303–327.
[15] Seena, A., Bushra, A. and Afzal, N., 2008, "Logarithmic Expansions for Reynolds Shear Stress and Reynolds Heat Flux in a Turbulent Channel Flow," ASME J. Heat Transfer, **130**, p. 094501.
[16] Gad-el-Hak, M., 2000, *Flow Control*, Cambridge University Press, Cambridge.
[17] Sreenivasan, K. R., 1989, "The Turbulent Boundary Layer," *Frontiers in Experimental Fluid Mechanics* (Lecture Notes in Engineering Vol. 46), M. Gad-el-Hak ed., Springer-Verlag, Berlin, pp. 159–209.
[18] Johansson, A. V., and Alferdsson, P. H., 1982, "On the Structure of Turbulent Channel Flow," J. Fluid Mech., **122**, pp. 295–314.
[19] Sreenivasan, K. R., 1987, "A Unified View of the Origin and Morphology of the Turbulent Boundary Layer Structure," *Turbulence Management and Relaminarisation, IUTAM Symposium*, Bangalore, H. W. Liepmann and R. Narasimha, eds., Springer-Verlag, Berlin, pp. 37–66.
[20] Long, R. R., and Chen, T. C., 1981, "Experimental Evidence of the Existence of the Mesolayer in Turbulent Systems," J. Fluid Mech., **105**, pp. 19–59.
[21] Procaccia, I., and Sreenivasan, K. R., 2008, "The State of the Art in Hydrodynamic Turbulence: Past Successes and Future Challenges," Physica D, **237**, pp. 2167–2183.
[22] Sreenivasan, K. R., and Bershadskii, A., 2006, "Finite-Reynolds-Number Effects in Turbulence Using Logarithmic Expansions," J. Fluid Mech., **554**, pp. 477–498.
[23] Zagarola, M. V., and Smits, A. J., 1998, "Mean-Flow Scaling of Turbulent Pipe Flow," J. Fluid Mech., **373**, pp. 33–79.
[24] Eyink, G.L., 2008, "Turbulent Flow in Pipes and Channels as Cross-Stream "Inverse Cascades" of Vorticity," Phys. Fluids, **20**, p. 125101.
[25] Seena, A., and Afzal, N., 2008, "Intermediate Scaling of Turbulent Momentum and Heat Transfer in a Transitional Rough Channel," ASME J. Heat Transfer, **130**, p. 031701.
[26] Seena, A. and Afzal, N., 2008, "Power Law Velocity and Temperature Profiles in a Turbulent Channel Flow, "ASME J. Heat Transfer, **130**, p. 091701.
[27] Metzger, M., Lyons, A., and Fife, P., 2008, "Mean Momentum Balance in Moderately Favourable Pressure Gradient Turbulent Boundary Layers," J. Fluid Mech., **617**, pp. 107–140.
[28] Bush, W. B., and Fendell, F. E., 1972, "Asymptotic Analysis of Turbulent Channel and Boundary Layer Flows," J. Fluid Mech., **56**, pp. 657–681.
[29] Wei, T., Fife, P., Klewicki, J., and McMurtry, P., 2005, "Scaling Heat Transfer in Fully Developed Turbulent Channel Flows," Int. J. Heat Mass Transfer, **48**, pp. 5284–5296.
[30] Hoyas, S., and Jimenez, J., 2006, "Scaling of the Velocity Fluctuations in Turbulent Channels up to Re=2003," Phys. Fluids, **18**, p. 011702.
[31] Morrison, J. F., McKeon, B. J., Jiang, W., and Smits, A. J., 2004, "Scaling of the Streamwise Velocity Component in Turbulent Pipe Flow," J. Fluid Mech., **508**, pp. 99–131.
[32] Abe, H., Kawamura, H., and Matsuo, Y., 2004, "Surface Heat-Flux Fluctuations in a Turbulent Channel Up to R_τ=1020 With Pr=0.025 and 0.71," Int. J. Heat Fluid Flow, **25**, pp. 404–419.
[33] Buschmann, M. H., and Gad-el-Hak, M., 2009, "Evidence of Non-Logarithmic Behavior of Turbulent Channel and Pipe Flow," AIAA J., **47**(3), pp. 535–541.
[34] Buschmann, M. H., and Gad-el-Hak, M., 2008, "Recent Developments in Scaling of Wall-Bounded Flows," Fifth AIAA Theoretical Fluid Mechanics Conference, Seattle, WA, June 23–28, AIAA Paper No. 2008–4238.
[35] Squire, H., 1948, "Reconsideration of the Theory of Free Turbulence," Philos. Mag., **39**(288), pp. 1–20.
[36] Afzal, N. , 2009, "Comment on "Evidence of Non-Logarithmic Behavior of Turbulent Channel and Pipe Flow" [AIAA Journal, 47, pp. 535–541 (2009)]," to be published.
[37] Klewicki, J. C., 2006, "Mean Momentum Balance: Implications for Turbulence Control," NUS-IMS Workshop on Transition and Turbulence Control, Vol. 8, Lecture Note Series, National University of Singapore, Singapore, pp. 283–396.
[38] Klewicki, J. C., and Moffit, J. L., 2007, "Measurement Considerations in Wall-Bounded Turbulent Flows: Wall Shear Stress," *Handbook of Fluid Mechanics*,

C. Tropea and J. Foss, eds., Springer-Verlag.
[39] Klewicki, J. C., and Fife, P., 2007, "On Discerning Dynamical Structure From the Once-Integrated Momentum Equation," 16th Australasian Fluid Mechanics Conference Crown Plaza, Gold Coast Australia, December 2–7, pp. 159–162.
[40] Klewicki, J., Priyadarshana, P. J. A., and Metzger, M. M., 2008, "Statistical Structure of the Fluctuating Wall Pressure and its In-Plane Gradients at High Reynolds Number," J. Fluid Mech., **609**, pp. 195–220.
[41] Morris, S. C., Stolpa, S. R., Slaboch, P. E., and Klewicki, J., 2007, "Near Surface Particle Image Velocimetry Measurements in a Transitionally Rough-Wall Atmospheric Boundary Layer," J. Fluid Mech., **580**, pp. 319–338.
[42] Mehdi, F., Klewicki, J. C., and White, C., 2008, "Refined Analysis of the Mean Momentum Balance in Rough-Wall Turbulent Boundary Layers," 61st Annual Meeting of the American Physical Society, Division of Fluid Dynamics meeting, November 23, 2008, San Antonio Texas.
[43] Priyadarshana, P. J. A., Klewicki, J.Treat, S., and Foss, J., 2007, "Statistical Structure of Turbulent-Boundary Layer Velocity-Vorticity Products at High and Low Reynolds Numbers," J. Fluid Mech., **570**, pp. 307–346.
[44] Phuong, M. L, and Papavassiliou, D. V., 2008, "On the Scaling of Heat Transfer Using Thermal Flux Gradients for Fully Developed Turbulent Channel and Couette Flows," Int. Commun. Heat Mass Transfer, **35**, pp. 404–412.

Closed Form Solutions For Mixed Convection With Magnetohydrodynamic Effect in a Vertical Porous Annulus Surrounding an Electric Cable

A. Barletta
e-mail: antonio.barletta@mail.ing.unibo.it

E. Magyari[1]
e-mail: magyari@bluewin.ch

S. Lazzari
e-mail: stefano.lazzari@mail.ing.unibo.it

Dipartimento di Ingegneria Energetica, Nucleare e del Controllo Ambientale (DIENCA),
Università di Bologna,
Via dei Colli 16,
I-40136 Bologna, Italy

I. Pop
Faculty of Mathematics,
University of Cluj,
R-3400 Cluj,
CP 253, Romania
e-mail: pop.ioan@yahoo.co.uk

Mixed convection Darcy flow in a vertical porous annulus around a straight electric cable is investigated. It is assumed that the flow is fully developed and parallel. Moreover, the Boussinesq approximation is used. The magnetic field with a steady electric current in the cable is radially varying according to the Biot–Savart law. Two flow regimes are investigated. The first is mixed convection with negligible effects of internal heat generation due to Joule heating and viscous dissipation. The second is forced convection with important effects of heat generation. In these two special cases, closed form expressions of the velocity profile and of the temperature profile, as well as of the flow rate and the Nusselt number, are obtained. The main features of these solutions are discussed.
[DOI: 10.1115/1.3085874]

Keywords: porous media, mixed convection, viscous dissipation, magnetohydrodynamics, analytical solution

1 Introduction

Natural and mixed convection flows in fluid saturated porous materials in the presence of an external magnetic field have been widely studied in the past years [1–11]. The technical interest of these investigations is very high both in the field of heat transfer and for electric engineering. Possible applications of these flow analyses are, for instance, in the thermal control of buried electric cables in cases where an electrically conducting fluid such as salt water is present in the soil. As it has been pointed out by Chamkha [3], other applications are in the design and flow control of magnetohydrodynamic (MHD) generators. The description of the modeling of MHD flows in porous media as well as a complete bibliography on this subject can be found in the book and paper by Nield and co-worker [12,1] and by Geindreau and Auriault [4]. Beyond the technical relevance, mixed convection in porous media in the presence of MHD effects deserves a special physical interest with respect to the analysis of the interaction between buoyancy force and magnetic force and their effects on fluid flow.

Al–Nimr and Hader [2] considered the fundamental solutions of the linear mixed convection problem in a vertical parallel plane channel filled with a fluid saturated porous medium and subject to an external transverse magnetic field. These authors analyzed the case of negligible effects of viscous dissipation and Joule heating in the fluid. The same heat transfer regime, i.e., negligible internal heat generation effects, has been investigated in the papers by Mahmud and Fraser [5], Postelnicu [6], Partha et al. [7], Rakoto Ramambason and Vasseur [8], Bhadauria [9,10]. On the other hand, viscous dissipation and Joule heating effects have been taken into account by Chamkha [3] and by Makinde and Sibanda [11]. Some of these papers present investigations of buoyant flows about a vertical surface [6,7,11]. Other authors have investigated natural convection heat transfer in cavities [5,8–10]. Chamkha [3] studied the effect of variable fluid properties for the flow with constant pressure gradient in a horizontal channel under the assumption of negligible buoyancy forces.

The aim of the present paper is to study mixed convection in a vertical porous annulus surrounding an electric cable carrying a stationary electric current. The main objective is to show that, in two special cases, closed form expressions of the velocity and temperature fields, as well as of the Nusselt number and the average velocity, exist. The two special cases are that of negligible heat generation effects and that of negligible buoyancy (forced convection). The study will be performed by assuming the validity of Darcy's law and of the Boussinesq approximation.

2 Governing Equations

Let us consider mixed convection flow in a fluid saturated vertical porous annulus surrounding a very long straight cable with radius R_1 carrying a constant electric current I (see Fig. 1). The following assumptions are made:

- The flow is steady, laminar, parallel, and fully developed.
- Darcy's law and the Boussinesq approximation hold.
- The cable is electrically insulated.
- The magnetic field created by the current I is not appreciably modified by the feedback field induced by the fluid flow in the porous medium (magnetic Reynolds number is small).
- The fluid is an electrically conducting liquid supposed to be practically opaque to thermal radiation.

On account of these assumptions, Biot–Savart law implies that the magnetic field $\mathbf{B}$ is given by

$$\mathbf{B} = B_0 \frac{R_1}{R} \hat{\mathbf{e}}_\theta, \quad B_0 = \frac{\mu_0 I}{2\pi R_1} \tag{1}$$

Moreover, the seepage velocity can be expressed as $\mathbf{U} = U\hat{\mathbf{e}}_Z$. Then, the mass balance equation requires $\mathbf{U}$ to be solenoidal, so that $U = U(R)$, while the momentum balance in the Z, R, and θ directions yields

$$\frac{\eta}{K} U = -\frac{\sigma B_0^2}{\phi} \frac{R_1^2}{R^2} U + \rho\beta g (T - T_{\text{ref}}) - \frac{\partial P}{\partial Z} \tag{2}$$

$$\frac{\partial P}{\partial R} = 0, \quad \frac{\partial P}{\partial \theta} = 0 \tag{3}$$

where the hydrodynamic pressure $P = p + \rho g Z$ is the difference between the pressure p and the hydrostatic pressure $-\rho g Z$. Equation

[1]On leave from Institute of Building Technology, ETH–Zürich, Switzerland.

Manuscript received February 27, 2008; final manuscript received December 3, 2008; published online April 10, 2009. Review conducted by Jamal Seyed-Yagoobi.

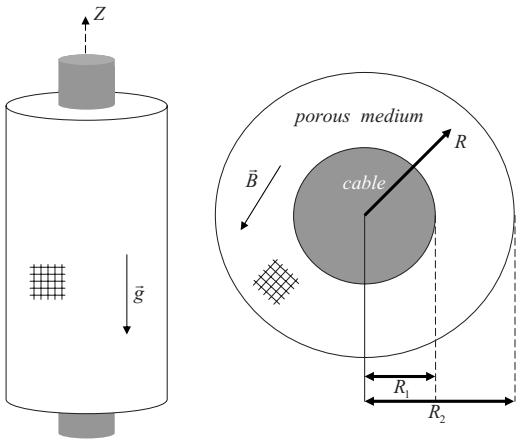

Fig. 1 Drawing of the system

(3) implies that $P=P(Z)$. In analogy with Morton's treatment [13], the reference temperature T_{ref} introduced in the buoyancy term is chosen as the fluid temperature at the heated boundary $R=R_1$, namely,

$$T_{\mathrm{ref}} = T|_{R=R_1} \tag{4}$$

The MHD body force appearing on the right hand side of Eq. (2) is evaluated, as suggested by Nield [1], by considering the intrinsic velocity $\mathbf{U}/\phi$ instead of the seepage velocity $\mathbf{U}$.

The inner boundary of the porous medium $R=R_1$ is subject to a uniform wall heat flux q_w due to the Joule heating inside the electric cable. The outer boundary $R=R_2$ is assumed to be isothermal at temperature T_w. Since the axial length of the annular porous medium is much greater than R_2, then it is reasonable to assume a purely radial heat flow, i.e., a temperature field T depending only on R. Therefore, on account of Eq. (2), one can easily infer that dP/dZ is a constant.

The local energy balance in steady regime for the fluid saturated porous medium can be expressed as

$$\frac{k}{R}\frac{d}{dR}\left(R\frac{dT}{dR}\right) + \frac{\sigma B_0^2}{\phi^2}\frac{R_1^2}{R^2}U^2 + \frac{\eta}{K}U^2 = 0 \tag{5}$$

The second and third terms on the left hand side of Eq. (5) represent the Joule heating and the viscous dissipation contributions, respectively.

The thermal boundary conditions are given by

$$-k\left.\frac{dT}{dR}\right|_{R=R_1} = q_w, \quad T(R_2) = T_w \tag{6}$$

Let us define the dimensionless quantities as follows:

$$r=\frac{R}{R_1}, \quad u=\frac{U}{U_{\mathrm{ref}}}, \quad t=\frac{T-T_{\mathrm{ref}}}{\Delta T}, \quad \gamma=\frac{R_2}{R_1}, \quad \mathrm{Gr}=\frac{\rho^2\beta g\Delta T K R_1}{\eta^2}$$

$$\mathrm{Re}=\frac{\rho U_{\mathrm{ref}}R_1}{\eta}, \quad \Xi=\frac{\mathrm{Gr}}{\mathrm{Re}}=\frac{\rho\beta gK\Delta T}{\eta U_{\mathrm{ref}}}, \quad \mathrm{Br}=\frac{\eta U_{\mathrm{ref}}^2R_1^2}{kK\Delta T} \tag{7}$$

$$M=B_0\sqrt{\frac{\sigma K}{\eta\phi}}$$

where ΔT and U_{ref} are, respectively, the reference temperature difference and the reference velocity is given by

$$\Delta T=\frac{q_wR_1}{k}, \quad U_{\mathrm{ref}}=-\frac{K}{\eta}\frac{dP}{dZ} \tag{8}$$

Equation (7) implies that $1\le r\le\gamma$. On account of Eqs. (7) and (8), the governing Eqs. (2) and (5) can be rewritten as

$$\left(1+\frac{M^2}{r^2}\right)u = \Xi t + 1 \tag{9}$$

$$\frac{1}{r}\frac{d}{dr}\left(r\frac{dt}{dr}\right) + \mathrm{Br}\left(1+\frac{M^2}{\phi r^2}\right)u^2 = 0 \tag{10}$$

The definition of t given in Eq. (7), Eq. (4) and the first thermal boundary condition (6) yield, respectively,

$$t(1)=0, \qquad \left.\frac{dt}{dr}\right|_{r=1} = -1 \tag{11}$$

The definition of the dimensionless temperature t contains the difference $T(R)-T(R_1)$. In fact, the natural input parameter is not the temperature $T(R_1)$ of the isoflux wall, but the temperature T_w of the isothermal wall $R=R_2$. However, after having determined the solution of Eqs. (9)–(11), the value of $T(R_1)=T_{\mathrm{ref}}$ can be easily obtained as $T(R_1)=T_w-t(\gamma)\Delta T$.

The heat transfer from the heated boundary $R=R_1$ to the cooled isothermal boundary $R=R_2$ is described through the Nusselt number defined as

$$\mathrm{Nu}=\frac{q_wR_1}{k[T(R_1)-T_w]}=-\frac{1}{t(\gamma)} \tag{12}$$

Another quantity of technical interest is the ratio between the average velocity in a transverse cross section.

$$U_m=\frac{2}{R_2^2-R_1^2}\int_{R_1}^{R_2}URdR \tag{13}$$

and the reference velocity U_{ref}, namely,

$$u_m=\frac{U_m}{U_{\mathrm{ref}}}=\frac{2}{\gamma^2-1}\int_1^{\gamma}urdr \tag{14}$$

The flow rate parameter u_m allows one to obtain the relation between the average velocity U_m and the vertical pressure gradient dP/dZ, as shown by Eqs. (8) and (14). In fact, one easily obtains the relation

$$U_m=-\frac{u_mK}{\eta}\frac{dP}{dZ} \tag{15}$$

It must be pointed out that the Darcy–Brinkman number (Br) represents an overall factor of the heat generation terms in the dimensionless energy balance (Eq. (10)). Thus, the limit $\mathrm{Br}\to 0$ determines the special case where both the viscous dissipation effect and the Joule heating contribution are negligible.

3 Closed Form Solutions of the Governing Equations

3.1 The Special Case Br→0. In this limiting case, the heat generation and viscous dissipation effects are neglected in the energy balance. As a consequence, the governing equations become linear and their solution is straightforward. If $\mathrm{Br}\to 0$, the solution of Eqs. (10) and (11) is given by

$$t(r)=-\ln(r) \tag{16}$$

so that, on account of Eq. (12), one has

$$\mathrm{Nu}=\frac{1}{\ln(\gamma)} \tag{17}$$

The logarithmic expression of $t(r)$ in Eq. (16) implies that the porous layer has, in this case, a pure conduction temperature field, i.e., the thermal behavior is not influenced by the fluid flow.

By substituting Eq. (16) into Eq. (9), one obtains

$$u(r)=\frac{r^2}{r^2+M^2}[1-\Xi\ln(r)] \tag{18}$$

From Eqs. (18) and (14), one obtains

$$u_m = 1 + \frac{\Xi}{2} - \frac{\Xi\gamma^2 \ln(\gamma)}{\gamma^2 - 1} + \frac{M^2}{\gamma^2 - 1}\left\{\ln\left(\frac{M^2+1}{M^2+\gamma^2}\right) + \Xi \ln(\gamma)\ln\left(\frac{M^2+\gamma^2}{M^2}\right) + \frac{\Xi}{2}\left[\mathrm{Li}_2\left(-\frac{\gamma^2}{M^2}\right) - \mathrm{Li}_2\left(-\frac{1}{M^2}\right)\right]\right\} \tag{19}$$

where $\mathrm{Li}_2(z)$ is Euler's dilogarithm function defined as [14]

$$\mathrm{Li}_2(z) = \sum_{n=1}^{\infty} \frac{z^n}{n^2} \tag{20}$$

Physically, Eqs. (16)–(19) allow one to describe buoyant MHD flow in the annular porous medium with reference to the special case of negligible viscous and Joule heating in the fluid. A special subcase is forced convection flow ($\Xi \to 0$) where

$$u(r) = \frac{r^2}{r^2 + M^2} \tag{21}$$

$$u_m = 1 + \frac{M^2}{\gamma^2 - 1}\ln\left(\frac{M^2+1}{M^2+\gamma^2}\right) \tag{22}$$

Another special subcase is the limit of vanishing pressure gradient $dP/dZ \to 0$. This limit corresponds to a flow driven only by buoyancy force and by MHD body force, and represents the MHD free convection regime. Obviously, when $dP/dZ \to 0$ or equivalently when $\Xi \to \infty$, the velocity scale U_{ref} used to define the dimensionless velocity becomes singular. However, both $u(r)/\Xi$ and u_m/Ξ tend to a finite limit, namely,

$$\lim_{\Xi\to\infty} \frac{u(r)}{\Xi} = -\frac{r^2 \ln(r)}{r^2 + M^2} \tag{23}$$

$$\lim_{\Xi\to\infty} \frac{u_m}{\Xi} = \frac{1}{2} - \frac{\gamma^2 \ln(\gamma)}{\gamma^2 - 1} + \frac{M^2}{\gamma^2 - 1}\left\{\ln(\gamma)\ln\left(\frac{M^2+\gamma^2}{M^2}\right) + \frac{1}{2}\left[\mathrm{Li}_2\left(-\frac{\gamma^2}{M^2}\right) - \mathrm{Li}_2\left(-\frac{1}{M^2}\right)\right]\right\} \tag{24}$$

Finally, a third special subcase is represented by the limit of negligible MHD body force $M \to 0$. In this limit, Eqs. (18) and (19) yield

$$u(r) = 1 - \Xi \ln(r) \tag{25}$$

$$u_m = 1 + \frac{\Xi}{2} - \frac{\Xi\gamma^2 \ln(\gamma)}{\gamma^2 - 1} \tag{26}$$

Equations (25) and (26) describe buoyant Darcy flow without viscous dissipation in an annular porous medium, in the absence of magnetic field effects.

3.2 The Special Case $\Xi \to 0$. In forced convection regime, buoyancy is neglected, so that the Grashof number tends to zero, i.e., $\Xi \to 0$. In this limit, there is no thermal feedback on the velocity distribution due to the absence of buoyancy effect. As a consequence, the presence or the absence of heating effects in the fluid saturated porous medium has no influence on the velocity distribution. Then, $u(r)$ and u_m are still given by Eqs. (21) and (22), whatever is the value of Br. On the other hand, Eqs. (10) and (11) lead to the expression

$$t(r) = -\ln(r) - \frac{\mathrm{Br}}{\phi}\int_1^r \frac{\bar{r}^3(\phi\bar{r}^2 + M^2)}{(\bar{r}^2 + M^2)^2}\ln\left(\frac{r}{\bar{r}}\right)d\bar{r}$$

$$= -\ln(r) + \frac{\mathrm{Br}}{4\phi(M^2+1)}\left\{2[\phi + M^2(2\phi - 1) + 2M^2(M^2+1)(2\phi-1)\ln(M)]\ln(r) - M^2(M^2+1)\ln(M^2+1)[1 - \phi + 2(2\phi-1)\ln(r)] - (M^2+1)[(r^2-1)\phi + M^2(\phi-1)\ln(M^2+r^2)] - M^2(M^2+1)(2\phi-1)\left[\mathrm{Li}_2\left(-\frac{r^2}{M^2}\right) - \mathrm{Li}_2\left(-\frac{1}{M^2}\right)\right]\right\} \tag{27}$$

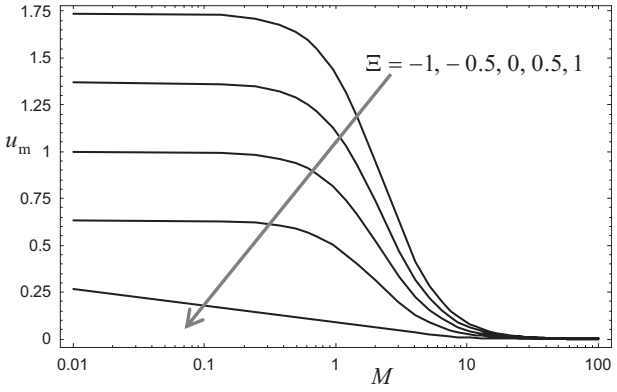

Fig. 2 Special case Br→0: plots of u_m versus M, for γ=3 and increasing values of Ξ

For each value of γ, Eqs. (12) and (27) allow one to obtain the Nusselt number Nu easily.

Equation (27) is drastically simplified when the effect of the magnetic field is negligible, i.e., in the limit $M \to 0$. In fact, one obtains in this case,

$$t(r) = \tfrac{1}{4}[\mathrm{Br}(1 - r^2) + 2(\mathrm{Br} - 2)\ln(r)] \tag{28}$$

4 Discussion of the Results

4.1 The Special Case Br→0. With the choice Eq. (4) of the reference temperature for modeling buoyancy, either in the absence of heat generation in the fluid (Br→0) or in the presence of heat generation, the buoyancy force is directed downward. Then, for Ξ=1, the buoyancy force $\rho\beta g(T - T_{\mathrm{ref}})$ and the hydrodynamic pressure force $-dP/dZ$ act in opposite directions. As a consequence, buoyancy tends to inhibit upflow. The effect of buoyancy vanishes at the inner boundary wall where, in fact, the dimensionless velocity is independent of Ξ. The inhibition of upflow can be so strong to cause a reversed flow, i.e., a flow in the direction of the hydrodynamic pressure gradient. Equation (18) allows one to conclude that u=0 when $\ln r = 1/\Xi$. In the case Ξ=1, one obtains zero velocity when $r = e \cong 2.71828$.

Figure 2 illustrates the dependence of u_m on M for different Ξ. The main feature displayed by this figure is that u_m rapidly decreases with M and, for $M \gtrsim 10$, flow is severely inhibited for all the considered values of Ξ.

4.2 The Special Case $\Xi \to 0$. The limiting case of forced convection corresponds to $\Xi \to 0$. In this special case, the dimensionless velocity field, given by Eq. (21), is not influenced by the temperature field, so that it does not depend either on Br or on ϕ. On the other hand, the temperature field, as well as the Nusselt number, depends on the Brinkman number and on porosity.

Figure 3 displays the dimensionless temperature distributions $t(r)$ for M=2. This figure refers to ϕ=0.5 and γ=3 and shows that the slope of $t(r)$ is fixed for r=1. In fact, this feature is a consequence of the definition of t and is formulated in Eq. (11).

5 Conclusions

Convective flow in a fluid saturated annular porous medium surrounding a vertical electric cable has been analyzed. Under the assumptions of laminar parallel Darcy flow, the balance equations have been written in a dimensionless form. It has been shown that

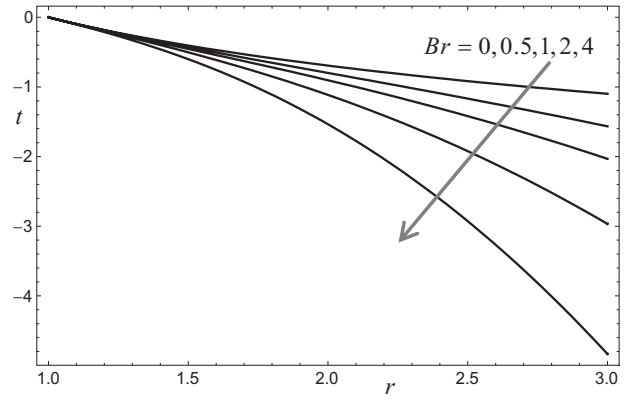

Fig. 3 Special case $\Xi \to 0$: plots of $t(r)$ for $\gamma=3$, $\phi=0.5$, and $M=2$

the governing parameters are the radial aspect ratio γ, porosity ϕ, Hartmann number M, Brinkman number Br, and the ratio $\Xi = \mathrm{Gr}/\mathrm{Re}$ between the Grashof number and the Reynolds number. Closed form solutions of the balance equations have been found in two limiting cases. The case $\mathrm{Br} \to 0$, that corresponds to negligible effects of internal heating due to Joule effect and viscous dissipation. The case $\Xi \to 0$, that corresponds to forced convection. In the first case, the absence of internal heat generation implies that the temperature profile is logarithmic exactly as in the case of pure heat conduction. On the other hand, in the second case (forced convection), Joule heating and viscous dissipation inside the fluid imply that the dimensionless temperature and the Nusselt number depend on the porosity, the Hartmann number, and the Brinkman number.

Nomenclature

$\mathbf{B}$ = magnetic field
B_0 = constant magnetic field, Eq. (1)
Br = Brinkman number, Eq. (7)
$\hat{\mathbf{e}}_\theta$, $\hat{\mathbf{e}}_Z$ = angular and axial unit vectors
g = acceleration due to the gravity
Gr = Grashof number, Eq. (7)
I = electric current
k = thermal conductivity of the fluid
K = permeability
Li_2 = Euler's dilogarithm function
M = Hartmann number, Eq. (7)
Nu = Nusselt number, Eq. (12)
p = pressure
P = hydrodynamic pressure, $p+\rho gZ$
q_w = wall heat flux at the internal boundary
r = dimensionless radial coordinate, Eq. (7)
R, θ, Z = radial, angular, and axial coordinates
R_1, R_2 = internal radius and external radius
Re = Reynolds number, Eq. (7)
t = dimensionless temperature
T = temperature
T_{ref} = reference temperature, Eq. (4)
T_w = temperature at the external boundary
u = dimensionless velocity
u_m = dimensionless average velocity in a transverse cross section, Eq. (14)
$\mathbf{U}$ = velocity
U = axial velocity component
U_m = average velocity in a transverse cross section, Eq. (13)
U_{ref} = reference velocity, Eq. (8)

Greek Symbols

β = volumetric coefficient of thermal expansion
γ = radial aspect ratio, Eq. (7)
ΔT = reference temperature difference, Eq. (8)
η = dynamic viscosity
μ_0 = magnetic permeability of vacuum
Ξ = dimensionless parameter, Eq. (7)
ρ = mass density
σ = electric conductivity of the fluid
ϕ = porosity

References

[1] Nield, D. A., 1999, "Modeling the Effects of a Magnetic Field or Rotation on Flow in a Porous Medium: Momentum Equation and Anisotropic Permeability Analogy," Int. J. Heat Mass Transfer, **42**, pp. 3715–3718.
[2] Al–Nimr, M. A., and Hader, M. A., 1999, "MHD Free Convection Flow in Open–Ended Vertical Porous Channels," Chem. Eng. Sci., **54**, pp. 1883–1889.
[3] Chamkha, A. J., 2001, "Unsteady Laminar Hydromagnetic Flow and Heat Transfer In Porous Channels With Temperature–Dependent Properties," Int. J. Numer. Methods Heat Fluid Flow, **11**, pp. 430–448.
[4] Geindreau, C., and Auriault, J.-L., 2002, "Magnetohydrodynamic Flows in Porous Media," J. Fluid Mech., **466**, pp. 343–363.
[5] Mahmud, S., and Fraser, R. A., 2004, "Magnetohydrodynamic Free Convection and Entropy Generation in a Square Porous Cavity," Int. J. Heat Mass Transfer, **47**, pp. 3245–3256.
[6] Postelnicu, A., 2004, "Influence of a Magnetic Field on Heat and Mass Transfer by Natural Convection From Vertical Surfaces in Porous Media Considering Soret and Dufour Effects," Int. J. Heat Mass Transfer, **47**, pp. 1467–1472.
[7] Partha, M. K., Murthy, P. V. S. N., and Raja Sekhar, G. P., 2006, "Soret and Dufour Effects in a Non-Darcy Porous Medium," ASME J. Heat Transfer, **128**, pp. 605–610.
[8] Rakoto Ramambason, D. S., and Vasseur, P., 2007, "Influence of a Magnetic Field On Natural Convection in a Shallow Porous Enclosure Saturated With A Binary Fluid," Acta Mech., **191**, pp. 21–35.
[9] Bhadauria, B. S., 2007, "Magnetofluidconvection in a Rotating Porous Layer Under Modulated Temperature on the Boundaries," ASME J. Heat Transfer, **129**, pp. 835–843.
[10] Bhadauria, B. S., 2008, "Combined Effect of Temperature Modulation and Magnetic Field on the Onset of Convection in an Electrically Conducting-Fluid-Saturated Porous Medium," ASME J. Heat Transfer, **130**, p. 052601.
[11] Makinde, O. D., and Sibanda, P., 2008, "Magnetohydrodynamic Mixed-Convective Flow and Heat and Mass Transfer Past a Vertical Plate in a Porous Medium With Constant Wall Suction," ASME J. Heat Transfer, **130**, p. 112602.
[12] Nield, D. A., and Bejan, A., 2006, *Convection in Porous Media*, 3rd ed., Springer, New York.
[13] Morton, B. R., 1960, "Laminar Convection in Uniformly Heated Vertical Pipes," J. Fluid Mech., **8**, pp. 227–240.
[14] Erdélyi, A., Magnus, W., Oberhettinger, F., and Tricomi, F. G., 1953, *Higher Transcendental Functions*, Vol. 1, McGraw-Hill, New York, p. 31.

Autonomous Thermal Control System for Highly Variable Environments

G. A. Richardson
Department of Mechanical and Aerospace Engineering,
University of Alabama in Huntsville,
Huntsville, AL 35899
e-mail: georgia.richardson@uah.edu

An autonomous thermal control system has been developed for instruments with steady temperature requirements that are exposed to widely varying environmental conditions. The active thermal control system uses thermo-electric (Peltier) coolers with a programmable power supply, digital temperature sensors, and on-board proportional differential logic to track and predict temperature variations. This system is designed for instruments with large thermal mass and thermally sensitive electronic components that would be effected by variabilities in the local outdoor environment including weather, sunrise, and sunset. Presented are the test results of the design showing the temperature stayed within ±0.125°C during smooth ambient temperature changes (27°C ambient change over 80 min), remained within +0.375/−0.6875°C under a sharp ambient temperature drop (27°C sudden drop), and remained within +0.25/−0.875°C when random variabilities in the ambient were introduced (2–10°C degree variabilities over the time frame of minutes). For the thermal control system and test results presented, it is shown that several calibration and design points must be considered for a large thermal mass system in order to achieve steady thermal control. The system presented is capable of maintaining steady thermal control within the given constraints. [DOI: 10.1115/1.3085826]

Keywords: thermo-electric cooling, thermal control, conduction, thermal management

1 Introduction

Passive thermal control is not adequate for scientific instruments with temperature limitations and constraints. Instead, cooling requirements are determined in real-time, and active thermal control is used to force heat transfer as needed. This study presents an autonomous thermal control system for high mass instruments with steady temperature requirements that are exposed to varying thermal environments.

Similar systems have been developed for low mass applications, specifically for microscale systems driven by the need for thermal control in computer microprocessors [1–4]. Our study of the thermal control of high mass systems utilizes thermo-electric coolers (TECs). Some fundamental limitations exist with these devices [5]. A further overview of current approaches and the need for customized techniques are given in Ref. [6].

Presented in this article is an overview of the system design and components including the proportional differential controller logic. Test results are given showing the system response for three environmental conditions: slowly changing ambient temperature (afternoon heating), sharp ambient temperature drop (sunset), and a varying ambient environment (shading and/or convective cooling due to weather or variabilities in power from electronic components).

Contributed by the Heat Transfer Division of ASME for publication in the JOURNAL OF HEAT TRANSFER. Manuscript received March 12, 2008; final manuscript received November 13, 2008; published online April 13, 2009. Review conducted by Cholik Chan.

2 System Description

Instrument configuration. The basic concept for the design is to actively cool a conductive plate to which the thermally sensitive components are mounted. The conductive plate is inside an insulated box, as shown in Fig. 1. A cut-through in the outer box allows TECs to be in contact with both the cooled plate and heat sinks. The heat sinks are external and blowers are used to remove the heat [7]. Four primary electronic components make up the thermal control system: one-wire 12 bit digital temperature sensors (DS18B20) [8], thermo-electric coolers (Melcor CP2-127-10L), a programmable switching power supply (Instek PSH-6012) [9], and microcontroller (ST10F269).

The system uses digital temperature sensors to monitor the components needing the most stable thermal control, and TECs to control heat flow out of the box. Temperature is measured over time, and predictions of the future temperature trends are made. Since each temperature sensor has a unique address, multiple temperature sensors can be included, allowing thermal gradients to be monitored. Communication between the microcontroller and DS18B20 initiates the measurement process through a series of handshake commands. Changes in the TEC voltage are applied based on the projected temperature, resulting in a change in the cooling power. The system is capable of different response times depending on the thermal mass. For a relatively large thermal mass such as the system described (cooled aluminum plate with a volume of $0.305 \times 0.203 \times 0.00635$ m^3), a longer response time is necessary. For testing purposes, heating resistors were used to simulate the thermally sensitive electronic components. Proper calibration should allow for a variety of systems [10].

Solid state TECs work based on the Peltier effect and are a type of heat engine. The Peltier effect works by applying a voltage potential across specific materials (as in the Seebeck effect for thermocouples) to cause a temperature differential. Since TECs come in a variety of sizes and power options, they are useful in customized systems. They are not as efficient as other heat engines, but their solid state design is ideal for small systems and outdoor environments. The TEC used in this project is capable of stabilizing a 20 W heat output while maintaining a 21.75°C temperature differential with the ambient, as shown in Table 1.

The 60 V/12 A programmable power supply has a resolution of 10 mV and a response time of less than 150 ms. The microprocessor receives the temperature measurements, calculates the necessary voltage change, and directs that change to the power supply that powers the TECs.

A pressure plate with springs was used to clamp the cooled plate, TECs, and heat sink to ensure good thermal contact. The springs allowed for maximum pressure without cracking the ceramic surfaces of the TECs. Materials with high thermal conductivity were used including an aluminum plate and copper heat sinks. Thermal grease helps to maximize the thermal contact.

Microprocessor logic. Proportional differential logic utilizing temperature readings determines trends and calculates corrective action. Initially a desired temperature must be determined. Based on continuous readings from the temperature sensors the processor determines if a change in cooling power is required. In order to reduce instrumentation errors, a number of readings are taken and then averaged. For the test system, ten readings are taken over 1 min and averaged. A pause is introduced (depending on the system response time, 30 s in this test case) before ten more readings are taken and averaged. A linear fit is done between the points to predict the future temperature and to determine if changes in the cooling power need to be made. The system is calibrated to determine the power response of the TECs. Once the amount of cooling increase or decrease is determined, the microprocessor sends that information to the power supply and changes are made. The system pauses to ensure the voltage changes take effect and the process repeats. A stop system is in place to prevent system overload in extreme cases (sensor failure or instrument malfunction).

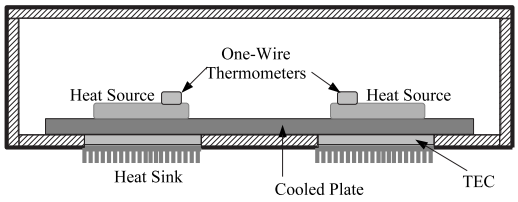

Fig. 1 System configuration: An aluminum plate is actively cooled using TECs. Thermally sensitive components are mounted directly to the cooled plate (0.305×0.203 ×0.00635 m^3) and temperature sensors are attached to the components.

Calibration and design considerations. There are several calibration points for this system. Depending on the thermal mass of the instrument, the thermal response time will vary. Also, the size of TEC that is used will determine the amount of heat being removed. The larger the cooling power of the TEC, the faster the thermal response, but power used to run the TEC must be accounted for. Too much power into a TEC can result in adverse effects. Finally, each TEC should be tested to determine the maximum temperature gradient between the plate and ambient, as shown in Table 1. The target temperature should fall within that gradient. Additional points to consider are the response times for the microprocessor, temperature sensors, and power supply.

3 System Testing

To simulate the heat load of the thermally sensitive electronics, 20 W of heat was generated inside the insulated test box and three thermal tests were performed with two TECs actively cooling the internal plate. *Test 1:* The box was installed in an environmental chamber and the ambient temperature was slowly increased from 23°C to 50°C (~2 h). *Test 2:* The ambient temperature was then rapidly reduced by opening the door of the chamber (Fig. 2). In Test 1, there is an initial time (~10 min) for the system to stabilize. During the time of temperature increase, the TECs regulated the internal temperature of the box within ±0.125°C. When the ambient temperature was suddenly dropped by 27°C in Test 2, the plate temperature varied by at most +0.375/−0.6875°C. *Test 3:* The ambient temperature was rapidly increased and decreased (from a minimum of 22°C to a maximum of 35°C) several times over a 40 min time period (Fig. 3). After an initial stabilization period similar to the first test, the regulated temperature stayed within +0.25°C and −0.875°C. The systematic uncertainties for these tests come from the temperature sensors. The DS18B20 has a resolution of 0.0.0625°C and an accuracy of 0.5°C [8]. The voltage accuracy for the power supply is given as 0.2% [9].

Table 1 Maximum temperature differential for a single TEC (CP2-127-10L-1.9) in contact with the aluminum plate. The temperature difference was measured after steady state conditions were reached. The temperature sensor was attached directly to the heat source.

Heat removed (W)	Max temperature difference[a] (°C)
0	31.56
5	29.38
10	26.56
15	23.75
20	21.75

[a]Box interior to ambient.

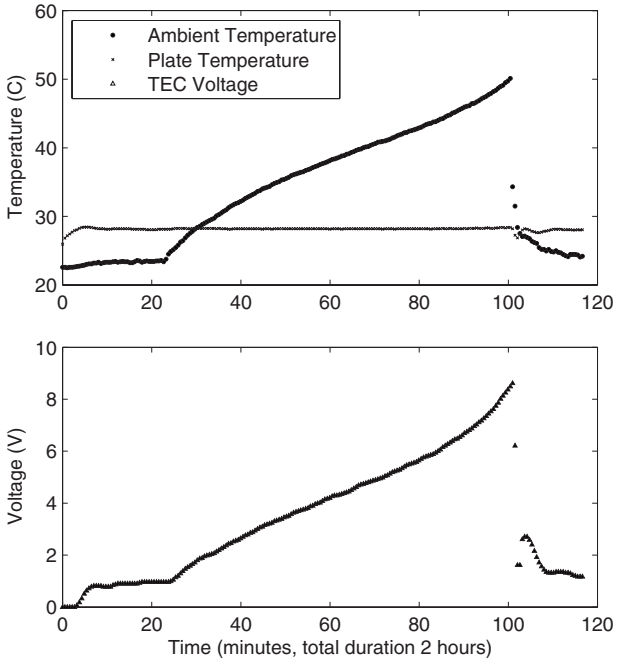

Fig. 2 Thermal test with 27°C sudden ambient temperature drop after a gradual increase. The maximum temperature change in the measurement is +0.375/−0.6875 deg.

4 Conclusions

For a system with a large thermal mass there are several calibration and design points, as shown in Sec. 2. Once calibrated properly this system maintained steady temperature control for three environmental simulations: (1) a slow environmental temperature increase (afternoon heating), (2) a sudden drop in environmental temperature (sunset), and (3) highly variable thermal changes (sudden weather changes or variabilities in an electronic

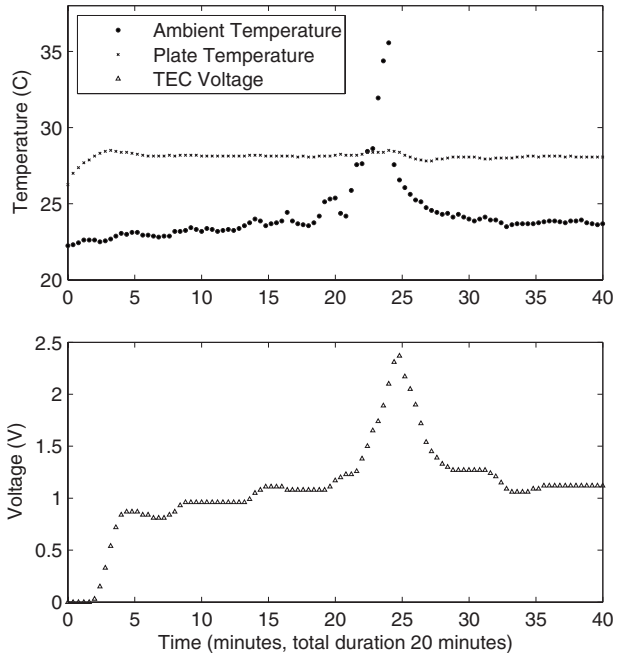

Fig. 3 Thermal test with a variable ambient temperature and 12°C sudden ambient temperature rise. The maximum temperature change in the control plate is +0.25/−0.875 deg.

component). The control system was fast to respond, and the temperature fluctuations remained within approximately 1 deg for each case. This basic design could be modified and configured for a wide variety of applications considering the availability of TEC options.

Acknowledgment

The early stages of this work were supported in part by the National Research Council Fellowship Program and the Chandra X-Ray Astronomy Group at the National Space Science and Technology Center.

References

[1] Li, D., Huxtable, S. T., Abramson, A. R., and Majumdar, A., 2005, "Thermal Transport in Nanostructured Solid-State Cooling Devices," ASME J. Heat Transfer, **127**, pp. 108–114.
[2] Dziurdzia, P., and Kos, A., 2000, "High Efficiency Active Cooling System," Semiconductor Thermal Measurement and Management Symposium, 16th Annual IEEE SEMI-THERM Symposium, pp. 19–26.
[3] Wan, J. W., Zhang, W. J., Torvi, D., and Wu, F. X., 2004, "An Analysis to Two-Heater Active Thermal Control Technology for Device Class Testing," IEEE Trans. Compon. Packag. Technol., **27**(3), pp. 577–584.
[4] McCarty, R., Hallinan, K. P., Sanders, B., and Somphone, T., 2007, "Enhancing Thermoelectic Energy Recovery via Modulations of Source Temperature for Cyclical Heat Loading," ASME J. Heat Transfer, **129**(6), pp. 749–755.
[5] Simons, R. E., Ellsworth, M. J., and Chu, R. C., 2005, "An Assessment of Module Cooling Enhancement With Thermoelectric Coolers," ASME J. Heat Transfer, **127**(1), pp. 76–84.
[6] Riffat, S. B., and Ma, X., 2003, "Thermoelectrics: A Review of Present and Potential Applications," Appl. Therm. Eng., **23**, pp. 913–935.
[7] Chein, R., and Huang, G., 2004, "Thermoelectric Cooler Application in Electronic Cooling," Appl. Therm. Eng., **24**, pp. 2207–2217.
[8] DS18B20 Datasheet, http://www.maxim-ic.com.cn/pdfserv/en/ds/DS18B20.pdf.
[9] PSH-6012 Datasheet, http://www.instek.com/PSH-H.htm.
[10] Huang, B. J., Chun, C. J., and Duang, C. L., 2000, "A Design Method of Thermoelectric Cooler," Int. J. Refrig., **23**, pp. 208–218.